

AD-774 967

NEW METHODS FOR GROWTH AND CHARACTERIZATION OF
GaAs AND MIXED III-V SEMICONDUCTOR CRYSTALS

UNIVERSITY OF SOUTHERN CALIFORNIA

30 JUNE 1973

DISTRIBUTED BY:

NTIS

National Technical Information Service
U. S. DEPARTMENT OF COMMERCE

Final Technical Report

1 July 1970 - 30 June 1973

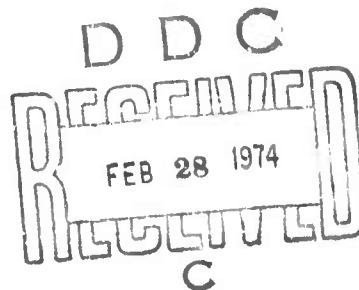
NEW METHODS FOR GROWTH AND CHARACTERIZATION OF GaAs
AND MIXED III-V SEMICONDUCTOR CRYSTALS

University of Southern California
Los Angeles, California 90007

Submitted to

ADVANCED RESEARCH PROJECTS AGENCY

ARPA Order Number 1628
Grants: DAHC 15-70-G14
DAHC 15-71-G6
DAHC 15-72-G7



Principal Investigator: William R. Wilcox (213) 746-6203

Investigators:	Worth P. Allred*	
	Clarence R. Crowell	746-6217
	Agerico Esquivel*	
	Murray Gershenzon	746-6215
	Eric Johnson*	
	Pat Leung*	
	Harry Stover*	
	Rong Wang*	
	James B. Whelan	746-6219
	David B. Wittry	746-2510

*No longer full time at USC.

The views and conclusions contained in this document are those of the authors and should not be interpreted as necessarily representing the official policies, either expressed or implied, of the Advanced Research Projects Agency or the U.S. Government.

UNCLASSIFIED

Security Classification

DOCUMENT CONTROL DATA - R & D

(Security classification of title, body of abstract and indexing annotation must be entered when the overall report is classified)

1. ORIGINATING ACTIVITY (Corporate author) Electronic Sciences Laboratory University of Southern California Los Angeles, California 90007		2a. REPORT SECURITY CLASSIFICATION UNCLASSIFIED	
		2b. GROUP	
3. REPORT TITLE NEW METHODS FOR GROWTH AND CHARACTERIZATION OF GaAs AND MIXED III-V SEMICONDUCTOR CRYSTALS			
4. DESCRIPTIVE NOTES (Type of report and inclusive dates) FINAL TECHNICAL REPORT			
5. AUTHOR(S) (First name, middle initial, last name) WILLIAM R. WILCOX			
6. REPORT DATE 1 July 1970 - 30 June 1973		7a. TOTAL NO. OF PAGES 343 344	7b. NO. OF REFS 122
8a. CONTRACT OR GRANT NO. DAHC 15-70-G14, 15-71-G6 and 15-72-G7.		9a. ORIGINATOR'S REPORT NUMBER(S) USCEE Report 460	
b. PROJECT NO.		9b. OTHER REPORT NO(S) (Any other numbers that may be assigned this report)	
c. ARPA Order No. 1628			
d.			
10. DISTRIBUTION STATEMENT Approved for public release; distribution unlimited.			
11. SUPPLEMENTARY NOTES		12. SPONSORING MILITARY ACTIVITY The Advanced Research Projects Agency	
13. ABSTRACT The purpose of this program was to develop new and improved methods for the growth and characterization of gallium arsenide (GaAs) and mixed III-V semiconductor crystals. This was accomplished by laboratory experiments and related theoretical research. New Czochralski, floating zone melting, gradient freeze, and liquid epitaxy techniques for GaAs growth were developed and studied. The travelling heater method for GaAs and III-V alloys was studied. Material was characterized by spark-source mass spectrometry, ion microprobe mass analyzer, glow-discharge spectroscopy, infrared absorption, dislocation etching, X-ray topography, cathodoluminescence, photoluminescence, Hall measurements, photothreshold, and C-V-W measurements on Schottky barriers. Dislocations generated by bending were observed by cathodoluminescence and the effect on electrical properties determined. A new technique for measuring and controlling oxygen in gallium melts was developed and studied.			

Reproduced by
NATIONAL TECHNICAL
INFORMATION SERVICE
U S Department of Commerce
Springfield VA 22151

DD FORM 1 NOV 65 1473

UNCLASSIFIED

Security Classification

UNCLASSIFIED

Security Classification

14. KEY WORDS	LINK A		LINK B		LINK C	
	ROLE	WT	ROLE	WT	ROLE	WT
Gallium arsenide, Czochralski, crystal growth, liquid epitaxial growth, travelling heater method, glow-discharge spectroscopy, cathodoluminescence, infrared absorption, C-V measurements, Schottky barriers, dislocations.						

UNCLASSIFIED

Security Classification

TABLE OF CONTENTS

	<u>Page</u>
List of Figures	vi
List of Tables	xi
Abstract	xiii
I. INTRODUCTION	1
II. BULK CRYSTAL GROWTH	3
A. Liquid-Seal Czochralski Technique for GaAs	3
1. Introduction	3
2. New Czochralski Technique	4
3. Discussion	17
B. Liquid Encapsulated Floating Zone Melting of GaAs	18
1. Introduction	18
2. Procedures for Encapsulated Float Zoning of GaAs	19
3. Float Zoning Problems Associated with Large Diameter Ingots	27
4. Summary of Experiments: Successes and Failures	30
5. Characterization of Encapsulated Float Zoned GaAs	30
6. Conclusions and Future Potential for the Technique	42
C. Vitreous Boron Oxide: Drying and Moisture Absorption	43
D. Horizontal Bridgman Growth	43
E. Vertical Gradient-Freeze Crystal Growth of GaAs	44
F. Travelling Heater Method Solution Growth	50
1. THM GaAs	50
2. THM Alloys	58
G. Crystal Growth of Gallium Nitride	58
III. LIQUID EPITAXIAL GROWTH OF III-V SEMICONDUCTORS	66
A. Dipping Technique	66
B. GaAs Junction Field Effect Transistor (JFET)	66
C. Measurement and Control of Oxygen Using Stabilized Zirconia Electro_yte	67
1. Zirconia Electrolyte	68
2. Liquid Epitaxial Growth with Oxygen Pumping	74
3. Related Projects	75
IV. STUDIES OF CRYSTAL GROWTH PHENOMENA	75
A. Transport Processes in Unidirectional Crystal Growth	75
1. Control of Interface Shape in the Bridgman- Stockbarger Technique	76
2. Control of Interface Shape in the Vertical Gradient-Freeze Technique	76

TABLE OF CONTENTS (Continued)

	<u>Page</u>
3. Heat Transfer in Vertical Zone Melting	77
4. Transport Processes in the Travelling Heater Method	77
5. Localized Interface Breakdown in Zone Melting and the Travelling Heater Method	78
B. Constitutional Supercooling in Multicomponent Systems	78
C. Foreign Particles and Gas Bubbles in Solidification	79
D. Influence of Pressure on Evaporation Rates	80
E. Movement of Solvent Inclusions in Centrifugal and Thermal Fields	80
F. Miscellaneous Crystallization Studies	80
V. CRYSTAL PROCESSING	81
A. Crystal Orientation by Cleavage Plane Reflected Laser Beam	81
B. Chemical-Mechanical Lapping and Polishing of GaAs	81
1. Substrate Thinning	83
2. Types of Chemical-Mechanical Polishes used for Gallium Arsenide	85
C. Contacts	87
VI. CHARACTERIZATION	89
A. Ion Microprobe Mass Analyses (IMMA)	89
B. Carbon in GaAs	92
C. Si Local Modes in GaAs	94
D. Oxygen in GaAs	97
E. Glow Discharge Spectroscopy for the Analysis of Thin Films	98
F. Dislocation Studies and Electrical Properties	101
1. Characterization of As-Grown GaAs by Etching and Optical Microscopy	101
2. Study of GaAs Crystals by X-Ray Topography	107
3. Plastic Deformation by Four-Point Bending at Elevated Temperatures	109
4. Cathodoluminescence Study of Deformed Regions in n-Type GaAs	117
5. Anisotropy of Electrical Properties from α and β Dislocations in Plastically Deformed GaAs	138
G. Electron Beam Characterization	154
1. Studies of Stimulated Emission from GaAs with Continuous Electron Beam Excitation	154
2. Infrared Modulation of Cathodoluminescence	156
3. Cathodoluminescence of the GaAs, GaP and GaAs _{1-x} P _x	162

TABLE OF CONTENTS (Continued)

	<u>Page</u>
H. Photoluminescence Measurements	166
1. Bulk GaAs	166
2. Films	167
I. Characterization of Epitaxial and Bulk GaAs by Capacitance-Voltage Profiling	167
J. Electrical Characterization of Bulk Interfaces in GaAs	176
1. Program Orientation	176
2. Hall and Resistivity Measurements	176
3. Capacitance/Conductance Analysis	183
VII. CONCLUSIONS, DISCUSSION AND RECOMMENDATIONS ON GALLIUM ARSENIDE GROWTH AND CHARACTERIZATION	219
REFERENCES	228
APPENDICES	235

LIST OF FIGURES

	<u>Page</u>
1. Diagram of the liquid-seal Czochralski GaAs grower	5
2. Photograph of a GaAs crystal grown by the liquid-seal Czochralski method	7
3. Diagram of apparatus for liquid encapsulated floating zone melting	21
4. Photograph of the liquid-encapsulated floating zone melting apparatus for growth of high purity GaAs and mixed III-V crystals	22
5. FZ-8 after six floating zone passes	34
6. FZ-8 sandblasted to show grain structure	34
7. Sectioned FZ-8	35
8. FZ-9 after ten floating zone passes	35
9. FZ-12 showing two regions, one at each end, in which a stable zone was moved for a short distance through a ~13 mm diameter GaAs rod	36
10. Diagram of the horizontal Bridgman apparatus	45
11. Diagram of initial loading of the growth ampoule	46
12. Diagram of system for measuring and controlling oxygen concentrations	70
13. Variation of oxygen fugacity at zirconia-Ga interface relative to reference oxygen fugacity	73
14. Wafers mounted on glass disc	82
15. Wafers being hand-lapped on flat glass plate	82
16. Chemical polisher	84
17. New lapping fixture	84
18. Lapping machine	85
19. IMMA of CZ23, with beam burning-in on one spot at a time, producing roughly parabolic pits	91
20. Infrared absorption at liquid nitrogen temperature of sample from Czochralski-grown crystal CZ-37	93
21. Absorption coefficient vs. frequency for three GaAs samples at liquid nitrogen temperature	96
22. Changes in $(P_{O_2}/P_{O_2Ref.})^{1/2}$ associated with additions of oxygen to the Ga solution	99
23. Changes in $(P_{O_2}/P_{O_2Ref.})^{1/2}$ upon dissolving GaAs samples	100
24. Dislocation etch pits resulting from use of Schell's reagent on A(111) surface of single crystal GaAs	104

LIST OF FIGURES (Continued)

	<u>Page</u>
25. Dislocation etch pits resulting from use of Schell's reagent + 0.5% butylamine	105
26. Dislocation etch pits resulting from use of Schell's reagent + 0.5% AgNO ₃	106
27. Lang ($\bar{2}20$) symmetric transmission topographs of (111) wafers of as-grown, Te-doped (10^{17} cm ⁻³) GaAs	110
28. Lang ($\bar{2}20$) transmission topographs of (111) wafers taken from back end of as-grown, Te-doped (10^{17} cm ⁻³) GaAs	111
29. ($\bar{2}4\bar{2}$) transmission Lang topograph of a (111) wafer cut from a horizontal Bridgman-grown GaAs crystal	112
30. ($\bar{2}42$) topograph of the crystal in Figure 29	113
31. Orientation of GaAs bend sample showing [$\bar{1}\bar{1}2$] bend axis and (111) slip plane	114
32. All-quartz four-point bend apparatus and furnace	116
33. Determination of dislocation densities on the (112) face of bent GaAs samples (CZ-16 and HB-105) using the nondestructive infrared cathodoluminescence (IR-CL) method	118
34. IR-CL micrographs of undoped GaAs and CL intensity line scan across sample	121
35. Cathodoluminescence infrared (IR-CL) micrographs of Te-doped GaAs and cathodoluminescence (CL) intensity line scan across sample	122
36. IR-CL micrographs and secondary electron emission micrographs of the tensile and compressive areas in a bent, undoped GaAs sample	124
37. Secondary electron emission-micrographs and IR-CL micrographs of bent area in undoped GaAs sample	125
38. Secondary electron emission (SEE) micrographs, infrared cathodoluminescence (IR-CL) micrographs and IR-CL intensity, I _C , line scans versus distance, d, in microns for the undoped, bent GaAs samples	126
39. SEE micrographs, IR-CL micrographs and IR-CL intensity line scans for the doped bent GaAs samples	128
40. Relative infrared cathodoluminescence (IR-CL) intensities taken from the center and tips of the as-grown, heated and bent GaAs samples (HB-105)	130
41. Relative IR-CL intensities for the as-grown, heated and bent (CZ-16) GaAs samples with different types and densities of dislocations	132

LIST OF FIGURES (Continued)

	<u>Page</u>
42. Relative IR-CL intensity as a function of position in a bent (HB-105) GaAs sample with a dislocation density, $\rho = 1.7 \times 10^{17} \text{ cm}^{-2}$	133
43. Relative IR-CL intensity as a function of position in a bent (CZ-16) GaAs sample with a dislocation density, $\rho = 1.5 \times 10^7 \text{ cm}^{-2}$	134
44. Hall coefficient vs. reciprocal temperature for Te-doped Czoehrsalski (CZ-16) and undoped horizontal Bridgman (HB-105) samples of as-grown, heated, and bent GaAs	135
45. Carrier concentration vs. reciprocal temperature for as-grown, heated, and bent horizontal Bridgman (HB-105) and Czoehrsalski (CZ-16) GaAs	140
46. Conductivity vs. reciprocal temperature for as-grown, heated, and bent horizontal Bridgman (HB-105) and Czoehrsalski (CZ-16) GaAs	141
47. Mobility vs. temperature for as-grown, heated, and bent horizontal Bridgman (HB-105) and Czoehrsalski (CZ-16) GaAs	142
48. Schematic diagram of the orientation of Te-doped GaAs (CZ-16) samples relative to the $[\bar{1}\bar{1}2]$ bend axis to introduce an excess of α -type dislocation and an excess of β -dislocations	146
49. Carrier concentration vs. reciprocal absolute temperature for the as-grown, heated and bent samples which were measured parallel or perpendicular to the bend axis (CZ-16)	147
50. Hall mobility vs. reciprocal absolute temperature for the as-grown, heated and bent samples (CZ-16)	148
51. Conductivity vs. reciprocal absolute temperature for the as-grown, heated and bent samples	149
52. Infrared image and scan profile on SE-3 Cr-doped GaAs sample using 40 kV electron beam	159
53. Infrared image and scan profile on CZ-43 Cr-doped GaAs sample using 40 kV electron beam	160
54. Infrared image and scan profile on GF-30 undoped GaAs sample using 40 kV electron beam	161
55. Composition dependence of the cathodoluminescence spectrum peak of $\text{GaAs}_{1-x}\text{P}_x$ crystals	163
56. Temperature dependence of the cathodoluminescence spectrum peak of $\text{GaAs}_{1-x}\text{P}_x$ crystals	164
57. Photoluminescence of GaN crystals annealed in Ga solution	168
58. Photoluminescence of GaN crystals grown over Ga boat	169
59. Carrier vs. depth profile of bulk GaAs (CZ-35) from capacitance-voltage measurements	172

LIST OF FIGURES (Continued)

	<u>Page</u>
60. Carrier profile from opposite end of CZ-35 from sample of Figure 59	173
61. Carrier profiles at various points of a slice from CZ-35	173
62. Impurity profile of a GaAs layer prepared by liquid epitaxial growth at USC, as determined by C-V measurements	174
63. Impurity profile of hyper-thin chemically vapor deposited epitaxial film of GaAs from the Monsanto Company as determined by C-V measurements	175
64. Correction factors for finite contact effect on resistivity measurement shown as a function of δ/λ	178
65. Correction factors for finite contact effect on Hall coefficient measurement as a function of δ/λ	179
66. Current source	180
67. Electrometer	181
68. Switching network for high impedance leads	182
69. Hall-effect carrier concentration vs. reciprocal temperature for high resistivity GaAs grown by the horizontal Bridgman method without intentional doping	184
70. Block diagram of the variable-frequency automatic capacitance/conductance measurement system as connected for the experimental studies on ring-guarded diodes	190
71. Connection of the analog computer unit for $\log_{10} (N(x))$ versus x output format	196
72. Bridged-T preamplifier for frequency-independent measurement of capacitance	200
73. Gain of the bridged-T preamplifier as a function of frequency when a capacitor equal to C_f is used as an input element	203
74. Phase shift between e_o and e_i for the bridged-T preamplifier when a capacitor is used as an input element	204
75. Expanded plot of the phase shift between e_o and e_i for the bridged-T amplifier when a capacitor is used as an input element	205
76. Detailed schematic of the bridged-T preamplifier unit.	207
77. Detailed schematic of the DC bias sweep supply	209
78. Detailed schematic of the signal source unit output section	214
79.	217
80. Capacitance-voltage measurements for Si Schottky diode at 10 kHz.	218
81.	220

LIST OF FIGURES (Continued)

	<u>Page</u>
82. Comparisons of step etched GaAs doping profile as determined by RRE impurity plotter and present system	221
83. Quantum-mechanical electron transmission coefficients for a Au-n-type GaAs Schottky barrier with electric field as a parameter	222
84. Corrections to the apparent photothreshold for a Au-n-type GaAs Schottky barrier with temperature and electric field as parameters	223
85. Corrections to the apparent photothreshold for a Au-n-type GaAs Schottky barrier with temperature and electric field as parameters	224
86. Comparison of exact corrections to the apparent threshold for a Au-n-type GaAs Schottky barrier with corrections synthesized by adding the corrections for tunneling at 0°K to the pure thermal correction	225

LIST OF TABLES

	<u>Page</u>
I. GaAs grown by the liquid seal Czochralski technique from June 1971 - June 1973	8
II. Mass spectrographic analyses of Czochralski-grown crystals	16
III. Summary of liquid encapsulated floating zone experiments	31
IV. Hall effect data for experiments FZ-3, FZ-8 and FZ-9	38
V. Mass spectrometric analyses of floating zone feed rods, zoned rods, and B ₂ O ₃ encapsulant	39
VI. Typical GaAs ingots grown by vertical gradient freeze method	47
VII. Hall measurement results for gradient freeze GaAs crystals grown from different starting materials	48
VIII. Spectrochemical analyses of gradient freeze GaAs	48
IX. Mass spectrometric analyses of GaAs grown by gradient freeze, horizontal Bridgman and liquid-seal Czochralski techniques	49
X. Summary of early travelling heater experiments on GaAs (July 1970-June 1971)	51
XI. Details of THM runs with different initial Ga zone lengths	53
XII. Summary of THM growth runs at different heater temperature and lowering rates	54
XIII. Details of THM runs at different temperature and lowering rates	55
XIV. THM runs with controlled seeding and doping	57
XV. Mass spectrometric analyses of feed rods and THM GaAs grown from them	59
XVI. Hall measurements of feed crystals and THM grown GaAs crystals	60
XVIII. Summary of travelling heater experiments on Ga _x In _{1-x} Sb	62
XIX. Summary of THM Ga _x Al _{1-x} As growth runs	63
XX. Ion microprobe mass analyses of GaAs	90
XXI. Dislocation densities and etchant data for GaAs A(111) and B($\bar{1}\bar{1}\bar{1}$) surfaces	103
XXII. Radii of curvature, dislocation types and densities in bent n-type GaAs	119
XXIII. Infrared cathodoluminescence intensity, half-width and peak position for control and bent GaAs samples	136

LIST OF TABLES (Continued)

	<u>Page</u>
XXIV. Relative changes in Hall parameters after heating and bending of n-type GaAs	143
XXV. Percent change in the Hall parameters of the bent Te-doped GaAs sample	150
XXVI. Summary of the anisotropic character of the conductivity, carrier concentration and mobility of bent semiconductor crystals	152
XXVII. Samples investigated by infrared modulation of cathodoluminescence	157

ABSTRACT

The purpose of this program was to develop new and improved methods for the growth and characterization of gallium arsenide (GaAs) and mixed III-V semiconductor crystals. This was accomplished by laboratory experiments and related theoretical research over a three-year period. Eventually this will have produced all or part of approximately 15 Ph.D. dissertations, 40 papers, and 3 patents.

A new Czochralski growth technique was invented and developed. A boron oxide seal is employed which is not in contact with the melt, permitting routine growth of low dislocation density or dislocation free GaAs using elemental Ga and As as the starting material. Sixty runs were made, producing crystals for sixteen different investigators both within and outside of USC. Mobilities ranged up to $3500 \text{ cm}^2/\text{volt-sec}$ and carrier concentrations ranged from semi-insulating to $6.5 \times 10^{18}/\text{cm}^3$. Mass spectrographic analyses of unintentional impurities were inconclusive.

Most of the technical problems associated with liquid encapsulated floating zone melting were overcome. Ten passes of a 10 mm diameter GaAs ingot were successfully performed. The boron oxide encapsulant greatly stabilized the zone in addition to preventing arsenic evaporation. However, within the time available we were unable to develop a control system for the radio-frequency generator. Such control is necessary for ingots above about 13 mm in diameter. Processed ingots were large-grained polycrystalline with mobilities up to $4400 \text{ cm}^2/\text{volt sec}$ and carrier concentrations down to $6 \times 10^{15}/\text{cm}^3$. The concentrations of B, P, K, Ca, Ti and Ni increased during zoning, while Al and Si were not appreciably changed, and Sb and Te were reduced.

It was shown that boron oxide can be dried more rapidly by bubbling a dry gas through it than by application of a vacuum, although the vacuum method is more convenient for removal of traces of moisture immediately prior to crystal growth. At room temperature, boron oxide rapidly absorbs water, forming a diffusion-limited coherent layer at first and later forming cracked boric acid. This surface moisture could be removed in a vacuum at room temperature, with rate constants of 1.21 hr^{-1} and 0.216 hr^{-1} .

Horizontal Bridgman growth was shown to be a convenient production method for GaAs crystals, whereas the vertical gradient freeze and vertical Bridgman-Stockbarger techniques are probable strong competitors.

The optimum conditions for growth of 1 cm diameter GaAs by the travelling heater solution-growth method with a 1 cm long heater were established as a heater temperature of about 980°C, a maximum travel rate of 1.5 mm/day, a solvent zone slightly shorter than the heater, a seed length of about one diameter and a feed length of over 2 diameters. Mobilities ranged up to 1007 cm²/volt-sec and carrier concentrations down to $3.3 \times 10^{15}/\text{cm}^3$. Impurity concentrations of the product were somewhat lower than the feed. Polycrystalline $\text{In}_{1-x}\text{Ga}_x\text{Sb}$ and $\text{Ga}_{1-x}\text{Al}_x\text{As}$ were also prepared by the travelling heater method in preliminary experiments.

Gallium nitride films were chemically vapor deposited on sapphire using gallium chloride and ammonia. Carrier concentrations were always about $10^{20}/\text{cm}^3$ n-type, regardless of processing changes.

GaAs, $\text{GaAs}_{1-x}\text{Sb}_x$ and $\text{Ga}_{1-x}\text{In}_x\text{As}$ films were grown on GaAs by liquid epitaxial growth (LEG) using the dipping technique first developed at USC. The Ga-In-As solid-liquid equilibria at 860°C were determined. Substrate orientations of (111) were superior to (100), (110), (211) and (311). The dependence of lattice constant on composition of $\text{GaAs}_{1-x}\text{Sb}_x$ was linear, obeying Vegard's Law. A mesa GaAs junction field effect transistor with a ring-dot configuration was prepared by LEG. Reverse currents at the 12V pinchoff voltages were 2×10^{-9} amperes. New techniques for measurement and control of oxygen activity during LEG are being developed. These primarily utilize zirconia as an electrolyte.

The influence of heat transfer and mass transfer conditions on interface position, shape and stability was investigated theoretically and experimentally for zone melting, the travelling heater, the gradient-freeze, and the Bridgman-Stockbarger techniques. New equations for constitutional supercooling in multi-component systems were developed. The influence of pressure and ambient gas on the evaporation rate of a melt was analyzed and compared with experiments performed at Sandia. The influence of boiling and convection on movement of solvent inclusions in a temperature gradient was studied experimentally. A theory was developed for movement in a centrifugal field which did not agree precisely with experiments. Reviews were published on mass transfer in crystal growth and on movies in crystal growth. A new twin and growth mechanism was discovered. Experiments at the Aerospace Corporation on off-eutectic zone melting were analyzed and interpreted.

Advances were also made in crystal processing. A new laser technique was developed for orientation of crystal ingots. New and improved methods for lapping, polishing and thinning GaAs were developed. Electrochemical techniques were developed for producing An-Sn contacts of desired composition and thick Cu layers for heat sinks. The most convenient ohmic contacts for Hall measurements proved to be indium dots carefully alloyed with a small hydrogen flame. Exposure to the flame had only a small effect on measured Hall parameters.

Mass spectrographic analyses were not as reproducible or sensitive as one would hope. Ion Microprobe Mass Analysis is useful for examination of surface contamination and composition variation, and can be used for oxygen, carbon, nitrogen and hydrogen analysis, unlike ordinary mass spectrographic analysis. For meaningful bulk analysis a clean surface is required, as best supplied by a recent cleavage. Sensitivity varies greatly from element to element, and so interpretation requires time and experience.

Carbon and silicon were observed in GaAs by infrared absorption measurements on our new liquid-seal Czochralski technique (referred to earlier). The influence of carbon on electrical properties is unknown. $\text{Si}_{\text{Ga}}\text{-Si}_{\text{As}}$ pairs were studied by isotope and other experiments. Using the zirconia electrolyte method, the oxygen concentration in two bulk GaAs crystals was estimated to be 10^{17} and 10^{18} atoms/cm³. Glow discharge spectroscopy was shown capable of determining the concentration of some elements in thin films. The detection limit for Sn in GaAs was 9×10^{17} atoms/cm³ at a sputtering rate of 1.4×10^{-5} cm³/min.

Dislocations in GaAs were revealed by etch pits, by X-ray topography and by infrared cathodoluminescence (IR-CL). Cathodoluminescence was more uniform for one of our Czochralski crystals than for a horizontal Bridgman sample. After bending GaAs samples, slip lines were apparent in the IR-CL. Heating at 600 to 700°C for 10 to 20 minutes caused changes in electrical properties; for example, a 17% decrease in carrier concentration and a 12% increase in mobility of a nominally undoped crystal, and a 15% decrease in mobility and no change in carrier concentration of a Te-doped sample. When the samples were bent during heating, additional anisotropic changes in electrical properties were observed.

We did not succeed in producing stimulated emission in GaAs by continuous electron beam excitation. Some GaAs samples exhibited infrared modulation of cathodoluminescence, while others did not. It decreased more rapidly with

increasing beam voltage than would be expected if it were entirely a bulk effect. It was only observed on high resistivity material. Cathodoluminescence of GaAs, GaP and $\text{GaAs}_x\text{P}_{1-x}$ was studied as a function of temperature. That of $\text{GaAs}_x\text{P}_{1-x}$ was also studied as a function of composition.

Low temperature photoluminescence measurements on five liquid-seal Czochralski crystals and one horizontal Bridgman crystal were made. Only the Bridgman-grown sample was pure enough to show some luminescence from free excitons or from excitons bound to neutral shallow donors or acceptors. Photoluminescence spectra of LEG films of $\text{GaIn}_x\text{As}_{1-x}$ and $\text{GaAs}_x\text{Sb}_{1-x}$ indicated that impurity-band transitions were responsible. Highly efficient photoluminescence of CVD GaN films was observed.

Two capacitance-voltage profiling systems were developed at USC. One was relatively simple and suitable for measuring carrier concentrations in the absence of deep impurity levels. The other involved detailed analyses and sophisticated circuit design and construction permitting one to obtain information on deep impurity levels. A high-impedance temperature-controlled Hall apparatus was designed and constructed. Correction factors were derived for finite electrodes in the van der Pauw geometry for Hall measurements. We determined the effects of thermal excitation and quantum-mechanical transmission on photothreshold determination of Schottky barrier height.

The following capital equipment was purchased under these three grants: ellipsometer, Cat to TTY interface, gas laser and power supply, polisher, high voltage power supply, four temperature controllers, programmer, power assembly for X-ray generator, volt-ohmmeter, sodium vapor lamp, analytical balance, two mechanical vacuum pumps, vacuum oven, cryogenic temperature controller, dewar and accessories, digital voltmeter, high purity water system, zone refiner, X-ray topographic camera, residual gas analyzer, cold trap, multipoint recorder, calculator, X-Y recorder, zoom lens and an interference attachment for the microscope.

I. INTRODUCTION

The purpose of this program was to contribute to the state of the art of growth and characterization of GaAs and III-V alloys. At the beginning, in July 1970, GaAs showed great potential for a variety of military and civilian applications, but had not yet reached commercial importance for any of these. Since then, light emitting diodes and related devices have begun to be produced on a large scale. This has stimulated feverish work on improvement of crystal growth techniques, which is leading to availability of crystals with more reproducible properties at lower prices. This availability, in turn, should lead to eventual commercialization of other GaAs-based devices, such as mixer and varactor diodes, Gunn-effect devices and various transistors.

At the present time, bulk GaAs is used only as substrate material for deposition of GaAs and III-V alloy films by chemical vapor epitaxial growth and liquid epitaxial growth. Although consideration has been given to use of bulk GaAs as a window for high-powered infrared lasers, other materials appear to be superior for this application. The ideal GaAs substrate material would be dislocation-free and of reproducible electrical resistivity and carrier mobility. Such material is not yet produced commercially, but fortunately is not required for currently produced devices. The primary goal of the present program was to assist with achievement of commercial production of such ideal material, both by developing and studying growth techniques and by various characterization studies.

Throughout this report we have used a code system to denote the origin of crystal slices. The code begins with two or three capital letters denoting the growth technique, followed by an ingot number and sometimes by numbers and letters identifying the particular slice. The growth technique code is as follows:

- CZ - Grown by our new liquid seal Czochralski technique.
- FZ - Grown by liquid-encapsulated floating zone melting.
- GF - Grown by the vertical gradient-freeze method.
- THM - Grown by the travelling hheater solution method.
- HB, HBT or WA - Grown by the horizontal Bridgman technique.

Several dissertations have resulted with partial or whole support by the present grants. Three of these have been issued as separate reports available through the Defense Documentation Center, and so are summarized only briefly here. Likewise, many papers have resulted from this program. In order to avoid unnecessary duplication, the most pertinent of these are included as appendices here, with only brief mention in the bulk of the report.

The first section of the report deals with our research on two new and three existing bulk growth techniques for GaAs and III-V alloys. Liquid epitaxial growth and our own exciting oxygen control techniques are discussed in the second section. In third section are described studies on heat and mass transfer in unidirectional crystal growth, interface stability, control of second phase defects, and evaporation of volatile melts. New polishing, orienting and contacting methods are discussed in the fourth section. Chemical analytical techniques and results, dislocation studies, electron beam interactions, photoluminescence, Schottky barrier properties, and Hall measurements are dealt with in the fifth section. This is followed by a discussion of the conclusions and suggestions for future work.

II. BULK CRYSTAL GROWTH

A. Liquid-Seal Czochralski Technique for GaAs

(P. C. Leung and W. P. Allred)

1. Introduction

Czochralski growth of gallium arsenide has presented some problems, primarily because of the volatility of arsenic. The arsenic vapor pressure at the melting point is about one atmosphere. A vapor space over the melt can permit transport of arsenic and condensation of solid arsenic on any cool portions of a sealed system. Condensation may be avoided by maintaining the entire enclosure at a temperature such that the vapor pressure of pure arsenic is greater than the arsenic partial pressure over the melt. Since the temperature needed to provide a stoichiometric pressure is 610°C , a problem arises in providing a seal for the pulling mechanism which will withstand this temperature. A second problem is the high reactivity of the arsenic vapor with many materials at 600°C . We report here the development of a new technique for Czochralski growth of gallium arsenide possessing some advantages over previous techniques. (1-5)

Several methods have been employed previously to avoid loss of arsenic from the melt. The earliest technique is the magnetic-type puller developed by Gremmelmaier. (6) This method uses magnets to support and rotate the seed rod which is sealed within the quartz chamber. Since there is no mechanical feed through, the temperature of the entire quartz envelope can be heated to a temperature in excess of 610°C . One of the major disadvantages of the magnetic puller is that the seed crystal, which is driven by rotating magnets, is subject to considerable vibration. This problem is caused by the loose coupling of the magnet and by the friction of the quartz bearing surfaces. In addition, the system is very complex, costly, and difficult to use.

A second method uses a liquid gallium seal to contain the arsenic vapor. (7) However, it proved to have little practical use because of its complexity and the fact that the arsenic in the growth chamber reacts with the gallium seal to form solid gallium arsenide. Arsenic is also lost through the gallium seal.

The third method is the liquid encapsulation technique. (8,9) This system uses a layer of molten B_2O_3 on the surface of the GaAs melt to prevent the escape of arsenic. The B_2O_3 enables the use of conventional Ge or Si growers for the growth of GaAs. The growing crystal is pulled through the B_2O_3

layer. A layer of B_2O_3 adheres to the crystal and generates stresses as it cools due to the differences in thermal expansion. Because the B_2O_3 is in contact with the melt, impurities in the B_2O_3 are thereby transferred directly to the melt, leading to erratic electronic properties in the crystal. It is also difficult to react elemental gallium and arsenic under the B_2O_3 layer, making it necessary to use prereacted GaAs for the starting material.

2. New Czochralski Technique

We present here a high temperature push-pull rotary seal that can be used with Czochralski growth of gallium arsenide. This technique overcomes many of the previously mentioned difficulties. This system uses a molten B_2O_3 seal, not in contact with the melt, to prevent arsenic escape. As shown in Figure 1, the pull rod rotates through the liquid seal so that a direct mechanical drive similar to that used in conventional Ge or Si growers can be used. The two resistance furnaces are used to maintain proper temperatures for different regions of the growth system during growth. A stoichiometric amount of gallium and arsenic is placed in the crucible. An additional amount of arsenic is added to provide an arsenic vapor pressure above the melt. A seed is fastened to the quartz pull rod and the bottom growth chamber containing the crucible and melt is then welded to the top section.

The high temperature, vacuum tight, rotating seal required for the growth of GaAs is formed by first placing solid B_2O_3 above the narrow quartz neck. The system is then closed and evacuated. After outgassing the B_2O_3 and the system under vacuum at about $300^\circ C$, the B_2O_3 is melted by heating the top furnace to $900^\circ C$. This temperature is maintained until all the moisture in the B_2O_3 is dissipated. The B_2O_3 is then driven between the pull rod and the surrounding small bore tubing by back filling the section above the B_2O_3 with helium or argon gas. The B_2O_3 is then cooled to between $610^\circ C$ and $650^\circ C$. The seal thus formed is vacuum tight and can be rotated and moved vertically without the loss of vacuum or arsenic vapor from the lower section. Due to the high viscosity of the B_2O_3 at $650^\circ C$, the differential pressure between the helium filled section and the growth chamber is not critical. A helium pressure of one or two atmospheres is used with consistent success.

After the seal is formed, the lower furnace is then heated to above $600^\circ C$ while the induction heater is used to react the gallium and arsenic and to bring

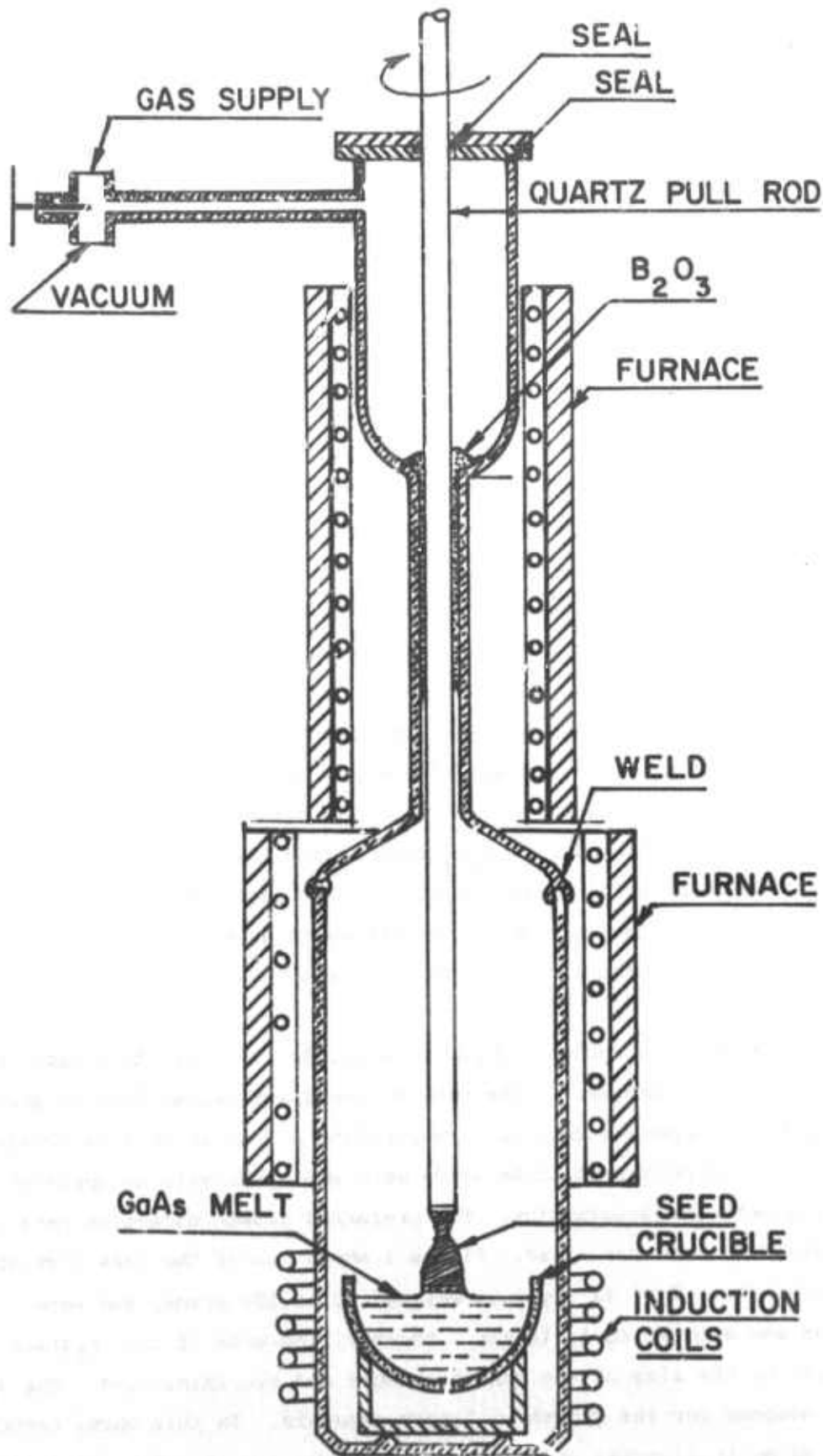


Figure 1. Diagram of the liquid-seal Czochralski GaAs grower.

the GaAs melt to the growth temperature. The seed is then lowered into contact with the melt and the crystal can be grown. After the crystal is grown, the furnaces are allowed to cool. The differences in thermal expansion of the B_2O_3 and the quartz causes the pull rod and the surrounding quartz tubing to fracture. This necessitates replacement of the quartz pull rod and the surrounding tubing for each crystal grown.

In the early experiments, arsenic tended to leak through the B_2O_3 seal. This was caused by formation of gas bubbles due to water which was present in the B_2O_3 . The water reacted with the arsenic vapor to form an oxide which dissolved in the B_2O_3 and was readily transported through the seal to the vacuum chamber above. The problem was solved by heating the B_2O_3 in a vacuum within the system, thus preventing pick-up of H_2O during the loading process. The B_2O_3 was further purified by first bleeding dry helium into the pulling chamber before melting of the B_2O_3 and then passing the helium up through the molten B_2O_3 at $900^\circ C$. This process was very effective in removing residual water from the B_2O_3 . Arsenic leakage was also caused by channeling of the B_2O_3 . The channels were formed when the pull rod was pushed down into the pulling chamber. The B_2O_3 tended to run down one side of the pull rod, leaving a void on the other side and permitting loss of arsenic. The channeling was eliminated by using helium pressure to push the B_2O_3 down around the pull rod in an even manner. A problem of poor visibility due to evaporated deposits was corrected by the addition of a view port which was heated to about $900^\circ C$ by a resistance heater. The window of the view port then remained clear during the entire growth period.

GaAs crystals undoped, or doped with Te, Zn, Si, Cr, etc., have been grown routinely by this technique. The crystal was first necked-down to about 1 mm diameter and then expanded to 1 to 2 cm yielding a 4 to 10 cm long crystal. Both Ga $\langle 111 \rangle$ seeds and polycrystalline seeds were employed, with no apparent difference in growth characteristics. The preferred growth direction resulting from a polycrystalline seed was $\langle 111 \rangle$. Figure 2 shows one of the GaAs crystals grown by this technique. Typical crystals weighed 50 to 100 grams, and were 1 to 2 cm in diameter and 4 to 10 cm in length. However, the size of the crystals is limited only by the size of the quartz chamber and crucibles used. The system can be easily adapted for the growth of larger crystals. In this work, carbon crucibles 50 mm in diameter and 20 mm high have been used. Table I lists the

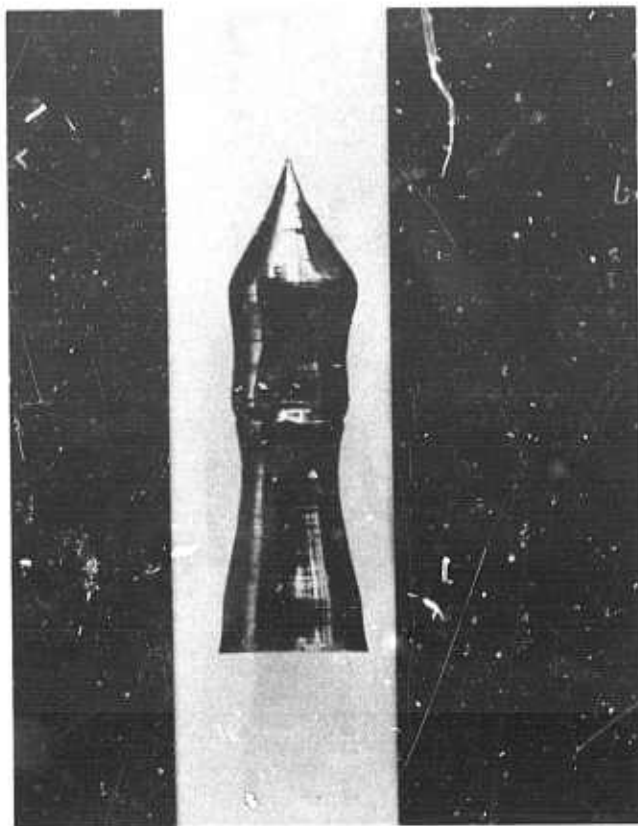


Figure 2. Photograph of a GaAs crystal grown by the liquid-seal Czochralski technique.

TABLE I. GaAs GROWN BY THE LIQUID-SEAL CZOCHRALSKI TECHNIQUE FROM
JUNE 1971 - JUNE 1973

Crystal Number	Dopant	Carrier Conc. (cm^{-3})	Mobility ($\text{cm}^2/\text{volt-sec}$)	Samples Sent to	Purpose	Remarks
CZ-16	Te	2.5×10^{17}	3500	A. L. Esquivel	Dislocation Studies and Electrical Properties.	See Sec. VI.F.
CZ-17	Si	6.5×10^{18}		J. Kung	Annealing Studies and Infrared Measurements.	No difference in annealing character- istics between Czochralski and Horizontal Bridgman samples.
						Carbon local modes observed. (10)
						See Sec. VI.B.
CZ-19	Undoped	1×10^{17}	3000	A. L. Esquivel	Dislocation Studies and Electrical Properties.	
CZ-20	Mg, Se	1.2×10^{18}		P. Leung	Local Mode Absorption Studies.	See Ref. 10.
CZ-22	Mg, S			P. Leung	Local Mode Absorption Studies.	Unpublished data.
CZ-23	Te			A. L. Esquivel	Dislocation Studies and Electrical Properties.	
				W. R. Wilcox	Ion Microprobe Mass Analysis.	See Sec. VI.A.
CZ-25	Undoped	High ρ		H. Huang	Substrates for Deposition of ALP Films.	

TABLE I. (Continued)

Crystal Number	Dopant	Carrier Conc. (cm ⁻³)	Mobility (cm ² /volt-sec)	Samples Sent to	Purpose	Remarks
CZ-25 (Contd.)				D. Gonzales	Calorimetric Studies with CO ₂ Laser.	High absorption at 10.6 μ .
				S. Nieh	Calorimetric Studies with CO ₂ Laser.	
				P. Leung	Local Mode Studies of Carbon in GaAs.	Carbon band observed, no additional bands.
				V. Yip	Seed Material for THM Growth.	
CZ-28	Undoped			P. Leung	Mass Spectrographic Analysis.	Si contamination.
CZ-32	Undoped (Quartz crucible)			P. Leung		
CZ-34	Undoped	High ρ		P. Leung		
CZ-35	Undoped	2.3×10^{16} (frcnt)	2800	A. L. Esquivel	X-Ray Topography.	
				C. R. Crowell	Temperature Dependent Hall Measurements.	
				D. Wittry	Cathodoluminescence Studies.	
				L. H. Skolnik (AFCRL)	Calorimetric Measurements.	
				P. Leung	Mass Spectrographic Analysis.	
				B. Gordon	Schottky Barrier Diodes C-V Profiling.	See Sec. VI.I.

TABLE I. (Continued)

Crystal Number	Dopant	Carrier Conc. (cm ⁻³)	Mobility (cm ² /volt-sec)	Samples Sent to	Purpose	Remarks
CZ-36	Te	4×10^{17} (back)	2160	C. R. Crowell	Hall, C-V Measurements. Schottky Barrier Diodes.	Carrier concentration too high to observe photo-conductivity.
				J. C. Corelli (RPI)	Radiation Induced Extrinsic Photoconductivity Measurements.	
CZ-37	Undoped	High ρ		L. H. Skolnik (AFCRL)	Calorimetric Measurements.	
				C. R. Crowell	Temperature Dependent Hall Measurements.	
				P. Leung	Local Modes Studies of Carbon in GaAs. Mass Spectrographic Analysis.	Carbon band observed.
				E. Miller	Substrate Material for CVD Epitaxial Growth.	
CZ-38	Zn	4.6×10^{17} P	120	D. Wittry	Cathodoluminescence Studies.	
				J. C. Corelli (RPI)	Radiation Induced Extrinsic Photoconductivity Measurements.	Carrier concentration too high to observe photo-conductivity.
CZ-40	Undoped	High ρ		E. Miller	Substrate Material for CVD Epitaxial Growth.	
CZ-41	Undoped			V. Yip	Seed Material for THM Growth.	See Sec. II.F.
CZ-42	Undoped			S. Nieh	Calorimetric Studies.	Absorption very high.

TABLE I. (Continued)

Crystal Number	Dopant	Carrier Conc. (cm ⁻³)	Mobility (cm ² /volt-sec)	Samples Sent to	Purpose	Remarks
CZ-43	Cr	High ρ		S. Nieh D. Wittry	Calorimetric Studies. Cathodoluminescence Studies.	Cr level observed.
CZ-44	Si			P. Leung	Carbon Local Modes Study. Check Control for Growth with ³⁰ Si.	
CZ-45	Si			P. Leung	Carbon Local Modes. Check Control for Growth with ³⁰ Si.	
CZ-46	Zn			P. Leung	Carbon Local Modes.	Two additional bands observed. May be due to Zn-C Pairs.
CZ-47	Te			P. Leung	Carbon Local Modes.	No additional bands. No enhancement or suppression of carbon band.
CZ-48	Cr			D. Wittry	Cathodoluminescence Studies.	Too much oxide on surface of melt, probably due to too much chromium doping. Ingot was polycrystalline.

TABLE I. (Continued)

Crystal Number	Dopant	Carrier Conc. (cm ⁻³)	Mobility (cm ² /volt-sec)	Samples Sent to	Purpose	Remarks
CZ-49	Undoped					Trial run with silicon susceptor and quartz liner. The susceptor was melted before the Ga and As could be reacted.
CZ-50	³⁰ Si	2.5×10^{18}		P. Leung	Si-Doped GaAs Local Modes.	Tried to control ³⁰ Si-doping. It appeared to have a slight amount of ²⁸ Si contamination, probably from the seed.
CZ-51	³⁰ Si	5.9×10^{18}		P. Leung	Si-Doped GaAs Local Modes. Mass Spectrographic Analysis.	See Sec. VI.C. Absorption spectrum showed little ²⁸ Si.
CZ-52	Undoped	8×10^{17}		P. Leung	Local Modes. Mass Spectrographic Analysis.	Trial run with carbon susceptor and quartz liner. Local mode measurements indicated much less carbon but an appreciable amount of Si contamination.
CZ-53	Undoped	9.2×10^{16}	2850	P. Leung	Local Modes. Mass Spectrographic Analysis.	Trial run with Al ₂ O ₃ crucible. No carbon local mode.

TABLE I. (Continued)

Crystal Number	Dopant	Carrier Conc. (cm^{-3})	Mobility ($\text{cm}^2/\text{volt-sec}$)	Samples Sent to	Purpose	Remarks
CZ-54	^{30}Si + ^{28}Si			P. Leung	Si Local Modes. Mass Spectrographic Analysis.	Regrowth of CZ-51 with added ^{30}Si and ^{28}Si . Absorption measurements showed too little ^{30}Si . See Sec. VI.C.
CZ-55	^{30}Si + ^{28}Si	6.1×10^{18}		P. Leung	Si Local Modes. Mass Spectrographic Analysis.	Regrowth of CZ-54 with ^{30}Si added. Measurements showed approximately equal concentrations of ^{28}Si and ^{30}Si . See Sec. VI.C.
CZ-56	Cr	High ρ		S. Nieh	Absorption at 10.6μ Region.	Much less than previous chromium doping was used. No problem with oxide forming on surface of melt. Ingot was single crystal.
				D. Wittry	Luminescence Measurements of Cr-Level.	
CZ-57	Undoped					Oxides formed on surface of melt.
CZ-58	Undoped	High ρ		W. G. Spitzer	Substrate Material for Ion Implantation Studies.	

TABLE I. (Continued)

<u>Crystal Number</u>	<u>Dopant</u>	<u>Carrier Conc. (cm⁻³)</u>	<u>Mobility (cm²/volt- sec)</u>	<u>Samples Sent to</u>	<u>Purpose</u>	<u>Remarks</u>
CZ-59	Undoped	High ρ		J. M. Whelan	Substrate Material for LPE Growth.	
CZ-60	Undoped					Diameter control not good. Problems with R-F generator and con- troller.

GaAs ingots grown by this technique during the period 1 July 1971 - 30 June 1973 and the characterization studies performed on samples from these ingots.

Dislocation densities of crystals grown in this system have been measured by etch pit and topographic techniques (see Section VI.F). Dislocation densities were low, with most crystals averaging $< 100/\text{cm}^2$ and with sizeable volumes dislocation-free.

Our undoped crystals had a resistivity of about 10^8 ohm-cm . Crystals doped with tellurium had low mobilities compared with crystals grown by the horizontal Bridgman method. This indicates the presence of a deep-level impurity. Mass spectrographic analysis (Air Force Cambridge Research Laboratories and Battelle Memorial Institute) have been performed on some of these crystals. As indicated in Table II, Al, Si and Cl were found, but no Cu. Infrared absorption measurements at USC (courtesy of Prof. W. G. Spitzer) failed to reveal the presence of Si, however.

Recent infrared absorption measurements over a higher frequency region have revealed the presence of carbon in our crystals, as described in Section VI.B of this report. It is suspected that carbon may be responsible for our low mobilities and high resistivities of undoped crystals. Other possible GaAs crucible materials were explored since carbon crucibles were a source of carbon in the crystals as well as a possible source of other impurities. A major effort was devoted to studying the feasibility of various materials to be used as crucibles during the last contract period.

a. Silica Crucible with Silicon Susceptor

Silicon was considered as a good possibility as a susceptor material since it has a higher melting point than gallium arsenide, and is easily heated by RF induction. A susceptor was machined from a polycrystalline silicon ingot. It was then oxidized at about 1100°C over 24 hours. Originally, it was planned to carbonize the surface and use it as a crucible. However, since carbon was found in material grown in a vitreous carbon crucible, a fused silica crucible was used instead, with the silicon as the susceptor. During the test run, there was no difficulty in coupling to the silicon susceptor. However, it was not possible to provide enough heat to form and melt the gallium arsenide without melting the Si. Perhaps the difference between the melting points of GaAs (1240°C) and Si (1420°C) is not large enough.

TABLE II. MASS SPECTROGRAPHIC ANALYSES OF CZOCHRALSKI-GROWN CRYSTALS (P_2 MW)

Element	AFCRL				Battelle		
	<u>CZ-13</u>	<u>CZ-37</u>	<u>CZ-32</u>	<u>CZ-35</u>	<u>CZ-37</u>	<u>CZ-52</u>	<u>CZ-53</u>
B	0.483 x 10 ⁻²	0.566 x 10 ⁻¹			0.002	<0.002	0.01
C	16.6	0.668	2.37	0.637			
O		0.524	5.37	0.173			
F		0.262 x 10 ⁻²		0.218 x 10 ⁻¹	<0.1	<0.1	<0.1
Al	0.990 x 10 ⁻¹	0.246 x 10 ⁻¹	0.544 x 10 ⁻¹	0.819 x 10 ⁻²	0.1	0.04	5.0
Si	0.990 x 10 ⁻¹	0.293	22.4	1.14	4.0	10.0	2.0
Cl	0.242 x 10 ⁻¹	0.173 x 10 ⁻¹		0.142	0.1	0.2	0.05
K		0.283 x 10 ⁻¹	3.71	0.436	0.03	0.6	0.1
N	0.110 x 10 ⁻¹						
Ca	0.178 x 10 ⁻¹				0.01	0.03	0.006
Cr	0.339 x 10 ⁻¹				0.04	0.02	0.01
S	0.249	11.6			<0.2	<0.2	<0.2
Li			0.658 x 10 ⁻²	0.171 x 10 ⁻²			
Mg				0.142			
P				0.214 x 10 ⁻¹	<0.05	<0.05	0.01
Fe				0.116	0.4	0.2	0.2

b. Silica Crucible with Vitreous Carbon Susceptor

With a fused silica crucible and a vitreous carbon susceptor, we expected less carbon in the material since the GaAs melt would not be in direct contact with the vitreous carbon. During the run, the diameter control was not good. Nevertheless, a crystal was grown. Local mode measurements made on this material showed that the carbon was much less compared to an undoped crystal grown in a vitreous carbon crucible. Local mode absorption data also showed that this material contained $\sim 8 \times 10^{17}/\text{cm}^3$ Si, probably from the silica crucible. This is in reasonable agreement with the results of a mass spectrographic analysis performed on this material which gives 10.0 (ppmw) or $\sim 5 \times 10^{17} \text{ cm}^{-3}$ (see Table II, CZ-52).

c. Alumina Crucible with Direct Coupling to the Melt

Early attempts with alumina crucibles were not successful because the crucibles fractured due to thermal stresses, allowing gallium to leak out. This problem was avoided by placing the Al_2O_3 crucible on top of another upside-down Al_2O_3 crucible. With radio frequency induction heating, the power had to be coupled directly to the GaAs melt, and the diameter control was considerably more difficult. Since there was no carbon in the material (as shown by local mode measurements), the electrical data would be expected to be much improved. However, the measured electrical resistivity of $0.025 \Omega\text{-cm}$, carrier concentration of $9.2 \times 10^{16}/\text{cm}^3$, and the mobility of $2850 \text{ cm}^2/\text{volt-sec}$ were close to the values for some of the undoped materials grown with the vitreous carbon crucible. This led us to suspect the present B_2O_3 seal material (99.95% (Optran grade from BDH Chemicals)) may not be pure enough. Impurities may have been introduced into the melt through vapor transport from the B_2O_3 seal. The purity of the crystals may be improved if a higher purity grade B_2O_3 (99.999% or 99.9999%) is used.

3. Discussion

A somewhat similar technique has been developed by using the principle of pressure balancing.⁽¹¹⁾ In this system, the dissociation pressure of the compound is dynamically balanced by a pressure of inert gas. The new liquid-seal technique presented here differs in that it does not attempt to balance the differential pressure. It utilizes the fact that the B_2O_3 is extremely viscous at 650°C . The liquid B_2O_3 seal remains in position during the entire crystal growth process and prevents the leakage of arsenic from the growth chamber. The complex pressure balancing apparatus is therefore unnecessary for the growth of GaAs.

The liquid-seal Czochralski technique has an advantage over the magnetic-type puller in that it does not use magnets to effect the vertical displacement and rotation of the seed crystal. This grower also has advantages over the liquid encapsulated Czochralski technique in that pre-reacted material is not necessary. In addition, the problem of B_2O_3 adhering to the crystal is eliminated. The most attractive feature of the technique is its simplicity. It is economical to construct, easy to load and keep clean. The size of the crystal is limited only by the size of the quartz chamber and crucibles used. The system can be easily adapted for the growth of larger crystals. In this work, carbon crucibles 50 mm in diameter and 20 mm high have been used. It has been shown that low- or zero-dislocation GaAs single crystals can be grown routinely using this technique. The purity of the crystals may be improved by using higher purity B_2O_3 , and a different crucible material such as Al_2O_3 with a pyrolytic graphite susceptor. Automatic diameter control may be developed to minimize the need for the operator to be present after the crystal has been expanded to its final diameter. With these improvements, the liquid-seal Czochralski can potentially become the easiest and most economical technique to produce high quality GaAs single crystals.

B. Liquid Encapsulated Floating Zone Melting of GaAs

(E. S. Johnson and W. P. Allred)

1. Introduction

The principle of liquid encapsulated floating zone crystal growth^(14,23) is a straightforward extension of the successful encapsulation technique used in the Czochralski growth of GaAs and GaP. In the encapsulated Czochralski technique a molten glass encapsulant is placed on the melt and a crystal is pulled through the encapsulant. In the encapsulated floating zone technique the feed rod is immersed in encapsulant, allowing repeated passes of a floating zone. The expected advantages of growth with the floating zone technique over Czochralski growth are the avoidance of crystal contamination by the crucible and the potential for the preparation of high purity bulk material through multiple floating zone passes. In addition, the liquid encapsulant would help support the floating zone, permitting the use of larger diameter feed then would be possible with a hot As atmosphere floating zone apparatus.⁽¹⁵⁾ In fact, if

the densities of encapsulant and semiconductor were equal, very large diameter feed could be processed.

Major questions regarding the value of the encapsulated floating zone technique are whether the encapsulant acts as a getter for impurities or as a source of contamination and the maximum diameter feed through which a stable floating zone can be passed for a given encapsulant-semiconductor system. Answers to these questions, and a description of the procedures for encapsulated float zoning which have evolved under the support of this grant are presented here. GaAs has been used because the As vapor pressure of ~ 0.9 atmospheres at the GaAs melt temperature is sufficiently large to require an encapsulation technique and yet is not excessive for a fused silica apparatus. B_2O_3 has been used as encapsulant.

2. Procedures for Encapsulated Float Zoning of GaAs

Briefly stated, the procedure for encapsulated float zoning consists of preparing feed material, drying the B_2O_3 encapsulant, immersing the feed in the encapsulant, performing the desired floating zone operations, and removing encapsulant from the zoned ingot. Each of these operations is described here in some detail.

GaAs crystals used as feed rods were grown by the horizontal Bridgman technique (Section II.D). The feed rods need only be relatively homogeneous and free of voids and inclusions for use in experiments testing the encapsulated zoning mechanical capabilities, whereas, in other cases, low impurity concentrations are also necessary. Pre-reacted "scrap" GaAs may be melted down to ingot form in the former case, while Ga and As of semiconductor purity are reacted in the latter. These ingots are usually grown in boats formed from bisected silica tube with the maximum ingot cross section limited by the bore of the Bridgman furnace. For GaAs ingots larger than this, a section of silica tube greater than 180° may be used to construct a boat if the boat is carbonized. Carbonization prevents the GaAs melt from wetting the silica and the subsequent breakage of the ingot by differential thermal contraction. The boat may be carbonized by heating it at 800 to 900°C in an atmosphere of helium containing acetone.

Bridgman-grown crystals approximately six inches long were cut into feed rods with square cross sections. The dimensions of the square were calculated to give the desired diameter when the feed is float zoned to circular cross section. The feed was then secured inside a hollow aluminum tube with only one end protruding. The end of the feed rod was then ground to the desired shape (threads at one end, a round at the other) using a threading jig and a conventional wafering saw. Final fitting of the ground ends of the GaAs feed to the rest of the apparatus was done by careful etching of the GaAs. The entire feed rod was lightly etched prior to assembly of the apparatus.

Silica used in the apparatus was cleaned with soap and water, rinsed in deionized water, etched in aqua regia, and rinsed in deionized water. The graphite chuck was heated white hot under vacuum to drive off volatile impurities. The silica pull rod, graphite chuck, GaAs feed rod, and silica containment tube for the B_2O_3 were assembled so that the volume of B_2O_3 needed for the particular experiment could be determined. The components were disassembled and dried. The correct weight of B_2O_3 was measured out and placed in the containment tube. The apparatus was then fitted to the motion table, with the radio frequency work coil and auxiliary furnaces in position. The assembled apparatus, with the feed in position for float zoning, is shown in Figure 3. Details of an early apparatus in operation are shown in Figure 4.

Several steps had to be completed, however, before the apparatus was ready for float zoning. The GaAs feed, graphite chuck, and silica pull rod were initially assembled so that the feed is placed above the upper auxiliary furnace. This was done so that the B_2O_3 encapsulant may be adequately dried prior to lowering the GaAs feed into position in the encapsulant. Without adequate drying, water vapor would be formed at the B_2O_3 -GaAs interface, producing uneven support for the molten zone and allowing the escape of As. There is also evidence that Ga and residual water react in the molten B_2O_3 to form an opaque oxide which would reduce the visibility of the floating zone. ⁽⁹⁾

Although the BDH "Optran" grade B_2O_3 commonly used for encapsulation purposes was nominally "dry", significant amounts of water remain, and additional water was absorbed from the air during loading of the B_2O_3 into the silica containment tube. The water was removed by heating the B_2O_3 in the upper auxiliary furnace at 1000°C for twelve hours under forepump vacuum. An additional two hours of drying at 1100°C under vacuum was performed before lowering the GaAs feed rod.

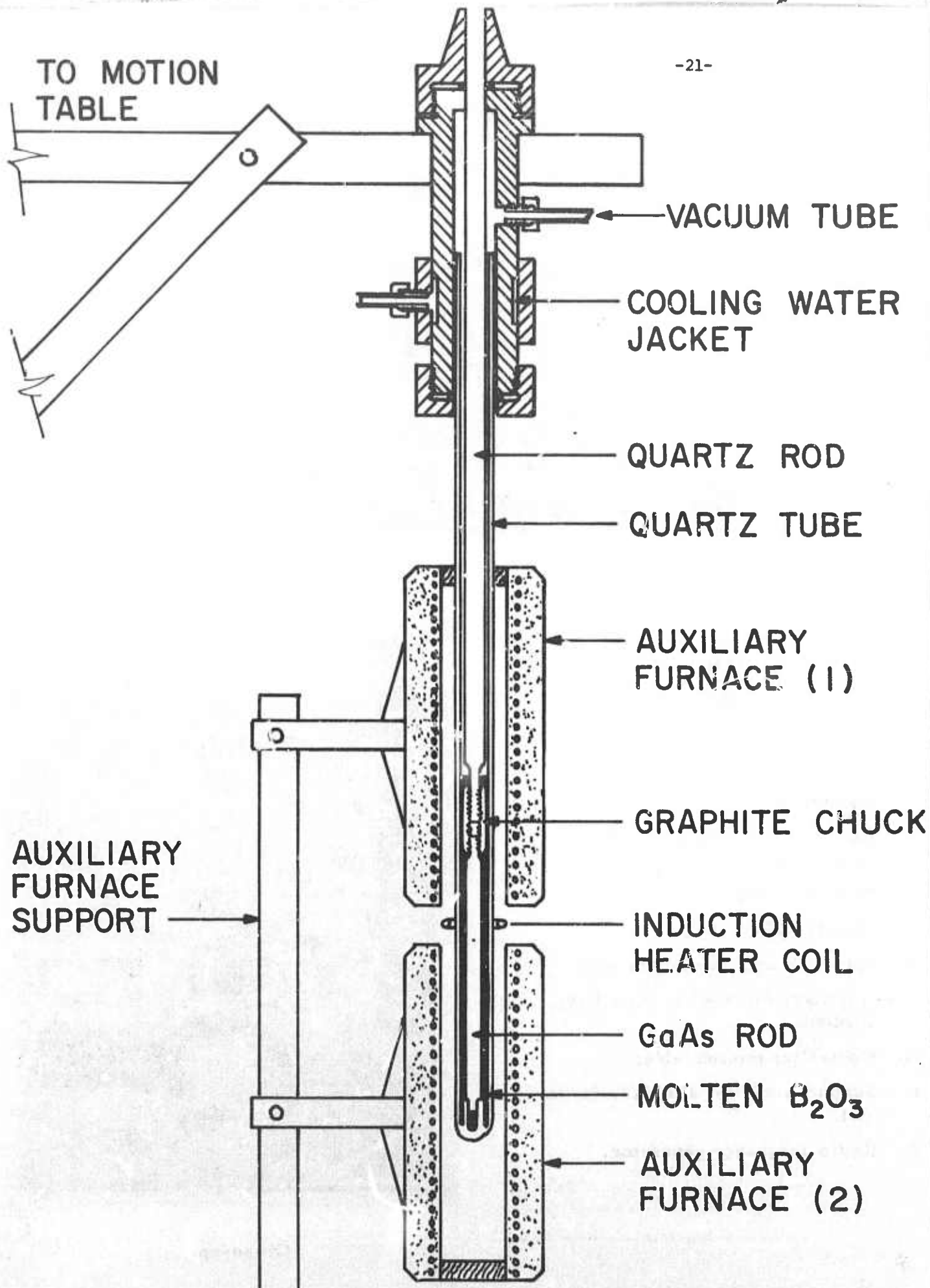


Figure 3

Diagram of apparatus for liquid encapsulated floating zone melting.

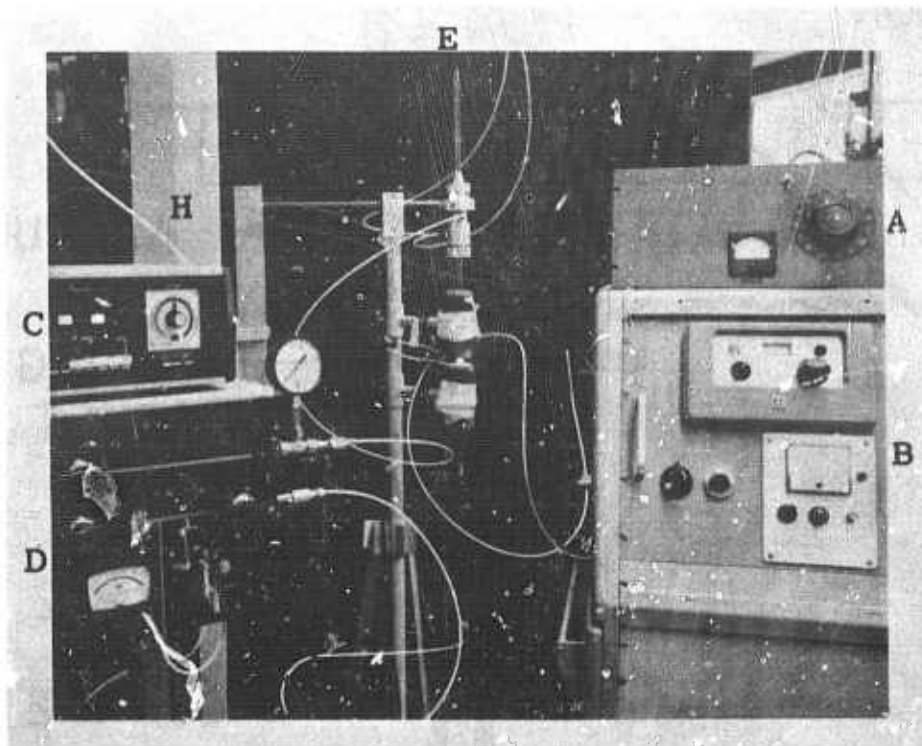
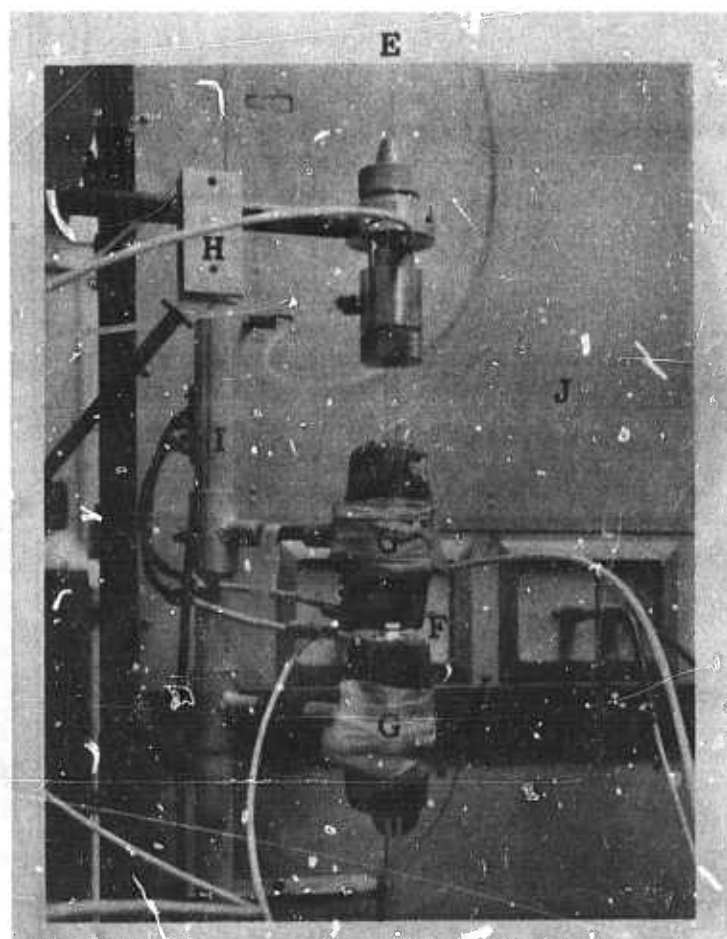


Figure 4. Photographs of the Liquid-Encapsulated Floating-Zone Melting Apparatus for Growth of High Purity GaAs and Mixed III-V Crystals.

- A. Control for auxiliary heaters (G).
- B. Controls for radio-frequency generator (J).
- C. Controls for controlled-motion table (H).
- D. Vacuum system.
- E. Quartz rod and tube.
- F. Induction coil and molten zone.
- G. Auxiliary furnaces to keep B_2O_3 molten.
- H. Controller motion table.
- I. Support stand for auxiliary furnaces (G).
- J. Radio-frequency generator.



Close-up.

An attempt was made with early apparatus to speed the removal of water by bubbling dry N_2 gas through the molten B_2O_3 . The gas was introduced by a capillary built into the bottom of the silica containment tube. A difficulty with this technique was that the molten B_2O_3 wets the silica capillary, and unless the capillary was also raised above the softening point of B_2O_3 , the encapsulant hardened and cracked the capillary. Thus, it was necessary to heat an ever increasing length of the capillary. This "creep" problem could be prevented by using a very thin (1 mm) capillary and starting the flow of dry N_2 gas through the capillary before the B_2O_3 had been melted. It was found that the use of dry N_2 gas did not appreciably speed B_2O_3 drying, and the approach was abandoned. This greatly simplified the silica fabrication.

In practice, a circular furnace twelve inches long was used for the upper auxiliary furnace and a six-inch long furnace was used for the lower auxiliary furnace. The B_2O_3 in the containment tube was dried by raising the motion table until the B_2O_3 was entirely within the twelve-inch furnace. The ends of the furnace were sealed with insulating wool and the drying begun. When bubbles stop appearing in the encapsulant during the $1100^\circ C$ heating, the B_2O_3 was considered to be "dry".

The GaAs feed-silica pull rod assembly was released and allowed to fall through the B_2O_3 under the force of its own weight. The immersion process was speeded by heating the B_2O_3 to $1000^\circ C$ to reduce its viscosity. At this temperature small bubbles of As vapor appeared on the immersed GaAs. This was not a problem if the As bubbles were not mistaken for water vapor and vacuum not re-applied in an effort to remove the bubbles. Some jostling of the pull rod was often necessary to introduce the rounded bottom of the GaAs feed into the corresponding indentation in the silica.

In early work, the GaAs feed rod was connected to the graphite chuck with hand-ground GaAs threads. These threads permitted sideways motion of the feed while lowering through the encapsulant and the horizontal forces would often fracture the GaAs rod at the threads. There were also large stresses upon the threads when the feed rod was rotated in the encapsulant and when it was pulled from the encapsulant upon completion of zoning. Procedures were developed for grinding high quality, uniform threads on the GaAs feed to provide the necessary strength and alignment. The round and shoulder at the bottom of the GaAs feed was designed so the feed rod sat upright and remained centered in the B_2O_3

containment tube-fitting after a floating zone had been established and support of the feed by the silica pull rod was removed.

The steps leading to the assembled apparatus for float zoning GaAs, shown in Figure 3, have been described. It is appropriate to include here a discussion of the various problems associated with applying RF power to the GaAs feed. The generator used was a 25 kW Lepel unit utilizing a tuned grid-tuned plate oscillator circuit for megahertz operation. The generator was normally operated at 4.2 megahertz, although higher frequencies were used for several experiments. Further discussion of the effects of frequency is found in Section II.B.3. The encapsulated floating zone apparatus was originally designed with the GaAs feed and containment tube remaining stationary while the RF work coil and auxiliary furnaces were attached to the motion table. This arrangement was found to be unsatisfactory because the long, flexible RF leads to the work coil radiated excessively, coupling to and disturbing the motion table control circuitry. The system was redesigned to its present configuration with the work coil and auxiliary furnaces stationary and the GaAs-silica attached to the motion table. This arrangement permitted stationary RF leads of under one foot in length and greatly limited interference with control circuitry.

A further problem in the early work was RF arcing to the silica and auxiliary furnaces. The work coil used then was a simple, five-turn coil to which a small transformer coil was attached. The small coil surrounded the silica and heated the GaAs. This high voltage, low current coil was replaced with a low voltage, high current "pie" coil with excellent results. No further problems have been encountered with arcing. The "pie" or "pancake" helical coil used here consisted of five turns with increasing radii, all turns lying in the same plane. The diameter of the innermost turn was large enough so that the B_2O_3 containment tube could be passed through. A circular copper plate with outer diameter equal to the outermost coil was soldered to the innermost coil and a hole was cut out of the center of the plate with diameter to pass the containment tube. Finally, a thin slot was cut along a radius of the plate at the point where the innermost coil completed its loop and the next coil began in such a manner that only the innermost coil was contacted by the plate.

Induction heating was easily initiated in low resistivity GaAs feed simply by increasing the generator power when the feed was properly positioned in the coil. Two techniques were developed to initiate RF coupling to high resistivity

GaAs feed. In the first, initial coupling was made to the graphite chuck. The GaAs feed rod near the chuck was thereby heated sufficiently so that coupling could be made to the semiconductor. With care, it was possible to move the unmelted but coupled region of the feed to the position where the floating zone was to be initiated. Great care had to be taken when moving the heated region off the chuck to avoid thinning or melting the GaAs near the chuck. In the second, preferred, technique, the encapsulated GaAs feed was heated to 1000°C in the upper auxiliary furnace and quickly repositioned in the RF coil. At this temperature, RF coupling could easily be initiated at any position.

Once induction heating was begun and molten GaAs was formed at a chosen position on the feed rod, the RF power was increased until melt-through was achieved. Melt-through (the presence of a floating zone) was determined when the section of the feed rod above the RF coil could be rotated independent of the lower section. The vapor pressure of As above GaAs at the melting point of GaAs (1238°C) is approximately 0.9 atmospheres. Atmospheric pressure above the encapsulant was not sufficient to prevent the formation of As bubbles, however, because the RF fields coupled only to a "skin depth" of the GaAs and the remaining material was heated to the melt temperature by radiation and conduction. Thus, the GaAs in the "skin depth" had to be heated above the melting point and consequently the As vapor pressure above the melt exceeded one atmosphere. The escape of As at melt-through could be prevented by applying an inert gas overpressure (5 lbs/in² is sufficient) to the B_2O_3 .

Floating zone stability for feed rods of diameter 10 mm or less was quite good. Visual observation of the floating zone shape and frequent checking for the presence of a floating zone were adequate indicators for control of the zone using manual control of the RF power. It was found that the loss of material from a zone too large to be contained by surface tension was not a serious problem. Excess molten GaAs that had broken from the zone froze and was held nearly stationary by the encapsulant. It could often be remelted and rejoined to the zone on a subsequent pass.

The early discovery of the ease with which a large encapsulated floating zone could be contained suggested that zoning at an RF power level significantly greater than that needed for melt-through could be used, thereby eliminating the risk that a small negative RF power perturbation might freeze the feed to the zoned crystal. Although a large zone could be contained, it was not possible

to control the zoned crystal's diameter nor achieve more than a single floating zone pass. The problems arose because a large zone badly sagged, resulting in insufficient melt at the top of the zone. This led to spatial separation of melt and RF coil (if the zone is moving up) or loss of diameter control (if the zone is moving down). Successful multiple-pass float-zoning requires that the RF power level be kept reasonably close to the minimum value necessary for melt-through. This power level produces only a slightly distorted zone which may be recognized visually after some practice.

Early experiments suggested that significantly lower RF power levels are needed for successive floating zone passes. This suggestion was not confirmed by later, more extensive experiments involving as many as ten passes, and the earlier results are now believed to have occurred because the RF generator was operated under conditions of poor stability. Arsenic lost through the B_2O_3 would be expected to lead to Ga enrichment of the zone, so that lower power levels would be needed at the completion of a pass than at the beginning. This does not appear to be a noticeable effect, probably because Ga was also lost to the B_2O_3 . Other workers⁽⁹⁾ have pointed to an interaction of Ga with water vapor in B_2O_3 , and it has been observed in this work that Ga placed in molten B_2O_3 slowly dissolved, thereby coloring the B_2O_3 and rendering it opaque. This tendency for the B_2O_3 to become opaque was also observed during the float zoning of GaAs. Visibility of the floating zone interfaces with solid was often hindered, but seldom completely lost.

A stable floating zone was passed along the feed at a speed ranging from 0.3 to 0.5 inches per hour. In order to use higher travel rates, the RF power had to be very carefully controlled. The floating zone apparatus could be placed in a "hold" position between passes by raising the motion table until the encapsulated GaAs was entirely within the upper, twelve-inch auxiliary furnace. The ends of the furnace could be plugged with insulating wool during the "hold".

After the desired number of passes had been made, the encapsulant had to be separated from the zoned ingot. This was done by gently pulling the ingot up out of the greater part of the encapsulant with the silica pull rod. Much of the encapsulant remaining on the ingot was removed by heating (1000°C) the ingot in the upper auxiliary furnace (with inert gas overpressure) for 12 to 24 hours. The apparatus could then be disassembled and the zoned ingot placed in boiling water until the last traces of B_2O_3 were removed. It was possible to recover

the zoned ingot without cracks or surface damage using this technique.

A further comment on ingot removal is pertinent. Care had to be taken during zoning that the passes did not all end at the same place on the feed rod, because impure, nonstoichiometric material built up in this manner had little structural strength and would break when the feed rod was pulled from the B_2O_3 .

3. Float Zoning Problems Associated with Large Diameter Ingots

One of the most important questions concerning the encapsulated float zone technique is to determine the maximum diameter ingot which may be used. While a great deal of effort has been put forth to develop techniques for zoning large ingots and to answering this question, a final answer was not obtained. We shall discuss here the various problem areas encountered, some possible solutions, and a reasonable estimate for the maximum diameter ingot possible for the B_2O_3 -GaAs system.

In general, zoning of large diameter GaAs was attempted by scaling up the techniques successful for 10 mm diameter feed. This required a scaling up of the fittings holding the containment tube, the silica, and the RF "pie" coil. A containment tube fitting was built using a variety of sleeve sizes to hold containment tubes of various diameters. Problems concerned with the growth and preparation of large GaAs feed rods have been discussed earlier.

A major problem area in zoning large ingots was control of the RF power at a constant value. Since the tuned grid-tuned plate oscillator circuit used in the Lepel is not self-stabilizing, some external control system would be necessary. In addition, it is necessary to learn under what conditions of grid tuning and for what values of tank circuit capacitance and inductance the RF oscillator is inherently most stable. An external control system may be constructed using a conventional set-point null-detector three-action controller technique to regulate an SCR unit which in turn controls the generator's saturable reactors. The difficulty in such a system is to develop a fast, accurate sensor producing a signal proportional to the RF power delivered to the load. Commonly used sensors such as thermocouples and photodetectors are not really applicable here for the following reasons. A thermocouple must be in contact with something heated by the RF fields. Since it is not possible to attach a thermocouple to the GaAs melt, a second load must be placed in the vicinity of the work coil to which the thermocouple may be attached. It was not possible to

construct a load for a thermocouple sensor with fast response time and low noise. A photodetector viewing the molten zone is not practical because of the tendency for the encapsulant to become nonuniformly opaque.

The sensor technique which was used with some success in this work was the RF pickup loop. A copper loop was mounted inside the RF generator near the tank coil and the ac signal induced in the loop was fed to a full wave rectifier. The resulting dc voltage was applied to the set-point unit. A second pickup loop-rectifier system was positioned near the work coil and its output applied to a chart recorder. This second sensor system served as a monitor to assess the performance of the automatic control system. This sensor system produced good control of the RF power for conditions of constant loading.

A photodetector technique, which was not tried but which appears promising, would place a small fluorescent lamp tube upon which a photodetector would be focused near the work coil. The RF fields would ionize the gas in the tube and excite the phosphor which in turn would produce a signal in the photodetector. Such a system would be "fast" and would produce a signal proportional to the induced fields.

Any RF sensor system which does not directly measure some quantity proportional to the power into the work piece is not suited for use with a fluctuating RF load impedance. In any RF heating application, a fraction of the fields produce heating of the work and the remaining fraction is radiated into space. Only if this fractional relationship stays constant will a sensor accurately reflect the power into the load. Thus, the pickup loop sensor, and the fluorescent lamp-photodetector sensor would not enable a controller to produce constant power to the load when the load impedance is not constant. Under certain conditions, floating zone growth of GaAs does not produce constant loading. Changes in zone shape result from power perturbations and effect coupling to the load. Rotation of the feed to confirm melt-through also changes loading if the feed is slightly off center, as was often the case. There are many other effects that can produce changes in loading. It can be seen that any change in loading produces a feedback loop which drives the power further from set point. For example, an increase in melt size, due perhaps to the motion of much of the zoned ingot into the hot lower auxiliary furnace, would increase the loading. The radiated fraction of the RF field would thus decrease. This decrease would be interpreted by the sensor as a decrease in power delivered by the generator. The controller

would increase the generator power, producing increased melt and further increased coupling to the load.

The choice of generator frequency is quite important in encapsulated float zoning and involves an important tradeoff. As frequency increases, the RF fields become more tightly confined around the work coil and the "skin depth" of the work is more shallow. These effects help greatly when initiating a melt, for only a very limited amount of GaAs couples well to the fields and is heated to the melting point. Thus, the amount of melt closely follows the applied power as melt-through is approached. There are several disadvantages inherent in high frequencies. The RF coupling to the load is very sensitive to geometry and slight changes in position greatly affect coupling. In addition, the shallow "skin depth" means that a large surface area must be melted to generate the heat needed for melt-through. This produces a long zone which has a strong tendency to become unstable. On the other hand, at lower frequencies, with more diffuse fields and deeper "skin depth", the power level must be high to initiate a melt since a large amount of feed must be heated to near the melting point. The power must be decreased quickly as the first material melts, because the increased coupling into melt relative to solid focuses the RF fields and the zone size is rapidly out of control. The high power and more diffuse fields also greatly increase the risk of coupling to the auxiliary furnaces. However, once a molten zone is established, it is generally short, stable, and relatively insensitive to geometry. Therefore, if a pickup loop control system is used, lower frequencies are necessary. In practice, frequency must be picked to give the best tradeoff of the various effects.

Experiments pointed up several minor points pertinent to the zoning of large diameter GaAs ingots. Feed rods of round cross section should be used instead of rods with square cross section because the corners of the square feed do not readily melt down. In addition, there should be several millimeters free space between the silica containment tube and the circular plate of the "pie" coil. This prevents the zone from approaching too close to the coil and being distorted by coupling with the RF lead connecting the innermost coil to the generator. Further attempts should be made in any future apparatus to improve centering for the silica pull rod.

4. Summary of Experiments: Successes and Failures

The encapsulated floating zone experiments performed are described here. The experiments, with various successes and failures, are outlined in Table III. A short summary of the table is given here. Experiments FZ-1 through FZ-9 were devoted to development of the mechanics of encapsulated float zoning, i.e., the procedures for drying B_2O_3 , introducing the feed rod, passing a floating zone several times along the length of the feed, and removing the zoned ingot intact from the encapsulant. This work was considered successfully completed following experiments FZ-8 and FZ-9, in which an ingot 8 mm in diameter was zoned six times and an ingot 10 mm in diameter was zoned ten times, respectively. Ingot FZ-8 is shown as grown, after sandblasting to reveal grain structure, and after lapping to show grain structure of a cross section in Figures 5, 6 and 7. Figure 8 shows the ingot FZ-9 as grown. Experiments FZ-10 through FZ-13 were attempts to increase the maximum diameter feed rod which could be zoned in the B_2O_3 -GaAs system. These experiments showed that the dominant experimental parameter effecting zone stability was the RF generator frequency. On several occasions, stable zones were carried for short distances in 13 mm feed rods (see Figure 9, for example). An attempt to move a stable zone through a 15 mm feed rod was not successful, although 15 mm feed may be possible with appropriate modifications of technique and apparatus.

5. Characterization of Encapsulated Float Zoned GaAs

Several GaAs ingots through which a stable floating zone was passed several times were characterized with respect to crystallinity and purity. In general, it appeared that the number of grains increased with the number of floating zone passes. This conclusion is derived from the following observations. In FZ-4, a single crystal GaAs feed rod was submitted to a single floating zone pass through a section of the feed. It was found that the zoned section remained single crystalline. However, FZ-8 and FZ-9, which initially had a seed section of but one or two grains, show that polycrystalline GaAs was produced with repeated passes. Comparison of FZ-8 with FZ-9 suggests that the grain size decreased for a greater number of passes. It is not clear what was causing nucleation of additional grains. We believe, however, that they were caused by fluctuations in the growth rate produced by changes in RF power, since the grains did not appear to originate at the GaAs- B_2O_3 interface. This interpretation is further

TABLE III. SUMMARY OF LIQUID ENCAPSULATED FLOATING ZONE EXPERIMENTS

Experiment Number	Successful Aspects	Unsuccessful Aspects
FZ-1	Assembly of apparatus with moving encapsulated GaAs rod, stationary auxiliary furnaces and RF coil. Familiarity with silica, graphite chuck, sample preparation.	Inadequate heating from auxiliary heaters to remove water from B ₂ O ₃ . Insufficient B ₂ O ₃ in containment tube, difficulty lowering GaAs rod into B ₂ O ₃ . Failure when silica broke out at bottom.
FZ-2	Redesign dry nitrogen input section of silica. Rebuild various mechanical parts. Weigh out correct volume of B ₂ O ₃ and modify graphite chuck to ease lowering of GaAs rod. A work coil was found which eliminated arcing from RF coil to other pieces of apparatus. Successfully carried molten zone ~1 1/2 inches.	B ₂ O ₃ leaking into dry nitrogen capillary forced dry N ₂ shutdown. Auxiliary furnaces still inadequate to dry B ₂ O ₃ . GaAs rod broken from graphite chuck prevents removal.
FZ-3	Rewound auxiliary furnaces with Hoskins 875 high temperature wire and built variac units to apply 210 V power to furnaces. Adequate drying of B ₂ O ₃ using auxiliary furnaces. Two passes of the floating zone and recovery of the crystal. Hall effect and mass spectrometer data.	B ₂ O ₃ leaking into capillary produces another failure of dry N ₂ drying. Continual loss of As bubbles from GaAs-B ₂ O ₃ interface. Drift of RF generator across floor.
FZ-4	Anchor RF generator to floor. Construction and successful use of 12-inch auxiliary furnace to replace 6-inch furnace. Modification of apparatus to apply He gas overpressure. Procedure found to avoid B ₂ O ₃ leaking into capillary. Successful control of As bubbles by applied overpressure.	Broke GaAs feed rod from graphite chuck upon lowering into B ₂ O ₃ . Incomplete melt-through and only a single pass.
FZ-5	Develop precision threads for feed rods. Successful techniques for lowering GaAs feed rod into B ₂ O ₃ as routine procedure. Successful drying of B ₂ O ₃ with no provisions for or use of dry N ₂ gas. One pass through feed rod under He gas overpressure.	Mistake of As bubbles for H ₂ O bubbles resulted in reapplication of vacuum and distribution of B ₂ O ₃ over much of the silica. B ₂ O ₃ froze and broke up silica. The feed rod could not be recovered. Feed rod tipped to side during melt-through.

TABLE III. (Continued)

Experiment Number	Successful Aspects	Unsuccessful Aspects
FZ-6	Redesign of auxiliary furnaces to prevent B_2O_3 solidification. Redesign of bottom of silica to provide GaAs feed rod support after melt-through. One pass through feed rod under He overpressure.	Failure to control zone diameter so that a second pass would be possible. Impossible to recover GaAs because of separation of ingot from chuck due to excessive heating.
FZ-7	Control of zone diameter to permit three passes. Discovery of apparent variation in RF power necessary for successive floating zone passes.	GaAs feed rod broke from chuck because of build up of structurally unsound material at position where floating zone passes ended.
FZ-8	Control of floating zone adequate for six passes; ingot diameter 8 mm. Successful recovery of zoned ingot from B_2O_3 . Evidence of purification from decreasing ease of coupling RF fields to GaAs. Hall effect and mass spectrometer data.	Zoned material has tendency to tip to side because the feed is poorly fit to bottom silica. Necessary to melt GaAs out of bottom silica fitting to remove ingot from B_2O_3 . Zoned material polycrystalline.
FZ-9	Floating zone passed through a high purity Bridgman-grown feed rod ten times; ingot diameter 10 mm. Successful recovery of zoned ingot from B_2O_3 . Hall effect and mass spectrometer data.	Tendency of zoned part of feed rod to tip to side, again due to poor bottom fittings. Continued evidence for self-nucleation of new grains during zoning. Slight chipping of ingot surface due to failure to remove all of B_2O_3 from ingot while in upper auxiliary furnace.
FZ-10	Growth and fabrication of larger diameter feed rods. Successful operation of new fittings with variable sleeves for use with GaAs feed rods from 10 mm to 20 mm. Floating zone moved for 1.6-inch along feed with a diameter of 13 mm.	Problems with initiating zone at 4.2 megahertz. Oscillator power instability produces freezing of zone; coupling into auxiliary furnace at high RF power levels produces arcing and destruction of 12-inch auxiliary furnace and control circuitry. Failure of RF generator heat exchanger. Loss of GaAs ingot.

TABLE III. (Continued)

Experiment Number	Successful Aspects	Unsuccessful Aspects
FZ-11	Develop understanding of use of automatic controller with a GaAs load. Familiarization with generator operation at 6.2 megahertz at various points on the grid tuning-power curve.	Automatic controller does not work well at 6.2 megahertz with GaAs load. Stable floating zone could not be obtained on either automatic or manual power control. Attempts to control power by maintaining constant frequency do not work.
FZ-12	Realization of the importance of RF generator frequency to obtaining a stable floating zone. A stable zone was passed for approximately a zone length along 13 mm diameter feed at 4.25 megahertz.	Unable to obtain a stable zone at 5.15 megahertz through 13 mm diameter feed rod.
FZ-13	None	Unable to obtain a stable zone at 4.05 megahertz with 15 mm diameter feed rod.

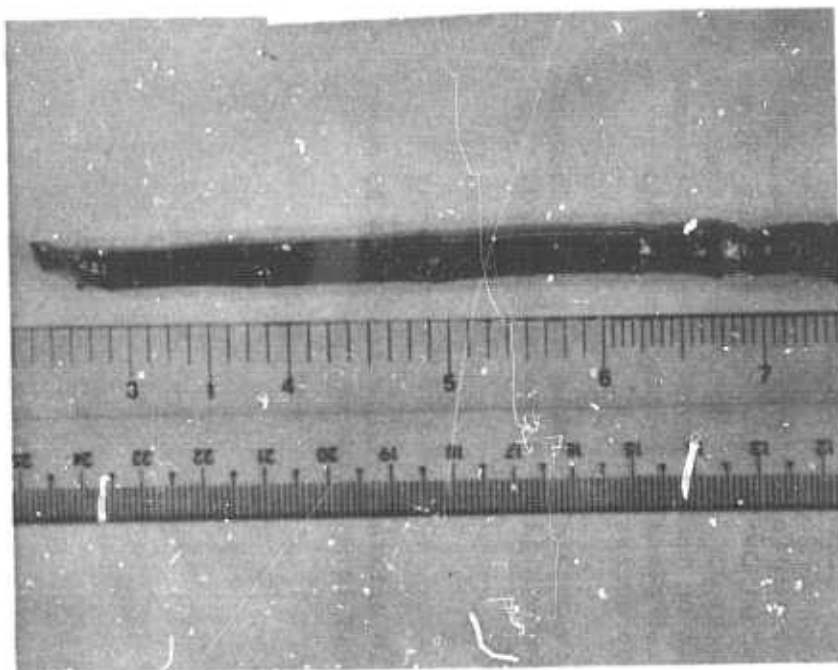


Figure 5. FZ-8 after 6 floating zone passes.

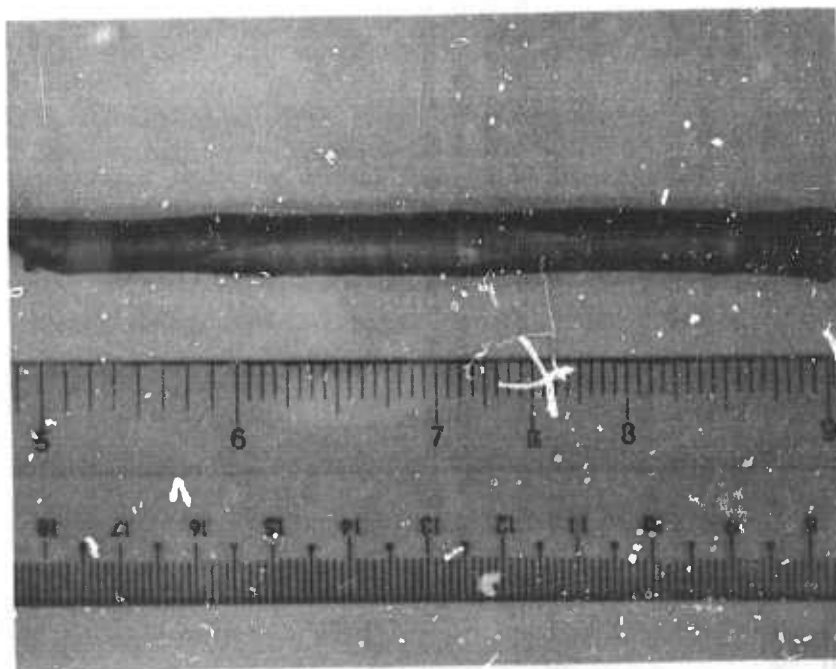


Figure 6. FZ-8 sandblasted to show grain structure.

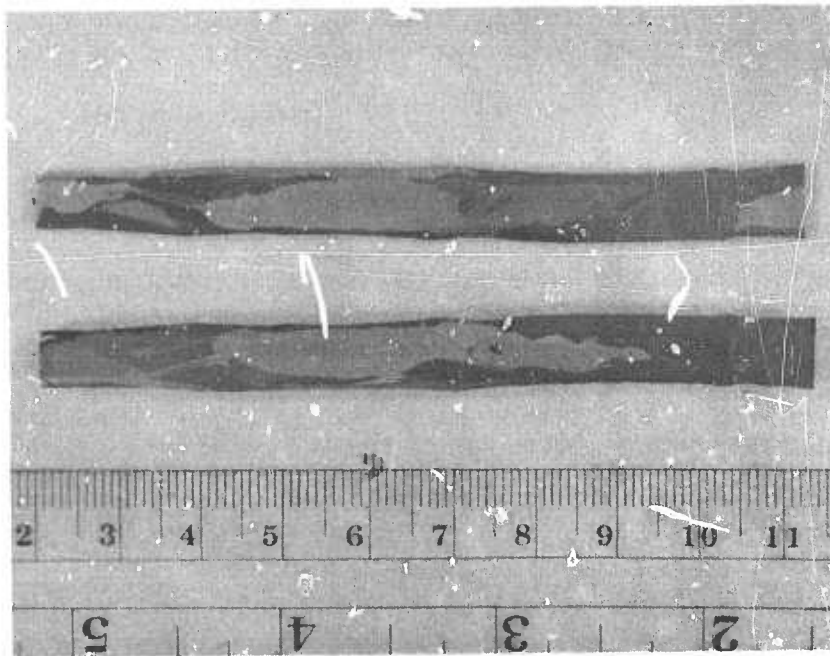


Figure 7. Sectioned FZ-8.

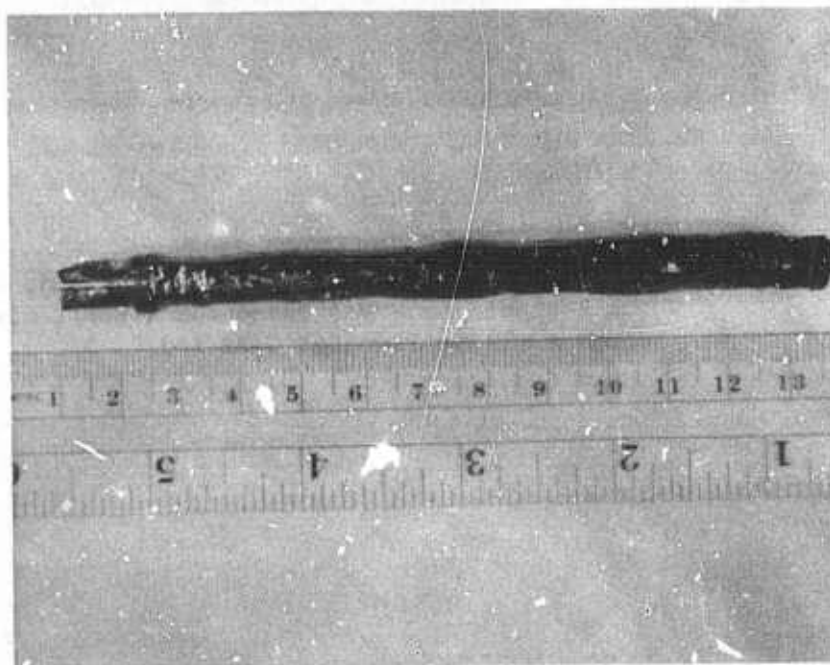


Figure 8. FZ-9 after 10 floating zone passes.

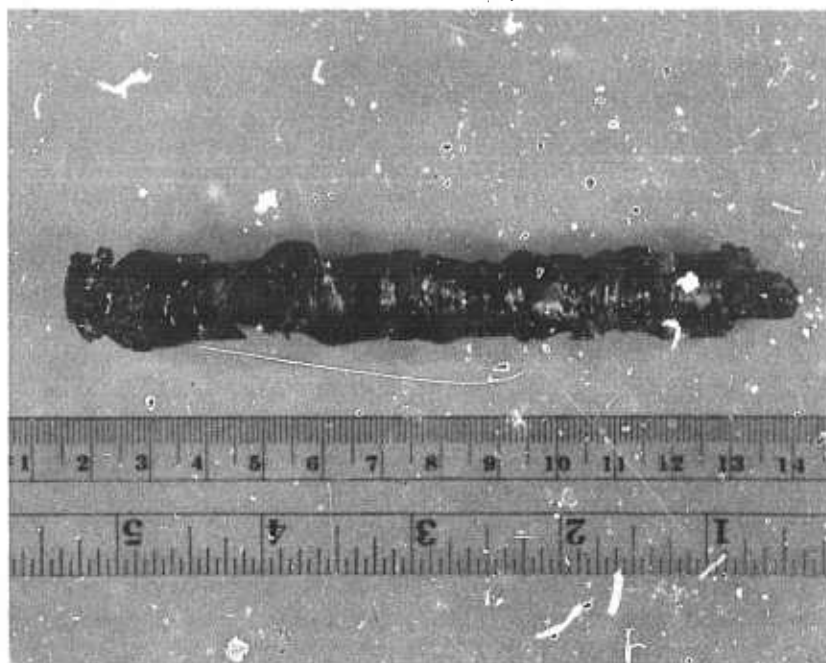


Figure 9. FZ-12 showing two regions, one at each end, in which a stable zone was moved for a short distance through a ~13 mm diameter GaAs rod.

supported by the fact that single crystals of GaAs can be grown using the liquid encapsulated Czochralski technique in which molten B_2O_3 , molten GaAs, and the growing GaAs crystal are all in contact.

The effects of encapsulated float zoning on GaAs purity were studied primarily by comparing the data from Hall effect measurements and mass spectro-metric analyses for material prior to and after zoning. Since it has been established in previous work that very high purity GaAs can be obtained by float zoning,⁽¹⁵⁾ this work attempted to determine the effect of the encapsulant on purity.

A qualitative answer is suggested from the fact that the GaAs feed rod of carrier concentration $\sim 10^{18}/\text{cm}^3$ coupled with ease to the RF fields without additional heating. After several floating zone passes coupling became quite difficult. This implies that $\sim 10^{18}/\text{cm}^3$ shallow impurity states were either being removed by float zoning or compensated by impurities from the B_2O_3 . The manufacturer's mass spectroscopy data for B_2O_3 and the growth of reasonably pure GaAs by the encapsulated Czochralski technique both show that impurity of this concentration is unlikely. A crude upper limit for B_2O_3 contamination may be placed at $\sim 10^{17}/\text{cm}^3$ based on these observations.

Optical absorption spectroscopy measurements on samples from experiment FZ-3 were compared with those for unzoned material from the same Bridgman-grown ingot. Both samples showed carbon and boron impurity concentrations below the detectability threshold. Although these thresholds are quite high ($\leq 10^{18}/\text{cm}^3$) for this method of analysis, the results are not insignificant, since carbon concentrations large enough to be detected have appeared in "as grown" GaAs from the liquid seal Czochralski apparatus, as discussed in Section VI.B. The results for boron are also important because they show that very large concentrations of boron were not being introduced from the B_2O_3 .

Samples for Hall effect measurements and mass spectrometer analyses were taken from the zoned ingot near the beginning of the floating zone pass. The comparison sample was taken from a similar position in the Bridgman-grown ingot from which the feed rod was cut. The floating zone passes were usually started at what would correspond to the seed end of the Bridgman ingot. Results for experiments FZ-8 and FZ-9, for which the procedures for encapsulated zone growth were well developed, are regarded with greatest confidence.

Hall effect data at room temperature for samples from three experiments are shown in Table IV. Samples were in the form of GaAs bars of dimensions 2 mm x 3 mm x 20 mm to which indium contacts were alloyed. Although the floating zone samples were polycrystalline, an effort was made to place a single grain between the Hall voltage contacts. Current flow through the long sample dimension was often difficult to obtain for polycrystalline samples, especially with the purest samples. Thus, the results for carrier concentration are believed to be reasonably accurate while the mobility values are lower limits due to uncertain influence of grain boundaries on resistivity.

FZ-8 showed a decrease in carrier concentration after six floating zone passes by a factor of ten, from $10^{18}/\text{cm}^3$ to $10^{17}/\text{cm}^3$. FZ-9 showed only a slight decrease in carrier concentration when the initial feed material was quite pure ($\sim 5 \times 10^{15}/\text{cm}^3$) for as many as ten floating zone passes.

TABLE IV. HALL EFFECT DATA FOR EXPERIMENTS FZ-3, FZ-8, AND FZ-9

Sample	Number of Passes	Carrier Concentration cm^{-3}	Mobility $\text{cm}^2 \text{ volt}^{-1} \text{ sec}^{-1}$
Feed for FZ-3	0	1.7×10^{18}	?
FZ-3	2	5×10^{17}	?
Feed for FZ-8	0	1.4×10^{18}	2000
FZ-8	6	1.6×10^{17}	3250
Feed for FZ-9	0	6×10^{15}	4400
FZ-9	10	3×10^{15}	?

Mass spectrometer analyses were performed under subcontract to the Battelle Columbus Laboratories by Mr. Dennis C. Walters, Research Chemist, Analytical Chemistry Division. The data, in ppm atomic, is shown in Table V. The lowest values listed in the table are comparable with the mass spectrometer sensitivities for GaAs given by Kane and Larabee.⁽¹⁶⁾ A mass spectrometer analysis of "Optran" grade B_2O_3 furnished by the manufacturer is also shown. As is common for mass spectrometer work, the elements C, O, N and the rare gases were not determined. Concentrations per cm^3 for GaAs may be obtained by multiplying

TABLE V. MASS SPECTROMETRIC ANALYSES OF FLOATING ZONE
FEED RODS, ZONED RODS, AND B_2O_3 ENCAPSULANT

Element	Feed FZ-3	Δ	Feed FZ-8	FZ-8	Δ	Feed FZ-9	FZ-9	Δ	Lowest Value Listed	B_2O_3
Li	<0.03	--	0.2	<0.03	-7	<0.03	<0.1	+3	<0.03	?
Be	0.32	+2.5	<0.08	<0.16	+2	<0.08	<0.024	-3	<0.024	< 0.02
B	<0.012	+1000	0.05	5	+100	0.03	0.6	+20	<0.012	--
Mg	<0.12	+2.5	0.6	0.09	-7	0.06	0.03	-2	0.03	< 0.2
Al	0.3	+2	0.3	0.5	+2	0.13	0.13	--	0.3	20
Si	5	--	2.5	2.5	--	<2.5	5	+2	0.5	40
P	0.1	+2	<0.01	0.23	+23	0.023	0.046	+2	<0.01	0.6
S	0.45	--	4.5	1.6	-3	0.45	0.45	--	<0.01	<10
Cl	0.4	+25	2	0.1	-20	0.2	0.1	-2	0.04	8
K	0.05	+8	1.2	1.2	--	0.04	0.2	+5	0.04	5
Ca	0.05	+7	0.35	0.035	-10	0.01	0.035	+3	0.01	2
Ti	<0.01	+10	0.03	0.06	+2	0.03	0.06	+2	<0.01	0.2
Cr	<0.03	+10	0.15	0.15	--	1.0	0.06	-17	0.015	0.02
Mn	<0.025	+3	<0.01	0.01	--	<0.01	<0.01	--	<0.01	0.02
Fe	0.25	+10	0.5	0.25	-2	0.25	0.25	--	0.25	0.2
Co	0.01	+10	<0.01	<0.01	--	<0.01	<0.01	--	<0.01	0.02
Ni	0.05	--	<0.01	0.02	+2	<0.01	0.06	+6	<0.01	0.3
Cu	0.02	--	<0.2	<0.02	-10	<0.01	<0.01	--	<0.01	0.18
Zn	8	--	<0.08	0.11	+1.5	0.04	<0.08	+2	0.02	< 0.04
Ge	<0.3	--	<0.3	<1.0	+3	<1	<0.5	-2	<0.3	< 0.08
Rb	<0.2	--	<0.2	0.3	+1.5	<0.1	0.2	+2	<0.04	< 1.0

TABLE V. (Continued)

Element	Feed FZ-3	FZ-3	Δ	Feed FZ-8	FZ-8	Δ	Feed FZ-9	FZ-9	Δ	Lowest Value Listed	B ⁰ ₂₃
Nb	<0.03	< 0.03	--	< 0.03	0.075	+2.5	<0.1	<0.1	--	<0.03	< 0.04
In	<0.03	0.3	+10	< 0.01	<0.01	--	<0.01	<0.01	--	<0.01	< 0.1
Sn	<0.04	< 0.04	--	0.04	0.12	+3	<0.03	<0.03	--	<0.03	< 0.06
Sb	<0.02	< 0.02	--	2.0	<0.02	-100	<0.02	<0.02	--	<0.02	< 0.1
Te	<0.03	< 0.03	--	20	0.1	-200	<0.03	<0.03	--	<0.03	< 0.06
Ta	<0.05	< 0.15	+3	< 0.15	<0.15	--	<0.15	<0.15	--	<0.15	?

the values in the table by 4.4×10^{16} . Only those elements are listed for which different concentrations were found for at least one of the three comparisons.

The following observations and conclusions may be taken from the data in Table V. 1) Boron contamination of GaAs occurred for all three cases and was certainly to be expected. The boron concentration appeared to saturate in the $10^{16}/\text{cm}^3$ to $10^{17}/\text{cm}^3$ region for experiments FZ-8 and FZ-9. There is every reason to suspect the oxygen concentration was also high. 2) Elements in addition to B which appeared to increase in concentration following zoning are P, K, Ca, Ti, and Ni. 3) Comparison of impurity concentrations for B_2O_3 and GaAs feed shows that Al, Si, S, Cl, K, Ca, and Rb might be expected to produce high levels of contamination. Ti, Ni, Cu, In, Sb, and Cs concentrations were also typically somewhat higher in B_2O_3 than in GaAs. 4) Elements which typically have comparable concentrations are Mg, Mn, Fe, Co, Nb, Sn, and Te. B_2O_3 impurities which would not be expected to contaminate GaAs are P, Be, Cr, Zn, and Ge.

Prediction of contamination effects based on impurity concentrations for B_2O_3 and GaAs requires knowledge of the impurity solubilities and effective distribution coefficients for the two materials. Only qualitative guesses are possible without this information. Of the six elements which appeared to increase, only P is believed to have been present in lower concentrations in B_2O_3 than in GaAs. The "leeching" of phosphorus into GaAs may be understood in terms of the greater than unity distribution coefficient for P in GaAs. and the fact that GaP is miscible in GaAs. It is not clear why contamination by Al, Si, S, Cl, or Rb was not observed. While the concentrations of Al and Si did not go up, they did not go down appreciably either, as their distribution coefficients suggest they should. ⁽⁴⁾ It may be that Al and Si existed as Al_2O_3 and SiO_2 in B_2O_3 and did not enter GaAs to a more significant degree because of the high stability of these oxides. A balance between contamination and purification appears to have occurred. Solubilities, effective distribution coefficients, and relative stabilities of possible compounds all influenced the final impurity concentration.

The purification effect of float zoning for elements with low distribution coefficients in GaAs where other effects do not interfere is shown for Sb and Te in experiment FZ-8. The purification of these elements is to be contrasted to that for Si. It is also seen that mass spectrometry loses much of its value as a characterization tool for the high purities used in experiment FZ-9 because many of the elements are at their detection limits.

The Hall effect and mass spectrometer data from experiments FZ-8 and FZ-9 which are presented here show clearly that purification did occur during encapsulated float zoning, but that the limiting purity level was approximately that of good undoped Bridgman-grown GaAs. It is significant that Si, an important impurity present in Bridgman-grown GaAs, is also a major impurity in commercial encapsulant-grade B_2O_3 , and that float zone refining GaAs using this encapsulant does not reduce Si concentrations.

Whelan and Wheatly⁽¹⁵⁾ showed that very pure GaAs ($\sim 10^{14}$ carriers/cm³) can be obtained by float zoning in a hot As atmosphere of GaAs feed prepared by the horizontal Bridgman technique. Distribution coefficients for impurities in GaAs are greater than unity only for Be and P.⁽¹⁷⁾ Both of these elements were present at levels of 10 to 50 parts per billion atomic in B_2O_3 sold for encapsulation purposes, which was designated 0.9995% pure. B_2O_3 powders with purities of five and six nines are commercially available. Thus, there appears to be no conceptual reason why high purity bulk GaAs should not be possible using the encapsulated float zone technique if high purity B_2O_3 is used as encapsulant.

6. Conclusions and Future Potential for the Technique

It is our belief that the encapsulated float zone technique has shown considerable promise as a special purpose crystal growth technique. However, a considerable amount of development work remains to be done to produce large size, high purity, single crystal GaAs. We have shown that GaAs ingots up to approximately 15 mm diameter can be immersed in encapsulant, float zone purified, and removed intact from the encapsulant. The maximum diameter previously possible using a hot As atmosphere floating zone apparatus was ~ 8 mm. The increase in circular cross-sectional area for encapsulated float zoning is 3.5 using a B_2O_3 encapsulant. There are several good reasons why development of this technique should continue. First, the technique is one of few with the potential of producing high purity, bulk GaAs. Theoretically, the ingot diameter may be as large as desired if the encapsulant and GaAs densities are equal, and thus the technique might be capable of producing large diameter GaAs infrared window material. In general, the development of a semiconductor growth technology which produces high purity bulk material has permitted new uses for the semiconductor.

Second, the technology developed here should be applicable to any volatile semiconductor or other material whose vapor pressure at the melt temperature is on the order of a few atmospheres. The most important class of materials would be the arsenic and phosphorus alloy semiconductors. In addition, it should be possible to modify the present liquid encapsulant system for the solution growth of GaP from an encapsulated Ga zone traveling through GaP feed at lower temperatures and phosphorus pressures than possible with melt growth. GaP grown by this new method should have the high luminescence efficiencies typical of solution grown material.

C. Vitreous Boron Oxide: Drying and Moisture Absorption

(C. E. Chang and W. R. Wilcox)

As noted in the preceding two sections and in the literature,^(9,12) moisture in boron oxide can be extremely deleterious to GaAs crystal growth. Therefore we studied methods of drying reagent-grade boron oxide and moisture absorption by vitreous boron oxide.^(13, Appendix 1) Frothing during heating can be avoided by a preliminary vacuum bake-out. Trace water is removed faster by bubbling dry nitrogen through molten boron oxide than by exposing it to vacuum, because of its high viscosity. At room temperature moisture is absorbed at the surface, at first in a diffusion-limited coherent layer and later as cracked boric acid. This surface moisture could be removed in a vacuum at room temperature, with two rate constants, 1.21 hr^{-1} and 0.216 hr^{-1} .

D. Horizontal Bridgman Growth

(T. Penna, E. Johnson and W. Allred)

Although developed prior to initiation of this grant, a horizontal Bridgman technique has been used for preparation of some of the crystals used here, and so it is appropriate to give a brief description of it now. Growth of partially dislocation-free GaAs by a similar technique was reported in the recent literature.⁽¹⁸⁾

Our furnace was constructed of Super-Kanthal elements, with the insulation removed in a strip along the top to allow positioning of fused silica view ports, enabling continuous viewing of the solid liquid interface position and approximate shape. The heating elements were surrounded by fire-bricks and

enclosed in a box of transite. The furnace was mounted on wheels which permitted movement along a rail, as shown in Figure 10. A sealed ampoule containing the growth boat was held in a stationary alumina tube, with a slot cut along the top, again to allow direct viewing of the interface.

In a growth run, gallium was initially loaded into the boat and arsenic was placed separately in the evacuated ampoule. The furnace was positioned such that the boat was under the two right view ports. The thermocouple inserted in the end and located at the seal regulated zones 1 and 2. It was initially set at 550°C and the temperatures in zones 3, 4 and 5 slowly increased until they exceeded 550°C , with 5 being at 900°C . Temperatures in all zones were gradually increased until all the arsenic had been transported to the boat and finally molten GaAs was present. The temperature at the seal was held at 635°C thereafter to prevent arsenic condensation there, which would cause breakage due to thermal expansion. The temperatures in 3, 4 and 5 were adjusted until a solid-liquid interface was in view and was slightly convex. The furnace was moved until all the solid was molten, allowed to sit for 10 hours, and then slow motion begun. Not only GaAs, but several other III-V's and dilute alloys have been prepared in this furnace.

E. Vertical Gradient-Freeze Crystal Growth of GaAs

(V. F. S. Yip and W. R. Wilcox)

Cylindrical rods of GaAs were needed for use as feed material in the liquid encapsulated floating zone melting and traveling heater method experiments. It was found that 1 cm diameter by 16 cm long rods could easily be cast by a vertical gradient-freeze technique.^(19,20) Either pre-reacted GaAs or elemental Ga and As were loaded into a 20 cm long fused silica tube closed at one end. This tube was then sealed in vacuum inside a 1.3 cm inside diameter by 45 cm long silica tube. This ampoule was placed inside a resistance heated furnace such that the maximum temperature was just above the surface of the GaAs. An auxiliary furnace at the top of the ampoule was used to control the total arsenic pressure. Slowly turning the furnace power down resulted in directional solidification of the GaAs melt.

Roughly the top half of each ingot was a single crystal, or occasionally a bi-crystal. Although the containing tube nearly always cracked badly, few or

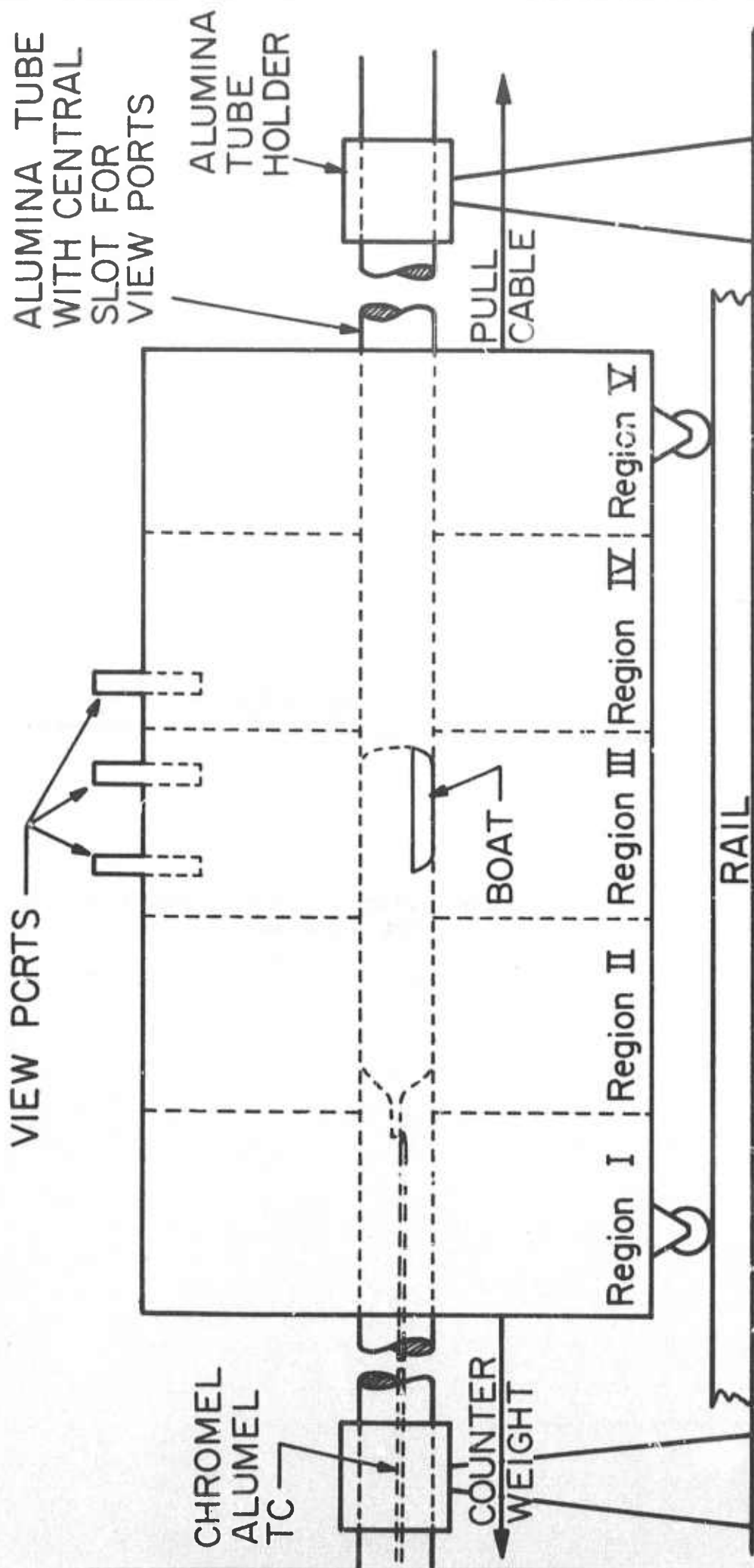


Figure 10. Diagram of the horizontal Bridgman apparatus.

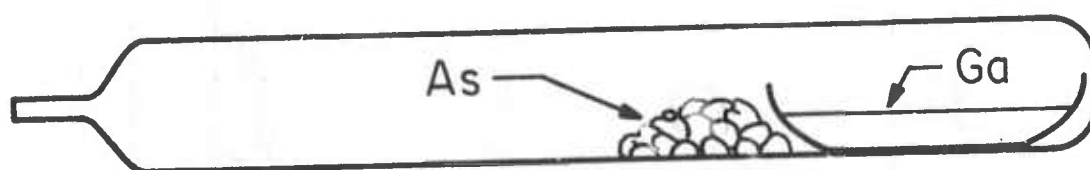


Figure 11. Diagram of initial loading of the growth ampoule.

little fractures were produced in the crystals. Cracking was avoided entirely by carbon coating the interior of the containing tube. Gas bubbles were often found at the periphery of the ingots. Occasionally there was a narrow central void, probably also due to gas. Dislocation densities ranged from 10^5 to $10^7/\text{cm}^2$.

Representative data on our gradient freeze runs are given in Tables VI-IX. When elemental Ga and As were used as starting materials, less Si was introduced into the gradient freeze crystals than into horizontal Bridgman and Czochralski crystals, probably reflecting the shorter time the material was molten. Cathodoluminescence showed that the gradient freeze crystals were inhomogeneous, probably indicating some interface breakdown due to the rapid freezing rates.

Although the purpose of these experiments was not to grow single crystals, they indicated that the vertical gradient freeze technique may be very useful for that. As noted in Section IV.A.2, selected cooling of the bottom of the ampoule should produce a convex interface and more rapid grain selection, so that a greater length of single crystal could be produced. Seeds could be employed. Much slower solidification rates should also be employed if high quality crystals are desired. These experiments indicate that the vertical gradient freeze technique, and probably also the vertical Bridgman-Stockbarger technique, could be employed to produce large GaAs crystals.

TABLE VI. TYPICAL GaAs INGOTS GROWN BY VERTICAL GRADIENT FREEZE METHOD

<u>Ingot</u>	<u>Starting Material</u>	<u>Cooling Rate</u>	<u>Results</u>
GF-1	Horizontal boat grown GaAs (undoped).	$3^\circ\text{C}/\text{min.}$	N-type, low resistivity.
GF-25	Czochralski grown GaAs (undoped).	$3^\circ\text{C}/\text{min.}$	N-type, low ρ .
GF-30	Six nines purity Ga + As.	$0.3^\circ\text{C}/\text{min.}$	N-type, high ρ .
GF-31	Six nines purity Ga + As.	$0.3^\circ\text{C}/\text{min.}$	N-type, low ρ .
GF-32	Czochralski grown undoped GaAs.	$0.3^\circ\text{C}/\text{min.}$	N-type, low ρ .

TABLE VII. HALL MEASUREMENT RESULTS FOR GRADIENT FREEZE GaAs CRYSTALS GROWN FROM DIFFERENT STARTING MATERIALS

Crystal	Resistivity, ρ $\Omega\text{-cm}$	Carrier Concentration cm^{-3}	Electron Mobility $\text{cm}^2/\text{volt-sec.}$
HBT-1 (Horizontal Bridgman)	0.0130	$2.75 \times 10^{17} \text{ n}$	1750
GF-1 (Grown from HBT-1)	0.0130	$3.00 \times 10^{17} \text{ n}$	1600
GF-1A (Grown from GF-1)	0.0100	$1.67 \times 10^{17} \text{ n}$	3747
GF-25 (Grown from Czochralski feed)	0.0336	$1.00 \times 10^{17} \text{ n}$	1890
GF-31 (Grown from Ga + As)	0.0164	$1.53 \times 10^{17} \text{ n}$	2500

TABLE VIII. SPECTROCHEMICAL ANALYSES OF GRADIENT FREEZE GaAs

Element	GF-1 wt. %	GF-25 wt. %	GF-30 wt. %	GF-31 wt. %
Ga	Rem.	Rem.	Rem.	Rem.
As	49	49	48	48
Si	nil	TR < 0.002	nil	nil
Mg	nil	TR < 0.0001	nil	nil
Cu	ND < 0.00002	0.000058	0.000041	0.000049
Ca	0.00022	0.00045	0.00021	0.00042
Li	ND < 0.005	ND < 0.005	ND < 0.005	ND < 0.005
Te	ND < 0.10	ND < 0.10	ND < 0.10	ND < 0.10
Other Elements	nil	nil	nil	nil

ND = not detected
TR = trace

TABLE IX. MASS SPECTROMETRIC ANALYSES OF GaAs GROWN BY GRADIENT FREEZE, HORIZONTAL BRIDGMAN AND LIQUID-SEAL CZOCHRALSKI TECHNIQUES

Element (ppm w)	GF-30	GF-31	HB-105	CZ-169
Li	< 0.003	< 0.003	< 0.003	< 0.003
Be	0.04	0.07	0.01	0.04
B	< 0.05	0.003	0.002	0.006
Mg	< 0.3	0.1	< 0.3	< 0.3
Al	< 0.1	< 0.04	< 0.07	< 0.07
Si	0.1	0.1	0.04	0.1
Cl	0.7	0.2	4	2
K	0.02	0.05	0.05	0.05
Ca	0.06	0.06	0.06	0.06
Cr	< 0.03	0.02	0.02	0.03
Mn	< 0.02	0.02	< 0.01	< 0.01
Fe	0.2	0.3	0.2	0.2
Co	0.03	0.02	< 0.01	< 0.01
Ni	0.1	0.06	0.03	0.02
Cu	0.6	0.04	0.02	0.04
Zn	0.2	0.1	0.1	0.2
Sn	0.1	< 0.06	< 0.06	< 0.06
Te	< 0.06	< 0.06	< 0.06	2
Pb	0.6	< 0.06	< 0.06	< 0.06

F. Traveling Heater Method Solution Growth

(V. F. S. Yip and W. R. Wilcox)

In the traveling heater method, a solvent zone is caused to move through a solid by means of movement of a heater. Essentially it is zone melting with a solvent zone rather than a melt zone. We have grown 1 cm diameter GaAs, $\text{Ga}_{1-x}\text{In}_x\text{Sb}$ and $\text{Ga}_{1-x}\text{Al}_x\text{As}$ by this technique, using a 1 cm long Pt-10% Rh resistance heater on a silica tube surrounded by bubbled alumina insulation. The zone could be viewed before and after runs by removal of the bubbled alumina. Correct preparation of the ampoule for experiments was a non-trivial process which required considerable experimentation to perfect, as described elsewhere. (20)

1. THM GaAs

Rather than merely grow crystals, experiments were performed to increase our understanding of the THM technique, as described in Tables X-XIV. The optimum heater temperature was about 980°C with a maximum travel rate of 1.5 mm/day. Inclusion formation due to constitutional supercooling increased as temperature decreased and travel rate increased. At a heater temperature of 1100°C , inclusion-free growth was obtained at a lowering rate of 20 mm/day. Higher temperatures result in higher impurity contents in the crystals, and heater temperatures above 1100°C caused the ampoule to stick to the heater tube and shortened the life of the heater.

When the seed below the heater was less than about 1 cm, the zone was shifted downward, which is a heat transfer effect. Likewise when the seed rod above the heater was less than about 2 cm, the zone was shifted upward. Thus a seed length of 1 cm and a feed length of over 2 cm were best for our apparatus, in order to avoid end effects.

A convex growing interface was found to be best for grain selection (see Section IV.A), although when the interface was strongly convex, twins were generated at the periphery with a $\langle 111 \rangle$ growth direction. Thus a slightly convex interface is recommended, and was achieved by having the solvent zone slightly shorter than the heater length (1 cm).

TABLE X. SUMMARY OF EARLY TRAVELLING HEATER EXPERIMENTS ON GaAs (JULY 1970-JUNE 1971)

Run THM No.	Heater Temp.	Original Seed length (cm)	Original Ga Zone length (cm)	Original Feed length (cm)	Lowering Rate (mm/day)	Results
1	1000°C	0.6 <111> direction	0.3	4.2	4.7	Seed was dissolved. Growth started by self-seeding and grains grew inwards towards center where Ga inclusions were found. Total growth about 3.5 cm.
2	1010°C	0.6 <111>	1.0	2.5	4.7	Seed dissolved. Self-seeded polycrystal measured 2.5 cm with large twinned crystals several mm in center. Evidence of nucleation near wall. No Ga inclusions.
3	1025°C	0.6 <111>	1.0	2.5	5.0	Seed dissolved. Large grain of 4 mm x 10 mm in center with polycrystalline nucleation near ampoule wall. No Ga inclusions. Total length 2.3 cm.
4	1055°C	0.3 <111>	1.0	2.0	5.0	Seed dissolved. Grains nucleated at bottom of ampoule and propagated along the length for 2.0 cm polycrystalline growth. No Ga inclusions.
6	1000°C	0.3 <111>	0.8	2.5	1.0	Growth was quenched after 1 cm growth from self-seeding (seed dissolved). The quenched solid-liquid interface was convex and the ingot showed grain selection.
7	950°C	1.3 <111>	0.8	2.5	2.0	Successfully seeded. 90% of the 1.5 cm grown was single crystal of <110> direction.

TABLE X. (Continued)

Run THM No.	Heater Temp.	Original Seed length (cm)	Original Ga Zone length (cm)	Original Feed length (cm)	Lowering Rate (mm/day)	Results
9	935°C	2.0 <110>	0.8	1.5	5.0	Successfully seeded and grown 1.0 cm. Ingot began single but rapidly became polycrystalline due to the fast growth rate.
11	950°C	0.8 <110>	0.8	1.0	3.0	Successfully seeded and grown 0.8 cm. Ingot was in <110> direction and nearly completely single crystal.

TABLE XI. DETAILS OF THM RUNS WITH DIFFERENT INITIAL Ga ZONE LENGTHS

Run THM No.	Heater Temp.	Original Seed length (cm)	Original Ga Zone length (cm)	Original Feed length (cm)	Lowering Rate (mm/day)	Results
61	980°C	1.0	0.55	3.8	1.5	2.8 cm successful growth. Grain selection by convex interface was apparent as grain boundaries grew outwards toward crucible wall.
40	980°C	1.0	0.75	3.8	1.5	3.0 cm growth. Seeded crystals appeared to have grown outwards due to presence of convex solid-liquid growth interface. Quality of crystal good with no Ga inclusion.
62	980°C	1.0	1.0	3.8	1.5	Growth interface was near-flat. As a result, the grain propagation was generally parallel to the growth direction.
41	980°C	1.0	1.55	3.8	1.5	2.8 cm polycrystalline growth completed. Grains appeared to have nucleated on wall and grown towards center due to the concave solid-liquid growth interface. Trains of Ga inclusions present in center of crystal.

TABLE XII. SUMMARY OF THM GROWTH RUNS AT DIFFERENT HEATER TEMPERATURES AND LOWERING RATES

Heater Temp. (°C)	Estimated Interface Temp. (°C)	Estimated As Solubility (wt. %)	Lowering Rate in mm/day							
			0.5	1.0	1.5	2.22	4.44	6.66	13.2	20.0
800	740	1.2%		#33 ^{**}						
850	775	2 %	#83 [*]	#45 [*]		#32 ^{**}	#31 ^{**}			
980	900	6 %			#61	#89	#39	#44 ^{**}		
1100	1010	12 %							#58	#79 [*]

^{*} Growth completed with some polycrystalline nucleation, but no Ga inclusions.

^{**} Growth run failed, Ga zone detached or Ga inclusions trapped.

TABLE XIII. DETAILS OF THM RUNS AT DIFFERENT TEMPERATURES AND LOWERING RATES

Run THM No.	Heater Temp.	Original Seed length (cm)	Original Ga Zone length (cm)	Original Feed length (cm)	Lowering Rate (mm/day)	Results
61	980°C	1.0	0.55	3.8	1.5	Successfully completed 2 to 8 cm of growth. Grain selection by convex interface quite evident. Growth rate could be considered ideal for growth.
89	980°C	1.0	0.55	3.8	2.22	Growth of 2 cm completed before run was terminated because of power shut down. Crystal contained a <111> twin. No inclusions were observed. It appeared that 2.22 mm/day was close to the maximum rate for single crystal growth at 980°C.
39	980°C	1.0	0.55	3.8	4.44	Successfully completed 3.5 cm growth. Polycrystalline with some Ga inclusions; travel rate apparently too fast for good quality crystal.
44	980°C	1.0	0.55	3.8	6.66	2.8 cm growth completed. Crystal very polycrystalline with trails of Ga inclusions.
58	1100°C	1.0	0.55	3.8	13.2	Completed 2.0 cm growth. No Ga inclusions present.
79	1100°C	self-seed	0.55	3.8	20	Good quality, inclusion free crystal.
33	800°C	1.0	0.75	3.8	1.0	Ga zone detached after 0.8 cm growth indicating 800°C is too low for THM growth, even at 1 mm/day.

TABLE XIII. (Continued)

Run THM No.	Heater Temp.	Original Seed length (cm)	Original Ga Zone length (cm)	Original Feed length (cm)	Lowering Rate (mm/day)	Results
83	850°C	1.0 <111> Ga	0.55	2.0	0.5	Ga inclusions were present, as well as small crystals scattered in the grown crystal.
45	850°C	1.0	0.75	3.8	1.0	Successfully completed 2.5 cm growth. Crystal quality poor, indicating 850°C and 1 mm/day as lower limit for THM growth.
32	850°C	1.0	0.75	3.8	2.22	Ga zone detached after 1 cm growth. Travel rate too fast for growth.
31	850°C	1.0	0.75	3.8	4.44	Ga zone detached after 0.7 cm growth.

TABLE XIV. THM RUNS WITH CONTROLLED SEEDING AND DOPING

Run THM No.	Heater Temp.	Original Seed length (cm)	Original Ga Zone length (cm)	Original Feed length (cm)	Lowering Rate (mm/day)	Results
71	980°C	0.6 <111> As	2.578 g Ga 0.001 g Te	3.8	1.5	2.0 cm single crystal with a separate small grain in the second cm.
72	980°C	1.0 <111> As	2.80 g Ga no dopant	3.5	1.5	95% single crystal. Three tiny strip-like (111) twins nucleated near the circumference and grew into the center of the crystal at 70.5° to <110>.
81	930°C	0.6 <111> Ga	2.95 g Ga 0.001 g Zn	2.0	1.5	Seeding poor. Polycrystalline from 0.5 cm to 1.5 cm.
84	980°C	1.0 <110>	3.39 g Ga 0.012 g Cr	2.0	1.5	After 0.3 cm growth in the <110> direction a (111) twin developed from the side and grew preferentially for the remaining 1.5 cm.
86	980°C	1.0 <110>	2.4 g Ga	2.0	1.0	Completely single.

Seeding directions tried were $\langle 111 \rangle$, $\langle \bar{1}\bar{1}\bar{1} \rangle$ and $\langle 110 \rangle$. Little difference was noted, except a $\langle 111 \rangle$ grain soon nucleated in the $\langle 110 \rangle$ run, so that $\langle 111 \rangle$ growth was obtained in that run as well.

The density of dislocations in the growth direction increased by about ten-fold at the seed interface, and then declined roughly exponentially with distance to $\sim 3 \times 10^3/\text{cm}^2$ in 2 cm if the crystal was cooled slowly after growth. Quenching caused the density to increase dramatically within about 1 cm of the final zone position. The density of dislocations normal to the growth direction was relatively constant at about $3 \times 10^4/\text{cm}^2$.

Chemical and electrical properties of the THM GaAs crystals are summarized in Tables XV to XVII.

The ability of the THM to produce high quality GaAs has been demonstrated. There is no fundamental limitation to the size of the crystals that can be grown, although larger diameters would require adjustments in the operating conditions.

2. THM Alloys

$\text{Ga}_x\text{In}_{1-x}\text{Sb}$ was grown with a Ga-In solvent zone at $\sim 550^\circ\text{C}$ and $\text{Ga}_x\text{Al}_{1-x}\text{As}$ was grown at 1000°C . Cast $\text{Ga}_x\text{In}_{1-x}\text{Sb}$ and GaAs with embedded Al wires were used as feed materials. No seeds were employed. A boron nitride crucible inside a silica ampoule was used for $\text{Ga}_x\text{Al}_{1-x}\text{As}$ because Al reacts with SiO_2 to form Al_2O_3 and Si. Large grain polycrystalline ingots were obtained with composition profiles as expected from the initial composition and the phase diagrams. Results are summarized in Tables XVIII and XIX.

G. Crystal Growth of Gallium Nitride*

(M. Gershenson)

Gallium nitride is a III-V semiconductor of interest as a luminescent material. Several methods have been used to grow GaN single crystals. The most successful method has been an open-tube vapor phase growth technique, in which Ga, transported to the deposition zone as a gaseous halide, reacted with NH_3 to form GaN epitaxially on a sapphire substrate. The GaN layer thickness was about

* Partly supported by U.S. Army Research, Durham (DA-ARO-D-31-124-70-G15), and the National Science Foundation (GK 12796).

TABLE XV. MASS SPECTROMETRIC ANALYSES OF FEED RODS
AND THM GaAs GROWN FROM THEM

(Concentrations in 10^{16} atoms/cm³)

Element (D - donor) (A - acceptor)	Feed CZ-41	Crystal THM-72	Feed GF-30	Crystal THM-76
Li (A)	< 0.14	< 0.14	< 0.14	< 0.09
Be	≤ 0.14	≤ 0.14	< 1.4	< 0.07
B	0.15	< 0.09	< 1.5	< 0.09
F	< 1.7	< 1.7	< 5.0	< 1.7
Mg (A)	0.4	0.4	< 1.3	≤ 0.04
Si (D/A)	<11.4	<11.4	8.0	6.8
Cl	0.9	0.9	0.02	0.04
K	< 1.6	0.8	0.49	0.26
Ca	< 2.4	< 2.4	0.24	< 0.48
Cr (A)	0.6	< 0.12	< 0.18	< 0.06
Mn (A)	< 0.02	< 0.12	< 0.12	< 0.06
Fe (A)	2.28	0.40	1.14	5.7
Co (A)	< 0.05	< 0.05	0.16	< 0.05
Ni (A)	< 0.22	< 0.22	0.54	< 0.11
Cu (A)	< 0.15	< 0.15	3.0	< 0.1
Zn (A)	0.47	0.47	0.9	< 0.09
Sn (D)	< 0.27	< 0.27	0.27	< 0.13
Te (D)	< 0.13	< 0.13	< 0.15	< 0.15
Pb (D)	< 0.09	< 0.09	0.9	< 0.09

TABLE XVI. HALL MEASUREMENTS OF FEED CRYSTALS AND THM GROWN GaAs CRYSTALS

Crystal	Resistivity Type	Resistivity ρ ohm-cm	Carrier Concentration cm ⁻³	Electron or Hole Mobility, μ cm ² /volt-sec.	Discussion
CZ-41 (undoped, liquid-seal Czochralski method grown.)	N	45.2	3.3×10^{15} n	very low	The presence of Cr in the mass spectrometric data could account for the moderately high ρ . The low μ could be due to Fe, C and other deep level acceptors.
THM-72 (grown from CZ-41 by THM growth.)	P	3.69	6.0×10^{15} p	275	Chromium concentration was reduced from CZ-41 and is represented in lower ρ . As in GaAs grown out of Ga, THM-72 was p type with reasonable hole mobility.
GF-30 (undoped, vertical gradient freeze grown.)	N	10^7 - 10^8	very low	very low	Sample apparently highly compensated. Mass spectrometric data show high concentration of Cr, Fe, Cu and other impurities.
THM-76 (grown from three passes on GF-30.)	P	0.042	2.5×10^{16} p	60.4	Quality of crystal improved from GF-30. Resistivity is low and impurity concentration very low as indicated by mass spectrographic data. Low hole mobility unexplained.

TABLE XVI. (Continued)

Crystal	Resistivity Type	Resistivity ρ ohm-cm	Carrier Concentration cm^{-3}	Electron or Hole Mobility, μ $\text{cm}^2/\text{volt-sec.}$	Discussion
THM-81 (Zn doping $\sim 0.5 \times 10^{19}$ atoms per cc Ga.)	P	1.166	2.6×10^{16} p	180	No mass spectrometric results obtained. Mobility is fair.
THM-71 (Te doping $\sim 1 \times 10^{19}$ atoms per cc Ga.)	N	0.022	2.8×10^{17} n	1007	No mass spectrometric results obtained. Electron mobility is low probably because of com- pensating impurities.

TABLE XVIII. SUMMARY OF TRAVELLING HEATER EXPERIMENTS ON $Ga_xIn_{1-x}Sb$

Run THM	Heater Temp.	Seed	Original Zone Composition	Original Feed Length and Composition	Lowering Rate (mm/day)	Results
68	420°C	Self seed	2.5 g Ga	3.0 cm $Ga_{0.7}In_{0.3}Sb$	2.0	No growth achieved.
69	420°C	Self seed	5.5 g In	3.0 cm $Ga_{0.7}In_{0.3}Sb$	2.0	No growth achieved.
74	420°C	$Ga_{0.7}In_{0.3}Sb$	1.32 g Ga 1.57 g In	1.5 cm $Ga_{0.7}In_{0.3}Sb$	1.0	Only 2 mm deposited on seed. Temperature apparently too low for growth.
75	600°C	Self seed	1.25 g Ga	2.0 cm $Ga_{0.7}In_{0.3}Sb$	1.0	Growth seemed successful.
77	600°C	Self seed	1.33 Ga 1.57 g In Atom ratio Ga/In = 1.4	3.5 cm $Ga_{0.5}In_{0.5}Sb$	2.0	3.3 cm polycrystal successfully grown. Large grains were present with no solvent inclusions.
87	600°C	Self seed	2.0 g Ga 0.82 g In Atom ratio Ga/In = 4.0	2.5 cm $Ga_{0.9}In_{0.1}Sb$	2.0	Large-grained polycrystal with no inclusions. There were cracks along the radial direction, as in THM-77.

TABLE XIX. SUMMARY OF THM $\text{Ga}_x\text{Al}_{1-x}\text{As}$ GROWTH RUNS

Run THM	Heater Temp.	Seed	Original Zone Content	Original Feed Length and Composition	Lowering Rate (mm/day)	Results
80	1100°C	Self seed	2.40 g Ga	13.12 g GaAs + 0.07 g Al $\approx \text{Ga}_{0.97}\text{Al}_{0.03}\text{As}$	4.0	White powder (Al_2O_3) on wall of quartz ampoule and on feed material. Unsuccessful.
82	1114°C	Self seed	2.0 g Ga	$\sim \text{Ga}_{0.94}\text{Al}_{0.06}\text{As}$	2.0	Same as THM-80.
88	1110°C	GaAs seed 0.75 cm dia. 1.5 cm long <111> As direction	1.025 g Ga +0.01 g Al	4.12 g GaAs + 0.024 g Al $\approx \text{Ga}_{0.97}\text{Al}_{0.03}\text{As}$	4.0	The growth took place inside a BN tube sealed inside the usual evacuated silica ampoule. No Al_2O_3 formed and 1.5 cm of GaAlAs was successfully grown. New grains nucleated near the BN crucible wall and propagated into the bulk of the ingot.

50 μ . It was colorless and always n-type with carrier concentrations on the order of 10^{20} cm^{-3} . Much effort was expended on the purification and the compensation of the crystals. First, oxygen was considered as the possible impurity. Since GaN deposits attack quartz walls, the system was liable to become contaminated with silicon and oxygen. Therefore, an alumina liner was put in the high-temperature reaction region and in the low-temperature deposition region. The ammonia was purified by passing it over a heated sodium-metal trap about 12 inches in length. The hydrogen tank was replaced with a hydrogen generator with purity of 10 ppb. However, with all those changes, no decrease was noted in the carrier concentrations. Later, water vapor was added intentionally to the growth system. It caused nucleation problems and produced yellow crystals. All measurements indicated that there was no noticeable resistivity change.

Native defects such as nitrogen vacancies are now suspected to be the cause of the high carrier concentrations. This is because the GaN crystal growth depends so strongly on the substrate surface which catalytically dissociates the ammonia to generate the active nitrogen required for the reaction for growth system without reacting or dissociating into nitrogen and hydrogen.

We also added PH_3 during growth, hoping that P would occupy nitrogen sites forming isoelectronic traps and eliminating nitrogen vacancies. However, the large covalent bond difference between P and N probably prevented P from entering the GaN crystals. Larger PH_3 pressures actually stopped the GaN crystals from growing.

There is no direct observation that nitrogen vacancies are the real cause of the high carrier density. We used catalysts such as titanium sponge in the substrate area. GaN crystals appeared to nucleate easier on the sapphire substrate under this condition, but the crystals still showed the same high carrier concentrations.

Chlorine atoms from the HCl transport species were probably not the electrically active impurities. Mass spectrometric analysis has not detected enough chlorine atom to account for the large density of free carriers.

Lattice mismatch between the substrate and the GaN may have caused local defects such as grain boundaries and dislocations. Indeed, the GaN resistivity increased with layer thickness and tended to saturate at higher thicknesses. However, the resistivity was still quite low, even in the thicker samples.

Single crystal GaAs, GaP, Ge, and Si were tried as possible substrates. Only polycrystalline GaN was deposited on the Ge and Si substrates. The GaAs and GaP substrates were etched away by the HCl which was used as the transport agent in the growth system.

III. LIQUID EPITAXIAL GROWTH OF III-V SEMICONDUCTORS

(J. M. Whelan, C. T. Lee, L. Yuan, P. D. Vijayakumar and S. Hoelke)

A. Dipping Technique

The liquid epitaxial growth dipping technique for producing thin films was under investigation at USC before initiation of the present grant. Films were grown on GaAs substrates by slow cooling of Ga solutions in a nearly isothermal environment. During this grant, the surface texture and substrate-interface regularity of GaAs films were significantly improved by the addition of arsenic to the hydrogen atmosphere under which the solution growth occurs. This permitted the growth of smooth films on substrates with the desired orientations, (211) and (311), and moderate dislocation densities ($\sim 5000/\text{cm}^2$). Comparable results were previously obtainable only with substrates with dislocation densities $\leq 100/\text{cm}^2$.

Variables affecting the characteristics of thin alloy films on GaAs substrates were elucidated. These included the determination of the Ga-In-As liquidus-solidus curve at 860°C , evaluation of film quality as a function of the substrate orientation and a comparison of the nucleation characteristics of two alloy systems. GaAs substrates with (111) orientations were superior to all other orientations tried--(100), (110), (211) and (311). The density of nucleation centers was markedly greater for the $\text{GaAs}_{1-x}\text{Sb}_x$ alloys than for the $\text{Ga}_{1-x}\text{In}_x\text{As}$ ones. For this reason the $\text{GaAs}_{1-x}\text{Sb}_x$ alloys are more likely to be useful when films $\sim 1 \mu\text{m}$ thick are required with energy gaps more than 0.04 eV less than GaAs. Difficulty with undercutting dissolution of the substrate was encountered in growth of concentrated alloy films. Bulk alloy substrates are needed to avoid nucleation and undercutting problems, but are not yet available.

The dependence of lattice constant on compositions of $\text{GaAs}_{1-x}\text{Sb}_x$ alloys has been measured. A linear variation with x was found, corresponding to Vegard's Law. Previous data had indicated a strong deviation from a linear variation. The new results are attributed to the improved homogeneity of our solution-grown alloy films.

B. GaAs Junction Field Effect Transistor (JFET)

The above improvements in thin film growth have been used to grow n-type layers on p-type GaAs substrates. The quality of the resulting pn

junctions were excellent, as judged by low reverse biased leakage currents. Good junctions were associated with highly regular substrate-film interfacial surfaces. Growth conditions which compromised the regularity always resulted in p-n junctions with enhanced leakage currents. A mesa GaAs JFET with a ring-dot configuration was built to demonstrate the gate junction quality of GaAs transistors with relatively large transconductances (6×10^{-3} mhos).

Reverse currents at pinchoff voltages, ≈ 12 V, were $\approx 2 \times 10^{-9}$ amp. Maximum processing temperatures required on the epitaxial films were under 430°C . This in part was due to the satisfactory performance of Au-Sn alloy contacts which are described in Section V.C.

C. Measurement and Control of Oxygen using Stabilized Zirconia Electrolyte

Low growth temperatures are desirable in that the temperature control requirements for controlling film thicknesses are less, impurity solubilities are lower, and chemical reactivities are reduced. It appears that the minimum growth temperature is limited by the presence of oxygen, which is probably chemisorbed on the substrate as a Ga-As-oxide more stable than Ga_2O_3 . In order to grow superior quality films it is necessary to remove this oxide prior to the growth. Manifestations of incomplete removal are irregular nucleation and the growth of films with poor surfaces.

Evidence was found for the presence of oxygen on the surface of GaAs substrates which was not reduced by H_2 in 30 minutes at 825°C . The mole ratio of H_2O to H_2 in the exhaust gas line of a liquid phase epitaxial system was monitored by the emf of a ZrO_2 -CaO cell operated at 700°K . The emf of this cell was stable to 1 mV and changed approximately 20 mV per decade change in the H_2O - H_2 mole ratio over its linear range. This was estimated to be the case for $\text{H}_2\text{O}/\text{H}_2$ ratios $\leq 10^{-6}$. For the reactor at 800°C the steady-state $\text{H}_2\text{O}/\text{H}_2$ ratio was $\sim 2 \times 10^{-6}$ with a H_2 flow rate of 100 cc/min. Without changing the flow conditions the emf of the ZrO_2 cell increased, indicating a lower $\text{H}_2\text{O}/\text{H}_2$ ratio when the reactor was cooled. This indicated that the reactor inlet H_2 was of higher quality and that it was degraded by the quartz reaction itself at 800°C . With the reactor at 800°C for several hours so that steady-state conditions pertained, the seed was lowered into the furnace to a position just above the melt and so maintained for 30 minutes. At the end of this period the $\text{H}_2\text{O}/\text{H}_2$ ratio was at its

original steady state value. Immersion of the seed in the Ga melt caused a momentary rise in H_2O/H_2 ratio. The Ga melt was slightly undersaturated. This rise indicated that the oxide on the substrate dissolved in the melt and the dissolved oxygen then reacted with the H_2 atmosphere to produce H_2O . Removal of the seed from the melt and subsequent immersion produced no detectable change in the exit H_2O/H_2 ratio. These experiences prompted the consideration of using an alternate method for removing oxygen from Ga melts.

One approach used in several laboratories elsewhere involves the use of carbon reactors contained in quartz. There are problems associated with adequately cleaning the carbon, avoiding reaction of carbon with the quartz and subsequent introduction of Si as an impurity. In principle, though, the carbon should be a good reducing agent for oxygen in Ga. Hydrogen is almost as good a reducing agent. The rates of removal are important. If one considers the dissolved oxygen in the Ga melt to be in equilibrium with the H_2 atmosphere (an optimistic assumption) and that the dissolved oxygen removal rate is proportional to the partial pressure of H_2O (which we optimistically take as 10 ppm or 10^{-5} atm) and a reasonable H_2 flow rate of $100 \text{ cc atm min}^{-1}$, the removal rate of oxygen from the melt at 1000°K is

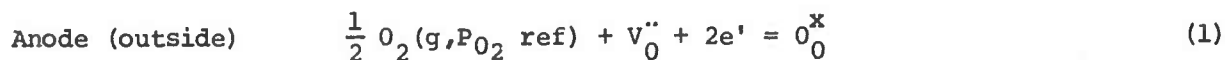
$$\begin{aligned} \text{moles of O removed from} &= \frac{10^{-5} \text{ atm} \times 100 \text{ cc/min}}{1000 \text{ deg} \times 82 \text{ cc atm mol}^{-1} \text{ deg}^{-1}} \approx 10^{-8} \text{ mol/min} \\ \text{melt per minute} & \\ &\approx 1 \text{ monolayer/cm}^2 \text{ of substrate/min} \end{aligned}$$

This slow removal rate caused us to consider using electrolytic pumping to remove dissolved oxygen. Calcia-stabilized zirconia operating with an ion current of only 10 mA can remove oxygen at a rate of 3×10^{-6} moles/min or 300 times faster than a clean H_2 atmosphere (work elsewhere has shown near unity transference numbers for oxygen ion). In addition, this pumping efficiency is to be anticipated for concentrations of oxygen below the saturation concentration at temperatures as low as 500°C .

1. Zirconia Electrolyte

Over a wide range of oxygen pressures and temperatures, zirconia ZrO_2 doped with a lower valent oxide such as CaO or Y_2O_3 is an oxygen ion conductor.

It is most conveniently used under conditions in which its electrical conductivity is essentially all due to oxygen ion movement. Additions of lower valent oxides enhance this by grossly increasing the oxygen ion vacancy concentration. The large concentration of oxygen vacancies, ~ 5 mol %, resulting from doping fixes the chemical potential of the vacancies with respect to oxygen pressure changes. Under these circumstances a cell can be constructed as in Figure 12 to produce a reversible emf resulting from differing oxygen pressures on two surfaces of the doped zirconia, such as the inside and outside of a tube. Suitable electrodes are required. Platinum paste (with inorganic glass fluxes) is a convenient electrode material for laboratory cells. Half cell reactions may be written as follows for a tubular cell in which the outside oxygen reference pressure, P_{O_2} ref, is greater than the inside oxygen pressure, P_{O_2} :



The reversible emf, ϵ , of the cell is $(-\Delta G_3/2F)$ where ΔG_3 is the Gibbs free energy change for the net cell reaction (3) and F is the Faraday (96,500 coul./g equ). Note that two equivalents of charge are transported per half mole of molecular oxygen gas or per g atom of oxygen. ϵ and ΔG_3 are related to the oxygen pressures which are assumed (and, in fact, are) low enough so that they are the corresponding oxygen fugacities. The relationships are:

$$\epsilon = -\Delta G_3/2F = \frac{-RT}{2F} \ln \left[\left(\frac{P_{O_2}}{P_{O_2} \text{ ref}} \right)^{1/2} \right] \quad (4)$$

Since we are primarily interested in low oxygen fugacities it was convenient to use oxygen reference pressures (fugacities) which were also low. This reduced the effects of leaks through the tube wall, such as diffusion along grain boundaries. Since Pd-diffused "pure" He gas at 1 atm was used on the inside of the tube, it was convenient to use hydrogen gas (1 atm) saturated with water vapor at 0°C for establishing the oxygen reference pressure. The following

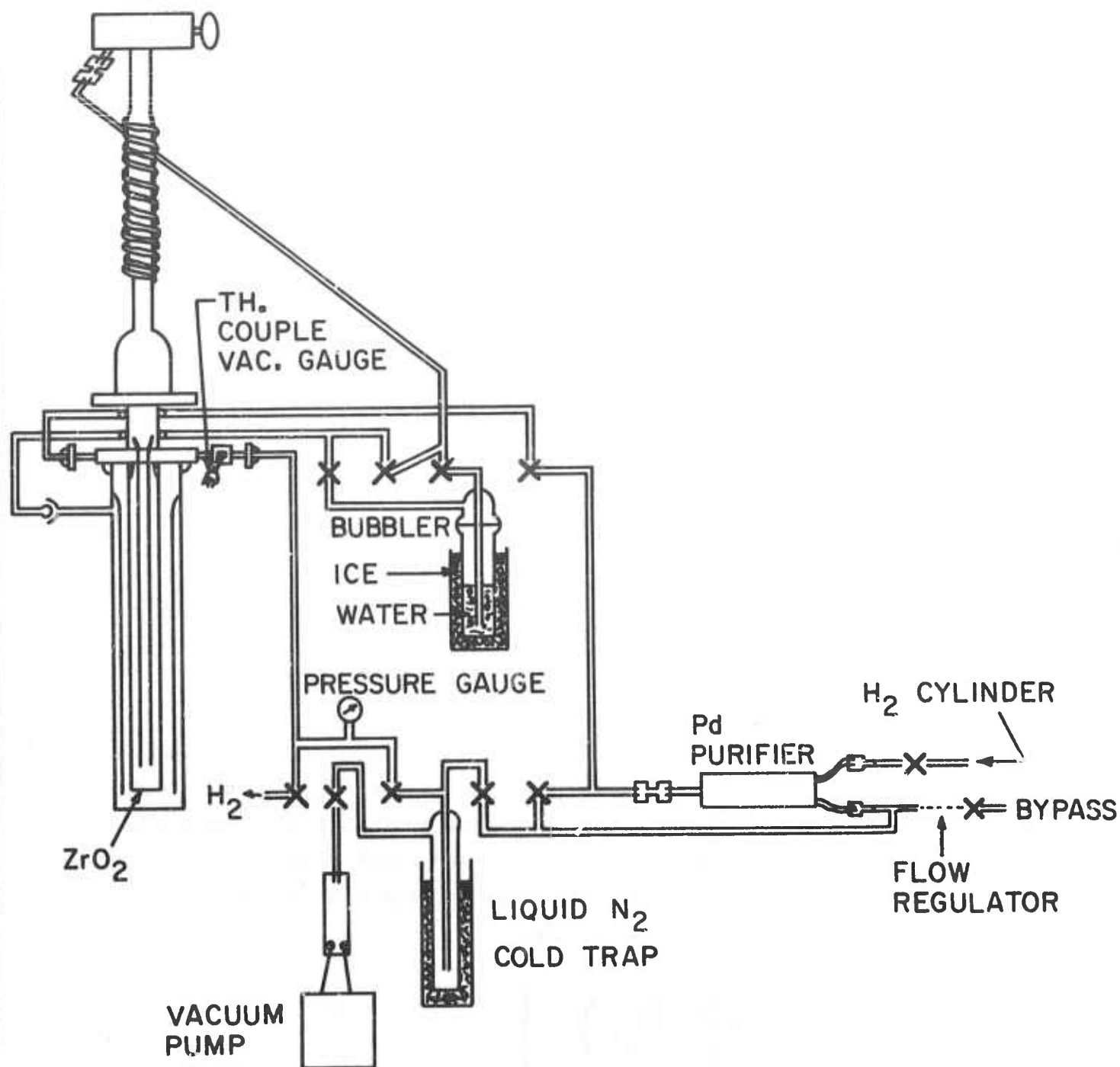


Figure 12. Diagram of system for measuring and controlling oxygen concentrations.

equilibrium was assumed:

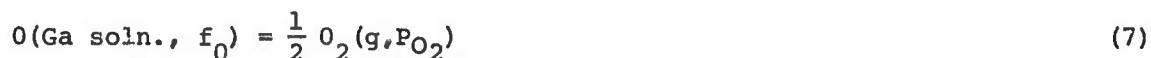
$$H_2O/P_{H_2O} = \text{v.p. } H_2O \text{ at } 0^\circ C = H_2(g, P = 1 \text{ atm}) + \frac{1}{2} O_2 (P_{O_2} \text{ ref}) \quad (5)$$

Establishment of this equilibrium was insured by use of the finely divided Pt paste electrode on the tube outside surface. Values of $P_{O_2} \text{ ref}$ are readily obtainable at various temperatures from data for the free energy of formation of H_2O . The cell can also be used to measure the water content in the "pure" H_2 gas flushed through the inside of the tube. This requires that the H_2 gas inside be equilibrated with the inner tube wall contacted by its electrode (Ga in our case). Equilibration at $500^\circ C$ required times as long as 24 hours, as contrasted with minutes for the outside Pt electrode. The emf of the cell is related to the H_2O partial pressure inside the tube by the equation:

$$\epsilon = \frac{RT}{2F} \ln \left[\frac{P_{H_2O\text{-outside}}}{P_{H_2O\text{-inside}}} \right] \quad (6)$$

where T is the absolute temperature at which the cell is operated. For H_2 flow rates of 100-200 cc/min, typical H_2O contents inside the tube were ~1-5 ppm at 500 to $700^\circ K$. Outgassing from the associated hot quartz tubing is believed to be the prime source of H_2O in the "pure" H_2 . Water contents increased with decreasing H_2 flow rates.

As has been noted, a lengthy time was required for the "pure" H_2 atmosphere to equilibrate with an inner Ga electrode weighing approximately 30 gm. Because of this, it was possible to reverse bias the cell and pump oxygen out of the Ga electrode or short circuit the cell through a suitable resistor and pump oxygen into the Ga. If oxygen is dissolved as atomic oxygen (or as a species containing a single oxygen atom) it has proved to be convenient to define an effective molecular oxygen pressure whose square root is proportional to the fugacity of oxygen in Ga, f_0 , i.e., the effective pressure of O_2 necessary to be in equilibrium with the dissolved oxygen at the same temperature. This may be represented by the reaction:



where

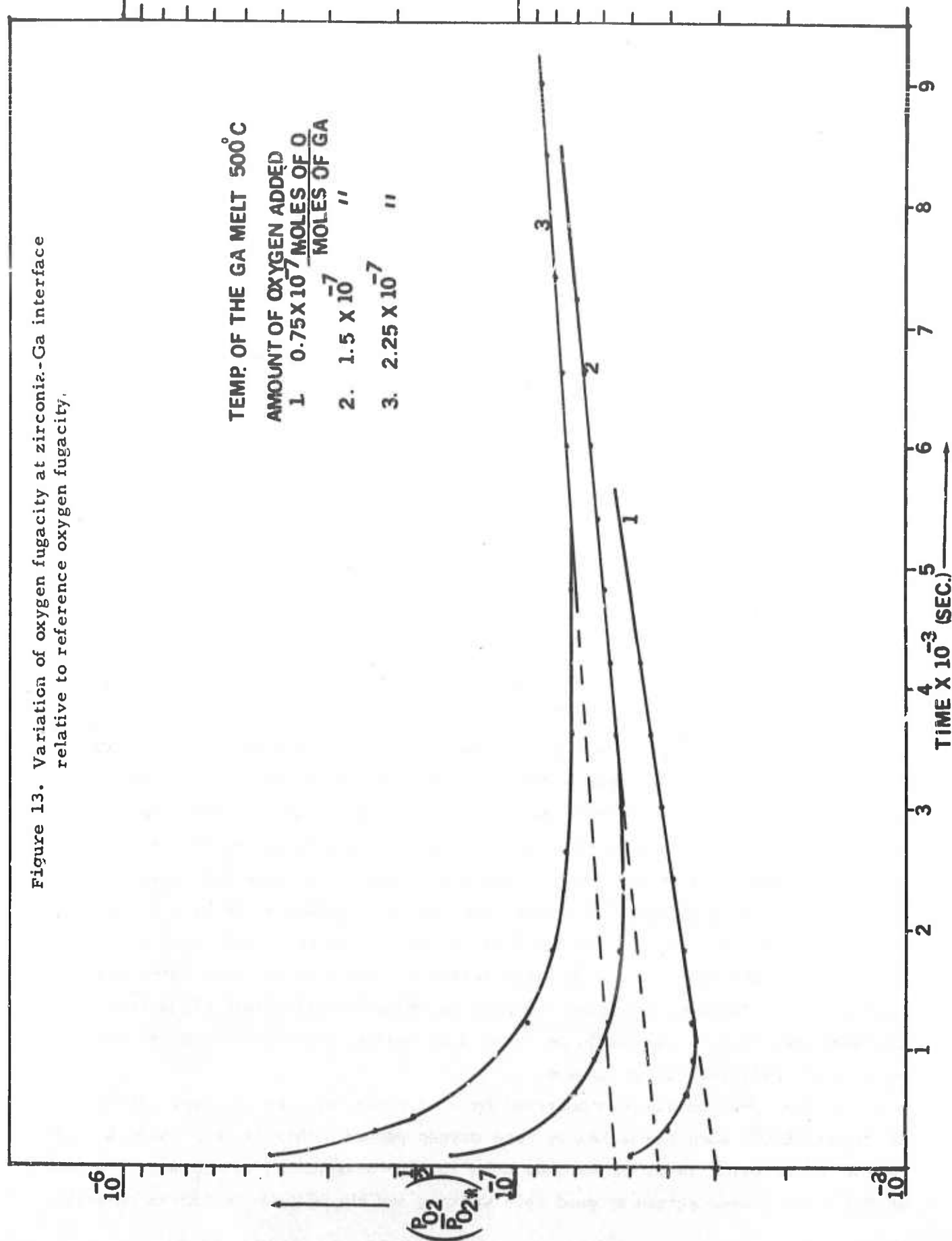
$$P_{O_2}^{1/2} = K_7 f_0 \quad (8)$$

and K_7 is the equilibrium constant for reaction (7) at $T^\circ K$. Experience has shown that oxygen in the Ga near the inside zirconia tube wall equilibrates with the tube wall rapidly for oxygen fugacities substantially below those corresponding to those fixed by the coexistence of Ga(l) and $Ga_2O_3(s)$. Thus, the measured value of the emf cell operating reversibly is given by Eq. (4), in which $P_{O_2}^{1/2}$ is that quantity appropriate for the Ga near the electrolyte. Upon relatively rapid additions or depletions of oxygen from the Ga electrode by electrolytic pumping, we observed relatively fast changes in the emf due to the diffusive/convective mixing of oxygen in the Ga solution and the much slower rate of exchange of the dissolved oxygen with the "pure" H_2 atmosphere. This is indicated by Figure 13, which shows the time dependence of $(P_{O_2}/P_{O_2 \text{ ref}})^{1/2}$ after adding various amounts of oxygen to the Ga by electrolysis. The additions were made to the Ga solution which had lower oxygen contents than required for equilibration with the "pure" H_2 atmosphere. The long linear variation of $\ln (P_{O_2}/P_{O_2 \text{ ref}})^{1/2}$ with time is expected if oxygen exchanges with the atmosphere at a rate proportional to the fugacity differences of the dissolved oxygen and its value upon equilibration. This corresponds to a first order rate process if the concentrations are linearly related to the fugacities or to $(P_{O_2}/P_{O_2 \text{ ref}})^{1/2}$, i.e., Henry's Law pertains. This will be shown to be so later. In Figure 13 the changes in $(P_{O_2}/P_{O_2 \text{ ref}})^{1/2}$ at the end of oxygen addition period were made by extrapolating the long time slopes to zero time.

It was previously indicated that the simple relations between emf and pressure fugacity depended on how reversible was the cell. Oxygen can be pumped from the Ga to concentration levels below which the inside zirconia surface is only partially an ionic conductor. The electronic conductivity causes a partial short circuit and the measured emf is below the reversible one. Under these circumstances, use of the measured emf in Eq. (4) leads to an over-estimate of $(P_{O_2}/P_{O_2 \text{ ref}})^{1/2}$ and the fugacity of dissolved oxygen. In this range, oxygen can be pumped from the Ga in order to lower its fugacity, but with an efficiency less than 100%. However, the fugacities cannot be well estimated except for their upper limits.

The apparatus used to obtain the data in Figure 13 and for the growth experiments is shown in Figure 12. Its basic features have been described.

Figure 13. Variation of oxygen fugacity at zirconia-Ga interface relative to reference oxygen fugacity.



Pure H_2 was circulated over the inside wall of the zirconia tube and flushed through the inside of an inner quartz guide tube. The H_2 then passed through a water bubbler at $0^\circ C$ and then over the outside surface of the zirconia tube. The upper portion of the apparatus was a windlass for lowering a GaAs seed into the Ga for either epitaxial growth or oxygen content determinations. Results for these are described separately below and in Section VI.D.

2. Liquid Epitaxial Growth with Oxygen Pumping

GaAs films have been grown on GaAs substrates at temperatures as low as $500^\circ C$ by the dipping technique with oxygen pumping. The majority of growth experiments were done at $600^\circ C$ on (100), (211) and (311) oriented substrates. These and the growth at $500^\circ C$ were made using Ga solutions in which the oxygen fugacities were four to five decades lower than obtainable with Ga melts equilibrated with Pd diffused H_2 , and exposed to quartz-ware at the growth temperature. (H_2 under these circumstances typically contains 1-10 ppm H_2O .) Faceted growth was characteristic of all growths at 500° and $600^\circ C$, with the exception of one very smooth film on a (211) substrate. Unfortunately that particular substrate was unique in that its history was unknown and it was suspected of having an unusually low dislocation density. Etching prior to growth by dissolving the chemically-polished surface region in the gallium melt nearly always produced a very rough surface. These results were discouraging in that they strongly suggest that surface mobility of Ga and/or As is limiting the growth of epitaxial films at 500° and $600^\circ C$. The effect of the oxygen pump was clearly evident. A growth at $600^\circ C$ without deliberate pumping was characterized by large randomly spaced areas which were not wetted by the melt and spotty nucleation in the remainder. Recently, the growth temperature has been increased to $700^\circ C$. Excellent wetting was noted for oxygen pumped melts and the faceting was absent. Surfaces of films on (311) oriented substrates had long wave-length ripples. Such features have been observed in conventionally-grown films from solutions at $800-850^\circ C$ and could be reduced by modifying the cooling rates and temperature profiles in the furnace.

Growth results may be summarized by noting that good wetting was achieved at 500 and $600^\circ C$ when the solutions were oxygen pumped. This is attributed to the removal of an oxide layer on the GaAs substrate by dissolution in the melt. Growth at $700^\circ C$ was characterized by good seed wetting and the absence of facets on (311)

substrates. Preliminary experiments at this temperature suggest that device-quality films can be grown at 700°C and possibly as low as 600°C.

3. Related Projects

These techniques will have numerous applications in addition to permitting liquid epitaxial growth of GaAs at lower temperatures. They will permit growth of crystals with a controlled and measured oxygen fugacity. For example, the electroluminescence efficiency in red-emitting GaP diodes is greatly reduced by the presence of oxygen. These techniques should permit growth of GaP with much lower oxygen concentrations than is currently possible.

A horizontal solution growth epitaxial system has been constructed for the growth of semiconductor films. It incorporates a novel feature which provides for the automatic control of oxygen fugacities in the films. Advantages are that large zirconia or thoria tubes are not required. Use of large tubes can be expected to be troublesome because of the poorly controlled purities of the commercial tubes and the difficulties in fabricating them.

A novel boat has been constructed for the growth of GaAs bulk crystals and those of other III-V semiconductors. It utilizes a semipermeable membrane which should restrict melt contamination by impurities such as silicon and oxygen.

IV. STUDIES OF CRYSTAL GROWTH PHENOMENA

A. Transport Processes in Unidirectional Crystal Growth

(C. E. Chang and W. R. Wilcox)

One of the most important parameters in directional crystallization is the shape of the crystallizing interface. Thermal stresses increase as the interface deviates from planarity. Grain selection is enhanced as the interface becomes increasingly convex, although we saw in Section II.F that a convex interface can give rise to twins in THM GaAs growth. A concept that has developed further under this grant is that the most important parameter influencing the shape of the interface is the furnace temperature immediately adjacent to the interface. Heat flow must be perpendicular to the interface when crystallization is not taking place and the solid is isotropic. A simple diagram⁽²⁵⁻²⁷⁾ then shows that when the interface is concave, heat must flow from crystal to surroundings, i.e., the surroundings must be at a lower temperature than the interface. The reverse is

true for a convex interface. The influence of transport processes on interface position and behavior was investigated both theoretically and experimentally in the present work. Experiments were performed on naphthalene, a low-melting transparent organic compound with a large entropy of fusion which has a non-faceted interface unless severe constitutional supercooling is present.

1. Control of Interface Shape in the Bridgman-Stockbarger Technique

Calculations have shown that the solid-liquid interface is convex when it is within the heater and concave when it is within the cooler.⁽²⁶⁾ (In this technique the interfacial position and temperature gradients may be independently controlled by varying the heater and cooler temperature.) As the lowering rate is increased the interface becomes more concave (or less convex). This may be overcome by moving the interface somewhat above its position at zero travel rate. When the interface is near either the top or the bottom of the tube its position is shifted either nearer to or further from the end, depending on the relative heat transfer from the end and the periphery. At low travel rates the dependence of interface position on travel rate, geometry of the ampoule, and on the relative temperatures of the heater and cooler increases as the effectiveness of heat transfer between ampoule and the surroundings diminishes and as the thermal conductivity of the material increases.

2. Control of Interface Shape in the Vertical Gradient-Freeze Technique

Calculations showed that a constant cooling rate for a very long ingot in a constant temperature gradient should produce only a concave interface when the thermal conductivity of the melt is greater than that of the crystal.^(20,25) When the thermal conductivity of the crystal is greater, a convex interface is expected when the freezing rate is below a critical value. For a 1 cm diameter by 10 cm long rod of GaAs freezing very slowly, it was predicted that the interface would be concave for the first 5.8 cm and convex for the last 4.2 cm. Calculations showed that by preferential cooling of the bottom of the ingot, the interface could be held convex the entire length. Experiments with naphthalene confirmed these predictions and showed additionally that the interface became much more concave (less convex) as the cooling rate was increased.

3. Heat Transfer in Vertical Zone Melting

In zone melting, vigorous free convection currents in the zone shift the zone upward relative to the heater. Consequently the upper interface is always more concave (less convex) than the bottom interface. The zone position depends on the free convection currents, which in turn depend on the zone position, making it difficult to predict. Heat transfer coefficients from heater to top and bottom interface were determined experimentally by use of direct thermocouple measurements and by overall heat balances combined with measurements of interface position.⁽²⁵⁾ These results were correlated versus heat transfer parameters so that one can now estimate interface positions in zone melting. As the diameter of the pyrex container tube decreased, the interfacial temperature gradient increased and the dependence of interface position and shape on travel rate decreased.

Shifts in interface position and shape due to large zone travel rates were also determined. As one would expect, the zone was shifted in the direction of travel of the ingot relative to the heater. The freezing interface became more concave thereby and the melting interface more convex.

When a stationary zone was shorter than the heater, a hump developed on the top interface. From this hump a jet of melt flowed, forming an indentation on the bottom interface. Whereas temperature fluctuations (due to irregular free convection) were largest at the top of a large zone, in this case they were largest near the bottom.

4. Transport Processes in the Travelling Heater Method

When solvent is present, solute must be transported across the zone as the zone moves. This produces a much larger shift in zone position than when no solvent is present.⁽²⁵⁾

Experiments were performed with benzoic acid as a solvent for the naphthalene. The critical travel rate for interface breakdown compared reasonably well with that calculated by the classical constitutional supercooling model. The critical travel rates were much higher for the top interface than for the bottom interface because the interfacial temperature gradients were larger there. The critical travel rate increases as the solvent concentration decreases and as the zone length increases.

5. Localized Interface Breakdown in Zone Melting and the Travelling Heater Method

Interface breakdown began at grain boundary grooves and spread across the interface. Some grain orientations were more stable than others. Breakdown of a convex bottom interface began at the center and spread to the periphery as the freezing rate increased. This was because the interfacial temperature gradient was greater at the periphery than at the center. Breakdown at a concave bottom or top interface began at the wall and spread to the center. At freezing rates near the critical, breakdown eventually disappeared at the wall, remaining only in the center. At the top interface this is understood by realizing that the melt flows from the center outward, so that the solvent or impurity concentration increases as it moves radially, unless the interface is broken down at the center. Thus initial breakdown is favored at the periphery where the impurity or solvent concentration is greatest, but once the center is broken down only the interfacial temperature gradient differs significantly from the center to the periphery. At the bottom interface secondary eddies inhibit mass transfer at the periphery, causing a similar buildup there unless the center is broken down.

B. Constitutional Supercooling in Multicomponent Systems

(V. F. S. Yip and W. R. Wilcox)

In a multicomponent fluid the diffusion flux of a given component depends not only on its own composition gradient, but also on the gradients of all other components as well via the equation⁽⁴⁵⁾

$$j_i = \frac{C^2}{\rho RT} \sum_{\substack{j=1 \\ j \neq i}}^n M_i M_j D_{ij} X_j \sum_{k=1}^n \left(\frac{\partial \mu_j}{\partial X_k} \right) \nabla X_k, \quad (9)$$

where j_i is the diffusion flux of component i , C is the total molar concentration, ρ is density, R is gas constant, T is absolute temperature, M_i is molecular weight (or atomic weight) of i , D_{ij} are multicomponent diffusion coefficients, X_j is the mole (or atom) fraction of j , and μ_j is the chemical potential (partial molar free energy) of j . If the composition of the crystal and melt are known, as they are in slow steady-state growth by the travelling heater method, then

this equation may be used to find an expression for constitutional supercooling with a multicomponent system. We have done this for a ternary system, which already yields a complex result.⁽²⁰⁾

C. Foreign Particles and Gas Bubbles in Solidification

(V. H. S. Kuo and W. R. Wilcox)

Foreign particles and gas bubbles constitute very common defects in crystals, often leading to dislocation, twin and grain formation. If the surface energy between a particle and the melt is less than the sum of the particle-solid and solid-melt surface energies, then the particle will be pushed by the interface if the freezing rate is low enough. Above a critical rate the particles are trapped. The influence of various parameters on this critical rate was studied using transparent organics and both Bridgman-Stockbarger and rotating horizontal zone melting.^(29,30,33, Appendix B) From these results one would expect less trapping of particles in the Czochralski technique as the rotation rate is increased. It was also shown that mixtures of particles can be separated by gradually increasing the freezing rate--a process we have called particle chromatography.^(29,31)

Gases are normally much more soluble in melts than in the corresponding solids. Thus, the gas concentration at the interface is increased during crystallization. We have shown theoretically that the concentration may become large enough for homogeneous nucleation during directional solidification without appreciable convection of the melt, as expected for the vertical gradient freeze and Bridgman-Stockbarger techniques.^(29,32) With convection and with solution growth the bubbles observed must have formed by heterogeneous nucleation either on foreign particles or the interface itself. Experiments confirmed the prediction that use of a vacuum over the melt greatly reduces bubble formation. A large liquid head and stirring also reduces bubble formation. Increasing the temperature at the melt surface may significantly alter the dissolved gas concentration, and therefore the tendency to form bubbles.

D. Influence of Pressure on Evaporation Rates

(W. R. Wilcox)

Experiments at Sandia Laboratories on evaporation of NaCl melts was explained by theoretical work at USC. (34, Appendix C) The $1/P^{1/3}$ dependence of the evaporation rate was explained as due to turbulent thermal free convection of the gas over the melt, with a transition to laminar flow at low pressures. Condensation of NaCl in the vapor with reflux back into the melt was predicted at USC and later observed at Sandia, resulting in decreasing net evaporation as pressure decreases. The large differences in evaporation rates between Ar, He and CO₂ was attributed to differences in thermal conductivity and to infrared absorption by the CO₂.

E. Movement of Solvent Inclusions in Centrifugal and Thermal Fields

(W. R. Wilcox and K. H. Chen)

Solvent inclusions are very frequently formed during growth from solutions. These inclusions can be moved through and out of the crystal by means of thermal, centrifugal, and electric fields. Reference 35 (Appendix D) reports on boiling and convection in aqueous and water-alcohol inclusions in alkali halides in a temperature gradient. Reference 36 (Appendix E) reports on the theory of movement of inclusions in a centrifugal field. Experiments on aqueous inclusions in KI gave somewhat different results, for unknown reasons.

F. Miscellaneous Crystallization Studies

(W. R. Wilcox)

Reviews have been prepared of mass transfer in crystal growth⁽³⁷⁾ and of movies on crystal growth.⁽³⁸⁾ A new twin and growth mechanism was discovered. (39, Appendix F) Experiments at the Aerospace Corporation on zone melting of off-eutectic melts to produce oriented composites were analyzed at USC.^{(40,} Appendix G)

V. CRYSTAL PROCESSING

A. Crystal Orientation by Cleavage Plane Reflected Laser Beam

(J. M. Whelan and J. E. Green)

It is frequently necessary to determine the crystallographic orientation of a nonfaceted sample of GaAs. We have developed a new and simple method for accomplishing this that does not involve X-ray techniques. (101-103, Appendix H) Reflection of a laser beam from a cleaved surface is employed. GaAs, for example, cleaves to a surface of flat mirror-like steps along {110} planes. Examination of GaAs cleaved surfaces by MacRae and Gobeli⁽¹⁰⁴⁾ with an optical microscope at 1000 X failed to resolve any imperfections. Electron microscope examinations showed the cleavages to be flat and parallel to within the resolution of the instrument, 30 to 40 Å in height, along steps that were 3,000 to 10,000 Å in length. Step heights ranged from 50 to 200 Å. Such cleaved surfaces can be used as mirrors to reflect a well collimated light beam back upon itself. The light beam serves as one reference coordinate in a convenient space coordinate system and a cleaved plane fixes one of the crystallographic coordinates. By knowing the location of two different (110) faces and the angle between them (60° or 90°), one can locate any other plane by performing the proper rotations.

B. Chemical-Mechanical Lapping and Polishing of GaAs⁽⁹⁹⁾

(T. Culbertson and H. Stover)

The preparation of bulk GaAs prior to fabrication of devices begins with lapping the GaAs substrate which has been previously sawed from a large crystal and oriented in the desired crystallographic direction. The preliminary lapping can be done with 3200 grit abrasive powders or pastes. The wafers to be lapped are usually mounted on a flat glass quartz or pyrex disc as shown in Figure 14. In some cases, the wafers may be mounted on a stainless steel cylindrical block. There are a large variety of low melting temperature waxes such as Apiezon black wax or refined bee's wax that can be used to mount the wafers to the disc. The wafers are then hand lapped on a flat glass plate approximately 15 inches square, as shown in Figure 15. A good quality plate glass has been found to be satisfactory. The final polishing is sometimes done with a fine diamond paste, but more recently chemical-mechanical polishing has proven to be superior.

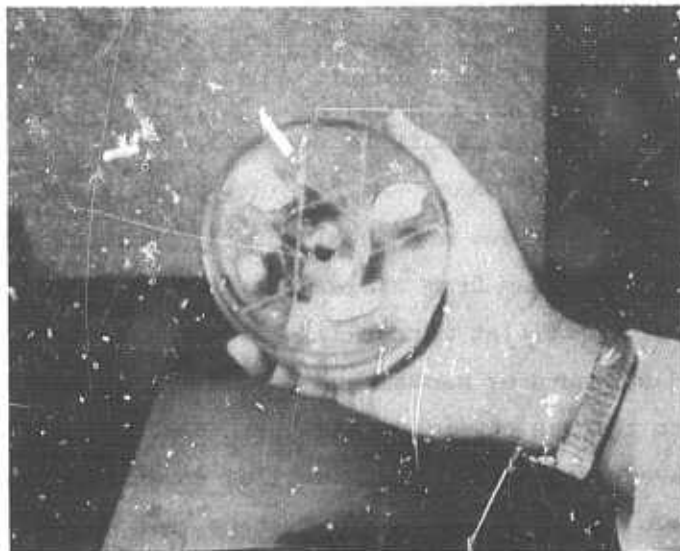


Figure 14. Wafers mounted on glass disc.

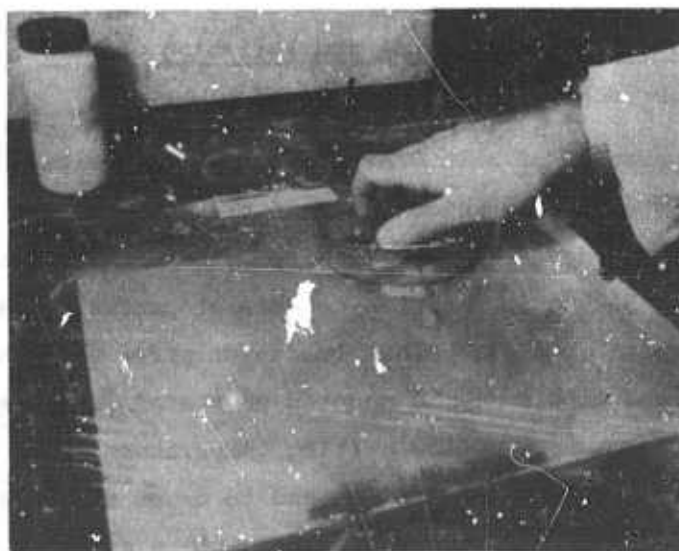


Figure 15. Wafers being hand-lapped
on flat glass plate.

Chemical-mechanical polishing utilizes a chemical solution which slowly attacks the semiconductor, while at the same time the semiconductor is rubbed against a soft cloth, paper, or synthetic such as Corfam. The preferred cloth for GaAs polishing is the Geoscience Polytex Pix. Sometimes the chemical agent also contains a colloidal suspension of SiO_2 or zirconium oxide. The chemical-mechanical polishing is generally very slow. Removal rates on the order of 0.1 to 1 mil per hour are typical. The removal rate can be accelerated somewhat by additives. The finished surface of the polished semiconductor can be damage-free and strain-free, whereas purely abrasive polishing leaves some damage and strain. Gallium arsenide is normally polished using a solution of methyl alcohol and bromine as described in reference 41. or a sodium hypochlorite solution as described in reference 42. The preferred solution is sodium hypochlorite because it gives a superior finish on the $\langle 111 \rangle$ A and B faces of gallium arsenide and because it is relatively safe to use. The bromine solution is noxious and corrosive. Special polishing machines with well-vented hoods are required for the bromine solution. Conventional commercially available polishing machines, such as manufactured by Buehler, Geoscience, Crane Packing Company, or Speedfam, may be used with the sodium hypochlorite solution. Both types of polishing apparatus are available at USC. Other chemical polishes, such as colloidal SiO_2 , have been tried but without much success.

A typical polishing set-up is shown in Figure 16.

The chemical-mechanical polish is finding wide use as the final polish for substrates for chemical vapor epitaxial growth. [Most devices require epitaxial layer(s).]

1. Substrate Thinning

In order to reduce the parasitic electrical series resistance of microwave devices, a very thin substrate is desired. Due to the slow cutting rates possible with the chemical-mechanical process, lapping jigs which allow entire slices to be lapped to dimensions on the order of ten microns have been made. (See Figure 17.) The very thin substrates also are beneficial in heat removal from microwave devices.

Successful thinning depends strongly on proper mechanical design of the apparatus which holds the semiconductor slice. The center post with the stainless steel flat must be precisely orthogonal to the outer support shell.

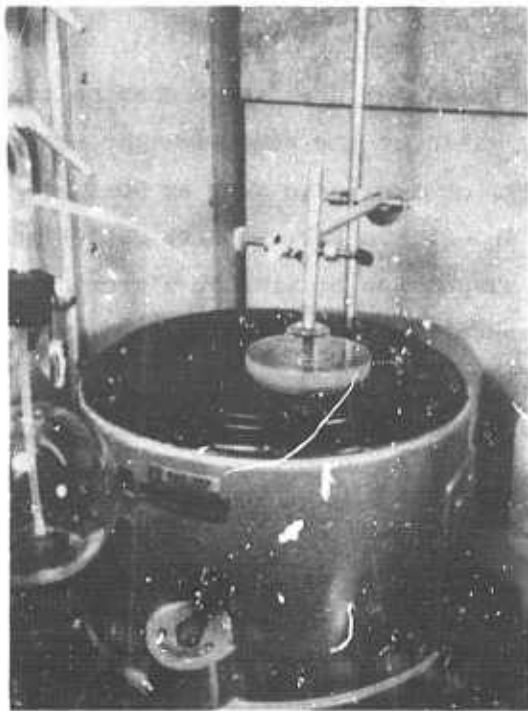


Figure 16. Chemical polisher.

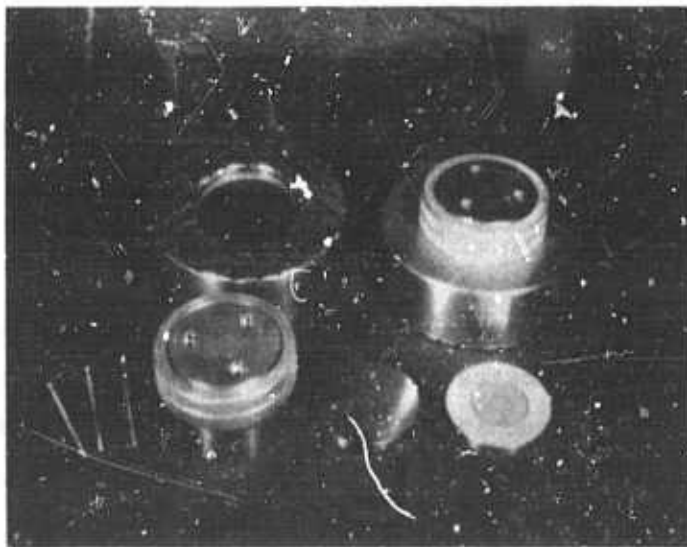


Figure 17. New lapping fixture.

Figure 18 shows the mechanical lapping machine (from Laser Technology) used at USC for wafer thinning. The abrasive slurry used is a diamond paste with kerosene lubricant. A different lapping wheel is used for each different diamond grit size. Diamond abrasives in the grit size of 45, 20, 9, 2 and 1 are being used. A typical removal rate for the 9-micron diamond grit is 4 mils per hour for silicon wafers. The wafers can only be thinned down to approximately 2-3 mils with the diamond abrasive due to the large number of scratches and microcracks which can reach to a depth of up to 1 mil.⁽⁴³⁾ The final steps in the wafer thinning process must be done with the chemical polish and/or an acid etch. The chemical polish technique is preferred because of the better geometrical control over the thickness.

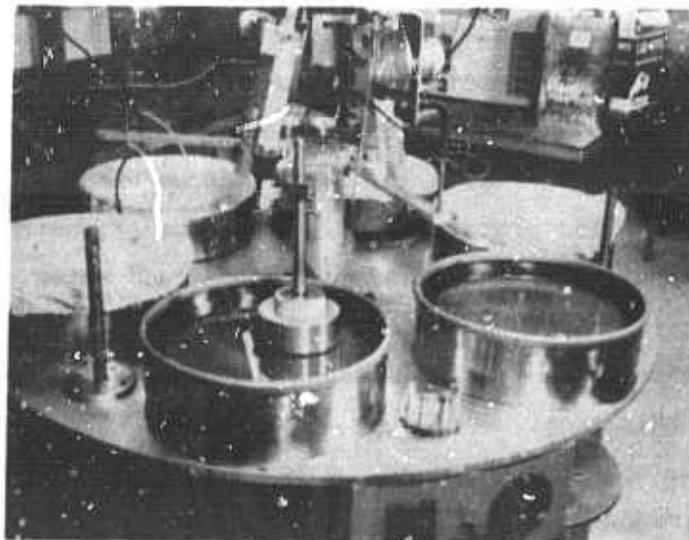


Figure 18. Lapping Machine

2. Types of Chemical-Mechanical Polishes
Used for Gallium Arsenide

a. Syton®

The Syton system is a colloidal suspension of SiO_2 particles in a basic aqueous solution with a pH in the range of 9.5. The particle size is on

® Registered trademark of Monsanto Chemical Company.

the order of 25 millimicrons. This suspension is known as a silica sol or silica aquasol. Other forms of SiO_2 useful for polishing are silica gel (a jelly-like suspension of SiO_2 with a particle size of 5 to 50 millimicrons), and silica organo-aquasol. The organo-aquasol contains an organic solvent such as ethylene glycol or glycerine.

The Syton process for polishing GaAs wafers is described in reference 44. This process was tried at USC, but the results were not entirely satisfactory for GaAs. The surface finish was not as good as that of other methods tried, and the polishing time required to obtain a good finish was longer. In addition, the pre-polishing steps are much more complicated, requiring two laps with alumina (1200 mesh and 3200 mesh), three successive laps with diamond paste (3-micron, 1-micron and 0.25-micron), and an ultrasonic cleaning operation between steps.

b. Sodium Hypochlorite

The method described by Reisman and Rohr in reference 42 has been used with minor modifications at USC. The solution used was reagent-grade NaOCl 5.0% assay diluted 15 (H_2O) to 1 (NaOCl) with deionized water. The solution is freshly prepared just prior to use. With this process, the wafers are mounted on a flat glass disc, as shown in Figure 16, using Apiezon black wax. They are then hand lapped on a flat glass plate, as shown in Figure 17, using an abrasive slurry of Buehler 3200 mesh extra fine grinding compound and water. This step is necessary in order to remove the surface damage due to sawing and to establish a coplanar surface for chemical polishing. About 1 to 3 mils are usually removed from the water in this step.

The wafers and the mounting plate are thoroughly cleaned to remove all traces of the abrasive powder.

Final polishing is done on a Buehler polishing machine having an 8-inch O.D. wheel covered with a Geoscience Polytex Pix polishing pad. The Pellon Pan W polishing cloth used by Reisman and Rohr was found to be unsatisfactory because of the rapid attack by the NaOCl solution. The solution was fed to the polishing wheel at a continuous rate of approximately 300 cc per hour. It was not found necessary to dispense the solution in bursts as described by Reisman and Rohr. A brilliant mirror-like finish is obtained in 1 to 1-1/2 hours. It is necessary to shut off the flow of NaOCl solution and flush the polishing wheel with de-ionized water for a few minutes prior to removing the wafers. This seems

necessary to prevent hazing. The speed of rotation of the wheel is in the range of 100 to 150 RPM.

After removing the wafers from the machine, they are rinsed in deionized water and blown dry with dry nitrogen or filtered air.

c. Methanol-Bromine

This method with minor modifications is that described by Sullivan and Kolb.⁽⁴¹⁾ A solution of 0.05% bromine in methanol is used. Prior to polishing, the wafers are mounted, lapped and cleaned as previously described. The wafers are polished on a special machine designed at USC. The apparatus is made of plastic to withstand the corrosive polishing fluid. The polishing wheel is made of a thick glass plate and covered with a Pellon PA-W polishing cloth with self-adhesive backing. The wheel is turned at 80 to 120 RPM. The wafer mounting plate is rotated counter to that of the wheel by a separate drive motor, but at a slower rate. The solution is fed to the wheel at a rate of about 500 cc per hour. The wafers achieve a mirror-like finish in about 1-1/2 to 2 hours.

After polishing, the wafers are rinsed in methyl alcohol and blown dry with dry nitrogen. It has not been found necessary to use the light source behind the polishing wheel as described by Sullivan and Kolb.⁽⁴¹⁾ Also, the wheel is not inclined, but horizontal.

C. Contacts

(J. M. Whelan, H. Stover, A. Esquivel, L. Yuan and T. Culbertson)

Fabrication of any semiconductor device ultimately requires reliable metal contacts to portions of the semiconductor. Reproducible formation of reliable contacts to GaAs appears to have been particularly elusive. We have developed a new technique yielding specific contact resistances as low as $\approx 1 \times 10^{-5} \text{ ohm cm}^{-2}$ (for GaAs with $n = 1 \times 10^{18} \text{ cm}^{-3}$). The contacts are ohmic for electron concentrations in the GaAs of $< 10^{13} \text{ cm}^{-3}$. They can be made by sputtering of tin or by a relatively simple short circuit electroplating of tin from a $\text{SnCl}_2\text{-KCl-NH}_4\text{Cl}$ salt bath on GaAs previously electroplated with gold. The other electrode of the molten salt short circuited cell is a Au-Sn alloy with the composition desired on the Au plated GaAs. It has been demonstrated that the average Au-Sn alloy composition can be easily regulated to within 2%. One can thermocompression

bond Au wires to these contacts. Required alloy temperatures are relatively low, 350-375°C.

A new method has been developed for assuring intimate contact between a device and a heat sink.⁽⁹⁹⁾ It is applicable to Gunn devices, avalanche diodes, etc. A copper heat sink is electroplated onto the entire semiconductor slice. Diodes are fabricated by etching from the reverse side. Individual diodes are separated by sawing the copper into small squares.

For heat sinks or mechanical support, a thick metal layer is frequently desired. To have good thermal conductivity and to be strain-free, the metal must be free of organic or chemical inclusions. We have developed a new copper electroplating technique which accomplishes this. Prior to plating a metal film is deposited by vacuum evaporation. The first metal layer is selected for good ohmic contact and adhesion. The top layer is gold approximately 4000 Å thick. After wax mounting a 0.3 to 0.5 mil layer of gold is electrodeposited from a 24-karat neutral bath. A copper lead wire is attached to the gold surface. Copper is plated from a fluoborate bath without additives or from an acid bath. Temperature is 54 to 71°C and current density 1/2 to 1 ma/cm².

Three methods were also investigated for producing ohmic contacts on bar-shaped samples for Hall-effect measurements (see Section VI.F.). The first method evaluated consisted simply of soldering indium at six points of the bar corresponding to the six arms in a Hall bridge sample. The contacts were non-ohmic, displaying nonlinear and asymmetrical voltage-current characteristics, and yielded a sample resistance of 4000 ohms or greater. The second method involved the evaporation of a Au-Ge eutectic alloy onto the current contacts of the sample after the method of Clawson and Wieder. To keep the Au-Ge film from curling up during the alloying process, a layer of indium oxide was evaporated on the Au-Ge film. Alloying of the Au-Ge with the GaAs surface was accomplished by exposing the sample to a 400°C heat lamp. The indium oxide was subsequently removed by gently abrading the contacts. The resulting contacts were ohmic and yielded a resistance of 0.4 ohm. The third method consisted of soldering a small amount of indium at the desired locations on the bar sample and applying momentarily the edge (not the tip) of a hydrogen flame to the spots of indium. This method assured proper alloying of the indium with the GaAs surface and yielded linear and symmetrical voltage-current curves with a sample resistance of 0.1 to 0.2 ohms.

The effect of heating during the flame soldering process was evaluated by comparing the Hall measurements taken from the same sample to which the two types of contacts were successively bonded. The first set of Hall measurements were taken after Au-Ge was evaporated onto the top surface of the bar ends (current contacts), while the second Hall data were measured after indium was flame soldered to the edge surfaces of the bar ends. Comparison of the Hall parameters taken at room and liquid nitrogen temperatures indicated a difference between the two methods of 2 to 3% in the resistivity data, and a difference of 5 to 8% in the Hall coefficient, mobility and carrier concentration. A similar range of differences was found between Hall measurements taken from the same sample after a first and then a second exposure to flame soldering.

This third method of attaching indium contacts by hydrogen flame soldering was subsequently adopted as standard because it yielded low resistance ohmic contacts, presented a bright and clean surface, and because the variations in the measurements were within experimental error. A further reason for using this method was that with the aid of a suitably designed sample holder, the leads could be attached to the sample with a minimum of sample handling, no subsequent cleaning, and thus eliminated possible sources of specimen contamination.

VI. CHARACTERIZATION

A. Ion Microprobe Mass Analyses (IMMA)

As summarized in various tables in Section II, several of our crystals were analyzed by ordinary mass spectrometry at the Air Force Cambridge Research Laboratories and at Battelle Columbus Laboratories. A few analyses were also performed at the Aerospace Corporation on their Applied Research Laboratories ion microprobe mass analyzer (IMMA) through a subcontract to USC. The results are summarized in Table XX. Comparison of Ga and As peaks shows that the yield varies considerably from element to element. Sensitivity seemed to be much higher for a N_2^+ beam than for an O^- beam. Comparison of the results for various points on the same Czochralski slice shows the great sensitivity to surface contamination on the one hand, and the great usefulness for determining the composition of microscopic deposits on a surface on the other hand. Surface effects are also demonstrated by Figure 19, which shows the variation of silicon

TABLE XX. ION MICROPROBE MASS ANALYSES OF GaAs
(Background or noise ~13 counts/sec.)

Counts/second for indicated mass number and probable element

Sample	Beam	1	12	14	16	23	24	25	26	27	28	29	30	39	40	41	48	56	69	71	75	113	115
		H	C	N	O	Na	Mg	Mg	Mg	Al	Si	Si	Si	K	Ca	K	Ti	Fe	Ga	Ga	As	In	In
CZ-23 ("clean" area)	O ⁻									16									10,390	6,380	14		
CZ-23 ("clean" area)	N ₂ ⁺					30	14			174	16	18	16	18	22	18			248,600	163,200	59		
CZ-23 ("dirt" spec)	N ₂ ⁺	16	15	19		89	163	72	93	1224	928	20	19	274	48	50	557	111	519,400	252,300	126		
CZ-23 (small spec)	O ⁻	16				16	22	13	15	568	100	14	14						1,336	14,470	15		
CZ-23 (particle)	C ⁻						14		13	24	37	13	13						5,194	3,710	15		
CZ-23 (drying spot?)	O ⁻	17	17	14		557	14			519	1560	252	24	70		17			315	445	14		
FZ8 Feed	N ₂ ⁺	15		16	14	22				14	14			22	14				445,200	222,600	193	27	1484
FZ8 Zoned	N ₂ ⁺	16		19		19				59	19	15		30	15	17			408,100	408,200	312	17	371
FZ9 Feed	N ₂ ⁺	17		19		17				16	18	14		63	26	19			408,200	408,200	371	26	853
FZ9 Zoned	N ₂ ⁺	54	14	23	23	740	16	13	14	35	16	16	13	965	171	52			408,200	408,200	315	141	3340

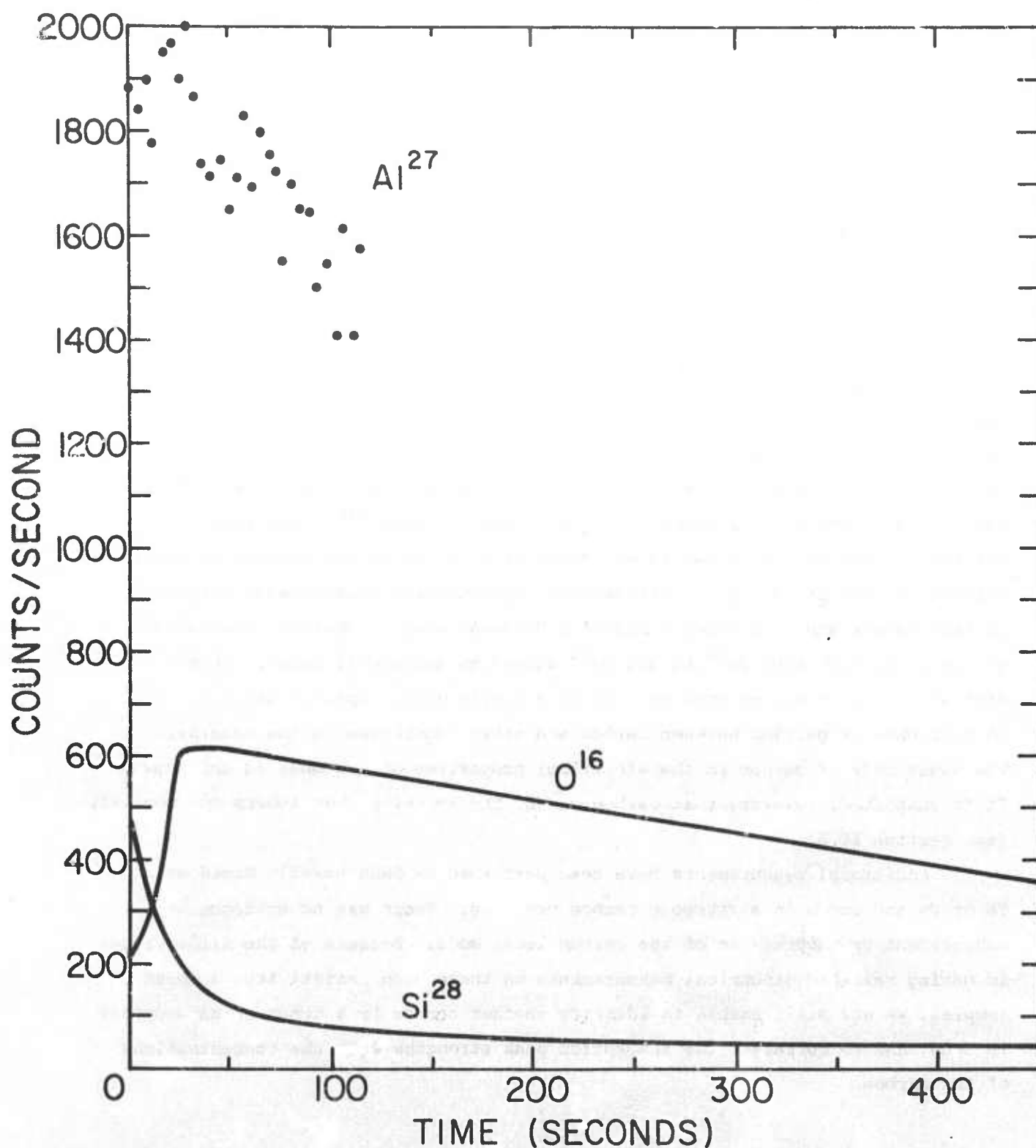


Figure 19. IMMA of C223, with beam burning-in on one spot at a time, producing roughly parabolic pits. O¹⁶ and Al²⁷ using N₂⁺ beam, Si²⁸ using O⁻ beam. O¹⁶ and Si²⁸ data gave relatively smooth curve, while Al²⁷ data fluctuated; using 1-second counts.

and oxygen contents with depth. Aluminum fluctuations probably resulted from growth rate fluctuations due to free convection fluctuations and rotation of the seed. The primary difference between the Czochralski slice and the liquid encapsulated floating zone samples is the much greater indium content of the floating zone samples, for which we have no explanation.

IMMA was also used in the studies described in Section VI.G.2.

B. Carbon in GaAs

(P. Leung)

We have performed infrared absorption measurements on some of our high resistivity Czochralski crystals over a higher frequency region. Figure 20 shows the liquid nitrogen temperature absorption coefficient versus wavenumber for an undoped sample. Note the distinct absorption band at $\sim 582.4 \text{ cm}^{-1}$. This band is due to the localized vibrational modes of carbon in GaAs.⁽⁴⁶⁾ The rise of the absorption coefficient at the lower frequencies is due to the two-phonon lattice absorption band at 528 cm^{-1} . Differential transmission measurements performed on this sample and an undoped horizontal Bridgman sample (WA-1000) over a frequency range from 5000 cm^{-1} to 350 cm^{-1} showed no additional bands. This indicates that carbon existed in GaAs as a single defect species and there were no complexes or pairing between carbon and other impurities in the material. The exact role of carbon in the electrical properties of our GaAs is not known. It is suspected, however, that carbon may be the impurity that lowers the mobility (see Section II.A).

Additional measurements have been performed on GaAs heavily doped with Te or Zn and grown in a vitreous carbon crucible. There was no evidence of enhancement or suppression of the carbon local mode. Because of the difficulties in making reliable electrical measurements on these high resistivity, undoped samples, we are still unable to identify whether carbon is a donor or an acceptor in GaAs, and to correlate the absorption peak strengths with the concentrations of the carbon.

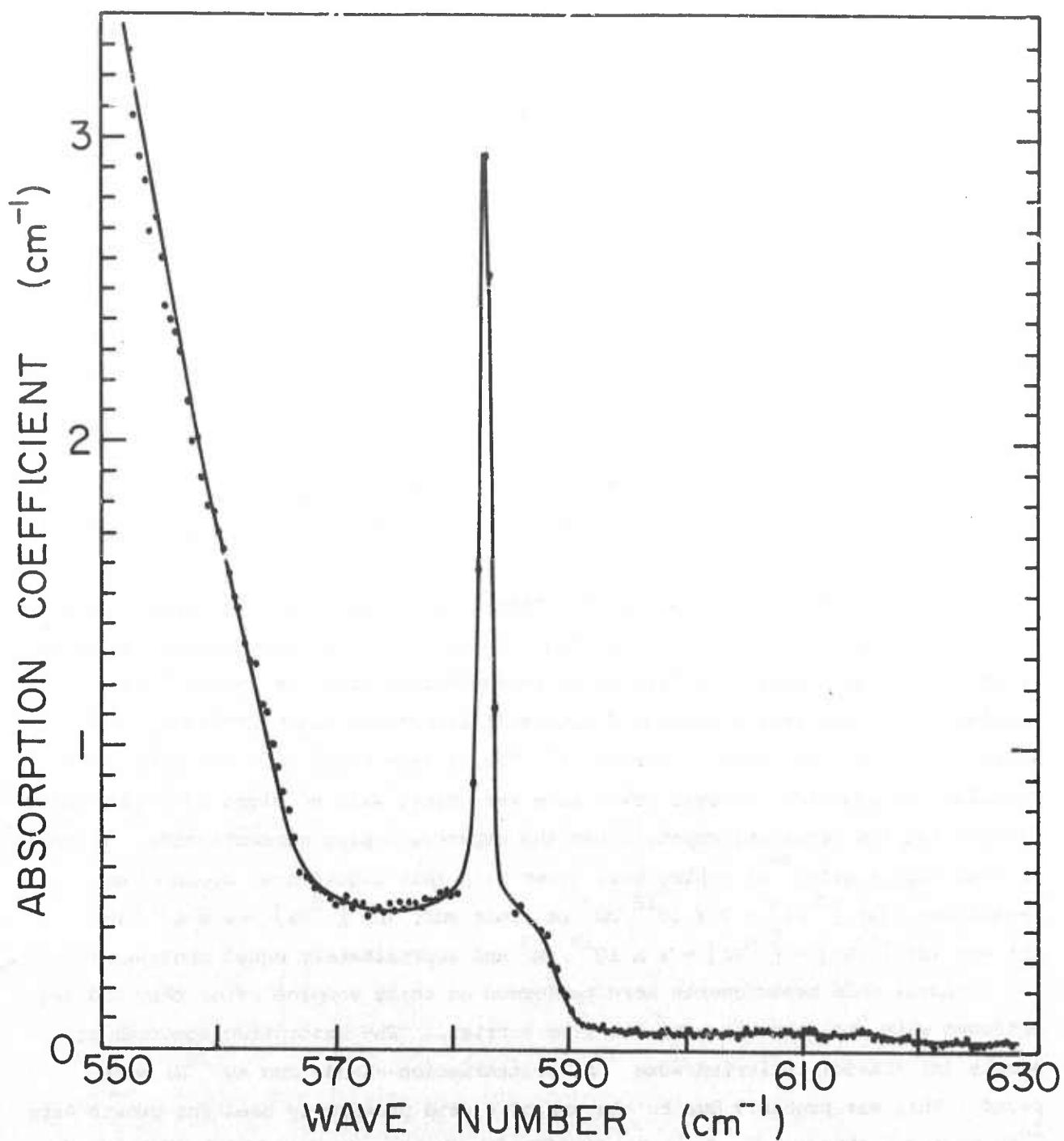


Figure 20. Infrared absorption at liquid nitrogen temperature of sample from Czochralski-grown crystal CZ-37.

C. Si Local Modes in GaAs

(P. Leung)

Local mode absorption is a very useful tool for studying the nature of defects in semiconductors. From the experimentally observed band frequency, strength, carrier concentration dependence, symmetry considerations, etc., the defect species for a particular local mode can be identified. Si-doped GaAs is a particularly interesting case since Si is an amphoteric impurity in GaAs, i.e., it can go substitutionally on the Ga site to form a donor (Si_{Ga}) or on the As site to form an acceptor (Si_{As}). In addition, there is the possibility of formation of Si-Si pairs and other complexes. Previous experimental studies^(47,48) on Si-doped GaAs have revealed many local mode absorption bands and have attributed them to Si_{Ga} , Si_{As} , $\text{Si}_{\text{Ga}}-\text{Si}_{\text{As}}$, $\text{Si}_{\text{Ga}}-\text{Li}_{\text{Ga}}$, etc. This work attempted to verify some of these band assignments, particularly those due to the $\text{Si}_{\text{Ga}}-\text{Si}_{\text{As}}$ pairs, by introducing a different silicon isotope (^{30}Si) as a dopant, singly and in combination with natural silicon (^{28}Si).

The main problem involved in performing this study was the preparation of the material with controlled ^{30}Si doping. To achieve this, the crystal had to be grown in a system relatively free of Si contamination from the system. The liquid-seal Czochralski technique (section II.A) offered this advantage. In addition, it was necessary to prevent the dopant from being oxidized before the material was reacted. Several trial runs were made, with no signs of oxides being formed, and the resultant crystals had the expected doping concentration. A total of four ingots with ^{30}Si doping were grown with this liquid-seal Czochralski technique: (a) $[\text{Si}] \sim 2 \times 10^{18}/\text{cm}^3$ at front end, (b) $[\text{Si}] \sim 2 \times 10^{19}/\text{cm}^3$, (c) and (d) $[\text{Si}] + [\text{Si}] \sim 2 \times 10^{19}/\text{cm}^3$ and approximately equal concentrations.

Local mode measurements were performed on these samples after they had been diffused with ^6Li to compensate the free carriers. The absorption spectrum of sample (a) (CZ-50) indicated some ^{28}Si contamination--bands due to ^{28}Si were noted. This was probably due to the use of a seed previously used for growth with ^{28}Si doping. Absorption of sample (b) (CZ-51) showed no noticeable bands due to ^{28}Si . In this case, the bands previously observed in ^{28}Si -doped GaAs at 367, 374, 379, 384, 393, 399, 405, 464 cm^{-1} due to $\text{Si}_{\text{Ga}}-\text{Si}_{\text{As}}$, $\text{Si}_{\text{Ga}}-\text{Li}_{\text{Ga}}$, $\text{Si}_{\text{Ga}}-\text{Li}_{\text{Ga}}$, Si_{Ga} , $\text{Si}_{\text{Ga}}-\text{Si}_{\text{As}}$, Si_{As} , $\text{Si}_{\text{Ga}}-\text{Li}_{\text{Ga}}$, $\text{Si}_{\text{Ga}}-\text{Si}_{\text{As}}$, etc., shifted to 356, 365, 369, 373, 383, 388, 394, 449 cm^{-1} , respectively. The shifts were close to the isotopic shift in the simple harmonic oscillator approximation. Sample (c) (CZ-54) represented the

first attempt to grow a crystal with approximately equal concentrations of $[^{28}\text{Si}]$ and $[^{30}\text{Si}]$. This was done by adding a small GaAs charge and ^{28}Si to the remainder of the previous ingot. Absorption measurements indicated that $[^{30}\text{Si}]$ was low and that $[^{28}\text{Si}]:[^{30}\text{Si}] \approx 2:1$. Probably the difficulty was in determining how much of the previous ingot was already used. Another ingot was then pulled with a small amount of ^{30}Si added. The results of sample (d) (CZ-55) indicated $[^{30}\text{Si}]:[^{28}\text{Si}] \approx 1:1$.

The absorption spectrum for the sample with mixed Si-isotopes doping showed the presence of all the bands in the ^{28}Si -doped and ^{30}Si -doped samples. Because of the many overlapping bands at the same or nearly the same frequencies, it was difficult to identify the mixed-isotope bands at the lower frequencies (350 to 420 cm^{-1}). Therefore, the band at 464 cm^{-1} was chosen for the analysis since it presented an unambiguous picture.

Figure 21 shows the composite plot of the liquid nitrogen temperature absorption coefficient versus frequency for sample I (CZ-99, ^{28}Si -doped, ^6Li -diffused), sample II (CZ-51, ^{30}Si -doped, ^6Li -diffused), and sample III (CZ-55, $^{30}\text{Si} + ^{28}\text{Si}$ -doped, ^6Li diffused). The bands at 470, 480 and 487 cm^{-1} were due to ^6Li vibrations of the $\text{Si}_{\text{Ga}}-^6\text{Li}_{\text{Ga}}$ pairs, and they were present in all three samples. The band at 464 cm^{-1} for sample I was shifted to 449 cm^{-1} . This shift of 15 cm^{-1} was as expected from the isotopic change. For sample III, the bands at 464 cm^{-1} and 449 cm^{-1} were both present. In addition, there was an intermediate band at 456 cm^{-1} .

Previous studies^(47,48) showed that the bands at 367, 393 and 464 cm^{-1} are from the same defect. The interpretation was that they are due to $\text{Si}_{\text{Ga}}-\text{Si}_{\text{As}}$ pairs. Elliott and Pfeuty⁽⁴⁹⁾ calculated the frequencies of the modes for this defect at 327, 369, 390 and 419 cm^{-1} . The lowest frequency band has not been observed since it is in a high lattice absorption region. The experimentally observed frequencies of the two intermediate bands at 367 and 393 cm^{-1} were very close to those predicted. The 464 cm^{-1} was substantially larger than the calculated $\omega = 419\text{ cm}^{-1}$, but this is the out-of-phase axial mode and its frequency should be extremely sensitive to the $\text{Si}_{\text{Ga}}-\text{Si}_{\text{As}}$ force constant which was not included in the calculation. Moreover, the overall splitting of these bands indicated a very strong coupling interaction, probably due to nearest neighbors, as compared to the much smaller splitting of the 374, 379 and 405 cm^{-1} bands for the substitutional neighbor pairs $\text{Si}_{\text{Ga}}-\text{Li}_{\text{Ga}}$. Although the interpretation is satisfactory, there

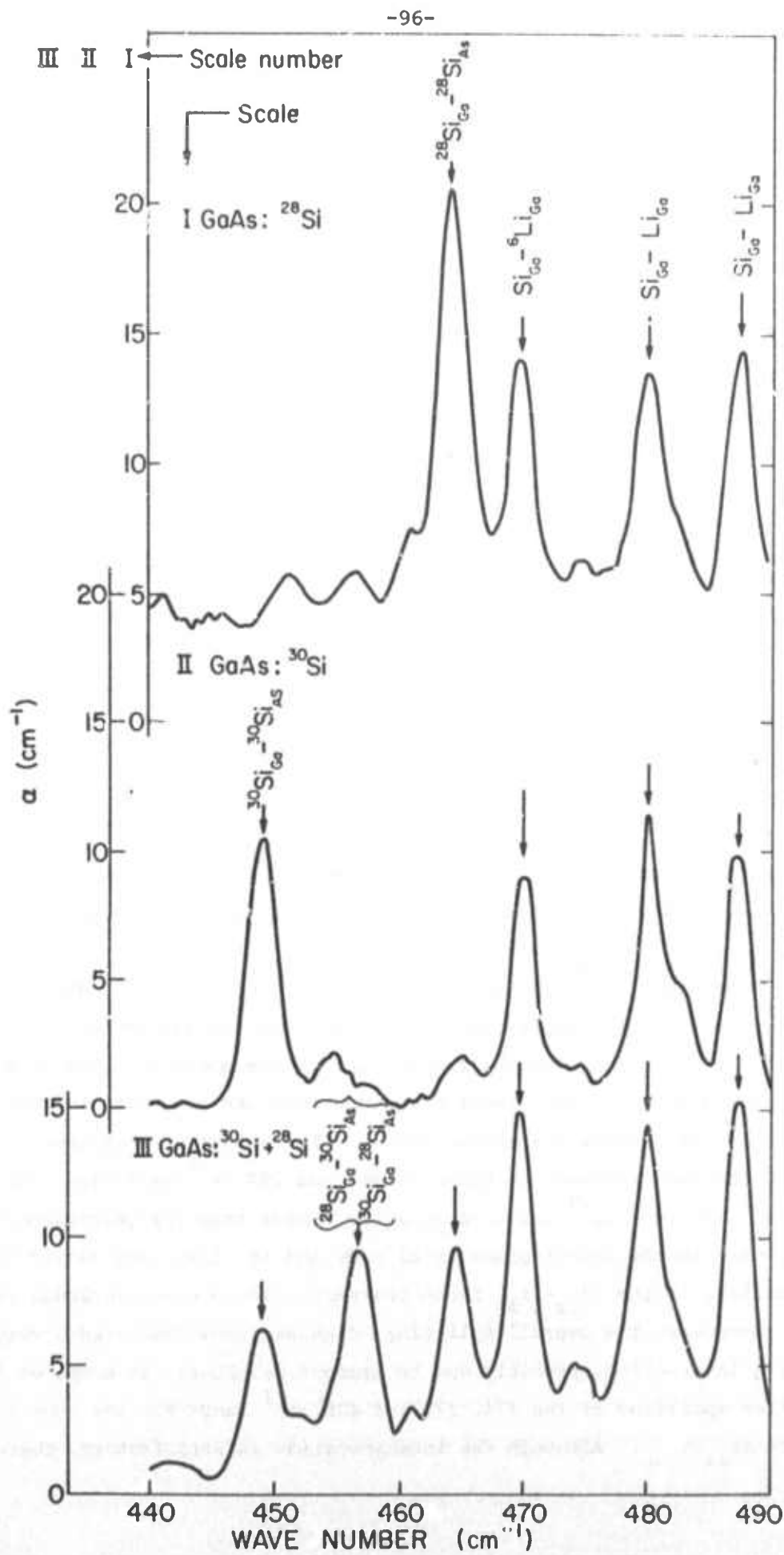


Figure 21. Absorption coefficient vs. frequency for three GaAs samples at liquid nitrogen temperatures.

remains the possibility that the bands at 367, 393 and 464 cm^{-1} may have been due to other complexes.

The presence of the intermediate band for sample III with the mixed $^{28}\text{Si} + ^{30}\text{Si}$ doping clearly established the fact that there was more than one silicon in the defect, since only the shifted band at 449 cm^{-1} would be expected if the defect involved only one silicon. The presence of one intermediate band with the frequency in the middle between the two pure isotope bands is only compatible with the model of two atoms in the defect with equivalent sites.⁽⁵⁰⁾ A three-atom model with equivalent sites gives at least two intermediate bands. In this particular case, the two sites in the defect may be slightly inequivalent. There may have been two bands too close in frequency to be resolved, giving rise to the larger half-width of the intermediate band compared to the two pure isotope bands. A local mode calculation using an iterative approximation computer program previously developed by Cosand⁽⁵¹⁾ predicted 456.4 and 456.9 cm^{-1} for $(^{28}\text{Si}_{\text{Ga}} - ^{30}\text{Si}_{\text{As}})$ and $(^{30}\text{Si}_{\text{Ga}} - ^{28}\text{Si}_{\text{As}})$ modes, respectively. This result is also in reasonably good accord with the experiments.

The absorption spectrum for a $^{30}\text{Si} + ^{28}\text{Si}$ -doped sample compensated by electron irradiation indicated additional absorption at 389 cm^{-1} which may be attributed to the mixed silicon isotope pairs, but no band at 362 cm^{-1} where the mixed isotope pair band should occur. The present results clearly establish the existence of $(\text{Si}_{\text{Ga}} - \text{Si}_{\text{As}})$ pairs and that the 464 cm^{-1} band is indeed due to a normal mode of this defect pair. It also appears likely that the previous identification of the 393 cm^{-1} band was correct and due to a vibrational mode of the same pair. The previous identification of the 367 cm^{-1} band is, however, questionable.

D. Oxygen in GaAs

(J. M. Whelan and P. D. Vijayakumar)

Although there has been much speculation on the role(s) of oxygen in GaAs, there is little solid information because of a lack of satisfactory techniques for determining the oxygen content of a crystal. The zirconia cell described in section III.C can be used for measuring oxygen in GaAs.

The apparatus shown in Figure 12 was first used to test the validity of Henry's Law for oxygen dissolved in Ga. Known amounts of oxygen were electrolytically pumped into the Ga and the corresponding changes in $[P_{\text{O}_2}/P_{\text{O}_2}^{\text{ref}}]^{1/2}$

noted as has been described. Typical changes corresponding to oxygen additions to Ga at 600°C are shown in Figure 22. The linear relationship (Henry's Law) between $(P_{O_2}/P_{O_2 \text{ ref}})^{1/2}$ and the amount of oxygen added can be extrapolated to $(P_{O_2}/P_{O_2 \text{ ref}})^{1/2} = 0$, at which the fugacity of the dissolved oxygen is zero, as is the mol fraction. This established the abscissa scale for the mol fraction of atomic oxygen.

With the information contained in Figure 22 one can estimate the concentrations of oxygen in GaAs by dissolving GaAs in Ga and noting the changes in its fugacity over a range in which it is proportional to $[P_{O_2}/P_{O_2 \text{ ref}}]^{1/2}$. The time dependence of $[P_{O_2}/P_{O_2 \text{ ref}}]^{1/2}$ is shown in Figure 23 before and after dipping and partially dissolving two GaAs samples. Based on the indicated extrapolations and weight changes the amounts of added oxygen correspond to oxygen concentrations in the GaAs samples of 10^{17} and 10^{18} atoms/cm³. For these calculations it is assumed that all of the oxygen associated with the GaAs was in the volume rather than on the surface. It is possible to separate the surface and volume sources.

E. Glow Discharge Spectroscopy for the Analysis of Thin Films

(J. E. Greene and J. M. Whelan)

Available techniques for the chemical analysis of epitaxial semiconductor films are limited due to typical sample thicknesses of 1 to 10 μm. The use of glow discharge spectroscopy was investigated as an analytical technique. (103, 105, Appendix I) GaAs was DC sputtered in argon and the glow discharge monitored for luminescence associated with one or more selected elements. The luminescent intensities combined with sputtering rates were used to estimate depth profile concentrations, e.g., the Sb concentrations in GaAs-GaSb alloy films on GaAs. The present detection limit for Sn in GaAs is 9×10^{17} atoms/cc for a sputtering rate of 1.4×10^{-5} cc/min. Sputtering yields have been measured over the range 0.5 - 3 kV and found to vary with orientation in the following order: (111)b, (111)a, (211), and (110).

noted as has been described. Typical changes corresponding to oxygen additions to Ga at 600°C are shown in Figure 22. The linear relationship (Henry's Law) between $(P_{O_2}/P_{O_2 \text{ ref}})^{1/2}$ and the amount of oxygen added can be extrapolated to $(P_{O_2}/P_{O_2 \text{ ref}})^{1/2} = 0$, at which the fugacity of the dissolved oxygen is zero, as is the mol fraction. This established the abscissa scale for the mol fraction of atomic oxygen.

With the information contained in Figure 22 one can estimate the concentrations of oxygen in GaAs by dissolving GaAs in Ga and noting the changes in its fugacity over a range in which it is proportional to $[P_{O_2}/P_{O_2 \text{ ref}}]^{1/2}$. The time dependence of $[P_{O_2}/P_{O_2 \text{ ref}}]^{1/2}$ is shown in Figure 23 before and after dipping and partially dissolving two GaAs samples. Based on the indicated extrapolations and weight changes the amounts of added oxygen correspond to oxygen concentrations in the GaAs samples of 10^{17} and 10^{18} atoms/cm³. For these calculations it is assumed that all of the oxygen associated with the GaAs was in the volume rather than on the surface. It is possible to separate the surface and volume sources.

E. Glow Discharge Spectroscopy for the Analysis of Thin Films

(J. E. Greene and J. M. Whelan)

Available techniques for the chemical analysis of epitaxial semiconductor films are limited due to typical sample thicknesses of 1 to 10 μm. The use of glow discharge spectroscopy was investigated as an analytical technique. (103, 105, Appendix I) GaAs was DC sputtered in argon and the glow discharge monitored for luminescence associated with one or more selected elements. The luminescent intensities combined with sputtering rates were used to estimate depth profile concentrations, e.g., the Sb concentrations in GaAs-GaSb alloy films on GaAs. The present detection limit for Sn in GaAs is 9×10^{17} atoms/cc for a sputtering rate of 1.4×10^{-5} cc/min. Sputtering yields have been measured over the range 0.5 - 3 kV and found to vary with orientation in the following order: (111)b, (111)a, (211), and (110).

Ga-Ga₂O₃ Equilibrium.

Temp. of Ga soln. : 600°C
 $P_{O_2Ref.}^{1/2} : 0.685 \times 10^{-14}$.

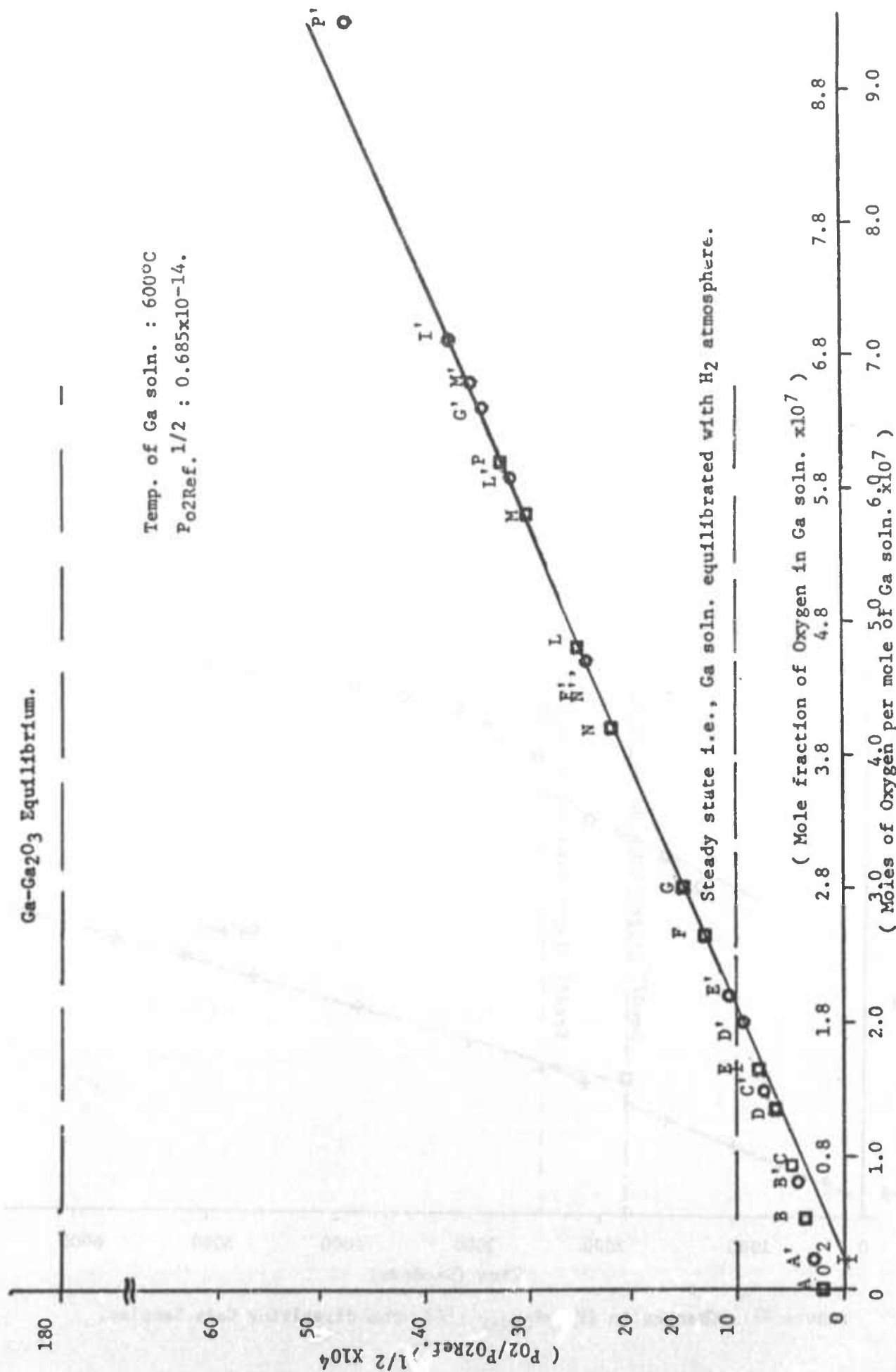


Figure 22. Changes in $(P_{O_2}/P_{O_2Ref.})^{1/2}$ associated with additions of Oxygen to the Ga soln. Changes are represented by unprime to corresponding prime letters.

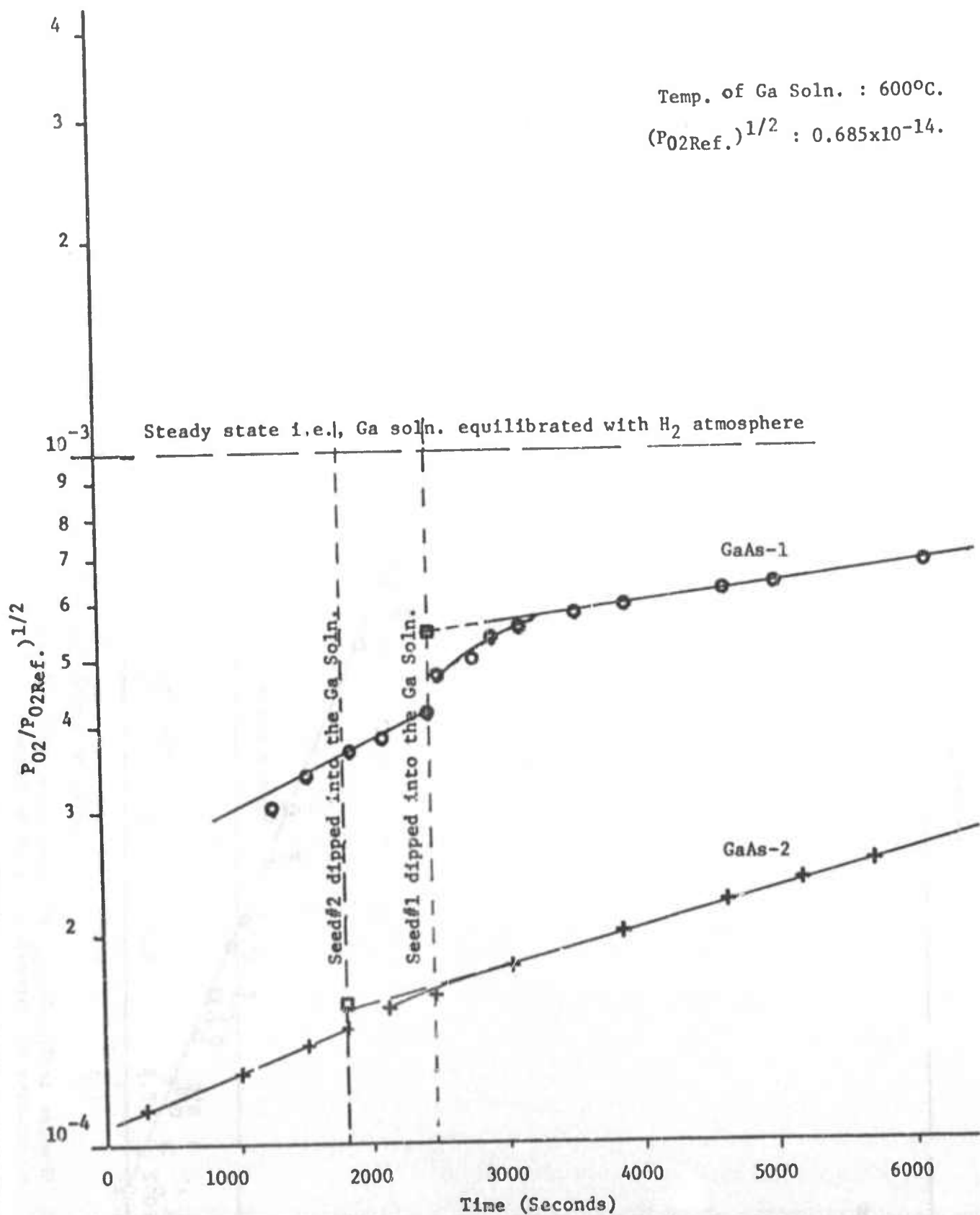


Figure 23. Changes in $(P_{O2}/P_{O2Ref.})^{1/2}$ upon dissolving GaAs Samples.

F. Dislocation Studies and Electrical Properties

(A. L. Esquivel, S. Sen, R. Wang and W. N. Lin)

Although it is well known that dislocations significantly affect the electrical properties of semiconducting crystals,⁽⁵²⁾ more than one method of characterization is necessary to fully describe their mechanical and electronic behavior. For the GaAs single crystals grown at USC, the grown-in dislocations were examined using conventional optical microscopy to distinguish between the A(111) and B($\bar{1}\bar{1}\bar{1}$) surfaces, and to determine the effect of etchants on surfaces with predominantly α (Ga)- or β (As)-type dislocations. Transmission Lang X-ray topography was used to bring out what appeared to be line defects within the bulk of wafers. Reflection Berg-Barrett topography was used to a limited extent to bring out features characteristic of the wafer surface. To examine the surfaces of plastically deformed bulk GaAs, the method of infrared cathodoluminescence (IR-CL) was utilized to point out surface features (related to dislocations) not previously observed. The IR-CL method also had the advantage of being nondestructive in that no etching was required, thus preserving the deformed and control samples for electrical measurements. Finally, from Hall measurements performed at near-liquid nitrogen temperatures to room temperature, the variation of the conductivity, carrier concentration and Hall mobility with temperature and deformation was examined in detail.

1. Characterization of As-Grown GaAs by Etching and Optical Microscopy

GaAs belongs to the class of A^{III}B^V semiconductor compounds which crystallize in a noncentrosymmetric zincblende lattice. Because this structure contains a polar axis it is customary to designate the {111} plane consisting of Ga atoms as the A(111) surface and the ($\bar{1}\bar{1}\bar{1}$) plane of As atoms as the B($\bar{1}\bar{1}\bar{1}$) surface. There are also two types of edge dislocations: α , when the extra half-plane of the dislocation ends on a row of Ga atoms, and β when the plane ends on a row of As atoms. Since different electrical and chemical properties are associated with these two types of surfaces, it is highly important, therefore, in the characterization of GaAs to be able to identify these two planes and two types of dislocations. As described below, we have studied etching methods for displaying the features of the A(111) and B($\bar{1}\bar{1}\bar{1}$) surfaces of GaAs.

A GaAs sample grown by a horizontal Bridgman technique was oriented along the $\langle 111 \rangle$ direction using standard Laue X-ray back-reflection methods. Wafers (3 mm x 10 mm) were sliced parallel to the (111) Bragg plane. Both top and bottom surfaces of the wafers were lapped on plate glass in a slurry of 3200 mesh powder. Surface damage was removed by immersing the samples in a chemical polishing solution consisting of one part HF, three parts HNO_3 and two parts H_2O .⁽⁵³⁾ The resulting thicknesses ranged from 0.1 to 0.8 mm.

The samples were separately etched in three different solutions⁽⁵³⁾ to reveal dislocation pits on either or both $A(111)$ and $B(\bar{1}\bar{1}\bar{1})$ surfaces. The density of these pits was calculated from several samples and from several areas of the same sample. The dislocation densities, chemical composition of the etchants and suitable etching times are listed in Table XXI.

The photomicrographs of the $A(111)$ and $B(\bar{1}\bar{1}\bar{1})$ surfaces etched by the three solutions are shown in Figures 24 through 26. Figure 24 shows that by using the first etchant (Schell reagent), dislocation pits appeared only on the $A(111)$ surface but not on the $B(\bar{1}\bar{1}\bar{1})$ surface. This designation of surfaces relative to etching behavior was established by other investigators for other $A^{\text{III}}B^{\text{V}}$ compounds.⁽⁵⁴⁻⁵⁶⁾ The $A(111)$ surface of sample E1 was characterized by well defined tetrahedral pits (Figure 24-a), while pits with defined geometrical shapes were not observed even at higher magnifications (up to 1000X) on the bottom or $B(\bar{1}\bar{1}\bar{1})$ surface of the same sample.

The absence of dislocation pits on the $B(\bar{1}\bar{1}\bar{1})$ surface has been attributed to the high sensitivity of the $B(\bar{1}\bar{1}\bar{1})$ surface to the dissolving power of Schell's reagent. By adding an inhibitor, butylamine (or amylamine) to Schell's reagent, etch pits were revealed on both $A(111)$ and $B(\bar{1}\bar{1}\bar{1})$ surfaces as shown in Figure 25. While the etch pits on the $A(111)$ surface of sample E2-a (Figure 25-a) were found to be similar in shape and size to those found in sample E1 (Figure 24-a) and observed at a lower magnification, the etch pits on the $B(\bar{1}\bar{1}\bar{1})$ surface of sample E2-B were found only at higher magnification and after longer etching times (Figure 25-b).

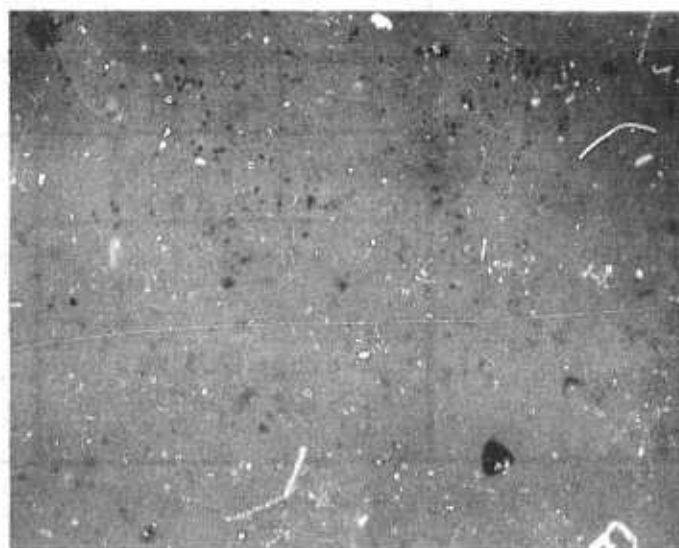
It was suspected, however, by other investigators that the second etchant revealed on the $B(\bar{1}\bar{1}\bar{1})$ surface only a portion of the total number of dislocations actually present.⁽⁵³⁾ Hence, a third etchant (Schell + 0.5% AgNO_3) was applied to both surfaces of sample E3. Figure 26 shows the dislocation etch pits resulting from the use of this third etchant. On the $A(111)$ surface,

TABLE XXI. DISLOCATION DENSITIES AND ETCHANT DATA
FOR GaAs A(111) AND B(111) SURFACES

Etchant No.	Etchant Composition and Etch Time	Dislocation Density, ρ (in cm^{-2})			
		A (111) Surface		B(111) Surface	
		Sample	ρ	Sample	ρ
1	Schell's Reagent: 1 - Part HNO_3 3 - Parts H_2O	E 1	0.6×10^4	No etch pits visible.	
		E 1-A	2.0×10^4 0.8×10^4 1.0×10^4 5.0×10^4		
	Average 1.9×10^4				
	15 minutes @ 80°C (Sample E 1)				
2	Schell + 0.5% Butylamine	E2-A	1.0×10^4	E2-B	4.3×10^5
		E2-C	1.2×10^4 2.8×10^4 1.1×10^4	E2-D	1.0×10^4 2.0×10^4
	15 Minutes @ 26°C (Sample E2-A) 25 Minutes @ 26°C (Sample E2-B)		Average 1.3×10^4		E2-E
				Average 1.6×10^4	
	3	Schell + 0.5% AgNO_3	E3	1.2×10^4	E3
E3-A			1.9×10^4 3.8×10^4	E3-A	3.0×10^4 6.0×10^4 0.2×10^4
		15 Minutes @ 80°C (Sample E3)	Average 2.3×10^4		E3-B
Average 2.8×10^4					



a. $A(111)$ surface 200X
Sample E1 No. 011

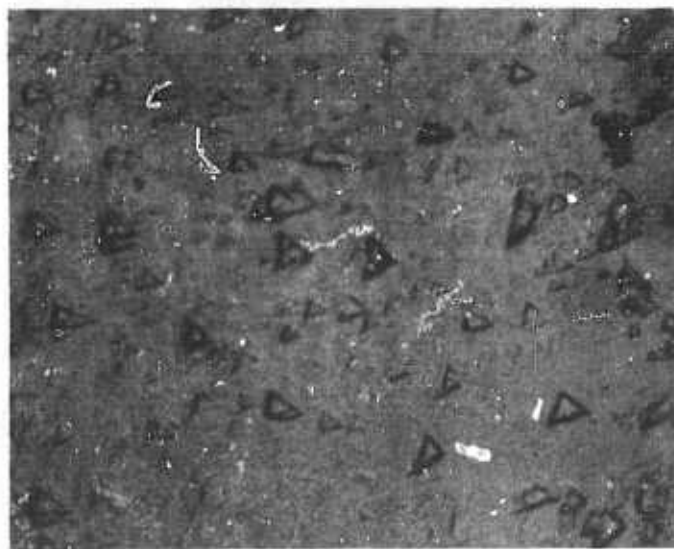


b. $B(\bar{1}\bar{1}\bar{1})$ surface 200X
Sample E1 No. 025

Figure 24. Dislocation etch pits resulting from use of Schell's reagent on $A(111)$ surface of single crystal GaAs. No etch pits appear on the $B(\bar{1}\bar{1}\bar{1})$ surface.

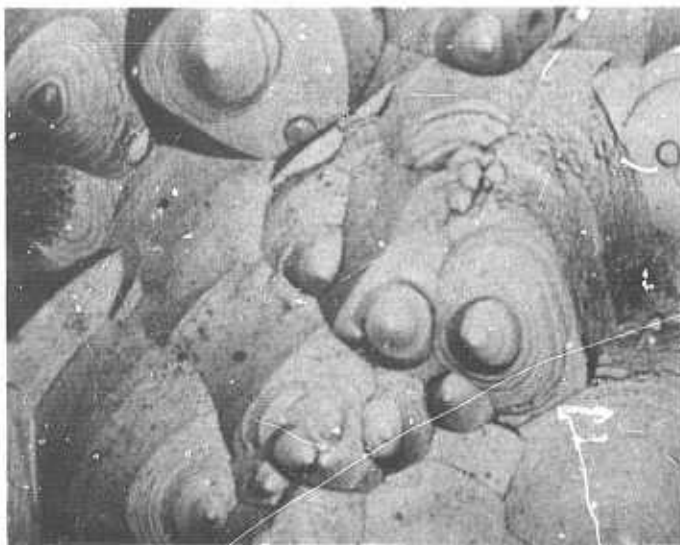


a. A(111) surface 200X
Sample E2-A No. 015



b. B(111) surface 500X
Sample E2-B No. 025

Figure 25. Dislocation etch pits resulting from use of Schell's reagent + 0.5% butylamine.



a. A(111) surface 200X
Sample E3 No. 013



b. B(111) surface 200X
Sample E3 No. 014

Figure 26. Dislocation etch pits resulting from use of Schell's reagent
+ 0.5% AgNO_3 .

conical pits instead of the tetrahedral pits shown in Figures 24-a and 25-a became visible (Figure 26-a). On the $B(\bar{1}\bar{1}\bar{1})$ surface of the same sample, E3, tetrahedral pits developed (Figure 26-b) with initial signs of overetching. Thus the tetrahedra appeared to break up into smaller rectangular parallelepipeds which were observed in earlier micrographs. Because these rectangular features might be mistaken for etch pits, Figure 26-b can be used as a guide when estimating the density of dislocations revealed by this etchant.

The three etchants may be characterized by the types of dislocations revealed on either surface. On the $A(111)$ surface, all three etchants reveal both α and β dislocations,⁽⁵³⁾ so that the dislocation densities on the three $A(111)$ samples should be about the same. Table XXI shows that the average dislocation densities are within the same order of magnitude.

While the first etchant (Schell's reagent) failed to reveal any dislocation pits on the $B(111)$ surface (Figure 24-b), the second etchant (Schell + 0.5% butylamine) revealed what are believed to be α -dislocations, subject to further verification by the bending experiments described later. The third etchant (Schell + 0.5% AgNO_3) is known to reveal both α and β dislocations, so that the dislocation densities observed in the third sample (Figure 26-b) should be higher than those found in the second (Figure 26-b). Table XXI shows that such is the case although the differences in dislocation densities observed in samples E2 and E3 were not as large as those reported by other workers.⁽⁵³⁾

2. Study of GaAs Crystals by X-Ray Topography

Within a GaAs crystal there are grown-in features such as dislocations and compositional fluctuations which are not typically visible in optical micrographs. For this reason, the method of Lang transmission topography was effectively used on several wafers. To prepare samples for the transmission method, slices were cut normal to the crystal growth direction from the top (seed) and bottom ends of Czochralski crystal CZ-16, from which bend samples were also prepared. In order to obtain topographs of the bulk defects, thin wafers (0.076 to 0.152 mm) of (111) GaAs had to be prepared by mechanical and chemical polishing methods.

The following steps were followed in the preparation of the GaAs wafers:

- (a) The crystal was mounted on a sample holder that could be used with the Laue camera and the cut-off wheel.

- (b) The crystal was oriented to the desired crystallographic direction (e.g., $\langle 111 \rangle$) to within 0.5 to 1.0 degree using standard Laue back reflection methods.
- (c) The desired number of 1.0-mm thick slices was cut from the crystal by mounting both crystal and holder on the platform of a diamond (or SiC) cut-off wheel.
- (d) Using a low melting temperature wax (Apiezon black wax) the slices were mounted on a flat quartz disk or on a stainless steel cylindrical block. The slices were then hand lapped on plate glass in a slurry of 3200 mesh abrasive powder.
- (e) To remove surface damage due to lapping, a method of simultaneous mechanical and chemical polishing was employed. The sample was polished on a rotating wheel covered with a soft cloth (Geoscience Polytex Pix) continuously wet with a polishing solution of "Mirrolite" powder (a patented powder developed at USC, see section V.B). The surface removal rate was 0.0025 to 0.025 mm/hour.
- (f) Because of the polarity of GaAs in the $\langle 111 \rangle$ direction, a solution of Mirrolite A was used on the A(111) surface, and plain Mirrolite for the B($\bar{1}\bar{1}\bar{1}$) surface. To determine the polarity of the (111) surface to be polished, a Schell etchant method was followed. Mirrolite A was used instead of the conventional bromine-methanol solution because of the toxic nature of the bromine gas evolved.
- (g) After polishing both surfaces to the desired thickness, the GaAs wafer (extremely brittle) was very carefully demounted from the holder by immersing the sample in acetone for three to six hours. After successively rinsing in acetone and deionized water, the wafer was dried in a slow jet of filtered air.

Lang ($\bar{2}20$) and ($\bar{2}4\bar{2}$) symmetric transmission topographs⁽⁵⁷⁾ of (111) Czochralski GaAs wafers were taken with a Krystallos Model 302 scanning X-ray

topographic camera using MoK α radiation. Topographs were recorded on 50-micron Ilford nuclear plates. Figure 27 shows ($\bar{2}20$) transmission topographs of slices taken from the front (Figure 27-a) and back end (Figure 27-b) of the crystal. Although a low dislocation density ($\sim 10^3 \text{ cm}^{-2}$) has been determined for this crystal, some features indicated by arrows may be associated with dislocations. The crystals in Figure 27 were also examined to a limited extent using skew-reflection, Berg-Barrett techniques. The resolution, however, of the ($\bar{1}\bar{1}2$) Berg-Barrett topographs (not shown) using CuK α radiation, did not permit closer examination of the dislocation-like features in Figure 27.

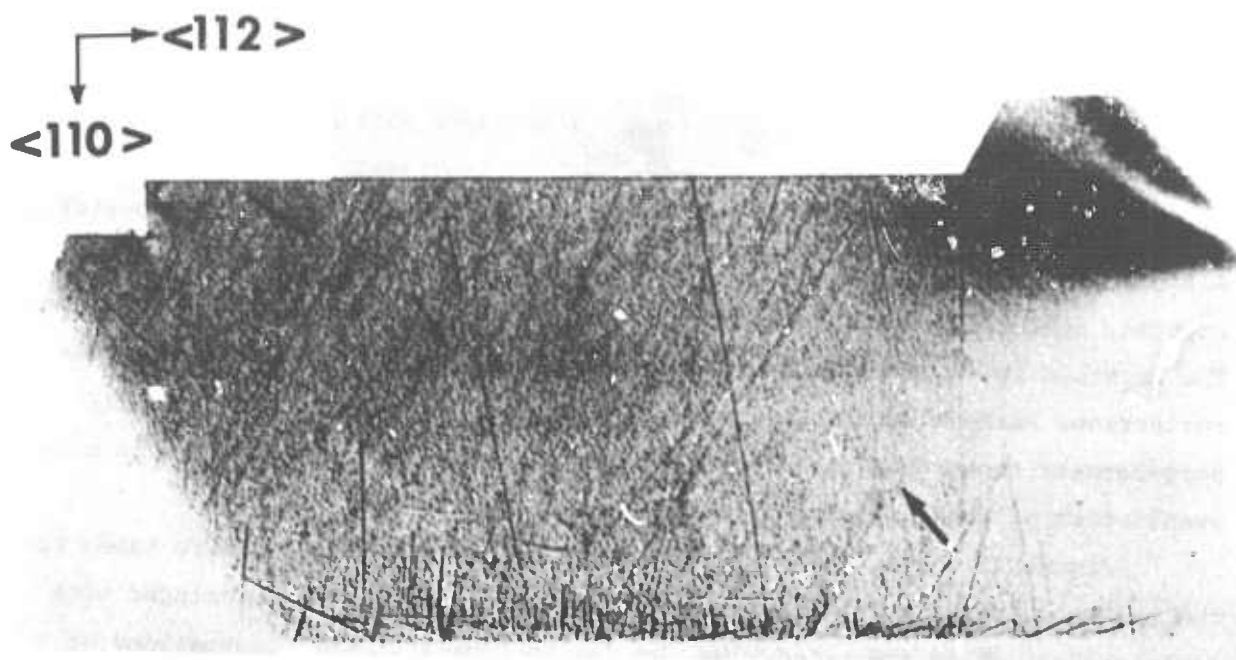
Figure 28 shows ($\bar{2}20$) transmission topographs of (111) wafers taken from the back end of the crystal. Striations in Figure 28 may be associated with dislocations, while the network may be due to compositional fluctuations or polishing artifacts.

Striation features similar to those depicted in the Czochralski sample (Figure 28-b) were also observed in a (111) wafer from a horizontal Bridgman grown GaAs. The ($\bar{2}4\bar{2}$) topograph of this wafer (Figure 29) shows a spiral-type defect (arrow a) which may be associated with a portion of a screw dislocation. The central section of the region shown in Figure 29 has been magnified to show in greater detail the spiral-type defect (arrow a in Figure 30) and numerous fine lines (arrow b) predominantly aligned along the $\langle 110 \rangle$ direction. Although these lines are strongly suggestive of dislocations, further X-ray topographic studies involving determination of Burgers vectors would show conclusively the nature of these defects.

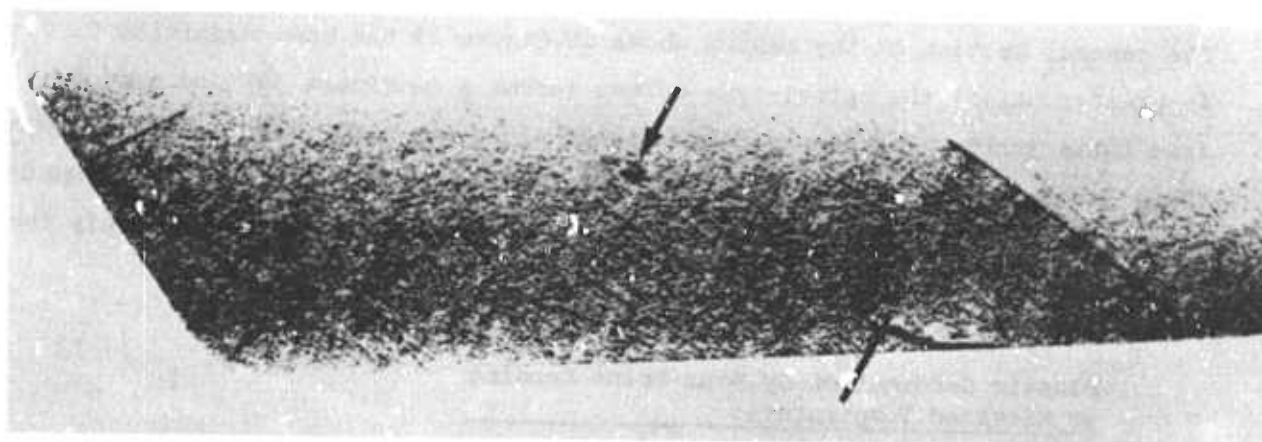
3. Plastic Deformation by Four-Point Bending at Elevated Temperatures

To determine the effects of crystal imperfections on the electrical properties of GaAs, dislocations were introduced in a controlled manner into the samples by four-point bending in an all-quartz bend-furnace. (58)

GaAs samples chosen for the bending experiments were taken from a Te-doped (10^{17} cm^{-3}) Czochralski crystal (CZ-16) and an undoped crystal grown by the horizontal Bridgman method (HB-105). After suitably orienting the crystals by a standard Laue X-ray technique, the samples were cut successively with a diamond wheel and a diamond impregnated wire saw such that the bars could be bent along the [$\bar{1}\bar{1}2$] direction (Figure 31).



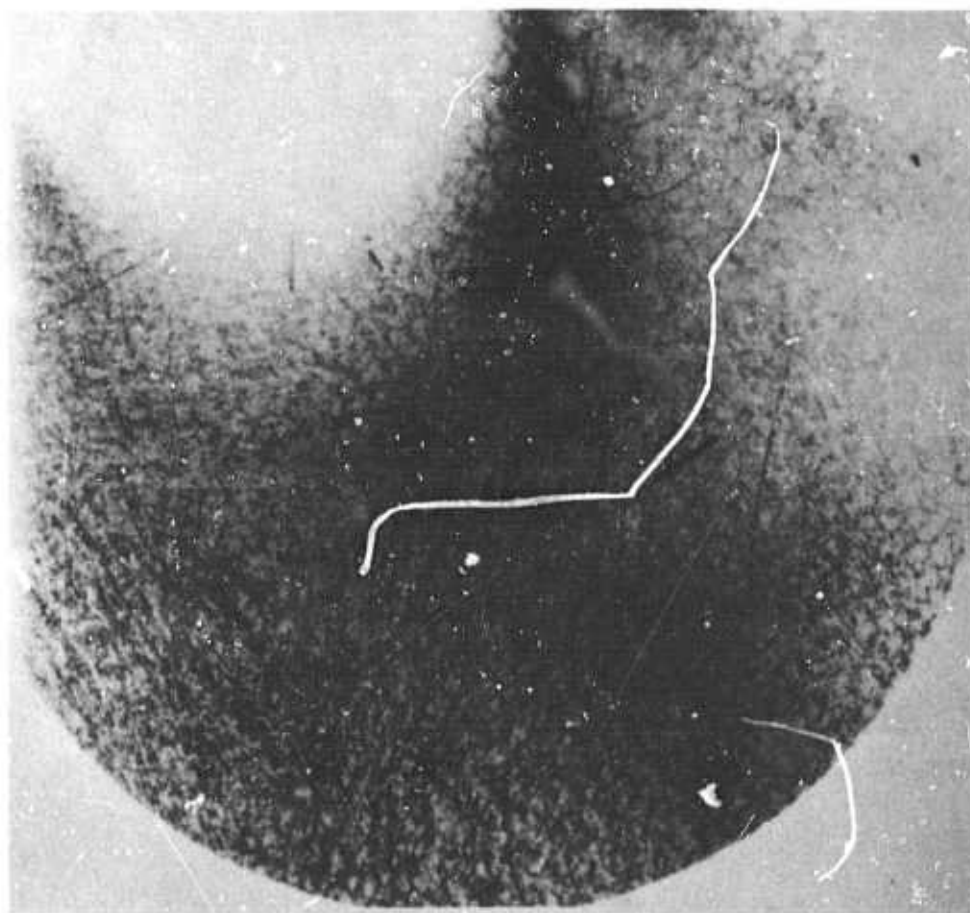
a



b

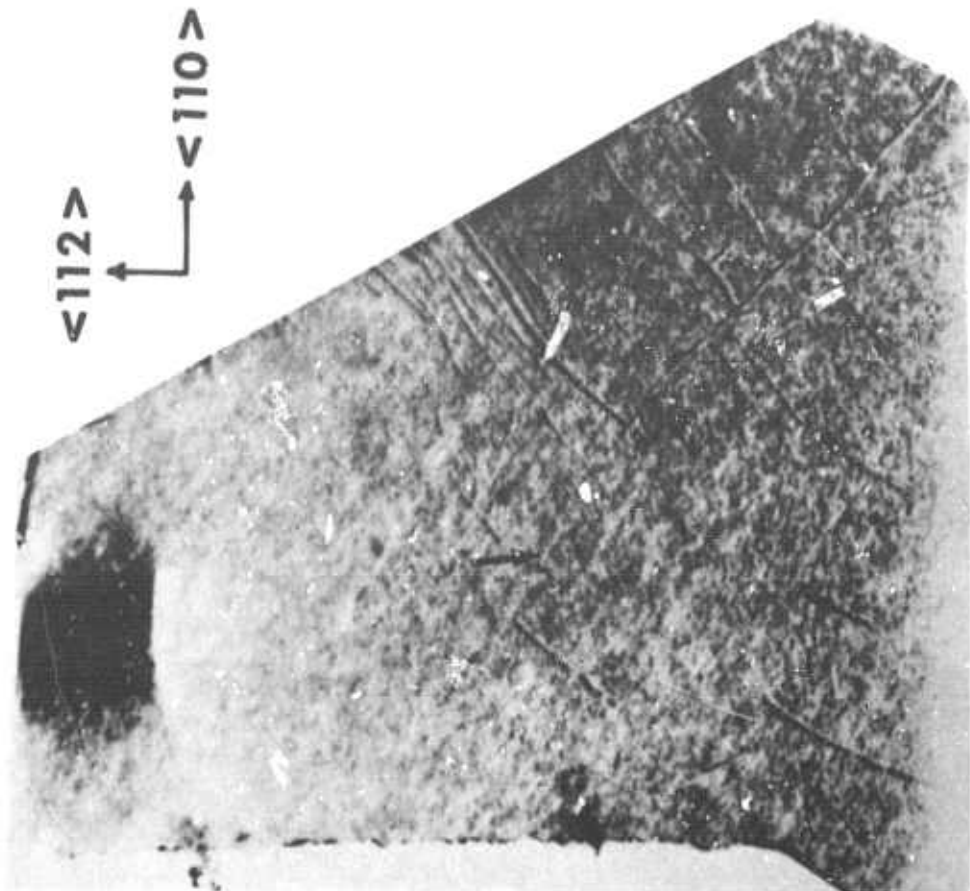
1 mm
└───┘

Figure 27. Lang ($\bar{2}20$) symmetric transmission topographs of (111) wafers of as-grown, Te-doped (10^{17}cm^{-3}) GaAs. Arrows refer to features associated with dislocations in (a) wafer taken from front (or seed) end, and in (b) wafer taken from back end of crystal. Crystal directions refer to both samples. Magnification: 15X. Sample nos. (a) CZ-16-13, (b) CZ-16-4.



a

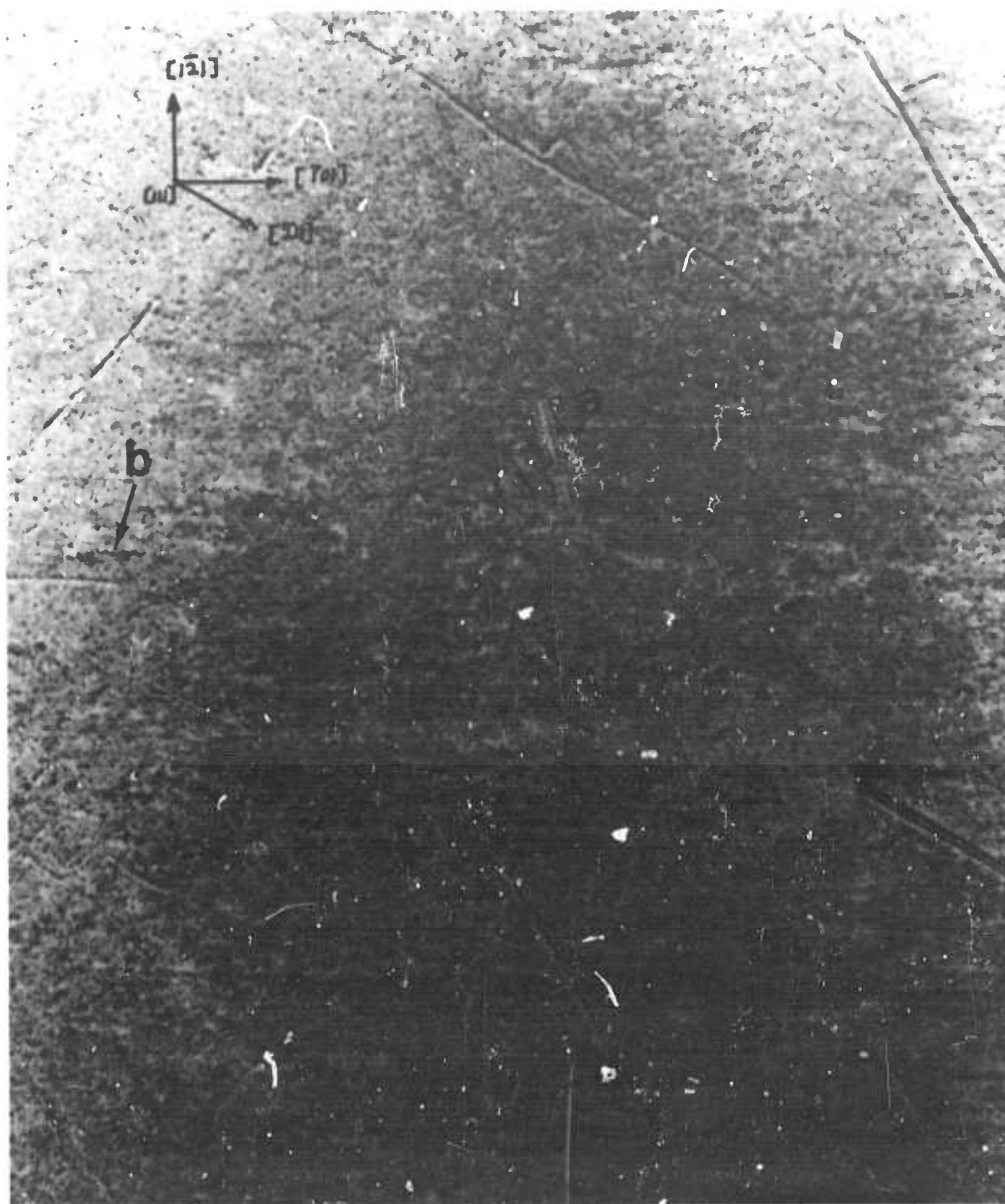
1 mm



b

1 mm

Figure 2a. Lang ($\bar{2}20$) transmission topographs of (111) wafers taken from back end of as-grown Te-doped (10^{17} cm^{-3}) GaAs. Arrows indicate possible dislocations in (a) and (b). Crystal directions refer to both samples. Magnification: (a) 12x, (b) 15x. Samples nos. (a) CZ-16-3; (b) CZ-16-2.



Imm

Figure 30. $(\bar{2}42)$ topograph of the crystal in Figure 29. (X20)

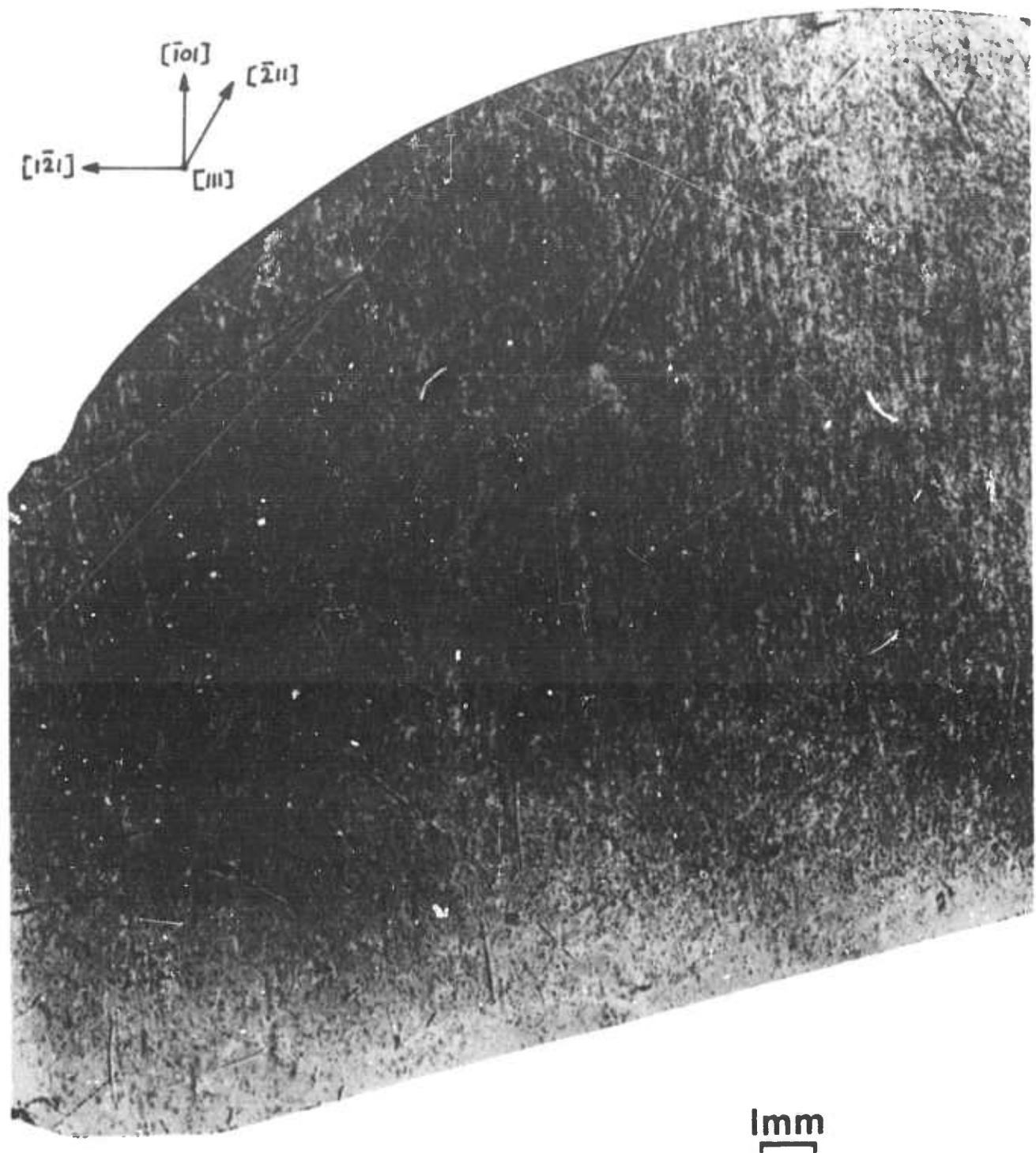


Figure 29. $(\bar{2}4\bar{2})$ transmission Lang topograph of a (111) wafer cut from a horizontal Bridgman-grown GaAs crystal. (X10)

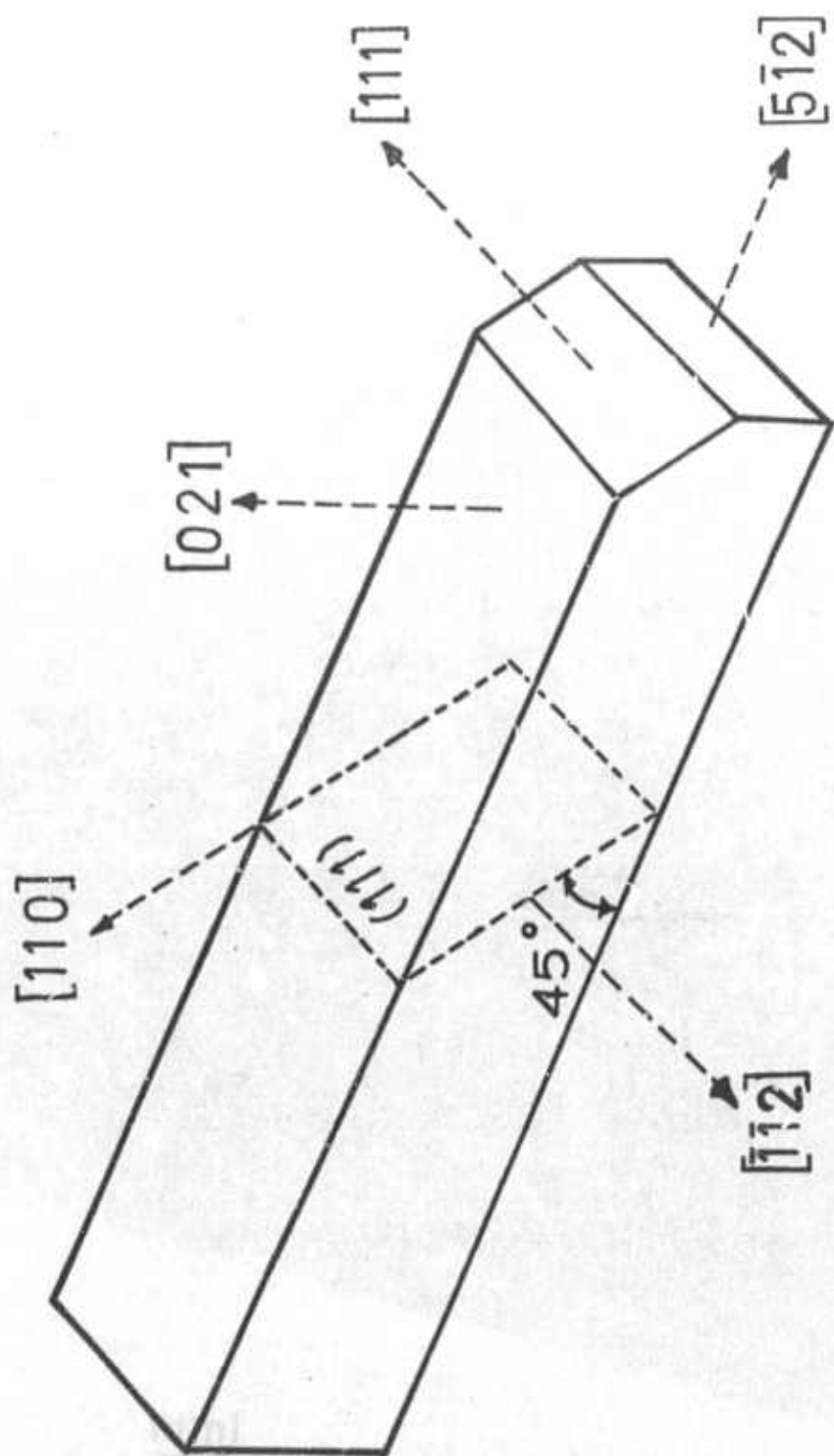


Figure 31. Orientation of GaAs bend sample showing $[112]$ bend axis and (111) slip plane.

The samples were 1.6 to 2.0 cm long, 0.12 to 0.17 cm wide and 0.10 to 0.15 cm thick. To remove any surface damage due to cutting, the rectangular bars were lapped in a slurry of 3200 mesh powder, etched in a hydrofluoric-nitric acid solution ($\text{HF}:\text{HNO}_3:\text{H}_2\text{O} = 1:3:2$) until about 50 microns were removed, and finally rinsed in deionized water. The resulting samples exhibited bright and shiny surfaces.

Six bar samples were cut from two adjacent slices (nos. 9 and 10) from approximately the center of crystal CZ-16. Two bars taken from slice 9 were used for control purposes (namely, as-grown and heated, not bent), while from slice 10, four bars were cut and bent to various curvatures. To introduce a majority of α -dislocations (namely, dislocations whose extra half-plane ends on a row of Ga atoms), the samples were bent according to the orientation shown in Figure 31. with $[\bar{1}\bar{1}2]$ as the bend axis. To introduce β -dislocations (whose extra half planes end on As atoms), the sample was rotated about the $[5\bar{1}2]$ direction such that the bend axis was parallel to the $[11\bar{2}]$ direction.

Because the slices from the front end of the Bridgman crystal were slightly smaller than the Czochralski slices, only three bars (one for bending, the other two for control) could be cut from each slice. Thus, the four Bridgman samples were taken from four adjacent slices instead of from a single slice. To insure cleanliness of the samples, both the control and the bend samples were etched lightly immediately prior to bending with the HF-HNO_3 solution and rinsed in deionized water.

The bending experiments were performed in an all fused silica apparatus (Figure 32) which was designed to eliminate sources of contamination likely to be present in a metallic or non-silica system. The bending apparatus consisted of a lower set of silica knife edges with a separation distance of $d_s = 1.24$ cm mounted on a movable stage (to permit easier alignment) and an upper set of knife edges ($d_s = 0.275$ cm) attached to the tip of a 1.5 cm diameter silica rod. The sample was set on the lower knife edges and kept in position by the upper knife edge. Bending was accomplished by turning the micrometer head a predetermined number of turns.

Prior to each bending operation, the silica platforms were removed from the bottle by means of the arch-shaped handles and washed with aqua regia, dilute HF, and rinsed in deionized water. To remove any residue from the cleaning, the entire bend apparatus was heated (minus the sample) to 700°C with two semi-

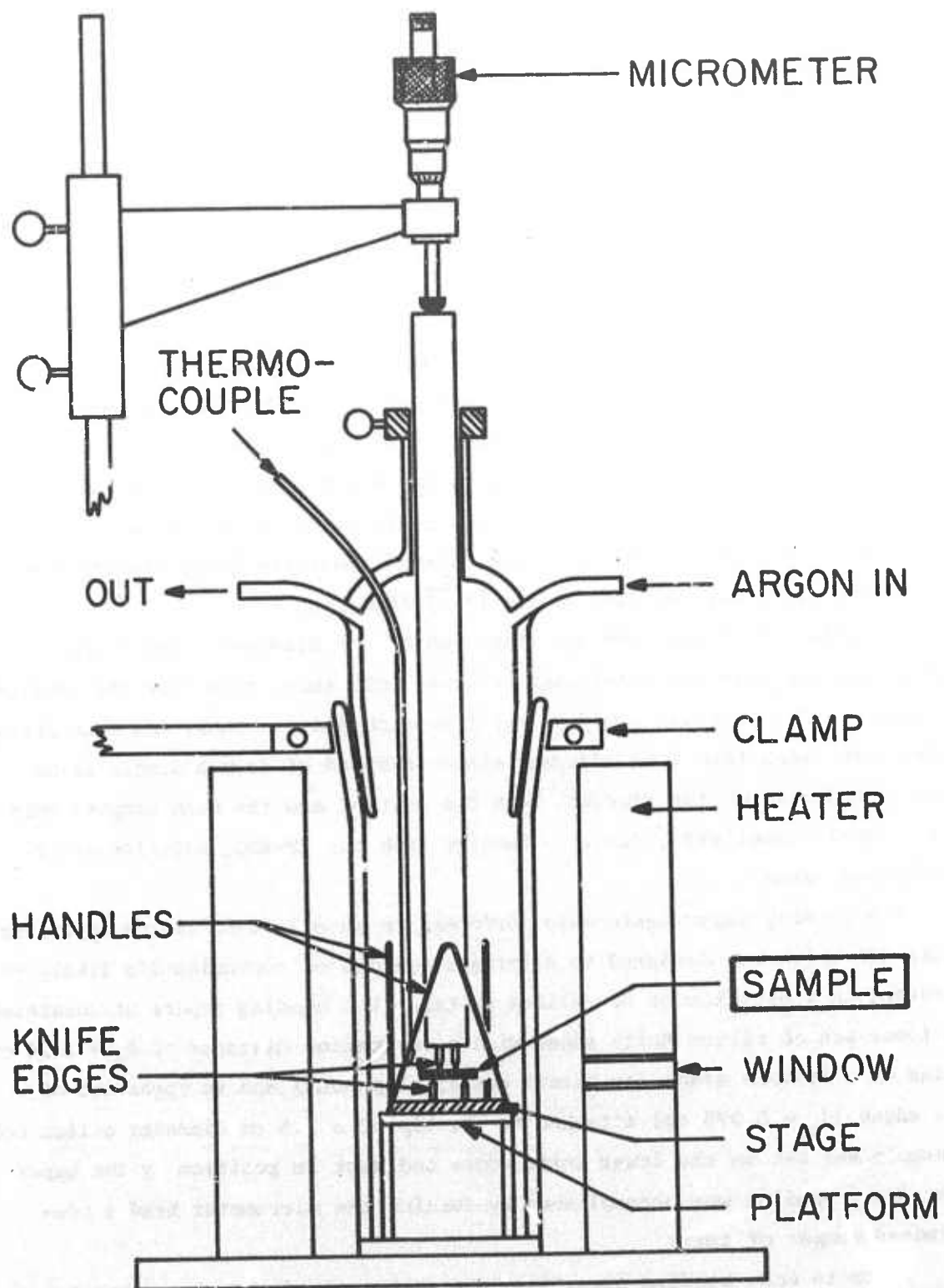


Figure 32. All-quartz four-point bend apparatus and furnace.

cylindrical heating elements which surround the silica bottle. Upon cooling, the platforms were again removed from the bottle and a sample positioned on top of the lower knife edges. For control purposes, another unbent sample was set beside the lower knife edges on the movable stage. After flushing the silica bottle for 15 minutes with purified argon, the furnace was heated to 700°C . Temperature was monitored by a previously calibrated chromel-alumel thermocouple which extended via a sealed silica tube to the inside of the bottle down to the sample level.

The bending temperature range of 650 to 725°C was reached 15 minutes from the moment power was turned on. The actual bending of the sample took 30 seconds. Immediately after bending, which was observed and monitored through a window, power was turned off and the sample cooled to room temperature by pulling the two heating elements away from the silica bottle. Upon removal from the furnace, the bent and control samples were always found to retain their original shiny surfaces.

Using this bending procedure, both α and β dislocations were introduced into the Zochralski and Bridgman grown GaAs samples. By bending these samples to various radii of curvature, R , which were measured graphically from enlarged photographs of the samples, different levels of dislocation densities were attained. The dislocation density, ρ , was calculated using Nye's relation,⁽⁵⁹⁾ $\rho = 1/(Rb \cos \theta)$, where b is the magnitude of the slip vector, $\vec{b} = (a/2) \langle 110 \rangle$, θ is the angle between the (111) slip planes and the neutral plane. The calculated values of dislocation densities lie along the solid line in Figure 33. Table XXII lists the measured bend radii and calculated dislocation densities of both α and β dislocations. Dislocation densities were also measured from cathodoluminescence micrographs (discussed in the next section) and these values are plotted in Figure 33.

4. Cathodoluminescence Study of Deformed Regions in n-Type GaAs

To characterize the surface and bulk regions of the bent and control samples without damaging the surfaces by chemical etching (in order to preserve the samples for the electrical measurements), an electron microprobe was used to study the electron beam excited cathodoluminescence from the deformed and undeformed GaAs crystals.^(60, Appendix J) The samples listed in Table XXII were examined in an

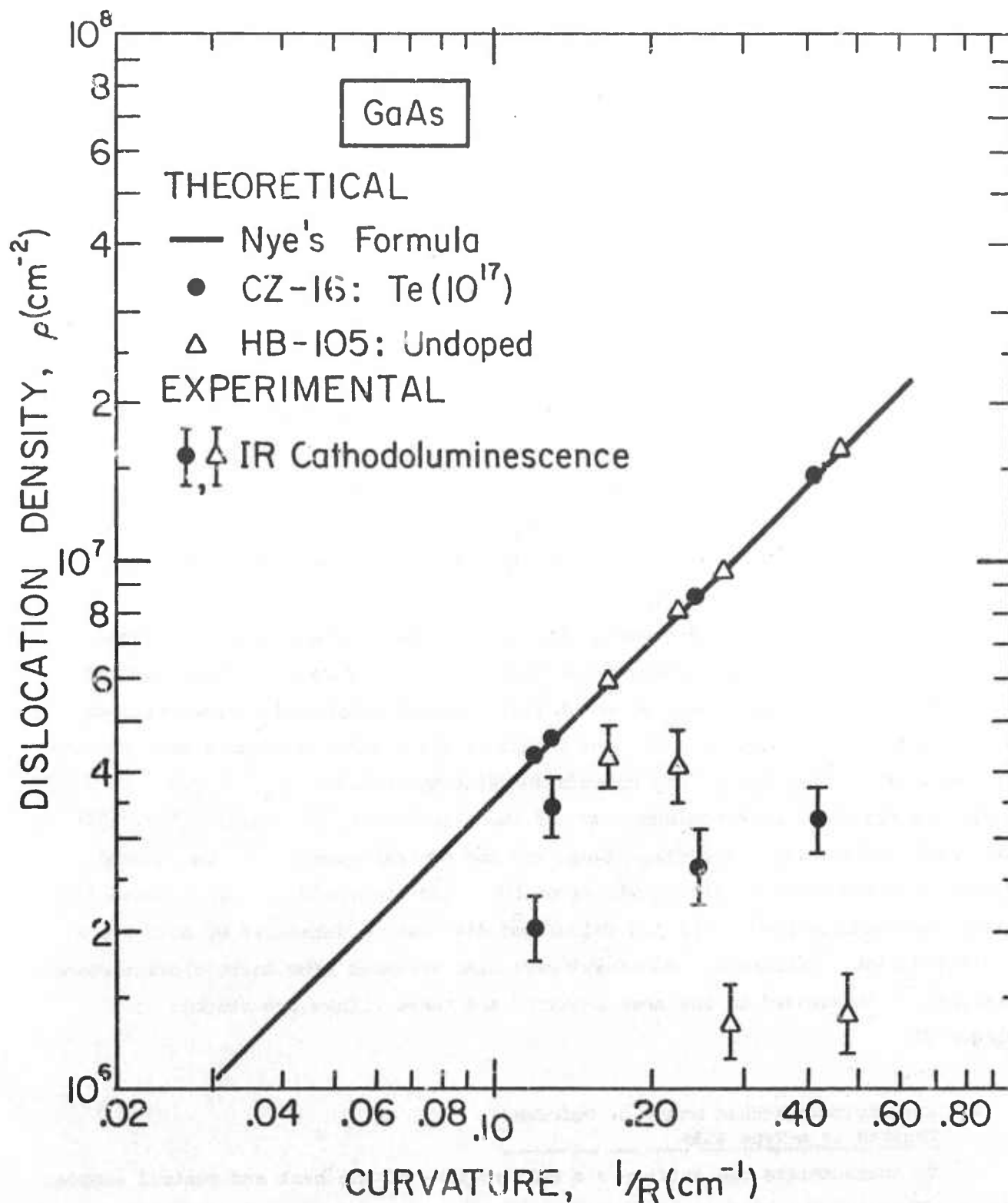


Figure 33. Determination of dislocation densities on the (112) face of bent GaAs samples (CZ-16 and HB-105) using the non-destructive infra-red cathodoluminescence (IR-CL) method. Deviation from the theoretical values can be improved by increasing the resolution of details in the IR-CL micrographs.

TABLE XXII

Radii of Curvature, Dislocation Types
and Densities in Bent n-Type GaAs

A. Czochralski: Te (10^{17} cm^{-3})

No.	Sample No. (CZ-16)	Disloc'n Type	Curve No.	Radius of Curvature R(cm)	Curvature $\frac{1}{R} (\text{cm}^{-1})$	Dislocation Density $\rho (\text{cm}^{-2})$	
						Calculated (a)	Exp'tl (b)
1	10-F-B1	α	B1	8.30	0.121	4.28×10^6	$(2 \pm 0.4) \times 10^6$
2	10-E-B2	β	-	7.62	0.131	4.64×10^6	$(3.4 \pm 0.5) \times 10^6$
3	10-C-B3	β	B2	4.13	0.242	8.57×10^6	$(2.6 \pm 0.6) \times 10^6$
4	10-D-B4	β	B3	2.42	0.414	1.47×10^7	$(3.3 \pm 0.5) \times 10^6$

B. Horizontal Bridgman: Undoped

No.	(HB-105)	Disloc'n Type	Curve No.	R(cm)	$\frac{1}{R} (\text{cm}^{-1})$	$\rho (\text{cm}^{-2})$	
						Calculated	Exp'tl
1	F13-C-B1	β	B1	4.98	0.167	5.91×10^6	$(4.2 \pm 0.6) \times 10^6$
2	F11-C-B2	α	-	4.44	0.225	7.97×10^6	$(4.0 \pm 0.8) \times 10^6$
3	F12-C-B3	α	B2	3.78	0.265	9.38×10^6	$(1.3 \pm 0.4) \times 10^6$
4	F10-C-B4	β	-	2.13	0.469	1.66×10^7	$(1.4 \pm 0.3) \times 10^6$

(a) Using Nye's formula

(b) From cathodoluminescence infra-red micrographs of (112) surface.

an electron microprobe operated at 40 kV and with sample currents ranging from 0.46 to 0.70 microamperes. Most of the micrographs were taken at 200X and the surfaces examined represent square areas from 350 to 400 μ along each edge.

Figure 34 shows the infrared cathodoluminescence (IR-CL) micrographs (a, b, and c) and the corresponding cathodoluminescence (CL) intensity line scans (d, e, and f) of the as-grown (A), heated but not bent (H), and bent (B) Te-doped GaAs. The micrographs were obtained from the ($\bar{1}\bar{1}2$) surface normal to the bend axis and at the center along the edge of each sample as indicated in the accompanying sketches. Dark stripes in Figure 34-a represent growth bands on (111) planes inclined at 45° relative to the (021) plane.

The IR-CL micrographs (Figure 34-a and 34-b) show the effect of heating on the growth bands and particles visible in Figure 34-a. Thus, after heating, the particles have coarsened and the distance between the bands appears to have increased, probably indicating that the dark material in the bands coalesced with the small particles to form larger particles. The mottled appearance in Figure 34 was observed only in the bent sample. It is believed that the dark patches were due to the termination of dislocation lines at the surface from which no radiative recombination took place. Thus, some estimate could be made of the dislocation densities in the bent samples, although because of the low resolution of the micrographs, the values determined from the pictures differ by 15 to 20 percent from the calculated densities (Table XXII).

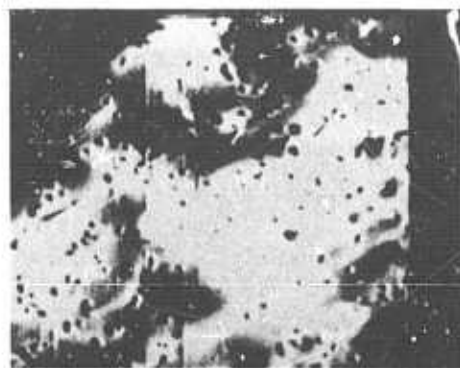
The CL intensity line scans (Figure 34-d, 34-e and 34-f) give a qualitative picture of the homogeneity of the samples along the region scanned by the electron beam. In Figure 34-d, the ordinate represents the relative CL intensity in arbitrary units, while the abscissa indicates distance along the sample surface. Based on the CL line scan, it appears that the as-grown Czochralski sample gave a more uniform profile than the as-grown horizontal Bridgman (undoped) sample shown in Figure 35.

Figure 35 shows the IR-CL micrographs (a, b, and c) and CL intensity line scans (d, e, and f) for the undoped GaAs. The notations are the same as those used in Figure 34. In contrast to the doped sample in Figure 34, the undoped Bridgman samples exhibited a higher particle density (Figure 35-b). Slip on the (111) planes was evident on the deformed ($\bar{1}\bar{1}2$) surface and what are believed to be end points of dislocations on the ($\bar{1}\bar{1}2$) plane appear as dark spots in Figure 35-c.

GaAs

-121-

HB-105-F13C

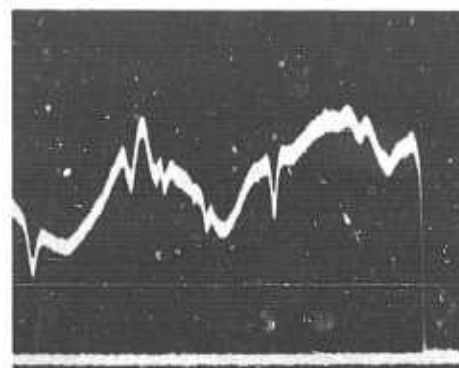


a

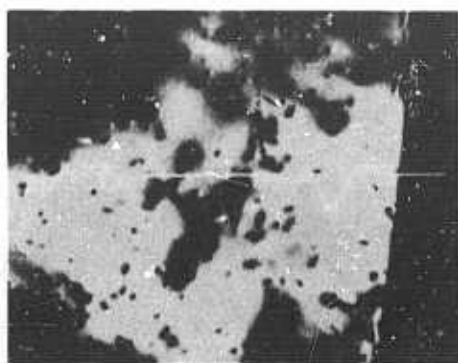
100 μ



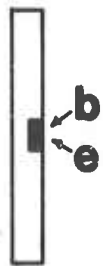
A



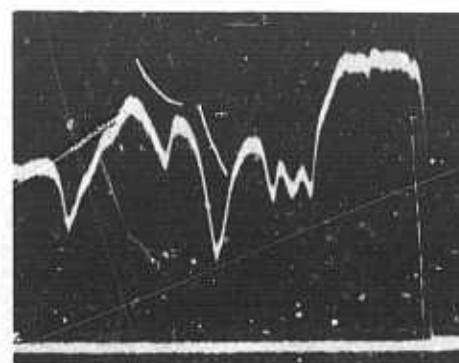
d



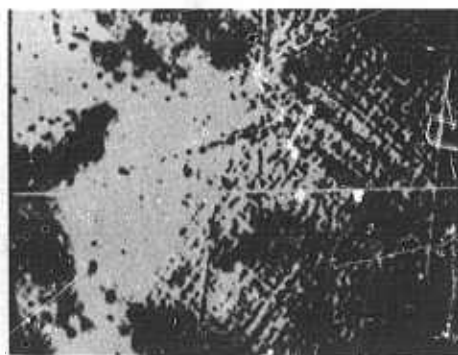
b



H



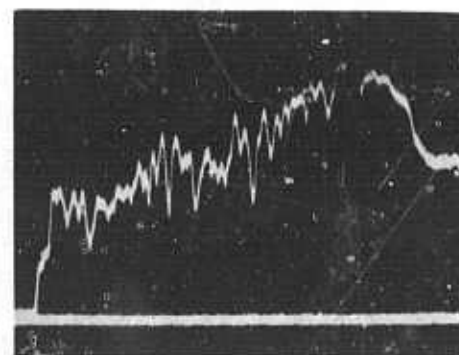
e



c



B



f

Figure 34. IR-CL micrographs of undoped GaAs (a, b, and c) and CL intensity line scans (d, e, and f) across sample. Areas in the as-grown (A) and heated (H) horizontal Bridgman (HB-105) samples are compared with the bent (B) sample.

GaAs

-122-

CZ-16-10 E

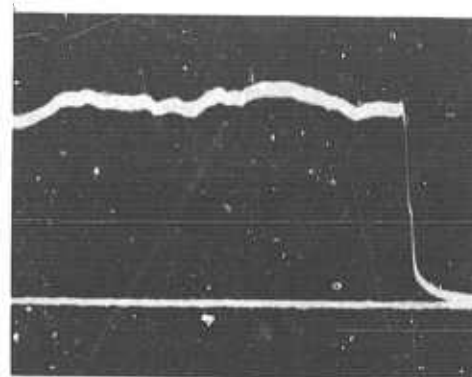


a

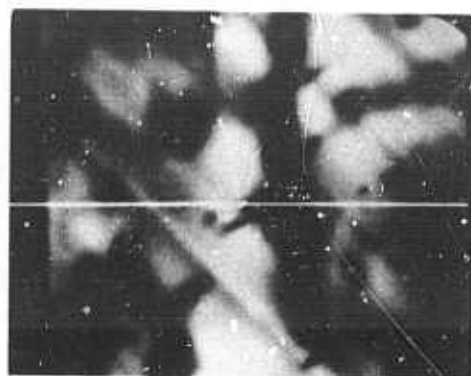
100 μ



A



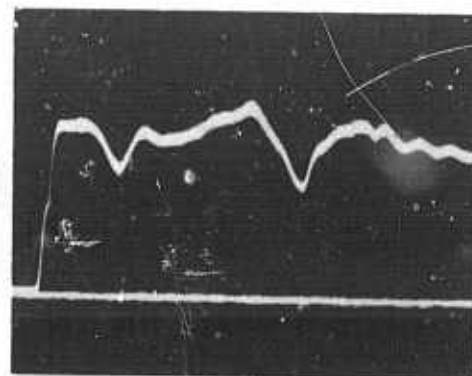
d



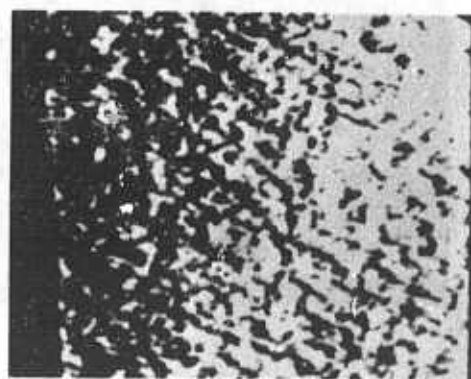
b



H



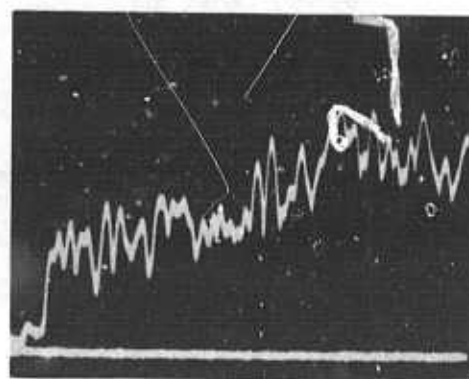
e



c



B



f

Figure 35. Cathodoluminescence Infra-red (IR-CL) micrographs of Te-doped GaAs (a, b, and c) and cathodoluminescence (CL) intensity line scan (d, e, and f) across sample. Areas examined are indicated schematically in the as-grown (A), heated (H), and bent (B) Czochralski (CZ-16) samples. The ordinate and abscissa in (d), (e), and (f) refer, respectively, to CL intensity (in arbitrary units) and distance across sample in microns.

Figure 36 shows that in a bent horizontal Bridgman sample, the mottled or checkered pattern on the (112) plane was restricted to the area near the center, and that the pattern disappeared the farther one moved away from the center (Figure 36-c, 36-d, and 36-e). Figure 36 also shows some microcracking along the upper edge (arrow), thus suggesting that the deformation was more severe on the tensile (Figure 36-a) than on the compressive side (Figure 36-c). The backscattered secondary electron image corresponding to the tensile and compressive surfaces of the bent region revealed a featureless surface in contrast to the checkered pattern shown by the IR-CL micrographs.

Figure 37 shows IR-CL micrographs taken on both the ($\bar{1}\bar{1}2$) surface, compressive side (Figure 37-c and 37-d), and on the (021) surface, tensile side (Figure 37-e and 37-f). Figure 37-a and 37-b shows featureless secondary electron images taken from two areas approximately 0.7 and 1.3 mm from the center on the ($\bar{1}\bar{1}2$) surface, compressive side. The IR-CL, however, exhibit slip traces of (111) planes on both the ($\bar{1}\bar{1}2$) and (021) surfaces.

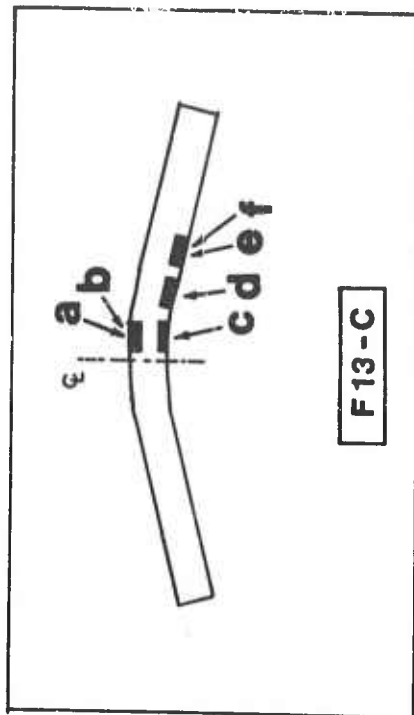
Thus, with the aid of electron beam excited cathodoluminescence, it was possible to reveal details not otherwise visible from optical or back-scattered secondary electron micrographs. Furthermore, without damaging the samples, we have delineated slip characteristics and examined features related to dislocation densities in plastically deformed GaAs.

Figure 38 shows secondary electron emission (SEE) micrographs (column 1), IR-CL micrographs (column 2), and IR-CL intensity, I_c , versus distance, d , (column 3) from the edge of the undoped horizontal Bridgman (HB-105) crystals. The micrographs were taken from the (112) surface at the center of the sample as indicated by the black rectangle in the schematic diagram in Figure 39. It was shown from Figures 34-37 that surface markings as well as growth striations became visible in the IR-CL micrographs. In the present set of photographs (Figure 38), a subsurface flaw not apparent in the SEE micrograph became visible when examined in the IR-CL mode as indicated by the arrows (Figure 38-a, column 2) and by the decrease in IR-CL intensity in column 3.

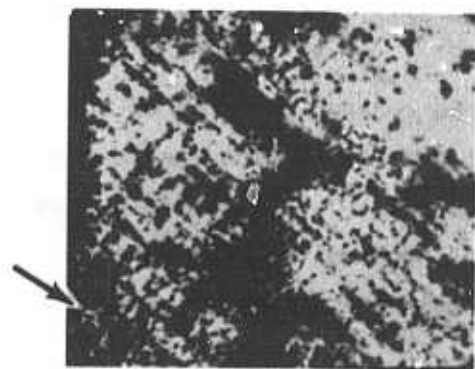
The set of pictures in Figure 38 describe the central portions of the bent horizontal Bridgman samples, while those in Figure 39 describe the corresponding areas in the Te-doped Czochralski sample (CZ-16). The micrographs were taken in the order of increasing calculated dislocation density (indicated in column 2) and as a function of the type of excess dislocation (α or β) present.

GaAs

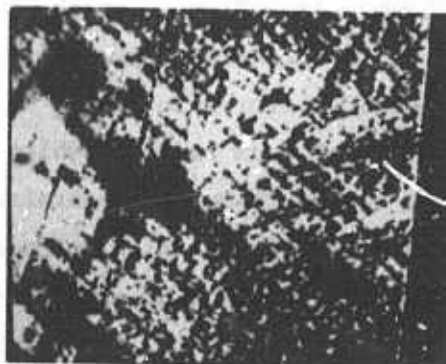
HB-105



100 μ



a



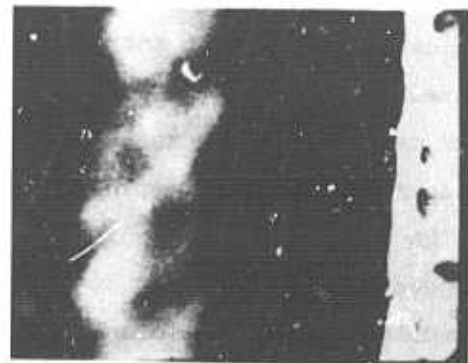
c



d



e



b



f

Figure 36. IR-CL micrographs (a, c, d, e) and secondary electron emission micrographs (b, f) of the tensile (a) and compressive (b) areas in a bent, undoped GaAs sample. Regions progressively removed from bend center are shown in (e) and (f).

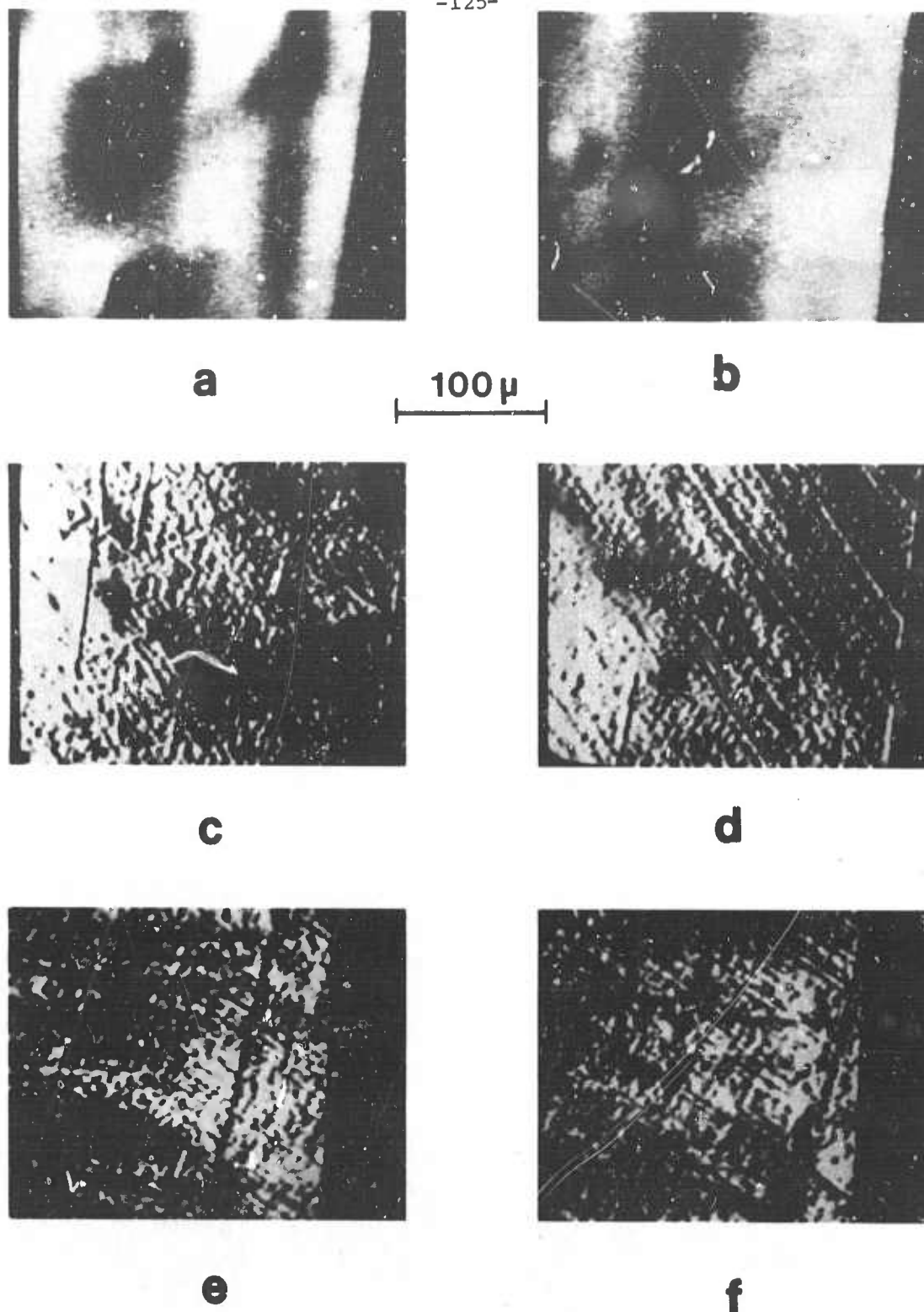


Figure 37. Secondary electron emission-micrographs (a, b) and IR-CL micrographs (c, d, e, f) of bent area in undoped GaAs sample (HB-105-F13C). Taken from $(\bar{1}\bar{1}2)$ face, compressive side are micrographs (a) and (c) (0.7 mm from bend center) and (b) and (d) (1.3 mm from bend center). Micrographs (e) and (f) were taken from (021) face, tensile side.

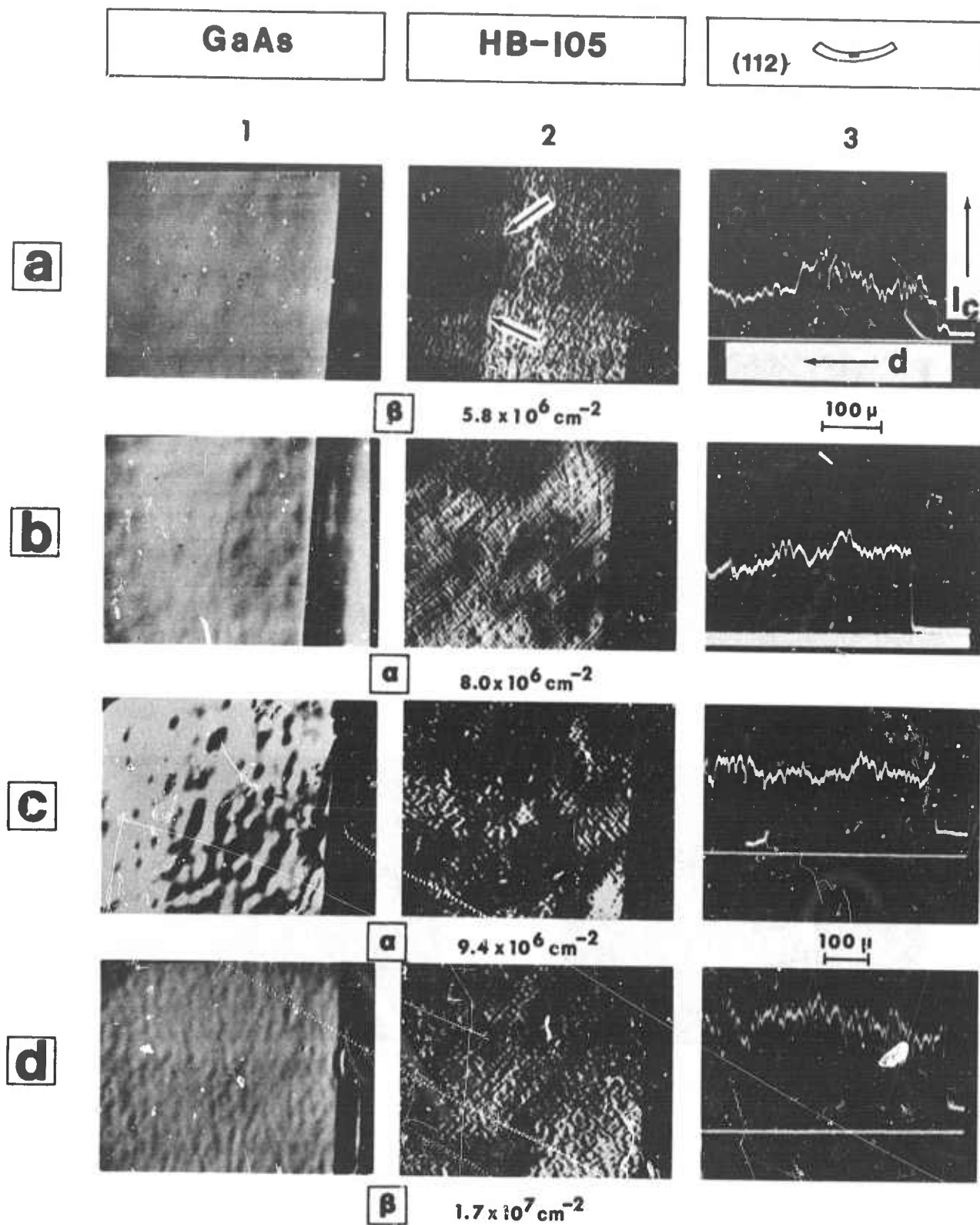


Figure 38. Caption on following page.

Figure 38. Secondary electron emission (SEE) micrographs (column 1), infra-red cathodoluminescence (IR-CL) micrographs (column 2) and IR-CL intensity, I_c , line scans versus distance, d , in microns (column 3) for the undoped, bent GaAs samples (HB-105). Areas examined were taken from the (112) surface at the center of the bend. Figures a, b, c, and d represent increasing dislocation densities (noted in column 2) and different types of excess dislocation (α and β). A subsurface flaw is indicated by arrows in (a) - column 2. Sample numbers: (a) F13-C-B1, (b) F11-C-B2, (c) F12-C-B3, (d) F10-C-B4.

(On Preceding Page)

Figure 39. SEE micrographs (column 1), IR-CL micrographs (column 2) and IR-CL intensity line scans for the doped (Te: 10^{17}cm^{-3}), bent GaAs samples (CZ-16). Figures a, b, c, and d represent increasing dislocation densities (noted in column 2) and different types of excess dislocation (α and β). Sample numbers: (a) 10-F-B1, (b) 10-E-B2, (c) 10-C-B3, (d) 10-D-B4.

(On Following Page)

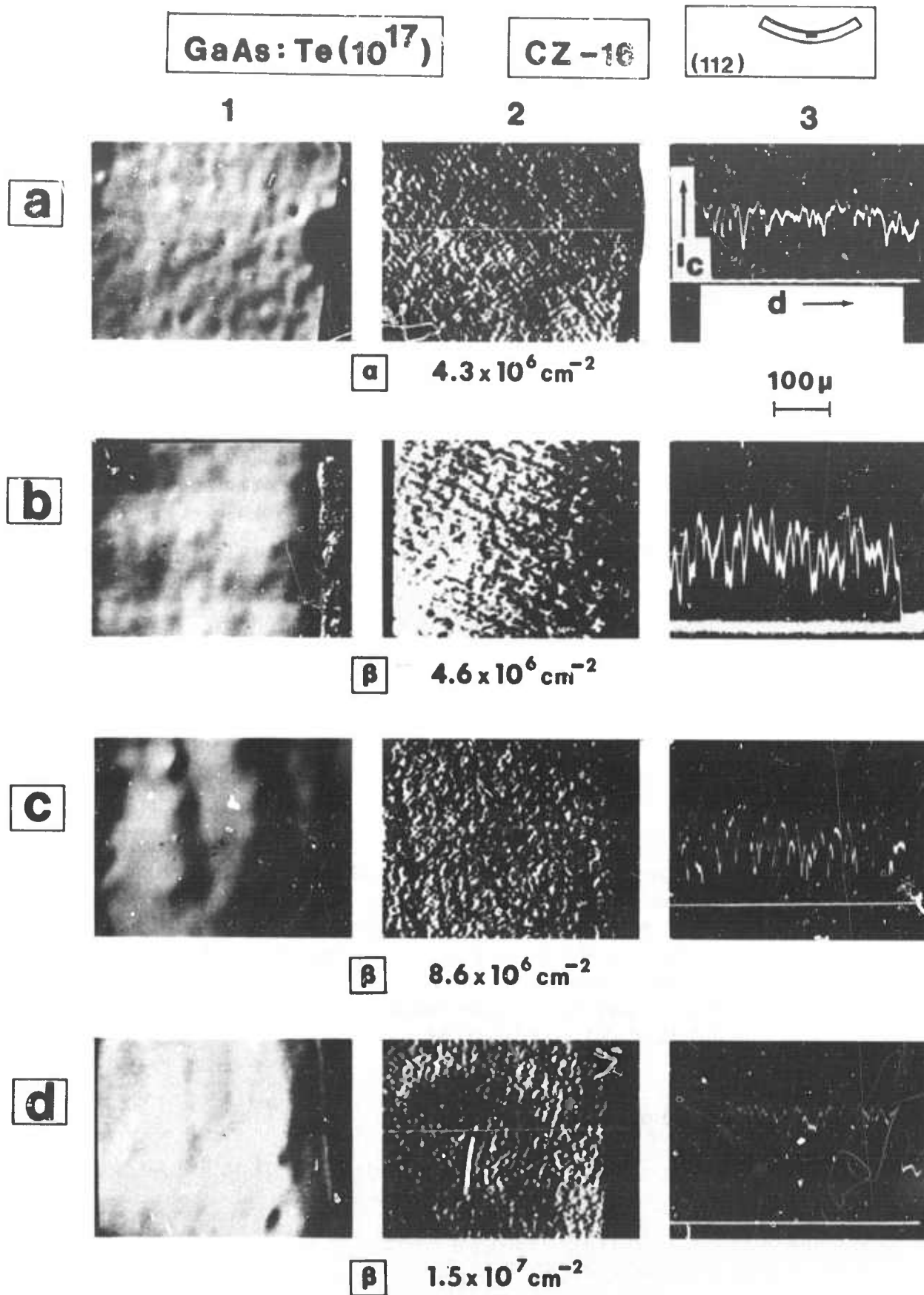


Figure 39. Caption on preceding page.

No significant features associated with the density or type of dislocation could be discerned from the micrographs. However, from the IR-CL micrographs, dislocation densities were estimated by taking average counts of the number of black dots visible in column 2 and the number of minima recorded by the line scans in column 3.

The results of the dislocation density measurements based on the IR-CL micrographs are shown in Figure 33. The deviation of some of the points from the calculated values was due mainly to the lack of resolution in the photomicrographs. However, from Figures 34-37 and from Figure 38-b-2, the black dots believed to be associated with the end points of dislocations could be resolved to a diameter of 3 μm . This resolution, however, can be improved by determining an optimum level for the bias control. For the present, the three points close to the theoretical values in Figure 33 indicate the potential application of the IR-CL method for measuring dislocation densities in a nondestructive way, namely, without chemically etching the sample surface.

To obtain samiquantitative data related to the type and density of dislocations, the intensity, peak position and half-width of the infrared (IR) peak at an emission energy of $E = 1.41 \text{ eV}$ ($\lambda_p = 8600 \text{ \AA}$) were recorded from the control and bent samples and from various positions within each bent or unbent sample. The observed IR spectra are shown in Figures 40-44. The spectra were taken from the areas indicated by black rectangles in the schematic diagrams of the samples. Also indicated in the figures are the type and density of dislocations in each sample. The curves indicate changes in IR peak intensity associated with heating or increase in dislocation density. No changes were observed in the peak position or half-width which could be related to the type or density of dislocations (Table XXIII).

For both the undoped and doped GaAs samples (Figures 40 and 41) an increase in IR intensity was noted after heating. This increase appeared genuine since the peak intensities recorded represented the average of twelve to nineteen measurements along the length of each sample. Furthermore, the peak intensity of the heated sample approximated the intensities observed from the tips of the bent doped and undoped samples (Figures 40 and 41). Thus, short term heating at 700°C for 15 minutes produces an annealing effect on the dislocations in the as-grown sample as well as a probable redistribution of impurities. Both these processes appear to enhance radiative recombination at the observed wavelength in the heated sample and in the relatively undeformed tips of the bent samples.

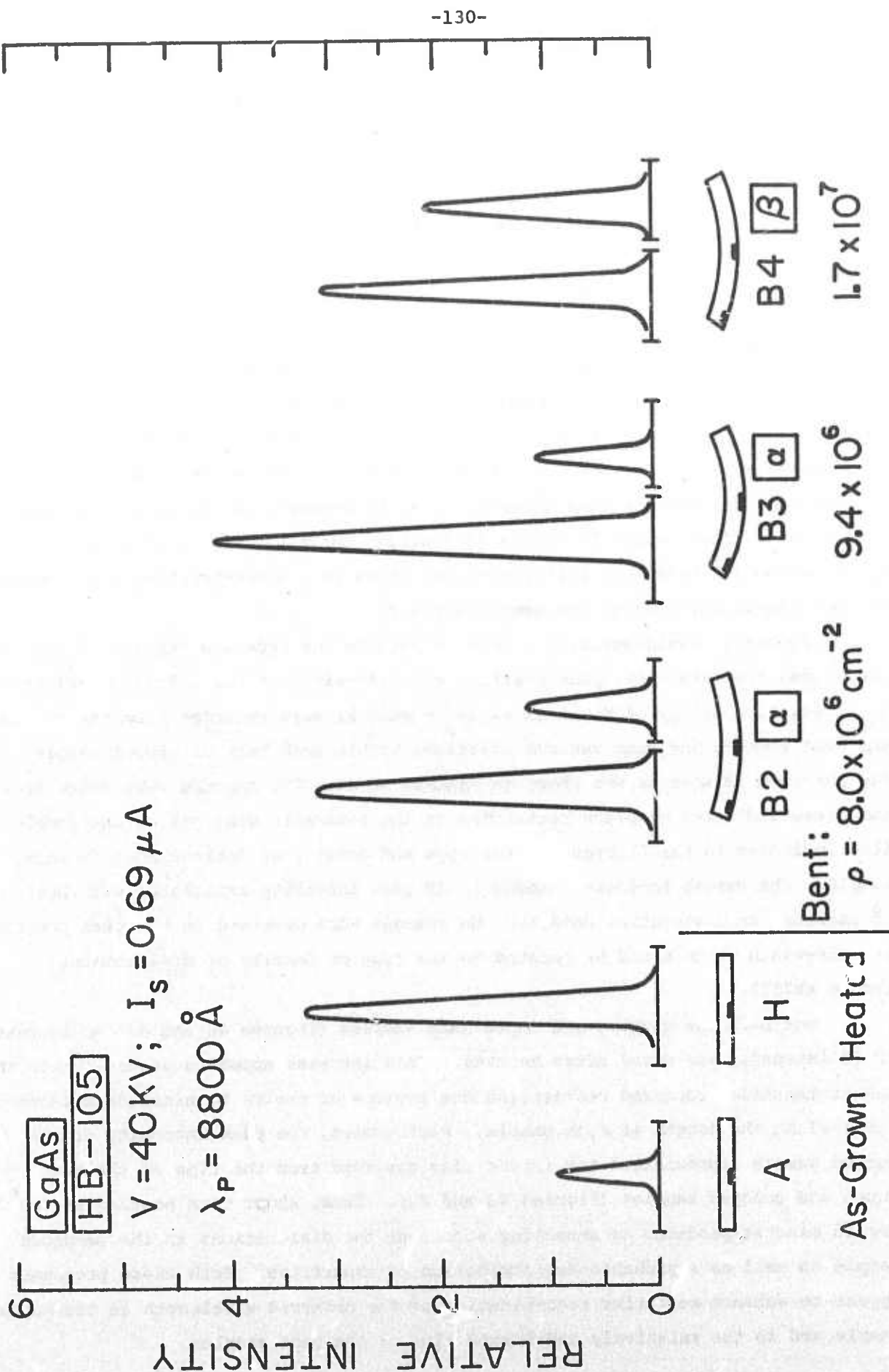


Figure 40. Caption on following page.

Figure 40. Relative infra-red cathodoluminescence (IR-CL) intensities taken from the center and tips of the as-grown (A), Heated (H) and bent GaAs samples (HB-105). Dislocation densities (ρ) and type of dislocation (α or β) are indicated. IR peak position is at $\lambda_p = 8800\text{\AA}$, at an accelerating voltage in the microprobe of 40 KV, and sample current of $0.69\mu\text{A}$. Areas examined are indicated by black rectangles in the schematic diagrams of the samples.

(On Preceding Page)

Figure 41. Relative IR-CL intensities for the as-grown (A), heated (H), and bent (CZ-16) GaAs samples with different types (α and β) and densities (ρ) of dislocations. Same scheme is followed as in Figure 33.

(On Following Page)

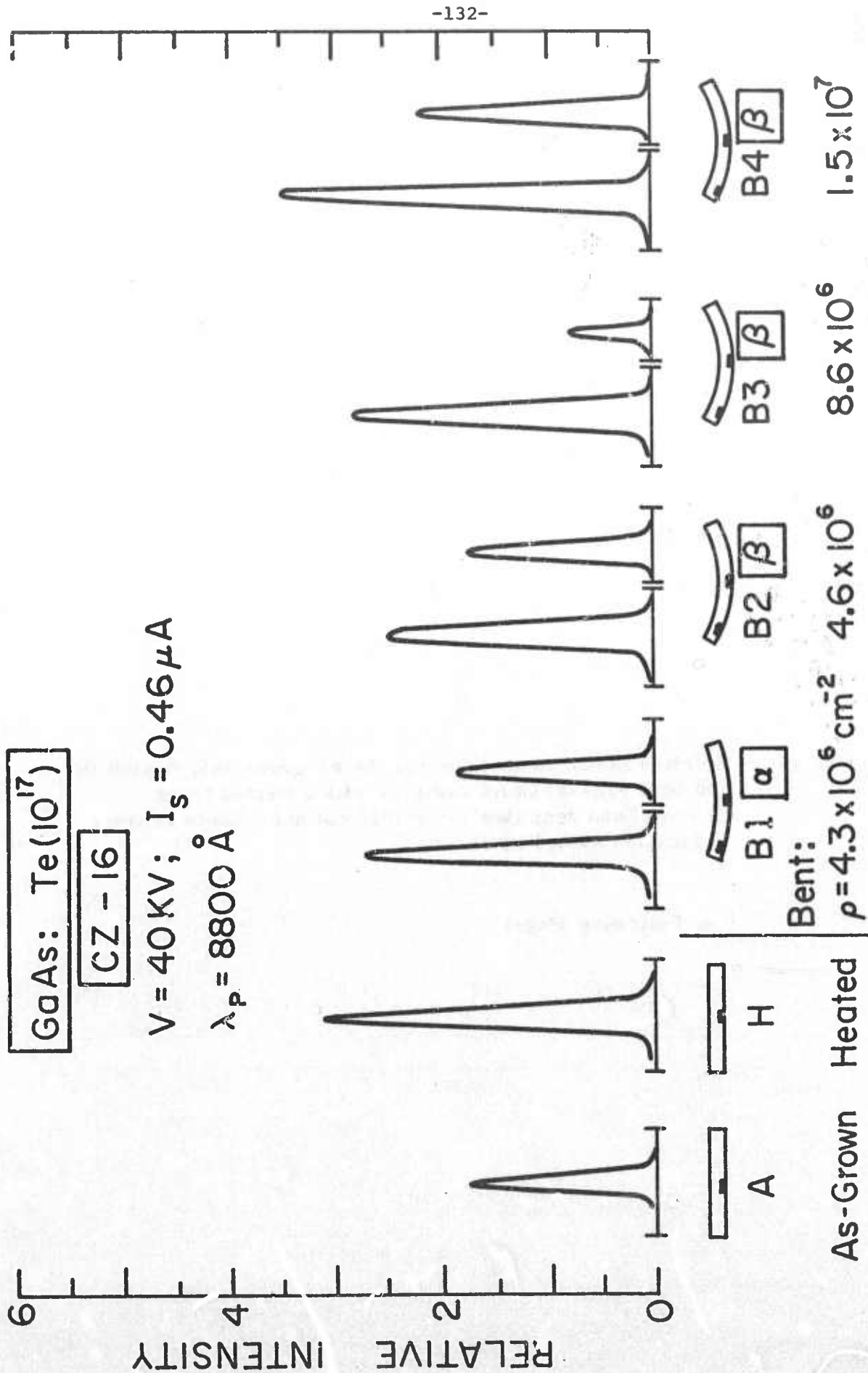


Figure 41. Caption on preceding page.

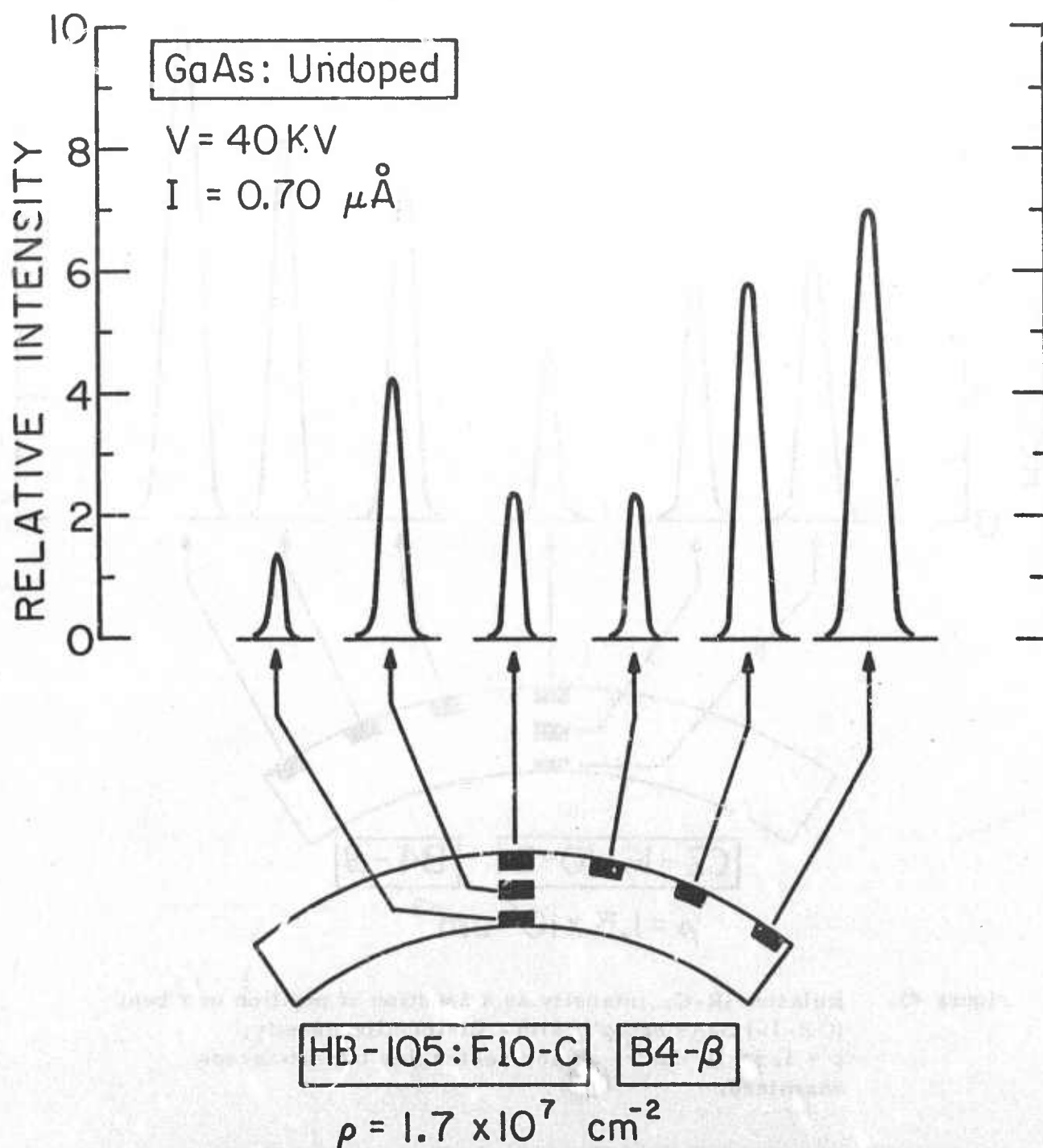


Figure 42. Relative IR-CL intensity as a function of position in a bent (HB-105) GaAs sample with a dislocation density, $\rho = 1.7 \times 10^7 \text{ cm}^{-2}$. Areas examined are indicated by black rectangles.

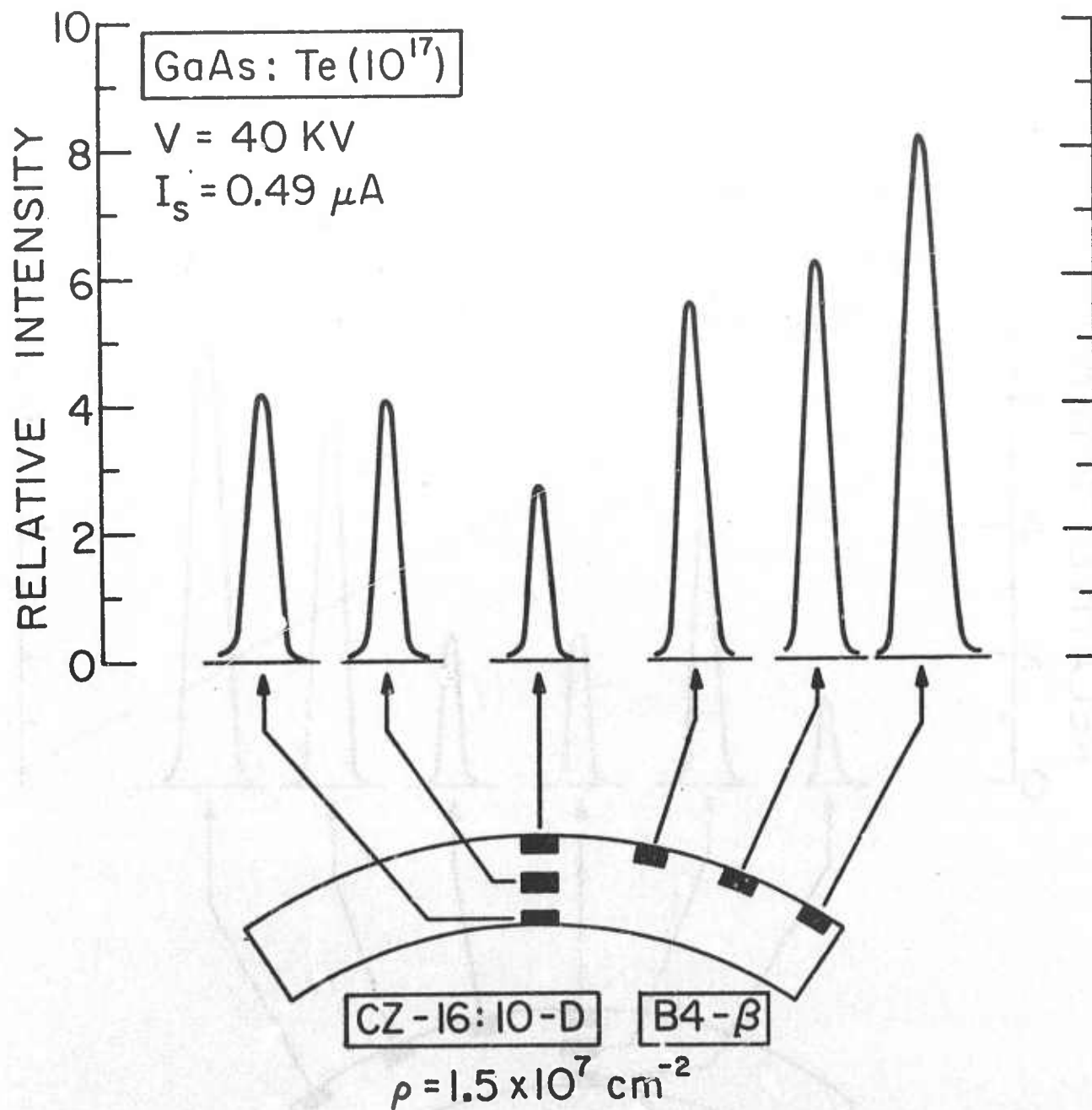


Figure 43. Relative IR-CL intensity as a function of position in a bent (CZ-16) GaAs sample with a dislocation density, $\rho = 1.5 \times 10^7 \text{ cm}^{-2}$. Black rectangles indicate areas examined.

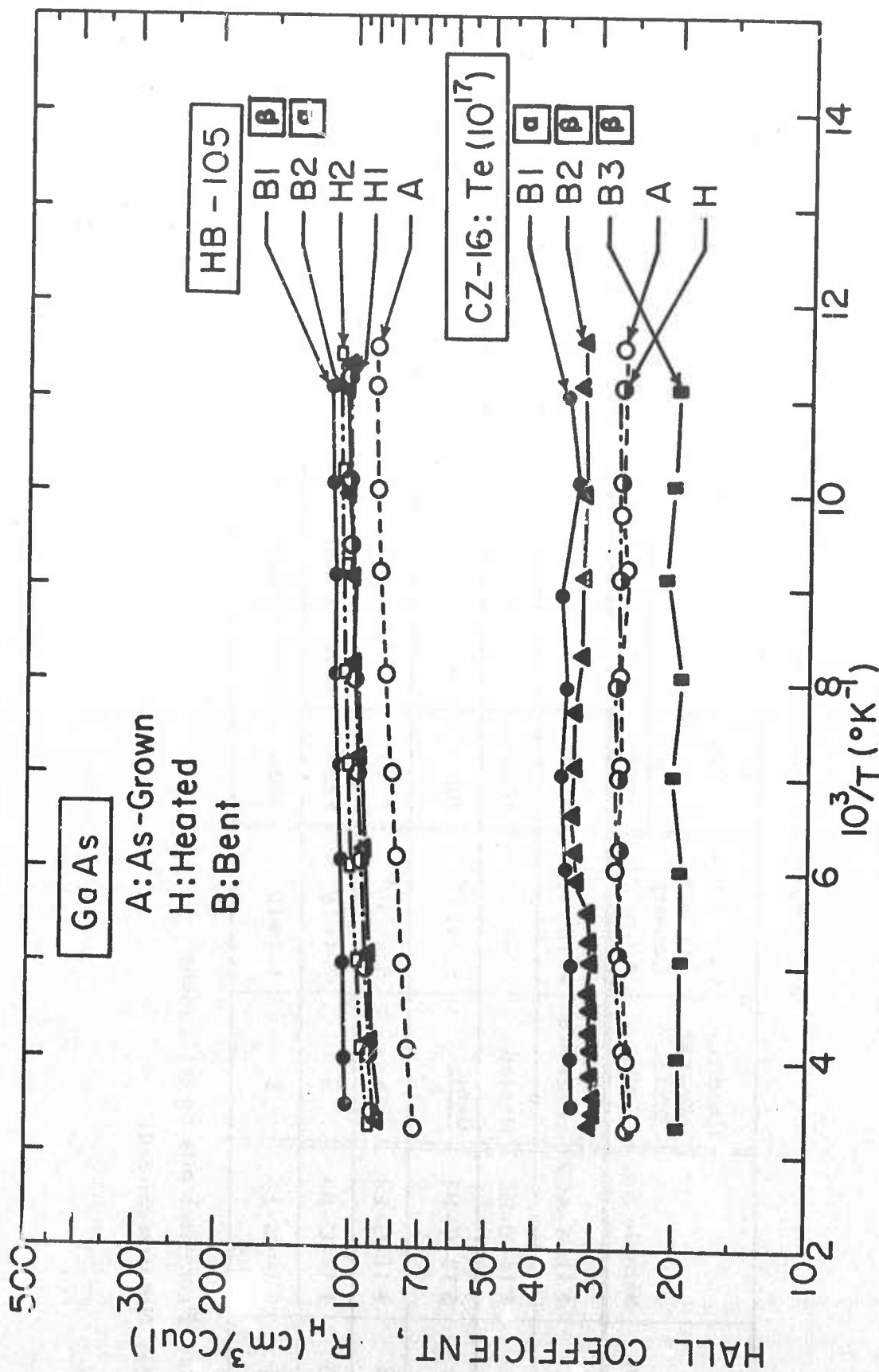


Figure 44. Hall coefficient vs. reciprocal temperature for Te-doped Czochralski (CZ-16) and undoped horizontal Bridgman (HB-105) samples of As-grown (A), heated (H, H1, H2) and bent (B1, B2, B3) GaAs. Majority dislocations introduced during bending are referred to by α and β .

TABLE XXIII
Infra-red Cathodoluminescence Intensity, Half-width and
Peak Position for Control and Bent GaAs Samples

A. Horizontal Bridgman (HB-105) Undoped

No.	Sample No.	Condition Excess Disloc'n Type	Calculated Disloc'n Density ρ (cm ⁻²)	Peak Pos'n λ_p (Å)		Half- Width HW (Å)		Relative Peak Intensity, I		% Change in Inten- sity Rela- tive to Tip
				Center	Tip	Center	Tip	Center	Tip	
1	F11-A-AG2	as-grown	$\sim 10^4$ (a)	8780	-	228	-	0.95	0.90	+5
2	F11-B-H2	Heated	—	8800	-	228	-	3.30	3.10	+6
3	F13-C-B1	Bent: $\frac{\alpha}{\beta}$	5.8×10^6	(b)	-	(b)	-	(b)	-	-
4	F11-C-B2	α	5.0×10^6	8790	8810	224	228	1.64	3.20	-49
5	F12-C-B3	α	9.4×10^6	8320	8830	228	228	1.62	4.08	-60
6	F10-C-E4	β	1.7×10^7	8830	8830	225	230	2.10	3.52	-40

(a) From etch pits on (111) plane.

(b) Not determined.

TABLE XXIII (Continued)

B. Czochralski (CZ-16) Doped Te (10^{17} cm^{-3})

No.	Sample No.	Cond'n	$\rho \text{ (cm}^{-2}\text{)}$	$\lambda_p \text{ (Å)}$		HW (Å)		Relative I		% Change in I
				Center	Tip	Center	Tip	Center	Tip	
1	9A-AG1	as-grown	$\sim 10^3 \text{ (a)}$	8780	-	245	-	1.75	1.60	+9
2	9B-H1	Heated	-	8780	-	240	-	3.06	3.44	-11
3	10F-B1	$\frac{\text{Bent:}}{\alpha}$	4.3×10^6	8790	8790	245	245	1.85	2.72	-32
4	10E-B2	β	4.6×10^6	8790	8790	250	240	1.74	2.47	-30
5	10C-B3	β	8.6×10^6	8780	8790	250	245	0.81	2.82	-71
6	10D-B4	β	1.5×10^7	8790	8790	245	246	2.21	3.54	-38

Although no systematic decrease in IR intensity was observed with increasing calculated dislocation density in the bent samples, it was observed that the IR intensity from the central portion of the bent sample was consistently lower than the intensity from the relatively undeformed tip of the same sample. This observation was found true for both the Bridgman and the Czochralski samples (Figures 40 and 41). To eliminate the possibility of excessive inhomogeneity within the same sample, the regions between the center and the tip as well as between the tensile and compressive surfaces of the bent samples were examined for changes in the IR intensity. The results shown in Figures 42 and 43 indicate a systematic decrease in IR intensity with increasing dislocation density. That the dislocation density increased upon approaching the bend center has been demonstrated in Figures 34-37.

Although the process of recombination of excess carriers at dislocations is not fully understood, it is known that dislocations in germanium introduce deep acceptor levels which act as traps for minority carriers.⁽⁶¹⁻⁶⁴⁾ Dislocations in GaAs would be expected to behave in the same way. Thus, in portions of the bent sample where the dislocation density is high, there is a corresponding high density of traps so that a decrease in radiative recombination takes place. There is also the possibility that dislocations act as recombination centers which emit IR radiation at a wavelength which falls beyond the range (0.6 to 1.1 μ) of our S-1 IR detector so that the observed low IR intensity represents merely a portion of the complete IR spectrum. Further study with a detection system capable of recording IR radiation at wavelengths greater than 1.1 μ should resolve this question.

5. Anisotropy of Electrical Properties from α and β Dislocations in Plastically Deformed GaAs⁽⁶⁵⁾

Parallelapiped bar samples were cut and ohmic contacts attached by the methods described in section V.C. Hall parameters were calculated from resistivity and Hall voltage data obtained at temperatures ranging from 83°K to 300°K from a DC Hall apparatus with a 5 kG magnet made available through the courtesy of Dr. H. Wieder of the U.S. Naval Electronics Center, San Diego.⁽⁶⁶⁾ Sample currents varied from 10 to 20 mA. Reproducibility of the measurements was 1 to 2% for the resistivity data and 2 to 5% for the Hall coefficient, mobility and carrier concentration.

The Hall parameters as a function of reciprocal temperature for the as-grown (A), heated (H) and bent (B) horizontal Bridgman (HB-105) and Czochralski (CZ-16) samples are shown in Figures 44-47. The letter-number combinations identifying the samples are referenced in Tables XXII and XXIII. The Greek symbols refer to the predominant type of dislocation introduced into the sample by bending. The samples are grouped such that there is one α - and one β -type bend sample from the undoped HB-105 and doped CZ-16. The B3 sample in the figures refer to a sample that was oxidized after bending and during the cooling period.

Although the Hall parameters of the individual samples displayed very little temperature dependence because of the high carrier concentrations present, the relative differences between the curves for the control and bent samples were sufficiently large to permit determination of the effects of bending and short term heating (10 to 20 minutes) in the temperature range of 600° to 700°C.

The effect of short term heating (measured relative to the as-grown sample) on the undoped GaAs crystal (HB-105) was to increase the Hall coefficient by 20% (Figure 44), decrease the carrier concentration by 17% (Figure 45), decrease the conductivity of 7% (Figure 46) and increase the mobility by 12% (Figure 47). For the Te-doped sample (CZ-16), heating had no effect on the Hall coefficient or carrier concentration and produced a 15% decrease in the conductivity and mobility. Thus, the decrease in the carrier concentration after heating was limited to the undoped sample, while little or no change in carrier concentration was noted in the doped sample. (Table XXIV). Because the role of impurities such as copper and carbon in GaAs is quite complex,⁽⁶⁷⁾ no definite mechanism has as yet been assigned to explain the observed phenomena. However, it is quite certain that heating, even though of short duration, has affected the electrical properties of GaAs, as has been observed by others.^(68,69)

The microstructure observed in both the doped (Figure 34-a and 34-b) and undoped heated samples (Figure 35-a and 35-b) appeared to have no direct relationship to the changes after heating in the carrier concentration or mobility. Thus, the increase in size of the particles in CZ-16 probably had no bearing on the decrease in mobility, nor did the absence of change in the particle size in HB-105 appear to be related to the increase in mobility.

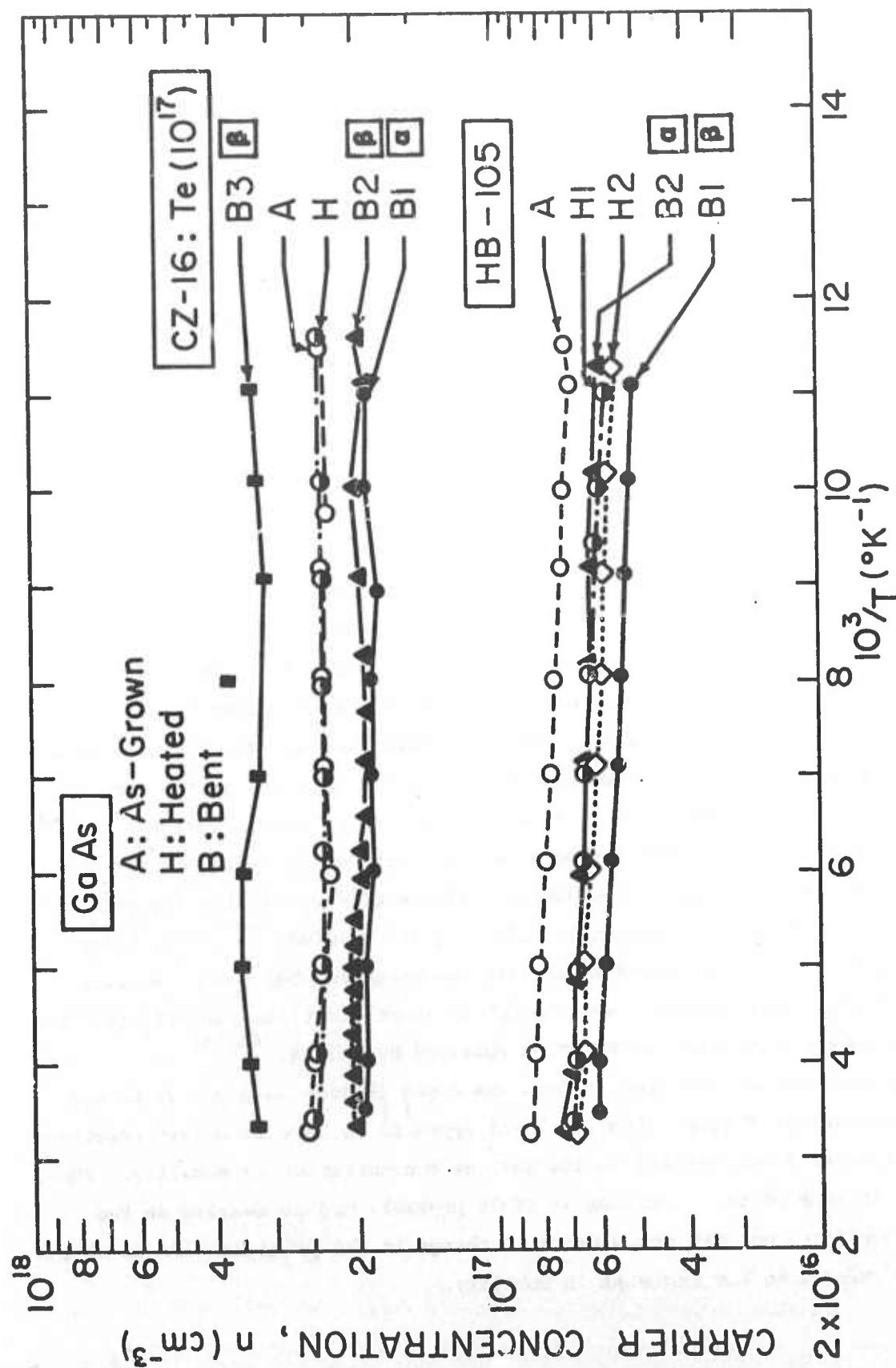


Figure 45. Carrier concentration vs. reciprocal temperature for As-grown (A), heated (H), and bent (B) horizontal Bridgman (HB-105) and Czochralski (CZ-16) GaAs.

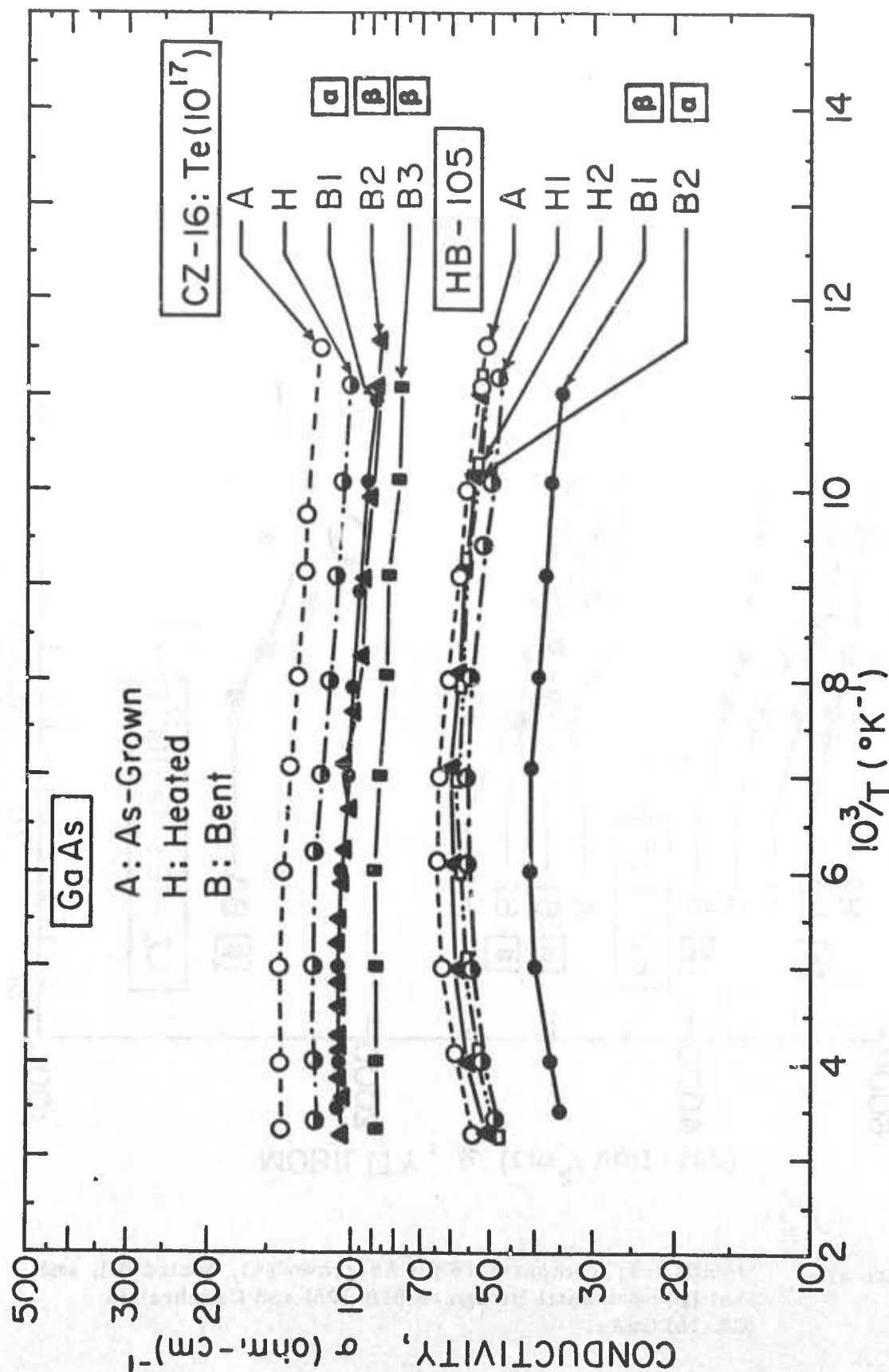


Figure 46. Conductivity vs. reciprocal temperature for As-grown (A), heated (H), and bent (B) horizontal Bridgman (HB-105) and Czochralski (CZ-16) GaAs.

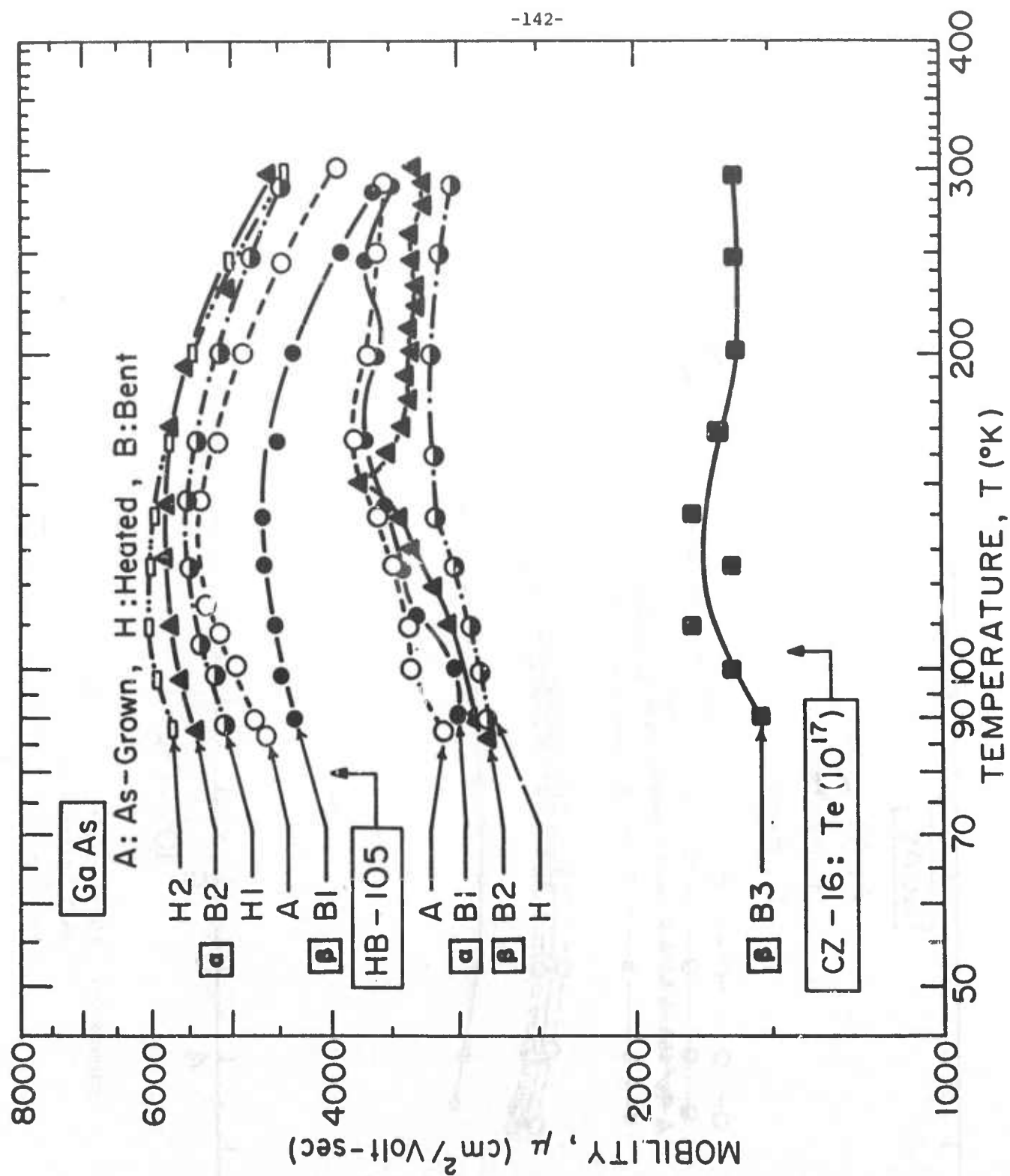


Figure 47.

Mobility vs. Temperature for As-grown (A), heated (H), and bent (B) horizontal Bridgman (HB-105) and Czochralski (CZ-16) GaAs.

TABLE XXIV

Relative Changes in Hall Parameters After Heating
and Bending of n-Type GaAs

A. Effect of Heating on the Unbent GaAs Relative to the As-Grown Sample

No.	Sample No.	Curve No. (a)	Percent Changes at 77°K			
			Hall Coeff. (R_H (cm ³ /conl))	Carrier Conc'n n (cm ⁻³)	Conduc-tivity σ (ohm-an) ⁻¹	Mobility μ (cm ² /V-sec.)
1	CZ-16 9-B-H	H	-0.2	+0.8	-14.7	-14.7
2	HB-105 F13-B-H1	H1	+19.8	-16.7	- 7.2	+11.5
3	HB-105 F12-B-H3	H2	+ 8.5	- 7.5	+ 6.2	+15.3

B. Effect of Bending on the Heated GaAs Relative to the Heated But Unbent Sample.

No.	Sample No.	Curve No. (a)	Dis-loc'n Type	Calcu-lated Dis-loc'n Density ρ (cm ⁻²)	Percent Changes at 77°K			
					R_H (cm ³ /conl)	n (cm ⁻³)	σ (ohm-cm) ⁻¹	μ (cm ² /V-sec)
1	CZ-16 10-F-B1	B1	α	4.28×10^6	+ 31.0	-21.3	-12.4	+14.7
2	HB-105 F12C-B3	B2	α	9.38×10^6	- 5.1	+ 5.4	+ 1.6	- 4.4
3	HB-105 F13C-B1	B1	β	5.91×10^6	+16.1	-14.8	-27.4	-15.5
4	CZ-16 10C-B3	B2	β	8.57×10^6	+22.4	-18.8	-14.3	- 4.85
5	CZ-16 10D-B4	B3	β	1.47×10^7	-22.45	+36.4	-23.53	-42.28

(a) refers to Hall Parameter vs. Reciprocal Temperature Curves.

The effect of bending on the Hall parameters of both the doped and undoped samples is shown in the same set of figures. Because of the two types of dislocations introduced and because of the varying dislocation densities involved, the changes in the Hall parameters of the bent samples are summarized for convenient reference in Table XXIV. It is to be noted that the changes recorded are those changes in the parameters after the effects of heating had already been taken into account.

The principal effects of dislocations (in other semiconductor materials) when these lie parallel to the bend direction and normal to the current flow have been: A decrease in carrier concentration, conductivity and mobility. (70-72) Table XXIV indicates that these effects appear verified in the case of β -dislocations (especially sample B3), but not consistently in the case of α -dislocations.

The large changes observed in the oxidized sample, B3, are noteworthy because it appears that the oxidation was not limited to the surface but also affected the bulk in such a manner as to produce a 36% increase in the carrier concentration, a 42% decrease in mobility, and a 23% decrease in conductivity. This observation does not appear consistent with the classification of oxygen as a trap. (67) Furthermore, the changes in the dislocation density appear to have no effect on the parameters. This is not surprising because the number of available donor or acceptor sites introduced by a dislocation density of $1.47 \times 10^7 \text{ cm}^{-2}$ (the maximum listed in Table XXIV) amounts to $2.65 \times 10^{13} \text{ cm}^{-3}$, assuming that the fraction of sites occupied is 0.1. Thus, with carrier concentrations ranging from 10^{16} to 10^{17} cm^{-3} , changes in the acceptor site density of 1.8×10^9 to $2.65 \times 10^{13} \text{ cm}^{-3}$ will not produce significant effects on the parameters unless other factors such as impurities also play a role.

Because the effects observed due to bending (after taking into account heating effects) are significantly large, they will have to be explained in terms of the complex interaction between the dislocations and impurities. Previous work with plastically deformed higher purity semiconductors has shown the directional property of charge carriers with respect to the orientation of dislocations. (70-72) Thus, the maximum decrease in the conductivity and mobility resulted when the current flow was normal to the dislocation lines, while little or no change was observed when the current flow ran parallel to the dislocations. This implies that impurities in a semiconductor do not have the directional properties of dislocations.

To sort out the effects due to dislocations from those due to impurities, a current could be passed in the bent sample parallel and perpendicular to the bend axis. The effect of impurities (whether or not precipitated on the dislocations) on the mobility and conductivity will be evident when current is run parallel to the bend axis. Similarly, the corresponding effect of dislocations (combined with the impurities) will be noted when current is normal to the bend axis. Thus, it will be possible to differentiate between the effects due to impurities only, and those due to a combination of dislocations and impurities, and finally those due to dislocations only.

Figure 48 shows how two adjacent slices of Te-doped (10^{17} cm^{-3}) Czochralski GaAs (CZ-16) were oriented to introduce single slip after four-point bending and to produce an excess of α or β dislocations. The figure also shows how each sample was cut to obtain sections parallel and perpendicular to the bend axis. In addition, a sample labeled "H \perp " (heated, perpendicular) was cut with the intention of providing a control sample from the same slice. It turned out, however, that the deformation extended to these samples such that their Hall curves approximated those for the $\alpha\text{-}\perp$ and $\beta\text{-}\perp$. Hence, the data from these samples were not included in the figures. The control samples, A (as-grown) and H (heated) were taken from a slice close to the α slice and their curves were taken from Figures 45-47.

Resistivity and Hall voltages were measured in a 5 kG magnetic field (aligned normal to the bend axis and the electric field) as a function of temperature (83° to 300°K) in the same Hall apparatus used earlier. The Hall parameters for the six samples as a function of reciprocal temperature are shown in Figures 49-51. Figure 49 shows that after heating no changes took place in the carrier concentration of the control samples, thus indicating an absence of contamination during the heating process. All the bent samples exhibited decreases in carrier concentration relative to the heated, unbent sample H, with the β samples showing a larger decrease than the α samples. A comparison of the $\alpha\text{-}\perp$ with $\alpha\text{-}\parallel$ shows that these two exhibited decreases in carrier concentration of 5 and 16 percent, respectively, while the $\beta\text{-}\perp$ showed a decrease of 28 percent compared to the 20 percent decrease of $\beta\text{-}\parallel$ (Table XXV). While the differences between the carrier concentrations in the parallel and perpendicular samples for the same type of dislocation are not significant, the decrease in carrier concentration relative to the heated control strongly suggests the introduction of acceptor sites in the bent α and β samples.

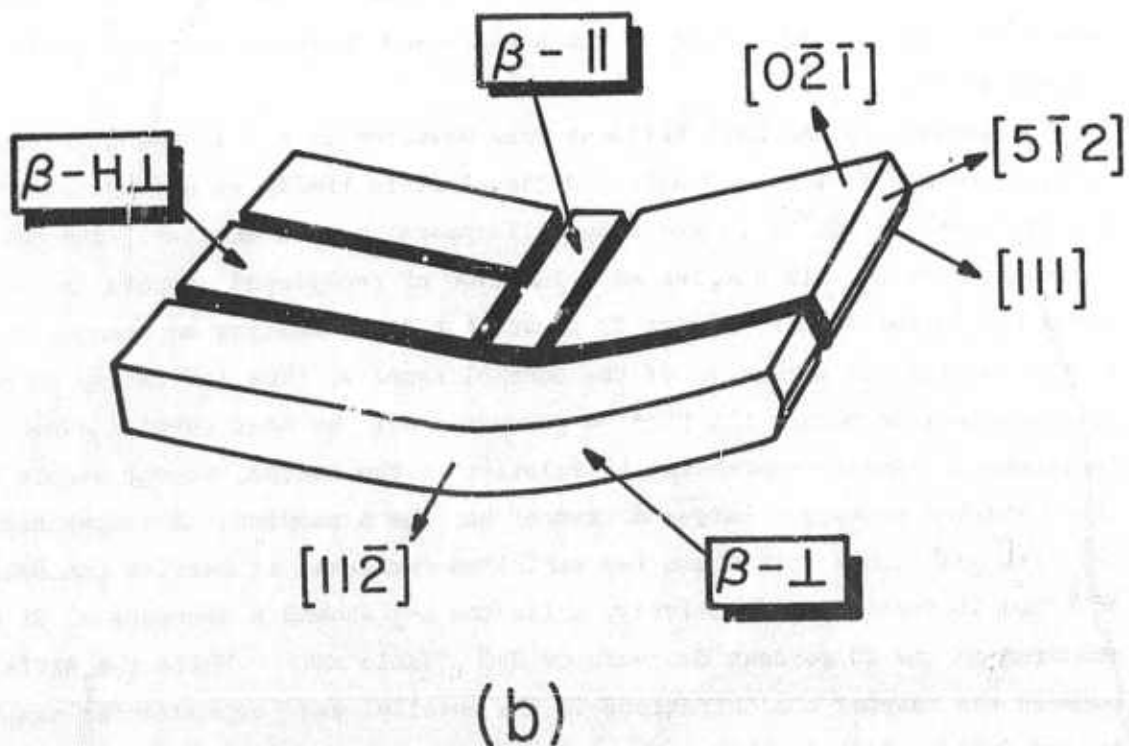
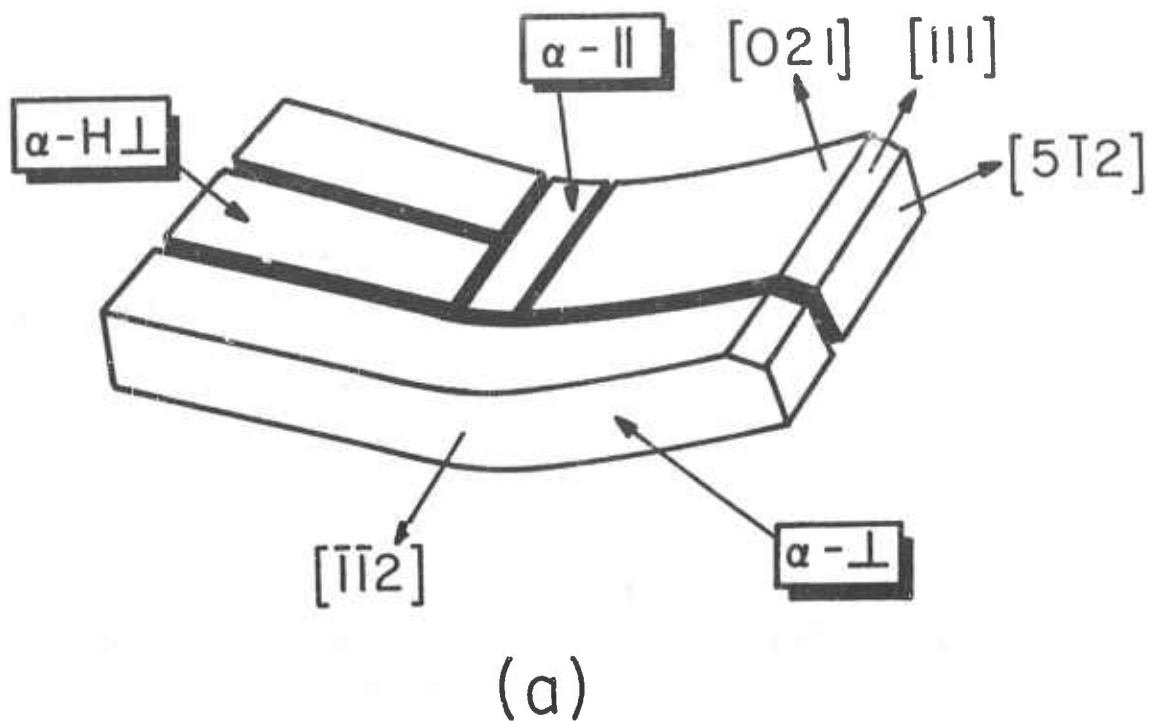


Figure 48. Schematic diagram of the orientation of Te-doped GaAs (CZ-16) samples relative to the $[1\bar{1}2]$ bend axis to introduce: (a) an excess of α -type dislocations and (b) an excess of β -dislocations. The samples were then cut to obtain slices perpendicular ($\alpha - \perp$, $\beta - \perp$) or parallel ($\alpha - \parallel$, $\beta - \parallel$) to the bend axis. The samples labeled $\alpha - H \perp$ and $\beta - H \perp$ represent heated-perpendicular slices.

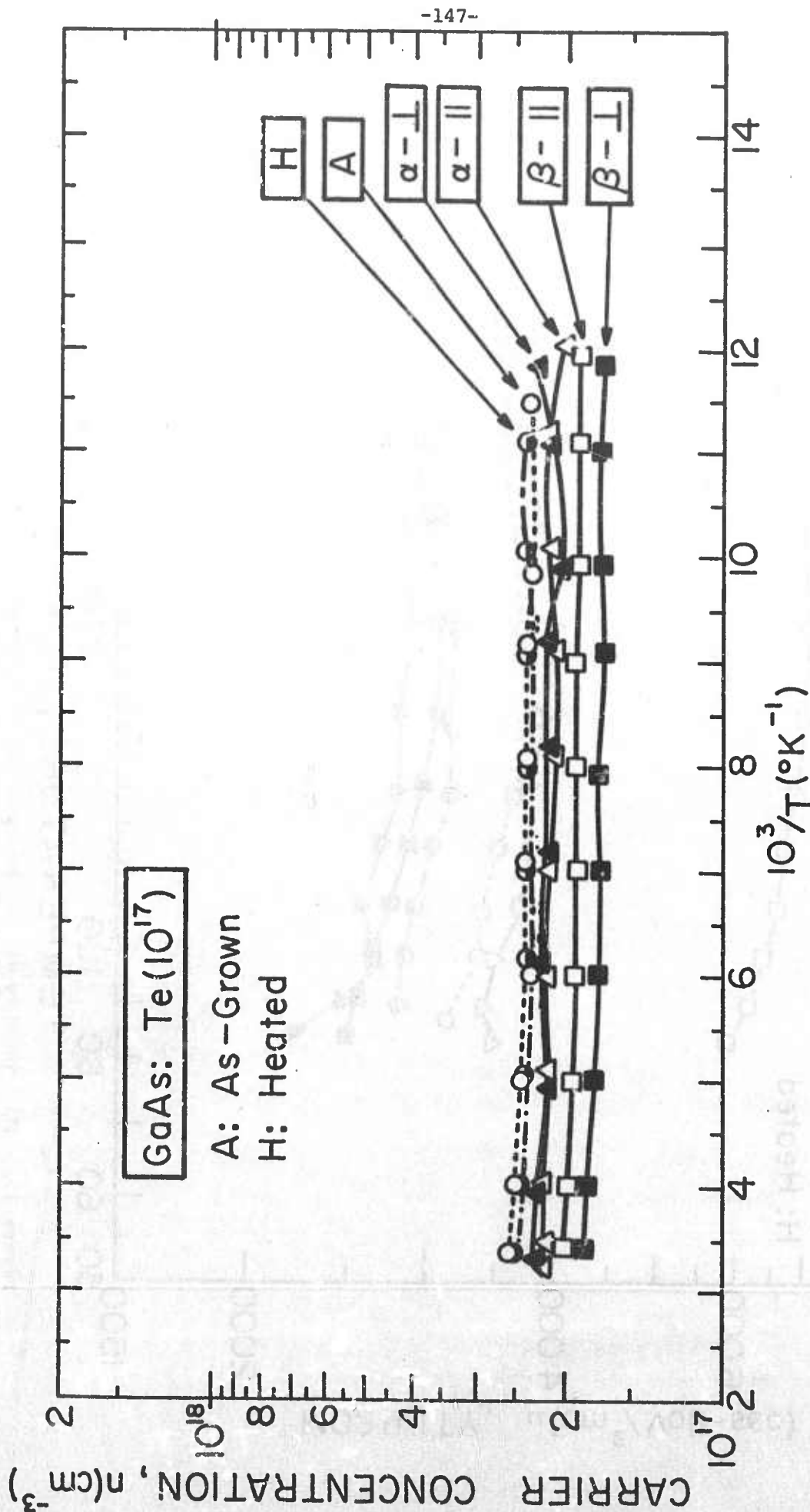


Figure 49. Carrier concentration vs. reciprocal absolute temperature for the as-grown (A), heated (H) and bent (α , β) samples which were measured parallel (\parallel) or perpendicular (\perp) to the bend axis (CZ-16).

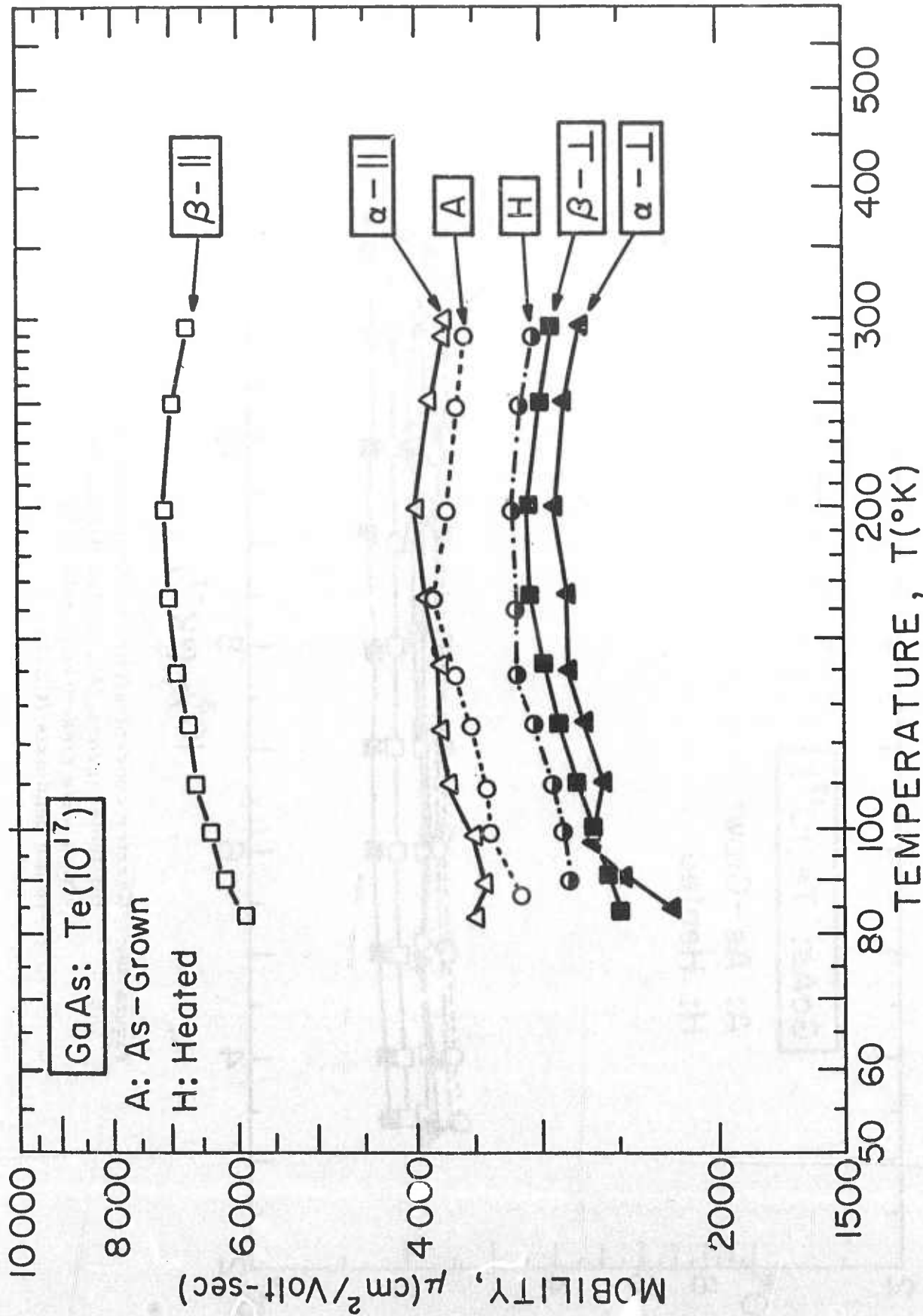


Figure 50. Hall mobility vs. reciprocal absolute temperature for the as-grown (A), heated (H) and bent samples ($\alpha - ||$, $\alpha - \perp$, $\beta - ||$, $\beta - \perp$) (CZ-16).

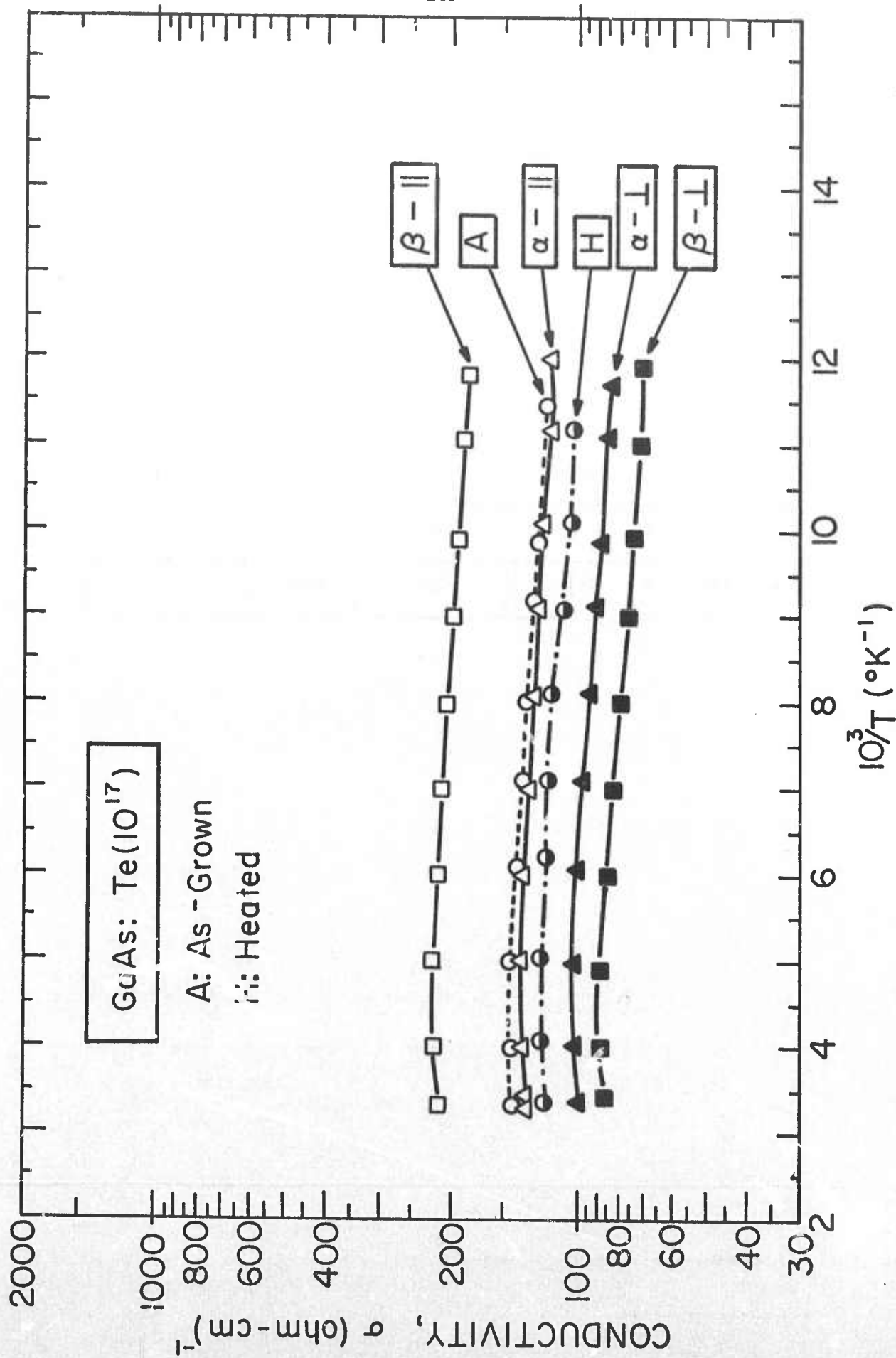


Figure 51. Conductivity vs. reciprocal absolute temperature for the as-grown (A), heated (H) and bent samples ($\alpha-||$, $\alpha-\perp$, $\beta-||$, $\beta-\perp$) (CZ-16).

TABLE XXV

Percent Change (Relative to the Heated Sample) in the
Hall Parameters of the Bent Te-Doped (10^{17} cm^{-3})
GaAs Sample (CZ-16)

No.	Sample Number	Dislocation Type and Direction	Percent Changes in:		
			Carrier Concentration	Mobility	Conductivity
1	11-E1	$\alpha \perp$	-5	-18	-19
2	11-E1	$\alpha \parallel$	-16	+29	+11
3	12-E2	$\beta \perp$	-28	-8	-34
4	12-E2	$\beta \parallel$	-20	+118	+73

Figure 50 shows the changes in mobility after bending, particularly in the β -|| sample. The effect of heating (relative to the as-grown condition) has been to decrease the mobility in sample H. Relative to the heated control, the effect of bending has been to decrease the mobility of the α -| and β -| by 18 and 8 percent, respectively--a decrease reflected in the corresponding drop of 19 and 34 percent in conductivity (Figure 51). This decrease in mobility and conductivity in the perpendicular direction similar to the ones shown in Figures 46 and 47 has been directly related to the scattering, either specular⁽⁷³⁾ or diffuse⁽⁷⁴⁾ or both at the dislocations acting as space charge tubes.

What is remarkably significant is the dramatic increase (relative to the heated control sample) in mobility (118%) and conductivity (73%) in the β -|| samples. A brief review of work by other investigators (Table XXVI) on the anisotropy of electrical properties in semiconductors shows that the mobility in the ||-direction is either equal to⁽⁷⁵⁾ or slightly less than the mobility of the control sample.⁽⁷⁶⁾ Read⁽⁷³⁾ assumed in his theory that only the perpendicular component of the momentum vector of the electrons will be scattered by the charged cylinder and that the parallel component should remain unaffected. Nowhere has it been predicted that the parallel component will be enhanced.

One principal difference between the earlier work on deformed Ga⁽⁷⁵⁾ and InSb⁽⁷⁶⁾ and the present study is the higher impurity concentration present in bulk grown GaAs. Hence, to explain the increase in the parallel mobility, one must include the role of impurities in the heating and bending process. Because of the fact that after heating no change was observed, while after bending there was a decrease in carrier concentration in both the parallel and perpendicular directions, it is highly probable that the combined process of heating and bending produced a migration of impurities to the dislocations and/or a sweeping away of the impurities by the dislocations. Thus, areas between neighboring dislocations would be cleared of impurities, while regions near or at the dislocations would have a high concentration of impurities. As a result, there would be in the sample an inhomogeneous distribution of impurities which could produce the high apparent mobilities predicted and observed by Wolfe et al.,⁽⁷⁷⁾ in inhomogeneous semiconductors.

On the basis of dislocation densities of the order of 10^7 cm^{-2} and assuming a uniform distribution of dislocations at the center of the bend (as indicated by the uniform array of black dots in the IR-CL micrographs), there

TABLE XXVI
Summary of the Anisotropic Character of the Conductivity, Carrier Concentration and Mobility of Bent Semiconductor Crystals

No.	Semi-conductor Mat'l	Net Carrier Conc'n, Nd-Na (cm ⁻³)	Excess Disloc'n Type	Disloc'n Energy Levels Ec-EDis (eV)	Type of Disloc'n Level	Anisotropic Behavior in:			Reference
						Conductivity	Carrier Conc'n	Mobility	
1	Ge	2×10^{14}	(a)	0.20	Acceptor	$\sigma_{ } < \sigma_o$ $\sigma_{\perp} < \sigma_{ }$	$n_{ } = n_o$ $n_{\perp} < n_{ }$	$\mu_{ } = \mu_o$ $\mu_{\perp} < \mu_{ }$	75
2	Ge	3.5×10^{14}	(a)	0.50	Acceptor	$\sigma_{ } < \sigma_o$ $\sigma_{\perp} < \sigma_{ }$	$n_{ } < n_o$ $n_{\perp} > n_{ }$	$\mu_{ } < \mu_o$ $\mu_{\perp} < \mu_{ }$	74
3	InSb	8.33×10^{13}	α (In)	0.12	Acceptor	$\sigma_{ } < \sigma_o$ $\sigma_{\perp} < \sigma_{ }$	$n_{ } < n_o$ $n_{\perp} = n_{ }$	$\mu_{ } < \mu_o$ $\mu_{\perp} < \mu_{ }$	76
			β (Sb)	0.22	Acceptor	$\sigma_{ } < \sigma_o$ $\sigma_{\perp} < \sigma_{ }$	$n_{ } < n_o$ $n_{\perp} = n_{ }$	$\mu_{ } < \mu_o$ $\mu_{\perp} < \mu_{ }$	
4	GaAs (Te-doped)	2.5×10^{17}	α (Ga)	(b)	Acceptor	$\sigma_{ } > \sigma_o$ $\sigma_{\perp} < \sigma_{ }$	$n_{ } < n_o$ $n_{\perp} > n_{ }$	$\mu_{ } > \mu_o$ $\mu_{\perp} < \mu_{ }$	This Work
			β (As)	(b)	Acceptor	$\sigma_{ } \gg \sigma_o$ $\sigma_{\perp} < \sigma_{ }$	$n_{ } < n_o$ $n_{\perp} < n_{ }$	$\mu_{ } \gg \mu_o$ $\mu_{\perp} < \mu_{ }$	

(a) Not indicated.
(b) Not determined.

would be a separation distance of $3\text{ }\mu\text{m}$ between dislocation centers. Using Read's⁽⁷³⁾ estimate of $1\text{ }\mu\text{m}$ as the typical diameter of the space charge cylinders, the actual space between the outer surfaces of the cylinders would then be $2\text{ }\mu\text{m}$. If this $2\text{ }\mu\text{m}$ region were swept clean of impurities, it would not be unreasonable to expect a corresponding increase in mobility and conductivity in the parallel direction as indeed has been observed for both the α -|| and β -|| GaAs samples.

G. Electron Beam Characterization

(D. B. Wittry, W. N. Lin, H. C. Marciniak and
J. C. Potosky)

Electron beam techniques can be very useful for study of semiconductors. In section VI.F.2 we showed how cathodoluminescence reveals information about plastic deformation in GaAs. Cathodoluminescence revealed inhomogeneities in our gradient freeze and travelling heater method GaAs crystals.⁽²⁰⁾ A new operational mode for the scanning electron microscope was developed which yields crystallographic information.^(78, Appendix K) A duoplasmatron with a quadrupole mass spectrometer has been constructed.^(79, Appendix L) An instrument for cathodoluminescence investigations between 25 and 400°K has been developed which has a clean vacuum electron beam column.^(80, Appendix M)

1. Studies of Stimulated Emission from GaAs with Continuous Electron Beam Excitation

Casey and Kaiser⁽⁸¹⁾ reported the observation of a second peak at lower energies than the principal peak usually observed in the recombination radiation from heavily doped n-type GaAs. The specimens they studied had a net carrier concentration of $2.8 \times 10^{18} \text{ cm}^{-3}$ and were excited at room temperature by a continuous electron beam focused to a diameter of 2 μm . These authors attributed the second peak to super-radiance because its intensity increased approximately as the square of the electron beam current above the usual distribution of recombination radiation (\sim proportional to the beam current).

In attempts to confirm the results of reference 81, we tried both at 300°K and 113°K on more than a dozen heavily doped n-type specimens of GaAs (typically $n_0 = 1$ to 4.5×10^{18}). These specimens had one or both sides chemically polished. One of the specimens studied was cut from the same ingot and was adjacent to the wafer used by Casey and Kaiser. Our excitation conditions were similar to those used by the previous authors; namely, a 40 kV beam focused to within 2 μm in diameter with a beam current ranging from 0.1 to more than 2 μA . However, our beam was chopped at 4 kHz (square wave) to facilitate phase sensitive detection. Our light collecting system also differed from that used in reference 81; we used a reflecting objective (N.A. ~ 0.4) coaxial with the electron beam as in the Applied Research Laboratories model EMX, whereas Casey and Kaiser use a light pipe added to a Cambridge Instruments Microscan. Hence, we also tried experiments on tilted specimens to reproduce the low take off-angle for the collected light

($\sim 70^\circ$ from the surface normal) that was employed in the previous experiments.

None of our experiments resulted in the second peak reported by Casey and Kaiser and attributed to super-radiance. At the higher excitation levels we found that the peak energy of the radiation decreased almost linearly with increasing beam current. The radiation intensity reached a maximum and then decreased with further increase in beam current. We believe that these effects were due to electron beam heating since estimates of the temperature of the bombarded region based on the temperature dependence of the energy bandgap agreed with the value calculated from beam heating equations within the expected accuracy. Furthermore, with certain beam focusing conditions, we observed local melting of the specimen so that we are sure that we had more than adequate beam current density to be able to observe the effects reported in reference 81.

Experiments were also performed on thin specimens ($\sim 50 \mu\text{m}$ in thickness) chemically polished on both sides so as to provide a cavity structure. Clear cavity modes were observed in the radiation from these specimens at 300°K and 113°K , but there was no evidence of stimulated emission; i.e., there was no superlinear increase of any cavity mode with increasing excitation.

Stimulated emission of recombination radiation in GaAs without feedback from a cavity has been observed with injection of excess carriers across a p-n junction by Kurbatov and coworkers.⁽⁸²⁾ The diode was excited by current pulses with a duration of 0.25 to 2 μsec . However, this mode of excitation does not cause the additional heating that is always present in electron beam excitation as a result of the low energy efficiency of carrier production ($\sim 33\%$).

In order to be able to observe stimulated emission in semiconductors, it is not only necessary to produce a high density of excess hole-electron pairs, it is also necessary that the carriers are not distributed over a large energy range by excess thermal energy. However, with electron beam excitation, the hot carriers produced by the electron beam transfer energy by collisions to the entire electron-hole gas and also transfer energy to the lattice.

For GaAs with a very short carrier lifetime, Popov⁽⁸³⁾ has made a calculation showing that with steady-state electron beam excitation the electron-hole gas temperature will be raised (above the lattice temperature) to an extent that carrier degeneracy which is necessary for a sufficient population inversion to occur would be annihilated and that it would be impossible to produce a "negative temperature".⁽⁸⁴⁾ On this basis, negative absorption coefficients would be

observed in a semiconductor only if the time of production of negative temperature is shorter than the lifetime of externally generated hot electrons and holes.

In our experiments it appears that stimulated emission could not be observed because of heating of the lattice but we are now analyzing the data more carefully to see if it is possible to determine both the lattice temperature and the electron temperature to verify the theory of Popov.⁽⁸³⁾ In any case, it appears that the work of Krubakov and coworkers⁽⁸²⁾ is a more reliable demonstration of stimulated emission without the benefit of feedback than the work of Casey and Kaiser.⁽⁸¹⁾

At present, we are not able to explain the results reported by Casey and Kaiser. However, it is possible that the fast-growing, lower-energy peak they observed is not due to super-radiance but is due to a different recombination mechanism that may become important at high excitation levels. One possibility is that the specimen contained deep acceptor-like impurities with multiple levels. In this case, the acceptor-like state may correspond to a higher energy level with no excitation (since the Fermi energy lies in the conduction band) than the state that is formed with excitation and trapping of holes. After trapping a hole, the impurity energy level may lie close to the valence band and when this state is filled by an electron, a quadratically increasing second peak might be produced. If this explanation is correct, then it would be necessary to postulate that we did not observe the results reported by Casey and Kaiser in spite of using similar specimens either because (a) some change took place in the specimens between the time of their measurements and ours (approximately 5 years), or (b) our measurement, which involved chopping of the electron beam at 1 kHz, did not yield the same average occupation of the state containing a trapped hole as their measurement which involved continuous electron beam excitation. A study of time-resolved spectra would clarify this latter possibility.

2. Infrared Modulation of Cathodoluminescence

Deep levels in direct gap semiconductors can be studied by illuminating the specimen with monochromatic infrared light of various frequencies while observing the band-edge radiative recombination. This technique has been applied to GAs as described in reference 85 (Appendix N).

The specimens we investigated included crystals grown by the Czochralski method, zone melting, and the gradient freeze technique, as summarized in Table XXVII. All of the specimens in which the effects described in the

TABLE XXVII

Samples Investigated by Infrared Modulation
of Cathodoluminescence

A. Samples that showed IR modulation effect:

1. CZ-43, Cr-doped GaAs

Cr concentration $\approx 6 \times 10^{16} \text{ cm}^{-3}$

$\rho \approx 10^8 \Omega\text{-cm}$ at 300°K

Czochralski grown (by P. Leung)

2. SE-3, Cr-doped GaAs

Cr concentration $\approx 6 \times 10^{16} \text{ cm}^{-3}$

$\rho \approx 10^8 \Omega\text{-cm}$ at 300°K

Zone melt grown.

3. GF-30, Undoped GaAs

$\rho \approx 10^9 \Omega\text{-cm}$

Grown by gradient freeze method (by V. Yip)

B. Samples that showed no IR modulation effect:

4. CZ-56, Cr-doped GaAs

Czochralski grown (by P. Leung)

5. THM-84, Cr-doped GaAs

Grown by V. Yip

6. THM-86, Cr-doped GaAs

Grown by V. Yip

appendix were observed were semi-insulating and had resistivities $> 10^8$ ohm-cm. Scanning images of the semi-insulating specimens were made using an electron multiplier phototube with S-1 response. Because of the current interest in semi-insulating GaAs, these images are shown in Figures 52-54, together with line scans that indicate the relative variations in efficiency for band-edge radiative recombination.

We believe that the local variations of the intensity in these images was due to local variations in the concentration of deep levels, but we were unable to verify this by ion microprobe mass spectrometry which was performed on one of the Cr-doped specimens through the courtesy of C. A. Anderson of Applied Research Laboratories, Inc. With regard to the ion microprobe results it may be useful to point out that the IMMA revealed a Cr concentration at the surface that was approximately an order of magnitude higher than the bulk concentration. We attribute this to the fact that Cr may be redeposited on the surface during the chemical polishing of the surface. We do not believe that the local variations in the images, or the infrared modulation of the cathodoluminescence were due to the chromium atoms on the surface, but we do plan to investigate this possibility further by studies of cleaved surfaces.

From the results that have been obtained up to now, it appears that infrared modulation of cathodoluminescence can be a useful technique to study deep levels in direct gap semiconductors. Moreover, it also appears that measurements of specimen current can provide similar results with considerable simplification in the experimental technique. When specimen current is used, the quantity that is indirectly being measured is the resistivity, so that the results should be similar to those obtained by conventional methods using photoconductivity. By using an electron beam, the present method avoids complications that result from additional barriers at the metal semiconductor contact.

It may be significant to note that we have not observed infrared modulation of cathodoluminescence or of specimen current for any GaAs specimens that were not semi-insulating. It is easy to understand why the modulation was not observed for specimen current (the specimen current cannot be influenced significantly by light if the specimen has a low resistivity in the dark). However, it is more difficult to understand why the cathodoluminescence was not modulated in more heavily doped specimens that had an appreciable concentration of deep levels.

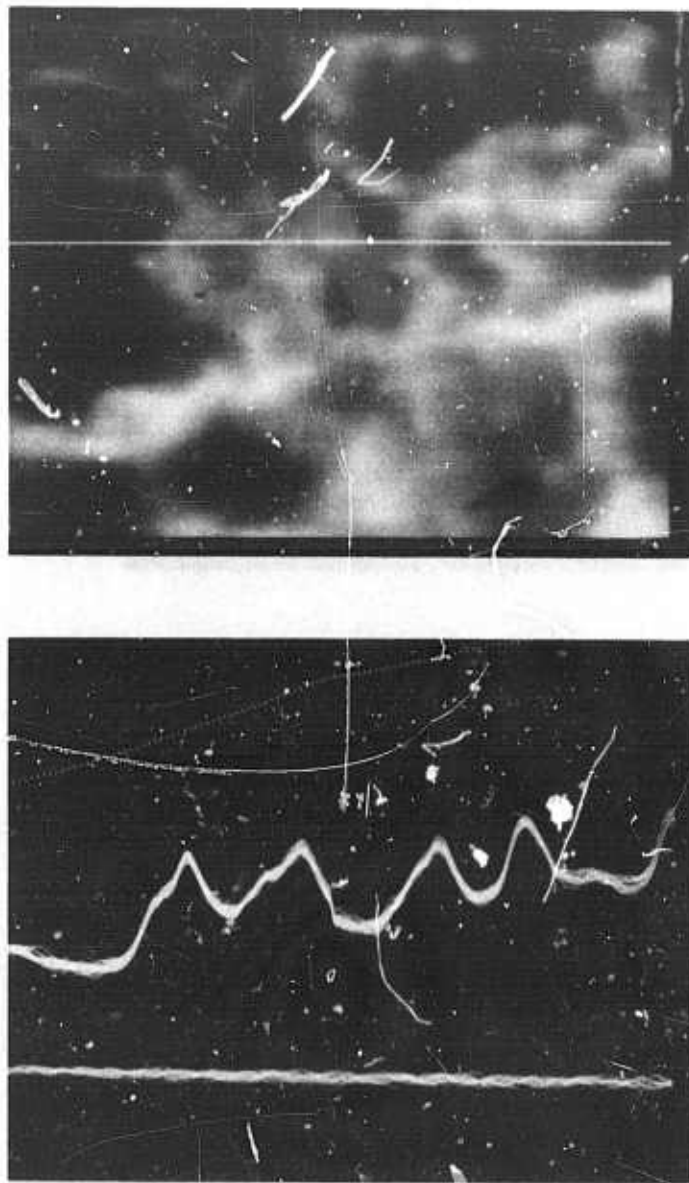


Figure 52. Infrared image and scan profile on SE-3 Cr-doped GaAs sample using 40 kV electron beam. Magnification = 220.

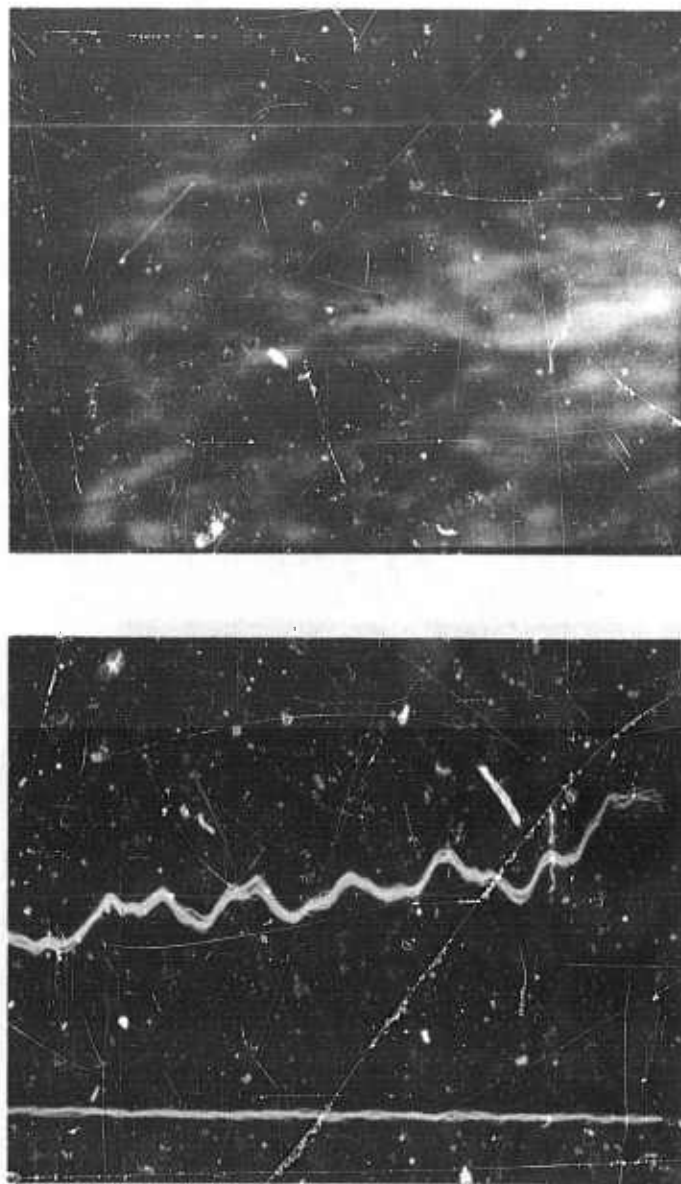


Figure 53. Infrared image and scan profile on CZ-43 Cr-doped GaAs sample using 40 kV electron beam. Magnification = 220.

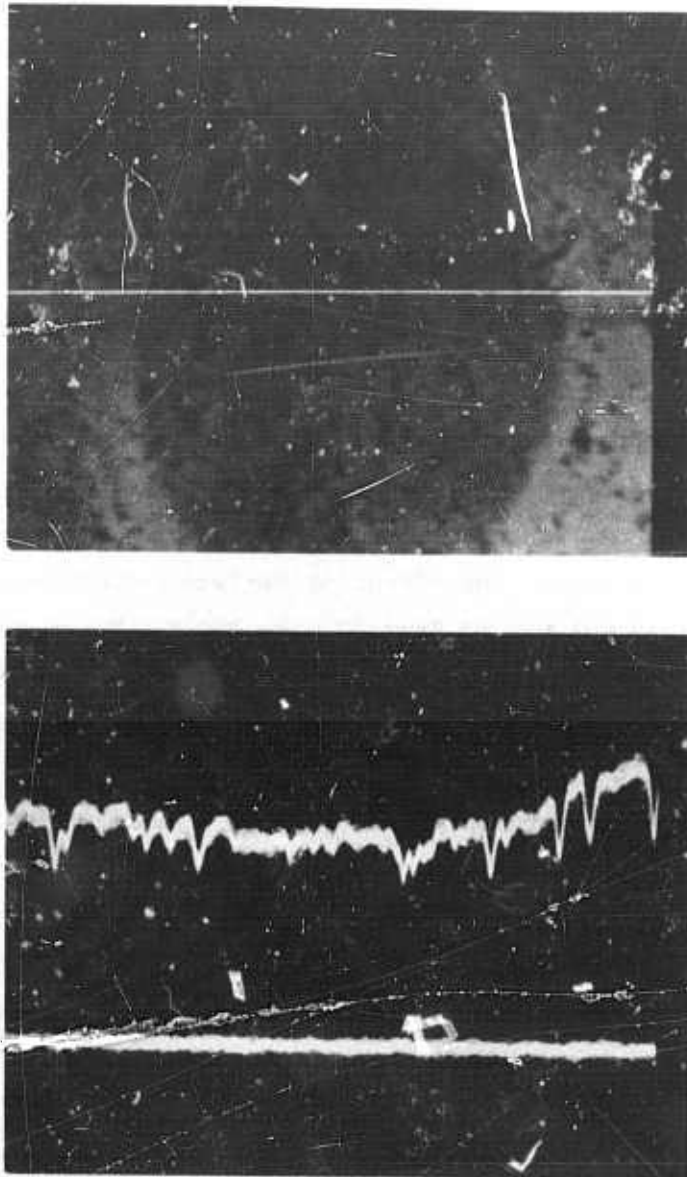


Figure 54. Infrared image and scan profile on GF-30 undoped GaAs sample using 40 kV electron beam. Magnification = 220.

In order to evaluate the limitations of the technique, we have conducted experiments to elucidate the mechanism for this effect. These experiments included studies of the influence of electron beam voltage, electron beam current, the frequency of chopping of the electron beam, the temperature of the specimen, and the intensity of the infrared light. While a large amount of data has been obtained, these data are not yet fully understood and therefore are not reproduced here. However, a significant finding is that the infrared modulation of cathodoluminescence decreases more rapidly with increasing beam voltage than would be expected if it were entirely a bulk effect. This result, combined with the fact that it is only observed on high resistivity GaAs, suggests that it may be related to processes that occur in the space charge region near the surface.

3. Cathodoluminescence of the GaAs, GaP and $\text{GaAs}_{1-x}\text{P}_x$

A clean vacuum electron beam column^(80, Appendix M) has been used to investigate the temperature dependence of cathodoluminescence of GaAs, GaP and $\text{GaAs}_{1-x}\text{P}_x$ semiconductors. All cathodoluminescence measurements were made using a beam voltage of 50 kV to reduce the effect of surface recombination. The temperature of the samples was varied from 27°K to 300°K. These samples were mounted on a copper sample holder using indium. The samples were passed into the indium either while it was hot or at room temperature. At no time was any sample contamination due to electron irradiation observed.

Cathodoluminescence measurements were made as a function of temperature and beam current on the $\text{GaAs}_{1-x}\text{P}_x$ mixed crystals. As x varies from 0 to 1, the mixed crystal changed from a direct to an indirect band gap semiconductor. This occurs at a value of $x = 0.4$ to $x = 0.5$.⁽⁸⁷⁻⁸⁹⁾ The samples were first analyzed to determine the composition using electron probe X-ray analysis and Colby's⁽⁸⁶⁾ MAGIC computer program. Some of the results of these measurements are shown in Figures 55 and 56.

Figure 55 shows the peak energies of the cathodoluminescence spectra as a function of crystal composition at 30°K (upper curve) and at 300°K (lower curve). The cross-over (direct to indirect band gap) point was at $x = 0.45$ to $x = 0.50$ which was close to the values of 0.4 and 0.45 reported.⁽⁸⁷⁻⁸⁹⁾ Differences could be due to different methods of measurement as well as differences in the samples measured.

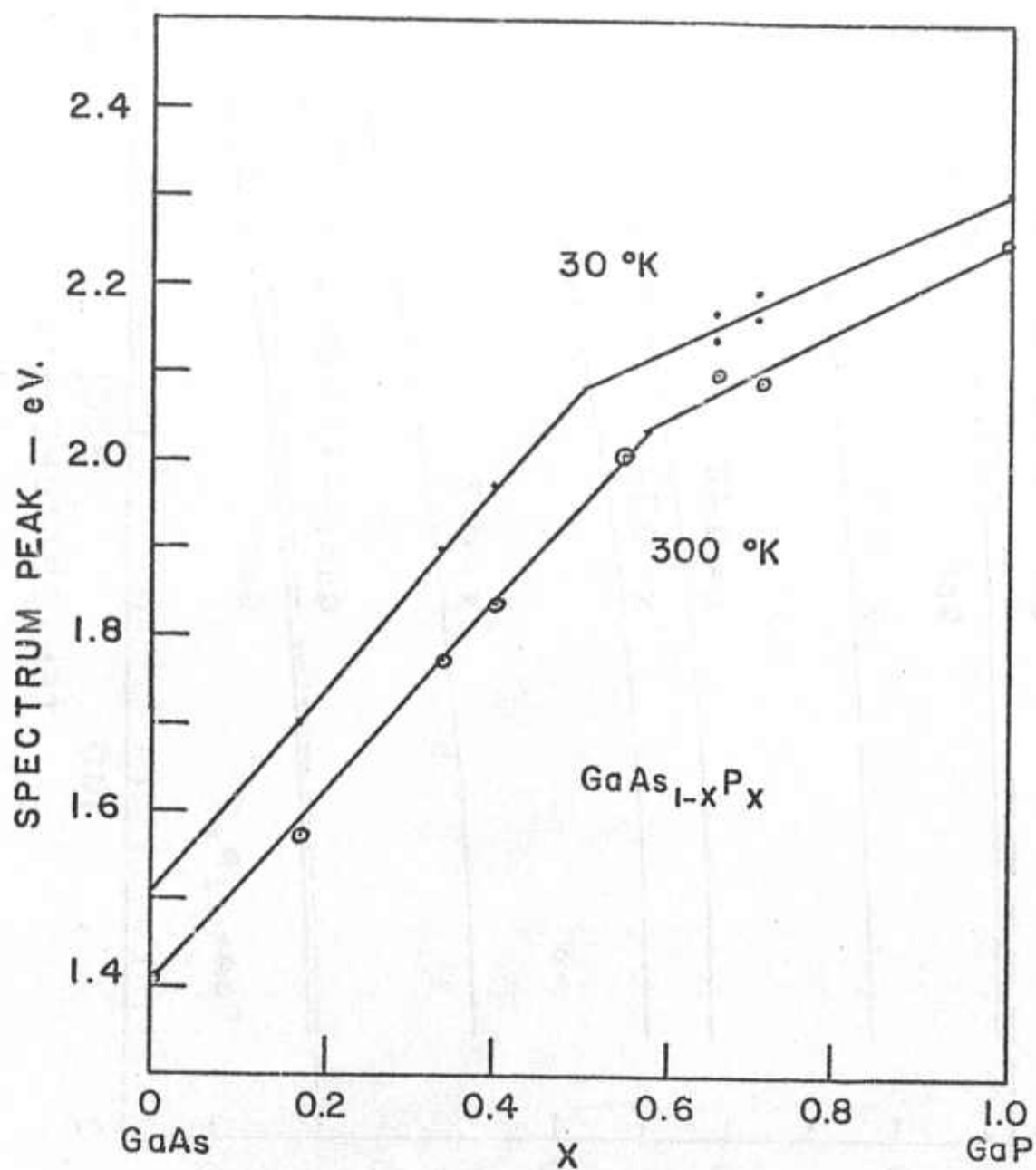


Figure 55. Composition dependence of the cathodoluminescence spectrum peak of $\text{GaAs}_{1-x}\text{P}_x$ crystals. Upper curve at 30°K, lower curve at 300°K.

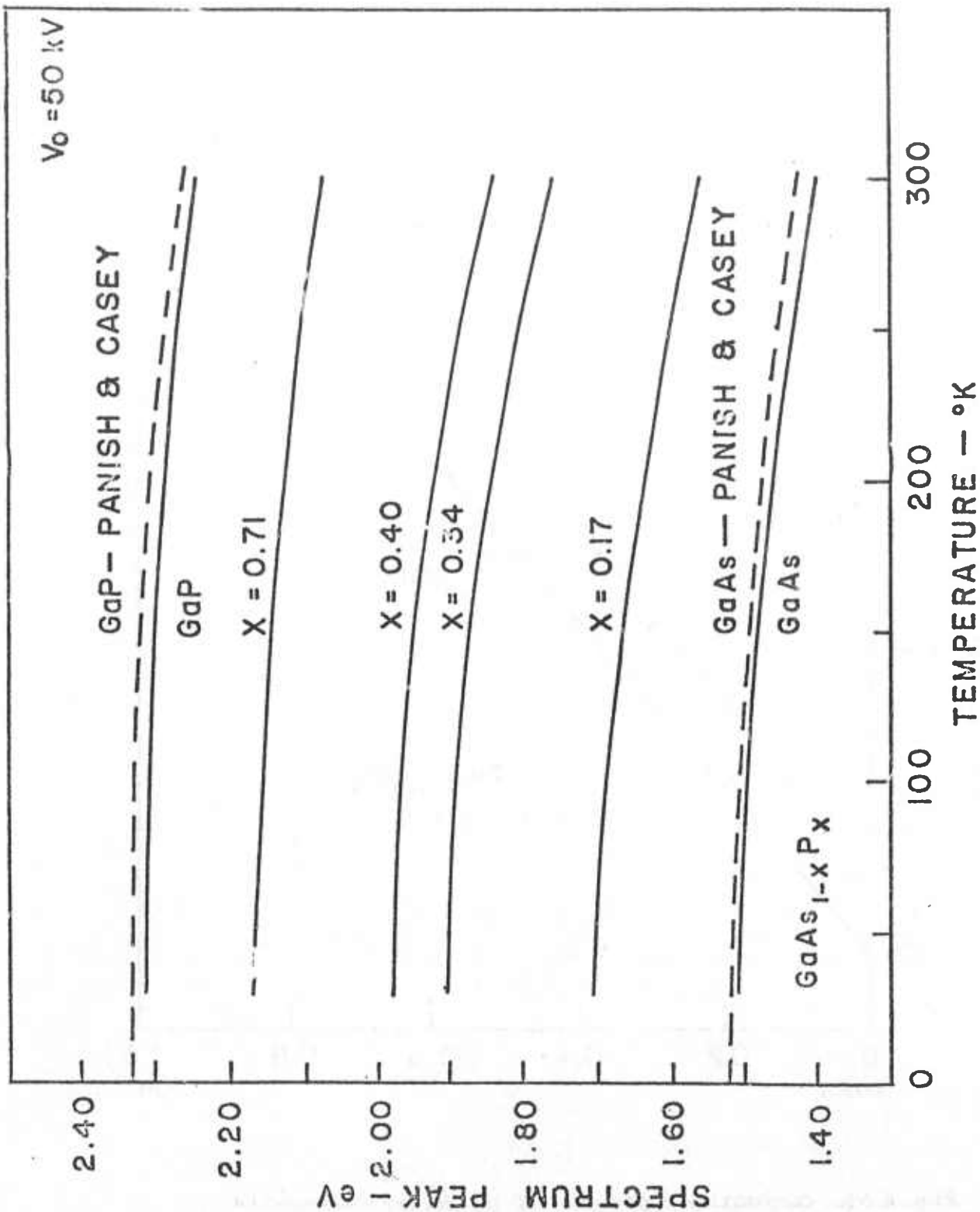


Figure 56. Temperature dependence of the cathodoluminescence spectrum peak of $\text{GaAs}_{1-x}\text{P}_x$ crystals.

Figure 56 shows the temperature variation of the energy peak of the cathodoluminescence spectra of some of the $\text{GaAs}_{1-x}\text{P}_x$ crystals investigated. The upper and lower dashed curves show the temperature dependence of the absorption edge of the GaP and GaAs according to Casey and Paniak.⁽⁹⁰⁾ The curves are all nearly parallel and show the same temperature dependence whether the material was direct or indirect in nature. Departure from this parallel behavior at higher temperatures and values of $x = 0.0$ to $x = 0.4$ can be explained by electron beam heating which was higher at these points because of lower thermal conductivity for these samples at these temperatures.^(91,92) The thermocouple, located about 0.5 cm from the beam spot, would not have detected this heating effect. For pure GaP no such heating has been observed at any sample current available with this instrument because the thermal conductivity of GaP is quite high compared to that of GaAs and $\text{GaAs}_{1-x}\text{P}_x$ for $x < 0.8$.

In one sample whose x value was 0.71, a 40 meV downward shift of the cathodoluminescence peak energy was measured as the sample current changed from 0.3 to 1.1 μA . According to the band gap variation with temperature, this corresponds to a temperature rise of 50°K . Using a value of $0.2 \text{ W/cm}^\circ\text{C}$ for the thermal conductivity and the formula for the temperature rise due to electron beam irradiation given by Almisi et al.,⁽⁹³⁾ which assumes an infinitely thick sample, we estimate a temperature rise of 40°K . The difference between this and the measured rise in temperature could be accounted for by differences in sample thickness and the nature of the indium contact with the sample.

Other results were presented at the 7th National Conference on Electron Beam Microanalysis.^(94, Appendix 10) More recently, samples of GaAs-GaP alloys have been obtained from Bell and Howell (now Electronic Materials Corp.), Pasadena, California. More information is available on the dopant species and concentration for these samples than for those previously studied. In some of these samples with $x < 0.3$, room temperature cathodoluminescence spectra were observed whose peaks corresponded to energies above the direct bandgap energy. This phenomenon has also been observed in photoluminescence experiments on $\text{GaAs}_{1-x}\text{P}_x$ at 77°K and was attributed to nitrogen traps.⁽⁹⁵⁾ Similar results were seen in photoluminescence measurements on $\text{In}_{1-x}\text{Ga}_x\text{P:N}$ at 77°K for $x < 0.71$ and attributed to a resonant N-trap state.⁽⁹⁶⁾ Relative intensities of radiation peaks and peak energies in multiple spectra taken at 30°K on $\text{GaAs}_{0.29}\text{P}_{0.71}$ as a function of electron beam excitation intensities showed variations

similar to those reported by N. Holonyak, Jr. et al.,⁽⁹⁷⁾ in photoluminescence measurements on $\text{GaAs}_{1-x}\text{P}_x\text{:N}$ at 77°K . Further investigations are in progress to determine how these peaks vary with temperature and electron beam excitation intensity.

H. Photoluminescence Measurements

(E. Johnson, B. Mroziewicz and M. Gershenson)

1. Bulk GaAs

Low-temperature photoluminescence measurements have been made on GaAs samples cut from six crystals grown at USC. Five of the samples were grown by the liquid-seal Czochralski technique (section II.A), the sixth was grown by the horizontal Bridgman technique (section II.D). One of the Czochralski-grown crystals and the Bridgman-grown crystal were not intentionally doped. The remaining crystals were doped with Te and combinations of Mg, S and Se. Photoexcitation was by helium-neon laser (6328 \AA , 1.96 eV), filtered to remove long-wavelength laser lines. Photoemission in the wavelength region 0.8 to 1.05μ (1.55 to 1.18 eV) was analyzed with a Perkin Elmer El monochromator and detected with a cooled RCA 7102 photomultiplier. The photomultiplier output was amplified by conventional phase-sensitive techniques and recorded on chart paper.

Luminescence measurements in GaAs are complicated by the fact that impurity banding occurs at very low impurity concentrations ($\sim 10^{16}/\text{cm}^3$) due to the low carrier effective masses. Such banding greatly broadens the energy levels associated with impurity-assisted recombination. Thus, when banding occurs it is often possible to determine the general class of impurity present (shallow donors, deep acceptors, etc.) and the transition mechanism involved, but it is not possible to identify impurity atomic species.

Of the samples examined, only the Bridgman-grown specimen was pure enough to show some luminescence from free excitons or from excitons bound to neutral shallow donors or acceptors. Even in this sample, the dominant luminescence appeared to involve free-to-bound or shallow donor-acceptor pair recombination. This result is in general agreement with the results of other characterization studies of this material which suggest compensation. The spectra from the Te-doped GaAs were dominated by possible free-to-bound transitions involving the Te donors existed in the more lightly doped sample. In the more heavily doped sample, contamination by deep acceptor impurities such as Fe, Zn, Cd, Cu, etc. is

suggested. The Mg: Se- and Mg:S-doped samples produced broadband luminescence which could be interpreted as donor-acceptor pair recombination. Other interpretations involve Si or some deep acceptor. More exact interpretation of the data simply is not possible due to the effects of impurity banding and the confused and often contradictory state of the GaAs photoluminescence literature. It should be pointed out that free and bound exciton recombination are not commonly observed in bulk GaAs and that nearly all such spectra reported come from high-purity epitaxially grown material.

2. Films

Photoluminescence spectra of liquid epitaxial grown films of $\text{Ga}_{1-x}\text{In}_x\text{As}$ and $\text{GaAs}_{1-x}\text{Sb}_x$ alloys were measured at room temperature and at the boiling points of helium and nitrogen. In general, the evidence was that impurity-band transitions were most likely for the detected luminescence. For both alloy systems the same dependence of the energy gap on x was observed as the values of $x \rightarrow 0$ (within estimated errors < 0.02 eV). Photoluminescent efficiencies of the alloys were encouragingly good, i.e., within a factor of ten of solution-grown GaAs for values of $x \leq 0.06$. Relative widths of the spectral and X-ray diffraction peaks were consistent with alloy homogeneities, $\Delta x/x$, of 0.1 or better.

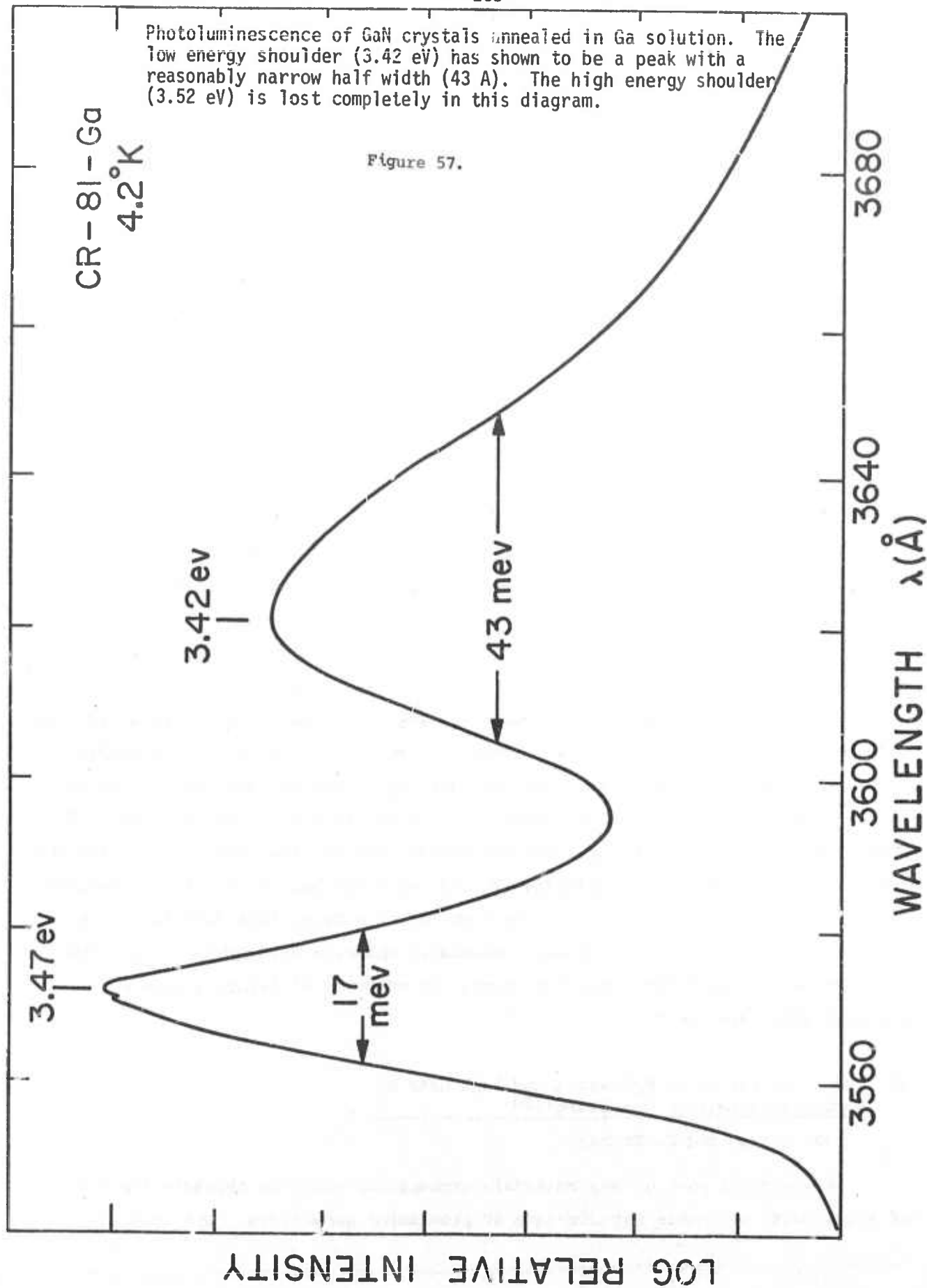
Highly efficient photoluminescence has been observed in GaN films at low temperatures and at room temperature. There are two peaks seen on all the samples measured: one at 3.47 eV which does not change with sample, and one at 3.42 or 3.448 eV depending on the sample used, as shown in Figures 57 and 58. The 3.47 eV peak is explained as due to free exciton transitions and the 3.42 eV (or 3.448 eV) may be due to bound exciton transitions. Li doped GaN has given a broad spectrum with high quantum efficiency. The spectrum covers a range from 3.57 to 3.16 eV.

Attempts were made to observe stimulated emission at liquid nitrogen temperature with a GaN Fabry-Perot structure. No evidence of lasing action was found in this experiment.

I. Characterization of Epitaxial and Bulk GaAs by Capacitance-Voltage Profiling(100)

(B. Gordon and H. Stover)

An integral part of any materials preparation study is characterization of the results to enable optimization of processing parameters. One technique



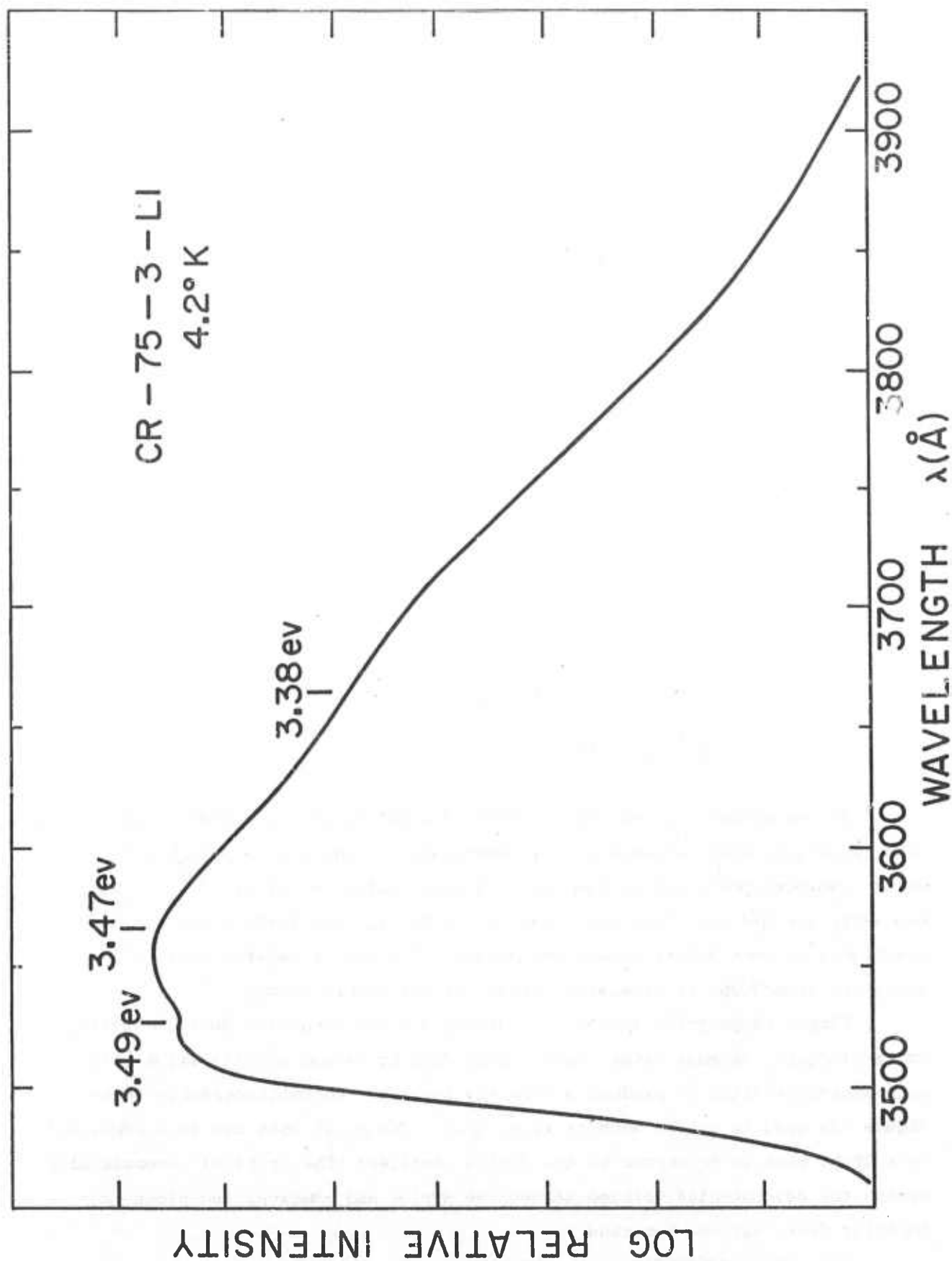


Figure 58. Photoluminescence of GaN crystals grown over Ga boat. The low energy shoulder which appears at 3.448 eV in this case has higher luminescence efficiency than the 3.47 eV peak.

that enables rapid, accurate determination of an electrically active impurity distribution in either epitaxial or bulk material is capacitance-voltage profiling. This procedure is based on well-known semiconductor junction expressions relating depletion-layer capacitance, depletion-layer width and doping at the edge of the depletion layer:

$$W(v) = \frac{\epsilon A}{C(v)}$$

and

$$N(v) = \frac{1}{e\epsilon A^2} \frac{C^3(v)}{dC/dv}$$

where

$W(v)$ = depletion layer width

$C(v)$ = depletion layer capacitance

e = charge on the electron

ϵ = dielectric constant of material

A = junction area

An instrument has been developed in the USC Solid State Devices Laboratory that implements these expressions electronically by the use of a capacitance meter, sweeping power supply and sophisticated analog circuitry. ⁽⁹⁸⁾ It has had extensive use profiling epitaxial layers for silicon devices and has been invaluable in controlling growth parameters. Its use is limited only by avalanche breakdown, or excessive leakage of the sample diode.

Sample preparation consists of making a diode structure on the material to be studied. In most cases, this can be done by vacuum metallization with an appropriate metal to produce a Schottky barrier. Photolithographic techniques are used to define dots of known area. The metal dots are then contacted by a probe that is connected to the doping profiler. The profiler automatically sweeps the reverse-bias voltage across the device and computes and plots the impurity distribution, N versus W .

The ease and rapidity with which measurements may be made enable many profiles to be measured over different portions of a sample. In this way,

uniformity of an epitaxial layer across a slice or differences in doping throughout a bulk crystal can easily be measured.

The accompanying profiles illustrate some typical characterization applications. Figures 59 and 60 are profiles of bulk GaAs from opposite ends of an ingot. Both are very uniform, but there is a difference in doping levels. The region of Figure 59 has a doping of $1.2 \times 10^{16}/\text{cm}^3$ while the doping in Figure 60 is $8.5 \times 10^{16}/\text{cm}^3$. The crystal was not deliberately doped and was grown by the liquid-seal Czochralski technique (section II.A).

Figure 61 illustrates a series of profiles taken across a single slice of bulk material cut from the crystal mentioned above. The slice was cut at an angle with respect to the growth direction ($\sim \langle 111 \rangle$).

Another application for impurity profiling is found in the characterization of epitaxial layers. As above, useful information on doping level and uniformity are easily obtained. If the doping and thickness of the sample permit, the epilayer can be completely depleted and the interface between the epitaxial layer and substrate can be observed.

Figure 62 is the doping profile of a liquid epitaxial GaAs growth layer. The impurity distribution is very uniform over a distance greater than 2 microns. The indicated sharp increase in doping at 2.3 microns is not real, but rather a result of avalanche breakdown. This was verified by I-V measurements. Figure 63 shows a profile of very thin CVD epitaxial layer obtained from Monsanto Corp. The impurity distribution is sharply graded and the $N-N^+$ interface is clearly discernible.

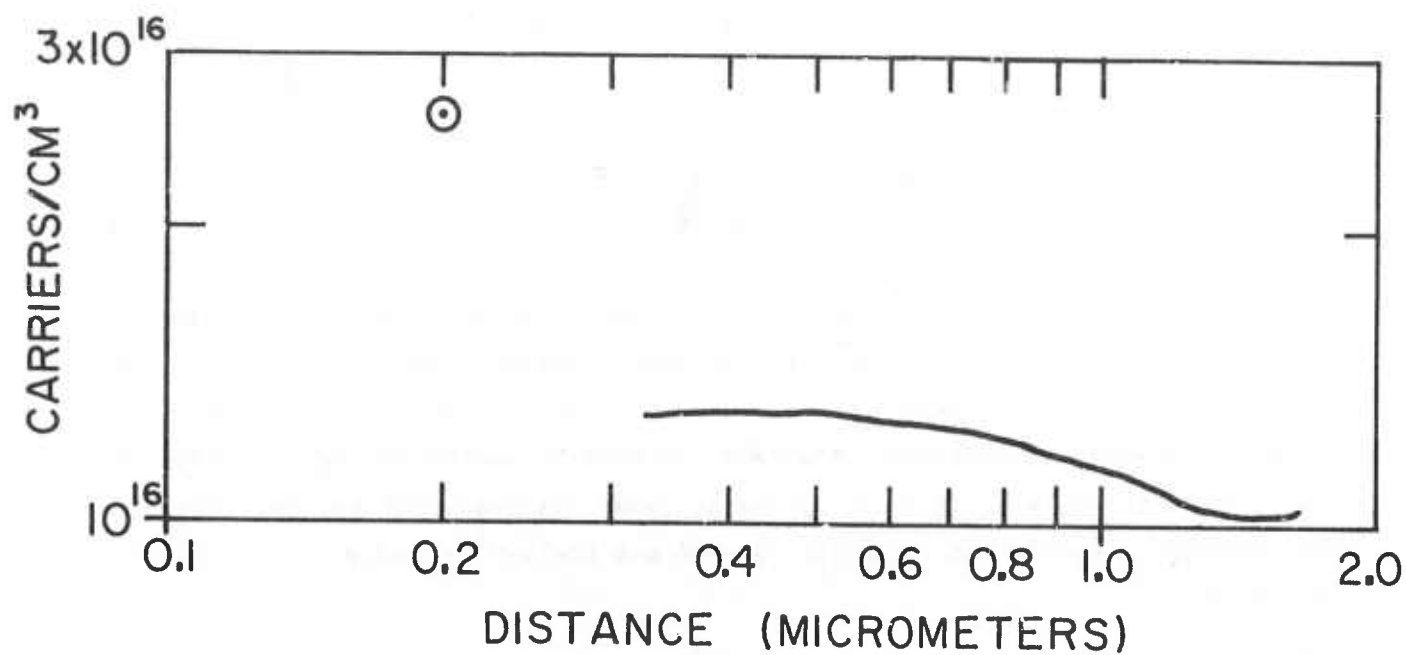


Figure 59. Carrier vs. depth profile of bulk GaAs (CZ-35) from capacitance-voltage measurements.

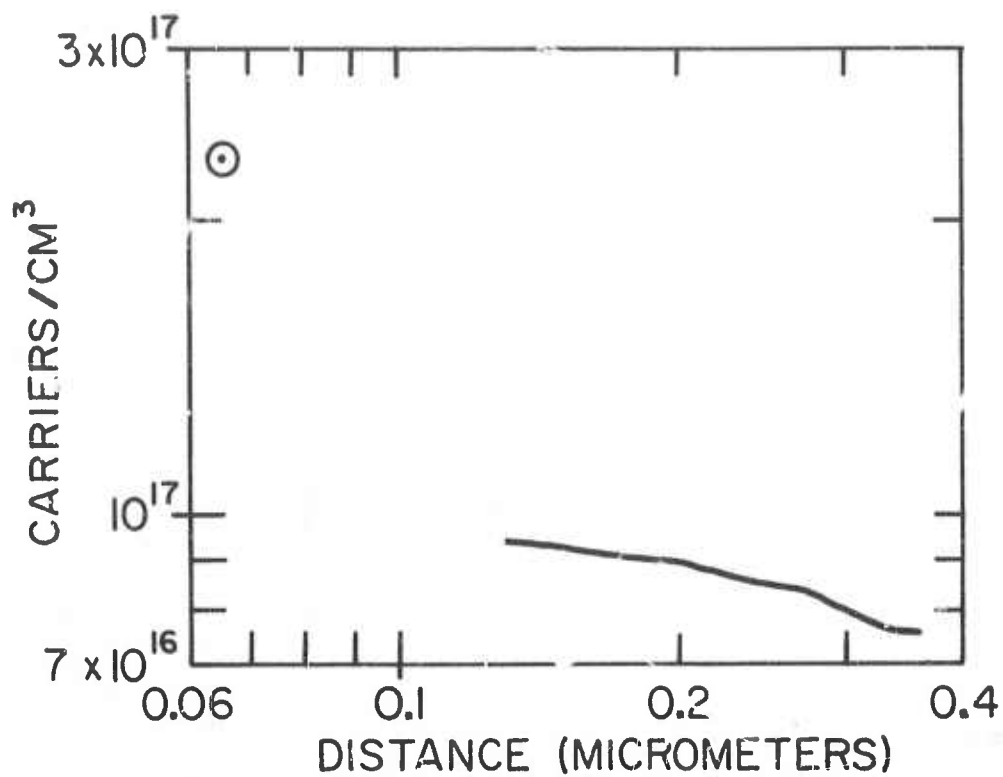


Figure 60. Carrier profile from opposite end of CZ-35 from sample of Figure 59.

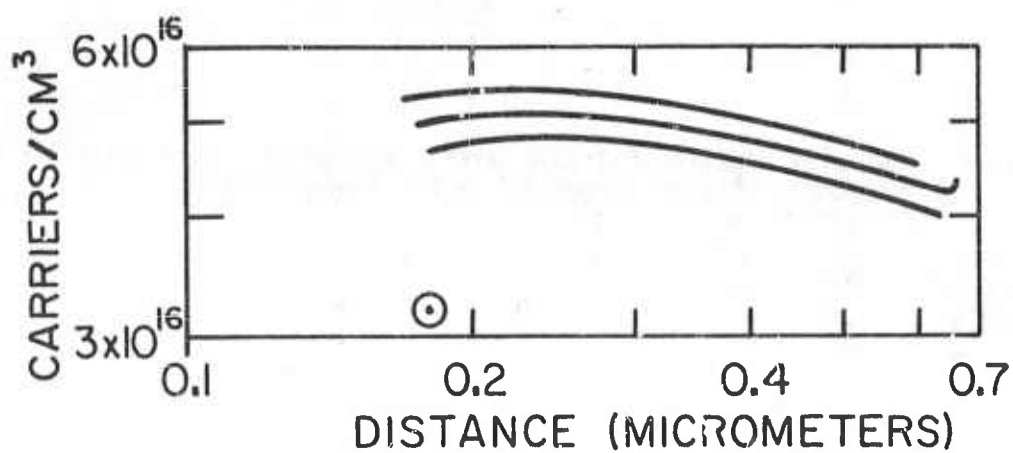


Figure 61. Carrier profiles at various points of a slice from CZ-35.

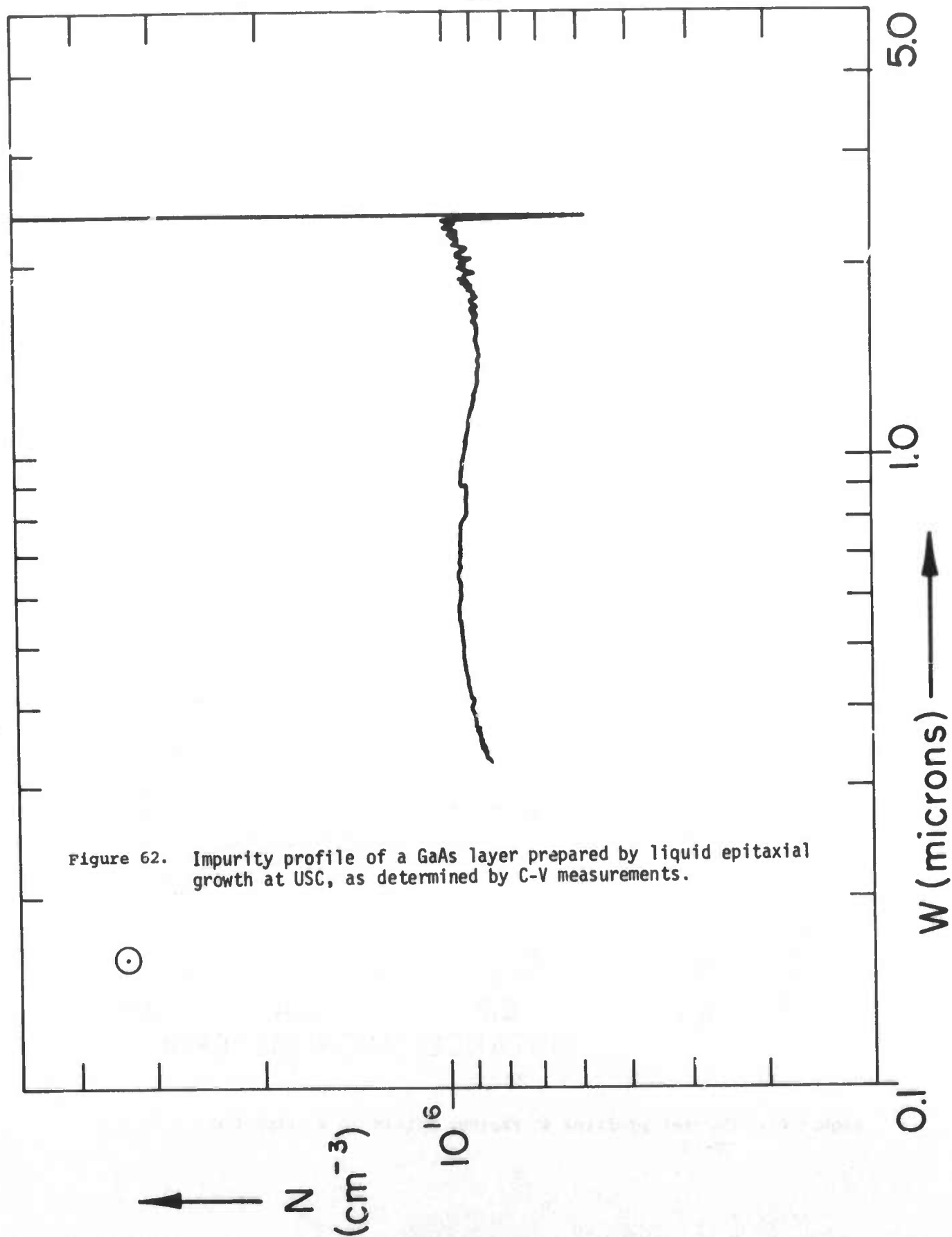
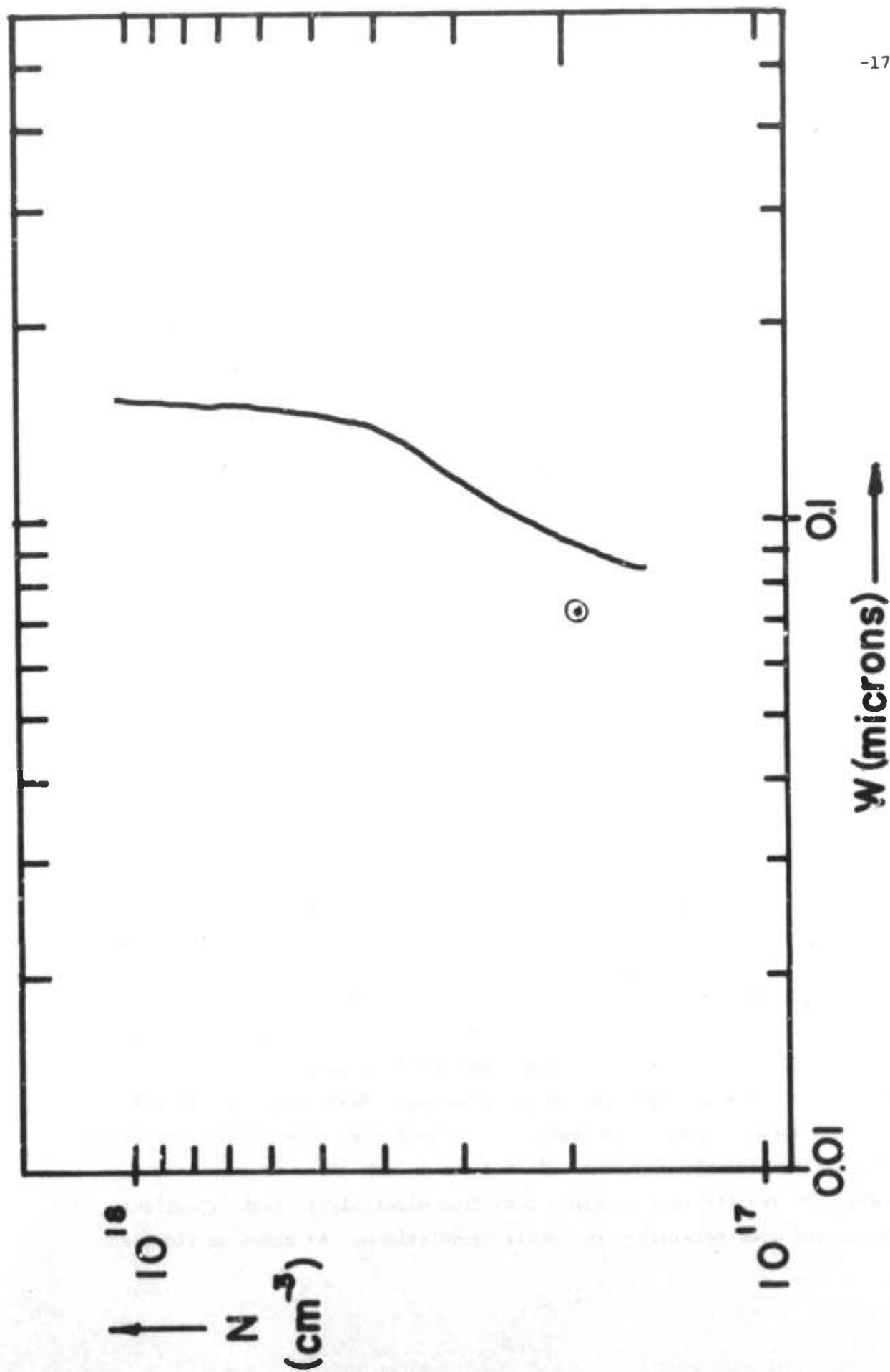


Figure 62. Impurity profile of a GaAs layer prepared by liquid epitaxial growth at USC, as determined by C-V measurements.



-175-

Figure 63. Impurity profile of hyper-thin chemically vapor deposited epitaxial film of GaAs from the Monsanto Company as determined by C-V measurements.

J. Electrical Characterization of Bulk Interfaces in GaAs

1. Program Orientation

(C. Crowell, M. Beguwala, S. Joshi, R. Chwang, B. J. Smith,
C. L. Anderson, M. Madden, K. Nakano, C. Huang, Y. Okuto,
R. Baron, T. W. Kao and V. L. Rideout)

At the initiation of this contract there were no on-campus facilities for high impedance variable temperature Hall measurements and no provisions other than manually balanced bridges for making capacitance measurements. Because of the importance of these tools in the analysis of the device performance of semiconductor materials, a program was undertaken to design and construct a high impedance Hall and resistivity measurement system which could be operated over the temperature range 4°K to 400°K and a capacitance/conductance analyzer with electronic self-balancing and frequency and voltage sweeping capabilities. The analyzer was intended to include a simple programmable analog computer designed to provide online output in a variety of formats suitable for the analysis of MOS, Schottky barrier and p-n junction configurations. In the course of the research supported by this program such facilities were designed, constructed and tested. Several illustrations of the use of these facilities are presented in this report. We also undertook to review the basic assumptions in relating such measurements to materials properties. From this study spring in particular investigations of the process of photoinjection at a metal-semiconductor interface and a study of contact size effects on van der Pauw Hall and resistivity measurements.

2. Hall and Resistivity Measurements

a. Hall and Resistivity Measurements

At the beginning of this program considerable attention was paid to the possible need for Hall samples in the conventional bridge and van der Pauw clover leaf form. These sample configurations are fragile and difficult to make and, if the contacts approach the infinitesimal ideal, are also of high resistance. Accordingly an investigation of contact size effects was undertaken. Correction factors for the apparent values derived from these measurements were determined. The results were obtained both from electrolytic tank experiments and computerized over-relaxation potential calculations. As shown in Figures

64 and 65, contacts of appreciable size relative to that of the sample can be a good approximation to van der Pauw's infinitesimal contact. With these correction factors, one can utilize the simplicity and other advantages of finite size ohmic contacts for these measurements and still obtain precise data.

b. High Impedance Hall System

We have completed the design and construction of a system for making Hall effect and resistance measurements on high impedance samples. The circuitry features electronic suppression of cable capacitance and leakage effects in both the current supply and voltmeter leads. The Hall sample current source is programmable and has an effective leakage resistance greater than 10^{12} ohms. The voltmeter circuit is balanced and has independent compensation for the leakage resistance of each lead to a level greater than 10^{11} ohms. The operational amplifiers used are varactor bridge amplifiers. The common of the voltmeter is also guarded to yield a common mode input resistance of the order of 10^{12} ohms. When the high impedance features are not required, this voltmeter can be bypassed and replaced by a balanced digital voltmeter with a decrease in noise level. The system is capable of measuring samples with a resistance of the order of 10^{10} ohms without applying more than 10 volts across the current terminals of the Hall sample. Figures 66-68 show the circuit diagrams for the current source, the electrometer and the switching network for the high impedance leads.

Our high impedance Hall system has been integrated with a Janis variable-temperature cryostat. In this system, temperature is specified in terms of the resistance of a platinum resistance sensor, which is also incorporated in the circuitry at the temperature controller. We have investigated errors due to sample placement relative to the sensor and the dependence on the flow rate of the exchange gas which provides cooling and also influences the heater power required.

The platinum resistance thermometer in the Hall cryostat was calibrated against another calibrated platinum sensor, using an extended Callender-van Dusen equation. The two temperature sensors were then used to obtain a table of potentiometer setting on the temperature controller versus temperature at the sample position with no flow of the exchange gas.

The potentiometer circuit of the temperature controller was modified to extend the high accuracy range below $\approx 300^{\circ}\text{K}$ to include the temperature range up to 400°K .

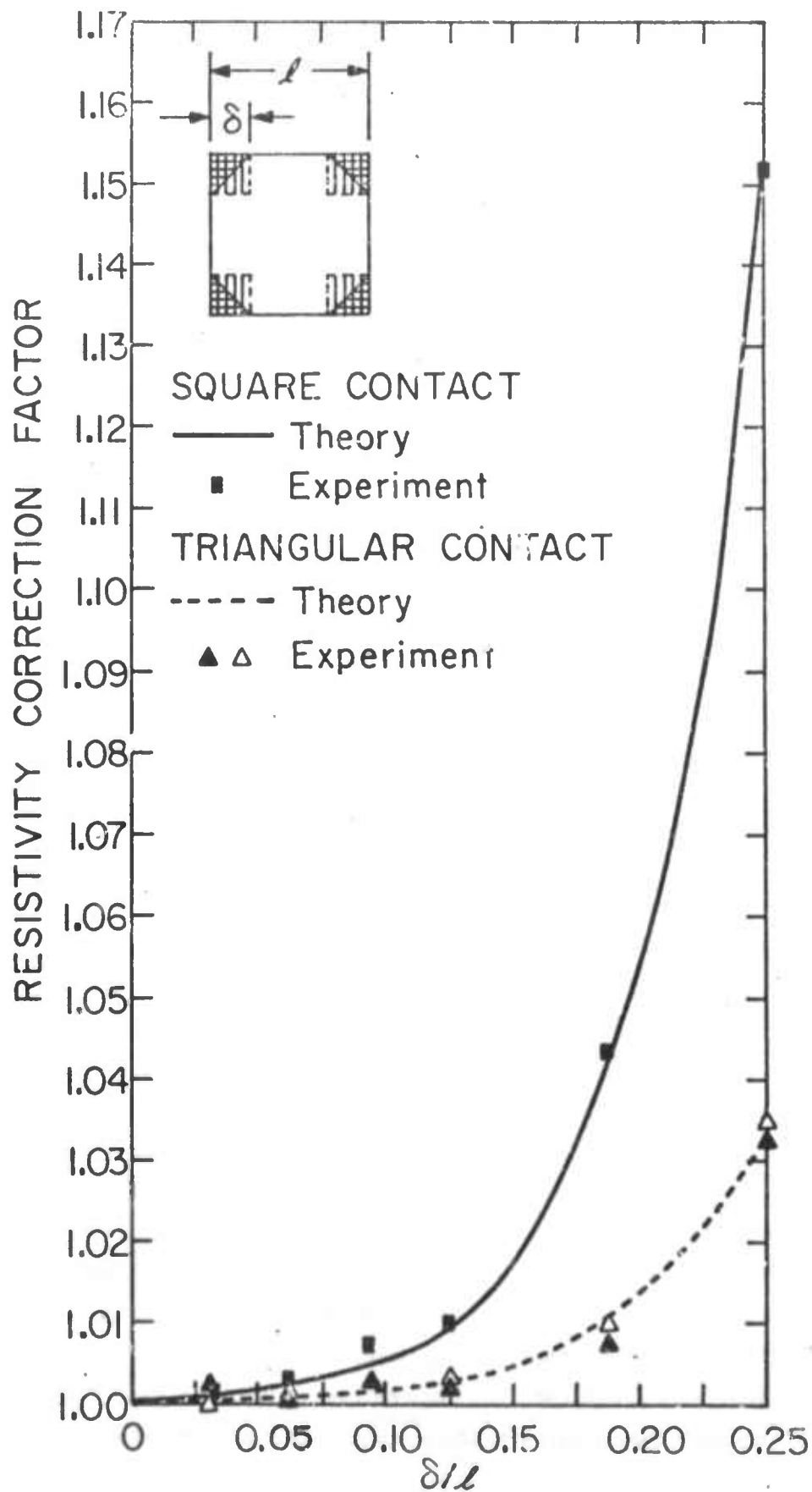


Figure 64. Correction factors for finite contact effect on resistivity measurement shown as a function of δ/l (parameters defined by insert). Result from computer calculation based on resistive network analogue is shown by solid and dashed curves for square and triangular contacts respectively. \square , Δ , \blacktriangle are the data obtained from the electrolytic tank experiment.

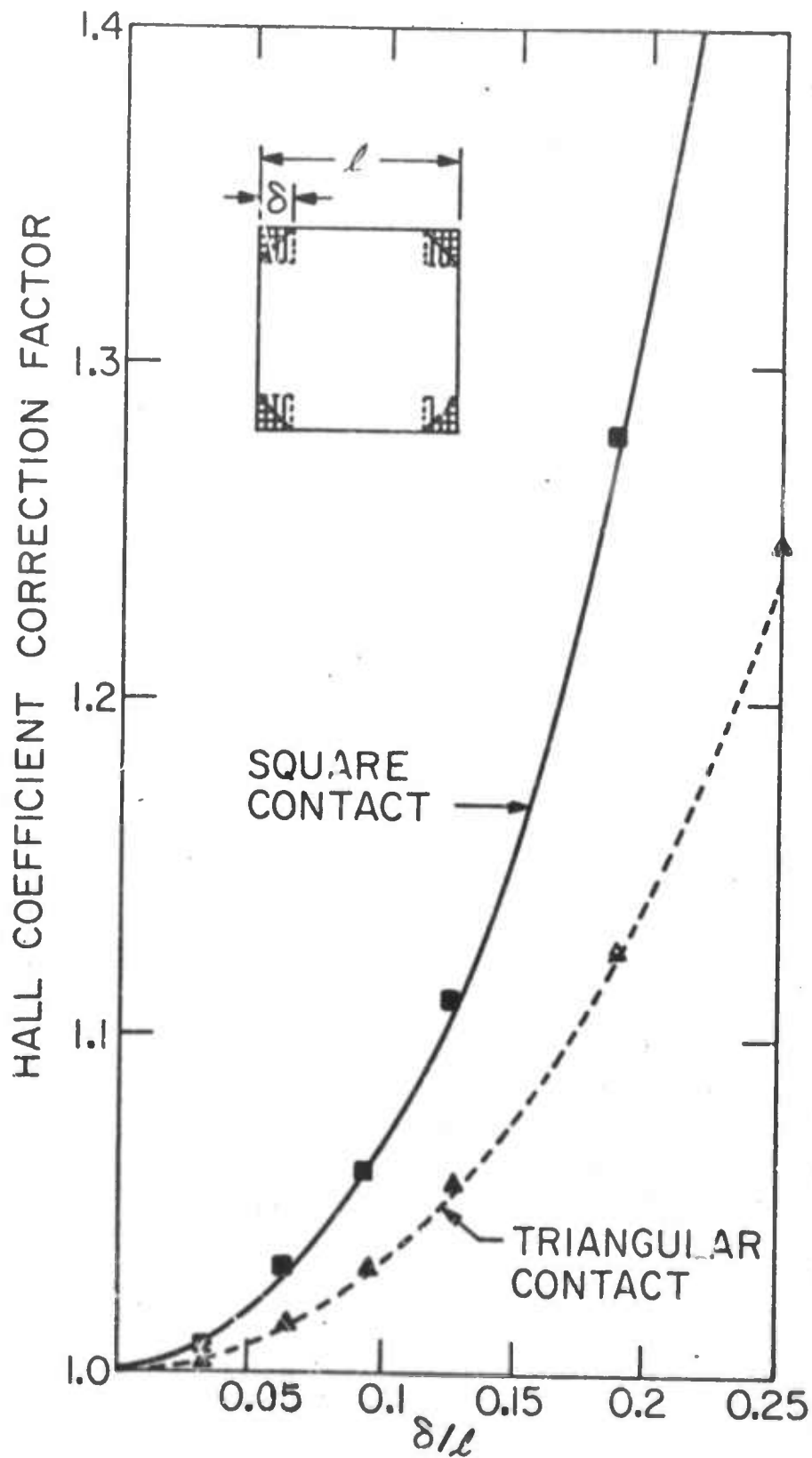


Figure 65. Correction factors for finite contact effect on Hall coefficient measurement shown as a function of δ/l . Result from computer calculation based on resistive network analogue is shown by solid and dashed curves for square and triangular contacts respectively. \blacksquare , \blacktriangle are data obtained from the electrolytic tank experiment.

Figure 66.

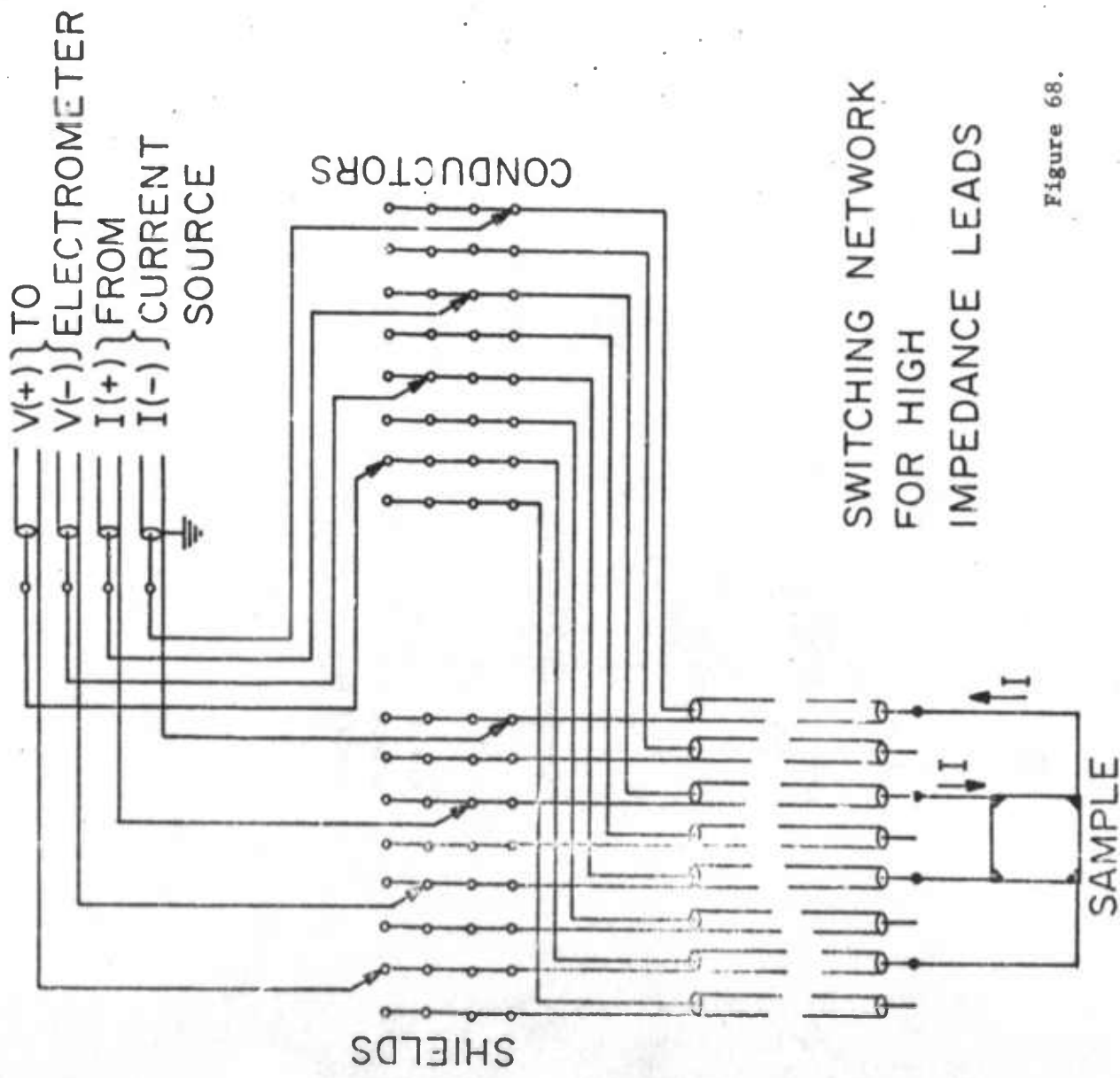


Figure 68.

The difference in temperature between the sample position and the sensor position for a finite flow of exchange gas and medium power dissipation (1.25 watts at liquid nitrogen temperature) was less than 0.02°K . Thus, with the present arrangement the absolute temperature can be set and controlled within an accuracy of about 0.05°K . The temperature controller gives a clear indication of temperature differences of 0.01°K .

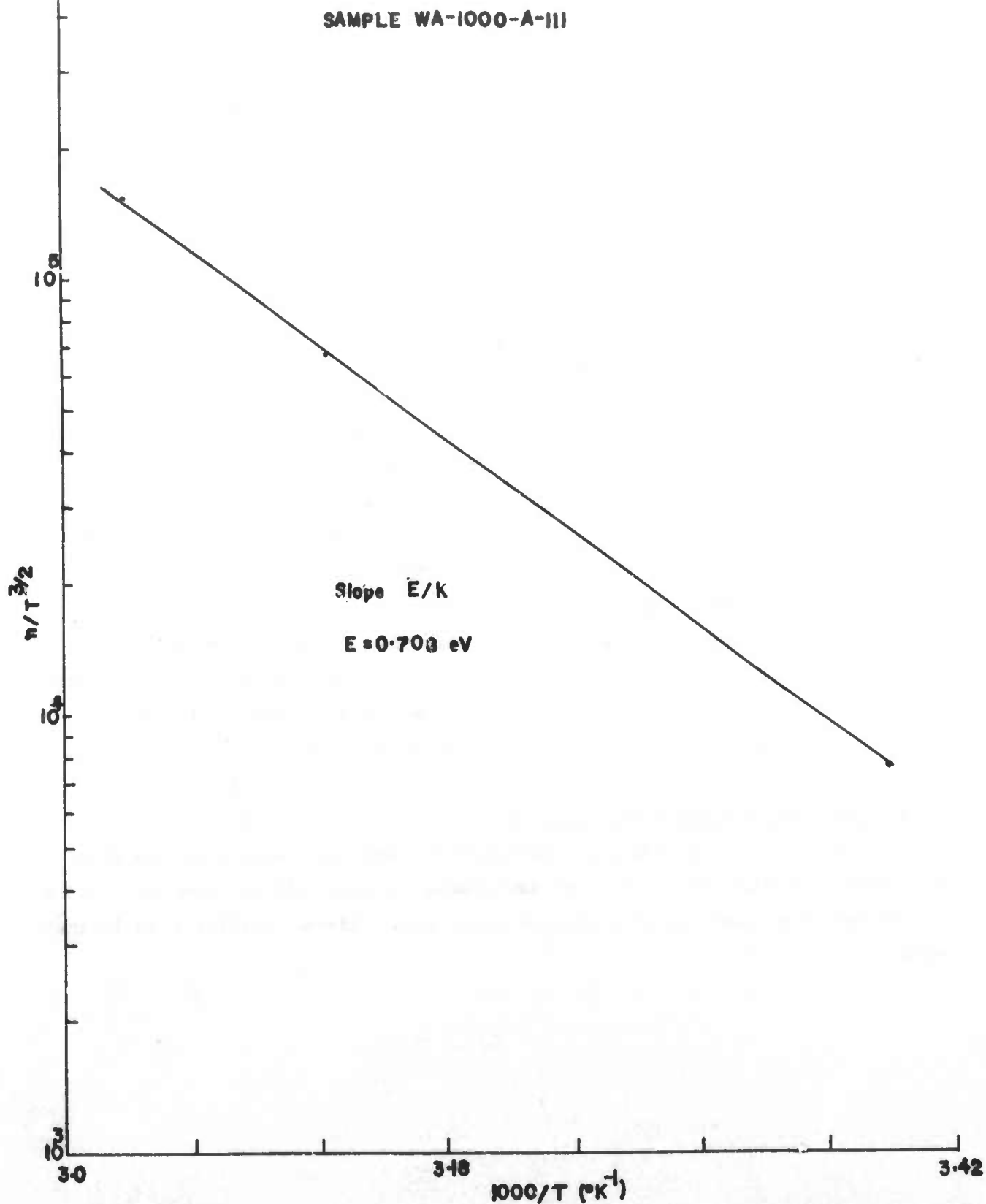
c. Example Applications

The system was routinely used to characterize GaAs grown here. The samples were prepared in a square van der Pauw configuration. The ohmic contacts were made by evaporating AuGe onto the corners of the square and alloying them at 450°C for 30 seconds in a forming-gas ambient. Temperature versus Hall effect measurements were performed on a number of samples. Figure 69 shows one such sample (WA-1000-AIII) of our typical high resistivity GaAs material. The room temperature resistivity, Hall mobility and carrier concentration of this sample were found to be $1.29 \times 10^8 \text{ ohm cm}$, $1238 \text{ cm}^2/\text{V sec}$ and $3.91 \times 10^7 \text{ cm}^{-3}$, respectively. The activation energy obtained from this plot was 0.708 eV, assuming that the material was compensated by deep impurities. Typical low resistivity samples (CZ-36 Te doped, CZ-53 undoped) were prepared from GaAs material grown by our Czochralski liquid-seal technique. The temperature dependence of the Hall effect on these samples in the temperature range of 300°K to 77.3°K did not show an appreciable change in the carrier concentration. To detect the shallow impurities, the temperature range of the experiment would have to be extended below 77.3°K . The room temperature resistivities and electron concentrations measured for CZ-36 were 0.0324 ohm cm and $1.08 \times 10^{17} \text{ cm}^{-3}$ respectively. The same parameters measured for CZ-53 were 0.0434 ohm cm and $8.85 \times 10^{16} \text{ cm}^{-3}$, respectively.

3. Capacitance/Conductance Analysis

The study of capacitance/conductance of junctions complements the bulk Hall effect studies and is of great importance for application since non-uniform doping and deep level impurity effects occur in a different fashion than in the bulk.

Figure 69. Hall-effect carrier concentration vs. reciprocal temperature for high resistivity GaAs, grown by the horizontal Bridgman method without intentional doping. Energy level from slope corresponds to Cr.



a. Theoretical Guidelines for Deep Level Analysis

A theoretical analysis⁽¹⁰⁹⁾ performed under ARO sponsorship provided the motivation for many of the features which were built into our capacitance/conductance analyzer.

b. Automatic Capacitance Voltage Measurements

The following describes the basic design criteria for the automatic capacitance analyzer. As constructed it has provisions for display of C-V, C^n -V where n may be chosen to be a number of discrete values (or with more complication any positive or negative value) and C- ω swept measurements. A 90° phase change permits corresponding measurements of the imaginary component of the capacitance. These features are of special interest in the analysis of deep level effects.

For impurity profiling a two-frequency technique is used to perform the measurement. Since this phase of operation is much less common than the above and has not been discussed at appreciable length in the literature, the balance of this section is devoted mainly to this topic.

The system consists almost entirely of commercial building blocks and uses phase-sensitive detection to achieve better than 40 dB isolation between capacitive and conductive signals. In the two-frequency intermodulation mode of operation the system can measure either capacitance, C, and dC/dV , or conductance, G, and dG/dV , over the frequency range 2 kHz - 200 kHz, where the derivatives are taken with respect to a low-frequency perturbation in the range 10 Hz - 2 kHz. A pinboard-programmable analog computer integral with the unit allows presentation of the data as impurity profiles. A simple change of circuit parameters permits measurement of C or G with amplitude response flat within 1% over the frequency range 20 Hz - 200 kHz. The computer may then be used to present the results in formats appropriate to Schottky barrier height, MOS interface state, or deep level evaluation. Particular attention has been paid to the problem of calibration and reduction of the sensitivity of the system to stray capacitance. All calibration signals are generated internally and are passed through the complete detection circuit, thereby eliminating the effects of drifts in detector gain adjustments and undetected phase shifts. The system uses an inverting operational amplifier input stage of high input impedance which degenerates the effect of cable capacitance and thereby allows the system

to be used with input cables of considerable length. Provisions are included to permit the elimination of voltage-independent offset capacitances and conductances associated with probe stations or device encapsulations.

The total charge, Q , stored in a semiconductor device biased to a voltage, V , may be expressed as a Taylor series expanded about a reference voltage, V_0 .

$$Q(V) = Q(V_0) + C(V_0) \cdot (V - V_0) + \left. \frac{dC}{dV} \right|_{V_0} \cdot \frac{(V - V_0)^2}{2} + \dots \quad (1)$$

where $C(V_0)$ is the differential capacitance of the device at voltage V_0 . The conduction current, I_c , passing through the device may be similarly expanded:

$$I_c(V) = I_c(V_0) + G(V_0) \cdot (V - V_0) + \left. \frac{dG}{dV} \right|_{V_0} \cdot \frac{(V - V_0)^2}{2} + \dots \quad (2)$$

where $G(V_0)$ is the differential conductance of the device at V_0 . If a simple parallel equivalent circuit is valid for the device being studied, the total current, I , passing through the device under the influence of a time-dependent input voltage may be expressed as the sum of a displacement current, I_d , derived from Eq. (1) and the conduction current given by Eq. (2). Thus

$$I = I_d + I_c = C(V_0) \cdot \frac{dV}{dt} + \left. \frac{dC}{dV} \right|_{V_0} \cdot (V - V_0) \frac{dV}{dt} + \dots$$

$$+ I_c(V_0) + G(V_0) \cdot (V - V_0) + \left. \frac{dG}{dV} \right|_{V_0} \cdot \frac{(V - V_0)^2}{2} + \dots \quad (3)$$

where the first line on the right-hand side is the displacement current and it is assumed that V_0 is constant or so slowly varying that terms involving dV_0/dt are negligible.

If the perturbation $\text{sign}(V - V_0)$ is the sum of a high frequency, ω_H , and a low frequency, ω_L , with $\omega_H \gg \omega_L$, then

$$(V - V_0) = V_H \sin \omega_H t + V_L \sin \omega_L t \quad (4)$$

and

$$\begin{aligned} I = & C(V_0) \cdot (\omega_H V_H \cos \omega_H t + \omega_L V_L \cos \omega_L t) \\ & + \left. \frac{dC}{dV} \right|_{V_0} \cdot \left(\left[\frac{\omega_H V_H^2}{2} \sin 2\omega_H t \right] + \frac{\omega_L V_L^2}{2} \sin 2\omega_L t \right. \\ & + \left\{ \frac{(\omega_H + \omega_L) V_H V_L}{2} \sin(\omega_H + \omega_L) t \right. \\ & \left. \left. - \frac{(\omega_H - \omega_L) V_H V_L}{2} \sin(\omega_H - \omega_L) t \right\} \right) + \dots \\ & + \left. \frac{dG}{dV} \right|_{V_0} \cdot \left(\left[\frac{V_H^2}{4} (1 - \cos 2\omega_H t) \right] + \frac{V_L^2}{4} (1 - \cos 2\omega_L t) \right. \\ & + \left\{ \frac{V_H V_L}{2} \cos(\omega_H - \omega_L) t - \frac{V_H V_L}{2} \cos(\omega_H + \omega_L) t \right\} \right) \\ & + \dots \end{aligned} \quad (5)$$

If no low-frequency perturbation signal is provided (i. e., $V_L = 0$), then the terms in curly brackets $\{ \}$ in Eq. (5) disappear, along with the terms in ω_L and $2\omega_L$. The terms in square brackets $[\]$ may be detected by an amplifier tuned to detect only signals at frequency $2\omega_H$. By employing phase-sensitive detection, either dC/dV or dG/dV may be measured by this "second harmonic" technique (110-115). Unless phase-sensitive techniques are used, however, dC/dV can only be separated from dG/dV if $\omega_H dC/dV|_{V_0} \gg dG/dV|_{V_0}$. (If the desired signal is dG/dV , this inequality is reversed.) Note also that the presence of any second harmonic distortion in the signal at frequency ω_H will generate terms proportional to $C(V_0)$ and $G(V_0)$ in the output of a second harmonic detector. These limitations can be overcome by careful filtering in fixed frequency operation (111,112). The purity required of the first harmonic signal necessary to obtain accurate dC/dV and dG/dV measurements (second harmonic distortion better than -100 dB) makes this technique impractical for sweep-frequency operation. For this reason we have adopted the two-frequency intermodulation technique to be described next. This system is also employed by the plotter designed by Gordon et al. (116) and in a commercial plotter designed by the Royal Radar Establishment (117). The internal details of both of these systems differ significantly from the construction of our system.

In the two-frequency intermodulation technique low-level signals at two frequencies, ω_H and ω_L , are applied to the device under test as in Eq. (4). The resulting cross-product terms,

shown in curly brackets { } in Eq. (5) are detected by a series demodulation technique. This method does not require excitation signals of extreme harmonic purity. It does, however, require careful control of intermodulation in the signal source unit and in the detection circuitry.

In the system being described, the current passing through the diode under test (DUT) is converted into a voltage signal by a preamplifier unit. See Figure 70. Note that the DUT is connected to the inverting input of a high gain operational amplifier. Since the differential voltage between the inverting and non-inverting inputs of such an amplifier never exceeds 1 mV under typical conditions, the system ground can be used as a high quality DC and AC guard point. The connection of the preamplifier for measurements on ring-guarded diodes is indicated in Figure 70. For capacitance measurements the operational amplifier is used with capacitive feedback. Then

$$e_o = - \frac{1}{C_f} \int I \, dt, \quad (6)$$

where e_o is the output voltage of the operational amplifier and C_f is the feedback capacitor. The signal is then sent through a high-pass filter to remove frequencies of the order of ω_L . In the actual preamp the integrator and high-pass filter are contained in a single unit.

The resultant preamplifier output, e_p , is given by

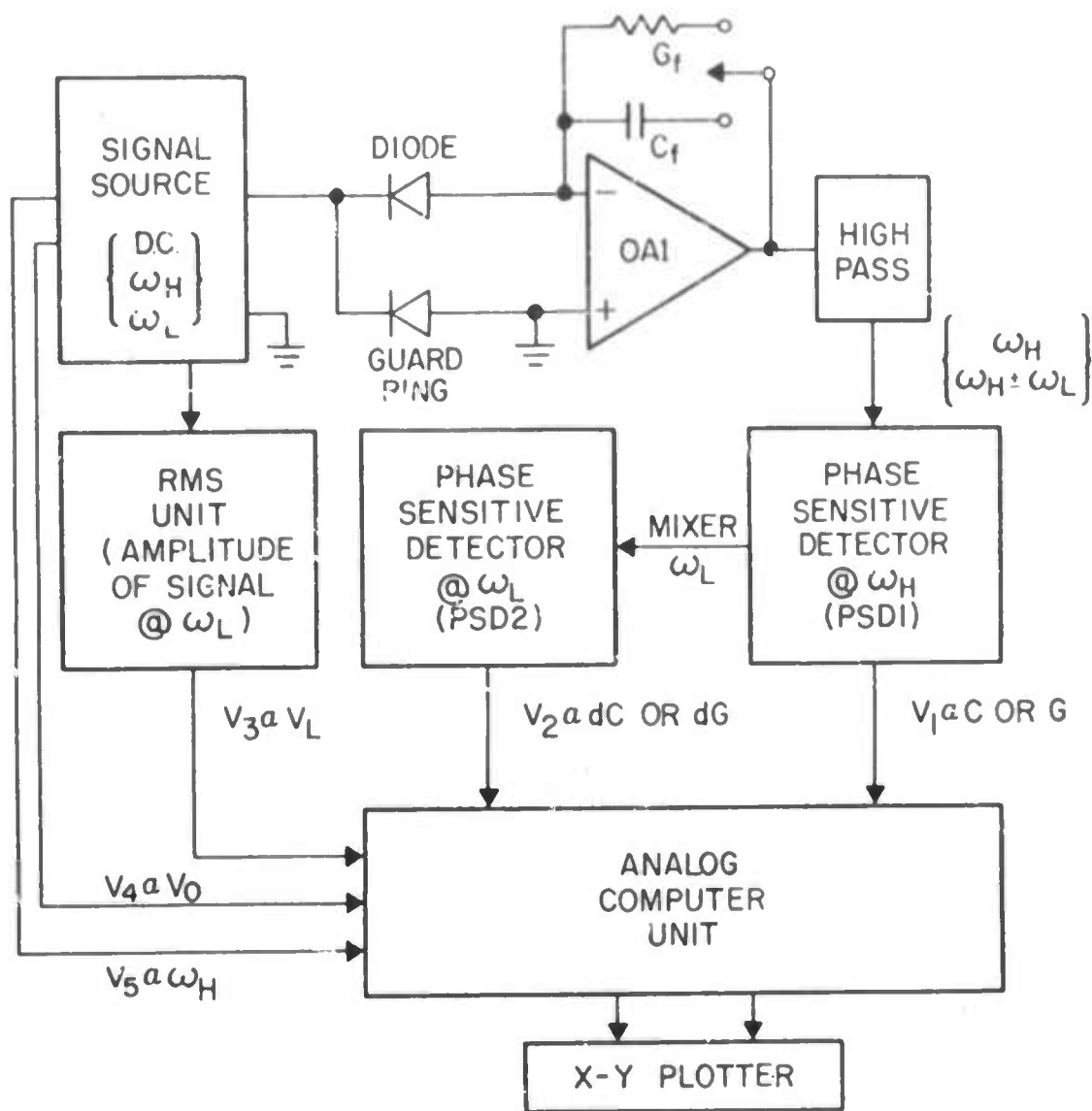


Figure 70. Block diagram of the variable-frequency automatic capacitance/conductance measurement system as connected for the experimental studies on ring-guarded diodes.

$$\begin{aligned}
 e_p = & - \frac{C(V_o)}{C_f} \cdot V_H \sin \omega_H t \\
 & + \frac{\left. \frac{dC}{dV} \right|_{V_o}}{C_f} \cdot \left(\frac{V_H^2}{4} \cos 2\omega_H t + \frac{V_H V_L}{2} \cos(\omega_H + \omega_L) t \right. \\
 & \quad \left. - \frac{V_H V_L}{2} \cos(\omega_H - \omega_L) t \right) + \dots \\
 & + \frac{G(V_o)}{\omega_H C_f} V_H \cos \omega_H t \\
 & + \frac{\left. \frac{dG}{dV} \right|_{V_o}}{C_f} \cdot \left(\frac{V_H^2}{8\omega_H} \sin 2\omega_H t + \frac{V_H V_L}{2(\omega_H + \omega_L)} \sin(\omega_H + \omega_L) t \right. \\
 & \quad \left. - \frac{V_H V_L}{2(\omega_H - \omega_L)} \sin(\omega_H - \omega_L) t \right) + \dots
 \end{aligned} \tag{7}$$

The frequency-tracking phase-sensitive detector, PSD1, (Princeton Applied Research Model 124L) demodulates the preamplifier output by multiplying it with a high-frequency sine wave signal $e_1 = \sin(\omega_H t + \varphi_1)$ where φ_1 is a high-frequency reference phase error. (The phase-sensitive detectors actually employed use square wave demodulation signals. If we use low level modulation signals, only the first Fourier component of the square wave need be retained, however, since the higher harmonics do not produce any significant low-frequency signals in the demodulator output.) Retaining only the low-frequency terms, the output of the demodulator, e_{d1} , is given by

$$\begin{aligned}
 e_{d1} = & \frac{V_H}{2} \left(-\frac{C(V_o)}{C_f} \cos \varphi_1 + \frac{G(V_o)}{\omega_H C_f} \sin \varphi_1 \right) \\
 & + \frac{V_H V_L}{2} \left[-\frac{\left. \frac{dC}{dV} \right|_{V_c}}{C_f} \cdot \sin \omega_L t \cos \varphi_1 \right. \\
 & + \frac{\left. \frac{dG}{dV} \right|_{V_o}}{C_f} \left(-\frac{\omega_L}{(\omega_H^2 - \omega_L^2)} \cos \omega_L t \cos \varphi_1 \right. \\
 & \left. \left. + \frac{\omega_H}{(\omega_H^2 - \omega_L^2)} \sin \omega_L t \sin \varphi_1 \right) \right] . \quad (8)
 \end{aligned}$$

The DC component of the demodulator output is amplified in the remainder of PSD1, giving an output voltage, V_1 :

$$V_1 = -A_1 \frac{V_H}{2C_f} \left(C(V_o) \cos \varphi_1 - \frac{G(V_o)}{\omega_H} \sin \varphi_1 \right) \quad (9)$$

where A_1 is the gain of PSD1. For perfect phasing ($\varphi_1 = 0$), V_1 is proportional to $C(V_o)$.

The demodulator output is also connected to a second phase-sensitive detector, PSD2, (Princeton Applied Research Model HR-8) where it is further demodulated by mixing with a low-frequency sine wave signal $e_2 = \sin(\omega_L t + \varphi_2)$, where φ_2 is a low-frequency reference phase error. The resultant signal is further DC amplified, giving an output signal, V_2 .

$$V_2 = A_2 \frac{V_H V_L}{4C_f} \cdot \left[- \frac{dC}{dV} \Big|_{V_0} \cdot \cos \varphi_1 \cos \varphi_2 + \frac{1}{\omega_H} \frac{dG}{dV} \Big|_{V_0} \cdot \left(\frac{\omega_H^2}{(\omega_H^2 - \omega_L^2)} \cos \varphi_1 \sin \varphi_2 - \frac{\omega_H \omega_L}{(\omega_H^2 - \omega_L^2)} \cos \varphi_1 \sin \varphi_2 \right) \right] \quad (10)$$

where A_2 is the gain of PSD2. For perfect phasing of both detectors V_2 is proportional to $dC/dV|_{V_0}$.

For conductance measurements the operational amplifier is used with resistive feedback. Then

$$e_0 = - \frac{1}{G_f} \quad (11)$$

where G_f is the conductance of the feedback resistor. Under these conditions the outputs corresponding to equations (9) and (10) are

$$V_1 = -A_1 \frac{V_H}{2G_f} \left(G(V_0) \cos \varphi_1 + \omega_H C(V_0) \sin \varphi_1 \right) \quad (12)$$

and

$$V_2 = -A_2 \frac{V_H V_L}{4G_f} \left[\frac{dG}{dV} \Big|_{V_0} \cdot \cos \varphi_1 \cos \varphi_2 + \frac{dC}{dV} \Big|_{V_0} \cdot (\omega_L \cos \varphi_1 \sin \varphi_2 - \omega_H \sin \varphi_1 \cos \varphi_2) \right] \quad (13)$$

Equations (9), (10), (11), and (12) determine the sensitivity of the system to reference phase errors. For a diode quality factor, $Q(\omega)$, equal to 1 ($\omega_H C(V_0) = G(V_0)$), measurement of $C(V_0)$ or $G(V_0)$ to 1 percent accuracy requires $\varphi_1 \leq 0.5^\circ$. Thus PSD1 must be phased carefully to obtain accurate capacitance measurements from lossy devices. Similarly, PSD1 must be phased carefully to obtain accurate conductance measurements from devices which exhibit high values of $Q(\omega)$ [$\omega_H C(V_0) \gg G(V_0)$].

The coefficient of the term in $\sin\varphi_1 \cos\varphi_2$ in Eqs. (10) and (12) is larger than the term in $\cos\varphi_1 \sin\varphi_2$ by a factor of about ω_H/ω_L , which is typically greater than one hundred. The term in $\sin\varphi_1 \cos\varphi_2$ can be eliminated by perfect phasing of PSD1. Thus the phasing of PSD1 is far more critical than the phasing of PSD2.

As indicated in the previous discussion, the basic signals provided by the detection system are DC outputs proportional to C , dC/dV , G , and dG/dV . In addition, a number of other DC signals are available for use as data (e.g., the DC bias voltage, V_0 ; the output of the RMS unit, $V_3 = 2.5 \sqrt{2} V_L$; and the voltage, V_5 , which is proportional to ω_H). The wide variety of combinations of these signals required in the various uses of the unit virtually precludes the use of a hard-wired, switchable analog computer unit for data reduction. Accordingly, we employ an analog computer unit consisting of a number of modular "building blocks" interconnected by a 25 x 25 matrix pinboard. The basic building blocks used are of two types: logarithmic amplifiers and operational amplifiers. The logarithmic amplifiers (Philbrick 4350 and 4351) can be used either as logarithmic

amplifiers (with gains of 2/3, 1, or 2 volts per decade) or as anti-logarithmic amplifiers (with gains of 1.5, 1, or 0.5 decades per volt). Both the gains and functions of these units are selected by the pinboard. By appropriate interconnections, therefore, logarithmic, exponential, or power law functions of any of the DC input signals can be generated. The operational amplifiers (Fairchild 741C or equivalent) have uncommitted outputs and inverting inputs controlled by the pinboard.

As an example of the use of the analog computer unit, Figure 71 indicates the connection of the analog computer unit to generate the logarithm of the "impurity profile" of an abrupt p-n junction or a Schottky barrier given by (118-121)

$$N(x_d) = - \left(q \epsilon_s S^2 \right)^{-1} \frac{C^3}{dV} \quad (14)$$

where

$$x_d = \frac{\epsilon_s S}{C} \quad (15)$$

and S is the area of the device.

Note that the output voltages in Figure 71 are labeled " $\log_{10} (N(x)/N_{ref})$ " and " $\log x$ ". Because of the number of variables involved (sensitivity settings of the phase-sensitive detectors, size of feedback capacitor, device area, semiconductor dielectric constant) and the wide range of values exhibited by some of these variables, it is much simpler (and probably more accurate) to calibrate the X-Y plotter

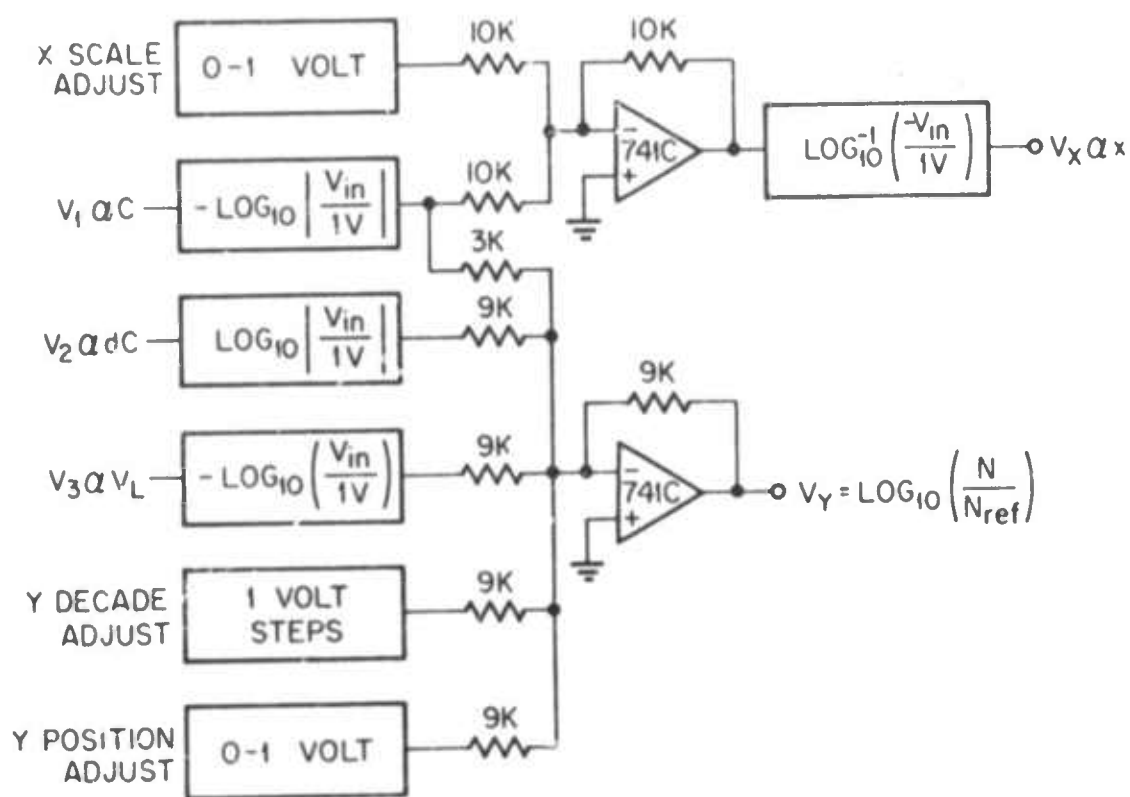


Figure 71. Connection of the analog computer unit for $\log_{10}(N(x))$ versus x output format.

input signals indirectly than to provide a sufficient number of switches and verniers to allow dialing in all the necessary independent variables. We therefore employ an indirect calibration technique to handle the DC portion of the logic. In this technique a calibration signal is injected into the preamplifier unit through one of a number of calibration elements. To calibrate the system for the measurement of capacitance, standard capacitors, C_s , are used as calibration elements. Standard resistors are used for conductance calibration. See the following section for a complete description of the preamplifier unit used for capacitance measurements. In normal operation, the amplitude of the high-frequency signal is 10 mV RMS. To calibrate the system for the measurement of C or G, the calibration signal is simply this 10 mV RMS signal. The resultant DC output from PSD1 therefore represents an admittance equal to the admittance of the calibration element selected, Y_s . The phase of PSD1 and the gains of the X-Y plotter can then be adjusted appropriately. To calibrate the system for measurements requiring simultaneous determination of C and dC/dV or G and dG/dV , an amplitude modulated sine wave of the form

$$(V - V_0) = 10 \sin \omega_H t \cdot (1 + M \sin \omega_L t) \text{ mV RMS} \quad (16)$$

is injected into the calibration element. Such a signal is readily available from the Wavetek model 136 used as the high-frequency oscillator. If the internal gains of PSD1 and PSD2 are known, M can be read directly on PSD2. Since both Y_s and M are known, M can be

directly related to device parameters. For example, M equal to unity is equivalent to a change of admittance equal to Y_s for a change in voltage equal to the amplitude of the low-frequency signal, V_L . Thus the calibration signal simulates a device with admittance Y_s and admittance derivative

$$\frac{dY}{dV} = M \frac{Y_C}{V_L} = \frac{5M Y_s}{\sqrt{2} V_3} \quad (17)$$

where V_3 is the output of the RMS unit. The signal appearing on the X-Y plotter is therefore identical to the response of the system to a device with the parameters given above. The system can therefore be calibrated as though an actual device were being measured.

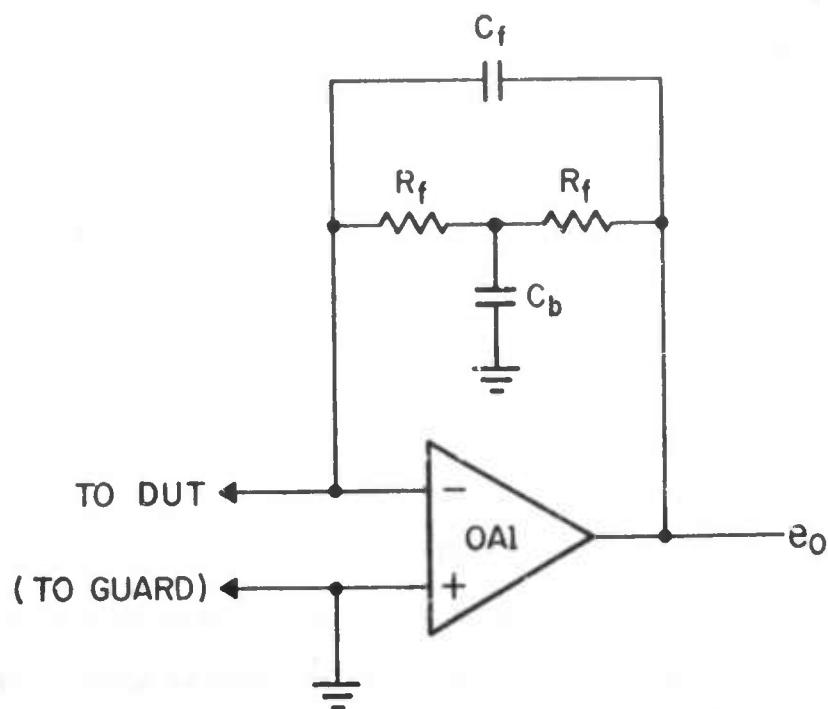
Additional calibration points can be provided by changing the calibration element or by applying voltage changes of known amplitude at the inputs of the elements of the analog computer or the X-Y plotter. An example of such a calibration voltage is the source marked "Y DECADE ADJUST" in Figure 26. As shown in Figure 71, a one volt change in the value of V_Y corresponds to a one decade change in N . Application of an incremental one volt signal from the source marked "Y DECADE ADJUST" therefore simulates a one decade change in N . Thus this source may be used as a calibration source to help adjust the gain of the Y axis of the X-Y plotter so that a one volt increment in V_Y will cause the pen on the X-Y recorder to move exactly one decade on a piece of semi-logarithmic graph paper.

c. Internal Design of the Variable-Frequency Automatic Capacitance/Conductance Measurement System

This section presents a detailed description of the internal operation of the variable-frequency automatic capacitance/conductance measurement system introduced in the preceding section. The design of the preamplifier unit used for the measurement of capacitance is discussed first. Finally the operation of the signal source unit is covered.

1: Capacitive-Feedback Preamplifier

A preamplifier for determination of the capacitance or conductance of devices with finite leakage current must be able to sink this leakage current. Thus some sort of resistive feedback or DC bypassing is necessary. Resistive feedback alone is sufficient to allow broadband determination of device conductance without the need for frequency-dependent corrections. Broadband capacitance measurements, however, are considerably simplified if the preamplifier unit exhibits essentially pure capacitive feedback with minimal phase shift over a wide frequency range. The bridged T feedback circuit illustrated in Figure 72 satisfies both these criteria. The resistors R_f provide DC feedback but are effectively removed from the feedback



$$\omega_0^2 = \frac{1}{R_f^2 C_b C_f}$$

$$\gamma = \frac{C_b}{4C_f}$$

Figure 72. Bridged-T preamplifier for frequency-independent measurement of capacitance.

loop by the tie-down capacitor C_b at high frequencies. The voltage gain $A(\omega)$ ($\equiv e_o/e_i$ where e_o is the output voltage of the preamplifier and e_i is the voltage applied to the input element) for an input element with admittance Y is given by

$$A(\omega) = - \frac{Y}{j\omega C_f} \cdot \frac{\omega^2 - (j\omega/\tau_B)}{(\omega^2 - \omega_o^2) - (j\omega/\tau_B)} \quad (18)$$

where

$$\tau_B = \frac{R_f C_b}{2} \quad \text{and} \quad \omega_o = \frac{1}{R_f^2 C_b C_f} \quad (19)$$

If ω_o is comparable to or greater than $1/\tau_B$, then for ω greater than a few ω_o , the preamplifier exhibits essentially pure capacitive feedback, i. e.,

$$A(\omega) = - \frac{Y}{j\omega C_f} \quad (20)$$

Values of the feedback elements are dictated both by device characteristics and by the immediate purpose for which the preamplifier is being used. The value of the resistors, R_f , is restricted by the maximum DC output voltage of the operational amplifier, V_{\max} , and the maximum DC leakage current of the device under test,

I_{\max} :

$$R_f < \frac{V_{\max}}{2I_{\max}} \quad (21)$$

The maximum value of the feedback capacitor, C_f , is determined in practice by the tolerance of the operational amplifier for capacitive loading. Values of R_f provided in the actual system range from 10^4 to 2×10^7 ohms. Values of C_f range from 5 to 1000 picofarads.

For a particular choice of R_f and C_f , the ratio of C_b to C_f is an important circuit parameter. Figures 73, 74, and 75 illustrate the gain and phase response of the circuit of Figure 72 for three values of a parameter $\gamma \equiv C_b/4C_f$ when a capacitor equal to C_f is used as an input element. From Figures 73, 74, and 75 it is quite apparent that increasing γ has little effect on the magnitude of A for frequencies above $3\omega_0$, but significantly improves the phase shift characteristic in this range. Additionally, an increase in γ may be used to lower ω_0 for low frequency measurements. The major disadvantage of operation with large γ is amplifier instability. For a pure capacitive input element, the response of the preamplifier to a unit step applied to the input element is given by

$$e_o = - \frac{C_{in}}{C_f} e^{-(t/2\tau_B)} \left[\cos \frac{\sqrt{4\gamma-1}}{2\tau_B} t + \sqrt{4\gamma-1} \sin \frac{\sqrt{4\gamma-1}}{2\tau_B} t \right] \quad (22)$$

where C_{in} is the input capacitance and $\gamma > 0.25$.

For $\gamma \gg 1$,

$$e_o \approx - \frac{C_{in}}{C_f} \exp - \frac{\omega_0 t}{2\gamma^2} \cdot \left(\cos \omega_0 t + \frac{1}{2\gamma^2} \sin \omega_0 t \right). \quad (23)$$

Note that large values of γ have relatively little effect on the amplitude of the output oscillations but significantly reduce the damping

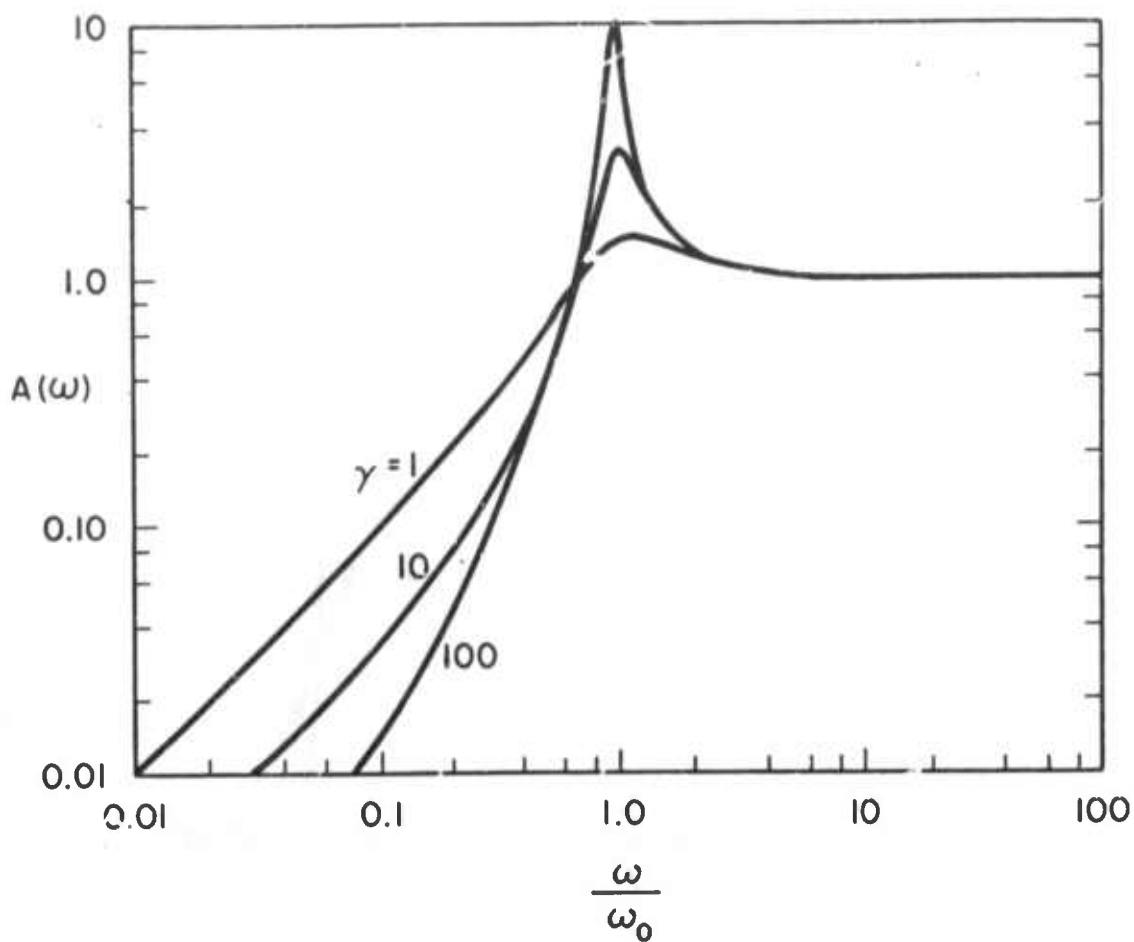


Figure 73. Gain of the bridged-T preamplifier as a function of frequency when a capacitor equal to C_f is used as an input element.

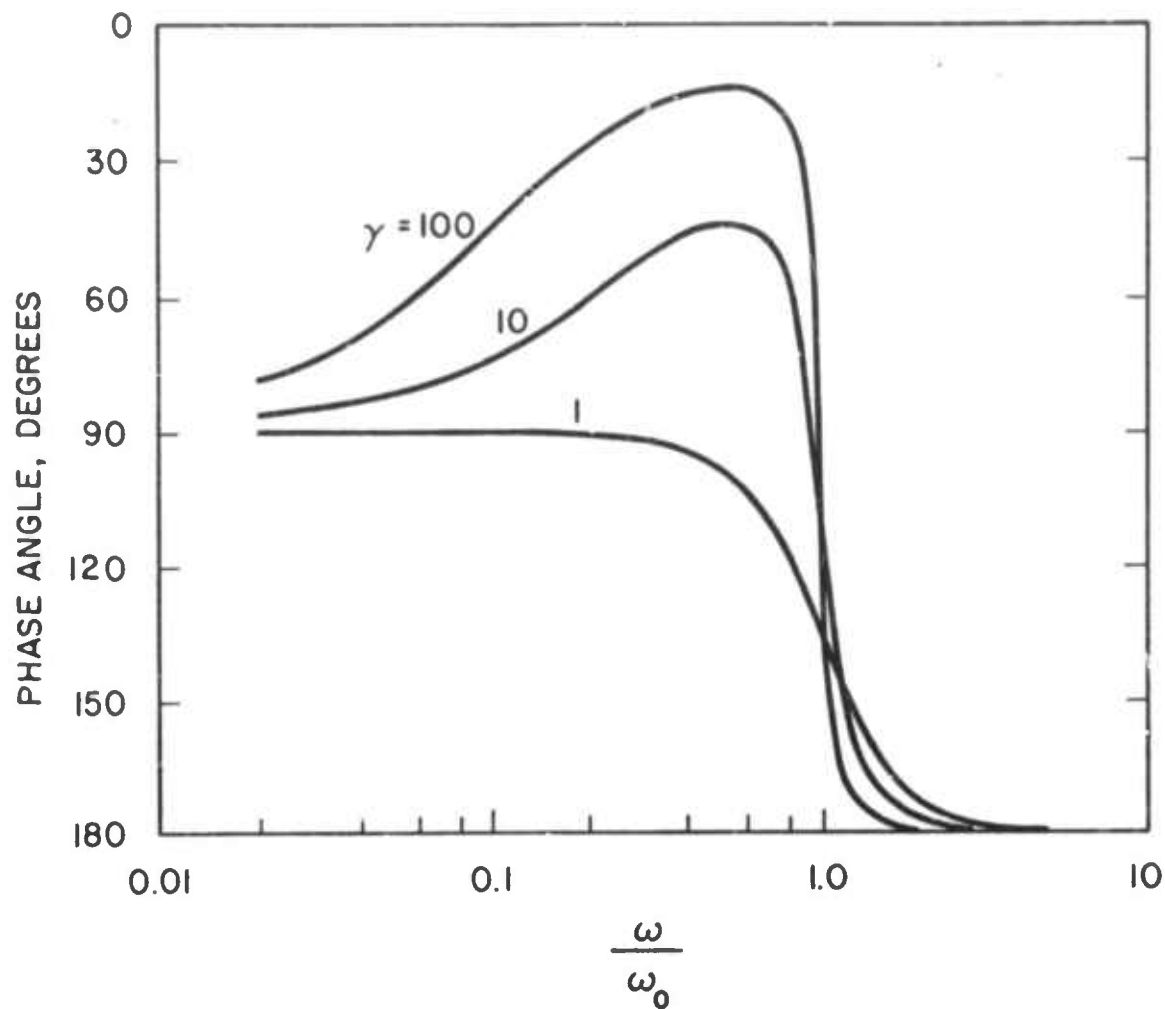


Figure 74. Phase shift between e_o and e_i for the bridged-T preamplifier when a capacitor is used as an input element.

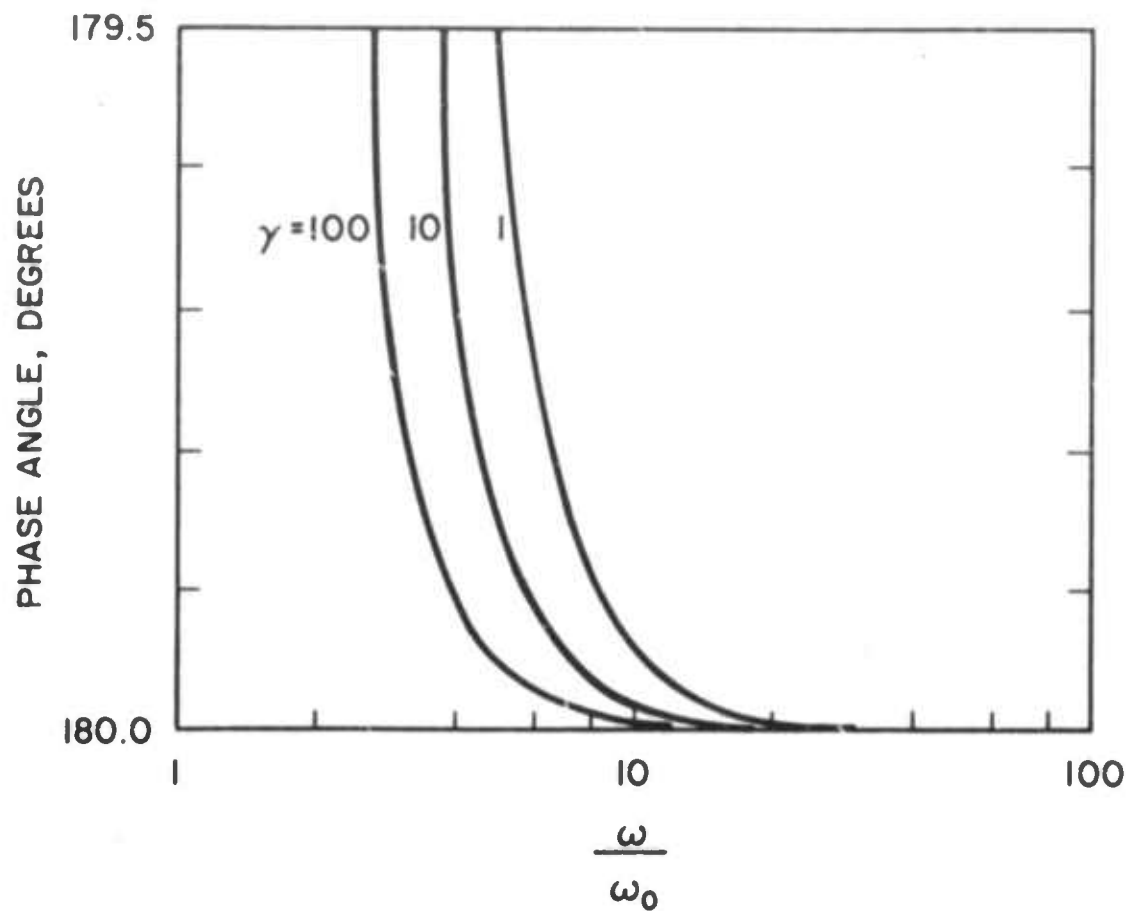


Figure 75. Expanded plot of the phase shift between e_o and e_i for the bridged-T preamplifier when a capacitor is used as an input element.

factor. An oscillation, once started, takes $\gamma^{1/2}/\pi$ cycles to decay by a factor of $1/e$. We have found $\gamma = 100$ affords sufficient stability for most purposes.

For calibration purposes it is desirable to provide a number of standard capacitances, C_s , at the input of the preamplifier. In addition, it is desirable to be able to change R_f and C_f independently while maintaining a constant value of γ . These features have been included in the preamplifier unit used in the actual system. The actual circuit employed is shown in Figure 76.

For broadband capacitance measurements it is frequently desirable to have ω_0 as low as possible. In impurity profiling using the two-frequency technique, however, an occasional device exhibits such a small derivative of capacitance with respect to voltage that if both the high- and low-frequency signals were allowed to pass through the preamplifier unattenuated, the very small intermodulation distortion in the phase-sensitive detectors would generate a cross-product signal comparable to that generated by the device. Therefore, for impurity profiling we exploit the high-pass character of the preamplifier response by placing the characteristic frequency of the preamplifier at approximately the geometric mean of the high and low frequencies. Under typical conditions ($\omega_H = 100$ kHz, $\omega_L = 100$ Hz, $\omega_0 = 3$ kHz, $\gamma = 100$) this technique reduces the intermodulation by more than 40 dB.

2: Signal Source Unit

As indicated by the discussion in section b, the signal source unit must be able to present a combination of DC bias,

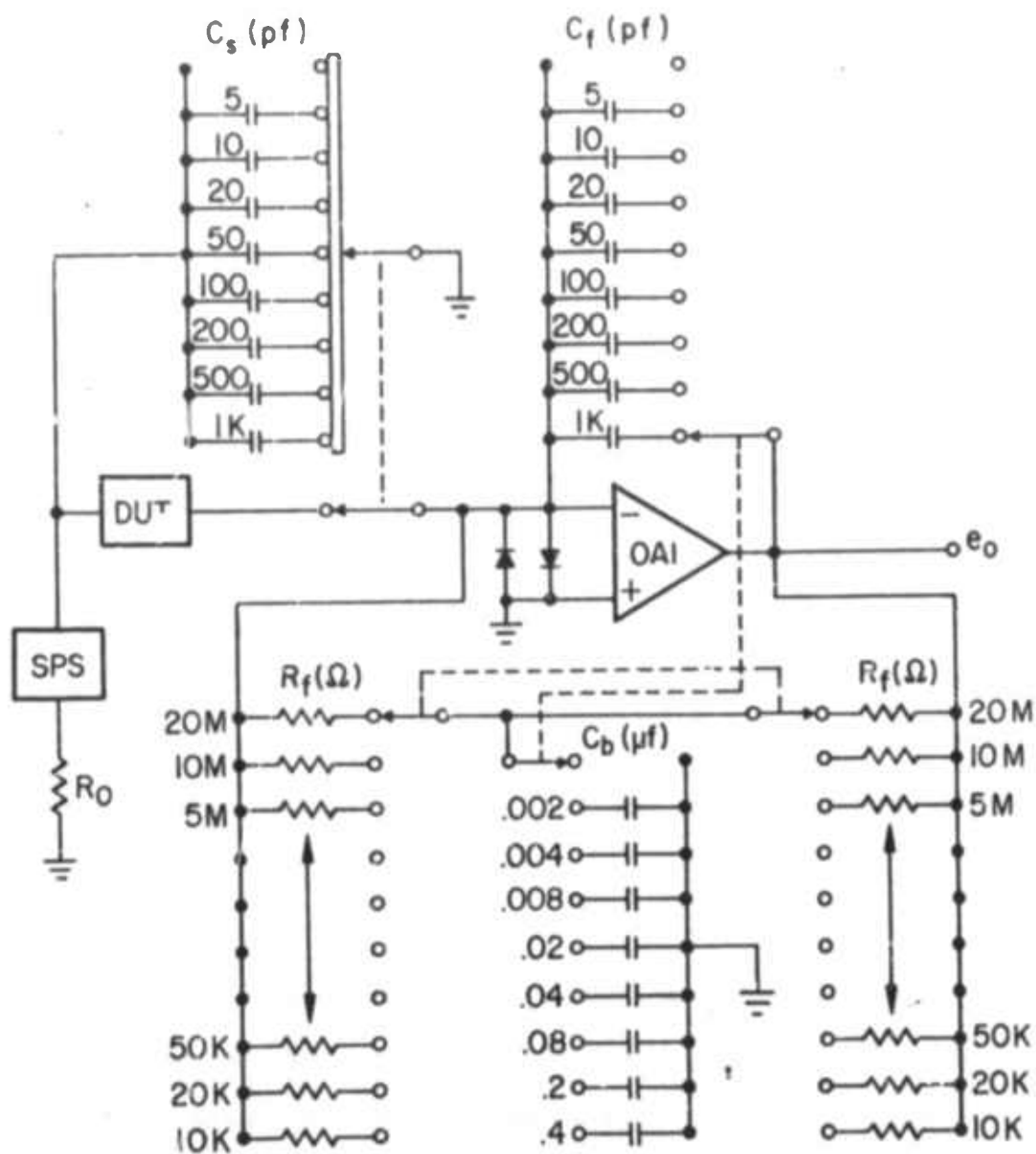


Figure 76. Detailed schematic of the bridged-T preamplifier unit.

high-frequency (up to 200 kHz) and low-frequency (up to 2 kHz) signals simultaneously to the device under test. The DC bias level must be able to be swept to allow automatic C-V, G-V, and impurity profile measurements. The high frequency must be programmable to permit automatic C- ω and G- ω measurements. Calibration of the unit (discussed in section b.) requires that the unit provide a high-frequency signal amplitude modulated at a low frequency. The combination of the disparity between the amplitudes of the DC bias (up to 250 V) and the AC signals (10 mV to 1 V RMS) with the distortion requirements to be discussed later in this section virtually eliminates the possibility of providing the complete signal with a single amplifier. For these reasons, we have adopted the procedure of providing the DC, low-frequency, and high-frequency signals from separate sources and employ a summing technique to supply the composite signal.

DC Bias Sweep

The sweeping DC bias signal is provided by a commercial 0-250 V power supply (Lambda LS516A) modified as shown in Figure 77. The internal bias sources of the LS516A are used to power a FET input operational amplifier, OA1, (Analog Devices AD503J) wired as a voltage follower. The voltage follower reduces the input bias current of the feedback regulator of the LS516A to approximately 15 pA. Thus the output voltage of the LS516A is controlled entirely by the combination of resistors R1 to R10 and capacitors C₁ and C_e. In operation the switch, S2, is placed in the "SET" position and the highest voltage to be applied to the DUT is set by adjusting the output

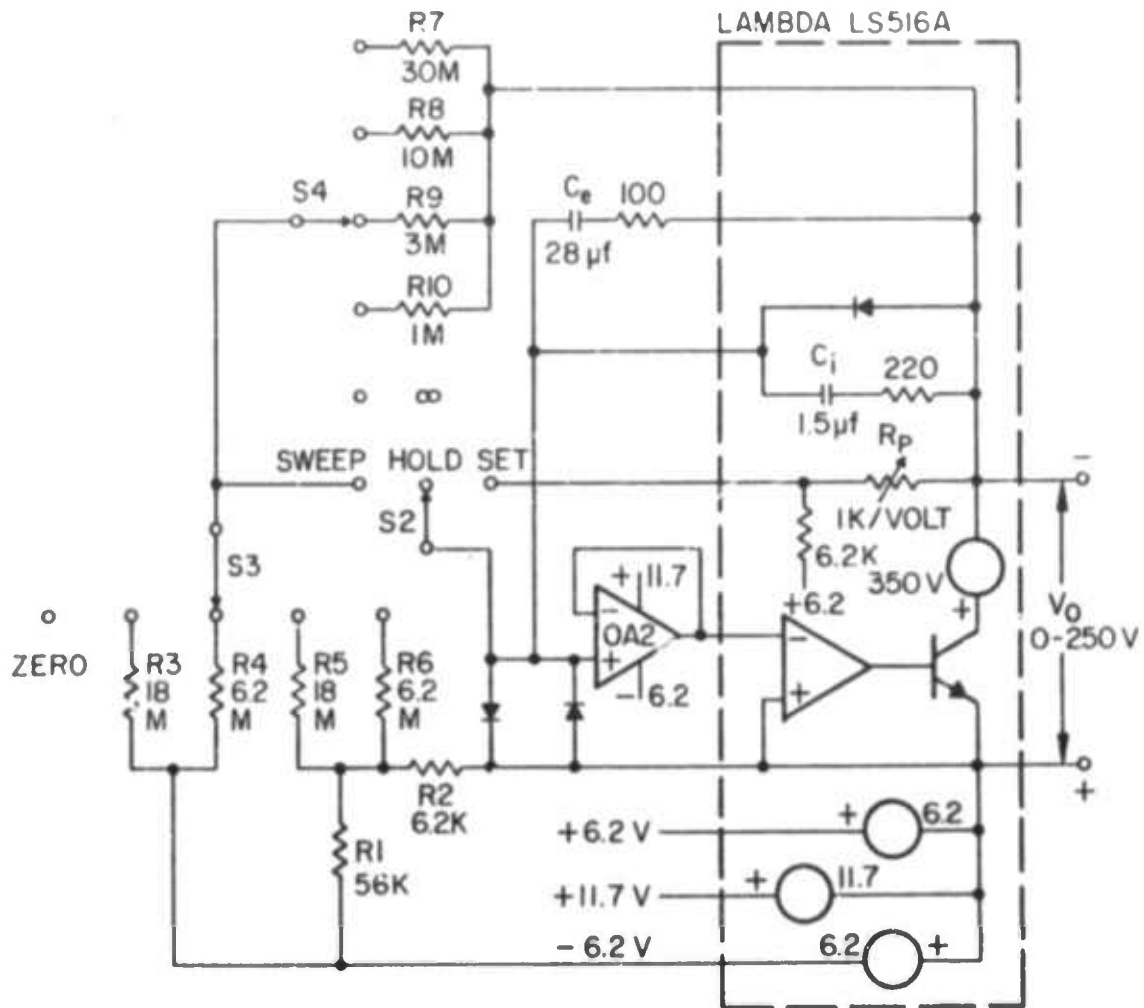


Figure 77. Detailed schematic of the DC bias sweep supply. All resistor values are in ohms.

voltage control, R_p , of the LS516A. S2 is then flipped to the "SWEEP" position and the voltage applied to the DUT begins to sweep. If S4 is set to the " ∞ " position and S3 is set to any position other than "ZERO", a linear sweep results. With the values of R1 to R6 shown, the linear sweep rate may be varied between .001 and .3 volts per second. The sweep terminates when the output voltage, V_o of the LS516A reaches a small negative voltage (about -0.3 volts). If S3 is set to the "ZERO" position and S4 is set to any position other than " ∞ ", a pure exponential sweep is produced and terminates when V_o reaches zero. With the values of R7 to R10 shown, the time constant of the exponential sweep may be varied between about 30 and 1000 seconds. If both S3 and S4 select finite resistors, the sweep is essentially exponential but terminates at a small negative voltage. Either S3 or S4 may be changed while the sweep is in progress without destroying the continuity of the sweep. The sweep may be terminated at any time by moving S2 to the "HOLD" position.

AC Modulation Limitations

The amplitudes of the high-frequency and low-frequency signals are constrained in many cases by basic device limitations. For an abrupt p-n junction or a Schottky barrier device, the relationship between the semiconductor band bending, V_D , and the depletion layer width, x_d , is given by

$$\frac{V_D}{(kT/q)} = \frac{x_d^2}{2L_D^2} \quad (24)$$

In this result the depletion approximation has been assumed. L_D , the

extrinsic Debye length, is given by

$$L_D = \sqrt{\frac{kT \epsilon_s}{q^2 N}} \quad (25)$$

ϵ_s is the semiconductor dielectric constant and N is the ionized impurity concentration. It is usually assumed that $N \gg n_i$, the intrinsic carrier concentration. If the band bending is changed by a small amount, ΔV , the depletion width will change by an amount

$$\frac{\Delta x_d}{L_D} = \frac{\Delta V}{\sqrt{2(kT/q)} V_D} \quad (26)$$

If $\Delta x_d/L_D < 1$, the resolution of the measurement will not be degraded. For many devices, a conservative estimate of the acceptable size of ΔV at zero bias can be obtained by assuming $\Delta x_d/L_D \leq 0.25$ (RMS) and $V_D = 0.5$ volts. Then at room temperature

$$\Delta V \leq 0.25 \sqrt{kT/q} \approx 40 \text{ mV RMS} \quad (27)$$

For $V \gg 1$ volt, $V_D \approx V$, and the corresponding result is

$$\Delta V \leq 0.25 \sqrt{2(kT/q) V} \approx 56 \sqrt{V_0} \text{ mV RMS} \quad (28)$$

Note that these results hold only for the case of a constant impurity concentration and are intended solely as guidelines.

In the two-frequency technique the total perturbation, ΔV , due to the high- and low-frequency signals should be held within the limits imposed by criteria such as Eqs. (27) and (28). In many devices, the capacitance, C , changes much less rapidly than dC/dV . For example, in an abrupt p-n junction or Schottky barrier device the capacitance is proportional to $V_D^{-1/2}$, whereas dC/dV is proportional to $V_D^{-3/2}$. Thus it is usually preferable to increase the size of the low-frequency perturbation signal faster than the high-frequency signal. On the basis of the above considerations we have adopted the following signal levels for use when operating in the two-frequency mode:

$V_H = 10$ mV RMS and

$$V_L = 20 \left(\frac{V_o + 5}{5} \right) \text{ mV RMS} \quad (29)$$

where V_o is in volts and is positive in reverse bias. The linear relationship, Eq. (29) was chosen to minimize circuit complexity. The total AC amplitude $\Delta V = \sqrt{V_H^2 + V_L^2}$ using these signal levels is less than the limitations given by Eqs. (27) and (28) for $V_o < 195$ volts and exceeds the limitation of Eq. (28) by about ten percent at $V_o = 250$ volts.

AC Summing Network

Because of the rapid variation of dC/dV relative to C exhibited by many devices and the fact that V_L is usually only a small fraction of a volt, the signal representing dC/dV in Eq. (5) is frequently smaller than the signal representing C by 40-60 dB. Since this signal appears as a modulation term at the input to the

first phase-sensitive detector, the circuitry preceding the first phase-sensitive detector must not intermodulate the high- and low-frequency signals by more than one part in 10^5 . In addition, the signal source unit must be able to drive cable, circuit, and device capacitances which may exceed 2000 pf. In light of the intermodulation limitations just described, use of a summing amplifier as an output element for the signal source unit is nearly impossible. For these reasons we have adopted a resistive summing technique, as shown in Figure 78. The modified LS516A DC power supply, SPS, floats on a 15 ohm AC summing resistor. The maximum AC excursion of the DC power supply is about 1 volt RMS. This technique was considered safer and more convenient than floating the oscillators and the associated circuitry. The operational amplifiers, OA3, OA4, OA5 (National LH0042C), and OA6 (Burr-Brown 3342/15C) in conjunction with the multiplier AM1 (Analog Devices AD426A) control of the amplitude of the low-frequency signal in accordance with Eq. (29). The switches, S5 and S6, change the polarity of the DC signal applied to the DUT and ensure that the low-frequency signal level increases in reverse bias and decreases in forward bias. An RMS unit (Intronics model R310) generates a DC signal equal to five times the RMS amplitude of the low-frequency signal.

The output resistor, R_o , is as small as the output capabilities of amplifier OA6 will allow. Without frequency compensation, however, R_o is not small enough that precise division ratios and constant phase shift can be maintained within acceptable limits under conditions of changing sample capacitance or a change in the length

ALL RESISTORS 0.01%

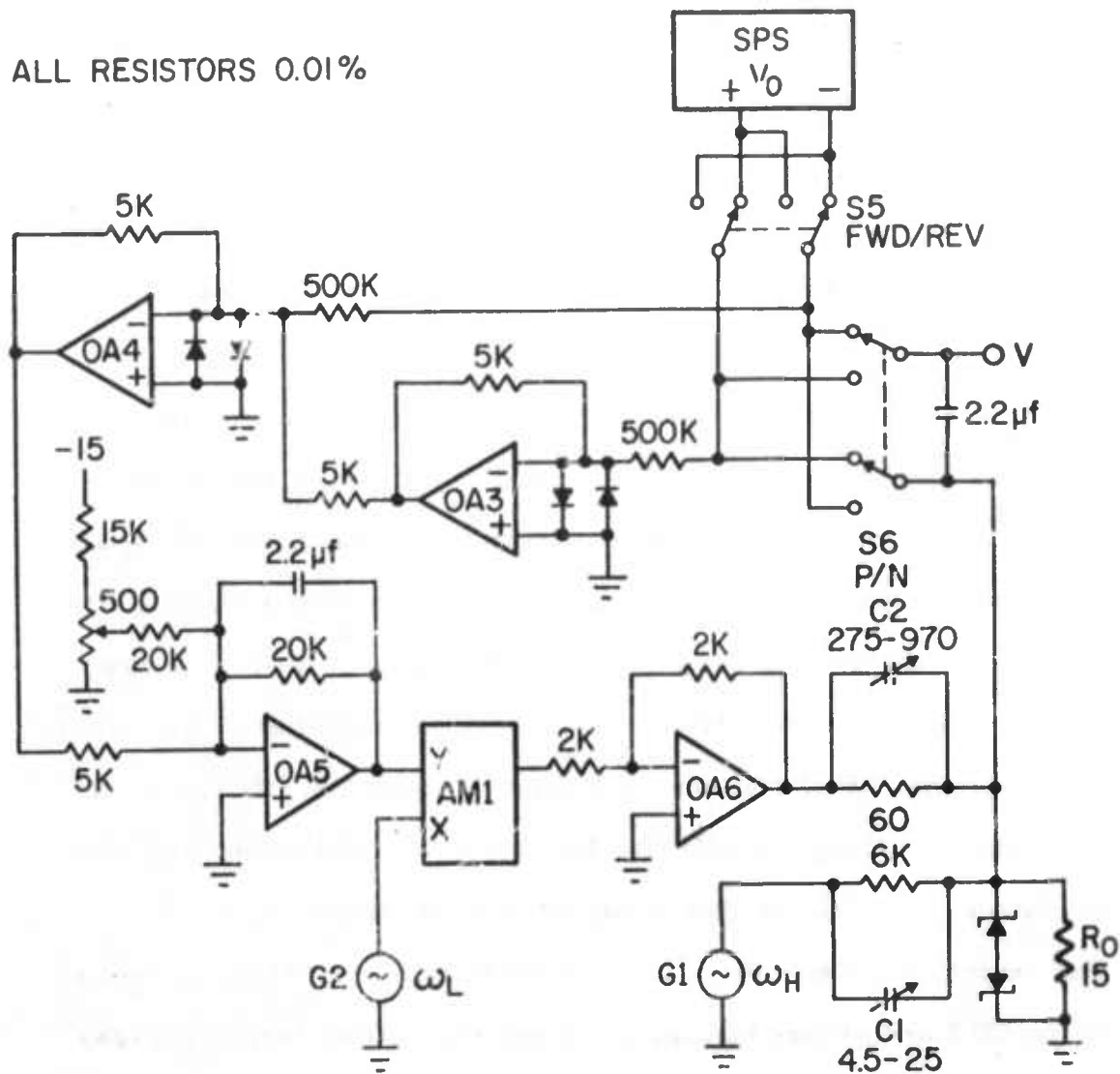


Figure 78. Detailed schematic of the signal source unit output section. All resistor values are in ohms.

of cable attached to R_o . For this reason we have taken precautions to maintain a large constant capacitive load on R_o and to frequency-compensate the summing network. As indicated in Figure 76, all the calibration elements of the preamplifier unit (approximately 2000 pf in parallel with 5 K ohms) plus the device under test appear to the signal source unit as loads to ground. In addition, the approximately 1000 pf of stray capacitance to ground of the LS516A power supply also loads R_o . Capacitors C1 and C2 are used for frequency compensation and are adjusted to produce accurate square wave outputs across R_o from high-frequency, square-wave signals generated by oscillators G1 and G2. When properly adjusted, the sensitivity of the summing network to changes in load is negligible in the vast majority of cases. For example, at the highest frequency of operation (200 kHz) a 600 pf change in the capacitive loading on R_o is necessary to produce an 0.5° phase shift of the signal source output relative to the output of G2. Thus the phase shift of the signal source is negligible for devices with capacitances of less than about 1000 pf or dynamic resistances greater than about 2500 ohms.

Changing the signal source unit from single-frequency to variable-frequency operation involves only minor modifications to the circuit configuration shown in Figure 78. For single-frequency operation the low-frequency oscillator, G1, is disconnected from M1 and the X input of M1 is grounded. The high-frequency oscillator, G2 (Wavetek model 136), has both VCG (FM) and VCA (AM) inputs. For sweep-frequency operation, the VCG input is driven by a 0-5 volt linear or exponential ramp. In this way a 100:1 frequency sweep is

produced. The frequency of oscillation of G2 is proportional to a control voltage equal to the instantaneous sum of the ramp voltage and a voltage dependent on the position of the frequency dial of the oscillator. This control voltage, V_5 , appears as a DC signal inside the Wavetek 136. An output terminal was provided to permit the use of V_5 as an indication of the instantaneous frequency of the oscillator during sweep-frequency operation.

c. Applications and Tests of the Analyzer System

The above analyzer as described above has now undergone considerable testing and calibration. Not included in the above description is a DC overload indicator for the preamp because the Bridged-T preamp circuit can be saturated by dc from the device under test without the PAR phase sensitive detector giving a clear indication of dc overload. Replacing the PAR 124 with a PAR 129 which has better frequency sweep capabilities and better phase orthogonality (with a slightly reduced frequency range) also provides improved performance. For impurity profiling the PAR 129 should be used for the high frequency detector and the PAR 124 for the low frequency detector. The following give some representative examples of use of the system.

Figure 79 shows a test of the system operated in the C- ω mode measuring a low loss fixed capacitor. The choice of R_f dictates the frequency range over which the system response is flat. Since the resistor R_g must pass the dc leakage current of the device under test, there is an obvious tradeoff between bandwidth and dc leakage current. Low leakage devices can, however, be examined down to 2 Hz with flat frequency response. The orthogonality between real and imaginary components of the capacitance is also excellent. The data shown here were taken both point-by-point and by scanning with a single phase adjustment made at 20 kHz. (C_1 was essentially zero on this scale of sensitivity.) This PAR 124 tracked to within $\pm 1^\circ$ over this frequency range. Much better precision at a single frequency is possible.

The phase error in profiling applications can be very serious as shown by the results in Figure 80. Here C^{-2} -V is shown for a Hf-p type Si Schottky barrier at 10 kHz and 300°K. This diode exhibits a maximum Q factor of the order of unity because of the low barrier height (≈ 0.6 eV). Note that with a phase error as little as $\pm 1^\circ$ that the slope of the $1/C^2$ vs. V plot (which is proportional to the inverse of the apparent doping concentration) changes

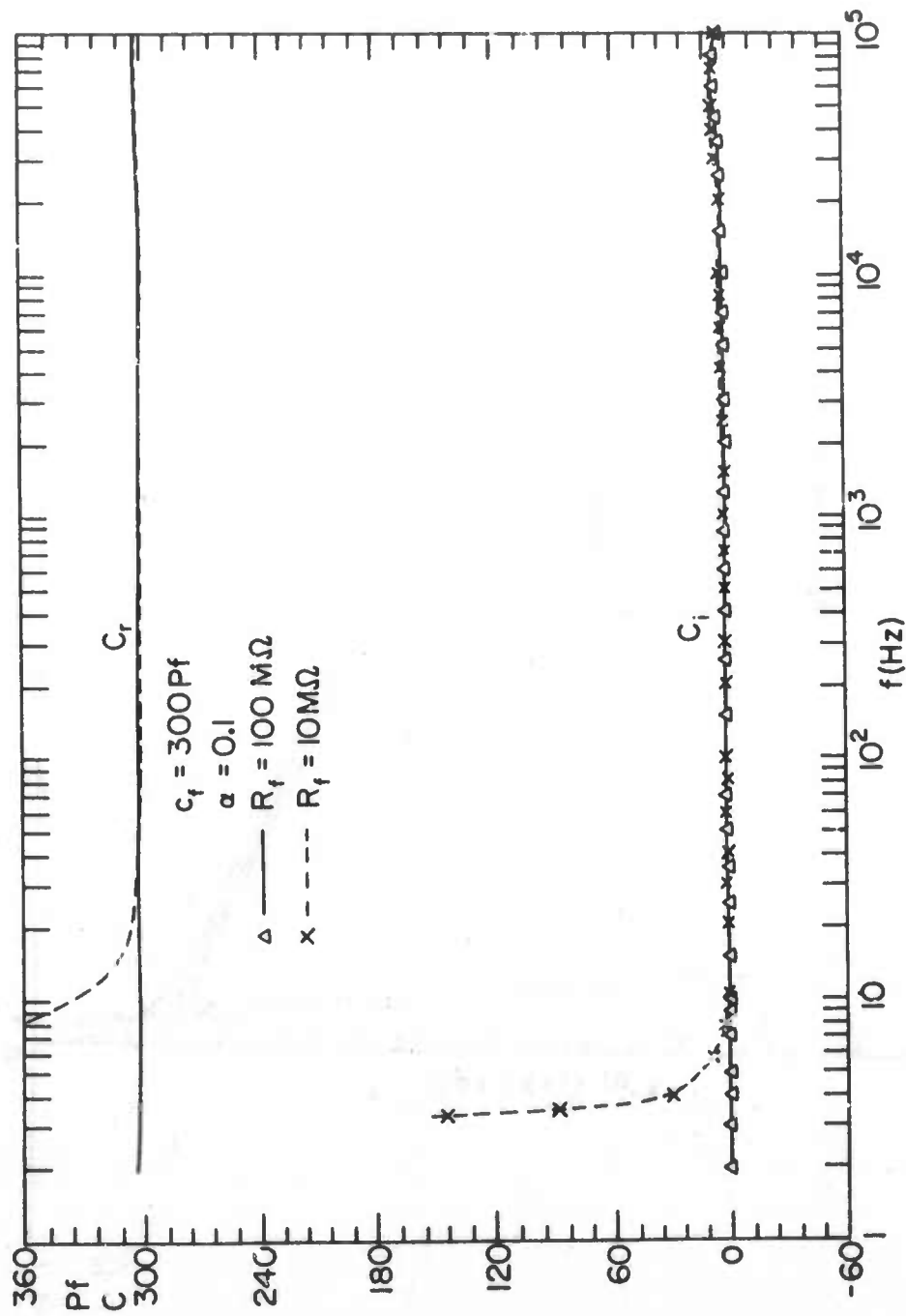


Figure 79.

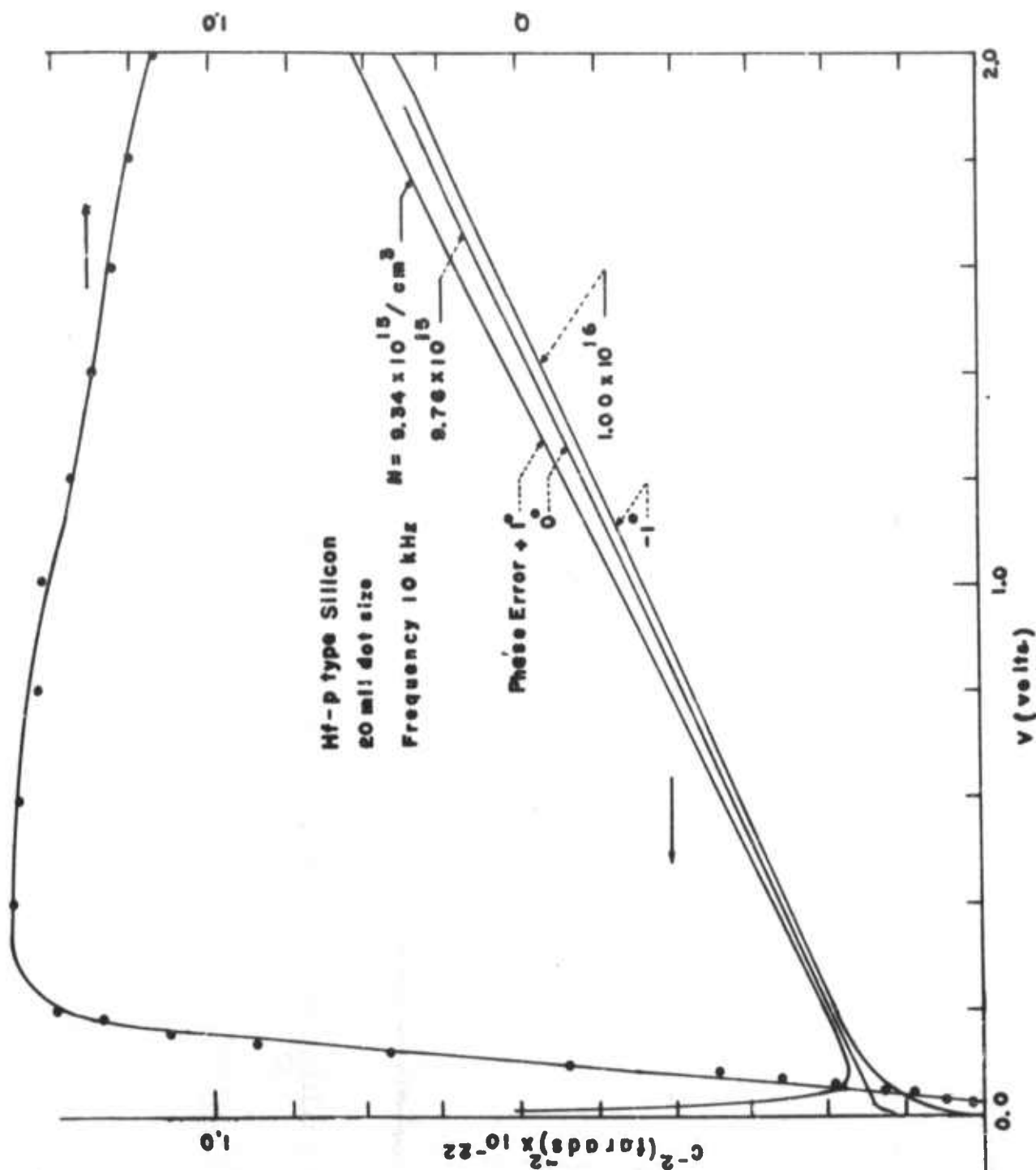


Figure 80. Capacitance-voltage measurements for Si Schottky diode at 10 kHz.

drastically when the diode Q falls below unity, but that proper phase adjustment allows profiling to be done with diode Q values well below 0.1.

The profiler operates very well. The accompanying Figure 81 shows a $4.5 \mu\text{m}$ epitaxial Si layer grown by the Hughes Research Laboratories, Malibu, Calif. Note that three orders of magnitude of doping can be covered without recalibration of the system. The diode used for this measurement was sufficiently leaky that the Stover profiler could only measure over a single decade of doping and the value of the doping appeared to be in error.

Figure 82 shows analogous results for a step etched epitaxial GaAs wafer.

In a recent paper (122) we determined quantum-mechanical electron transmission probabilities by numerical integration of the Schrodinger equation for a Schottky barrier model which includes Thomas-Fermi shielding in the metal, image force lowering in the semiconductor, and conservation of transverse $\langle 111 \rangle$ n-type Si and n-type GaAs (Figure 83). In the case of Si, conservation of transverse momentum at the interface produces a discontinuity in the electron kinetic energy associated with momentum normal to the interface. Using these results, the difference between the true barrier height, $q\phi_B$, and the apparent barrier height, $q\phi_A$, was calculated as a function of temperature, doping, and electric field at the metal-semiconductor interface. $q\phi_A$ is defined as the intercept on the $h\nu$ axis of the slope of a plot of (photocurrent per absorbed photon) $^{1/2}$ versus quantum energy, $h\nu$. Doping effects are negligible for impurity densities below about 10^{18} cm^{-3} for Si and 10^{17} cm^{-3} for GaAs. Values of $q(\phi_B - \phi_A)$ approaching 50 meV occur in many cases. The corrections derived are used to reinterpret previously reported measurements of the dependence of Schottky barrier height on temperature and impurity concentration. A normalized treatment of the purely thermal effects on the apparent photothreshold has also been published (Appendix S).

VII. CONCLUSIONS, DISCUSSION AND RECOMMENDATIONS ON GALLIUM ARSENIDE GROWTH AND CHARACTERIZATION

The following comments are based on the judgement of the principal investigator. Some, if not all, would be disputed by at least one member of the project team. The comments will be confined to techniques for growth and characterization of GaAs.

Our information is that bulk GaAs single crystals are being grown commercially primarily by the horizontal Bridgman technique and by liquid-encapsulated Czochralski growth. In our judgement, the Bridgman technique is superior because it is a one-step process not requiring pre-reacted GaAs and because it is

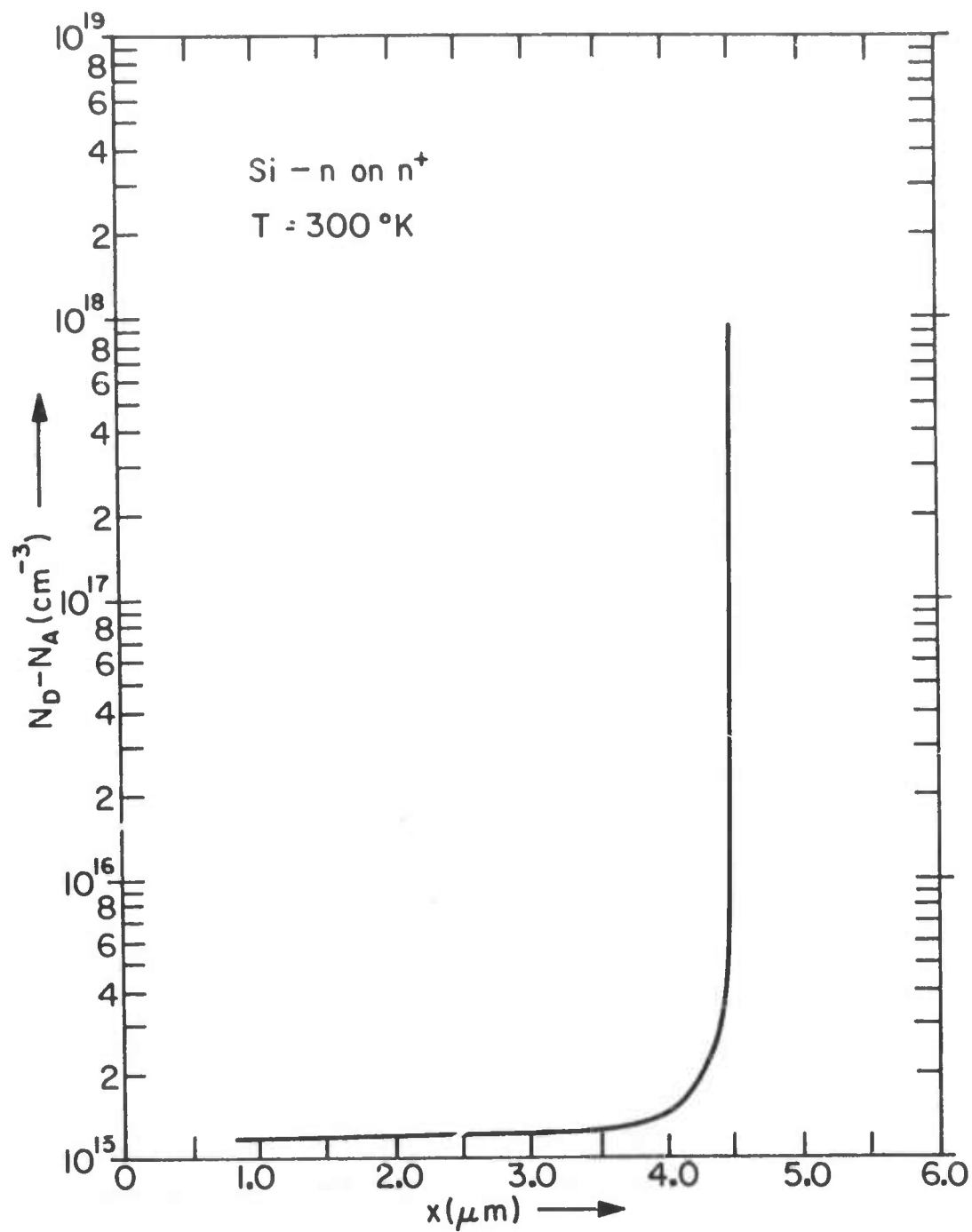


Figure 81.

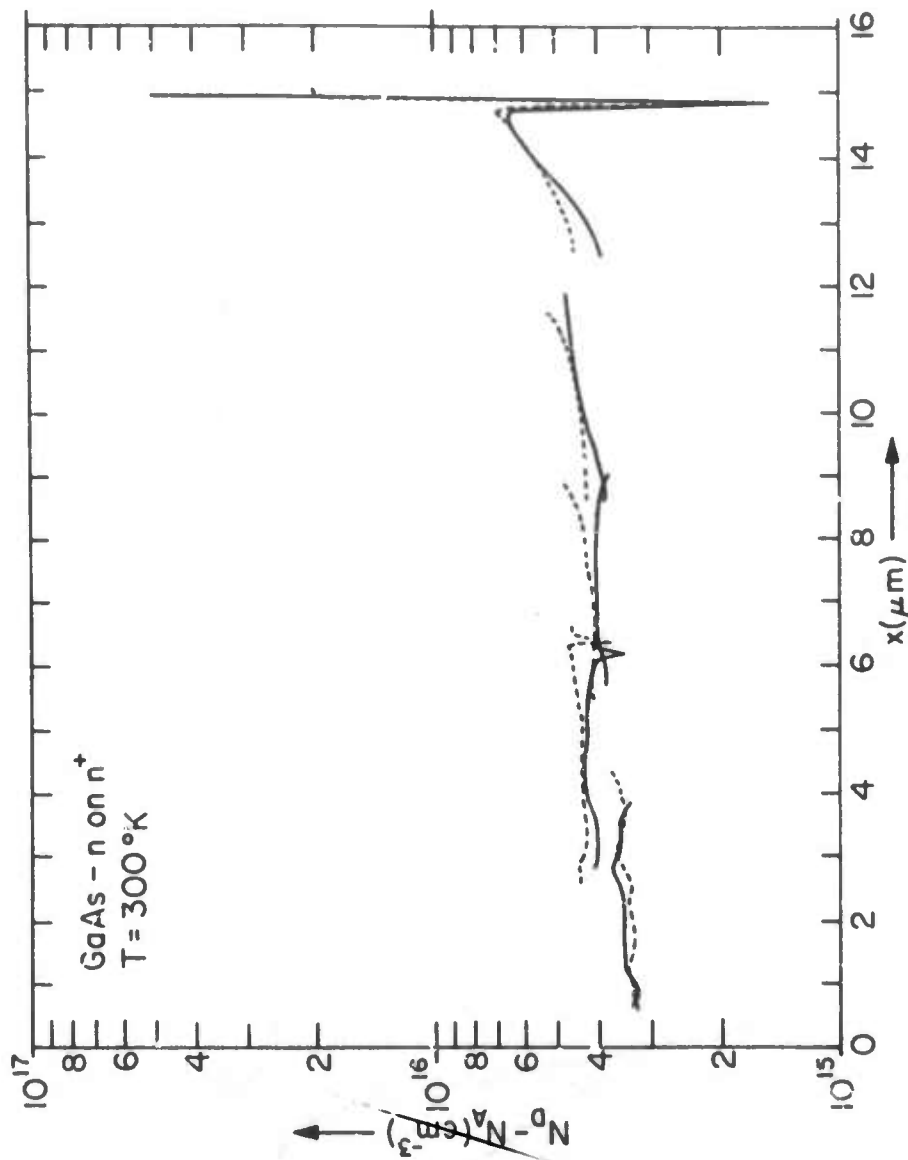


Figure 82. Comparison of a step etched GaAs doping profile as determined by RRE impurity plotter (dashed lines) and present system (solid lines). RRE data and sample courtesy of D. J. Ashen.

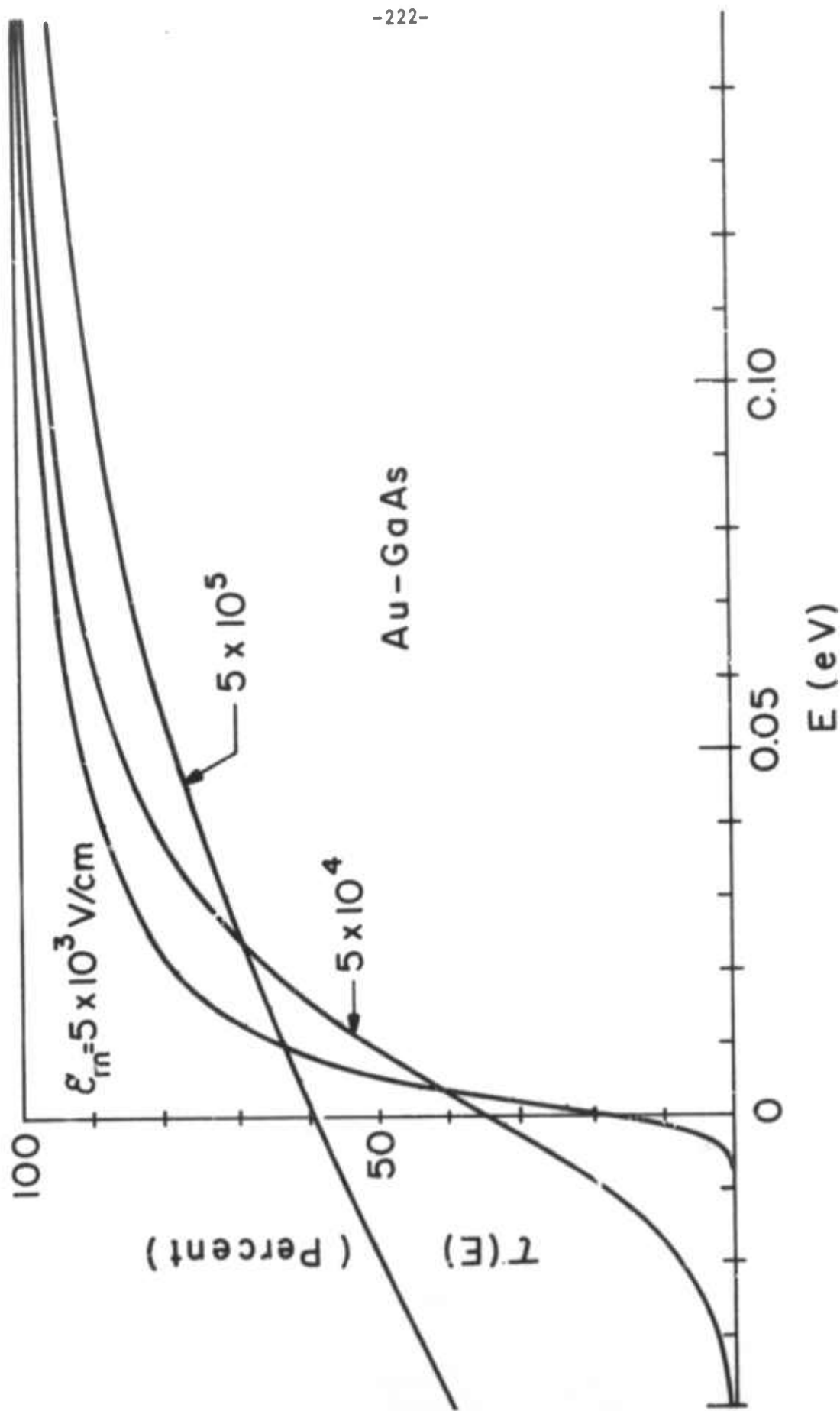


Figure 83. Quantum-mechanical electron transmission coefficients for a Au-n-type GaAs Schottky barrier ($\phi_B = 6.4 \text{ eV}$) with electric field, \mathcal{E} , as a parameter. Impurity concentration $\leq 10^{17} \text{ cm}^{-3}$.

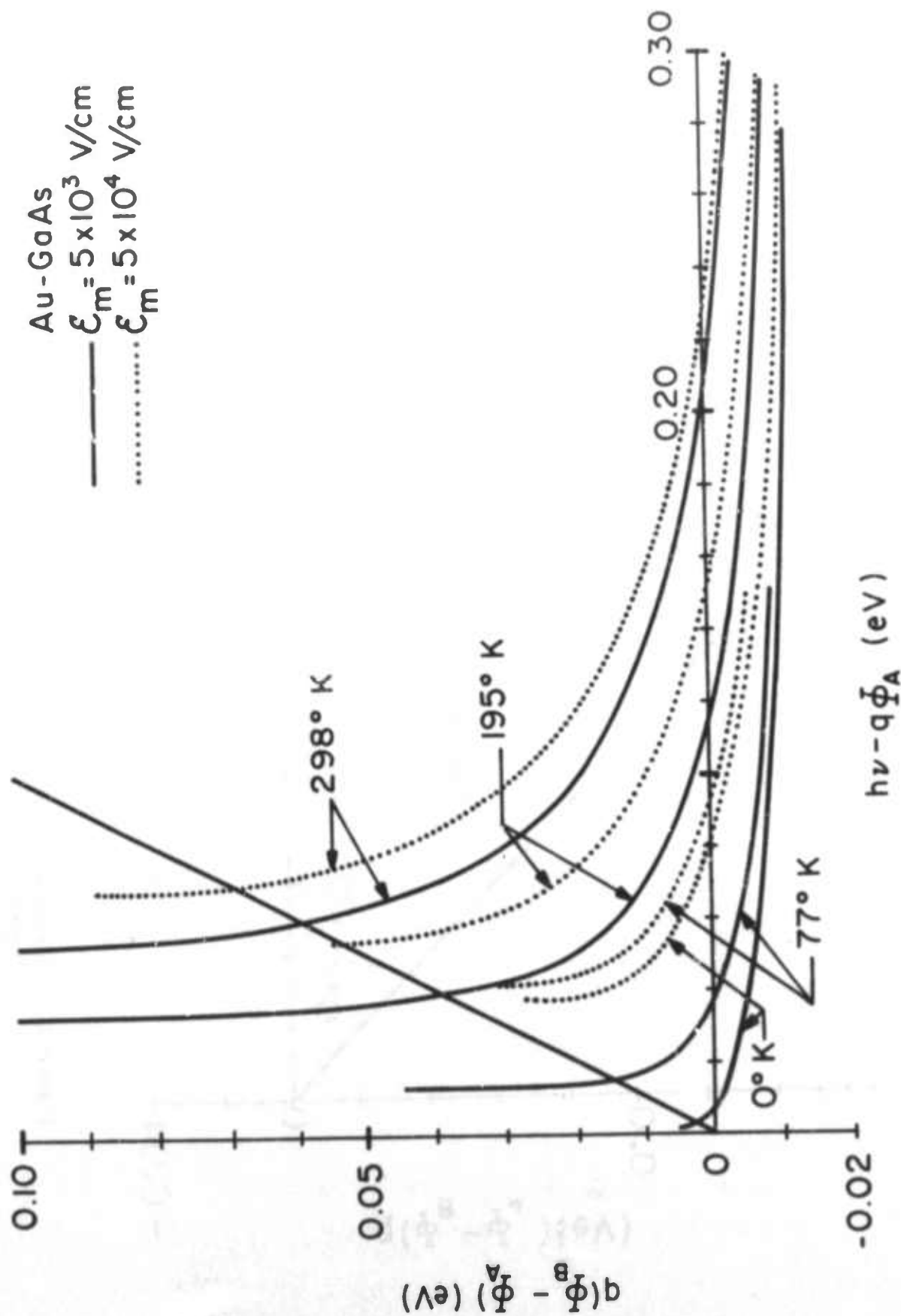


Figure 84. Corrections to the apparent photothreshold for a Au-n-type GaAs Schottky barrier with temperature and electric field, ξ , as parameters.

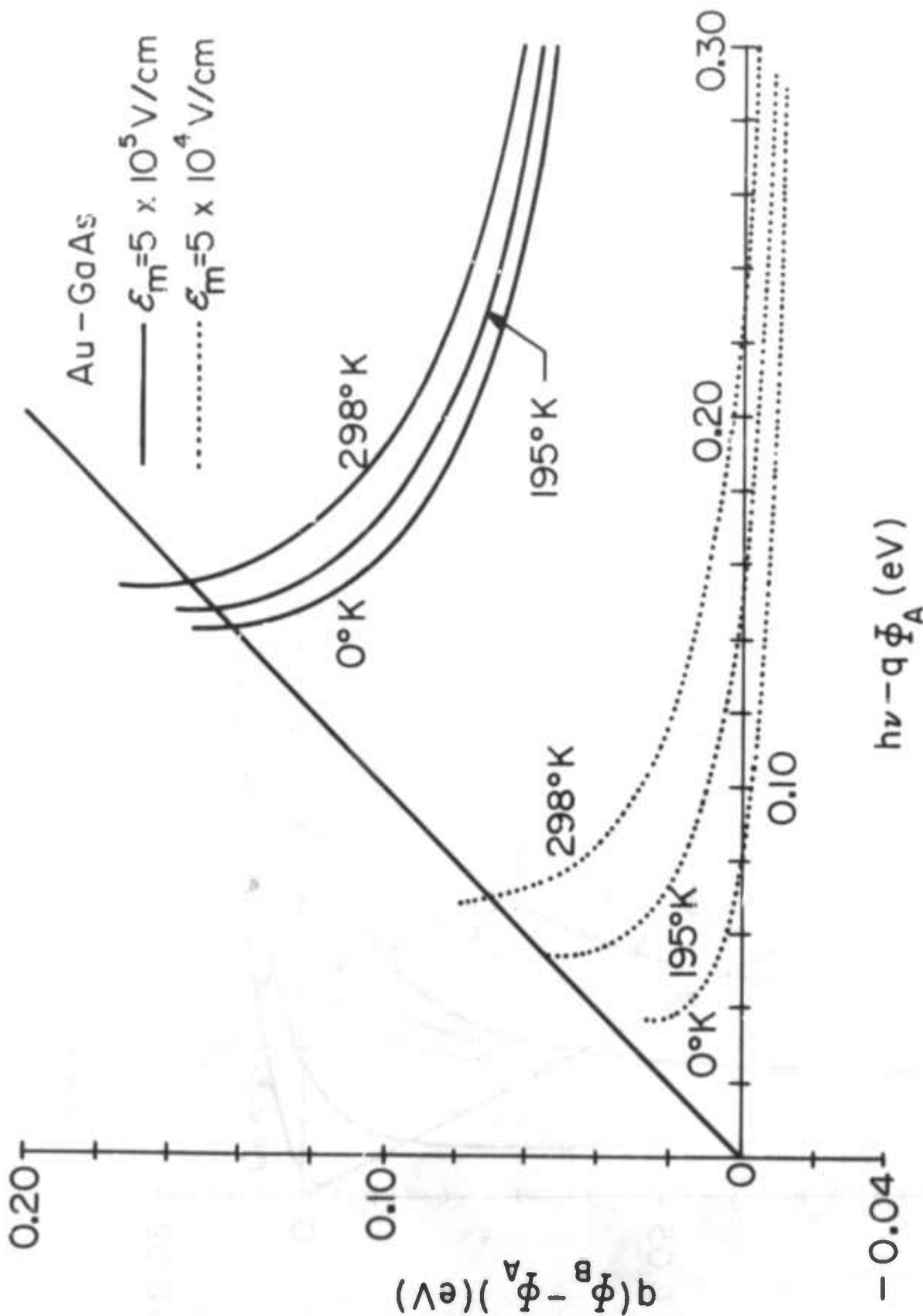


Figure 85. Corrections to the apparent photothreshold for a Au-n-type GaAs Schottky barrier with temperature and electric field, ϵ_m , as parameters. Legend: = $5 \times 10^4 \text{ V/cm}$; — $\epsilon_m = 5 \times 10^5 \text{ V/cm}$.

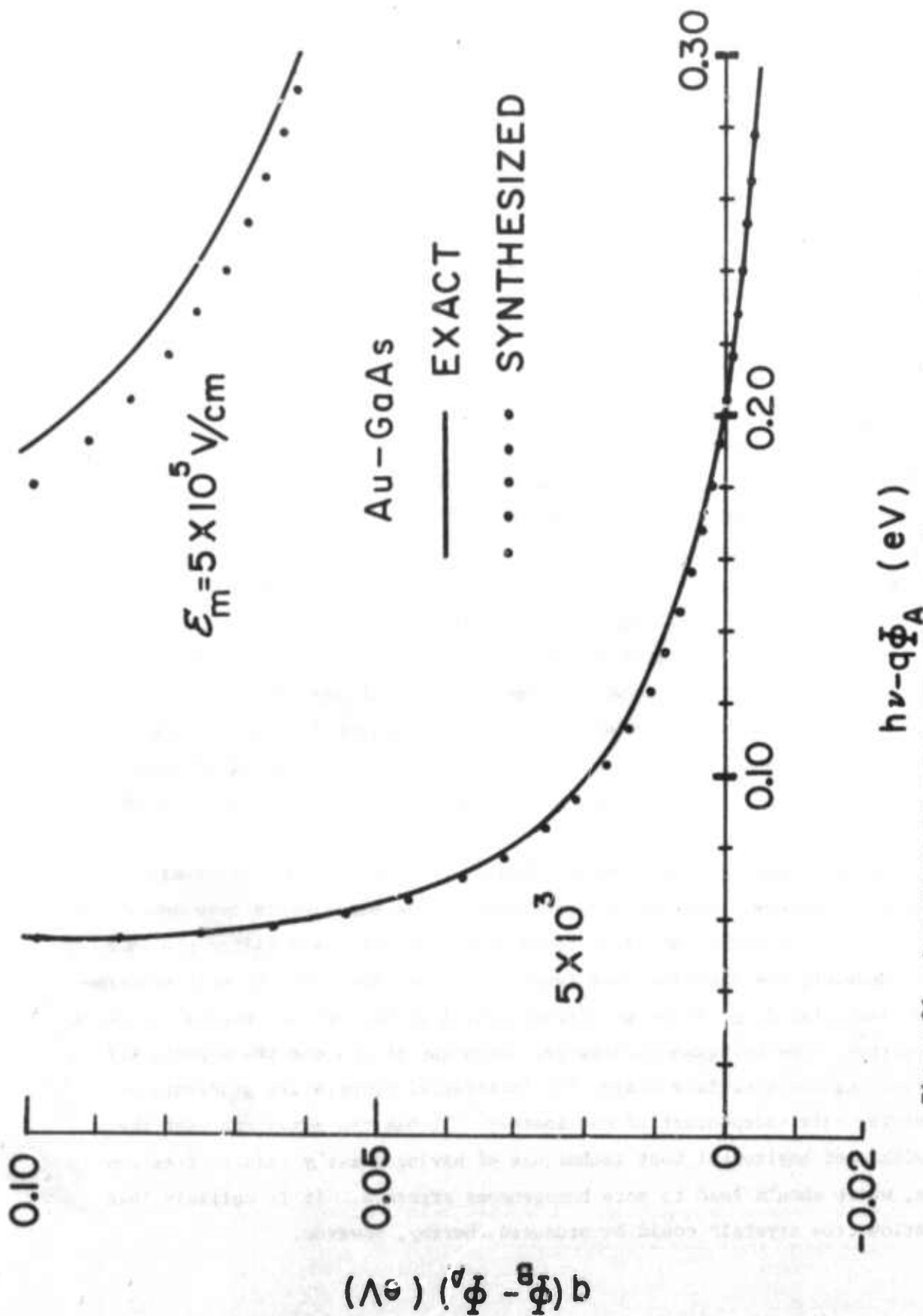


Figure 86. Comparison of exact corrections to the apparent threshold for a Au-n-type GaAs Schottky barrier at 298°K with corrections synthesized by adding the corrections for tunneling at 0°K to the pure thermal correction. Legend: — exact corrections; . . . synthesized corrections.

mechanically simpler. In addition, the resistance heating normally used with Bridgman growth is intrinsically more reliable and inexpensive than the induction heating normally used with Czochralski growth. Probably the labor required for horizontal Bridgman growth is less, as well. Our evidence also indicates that boron oxide can contribute appreciable quantities of impurities, indicating that the purity of Bridgman crystals should be greater and more reproducible.

Allred's new liquid-seal Czochralski technique invented and developed here is not yet a commercial method, although not much additional work is required to scale it up and make it so. Should dislocation-free GaAs ever be required on a large scale, it is believed that further development would be desirable. Although dislocation-free GaAs can be grown by horizontal Bridgman and by liquid-encapsulated Czochralski growth, it does not appear to be as fundamentally easy as it is with our new technique.

Further development of Allred's liquid-encapsulated floating-zone melting technique is unwarranted until truly high purity encapsulants become available. At that point, it could be developed to produce high purity large diameter GaAs, but only with considerable additional effort.

Although GaAs bulk single crystals can be grown by the Pfann-Tyco travelling heater method, it does not seem that it will ever be competitive. The properties are certainly no better and the production rate is too low. For alloy crystals with a volatile component it may possess strong advantages to the traditional melt techniques, and further effort in that direction seems very desirable.

A strong candidate for commercialization is the vertical Bridgman-Stockbarger technique. Our vertical gradient-freeze experiments have demonstrated that cylindrical crystals can be produced even when the fused silica crucible cracks. However, the freezing rate tends to be too large and the melt temperature too large for large diameter single crystal growth by the vertical gradient freeze method. The Bridgman-Stockbarger technique offers one the opportunity of controlling the interface shape, the interfacial temperature gradient, and the freezing rate independent of one another. It has the advantage over the Czochralski and horizontal boat techniques of having greatly reduced free convection, which should lead to more homogeneous crystals. It is unlikely that dislocation-free crystals could be produced thereby, however.

Whelan's experiments on oxygen sensing and pumping with oxide electrolytes are not only exciting for liquid epitaxial growth, but also open exciting possibilities for crystal growth whenever oxygen is suspected to be important. For example, one could imagine an oxygen sensor and an oxygen pump in series in a gas stream, permitting one to control the oxygen activity in the gas at any desired level. One could study thereby the influence of oxygen activity on chemical vapor deposition kinetics and morphology and on the properties of the films.

Traditional Hall measurements at two or more temperatures is still a very useful overall characterization method, although it does not provide many details. The ion microprobe mass analyzer appears to be a strong competitor with the usual mass spectrographic method for bulk analyses, as well as offering the possibility of investigating homogeneity and surface contaminants.

Infrared absorption and glow-discharge spectroscopy appear to be of occasional great value. All of these chemical analytical techniques are limited and variable in their sensitivity, generally being of little value for trace impurities. Carrier concentration profiles may be quickly determined by capacitance-voltage techniques. Capacitance-voltage-frequency measurements appear capable of elucidating information about deep carriers and might even be useful for chemical analyses. Unfortunately this was not actively pursued in the present project.

Although etching still appears to be the most convenient method for determining dislocation densities in GaAs, there are indications that cathodoluminescence may be capable of revealing even individual dislocations. Further work directed toward the cathodoluminescence behavior of grown-in dislocations is needed. Cathodoluminescence has demonstrated its value in quickly and non-destructively indicating the homogeneity of bulk GaAs.

REFERENCES

- *1. F. C. Leung and W. P. Allred, "Liquid-Seal Czochralski Growth of Gallium Arsenide," J. Crystal Growth, 19, 356 (1973) (Appendix Q).
- *2. P. C. Leung and W. P. Allred, "Improved Czochralski Growth for Gallium Arsenide," Houston Electrochemical Society Meeting (1972).
- *3. W. P. Allred, U.S. Patent applied for.
- *4. W. P. Allred, "GaAs Crystal Growth," meeting of Los Angeles section of the Electrochemical Society (1972).
- *5. W. R. Wilcox, "GaAs Crystal Growth," seminar at University of California at Los Angeles (1972).
6. R. Gremmelmaier, Z. Naturforsch. 11a, 511 (1956).
7. J. L. Richards, J. Appl. Phys. 34, 289 (1957).
8. J. B. Mullin, B. W. Straughan and W. S. Brickell, J. Phys. Chem. Solids 26, 782 (1965).
9. M. E. Weiner, D. T. Lassota and B. Schwartz, J. Electrochem. Soc. 118, 301 (1971).
10. P. C. Leung, L. H. Skolnik, W. P. Allred and W. G. Spitzer, J. Appl. Phys. 43, 4096 (1972).
11. J. B. Mullin, W. R. Macewan, C. H. Holliday and A. E. V. Webb, J. Cryst. Growth 13/14, 629 (1972).
12. S. F. Nygren, C. M. Ringel and H. W. Verleur, J. Electrochem. Soc. 118, 306 (1971).
- *13. C. E. Chang and W. R. Wilcox, "Vitreous Boron Oxide: Drying and Moisture Absorption," Mat. Res. Bull. 6, 1297 (1971).
- *14. E. S. Johnson and W. P. Allred, "Liquid Encapsulated Zone Refining of Gallium Arsenide," Princeton Meeting of American Association for Crystal Growth (1972). Paper in preparation.
15. J. M. Whelan and G. H. Wheatley, J. Phys. Chem. Solids 6, 169 (1958).
16. P. F. Kane and G. B. Larrabee, in Characterization of Semiconductor Materials, McGraw-Hill, New York (1970) pg. 114.

*Partially or wholly supported by ARPA.

17. R. K. Willardson and W. P. Allred, in Proceedings of the International Symposium on Gallium Arsenide, Reading, September 1966, edited by A. C. Strickland (Institute of Physics and Physical Society, 47 Belgrave Square, London, S.W. 1, 1967) pg. 35.
18. T. S. Plaskett, J. M. Woodall and A. Seegmüller, J. Electrochem. Soc. 118, 115 (1971).
- *19. V. F. Yip, C. E. Chang and W. R. Wilcox, "Vertical Gradient Freeze Crystal Growth of GaAs: Theory and Practice," Princeton AACG meeting, 1972 (paper in preparation).
- *20. V. F. S. Yip, "Growth and Characterization of GaAs and Mixed III-V Semiconductor Compounds," Ph.D. Dissertation and USCEE Report 455 (June 1973) (obtain from DDC or W. R. Wilcox).
- *21. V. F. S. Yip and W. R. Wilcox, Bull. Am. Phys. Soc. 15, 1624 (1970).
- *22. V. F. S. Yip and W. R. Wilcox, Bull. Am. Phys. Soc. 17, 1185 (1972).
- *23. E. S. Johnson and W. P. Allred, Bull. Am. Phys. Soc. 17, 1185 (1972).
- *24. C. E. Chang and W. R. Wilcox, Bull. Am. Phys. Soc. 17, 1185 (1972).
- *25. C. E. Chang, "Transport Processes in Unidirectional Crystal Growth," Ph.D. Dissertation and USCEE Report 450 (June 1973) (obtain from DDC).
- *26. C. E. Chang and W. R. Wilcox, "Control of Interface Shape in the Vertical Bridgman-Stockbarger Technique," submitted to J. Crystal Growth.
27. W. R. Wilcox, Ch. 6 in "Fractional Solidification," M. Zief and W. R. Wilcox, editors, Marcel Dekker, Inc., New York (1967).
- *28. C. E. Chang and W. R. Wilcox, "Localized Interface Breakdown in Zone Melting and the Travelling Heater Method," submitted to J. Crystal Growth.
- *29. V. H. S. Kuo, "Removal and Separation of Particles by Solidification," Ph.D. Dissertation and USCEE Report 435 (November 1972) (obtain from DDC).
- *30. V. H. S. Kuo and W. R. Wilcox, "Removal of Particles by Solidification," I&EC Proc. Des. Dev. 12, 376 (1973) (Appendix B), San Francisco AIChE meeting (1971).
- *31. V. H. S. Kuo and W. R. Wilcox, "Particle Chromatography," Sep. Sci., 8, 375 (1973) (Appendix R).
- *32. W. R. Wilcox and V. H. S. Kuo, "Formation of Gas Bubbles during Crystallization," J. Crystal Growth 19, 221 (1973) (Appendix P).

- *33. V. H. S. Kuo and W. R. Wilcox, "Some Factors Influencing the Pushing of Foreign Particles during Solidification," Princeton AACG meeting (1972).
- *34. R. J. Baughman, R. A. Lefever and W. R. Wilcox, "Evaporation of Sodium Chloride Melts," J. Crystal Growth 8, 317 (1971) (Appendix C).
- *35. K. A. Chen and W. R. Wilcox, "Boiling and Convection during Movement of Solvent Inclusions in Crystals," I&EC Fund. 11, 563 (1972) (Appendix D), Princeton AACG meeting (1972).
- *36. W. R. Wilcox, "Movement of Liquid Inclusions by Centrifugation," J. Crystal Growth 13/14, 787 (1972) (Appendix E).
- *37. W. R. Wilcox in "Preparation and Properties of Solid State Materials," R. Lefever, ed., Marcel Dekker, Inc., New York (1971).
- *38. W. R. Wilcox and P. J. Shlichta, "A Survey of Movies on Crystal Growth," J. Crystal Growth 15, 61 (1972).
- *39. W. R. Wilcox and A. Leon, "Twinning of Potassium Bromide," J. Crystal Growth 8, 230 (1971) (Appendix F).
- *40. R. T. Pepper and W. R. Wilcox, "Directional Solidification of an Off-Eutectic Aluminum-Beryllium Alloy," J. Comp. Mat. 5, 468 (1971) (Appendix G).
- 41. M. V. Sullivan and G. A. Kolb, "The Chemical Polishing of Gallium Arsenide in Bromine-Methanol," J. Electrochem. Soc. V. 110, 585 (June 1963).
- 42. A. Reisman and R. Rohr, "Room Temperature Chemical Polishing of Ge and GaAs," J. Electrochem. Soc. V. 111, 1425 (December 1964).
- 43. D. Laister and G. M. Jenkins, "Mechanically Induced Surface Damage in Gallium Arsenide," Solid State Electronics, 13, 1200 (1970).
- 44. R. J. Walsh and A. H. Herzog, U.S. Patent 3,170,273 (23 February 1965). Assigned to Monsanto Chemical Co., St. Louis, Mo.
- 45. R. B. Bird, W. E. Stewart and E. N. Lightfoot, "Transport Phenomena," Wiley and Sons, New York (1960), Eq. 18.4-8 on p. 567.
- 46. R. C. Newman, F. Thompson, M. Hyliards and R. F. Peart, Solid State Comm. 10, 505 (1972).
- 47. O. G. Lorimor and W. G. Spitzer, J. Appl. Phys. 37, 3687 (1966).
- 48. W. G. Spitzer and W. P. Allred, J. Appl. Phys. 39, 4999 (1968).
- 49. R. J. Elliott and P. Pfeuty, J. Phys. Chem. Solids 28, 1789 (1967).
- 50. M. E. Levy, Ph.D. Dissertation, Univ. of Southern California (1973).

51. A. E. Cosand, J. Appl. Phys. 42, 5230 (1971).
52. W. Bardsley, Progress in Semiconductors 4, 156 (1960).
53. P. L. Petrusevich and E. S. Sollertinskaya, Sov. Phys. Crystallography 8, 182 (1963).
54. E. P. Warekcois and P. H. Metzger, J. Appl. Phys. 30, 960 (1959).
55. H. C. Gatos and M. C. Lavine, J. Phys. Chem. Sol. 14, 169 (1960).
56. H. C. Gatos and M. C. Lavine, J. Electrochem. Soc. 107, 427 (1960).
57. E. S. Meieran, Siemens Review 37, 39 (1970).
- *58. A. L. Esquivel and S. Sen, Bull. Amer. Phys. Soc. 17, 61 (1972).
59. J. F. Nye, Acta Met. 1, 153 (1953).
- *60. A. L. Esquivel, W. N. Lin and D. B. Wittry, "Cathodoluminescence Study of Plastically Deformed GaAs," Appl. Phys. Lett. 22, 414 (1973) (Appendix J).
61. S. R. Morrison, Phys. Rev. 104, 619 (1956).
62. T. Figielski, Phys. Stat. Sol. 6, 429 (1964).
63. T. Figielski, Phys. Stat. Sol. 9, 555 (1965).
64. T. Figielski, Phys. Stat. Sol. 10, 75 (1965).
- *65. A. L. Esquivel and S. Sen, Bull. Amer. Phys. Soc. 17, 1195 (1972).
66. A. Clawson and H. Wieder, U.S. Patent No. 3,532,562 (6 Oct. 1970).
67. L. R. Weisberg, F. D. Rosi and P. G. Herkart, in "Properties of Elemental and Compound Semiconductors," H. C. Gatos, ed., Interscience Publishers, New York (1960) p. 49.
68. A. F. Kravchenko, A. M. Palkin and V. P. Rulera, Soviet Physics-Semiconductors, 1, 922 (1968).
69. S. P. Grishina, M. G. Mil'vidskii, V. B. Osvenskii and V. I. Fistul', Soviet Physics-Semiconductors, 4, 240 (1970).
70. R. A. Logan, G. L. Pearson and D. A. Kleinman, J. Appl. Phys. 30, 885 (1959).
71. U. Baitinger, J. Arndt and D. Schnepf, J. Mat. Sci. 4, 396 (1969).
72. R. L. Bell and A. F. W. Willoughby, J. Mat. Sci. 5, 198 (1970).

73. W. T. Read, Jr., Phil. Mag. 47, 111 (1955).
74. R. M. Broudy, Adv. Phys. 12, 135 (1963).
75. R. A. Logan, G. L. Pearson and D. A. Kleinman, J. Appl. Phys. 30, 885 (1959).
76. R. L. Bell and A. F. W. Willoughby, J. Mat. Sci. 5, 198 (1970).
77. C. M. Wolfe, G. E. Stillman and J. A. Rossi, J. Electrochem. Soc. 119, 250 (1972).
- *78. D. B. Wittry, "Crystallographic Information from Scanning Electron Microscope Images," in "Proceedings of the Sixth International Conference on X-ray Optics and Microanalysis," p. 471, G. Shinoda, K. Kohra and T. I. Chinoksawa, eds., Univ. of Tokyo Press (1972) (Appendix K).
- *79. J. C. Potosky and D. B. Wittry, "Study of a Duoplasmatron with a Quadrupole Mass Spectrometer," in "Proceedings of the Seventh National Conference on Electron Probe Analysis" (1972) (Appendix L).
- *80. H. C. Morciniak and D. B. Wittry, "A Clean Vacuum Electron Beam Column for Cathodoluminescence Investigations," Rev. Sci. Instr. 42, 1810 (1971) (Appendix M).
81. H. C. Casey, Jr., and R. L. Kaiser, Appl. Phys. Lett. 8, 113 (1966).
82. L. N. Kurbatow, et al., Sov. Phys.-Semiconductors 4, 1739 (1971).
83. Y. M. Popov, Sov. Phys.-Solid State 6, 1938 (1965).
84. O. N. Krokhim and Y. M. Popov, Sov. Phys. JETP 11, 1144 (1960).
- *85. W. N. Lin and D. B. Wittry, "Study of GaAs using Infrared Modulated Cathodoluminescence," Eighth National Conference on Electron Probe Analysis (1973) (Appendix N).
86. J. W. Colby, "MAGIC - A Computer Program for Quantitative Electron Microprobe Analysis," Bell Telephone Laboratories, Inc., Allentown, Pennsylvania.
87. W. K. Subashiev and S. A. Abagyan, "Band Structure of $\text{GaAs}_{1-x}\text{P}_x$ Crystals," in "Proceedings of the International Conference of the Physics of Semiconductors," Dunod, Paris (1964).
88. W. G. Spitzer and C. A. Mead, Phys. Rev. 133, A 872 (1964).
89. D. A. Cusano, G. E. Genner and R. O. Carlson, Solid State Comm. 2, 353 (1964).

90. M. B. Panish and H. C. Casey, J. Appl. Phys. 40, 164 (1966).
91. M. G. Holland, Phys. Rev. 134, A471 (1969).
92. H. Weiss, Ann. Physik 4, 121 (1959).
93. G. S. Almasi, J. Blair, R. E. Ogilvie and R. J. Schwartz, J. Appl. Phys. 36, 1848 (1965).
- *94. H. C. Marciniak and D. B. Wittry, "Temperature Dependence of Cathodoluminescence of GaAs, GaP, and GaAs_{1-x}P_x," Proc. of 7th National Conf. on Electron Probe Analysis, San Francisco, California (1972) (Appendix O).
95. D. R. Scipes, N. Holonyak, Jr., C. B. Duke, G. G. Keinmore, A. B. Kung, M. G. Craford, W. O. Grmes and A. H. Herzog, Phys. Rev. Lett. 27, 191 (1971).
96. H. Ma Macksey, N. Holonyak, Jr., R. D. Dupuis, J. C. Campbell and G. W. Zick, J. Appl. Phys. 44, 1333 (1973).
97. N. Holonyak, Jr., R. D. Dupuis, H. M. Macksey, M. G. Craford and W. O. Grmes, J. Appl. Phys. 43, 4148 (1972).
98. B. J. Gordon, H. L. Stover and R. S. Hard, "A New Impurity Profiler for Epitaxy and Devices," Silicon Device Processing, NBS Special Publication 337, Washington, D.C., Government Printing Office (1970).
- *99. T. Culbertson, "The Punch-Through Injection Diode: A New Microwave Source and Technology Related to its Fabrication," Ph.D. Dissertation (January 1972).
- *100. B. J. Gordon, "DC and Microwave Analysis and Characterization of the Punched-Through Injection Transit-Time Oscillator," Ph.D. Dissertation, (February 1973).
- *101. J. E. Greene and J. M. Whelan, Bull. Am. Phys. Soc. 15, 1614 (1970).
- *102. J. E. Greene and J. M. Whelan, "Crystal Orientation by Cleavage Plane Reflected Laser Beam," Sci. Instr. 5, 975 (1972). (Appendix H).
- *103. J. E. Greene, "Glow Discharge Spectroscopy," Ph.D. Dissertation (1971).
104. A. U. MacRae and G. W. Goveli, J. Appl. Phys. 35, 1629 (1964).
- *105. J. E. Greene and J. M. Whelan, "Glow-Discharge Optical Spectroscopy for the Analysis of Thin Films," J. Appl. Phys. 44, 2509 (1973) (Appendix I).
- *106. C. T. Li, "Preparation and Properties of GaAs, GaAs_xSb_{1-x} and Ga_xIn_{1-x}As Thin Films by Epitaxial Growth Techniques," Ph.D. Dissertation (1971).
- *107. L. T. Yuan, "Contributions to GaAs Technology," Ph.D. Dissertation (1971).

- *108. R. Chwang, B. J. Smith and C. R. Crowell, "Contact Size Effects on the van der Pauw Method for Resistivity and Hall Coefficient Measurement," Solid State Electron. (in press).
- 109. M. Beguwala and C. R. Crowell, "Characterization of Multiple Deep Level Systems in Semiconductor Junctions by Admittance Measurements," (in press).
- 110. N. I. Meyer and T. Galbrandsen, Proc. IEEE 51, 1631 (1963).
- 111. J. A. Copeland, IEEE Trans. on Electron Devices ED-16, 445 (1969).
- 112. R. R. Spivak, IEEE Trans. on Instrumentation and Measurement IM-18, 197 (1969).
- 113. G. R. Branner, E. M. Friar and G. Medicus, Rev. Sci. Instr. 34, 231 (1963).
- 114. W. R. Patterson and J. Shewchun, Rev. Sci. Instr. 35, 1704 (1964).
- 115. D. E. Thomas and J. M. Rowell, Rev. Sci. Instr. 36, 1301 (1965).
- 116. B. J. Gordon, H. L. Stover and R. S. Harp, "A New Impurity Profile Plotter for Epitaxy and Devices," Proc. Symp. on Silicon Device Processing, Gaithersburg, Md., Nat. Bur. Std. Spec. Pub. 337 (1970).
- 117. R. J. Baxandall, D. J. Colliver and A. F. Fray, J. Phys. E. 4, 213 (1971).
- 118. A. M. Goodman, J. Appl. Phys, 34, 329 (1963).
- 119. M. Schottky, Z. Physik 118, 539 (1942).
- 120. J. Hilibrand and R. D. Gold, RCA Rev. 21, 245 (1960).
- 121. C. O. Thomas, D. Kahng and R. C. Manz, J. Electrochem. Soc. 109, 1055 (1962).
- *122. C. L. Anderson, T. W. Kao and C. R. Crowell, "Effects of Thermal Excitation and Quantum-Mechanical Transmission on Photothreshold Determination of Schottky Barrier Height," Solid State Electron (to be published).

APPENDICES

Most relevant publications acknowledging
support of these grants.



VITREOUS BORON OXIDE: DRYING AND MOISTURE ABSORPTION

Chong E. Chang and William R. Wilcox
Chemical Engineering and Materials Science Departments
University of Southern California, Los Angeles, California 90007

(Received October 26, 1971; Communicated by R. A. Huggins)

ABSTRACT

Frothing of reagent-grade boron oxide during heating can be avoided by a preliminary vacuum bake out. The rate of removal of trace water is much larger when dry nitrogen is bubbled through the melt than when a vacuum is applied. The moisture absorbed by vitreous boron oxide when exposed to air at room temperature is confined to the neighborhood of the surface. Eventually boric acid is formed. This surface moisture can largely be removed by a vacuum at room temperature. The kinetics of water removal and absorption were measured.

Introduction

The liquid encapsulation (Zochralski technique has proven to be very useful for the growth of III-V and II-VI semiconductor crystals, especially GaAs and GaP (1-5). In this technique a layer of molten boron oxide (B_2O_3) is placed on the surface of the melt in order to prevent evaporation of the group V or group VI element. The presence of water in the B_2O_3 is very deleterious. Large amounts of water lead to severe bubbling when the B_2O_3 is heated and can cause a loss of up to 50% of the B_2O_3 by bubbling over the side of the crucible (5). Small amounts of water cause formation of bubbles which can bring up particles from the semiconductor melt, clouding the B_2O_3 and causing loss of visibility (4). Trace amounts of water appear to cause defect formation in the crystal and may be responsible for the poor performance of melt grown GaP as a light emitting diode (4,5). In this paper we review methods of drying boron oxide and present measurements of the kinetics of drying and of the kinetics of surface moisture absorption by vitreous B_2O_3 .

We have found that ordinary reagent grade boric oxide contains about 3 wt % water. Most of this water may be removed by heating slowly in a vacuum oven to 260-270°C and then maintaining this temperature for 6 hours (6). Pressures above 40 mm Hg or too rapid heating cause sintering and greatly hinder water removal (6). Alternately, the B_2O_3 may be heated to melting. Although vigorous frothing occurs at 700-800°C even at atmospheric pressure, we have succeeded in controlling the frothing by breaking the viscous bubbles with a stirring rod. However, no frothing occurs if the boron oxide is given an initial vacuum bake-out. The foregoing treatments are insufficient to lower the water content to that required for crystal growth. More complete drying may be obtained by heating to 1200-1300°C in a vacuum. Water vapor bubbles are produced for a time, but then the water content becomes too low to nucleate bubbles and the water is removed only through the melt surface, which is very slow. More rapid drying is obtained by bubbling dry nitrogen through the melt, because fresh surface is continuously generated. We have found that the gas stream tends to form an inefficient channel rather than the desired bubbles below about 1000°C, because of the high viscosity of the melt. Boow's viscosity measurements showed that 1 hour of bubbling nitrogen removed as much moisture as about 15 hours of simply heating at 1200-1250°C (7). Napolitano, Macedo and Hawkins (8) showed by viscosity measurements that bubbling of nitrogen reduced the water content below the steady state value reached at 1300°C without bubbling. Four hours of bubbling were required to reach a constant viscosity. The equilibrium water content can be calculated from the results of Franz (9) if the water partial pressure and temperature are known. He showed that solubility is proportional to the square root of water partial pressure and decreases as the temperature increases.

Drying may also be hastened by the use of various chemical reactions. Some crystal growers are reportedly adding aluminum to remove moisture, but this results in the introduction of Al_2O_3 into the B_2O_3 . Harrison (10) removed the 2.84-micron OH absorption band (11) in B_2O_3 by bubbling BCl_3 through the melt. Although this appears to completely dehydrate the B_2O_3 , chloride is introduced into the melt and this is equally difficult to remove (12). Poch (13) reduced the moisture content to as low as 0.001 wt % (10 ppm) by heating in a graphite crucible at 1300°C and 1 Torr pressure. He attributed the final drying to the water-gas reaction whereby H_2O reacts with C to produce CO and H_2 .

Experimental Methods

Initially, drying was accomplished by (a) heating to 700-800°C while breaking the bubbles with a rod, (b) heating to 1200°C when bubbling subsided, and (c) bubbling nitrogen through the melt at 1200°C. The nitrogen was obtained by vaporization of liquid nitrogen, while taking care not to evaporate all of the liquid nitrogen. Later it was found that the frothing at 700-800°C could be avoided by a three-day vacuum bake-out at 260-270°C.

In order to determine the amount of water in the boron oxide, infrared absorption measurements were made at room temperature. Samples were prepared by slowly pulling a platinum foil from a melt in air at about 700°C, resulting in a sheet of vitreous B_2O_3 hanging from the foil. Resulting spectra are shown in Figure 1.

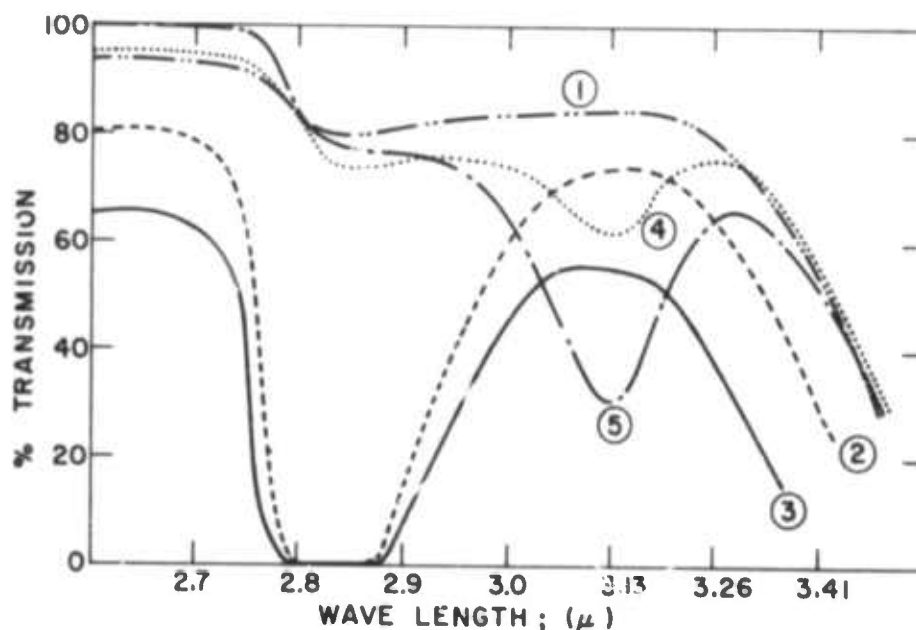


FIG. 1

Infrared Transmission of Vitreous Boron Oxide at Room Temperature.

- Curve 1: Dried by bubbling dry nitrogen at 1200°C for 10 hours. 0.114 mm thick. Measured in vacuum.
- Curve 2: Heated at 900°C for 1 hour in dry nitrogen. 0.259 mm thick. Measured in vacuum.
- Curve 3: Dry nitrogen bubbled through for 1 hour at 950°C. 0.528 mm thick. Measured in vacuum.
- Curve 4: Dried sample with $1.1 \mu g H_2O/cm^2$ of surface moisture. 0.104 mm thick. Measured in nitrogen.
- Curve 5: Dried sample with $4.1 \mu g H_2O/cm^2$ of surface moisture. 0.116 mm thick. Measured in nitrogen.

Curve 1 shows the absorption spectrum for B_2O_3 dried by the above methods. Using an extinction coefficient of 141 liter/mole cm at 2.84 microns (9), we estimate a moisture content of 0.06 wt %, which corresponds to a water partial pressure of 0.02 atm. at 700°C (9). This in turn corresponds to a relative humidity of about 65% at room temperature, which is a typical value for Los Angeles and indicates that the melt and sample sheet had reabsorbed moisture from the air during pulling of the sheet. Curves 2 and 3 show the OH absorption at 2.84 microns in partially-dried boron oxide. Curves 4 and 5 show an absorption band at 3.13 microns which has been attributed to moisture on the surface of vitreous boron oxide (11). Note that the bulk OH band at 2.84 microns was unaffected by exposure to air, indicating that the solid state diffusion of water in vitreous boron oxide is negligible at room temperature. Furthermore the 3.13-micron surface band rapidly disappeared at room temperature in a vacuum.

Kinetics of Drying Molten Boron Oxide
by Bubbling of Nitrogen

The water content of a boron oxide melt at 1200°C as a function of the time of bubbling was determined experimentally. About 200 g of vacuum-oven dried B_2O_3 was melted in a 2.5-inch diameter x 5-inch tall graphite crucible. Nitrogen gas was bubbled in at 2000 cc/min. Sample sheets were pulled periodically and the water content analyzed by infrared absorption. Unfortunately, the experimental results shown in Figure 2 are inaccurate because of air admission during drawing of the sheet samples, resulting in water reabsorption during drawing and a much higher water content value in thin samples than in thick samples.

It is reasonable to suppose that the rate of water removal during bubbling of nitrogen is proportional to the difference between the actual water content (weight fraction) W and the water content in equilibrium with the gas W_∞ , or mathematically:

$$\text{Drying rate} = -M \frac{dW}{dt} = K(W - W_\infty) \quad (1)$$

Here M is the total mass of the melt and K is a constant which depends on temperature, gas flow rate, viscosity, diffusion coefficient of water (or OH), and the shape and dimensions of the system. Integrating Eq. (1) we obtain the predicted dependence of the water content on time t :

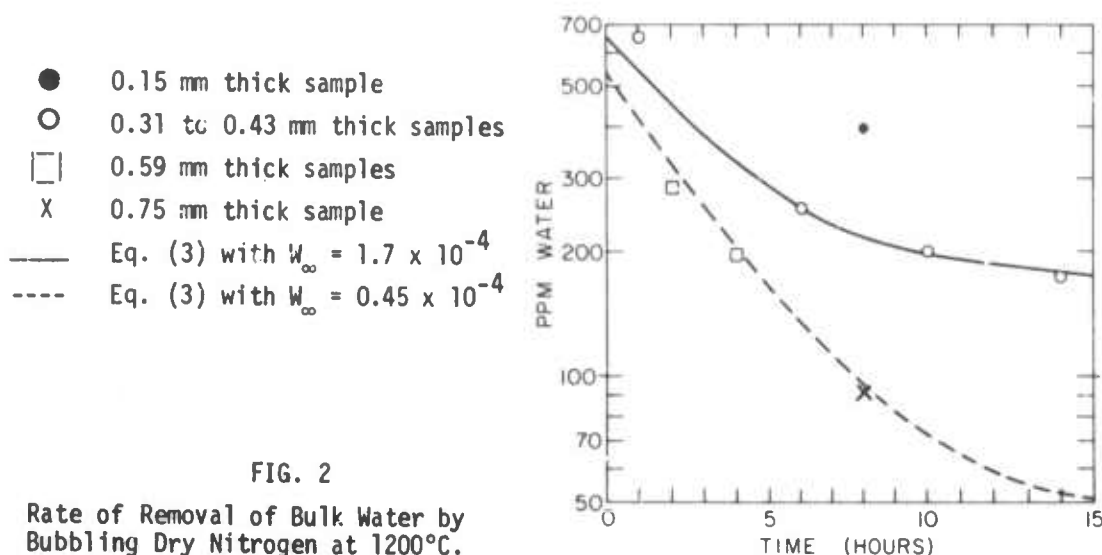


FIG. 2

Rate of Removal of Bulk Water by
Bubbling Dry Nitrogen at 1200°C.

$$W = W_{\infty} + (W_0 - W_{\infty}) \exp(-Kt/M), \quad (2)$$

where W_0 is the moisture content at time $t = 0$ and W_{∞} is the moisture content at time $t \rightarrow \infty$. From Figure 2 we see that $W_{\infty} \approx 0.00017$ for 0.31 to 0.43 mm thick samples, while $W_{\infty} \approx 0.000045$ for thicker samples. Using these values we obtain

$$W = W_{\infty} + 0.00049 \exp(-0.29 t), \quad (3)$$

which is shown as the curves in Figure 2.

Kinetics of Water Absorption on the Surface of Vitreous Boron Oxide

We have already noted the spectroscopic evidence for absorption of water on the surface of boron oxide. Exposure of vitreous boron oxide to air causes the surface to slowly assume a frosted appearance. Examination under the optical microscope after lengthy exposure reveals a rough powdery or globular deposit on the surface. X-ray diffraction shows peaks only for boric acid H_3BO_3 and no evidence for metaboric acid HBO_2 , in agreement with the results of Takamori (14). In order to determine the rate of water absorption, a sheet of vitreous boron oxide was exposed to air of $74 \pm 2\%$ relative humidity at 24°C and periodically weighed. The results are shown in Figure 3. The initial portion, up to ~10 hours, follows the equation

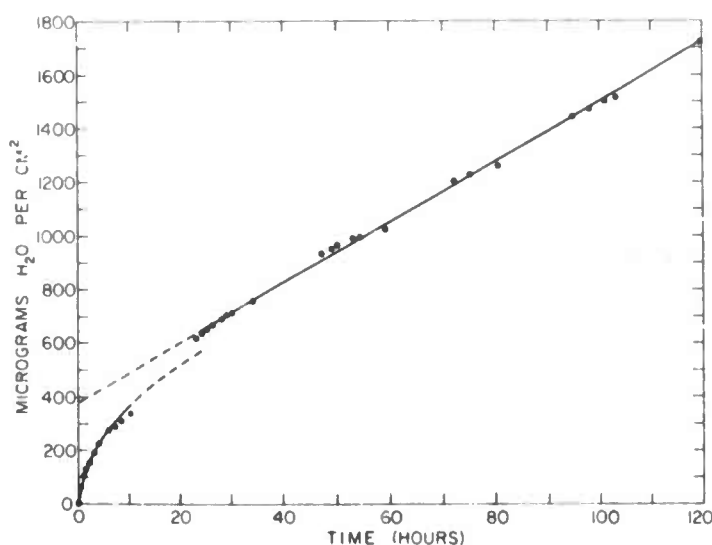


FIG. 3

Rate of Water Absorption on Surface of Vitreous B_2O_3
in Air at 74% Relative Humidity and 24°C

$$\rho_s = 1.16 \times 10^{-4} \sqrt{t - 0.29} \quad (4)$$

where ρ_s is g water/cm² surface. This indicates a diffusion controlled process, which would be expected if the surface of the boron oxide remains planar, as observed microscopically. After about one day the rate became constant, following the equation

$$\rho_s = (0.112 t + 3.76) \times 10^{-4}, \quad (5)$$

which indicates a damaged surface (as observed) permitting continued access by the water. (Parabolic and linear rates are commonly observed in oxidation of metals, but rarely are both observed for the same metal.)

Rate of Removal of Water from the Surface of Vitreous Boron Oxide

As noted earlier, we have observed that surface moisture may be removed at room temperature by means of a vacuum. The rate of removal was measured by monitoring the 3.13 μ absorption band of a sample which had developed a slightly cloudy surface during storage in a calcium sulfate desiccator for 40 days. The results are shown in Figure 4 and obey the equation

$$\rho_s = \{16 \exp(-1.21 t) + 2.11 \exp(-0.216 t)\} \times 10^{-6}, \quad (6)$$

which indicates that there are two different mechanisms of drying. Perhaps water is easy to remove from boric acid, but difficult to remove from the boron oxide structure. A marked reduction in surface cloudiness was noted after the vacuum treatment.

Conclusion

Many, if not most, crystal growers presently purchase pre-dried boron oxide. During loading of their apparatus the boron oxide is exposed to air and picks-up some moisture. Normally this is removed by melting the boron oxide and exposing it to a vacuum overnight or longer. We have learned here that the moisture is held on or near the surface of the boron oxide and can be removed by a vacuum at room temperature. Melting the boron oxide permits the water to mix into the bulk and may actually make its removal much more difficult.

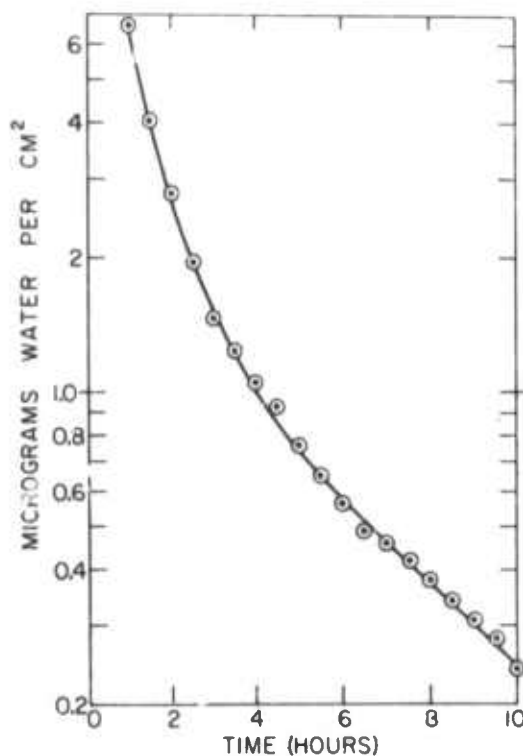


FIG. 4

Rate of Removal of Surface Moisture in Vacuum at 24°C. Curve follows Eq. (6).

Acknowledgements

This research was supported by the Advanced Research Projects Agency of the U.S. Department of Defense under Grant No. DAHC 15-70-G-14. The writers wish to thank L. Skolnik, P. Leung, and J. Kung for assistance with the infrared measurements.

References

1. S. J. Bass and P. F. Oliver, *J. Crystal Growth* **3**, 4, 286 (1968).
2. J. B. Mullin, B. W. Stroughan and W. S. Brickell, *J. Phys. Chem. Solids* **26**, 782 (1965).
3. E. P. A. Metz, R. C. Miller and R. Mazelsky, *J. Appl. Phys.* **33**, 2016, (1962).

4. S. F. Nygren, C. M. Ringel and H. W. Verleur, J. Electrochem. Soc. 118, 306 (1971).
5. M. E. Weiner, D. T. Lassota and B. Schwartz, J. Electrochem. Soc. 118, 301 (1971).
6. The Encyclopedia of Chemical Technology, Vol. 3, 2nd ed., edited by D. F. Othmer, Interscience/Wiley, New York, 1963.
7. J. Boow, Phys. Chem. Glasses 8, 45 (1967).
8. A. Napolitano, P. B. Macedo and E. G. Hawkins, J. Am. Ceram. Soc. 48, 613 (1965).
9. H. Franz, Glastechnische Berichte 38, 54 (1965).
10. A. J. Harrison, J. Am. Ceram. Soc. 30, 362 (1947).
11. R. V. Adams, Phys. Chem. Glasses 2, 39 (1961).
12. R. Bueckner, Glastechn. Ber. 37, 413 (1965); through Chem. Abstr. 62, 302b (1965).
13. W. Poch, Glastechnische Berichte 37, 533 (1964).
14. T. Takamori, J. Am. Ceram. Soc. 48, 170 (1965).



Removal of Particles by Solidification

Vincent H. S. Kuo¹ and William R. Wilcox*

University of Southern California, Los Angeles, California 90007

Removal of insoluble foreign particles from organics by solidification was studied by means of vertical Bridgman-Stockbarger experiments and by horizontal zone melting with rotation. By slowly increasing the freezing rate it was found that all particles were pushed by the advancing solid as long as the freezing rate was below a critical value, which depended on a variety of experimental parameters. A convex interface caused particles to be trapped at the wall of the glass container at lower freezing rates than at the center. Gas bubbles formed under some conditions and caused irregular incorporation of particles at low freezing rates. With carbon particles in naphthalene, critical velocities differed by about 20% between the different grains of the solid. In horizontal zone melting, the critical velocity for trapping at the center of the tube increased with increasing rotation rate, while that near the tube wall decreased with increasing rotation.

Many substances are contaminated by foreign particles, including most reagent-grade organic chemicals, most natural waters, and many metals. Nearly all such particles can be removed by slow solidification of a melt containing a suspension of the particles. Similarly, particulates in fruit juices and beverages could be concentrated along with dissolved components by crystallization and removal of the ice. On the other hand, materials of construction may be strengthened by incorporation of particles.

A necessary, but not sufficient, condition for pushing of a particle by a growing crystal is that the surface energy between the particle and the crystal be greater than that between the particle and the fluid plus that between the crystal and the fluid (Correns, 1949). Corte (1962), Uhlmann, Chalmers, and Jackson (1964), Hoekstra and Miller (1967), Cisse and Bolling (1971a,b), and Pikunov (1957) showed that there is a critical freezing rate V_c for a particle in a melt below which the particle is pushed by the moving solid-melt interface and above which it is trapped. This critical freezing rate was found to be sensitive to the particle-melt system. There was a rough correlation with melt viscosity, with less viscous melts generally being able to push a given particle at a higher rate. For spherical particles, the critical freezing rate was roughly inversely proportional to the particle diameter. The critical rates for rough particles were less sensitive to particle size. Bolling and

Cisse (1971) made the most recent theoretical analysis of particle pushing for materials containing no soluble impurities. Basically they solved the problem in which the pushing rate is limited by transport of melt to the interface adjacent to a spherical particle, taking into account the hydrodynamic forces on the particle and the deformation of the interface caused by the presence of the particle.

The research reported here was undertaken to provide information for design of industrial separation techniques utilizing pushing of foreign particles by solidification. The previous studies quoted above did not provide such information as, for example, the influence of stirring, interface shape, and gas bubbles.

Experimental Methods

Two experimental methods were employed (Kuo, 1973). First was a vertical Bridgman-Stockbarger technique with a sealed 10.5-mm i.d. Pyrex tube containing the suspension slowly lowered from a wire-wound resistance heater into a temperature-controlled cooling bath. Second was horizontal zone melting with rotation of the 10.5- or 19-mm i.d. Pyrex tube about its axis (Pfann, Miller, and Hunt (1966)). One or two loops of 3-mm wide nichrome ribbon were used as heaters with no shielding about the tube. In order to determine the critical velocity C_c , the freezing rate was slowly increased by about 2 mm/hr every 30 min by changing the lowering rate of the tube or the zone travel rate. After a change in the mechani-

¹ Present address, Allied Chemical Corporation, Solvay, N. Y.

Table I. Critical Trapping Velocities for Bridgman-Stockbarger Experiments

Organic matrix	Particle	V_c , mm/hr	Remarks
Naphthalene	C (0.5-2.5 μ m)	12	Agglomerate particles
		21	Ultrasonically dispersed
		16	Trapped next to glass wall due to convex interface
	Cu (8.5-55 μ m)	30-39	Stirring
		18	Trapped next to glass wall due to convex interface Calculated by equation of Bolling and Cisse (1971) using estimated properties
		14	
	1- μ m sphere	767	
	10- μ m sphere	24.6	
	C (0.5-2.5 μ m)	7	
	Fe ₂ O ₃ (0.45-1.8 μ m)	Not pushed at 6	
Salol	Zn	Not pushed at 6	Calculated by equation of Bolling and Cisse (1971)
	Si (<150 μ m)	Not pushed at 6	
	1- μ m sphere	82	
	10- μ m sphere	2.5	
	C (0.5-2.5 μ m)	Not pushed at 2	
Camphor	1- μ m sphere	85	Calculated by equation of Bolling and Cisse (1971)
	10- μ m sphere	2.7	

cal velocity, a small shift in interface position would occur before the freezing rate became equal to the mechanical motion rate. Particle trapping was observed with a low power microscope when possible. The critical velocity was also determined after each run by noting the position of the particle band and estimating the freezing rate when the interface was at that position. In the Bridgman-Stockbarger method, the interface shape could be made either concave into the solid, or planar or convex into the melt by adjusting the temperatures of heater and cooler. The freezing interface was concave in all but two of the zone melting experiments. In both techniques the interface became more concave (or less convex) as the freezing rate was increased during a run. The interface of the naphthalene was always nonfaceted, even though it is a high entropy of fusion material and might be expected to be faceted according to Jackson's criterion (Jackson, 1958). At high temperature gradients the interface of salol was faceted at freezing rates above 8 mm/hr and nonfaceted below 6 mm/hr, in accordance with the predictions of Wilcox (1970).

In order to prepare a tube for a zone melting run, a small amount of a melt-particle mixture was first poured into a tube with a tight-fitting Teflon plug placed about 3 cm above the sealed bottom. Melt containing no added particles was poured on top of this mixture after it had solidified. Because of liberation of dissolved gases the resulting charge was porous. During zoning a gas bubble formed in the zone and gradually increased in size. This bubble adversely affected particle pushing when it occupied more than one-third of the zone volume. Therefore a preliminary zone pass on the particle-free portion of the charge was performed in order to remove excess gas. The particle pushing experiment was initiated by melting the particle-containing portion.

Reagent grade naphthalene, camphor, salol, and benzophenone were used for the experiments. In some cases the naphthalene and camphor were first zone refined at 4 mm/hr (Fisher zone refiner) with no noticeable influence on the critical velocities. Ironically, this preliminary vertical zone

refining did not remove most of the small native particles originally present in the reagents. Fortunately the critical velocity for the native particles was much lower than for the added particles, so that no interference was observed. Particles used were rough and irregular-shaped carbon (0.5-2.5 μ m), irregular globules of copper (8.5-55 μ m), red ferric oxide (0.45-1.8 μ m), <74 μ m spherical silver and zinc, and <150 μ m silicon, where the size distributions are the 5 to 95 percentiles. Because of the various sizes and shapes present in most particles studied, a range of trapping velocities was observed. The critical freezing rates reported are those at which trapping first occurred, and are probably V_c for the largest, most spherical particles, which would be trapped most easily. As shown in Table I, early results with carbon gave higher values for V_c if the agglomerates were broken and the particles uniformly dispersed by placing melt plus particles in an ultrasonic field. Therefore ultrasonic dispersion was employed for all subsequent experiments. In the vertical Bridgman-Stockbarger technique, all but the smallest carbon and iron oxide particles settled to rest on the solid-liquid interface shortly after beginning the experiments. In the horizontal zone melting with rotation, the particles remained well suspended.

In two of the Bridgman-Stockbarger runs with naphthalene, the approximate axial temperature profile was determined by a 36-gauge copper-constantan thermocouple centered in the tube with the leads up the axis.

Experimental Results and Discussion

Table I summarizes the Bridgman-Stockbarger results. Note that both copper and carbon were trapped at lower velocities at the glass wall when the interface was convex. With a convex interface the particles tended to move to the groove or acute angle formed between the interface and the Pyrex container. Thus, when these particles were pushed they were forced to drag along the glass surface. (This observation throws doubt on those previous results obtained using a film of organic held between glass slides.) As a result, all later ex-



Figure 1. Surface-driven flows circulating particles around a gas bubble during freezing of naphthalene

periments were performed with a concave interface and trapping took place away from the tube wall.

A frequent problem in the Bridgman-Stockbarger technique was liberation of gas bubbles at the freezing interface. This occurred because gas (air) is much more soluble in melt than in crystal. Thus gas is rejected by a growing crystal. When the gas concentration becomes sufficient at the interface, nucleation of a bubble can take place. In our experiments, bubble formation was enhanced by rapid freezing and was influenced by the type of particle present (Wilcox and Kou, 1973.) With salol and naphthalene, such bubbles often remained attached to the interface. Continued gas evolution often caused gas holes to form in the solid. The presence of bubbles had a dramatic influence on particle trapping. As shown in Figure 1, vigorous surface-driven flows took place about gas bubbles in naphthalene. (Fluid flow caused by a variation in surface tension along a fluid-fluid interface. In crystal growth, variations in surface tension are caused both by temperature gradients and compositional variations (Wilcox, 1969).) This caused particles to settle in the depressions which formed about the bubble. Sometimes a bubble moved rapidly back into its hole or into a crack (caused by thermal stresses) and deposited a large number of particles in the solid. Occasionally a bubble broke free of the interface and floated away. This caused momentary rapid freezing and local trapping of particles at the former site of the bubble. The bubble problem was greatly reduced by a slight evacuation of the tube containing the melt, cooling to cause solidification, and then sealing of the tube at below 10 Torr vacuum before beginning an experiment. In the rotating zone melting experiments, bubbles did not adhere to the interface and so no such problems were encountered.

The critical freezing rate for carbon in naphthalene varied by over 20% from grain to grain, with the values shown in Table I being the smallest values observed. Thus there was a dependence of V_c on grain orientation. Although an orientation dependence was not predicted by the theory of Bolling and Cisse (1971), older work (Correns and Steinborn, 1939; Bokii, 1940) on "crystallization pressure" during growth of alum from aqueous solutions revealed a strong orientation dependence. However, these results are not sufficient to cause one to conclude that surface energy interactions between crystal and foreign solid are responsible for the orientation dependence. It may, for example, have been caused by the orientation dependence of growth-step height or mobility of surface adsorbed molecules.

Table II. Effect of Temperature Gradient on the Critical Velocity of the Naphthalene-Carbon System

Bath temp, °C	Heater input, W	Interfacial temp gradient, °C/cm	Critical velocity, mm/hr
-20	6.8	~27	~12
0	5.0	~6	~12
10	4.5		~12
20	4.5		~12

Table III. Optimum Rotation Rates for Separation of Particles from Naphthalene by a Horizontal Zone Refiner with Rotation

Particles	Tube size, mm (i.d.)	Optimum rotation, rpm	V_c , mm/hr
Carbon	10.5	33	30
	19	30	36
Copper	10.5	55	70
	19	50	<90
Iron oxide	10.5	40	35
	19	~25	~38

In 10.5-mm i.d. tubes, the solidified naphthalene normally consisted of 2 to 4 grains in a cross section, while salol typically had about 12 grains. These grains were easily separated and the grain-boundary surfaces examined under the microscope. Grain boundaries in salol had preferentially trapped carbon particles, while naphthalene grain boundaries did not. The theory of Bolling and Cisse (1971a) predicted better particle pushing by grain boundary grooves. However, the theory was developed for an isotropic nonfaceting material, rather than a faceted interface such as salol.

The influence of temperature gradient was studied for carbon agglomerates in naphthalene using the Bridgman-Stockbarger method. As shown in Table II, the temperature gradient did not have an observable influence on critical velocity. Cisse and Bolling (1971a) obtained similar results. The reason may be related to the influence of temperature gradient in the solid on the deformability of the interface, which has a strong influence on particle trapping. In rapid solidification of poor thermal conductors, the temperature gradient in the solid is determined almost entirely by the rate of latent heat liberation. (Examination of Tien's (1968) data showed this to be true for naphthalene.) The contribution by transport from the melt is made even smaller by movement of the interface away from the heater at high freezing rates.

Stirring of the melt is an important process variable which had not been previously investigated. It proved inconvenient to provide adequate stirring in the Bridgman-Stockbarger technique, although one run yielded very encouraging results, as shown in Table I. Therefore, the horizontal zone melting technique was used to study the influence of convection in the melt on critical freezing rates.

In horizontal zone-refining of naphthalene with rotation, the carbon particles gradually accumulated near the center of the concave interface and adhered there as the freezing rate was increased. (In view of the fact that carbon is more dense than naphthalene, this is perhaps surprising.) When V_c was exceeded, the length of the ingot over which particles were trapped was shorter for higher zone travel rates. When the zoning rate was kept at V_c , periodic trapping was observed. In other words, particles periodically accumulated at the interface and were trapped. This continued until all

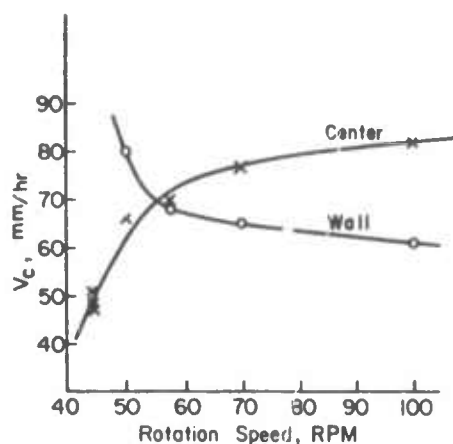


Figure 2. Influence of tube rotation on incorporation of copper particles by naphthalene during horizontal zone melting (10.5-mm i.d. tube)

particles originally present in the zone were trapped. Iron oxide was similarly trapped near the center of growing naphthalene. On the other hand, copper particles tended to be trapped uniformly. The foregoing were for the normal concave freezing interface. When the interface was kept planar by means of a second heater, carbon particles were trapped uniformly in naphthalene and V_c was increased from 30 to 35 mm/hr.

When the influence of tube rotation was studied, two values for V_c were observed, one in the center of the ingot and one near the tube wall. As shown in Figures 2-4, increasing the rotation rate increased V_c at the center and decreased V_c at the wall. Thus there was an optimum rotation rate. Note that the strongest influence of rotation rate on V_c was obtained with copper particles, which were the largest and most dense of those studied. This is what one would expect on the basis of the centrifugal and gravitational forces which act on the particles during rotation. As shown in Table III, larger diameter tubes gave smaller optimal rotation rates and larger critical velocities, again as one might expect.

Interestingly, most of the native particles in naphthalene were removed at 28 mm/hr with a tube rotation of 5 rpm, which is near V_c for carbon particles.

One can only speculate on the reasons for increases of V_c by stirring. Partly this may have been due simply to suspension of the particles. However, the primary mechanism must have to do with motion of the particles along the interface, so that there was less time for the interface to deform and make transport of melt between particle and interface more difficult.

Conclusions

Pushing of particles by a freezing interface was shown to be a complex process which is not yet completely understood. Bubbles, grain orientation, grain boundaries, container, and stirring were all shown to have a profound influence. The best results were obtained with horizontal zone melting with rotation about the tube axis. It was found that there was an optimum tube rotation rate which yields the best conditions for particle pushing. This optimum and the maximum pushing rate depend on tube diameter, particle-melt system, and probably to some extent on the exact shape and gas content of the zone as well.

It is certainly possible to develop other solidification schemes utilizing stirring which will also permit total removal of foreign particles in one step.

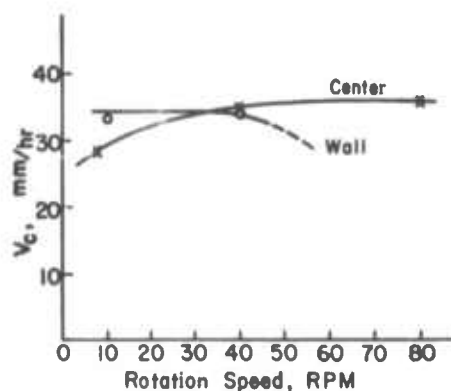


Figure 3. Influence of tube rotation on incorporation of iron oxide particles by naphthalene during horizontal zone melting (10.5-mm i.d. tube)

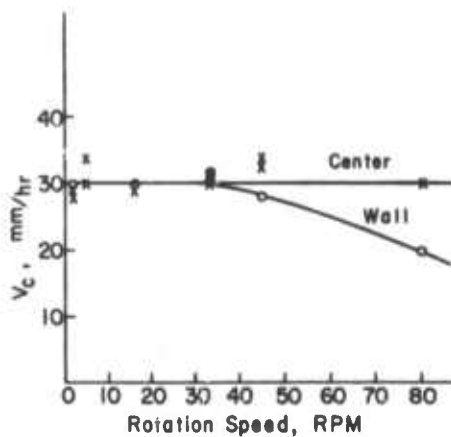


Figure 4. Influence of tube rotation on incorporation of carbon particles by naphthalene during horizontal zone melting (10.5-mm i.d. tube)

Literature Cited

- Bokii, G. B., *Tr. Inst. Kristallogr. Akad. Nauk SSSR*, **5**, 143 (1940).
- Bolling, G. F., Cisse, J., *J. Crystal Growth*, **10**, 56 (1971).
- Cisse, J., Bolling, G. F., *J. Crystal Growth*, **10**, 67 (1971a).
- Cisse, J., Bolling, G. F., *J. Crystal Growth*, **11**, 25 (1971b).
- Correns, C. W., Steinborn, W., *Z. Krist., Abt. A*, **101**, 117 (1939).
- Correns, C. W., *Discuss. Faraday Soc.*, **5**, 267 (1949).
- Corte, A. E., *J. Geophys. Res.*, **67**, 1085 (1962).
- Hoekstra, P., Miller, R. D., *J. Colloid Interface Sci.*, **25**, 166 (1967).
- Jackson, K. A., in "Liquid Metals and Solidification," American Society for Metals, Cleveland, Ohio, 1958, p 174.
- Kuo, V. H. S., Ph.D. Dissertation, University of Southern California, Los Angeles, 1973.
- Pfanz, W. G., Miller, C. E., Hunt, J. D., *Rev. Sci. Instrum.*, **37**, 649 (1966).
- Pikunov, M. V., *Metallurg. Obrab. Tverd. Metal. Splavov, Sb. State*, **55** (1957); *Chem. Abstr.*, **52**, 16826c (1953).
- Tien, L., Ph.D. Dissertation, University of Michigan, Ann Arbor, 1968.
- Uhlmann, D. R., Chalmers, B., Jackson, K. A., *J. Appl. Phys.*, **35**, 2896 (1964).
- Wilcox, W. R., *Sep. Sci.*, **4**, 95 (1969).
- Wilcox, W. R., *J. Crystal Growth*, **7**, 201 (1970).
- Wilcox, W. R., Kuo, V. H. S., *J. Crystal Growth*, submitted for publication.

RECEIVED for review December 11, 1972

ACCEPTED March 12, 1973

This paper is based on a dissertation submitted by V. H. S. Kuo in partial fulfillment of the requirements for the Ph.D. degree in Chemical Engineering at the University of Southern California. This research was supported by Grant No. 4528-AC6 from the Petroleum Research Fund (administered by the American Chemical Society) and by Grant No. DAH015-72-G7 from the Advanced Research Projects Agency of the Department of Defense.



EVAPORATION OF SODIUM CHLORIDE MELTS*

R. J. BAUGHMAN and R. A. LEFEVER

Sandia Laboratories, Albuquerque, New Mexico 87115, U.S.A.

and

WILLIAM R. WILCOX

University of Southern California, Los Angeles, California 90007, U.S.A.

Received 29 June 1970; revised manuscript received 10 November 1970

The evaporation rate of molten NaCl in the presence of various gases was measured at gas pressures between 0.74 and 212 psia. In induction heated crucibles the rate was a linear function of $(1/P)^{1/2}$, with different slopes at high and low pressures. The $(1/P)^{1/2}$ dependence is shown to be expected for turbulent free convective mass transport. Under some conditions the evapora-

tion rate decreased with decreasing pressures. This observation is attributed to condensation of NaCl in the gas with NaCl particles being carried back into the melt by a reflux process. The large difference in evaporation rates between Ar, He, and CO₂ is attributed not only to differences in thermal conductivity but also to infrared absorption by the CO₂.

1. Introduction

Interest in crystal growth of moderately high vapor pressure materials from the melt requires the use of special growth techniques¹⁻⁵ if one is to maintain a reasonable stoichiometric balance in the melt and growing crystal. Due to the recent commercial availability of high pressure crystal growth furnaces^{6,7}, the use of gas overpressure as a means of suppressing melt vaporization has gained widespread interest. Information on the value of a gas overpressure as a means of suppressing vaporization during crystal growth is very limited. Recent work on the single crystal growth of LiGaO₂ and Y₃Ga₅O₁₂ using relatively small gas overpressures has been reported^{8,9}. Table 1 summarizes the vapor losses for these materials at three levels of overpressure and in two separate atmospheric environments, with air at one atmosphere as a point of reference.

The present study was initiated to characterize the effect on melt vaporization losses caused by manipulation of several of the environmental parameters. Sodium chloride was selected as the experimental

* The research conducted at Sandia Laboratories was supported by the U.S. Atomic Energy Commission while that performed at the University of Southern California was supported by the Advanced Research Projects Agency of the Department of Defense under Grant No. DAHC 15-70-G-14.

TABLE I
Materials losses (wt%)

Atmosphere	Air		Argon				Carbon dioxide		
Pressure (psig)	0	30	150	300	30	150	300	30	150
LiGaO₂*									
Melt	3.40	4.41	2.54	2.46	2.71	0.59	—	—	—
Crucible (1r)	4.19	0.08	0.08	0.07	0.36	0.48	2.10	—	—
Y₃Ga₅O₁₂**									
Melt	22.94	18.01	11.32	8.46	3.20	—	—	—	—
Crucible (1r)	10.35	0.16	0.15	0.15	1.73	—	—	—	—

* After 3 hr at 1610-1615 °C.

** After 3 hr at 1770-1775 °C.

material because it has a relatively low melting point (801 °C), is compatible with a platinum crucible, has a reasonable vapor pressure, is readily available in high purity levels, and requires no special handling procedure or environment when melted.

2. Experimental methods and results

Most of the evaporation rate measurements were made with the experimental arrangement shown in fig. 1. The sodium chloride melt was contained in a 1½-inch diameter by 1½-inch high platinum crucible. A zirconia plate supported the crucible and provided thermal insulation. A boron nitride pedestal served as an electrical insulator between the support shaft and the crucible. Radio-frequency induction heating of the

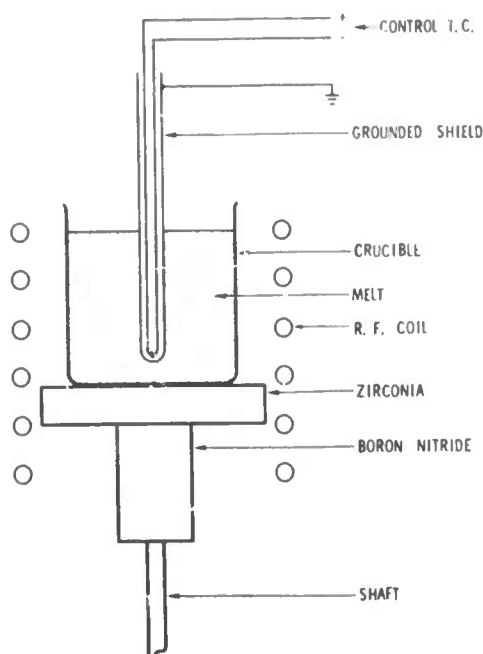


Fig. 1. Schematic of furnace assembly.

crucible was employed. Temperature was controlled by means of a Pt/Pt-10% Rh thermocouple located approximately $\frac{1}{8}$ -inch above the bottom of the crucible. The thermocouple leads passed vertically through the melt and were contained in a $\frac{1}{8}$ -inch diameter grounded sheath of stainless steel. This entire configuration was placed in a model MP crystal growing furnace manufactured by the Arthur D. Little Co. This apparatus constitutes an 8-inch diameter by 20-inch high water-cooled heat sink and NaCl vapor sink.

To determine evaporation rates the platinum crucible was charged with approximately 53 g of NaCl, which, when melted, filled the crucible to within $\frac{1}{8}$ -inch of the lip. To initiate an evaporation run, RF power was turned on and increased at a constant rate. When the salt had melted, the control thermocouple was lowered into position and the power then controlled automatically. The melt was held at the control temperature for six hours, which was sufficient to produce an evaporation loss large compared to start-up and shut-down losses. After six hours the control thermocouple was withdrawn and the power turned off. The evaporation loss was determined by weight change of crucible plus contents. The data were reproducible to within $\pm 2\%$ of the experimental value.

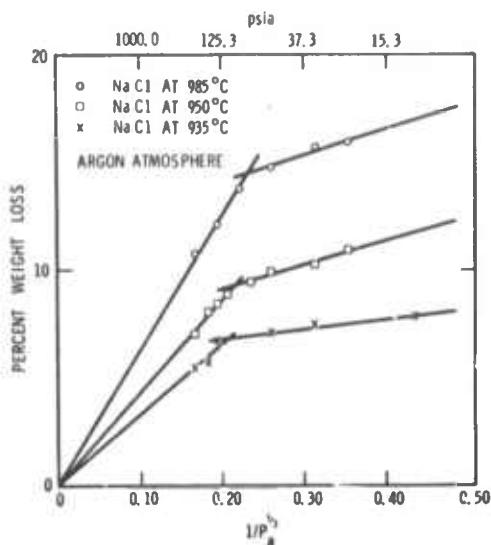


Fig. 2. Effect of pressure and temperature on evaporation rates.

In the first set of experiments the crucible was placed as shown in fig. 1. The evaporation rate was determined as a function of control temperature and pressure of argon gas. The results are shown in fig. 2. The evaporation rate increased with increasing temperature and decreasing pressure, as might be expected. Of the various elementary relationships examined, the best fit to the data was obtained with evaporation rates taken to be linear functions of $(1/P)^{1/2}$. Consequently, all data are shown plotted versus $(1/P)^{1/2}$.

The influence of the vertical position of the crucible relative to the RF coil was investigated using a CO_2 atmosphere. Fig. 3 shows that at low pressures the evaporation rate with the crucible fully within the coil

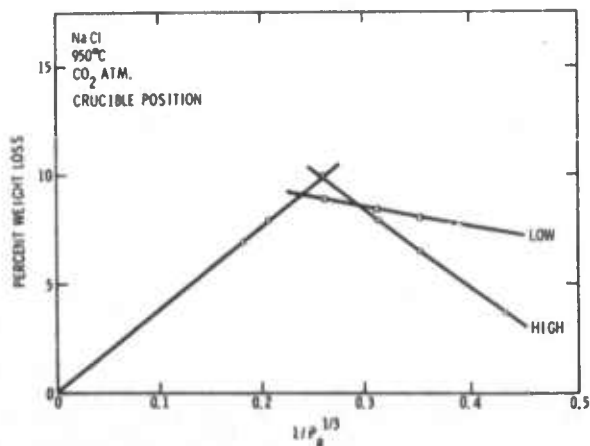


Fig. 3. Effect of vertical position of the crucible on evaporation rate versus pressure.

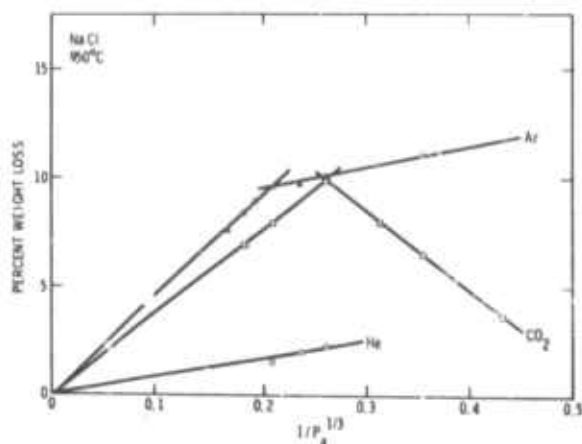


Fig. 4. Effect of atmosphere on evaporation rate versus pressure.

(low position) was greater than when the crucible was positioned as shown in fig. 1 (high position).

The influence of different gas atmospheres was investigated with the crucible in the high position. As shown in fig. 4, the evaporation rate was considerably higher for CO_2 and Ar than for He, although the rate for CO_2 fell rapidly at lower pressures. (Data for He could not be taken at lower pressures because of arcing from the RF coil to the crucible and furnace chamber walls.)

The effect of stirring was studied by use of a crucible with helical vanes welded on the interior. Fig. 5 shows that with an argon atmosphere the evaporation rate was higher when the crucible was rotated to produce stirring.

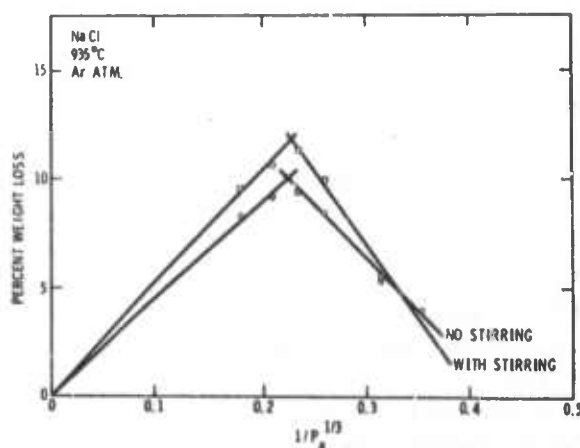


Fig. 5. Effect of melt stirring on evaporation rate versus pressure.

To obtain data at lower pressures a thermogravimetric apparatus was employed. In this apparatus a 1-inch diameter by $\frac{3}{4}$ -inch high platinum crucible was heated by convection and radiation from the hot wall of a vertical $1\frac{1}{2}$ -inch ID by 18-inch long alumina tube with a 13-inch hot zone. The crucible was located within a 2-inch region where the vertical temperature gradient was less than $0.5^\circ/\text{inch}$. The melt initially weighed 9.14 g and had a surface area of 4.74 cm^2 . The results are shown in fig. 6. Below 4 psia the evaporation rate varied as $1/P$.

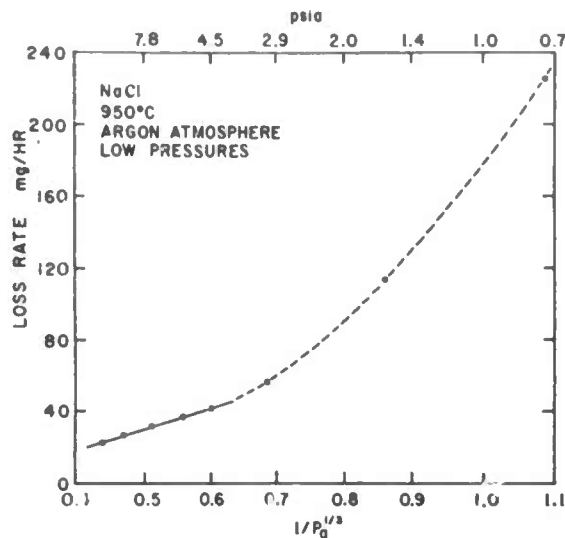


Fig. 6. Effect of pressure between 9.0 and 0.91 psia on evaporation rate. Dashed line is a $1/P$ curve that passes through the low-pressure data points.

3. Theory and discussion

Evaporation of liquids by heating depends on both heat transfer and mass transfer processes which interact in complex ways. We will discuss primarily those processes likely to be important with the experimental conditions employed here.

Since there was no gas flow in the system, the mass transfer in the RF heated experiments took place by free convection. The driving force for free convection is density variation, caused primarily by temperature variations (since the vapor pressure p_v was much less than the total pressure P). The evaporation rate is given by

$$J = K(C_s - C_\infty), \quad (1)$$

where J is the number of moles evaporated per unit

area per unit time, C_s is the molar concentration at the melt surface, C_a is the concentration in the ambient gas, and K is the mass transfer coefficient. The heat transfer flux is similarly given by

$$q = h(T_s - T_a), \quad (2)$$

where T_s and T_a are temperatures at the melt surface and in the bulk gas, respectively, and h is the heat transfer coefficient. For a heated square horizontal plate facing up it has been shown^{10,11}) that in the turbulent range ($\text{GrPr} > 2 \times 10^7$)

$$hL/k = 0.14 (\text{GrPr})^{1/4}, \quad (3)$$

and

$$KL/D = 0.14 (\text{GrSc})^{1/4}, \quad (4)$$

where L is the width of the square, k is the mean value of thermal conductivity between surface and bulk gas, D is the mean diffusion coefficient for the evaporating specie, $\text{Pr} = c_p \mu / k$ is the Prandtl number, c_p is the mean heat capacity, μ is the mean viscosity, $\text{Sc} = \mu / \rho D$, ρ is the mean density, $\text{Gr} = L^3 g \rho (\rho_a - \rho_s) / \mu^2 = L^3 g \rho^2 \beta (T_s - T_a) / \mu^2$ is the Grashof number, g is the gravitational constant, ρ_a and ρ_s are gas densities in the bulk gas and at the melt surface, respectively, and $\beta = -(\partial \rho / \partial T) / \rho$ is the thermal densification coefficient. For laminar free convection ($10^5 < \text{GrPr} < 2 \times 10^7$) over a heated square plate^{10, 11})

$$hL/k = 0.54 (\text{GrPr})^{1/4}, \quad (5)$$

and

$$KL/D = 0.54 (\text{GrSc})^{1/4}. \quad (6)$$

Within the pressure range investigated here, an appreciable pressure dependence is expected only for D , ρ , ρ_a , and ρ_s ¹²). Noting that D varies as $1/P$ and the densities as P , we predict that the evaporation rate should vary as $(1/P)^{1/4}$ for turbulent convection and as $(1/P)^{1/4}$ for laminar convection. Heat transfer should vary as $P^{1/4}$ for turbulent conditions and as $P^{1/4}$ for laminar. At high pressures, conditions should be turbulent and at low pressures laminar. Thus, it is tempting to attribute the break in the curves of fig. 2 to the turbulent-laminar transition. However, the pressure dependence for laminar convection is greater and, as a result, the slopes of the curves through the low pressure data would be expected to be greater than those for high pressures. Experimentally, the slopes were less on the low pressure legs.

At this point it is useful to perform some numerical calculations for argon at 110 psia, which is near the breaks in the curves of fig. 2. Properties are estimated¹¹⁻¹³) at a film temperature of 600 °C to be $\mu = 0.05$ centipoise, $\text{Pr} = 0.66$, $k = 9.3 \times 10^{-5}$ cal/°C cm sec, $D = 0.23$ cm²/sec (an alternate estimate of 0.1 cm²/sec has also been made), $\text{Sc} = 1.3$ (assuming NaCl molecules in gas). From the ideal gas law $\rho = MP/RT$ and $C_s = p_s/RT$, where M is molecular weight and R is the gas constant. Assuming the surface temperature T_s is 985 °C and the bulk gas temperature T_a is 100 °C, we calculate that $\rho = 4.2 \times 10^{-3}$ g/cm³, $\rho_a - \rho_s = 6.9 \times 10^{-3}$ g/cm³, and $C_s = 8.3 \times 10^{-8}$ mole/cm³. If we let $L = 3.8$ cm (the diameter of the crucible), then $\text{GrPr} = 4 \times 10^6$. This compares with the predicted laminar-turbulent transition at $\text{GrPr} = 4.5 \times 10^7$. Since the experimental geometry differed appreciably from a square plate, the difference may not be significant. The predicted evaporation rate is 5×10^{-5} g/sec [from eqs. (1) and (4)] as compared with the observed rate of 3.7×10^{-4} g/sec. Deviations between fig. 2 and expected behavior will be discussed further at a later point.

Fig. 2 also shows the dependence of evaporation rate on temperature. Eq. (1) indicates that the evaporation rate should be proportional to the vapor pressure which, in turn, depends on temperature¹³). Experimentally the evaporation rate is found to be very nearly proportional to the vapor pressure at the indicated temperature of the run in fig. 2. The data extrapolate to 0 at zero evaporation rate, indicating $C_a \approx 0$.

Fig. 3 shows that with CO₂ the evaporation rate drops at low pressures, especially with the crucible high in the RF coils. It is tempting to explain this observation on the basis of cooling of the surface by convective heat transport and expenditure of the latent heat of evaporation. Heat lost at the surface must be transported from the crucible walls where it is liberated. This required a temperature drop between the bottom of the crucible, where temperature is controlled, and the surface of the melt, where evaporation takes place.

The convective heat transport from the melt surface under the conditions previously given is found from eqs. (2) and (3) to be 3.87 cal/sec. The rate of latent heat liberation for 10% weight loss is calculated to be 0.17 cal/sec from the latent heat of 40810 cal/mole

for NaCl^{13}). The temperature drop ΔT in the melt is found by substituting this value into eqs. (2) and (5) along with the appropriate properties for molten salt¹⁴): $\mu = 0.82$ centipoise, $\rho = 1.475 \text{ g/cm}^3$, $k = 0.01 \text{ cal/}^\circ\text{C cm sec}$, $\beta = 3.7 \times 10^{-4} \text{ }^\circ\text{C}^{-1}$, $c_p = 16 \text{ cal/}^\circ\text{C mole}$, and $\text{Pr} = 0.25$. The temperature drop is calculated to be $5.4 \text{ }^\circ\text{C}$, which corresponds to an 11% drop in vapor pressure and evaporation rate. This value is very near the results shown in fig. 5. However, the convective heat loss from the surface diminishes as pressure decreases, which would predict a continually smaller difference between high and low position as pressure decreases (fig. 3). This discrepancy will be discussed later.

Fig. 4 shows data for different gases. The data for high pressures are easily explained by the drop in surface temperature caused by thermal losses and latent heat liberation. The thermal conductivity for CO_2 is 60% greater than for Ar while that for He is 7.4 times as large. The low pressure data for Ar and CO_2 are another matter. The only major difference in physical properties between CO_2 and Ar is infrared absorption. CO_2 absorbs heavily in the IR while Ar and He do not. It is necessary, therefore, to consider the effect of radiant heat transfer.

The platinum crucible not only loses heat by convection and conduction but also by radiation into the gas on the outside and radiation into the melt on the inside. For a refractive index of 1.53 for NaCl^{15}) and an emissivity ϵ of unity, the maximum amount of radiant energy is emitted at $1.62 \text{ } \mu\text{m}^{16}$), with 9.33% of the radiation emitted below $6.2 \text{ } \mu\text{m}$. For $\epsilon = 1$ the radiant heat flux at $950 \text{ }^\circ\text{C}$ is $3.04 \text{ cal/sec cm}^2$, which is about 10 times the convective heat flux. The IR absorption in this wavelength region is negligible for solid NaCl at room temperature, and it is assumed to be negligible for molten NaCl . Thus, when Ar and He are above the crucible, the radiation passes practically unhindered to the chamber walls. CO_2 absorbs the radiation, however, and is heated. This effectively increases T_g , lowers Gr , decreases the convection and decreases the evaporation rate. This explains part of the difference between Ar and CO_2 but not the increasing divergence as P decreases.

To explain the above anomalies it is necessary to invoke some other mechanism. It is proposed that condensation of NaCl occurs a short distance from the

melt surface. Consider the changes in temperature and NaCl concentration as distance from the melt increases. Both decrease at nearly the same rate. However, the equilibrium vapor pressure, being strongly dependent on temperature, decreases much more rapidly than temperature. Thus, the vapor a short distance from the interface is supersaturated. One expects NaCl melt, or more probably crystals, to nucleate and form a fine mist. Under turbulent conditions this mist would be swept away. The evaporation rate would be accelerated if nucleation occurred within the stagnant film (of thickness $\delta_h = k/h = 1.59 \text{ mm}$ at 110 psia) because the NaCl partial pressure drops when nucleation occurs and increases the concentration gradient at the melt surface. This provides a possible explanation for the experimental rate (fig. 2) being much higher than the predicted rate. Unfortunately, the theory for mass transport under such conditions apparently has not yet been worked out quantitatively.

Under laminar flow conditions, at low pressures, some of the condensed NaCl will find its way back into the melt — i.e., reflux occurs. Because the refluxing would increase heat transfer, the surface temperature would be lowered to cause an additional reduction in net evaporation rate. As pressure is decreased, convection is decreased and it becomes increasingly easy for the NaCl particles to fall back or be carried back into the melt. A vortex of dense particulate material can be clearly seen immediately above the melt at relatively low pressures. Material is transported upward along the outside of the vortex (near the crucible walls) and downward toward the melt in the center. Very little material leaves the vortex (in the form of thin streamers) at low pressures. As pressure over the melt is increased, the vortex gradually disintegrates, with the formation of numerous localized turbulent regions. Disintegration of the vortex is accompanied by a substantial increase in particulate material carried away from the melt (in the form of dense streamers). It appears likely that the vortex plays a major role in producing reflux action and accounts for the unexpectedly low evaporation rates associated with slope reduction or reversal of some of the evaporation curves at low pressures.

Returning to fig. 3, the difference in slope between the high position and low position data at low pressures is now better understood. In the low position

the crucible walls above the melt are much hotter than when the crucible is located in the high position. The CO_2 plus condensed NaCl is thus more effectively heated in the low position, which reduces the reflux action. Returning to fig. 4, the combined effect of IR scattering by NaCl particles and IR absorption by CO_2 is to cause a much lower temperature gradient with CO_2 than with Ar. The lower temperature drop increases the reflux action, permitting the NaCl particles to be more easily carried back into the melt.

In fig. 5 the difference between the two curves is now understood to have been caused by the larger drop in surface temperature without stirring. The decrease in rate at low pressures is probably due to the reflux mechanism.

The experimental apparatus used to take the data of fig. 6 differed primarily in that heating of the crucible occurred by conduction and convection from the tube walls. Thus, the temperature gradient at the melt surface was much lower than with induction heating. If the thermal conditions were the same, a film thickness of about 5 cm would be predicted at 0.7 psia. With the lower gradient the thickness would be even larger. In other words convective transport is negligible at very low pressures, especially in this apparatus. Evaporation takes place solely by diffusion and obeys the law

$$J = D(C_s - C_w)/W, \quad (7)$$

where W is distance from evaporating to condensing surfaces and C_w is the concentration at the wall. Using data for 0.73 psia of 225 mg/hr evaporation rate, $D = 48 \text{ cm}^2/\text{sec}$, $C_s = 5.06 \times 10^{-8} \text{ moles/cm}^3$, $C_w = 1.6 \times 10^{-9} \text{ moles/cm}^3$, and a surface area of 4.74 cm^2 , we calculate $W = 10.4 \text{ cm}$, which is a reasonable value. It should be noted that where the total pressure decreased to the order of the vapor pressure, further complications would arise. The net gas flow from the surface would become appreciable and give rise to a streaming mass transport flux of the same order as the diffusive and convective fluxes^{11,17}). This accelerates evaporation significantly. In addition, the influence of the vapor on gas density variation must be accounted for in free convection calculations. When the total pressure is equal to or less than the vapor pressure, the evaporation rate becomes limited by heat transfer and by interfacial kinetics. The limiting rate of evaporation for NaCl at 967 °C is found from the Langmuir equa-

tion to be $6.34 \times 10^{-2} \text{ g/cm}^2 \text{ sec}$, as compared to the maximum rate observed at 0.74 psia of $1.3 \times 10^{-5} \text{ g/cm}^2 \text{ sec}$.

If evaporation of a single component from a multi-component melt is considered, the resistance to mass transport in the melt as well as in the gas must be taken into account. If the two-film theory is used then the rate of evaporation may be expressed as

$$J = K_{0g}(mC_l - C_g), \quad (8)$$

where m is the ratio of the concentration in the gas to that in the liquid at the interface (at equilibrium), C_l is the concentration of the evaporating component in the bulk liquid, C_g is its concentration in the bulk gas, and K_{0g} is the overall gas mass transfer coefficient. K_{0g} is related to the mass transfer coefficient in the liquid K_l and that in the gas K_g by

$$K_{0g} = \frac{1}{1/K_g + m/K_l}, \quad (9)$$

which constitutes adding of resistances to mass transfer. Under the experimental conditions employed here these two resistances are of the same order of magnitude and must both be considered. Roughly speaking the liquid transport resistance may only be ignored if the vapor pressure of the pure evaporating component is very much less than the total pressure.

4. Conclusions

Evaporation from heated melts is a complex process. The evaporation rate is influenced not only by temperature and pressure but also by the mode of heating, by the ambient gas, by geometry, and so forth. The observation that evaporation rate for inductively-heated sodium chloride melts is a linear function of $(1/P)^{1/2}$ is interpreted to result from mass transport by turbulent free convection. A change in slope as pressure is decreased appears to correspond to the onset of laminar flow conditions. Low vaporization rates and decreasing rates with decreasing pressure at low pressures can be explained on the basis of a reflux process.

Acknowledgements

The authors wish to thank Michael Bencoe and Luis Lucero for technical assistance and D. A. Northrop for taking the data at pressures below one atmosphere.

References

- 1) P. F. Weller, J. Electrochem. Soc. **113** (1966) 90.
- 2) J. F. Miller, J. W. Moody and R. C. Himes, Trans. Met. Soc. AIME **239** (1957) 342.
- 3) J. D. Broder and G. A. Wolff, J. Electrochem. Soc. **110** (1963) 1150.
- 4) R. J. Baughman and R. A. Lefever, Mater. Res. Bull. **4** (1969) 721.
- 5) R. Sirrine, J. Electrochem. Soc. **111** (1964) 750.
- 6) Arthur D. Little, Inc., Acorn Park, Cambridge, Mass. 02140.
- 7) Metals Research Instrument Corp., 40 Robert Pitt Dr., Monsey, New York 10952.
- 8) R. J. Baughman and R. A. Lefever, Mater. Res. Bull. **3** (1968) 457.
- 9) R. J. Baughman and R. A. Lefever, Crystal Syntheses **1** (in press).
- 10) W. H. McAdams, *Heat Transmission*, 3rd ed. (McGraw-Hill, New York, 1954).
- 11) W. R. Wilcox, in: *Preparation and Properties of Solid State Materials*, Vol. 1, Ed. R. A. Lefever (Dekker, New York, in press).
- 12) R. C. Reid and T. K. Sherwood, *The Properties of Gases and Liquids* (McGraw-Hill, New York, 1958).
- 13) R. H. Perry, C. H. Chilton and S. D. Kirkpatrick, Eds., *Chemical Engineers' Handbook*, 4th ed. (McGraw-Hill, New York, 1963).
- 14) M. Blander, Ed., *Molten Salt Chemistry* (Interscience/Wiley, New York, 1964).
- 15) R. A. Smith, F. E. Jones and R. P. Chasmar, *The Detection and Measurement of Infra-Red Radiation*, 2nd ed. (Clarendon Press, Oxford, 1968).
- 16) E. M. Sparrow and R. D. Cess, *Radiation Heat Transfer* (Brooks/Cole, Belmont, Calif., 1966).
- 17) W. R. Wilcox, Mater. Res. Bull. **4** (1969) 265.

D

Boiling and Convection during Movement of Solvent Inclusions in Crystals

Kuo-Hung Chen and William R. Wilcox*

Chemical Engineering and Materials Science Departments, University of Southern California, Los Angeles, Calif. 90007

Boiling occurred in solvent inclusions in alkali halide crystals when the temperature was sufficiently high. Such boiling reduced the rate of movement in a temperature gradient. The rate of movement without boiling increased as the temperature increased and as the temperature gradient increased. It was generally higher with a horizontal temperature gradient than with a vertical gradient, indicating that free convection played a role in movement kinetics. Usually the hot side of the inclusion moved more rapidly than the cold side, causing the inclusion to lengthen and eventually to break up. The presence of gas bubbles or boiling usually caused the cold side to move in the opposite direction.

During crystallization from solution, some of the solution is nearly always trapped in the crystal as small inclusions. It has been shown that these solvent inclusions can be moved through the crystals by application of a temperature gradient (Anthony and Cline, 1971; Wilcox, 1968) or a centrifugal field (Anthony and Cline, 1970; Wilcox, 1972a; Wilcox and Shlichta, 1971). When a temperature gradient is applied, the inclusion normally moves toward the heat source. However, the presence of a gas bubble may cause all or part of the inclusion to move in the opposite direction (Anthony and Cline, 1972; Wilcox, 1969a,b).

The purpose of the present work was to investigate the influence of gravity, temperature, and solvent composition on the movement of inclusions in a temperature gradient. During the course of the experiments it was discovered that boiling can occur if the temperature is increased sufficiently. Thus the influence of boiling on movement of inclusions was also investigated.

These results have application to the drying of chemicals, to removal of inclusions from solution-grown single crystals (Chase and Wilcox, 1966), to interpreting the geological significance of inclusions (*e.g.*, Roedder, 1966, 1972) and to storage of radioactive waste materials in abandoned salt mines (Anthony and Cline, 1972).

Experimental Section

Inclusions were prepared in NaCl, KCl, and KI as follows. Melt-grown crystals from the Harshaw Chemical Co. were cleaned and drilled with ~ 0.5 -mm holes. These were filled with solvent and placed in saturated solutions so that growth occurred and sealed in the solvent. Both water and 50 vol % ethyl alcohol-water were used as solvents. Such samples were then placed between a brass heating plate and a cooling plate so that temperature gradients were perpendicular to the axes of the cylindrical inclusions. The exposed sides of the crystal were insulated with microscope slides and glass wool. The

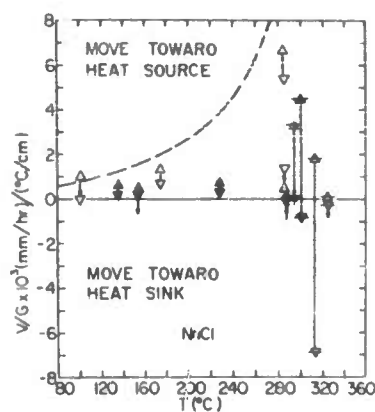


Figure 1. Rate of movement of solvent inclusions in NaCl-imposed temperature gradient. T is average temperature within inclusion: Δ , hot side of inclusion; ∇ , cold side of inclusion; \triangle , boiling taking place; \blacktriangle , 50 vol % alcohol-water solvent rather than water; arrow indicates direction of heat flow for vertical temperature gradient; ----, calculated for water as solvent from eq 5

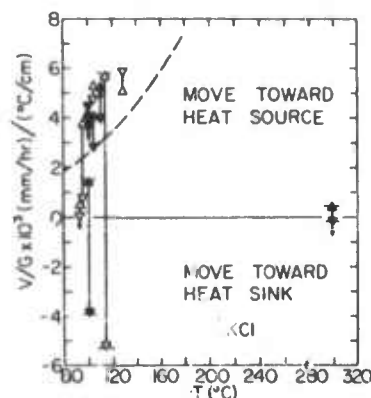


Figure 2. Rate of movement of solvent inclusions in KCl-imposed temperature gradient. Same notation as Figure 1, plus the following: Δ , air bubble present in inclusion

temperature of the heating and cooling plates was monitored with thermocouples while the inclusions were recorded by time-lapse photomicrography at 100X. The rate of movement was later measured from the movie film. Temperature gradients ranged from 61 to 435°C/cm. The movement rates of the two sides of the inclusion were rarely identical and in fact were sometimes of opposite sign.

Results

Experimental values of the movement rate V divided by the imposed temperature gradient G are shown in Figures 1, 2, and 3. Within experimental accuracy V appears to be proportional to G . Points representing the rates for the two sides of the inclusion are connected by a line. Arrows indicate the direction of heat flow, with the absence of an arrow signifying side heating. Horizontal lines indicate boiling, while a pair of tilted lines signifies the presence of an air bubble in the inclusion. Points for alcohol-water solvent are solid. It was found that each solvent inclusion possessed a fairly definite boiling point, as summarized in Table I.

Cline and Anthony (1972) observed boiling points of 420 and 395°C for water in NaCl and KCl. The inclusions were an order of magnitude smaller and the temperature gradient was near zero. Furthermore, our boiling point for water in KCl is

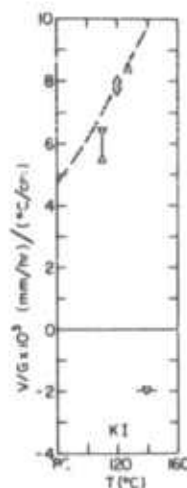


Figure 3. Rate of movement of aqueous inclusions in KI-imposed temperature gradient. Same notation as Figure 1

Table I. Inclusion Boiling Points

Crystal	Solvent	Bp, °C
NaCl	Water	331
NaCl	Water-alcohol	268
KCl	Water	249
KCl	Water-alcohol	209
KI	Water	137

below the minimum possible calculated by Cline and Anthony. A remarkable coincidence is that the change in weight fraction solubility (Landolt-Bornstein, 1962) between room temperature and our observed boiling point is about the same for NaCl, KCl, and KI; i.e., 12.8, 11.8, and 10.8%.

When boiling first occurred with side heating, the bubbles formed on the hot side of the inclusions and condensed on the cold side. This caused dissolution on the cold side with a movement rate of about 10X faster than that of the hot side (in the opposite direction). Projections formed in which the bubbles condensed, as shown in Figure 4. Soon, however, movement of the cold side nearly ceased, even though boiling continued. With top heating, the bubbles were produced on the top side of the inclusion and remained there. At first, upward movement of the top continued at several locations to form rough projections. Soon movement of both sides of the inclusion came to a virtual halt while boiling continued. Bubbles were much larger in KCl-H₂O than in NaCl-H₂O inclusions with top heating.

Air bubbles in KCl with both water and water-alcohol likewise caused the two sides of the inclusion to move in opposite directions, as observed previously (Anthony and Cline, 1972; Wilcox, 1969a). No essential difference in behavior was noted between water and water-alcohol solvents.

Theory

From the experimental results in Figures 1, 2, and 3, it appears that free convection plays a role in movement of 0.5-mm diameter inclusions. If we regard the inclusion as stationary, then there is a flux through the solid which must be equal to the solute flux through the inclusion, or mathematically

$$VC_o = V_{ci}C_i + K\left(\frac{GL}{m} - \frac{V}{a}\right) \quad (1)$$

where V is the movement rate, C_s and C_l are the solute concentration in solid and in liquid, V_{cl} is the crystallization flow (Wilcox, 1972b), F is the mass transfer coefficient between the hot side and the cold side of the inclusion, G is the temperature gradient across the inclusion, L is the width of the inclusion, and m is the slope of the liquids (solubility curve), $\partial T/\partial C$. The last term, V/a , is a correction for the concentration drop required to drive the interface kinetics of growth and especially dissolution. Solving for V we obtain for an anhydrous crystal

$$V = \frac{GL}{m} \left(\frac{C_s(1 - F_l)}{K} + \frac{1}{a} \right)^{-1} \quad (2)$$

where F_l is the volume fraction of salt in the inclusion. Note that GL/m is the driving force for movement, $C_s(1 - F_l)/K$ is the mass transfer resistance, and $1/a$ is the interface kinetics resistance. Thermal diffusion (Soret effect) and interface curvature effects (Anthony and Cline, 1971) have been neglected.

Since K and a are both unknown it is not possible to determine individual values from these experiments. In order to make some comparison of experiment with theory we examine the case of $a \rightarrow \infty$ (zero interface kinetic resistance) and $K = D/L$ (zero convection). We also assume that G is the same as the imposed temperature gradient. The thermal conductivity of the occluded solution is less than that of the crystal, which would tend to make G slightly larger than the imposed gradient. However, convection would have the reverse effect. Since solubility data are normally given in weight fractions w , we prefer to use

$$m_w = \partial T/\partial w = (\partial T/\partial C)(\partial C/\partial w) = \frac{mv_s M/M_s}{\{wv + (1 - w)v_s M/M_s\}^2} \quad (3)$$

where v and v_s are the partial molar volumes of the salt and the solvent in solution, and M and M_s are their molecular weights. Likewise we note that

$$F_l = \frac{wv}{wv + (1 - w)v_s M/M_s} \quad (4)$$

and that $C_s = \rho_s/M$, where ρ_s is the density of the crystal. Thus we find

$$\frac{v}{G} = \frac{DM}{\rho_s m_w (1 - w)[wv + (1 - w)v_s M/M_s]} \quad (5)$$

Curves calculated from this equation are shown in Figures 1-3. Values for the diffusion coefficient D were estimated by extrapolating lower temperature data from Landolt-Bornstein on a log D vs. $1/T$ plot, with log T/η as a guide (η is solution viscosity). It was assumed that the coefficient of expansion is about the same for crystal and solute and solvent in solution, so that room temperature values of ρ_s , v , and v_s were used. The predicted movement rates increase rapidly with temperature, since D and w increase and m decreases as temperature increases.

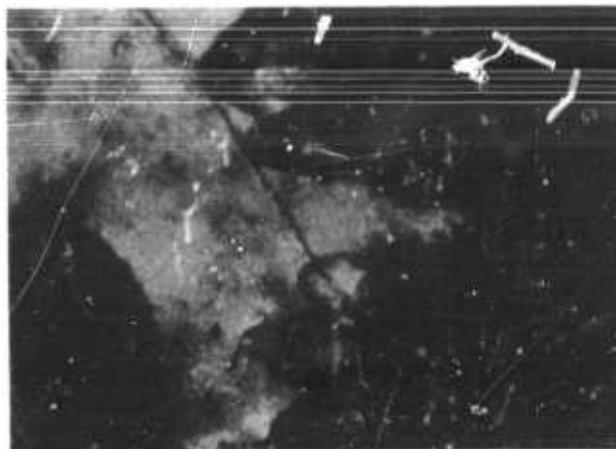


Figure 4. Boiling in KI. Frame from motion picture

Discussion and Conclusions

With only one exception, movement rates were higher when the temperature gradient was horizontal than when it was vertical. A reasonable explanation is that in an enclosed space free convection is greater with a horizontal density gradient. The density gradient is approximately proportional to $\beta + \alpha/m_w$ (where $\beta = (\partial \rho/\partial T)_w < 0$ and $\alpha = (\partial \rho/\partial w)_T > 0$). This is not exact since $Pr \neq Sc$. For KI and KCl, $\beta + \alpha/m_w$ is always positive, so that concentration densification dominates—the solution on the hot side of the inclusion is most dense. For NaCl, $\beta + \alpha/m_w$ is negative below about 250°C, which means that the solution on the cold side is most dense.

Movement rates are generally lower than predicted from eq 5, indicating considerable interface kinetics resistance. Several points for KCl are higher, however, indicating that interface kinetics may be more rapid for KCl.

Alcohol additions reduced the movement rate of inclusions in NaCl but had no appreciable effect on those in KCl. Using available data, eq 5 predicts that alcohol should actually increase the rate in NaCl slightly. Thus one is forced to attribute the reduction to retardation of the interface kinetics.

Acknowledgment

This research was supported by the Advanced Research Projects Agency of the Department of Defense under Grant No. DAH15-71-G6.

Literature Cited

- Anthony, T. R., Cline, H. E., *Phil. Mag.* **22**, 893 (1970).
- Anthony, T. R., Cline, H. E., *J. Appl. Phys.* **42**, 338 (1971).
- Anthony, T. R., Cline, H. E., *Acta Met.* **20**, 247 (1972).
- Chase, A. B., Wilcox, W. R., *J. Amer. Ceram. Soc.* **49**, 460 (1966).
- Cline, H. E., Anthony, T. R., *Phil. Mag.* in press (1972).
- Landolt, H. H., Ed., "Landolt-Bornstein Zahlenwerte und Funktionen," 6th ed, Springer-Verlag, Berlin, 1932.
- Roedder, E., *Econ. Geol.* **66**, 777 (1966).
- Roedder, E., in "Proceedings of IAGOD-IMA Meeting," Tokyo, Kyoto, Aug-Sept 1970, 1972.
- Wilcox, W. R., *Ind. Eng. Chem.* **60** (3), 13 (1968).
- Wilcox, W. R., *Ind. Eng. Chem.* **61** (3), 76 (1969a).
- Wilcox, W. R., *Sep. Sci.* **4**, 95 (1969b).
- Wilcox, W. R., *J. Cryst. Growth* **13/14**, 787 (1972a).
- Wilcox, W. R., *J. Cryst. Growth* **12**, 93 (1972b).
- Wilcox, W. R., Shlichta, P. J., *J. Appl. Phys.* **42**, 1823 (1971).

RECEIVED for review January 28, 1972

ACCEPTED July 13, 1972

E

MOVEMENT OF LIQUID INCLUSIONS BY CENTRIFUGATION

WILLIAM R. WILCOX

Chemical Engineering and Materials Science Departments, University of Southern California, Los Angeles, California 90007, U.S.A.

A theory is developed for movement of solvent inclusions in crystals by a centrifugal field. It is necessary to account for the electric field generated by the differential migration rates of the different ions. The theory predicts a centripetal movement rate which increases as the solubility increases, which usually means as the operating temperature increases. Experimentally, the rate of movement of aqueous inclusions in potassium iodide decreases with increasing temperature and becomes centrifugal above about 30 °C. The origin of this discrepancy between experiment and theory is presently unknown.

When crystals grow from solution they almost invariably trap some of the solution as inclusions. One method to remove these inclusions is to place the crystal in a temperature gradient, which causes the inclusions to move¹). Recent experiments have shown that a centrifugal field can similarly cause the inclusions to move through the crystal^{2,3}). Comparison of the rates of movement with theoretical expressions yields information on the interfacial kinetics of growth and dissolution.

The theoretical expressions for inclusion movement in the ultracentrifuge are given in refs. 2 and 3 as, respectively

$$V = \frac{\omega^2 r D}{RT} \left\{ \frac{\frac{M - v_f \rho_f}{v} + \Delta_c^f v \rho_f}{\left(\frac{C_c}{C_f} - \frac{\rho_c}{\rho_{cf}} \right) + \frac{D}{LC_f} \left(\frac{1}{\mu_L} + \frac{1}{\mu_0} \right)} \right\}, \quad (1)$$

$$V = \frac{C_f D}{(C_c - C_f)(RT)} [(M - \rho_f v_c)g - K/L], \quad (2)$$

where ω is the angular rotation rate of the sample, r is the radial position of the inclusion, g is the acceleration field at the inclusion ($= \omega^2 r$), D is the diffusion coefficient, R is the gas constant, T is the absolute temperature, C_f is the concentration of crystalline material in the inclusion (solubility), C_c is the solute concentration in the crystal, M is the molecular weight of the same species for which D and C apply, ρ_f and ρ_c are fluid and crystal densities, ρ_{cf} is the density the crystal would have if its components possessed their partial molal

volumes in the solution, $\Delta_c^f v$ is the change of partial molal volume upon solution, v_c is the molal volume of the solid ($= v_f - \Delta_c^f v$), v_f is the partial molal volume in the fluid, v is the number of ions into which each molecule of solute dissociates in solution ($= 2$ for alkali halides in water), L is the length of the inclusion, and μ_L , μ_0 and K are all corrections for finite interface kinetics. It may not be immediately obvious, but these expressions are nearly identical for infinite interface attachment kinetics ($K = 0$, $\mu_L = \mu_0 = \infty$). Nevertheless, both equations are incorrect. The correct derivation is given below. It is seen that the error in eq. (2) arose from neglecting dissociation into ions, while in eq. (1) dissociation was considered only in the sedimentation flux (first term in the numerator) and neglected in the diffusion flux (second term in the numerator).

When an ionized solute undergoes any form of mass transfer, the different ions tend to migrate at different rates. This generates an electric field which in turn influences the migration of the charged ions. Thus we must consider separately the migration of the different ions and connect the migration rates by the electric field and the net fluxes. The net flux of ion i into the solid is equal to the convective flux in the liquid plus the migration due to the gradient of electrochemical potential, η_{fi} , or

$$VC_{fi} = VC_{fi} \frac{\rho_c}{\rho_{cf}} + B_i C_{fi} \frac{\Delta \eta_{fi}}{L}, \quad (3)$$

where B_i is the mobility and ρ_c/ρ_{cf} represents the

change in convective flow in the inclusion from that in the solid due to the partial molal volume differences⁴). The change in electrochemical potential in the liquid across the inclusion is equal to the change in the crystal minus the energy necessary to drive interfacial processes, $\Delta\eta_{ki}$, or

$$\frac{\Delta\eta_i}{L} = \frac{\Delta\eta_{ci} - \Delta\eta_k}{L} = (M_i - \rho_i v_{ci})g + \frac{z_i F \Delta\phi}{L} - \frac{\Delta\eta_{ki}}{L}, \quad (4)$$

where z_i is the charge on the i th ion and F is the Faraday constant. Strain effects in the solid are neglected for the simple reason that we are not certain how to take them into account.

For convenience we consider a binary solute $(S_1)_{v_1}(S_2)_{v_2}$ which dissociates completely in the solvent to $v_1 S^{z_1}$ and $v_2 S^{z_2}$. Since the solid must be stoichiometric, the liquid is likewise stoichiometric, so that

$$C = C_1/v_1 = C_2/v_2. \quad (5)$$

Substituting eqs. (4) and (5) into eq. (3) and writing the result for S^{z_1} and S^{z_2} we find that

$$\begin{aligned} \frac{\Delta\phi}{L} = & \left\{ B_2 \left[(M_2 - \rho_i v_{c2})g - \frac{\Delta\eta_{k2}}{L} \right] \right. \\ & \left. - B_1 \left[(M_1 - \rho_i v_{c1})g - \frac{\Delta\eta_{k1}}{L} \right] \right\} \\ & \times [F(B_1 z_1 - B_2 z_2)]^{-1}. \end{aligned} \quad (6)$$

and

$$V = \left\{ z_1 \left[(M_2 - \rho_i v_{c2})g - \frac{\Delta\eta_{k2}}{L} \right] \right.$$

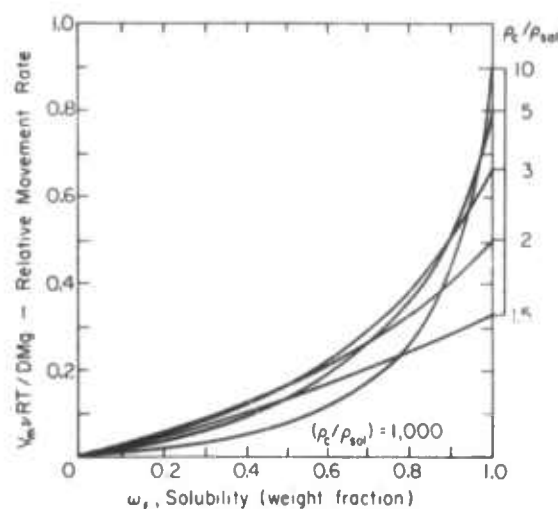


Fig. 1. Relative maximum inclusion movement rate as a function of solubility and relative densities of crystal and solvent, according to (approximate) eq. (20).

$$\begin{aligned} & - z_2 \left[(M_1 - \rho_i v_{c1})g - \frac{\Delta\eta_{k1}}{L} \right] \\ & \times \left[\left(\frac{C_c}{C_i} - \frac{\rho_c}{\rho_{ci}} \right) \left(\frac{z_1}{B_2} - \frac{z_2}{B_1} \right) \right]^{-1}. \end{aligned} \quad (7)$$

This may be made more useful by noting that

$$v = v_1 + v_2, \quad (8)$$

$$v_1 z_1 = -v_2 z_2, \quad (9)$$

$$M = v_1 M_1 + v_2 M_2, \quad (10)$$

$$v_c = v_1 v_{c1} + v_2 v_{c2}, \quad (11)$$

TABLE I
Inclusion movement rates (centripetal)

Crystal	M	ρ_c (g/cm ³)	T (°C)	w_i	v_i (cm ³ /m)	$D \times 10^5$ (cm ² /sec)	$\frac{\partial \log \gamma}{\partial \log C}$	g	V (mm/hr)		Exp. Ref.
									Calc.	Exp.	
AgNO ₃	170	4.35	20	0.687	32.9	(1)	-0.503	210,000	0.14		
KCl	75	1.98	20	0.256	30.9	1.7	-0.164	53,600	0.0042	≤0.0018	3
KCl	75	1.98	40	0.287	(30.9)	(2.6)	(-0.164)	210,000	0.028	0.022	2
KBr	119	2.75	20	0.394	37.7	1.8	-0.099	210,000	0.043		
KI	166	3.13	5	0.567	(47.9)	(1.4)	(-0.065)	144,000	0.05	0.05	2
KI	166	3.13	24.3	0.597	47.9	2.5	-0.065	210,000	0.14	0.06	2
KI	166	3.13	40	0.615	(47.9)	3.5	(-0.065)	210,000	0.19	-0.06	2
NH ₄ Cl	54	1.53	20	0.272	39.2	2	(-0.08)	210,000	0.013		
NaCl	59	2.17	20	0.264	21.2	1.4	-0.055	210,000	0.0081		
PbI ₂	461	6.16	20	0.001	(63.7)	(1)	(-0.01)	210,000	0.00006		
Pb(NO ₃) ₂	331	4.53	20	0.343	55.7	(1)	(-0.04)	210,000	0.028		
Sucrose	342	1.58	20	0.670	215	0.15	(0)	210,000	0.031		
Urea	60	1.32	20	0.517	44.2	1.1	(0)	210,000	0.020		

Data from refs. 8-10. Values in parentheses are author's estimates.

$$\Delta\eta_k \equiv K = v_1\Delta\eta_{k1} + v_2\Delta\eta_{k2}, \quad (12) \quad \text{equation}$$

and that the conventional tabulated diffusion coefficient may be written as^{5,6)}

$$D = \left[\frac{1}{z_1} - \frac{1}{z_2} \right] \left[1 + \left(\frac{\partial \ln \gamma}{\partial \ln C} \right)_{T,P} \right] RT \times \left[\frac{1}{B_1 z_1} - \frac{1}{B_2 z_2} \right]^{-1} \quad (13)$$

$$= z_1 v \left[1 + \left(\frac{\partial \ln \gamma}{\partial \ln C} \right)_{T,P} \right] RT \times \left\{ v_2 \left[\frac{z_1}{B_2} - \frac{z_2}{B_1} \right] \right\}^{-1}.$$

Substituting eqs. (9)–(13), eq. (7) becomes

$$V = D[(M - \rho_f v_c)g - \Delta\eta_k/L] \times \left\{ vRT \left(\frac{C_c}{C_f} - \frac{\rho_c}{\rho_{cf}} \right) \left[1 + \left(\frac{\partial \ln \gamma}{\partial \ln C} \right)_{T,P} \right] \right\}^{-1}. \quad (14)$$

When the crystal contains no solvent we find further that

$$\rho_c/\rho_{cf} = v_f/v_c, \quad (15)$$

$$C_c = 1/v_c = \rho_c/M, \quad (16)$$

and

$$C_f = F_f/v_f = w_f \rho_f/M, \quad (17)$$

where F_f and w_f are the volume fraction and weight fraction of solute in the occluded solution. With these, eq. (14) becomes

$$V = \frac{D[M(1 - \rho_f/\rho_c) - \Delta\eta_k/L]}{vRT(\rho_c/w_f \rho_f)(1 - F_f) \left[1 + \left(\frac{\partial \ln \gamma}{\partial \ln C} \right)_{T,P} \right]}. \quad (18)$$

In order to further elucidate the influences of solubility and crystal density we estimate the maximum movement rate V_m for an ideal solution with $v_c = v_f$ (no volume change on dissolution) and

$$\rho_f \approx \left(\frac{w_f}{\rho_c} + \frac{1 - w_f}{\rho_{sol}} \right)^{-1}, \quad (19)$$

where ρ_{sol} is the density of the solvent. This yields the

$$\frac{V_m v RT}{DMg} \approx \left(\frac{\rho_c}{\rho_{sol}} - 1 \right) \times \left[\frac{\rho_c}{\rho_{sol}} \left(1 + \frac{1 - w_f}{w_f} \frac{\rho_c}{\rho_{sol}} \right) \right]^{-1}. \quad (20)$$

which is plotted in fig. 1. Note that the movement rate is influenced mostly by the solubility, increasing as the solubility increases. For $0 \leq w_f \leq 0.5$, the movement rate is maximum for $\rho_c \approx 2\rho_{sol}$. For $0.5 \leq w_f \leq 0.9$ the maximum movement rate occurs for $\rho_c \approx 3\rho_{sol}$.

Experimental results are also shown in table 1 for KI and KCl. The fact that the experimental results are lower than the theoretical results indicates that finite interface kinetics reduced the rate. However, the data of ref. 2 on KI indicate both a decrease of travel rate with increasing temperature and a reversal to centrifugal travel above about 30 °C. These observations are contrary to the predictions of the present theory, i.e., a centripetal movement which increases in velocity as the temperature increases. Possible explanations might involve strain in the solid, free convection, or sedimentation across a gas bubble (similar to the results of ref. 7).

Acknowledgement

This research was supported by the Advanced Research Projects Agency of the U.S. Department of Defense under Grant No. DAHC 15-70-G-14.

References

- 1) W. R. Wilcox, *Ind. Eng. Chem.* **60** (1968) 13.
- 2) W. R. Wilcox and P. J. Shlichta, *J. Appl. Phys.* **42** (1971) 1823.
- 3) T. R. Anthony and H. E. Cline, *Phil. Mag.*, **22** (1970) 893.
- 4) W. R. Wilcox, *J. Crystal Growth*, in press.
- 5) Haskell, *Phys. Rev.* **21** (1908) 149.
- 6) J. R. Vinograd and J. W. McBain, *J. Am. Ceram. Soc.* **63** (1941) 2008.
- 7) W. R. Wilcox, *Ind. Eng. Chem.* **61** (1969) 76.
- 8) *International Critical Tables* (McGraw-Hill, New York, 1923).
- 9) Landolt-Börnstein, *Zahlenwerte und Funktionen*, 6th ed. Springer, Berlin, 1960).
- 10) *Handbook of Chemistry and Physics*, 51st ed. (Chemical Rubber Publ. Co., Cleveland, 1970–1971).



TWINNING OF POTASSIUM BROMIDE

WILLIAM R. WILCOX and ALBERTO LEON

University of Southern California, Los Angeles, California 90007, U.S.A.

Received 5 February 1970; revised manuscript received 26 October 1970

Large numbers of [211] penetration twins were formed when KBr reagent from one supplier was crystallized from water by evaporation. Most of these were butterfly twins while a few were interpenetrating cubes. Some lots of reagent from another supplier also produced twins while other lots did not. The non-twinning KBr was of an overall higher purity than that which produced twins. Twin formation appeared to be stimulated by Na^+ , Cl^- , and Thiazine Red R. Trace amounts of PbCl_2 pre-

vented twinning. The maximum yield of twins was obtained at intermediate growth rates. The interface surface was not a twin plane but varied widely in orientation. A model showed that the twin intersection forms a step much like that of a screw dislocation at the tip of the butterflies. Experimentally it was found that growth layers originated from this tip and later coalesced to form large waves which trapped tubular inclusions.

1. Introduction

The purpose of the present work was to describe solution grown [211] KBr twins and the conditions favoring their formation.

During the course of growing KBr crystals for inclusion-movement experiments¹⁾ an unusual twin formation was observed. Butterfly twins projected up from the bottom of the beaker during evaporation of saturated solutions made with reagent from the Mallinckrodt Chemical Works. Squat penetration twins and several other varieties were also occasionally observed, as illustrated in fig. 1. Measurement of the angles between the two portions of the twins showed the orientation to be [211].

A literature search revealed that similar twins were found in a collection of KBr crystals from Mallinckrodt in 1908²⁾. Although the twin orientation was not given, the sketch which was shown looks very much like our butterfly twins, only without the extra thin (and fragile) side wing usually found on our twins.

In 1934 Löffler reported on the formation of stocky penetration twins of NaCl and KCl during growth from aqueous solutions³⁾. Temperature changes produced no twins. NaCl twinned in the presence of MnCl_2 , LiCl , FeCl_3 , NaClO_3 and CdCl_2 . KCl formed twins in the presence of PbCl_2 , SrCl_2 , and NaCl but

not with LiCl , FeCl_3 , or MnCl_2 . A study of the influence of KClO_3 concentration on KCl twinning revealed a sharp maximum at 1 mg/cm^3 . Although the twins are reported as following the "bekannten Gesetz [111]", the observed angle between the twins was $131^\circ 49'$. This corresponds to a [211] twin, which should exhibit an angle of twice that between {100} and {211} or $2(65^\circ 54') = 131^\circ 48'$. In addition, Löffler's sole photograph of a NaCl twin looks like our stocky twins.

In 1948 Deicha reported the formation of small twins on larger crystals when NaCl was nucleated from supersaturated solutions⁴⁾. Occasionally twins occurred on each of three faces of the crystal. Deicha claims the twin orientation was probably [233]. Possibly these results are the consequence of polynucleation with oriented adhesion of nuclei onto established crystals, as observed by Shaskolsky and Shubnikov⁵⁾ with alum.

Ludemann has studied thin films of alkali halides deposited by evaporation and condensation⁶⁻⁸⁾. Electron diffraction revealed [111] twinning whenever the substrate temperature was below a critical temperature. The critical temperature appeared to depend only on the composition of deposited film and not on which alkali halide was employed as a substrate. The critical temperature was 80°C for KBr films on KBr substrates.

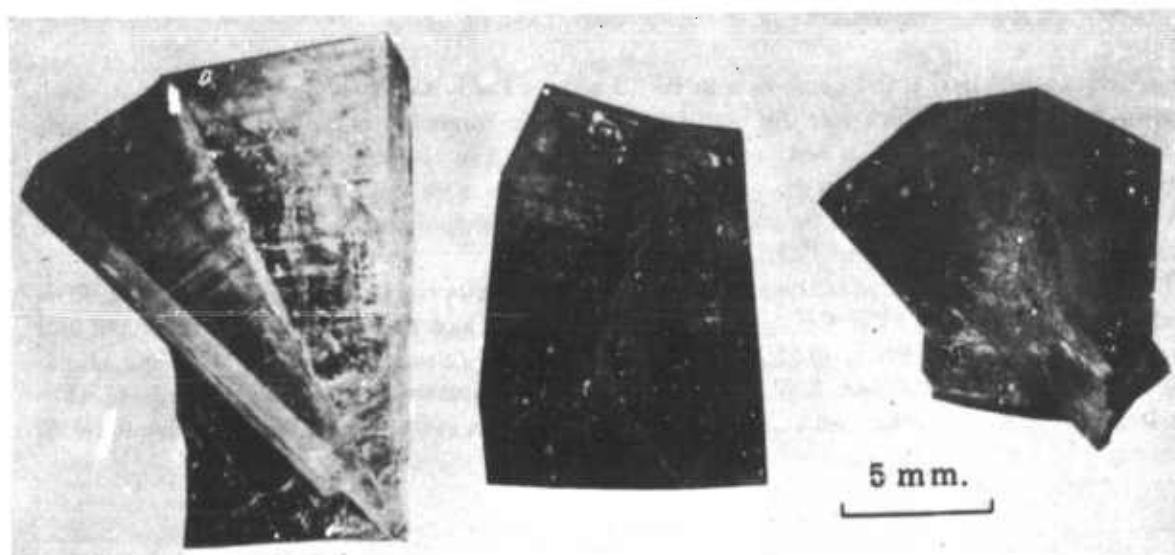


Fig. 1. KBr twins. Left to right: butterfly twin; tetragonal-winged twin, squat penetration twin.

2. Experimental

All experiments were performed at room temperature using saturated solutions in beakers covered with filter paper. Crystals grew on the bottoms of the beakers. Initial experiments were performed in 500 ml beakers. Twins were consistently observed with Mallinckrodt reagent but not with KBr from J. T. Baker Chemical Co. No difference was noted between purchased distilled water and laboratory deionized water as solvents. In any event the majority of the crystals were not twinned. The most spectacular twins were the butterfly twins that rapidly grew up from the bottom at rates up to 5 mm/day. In addition to the two thick wings of the twin, one half usually projected beyond the other to form a wing which was as thin as 30 μm . This thin wing was on the left side of approximately 75% of the twins (with the twin opening toward the viewer and the pointed end down), as in fig. 1. Although these thin wings appeared very planar, interference microscopy revealed ripples in the surface. When the butterfly twins lay sideways on the bottom of the beaker they did not grow so fast lengthwise but the wings were about as thick as when vertical. At the opposite end of the habit spectrum were squat penetration twins resembling very much the NaCl twin shown by Löffler²). These grew at about the same rate as the normal cubes beside them. Often one of the twins

would disappear as one half incorporated the other. Habits between the extremes of butterflies and penetration twins were also observed and rarely possessed the extra thin wing. Occasionally one of the major wings of a butterfly formed a hollowed-out tetragonal body, as if the wing had folded back on itself to produce a square cross section.

It is not clear whether the butterfly twins originated during nucleation or on a previously formed crystal since the bottom of the crystal was always imbedded in a mass of other crystals. Since multiple twinning was never observed, the authors' inclination is to believe that the twins originated in nucleation. No one phase of the evaporation seemed to favor twin formation, as twins were initiated both near the beginning and later in the experiments.

To investigate the effect of growth conditions on twinning, numerous experiments were performed using 50 ml beakers. The beakers were placed in a laboratory cabinet to yield an evaporation rate of 0.6 ml/day. The pH of the Mallinckrodt solution was 6.3 and the Baker solution 5.3. KOH and HBr were used to produce a pH of 5.0 in the Mallinckrodt solution and 9.8 in the Baker solution. No twins formed in either of these solutions.

The influence of impurities was investigated by making additions to a saturated solution of non-twinning Baker reagent. In several instances not all of

the added chemical dissolved and some had to be removed by filtration. A few thick butterfly twins resulted from addition of NaBr (1%), NaCl (1%) and Thiazine Red R (0.3%). (Percentages are weight % relative to KBr content of solutions). Squat penetration twins were produced by addition of KCl (< 5%), NaCl (1% and < 5%), and KI (1%). No twins resulted from additions of NaBr (< 5%), CaBr₂ (< 1%), K₂SO₄ (1%), FeCl₃ (0.3%), PbCl₂ (0.3%), KBrO₃ (0.3%), KF (1%), Naphthol Green B (0.3%), and Trypan Red (0.3%). On the other hand, addition of

5 ppm of PbCl₂ to the Mallinckrodt solution eliminated twin formation in 500 ml beakers in the open laboratory. This also caused the crystals to grow much smaller and more numerous, and greatly increased creeping of evaporating solution over the top of the beaker.

To investigate the influence of growth rates, 50 ml beakers were also placed in the open room and in a hood to produce evaporation rates of 1.2 and 3.0 ml/day. The non-twinning Baker reagent produced whiskers and plates at the higher rate, in addition to cubes.

TABLE 1
Manufacturers' analyses* of KBr in ppm

	Mallinckrodt (produced twins)	Baker Lot 35465 (no twinning)	Baker Lot 37363 (produced twins)
Barium	< 20	10	10
Bromate	≤ 10	1	10
Ca, Mg, R ₂ O ₃ (ppt)	< 50	1	20
Chloride	< 2000	1600	1000
Heavy metals (as Pb)	< 5	1	2
Iron	< 5	2	2
Nitrogen compounds (as N)	< 10	20	10
Sodium	< 200	20	40
Sulfate	< 50	10	30
Insoluble matter	< 50	5	30
pH of 5% solution	5.0-8.0	5.8	6.0

* "Maximum Limits" for Mallinckrodt, "Actual Analysis" for Baker.

TABLE 2
Analyses of KBr in ppm

Source Lab.*	M. Lot NMD (twinned)		B. Lot 35465 (no twins)		B. Lot 37363 (twinned)			M. Lot TKL (twinned)		Twins from B. Lot 37363		Twins from Early M. Lot	
	P*	G*	P	G	P	G	B*	B		P	G	B	
Al	N.D.**		N.D.		N.D.		20	5		N.D.		10	
Cr	59		13		73		70	< 50		41		< 50	
Cl	—	276	—	190	—	272	—	—		—	370	—	
Cu	< 0.8		< 0.8		1.1		N.D.	N.D.		0.82		N.D.	
Fe	< 8		< 8		8.1		N.D.	N.D.		9.9		N.D.	
Pb	< 60		< 60		< 60		N.D.	N.D.		< 60		N.D.	
Mg	2.4		1.9		5.3		20	7		3.1		30	
Mn	N.D.		N.D.		N.D.		50	50		N.D.		70	
Ni	N.D.		N.D.		N.D.		50	70		N.D.		70	
Si	N.D.		N.D.		N.D.		10	5		N.D.		5	
Na	55		45		73		100	< 100		74		< 100	
Other elements	N.D.		N.D.		N.D.		N.D.	N.D.		N.D.		N.D.	

* Laboratory performing analyses. P = Spectrochemical Analyses by Pacific Spectrochemical Laboratory, Inc., Los Angeles; B = Spectrochemical Analyses by J. T. Baker Chemical Co. through M. Zief; G = Neutron Activation Analysis by Gulf General Atomics, San Diego.

** N.D. = Not Detected.

The twin-producing Mallinckrodt reagent produced the maximum yield of twins at 1.2 ml/day, with mostly plates and needles produced at 3.0 ml/day.

Two new bottles of reagent were obtained from each supplier for chemical analyses. The suppliers' specifications are listed in table 1. Both lots of Mallinckrodt reagent produced twins during evaporation from covered 500 ml beakers in the open laboratory. One lot of Baker KBr produced twins while the other did not. Spectrochemical analyses were performed for cation impurities and neutron activation analyses for Cl^- , both for the reagents and for butterfly twins. The results shown in table 2 suggest that twinning is favored by a higher impurity content in the reagent.

3. Twinning model

A model of the KBr butterfly was made with a $\{211\}$ interface and is shown in figs. 2 and 3. Notice that if the twin interface surface is coherent (i.e., a $\{211\}$ twin plane), then the sum of the thicknesses of the wings on the left must be equal to the combined thickness of the wings on the right. Experimentally this has been found to be *not true*. The thick twinned wing on the left was

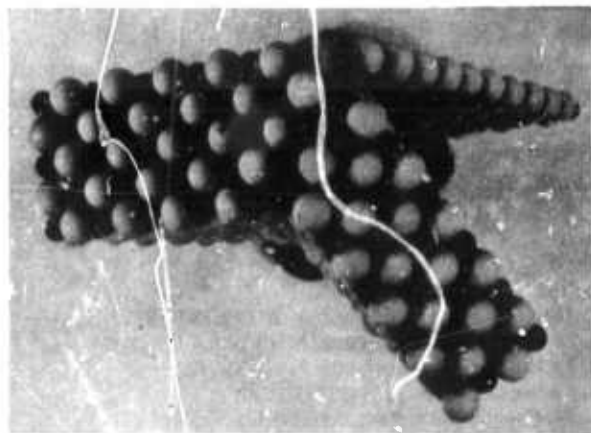


Fig. 2. Top view of model of KBr butterfly twin with major wings slightly separated at $\{211\}$ interface.

usually slightly thicker than the one on the right, but the ratio varied widely. This indicates that the twin interface surface did not follow a definite orientation. Breaking the twins apart revealed irregular surfaces, but it is not entirely certain that these represented the interfaces or were instead fracture surfaces (although

$\{100\}$ steps were not produced). By one definition⁹) twins possessing a non-coherent interface are called "penetration twins".

The $\{211\}$ planes from the two halves of the twin model do not fit together exactly. Many voids, smaller than Br^- , remain and form tubes. One may imagine

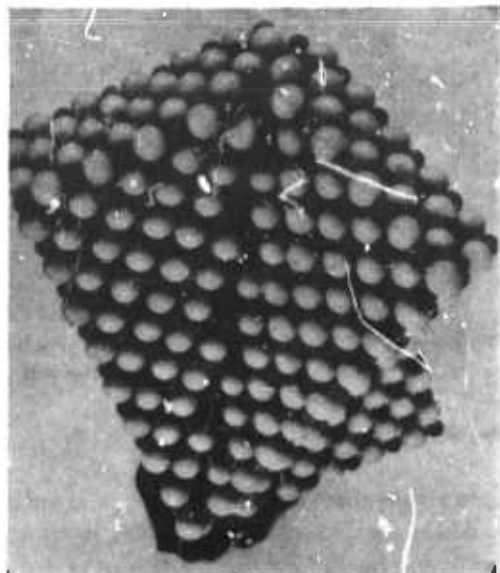


Fig. 3. Front view of model of KBr butterfly twin with major wings slightly separated to reveal $\{211\}$ interface.

that smaller ions might fill these voids and lower the interfacial energy. This is one possible explanation for the enhancement of twin formation by certain impurities.

If one examines the top peak of the twin model it is found that the two major $\{100\}$ planes that meet there are at an angle to one another and form a pseudo-screw dislocation. It is clear that this angled step can provide a continuous source of growth layers. Experimentally, growth waves were observed on the three narrow $\{100\}$ surfaces meeting at the peak and do appear to have been moving away from the peak, as expected. One of these waves on the thin wing is shown in fig. 4. Note that the wave was forming a tubular inclusion. Long inclusions were similarly found on the other two wings. Occasionally these would contain gas bubbles as well as solution. Very often the two large wings contained large flat inclusions interconnected with one another, i.e., the thick wings were often somewhat hollow.

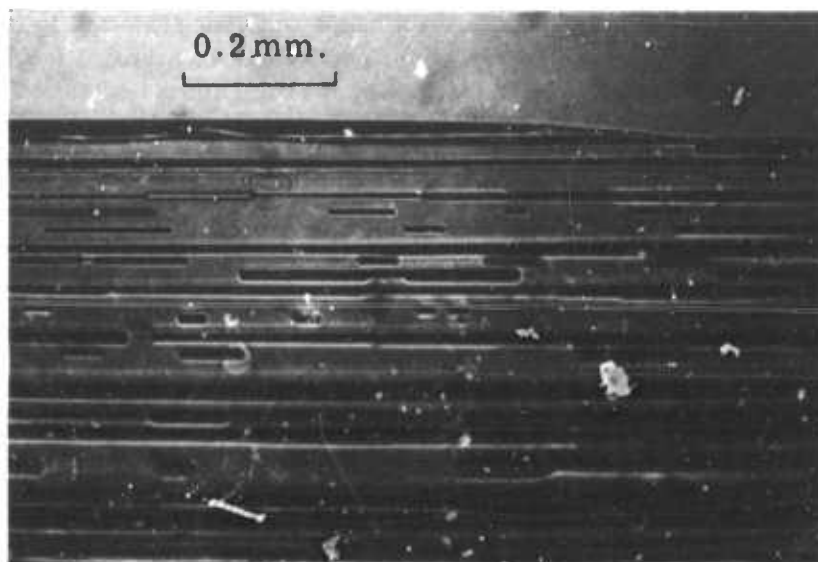


Fig. 4. Thin wing of KBr butterfly twin showing growth wave moving to right from tip and tubular inclusions formed by previous growth waves.

4. Conclusions

It has been shown that $[21\bar{1}]$ penetration twins are a common occurrence during growth of KBr from aqueous solutions by evaporation. A range of twin habits was observed from thin winged butterflies to interpenetrating cubes. Twin formation appeared to be favored by certain impurities and was inhibited by trace amounts of Pb. Twinning was sensitive to growth rate, with intermediate rates being most efficacious. The interface surface gives rise to a pseudo-screw dislocation at the top peak of the butterfly twins which generates growth layers. The origin of the twins is not certain. Multiple twinning did not occur, so twin generation may have occurred at nucleation. Small impurity ions are predicted to lower the interfacial energy and thus promote twin formation. On the other hand, impurities may act to poison an emerging screw

dislocation growth spiral on an existing crystal to generate the twin.

Acknowledgments

This research was supported by the Joint Services Electronics Program and by the Advanced Research Projects Agency, both of the U.S. Department of Defense, under Grants No. AFOSR-69-1622A and DAHC 15-70-G-14.

References

- 1) W. R. Wilcox and P. J. Shlichta, *J. Appl. Phys.*, in press.
- 2) V. Rosicky, *Z. Kryst. Mineral.* **45** (1908) 392.
- 3) M. Loffler, *Neues Jahrb. Mineral. Geol. Paleontol.* **68A** (1934) 125.
- 4) G. Deicha, *Experientia* **4** (1948) 67.
- 5) M. Shaskolsky and A. Shubnikov, *Z. Krist.* **85** (1933) 1.
- 6) H. Ludemann and H. Raether, *Acta Cryst.* **6** (1953) 873.
- 7) H. Ludemann, *Z. Naturforsch.* **9a** (1954) 252.
- 8) H. Ludemann, *Z. Krist.* **108** (1957) 397.
- 9) R. W. Cahn, *Advan. Phys.* **3** (1954) 363.



Directional Solidification of an Off-Eutectic Aluminum-Beryllium Alloy*

R. T. PEPPER

The Aerospace Corporation, El Segundo, California

AND

W. R. WILCOX

*School of Engineering
University of Southern California, Los Angeles, California*

(Received June 25, 1971)

ABSTRACT

Aligned fibers of beryllium in aluminum were obtained by zone melting of an aluminum-20 wt% beryllium alloy. Unfortunately, the fiber length was limited by banding caused by freezing rate fluctuations. Thus, the ultimate strength was only about 11×10^3 psi and elastic modulus 15×10^6 psi. Analytical expressions were found for the concentration perturbation caused by changes in freezing rate, both for progressive freezing with no convection and for zone melting with much liquid mixing.

I. INTRODUCTION

DIRECTIONALLY solidified beryllium-fiber reinforced aluminum matrix composites are potential materials for weight-critical structures because of their possible high strength-to-density and modulus-to-density ratios. This potential is based on the assumption that the beryllium fibers, grown *in situ* in aluminum, are dislocation-free single crystals that would have a modulus of elasticity of 45 million psi and a theoretical strength of 2.2 million psi [1]. The aluminum-beryllium alloy system [2] is a simple eutectic system that contains no intermetallic compounds and whose elements are nearly mutually insoluble in the solid state [3]. The eutectic composition [4, 5] in the aluminum-beryllium system, about 0.9 wt%, is at a volume fraction of beryllium too low for significant mechanical reinforcement of the aluminum matrix. This paper describes a study of the solidification behavior of a hypereutectic aluminum 20 wt% beryllium alloy (27 vol%). A theoretical analysis of the problems and phenomena encountered in zone melting of off-eutectic alloys at low rates is also given.

*This work was supported by the U.S. Air Force under Contract No. F04701-70-C-0059. The theoretical work was performed at the University of Southern California, supported by the Advanced Research Projects Agency under Grant No. DAHC 15-70-G14.

Solidification of Off-Eutectic Al-Be Alloy

Progressive freezing techniques have been used successfully in preparing off-eutectic composites [6,7]. High-temperature gradients are required in order to avoid interface breakdown, at least at low freezing rates. For solidification of two phases of off-eutectic composition, care should be taken to assure very little liquid mixing. When appreciable liquid mixing occurs, one component solidifies alone until the melt approaches the eutectic composition, thereby defeating the purpose of the technique. Zone melting, or really zone leveling, was selected as the preparative technique for the present program. With this technique, steady-state production of off-eutectic composites is possible even with large amounts of convection in the zone

[8,9]. The presence of convection simplifies the experimental method and offers the advantage of reducing the maximum melt temperature for a given temperature gradient at the freezing interface.

Trottier and Graf [5] previously prepared fibrous composites of aluminum and beryllium by directional solidification of slightly hypoeutectic mixtures. The beryllium fibers were found to have a preferred orientation with respect to the aluminum, producing fibers of approximately hexagonal cross section. The aluminum grew in the [011] direction while the beryllium grew in the [001] direction.

II. EXPERIMENTAL TECHNIQUES

A diagram of the zone melting apparatus is shown in Figure 1. An aluminum strip 1-in. wide and 0.1-in. thick, containing a beryllium insert, was progressively fed into the furnace, which was maintained at 1150°C. The zone initially contained only aluminum and was about 1-in. long. Analyses of directionally solidified bars showed that complete mixing of the aluminum and beryllium charge occurred in the melt. The aluminum and the beryllium used in the work were 99.90% and 99.8% pure, respectively.

Cooling at the freezing interface was accomplished by blowing helium gas through a heat exchanger that consisted of boron nitride rollers contacting the surface of the specimen. Measurement of the temperature gradient at the

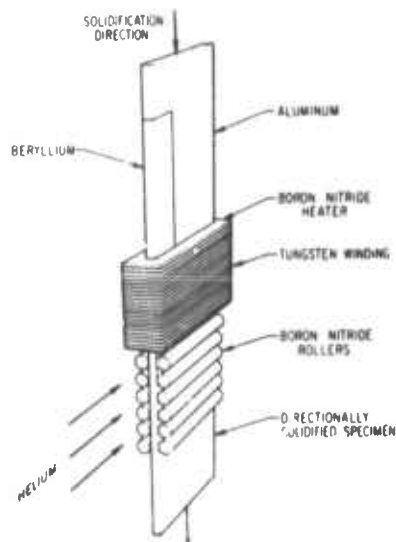


Figure 1. Diagram showing the principal features of the solidification apparatus.

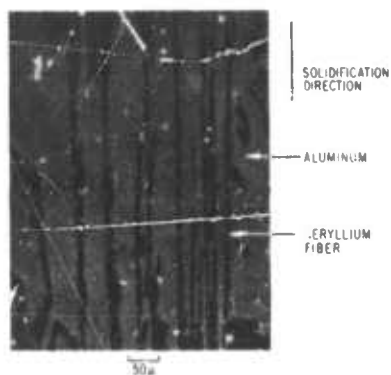


Figure 2. Longitudinal section showing aligned beryllium fibers in an aluminum matrix.

freezing interface with a traveling thermocouple revealed the gradient to be $\sim 1000^{\circ}\text{C}/\text{cm}$. The average freezing rates were on the order of $1 \text{ mm/hr} = 16.7 \mu/\text{min}$. Unfortunately, the freezing alloy occasionally adhered to the wall of the boron nitride heater. Therefore, the zone movement was not always uniform.

III. EXPERIMENTAL RESULTS

As previously mentioned, the zones initially contained only aluminum and, as expected, aluminum solidified alone at first. Metallographic sections revealed that irregular rods of beryllium soon appeared. The fraction of beryllium present gradually increased to an average of 20 wt%. Microstructures of the composite are shown in Figures 2-4. Alignment of beryllium fibers (Figure 2) was obtained in a direction parallel to the solidification direction for distances of up to 0.1 in. This aligned structure was approximately periodically interrupted by distinct bands of aluminum-rich and beryllium-rich alloy oriented in a direction perpendicular to the solidification direction (Figure 3). Figure 4 shows a transverse section of the aligned structure. Many of the beryllium fibers were observed to be hollow with well-defined crystal facets on their outer surfaces and with irregularly shaped inner surfaces. Davies obtained similar results with Cu_6Sn_5 fibers in Sn produced by zone melting of off-eutectic mixtures [10]. The hexagonal cross-sectional shape of the beryllium fibers (Figure 4) suggests that the basal plane of the close-packed-hexagonal beryllium lattice was perpendicular to the solidification direction. In many cases, the facets on the outer surfaces of neighboring beryllium fibers were observed to be roughly parallel to each other. This indicates preferred growth directions and orientation between beryllium and aluminum, as observed in Reference 5. Upon completion of each run, the heater power was turned off and rapid solidification of the molten zone occurred. It is significant that large beryllium needles containing no aluminum cores were obtained in this quenched zone.

The longitudinal tensile strength and modulus of elasticity of the directionally solidified aluminum 20 wt% beryllium alloy specimens were found to be 11,000 and 15×10^6 psi, respectively. Examination of the fracture surfaces of the specimens revealed that plastic deformation and fracture occurred in the bands of aluminum-rich alloy, which were oriented perpendicular to the solidification direction.



Figure 3. Longitudinal section showing the aluminum-rich and beryllium-rich bands.

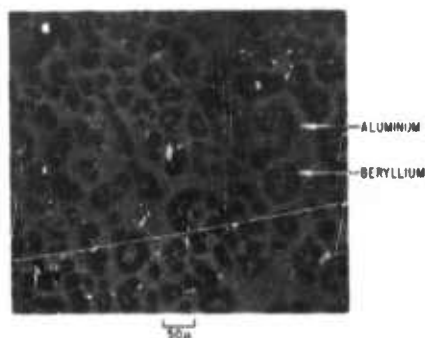


Figure 4. Transverse section of the aligned structure.

IV. THEORY OF OFF-EUTECTIC ZONE MELTING

A schematic diagram of the concentration profile reached at steady state during zone leveling of off-eutectic mixtures is shown in Figure 5. The variation in concentration across the zone is greatly amplified over that which occurred in the present experiments. Because aluminum is being rejected from the beryllium fibers and beryllium from the aluminum matrix, there is also a compositional variation parallel to the freezing interface. Jackson and Hunt [11] gave the solution to this problem when no liquid mixing occurs. This perturbation decreases rapidly as one moves away from the interface into the bulk melt, and in fact becomes negligible at a distance equal to about one-half the fiber spacing, or $\sim 20\mu$ in the present experiments. If we ignore the

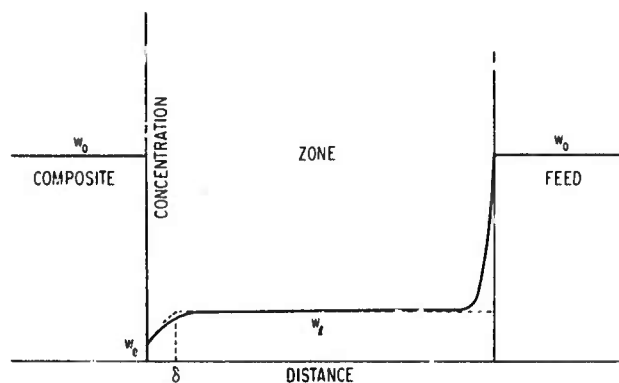


Figure 5. Schematic concentration profile for zone leveling of off-eutectic mixture.

————— Concentration
 assumed concentration

perturbation, then the mass transport problem becomes a linear one given by the differential equation

$$D \frac{\partial^2 w}{\partial x^2} + V \left(\frac{\rho_s}{\rho_l} \right) \frac{\partial w}{\partial x} = \frac{\partial w}{\partial t} \quad (1)$$

when no convective mixing occurs. In Equation (1), D is the diffusion coefficient, w is the melt composition in weight fraction at distance x from the freezing interface, V is the freezing rate, ρ_s is the average density of the solid, and ρ_l is the density of the melt [12]. The average solid composition w_s is given by

$$w_s = \frac{\rho_l}{\rho_s} w_i + \frac{D}{V} \frac{\rho_l}{\rho_s} \left(\frac{dw}{dx} \right)_i \quad (2)$$

where the subscript i denotes values at the interface ($x = 0$). At steady state, $\partial w / \partial t = 0$, $w_s = w_0$ (the feed concentration), and $w_i = w_e$ (the eutectic composition). When some convective mixing occurs, we assume the stagnant film model, so that Equation (1) may be used with the boundary condition that

$$x = \delta, w = w_i, \quad (3)$$

where δ is the film thickness and w_i is the bulk melt composition [13, 14].

The transient problem of progressive freezing ($\delta \rightarrow \infty$) of an off-eutectic melt with no mixing was solved analytically by Wilcox [15] and numerically by Mollard and Flemings [16]. It was predicted that the excess component freezes out pure until the melt at the freezing interfaces reaches the eutectic

Solidification of Off-Eutectic Al-Be Alloy

composition. The effects of changes in freezing rate on the solid composition have also been investigated numerically [16]. If steady state is attained at V_1 and the freezing rate is instantaneously changed to V_2 , Laplace transforms can be used to show that for equal densities in solid and melt ($\rho_s = \rho_l$),

$$\begin{aligned} \frac{w_s - w_o}{w_e + w_o} = & \frac{1}{2} \operatorname{erfc} \frac{1}{2} \left(\frac{z V_2}{D} \right)^{1/2} - \left(\frac{D}{\pi z V_2} \right)^{1/2} \exp \left(-\frac{z V_2}{4D} \right) + \exp \left[\frac{z V_1}{D} \left(\frac{V_1}{V_2} - 1 \right) \right] \\ & \times \left\{ \frac{1}{2} - \frac{V_1}{V_2} + \left| \frac{V_1}{V_2} - \frac{1}{2} \right| \operatorname{erf} \left(\left| \frac{V_1}{V_2} - \frac{1}{2} \right| \left(\frac{z V_2}{D} \right)^{1/2} \right) \right. \\ & \left. + \left(\frac{D}{\pi z V_2} \right)^{1/2} \exp \left[-\left(\frac{V_1}{V_2} - \frac{1}{2} \right)^2 \frac{z V_2}{D} \right] \right\} \quad (4) \end{aligned}$$

where z is the distance down the ingot from where the freezing rate change occurred.

Wilcox [8] used the quasi-steady state approach to determine the solid concentration profile for zone melting with mixing. An overall material balance across the zone yields

$$\frac{\rho_s}{\rho_l} \frac{dz}{l} = \frac{dw_l}{w_o - w_s} \quad (5)$$

where z is the distance moved by a zone of length l and w_o is the composition of the solid being fed into the zone [9]. If the relationship between w_s and w_l is known, this equation can be integrated to yield the average solid concentration as a function of distance. This may be accomplished by solving Equation (1) for $\partial w / \partial t = 0$ with $w = w_l$ at $x = 0$ to yield

$$w = \frac{w_l - w_i \exp \left(-\left(\frac{\delta V}{D} \frac{\rho_s}{\rho_l} \right) \right) + (w_l - w_i) \exp \left(-\left(\frac{x V}{D} \frac{\rho_s}{\rho_l} \right) \right)}{1 - \exp \left(-\left(\frac{\delta V}{D} \frac{\rho_s}{\rho_l} \right) \right)} \quad (6)$$

and

$$\left(\frac{\partial w}{\partial x} \right)_i = \frac{V}{D} \frac{\rho_s}{\rho_l} \frac{(w_l - w_i)}{1 - \exp \left(-\left(\frac{\delta V}{D} \frac{\rho_s}{\rho_l} \right) \right)} \quad (7)$$

If $w_l < w_e$, $w_s = 0$, and if $w_l > w_e$, $w_s = 1$. For the zone initially of composition w_o , Equations (2), (5), and (7) may be combined to determine the

distance over which the excess component comes out alone before $w_i = w_e$, as was done in Reference 8. In the present case, $w_i = 0$ initially (where w is the weight fraction of beryllium). Therefore, $w_s = 0$ initially. Integrating Equation (5) we find that w_i at any point is given by

$$\frac{\rho_s}{\rho_l} \frac{z}{l} = \int_0^{w_i} \frac{dw_i}{w_o} = \frac{w_i}{w_o} \quad (8)$$

The length of pure aluminum z_p can be found by substituting Equation (8) into Equation (7) and these results into Equation (2), letting $w_s = 0$ and $w_i = w_e$ to yield

$$z_p = l \frac{\rho_l}{\rho_s} \frac{w_e}{w_o} \exp \left(- \frac{\delta V}{D} \frac{\rho_s}{\rho_l} \right). \quad (9)$$

Subsequently $w_i = w_e$, and by substituting Equation (7) into Equation (2) and this result into Equation (5) we obtain:

$$w_s = w_o \left\{ 1 - \exp \left[- \frac{z - z_p}{l} \frac{\rho_s}{\rho_l} \frac{1}{1 - \exp \left(- \frac{\delta V}{D} \frac{\rho_s}{\rho_l} \right)} \right] \right\} \quad (10)$$

The effect of freezing rate changes on solid composition can be seen qualitatively by examination of Equation (2). If we consider that $o \neq w_i \neq 1$ both before and after the change in freezing rate, then $w_i = w_e$ is unchanged as is $(dw/dx)_i$. Only V changes. In our case, $(dw/dx)_i > 0$. Thus, if V increases, w_s decreases and approaches the eutectic composition. If V decreases, w_s increases and may actually achieve unity (pure beryllium), although if $w_s \rightarrow 1$, it is no longer required that $w_i = w_e$. Gradually $(dw/dx)_i$ changes and w_i approaches the steady state value. Freezing rate changes not only perturb the relative amounts of the two phases solidifying but also alter the fiber size and spacing. It is well known that fiber spacing is inversely proportional to the square root of the freezing rate [11].

We now consider quantitatively the change in w_s caused by a sudden change in freezing rate after steady state is established at the initial freezing rate V_1 . The initial concentration at V_2 is determined first by solving for the steady state $(dw/dx)_i$ using Equation (2) and letting $w_s = w_o$, $w_i = w_e$, and $V = V_1$. If this is substituted back into Equation (2), letting $w_i = w_e$ and $V = V_2$, we find that initially

$$w_s = w_e \left(1 - \frac{V_1}{V_2} \right) + \frac{V_1}{V_2} w_o \quad (11)$$

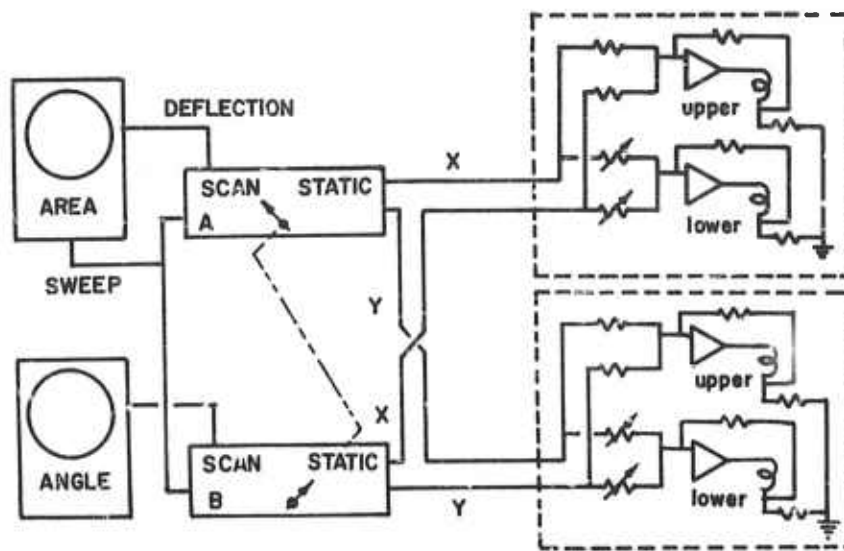


Fig. 2. A control and display system that provides for obtaining either angle scans or area scans.

two fixed ratios, one used for the area scan mode and a second used for the angle scan mode. To provide for change of the angle during an area scan, a dc signal is superposed on the ac signal, the ratio of coil drives being that normally employed for an angle scan. By interchanging the ac and dc drives one shifts from an area scan to an angle scan.

In practice, it is necessary that the dc signal imposed on the deflection coils be independently adjustable for the area and the angle scan modes. It may also be desirable to provide for different scan amplitude for the area and angle scans. Hence, two separate scan generators of the type commonly used are required. Figure 2 shows schematically how these scan generators would be connected. It is useful, although not essential, to provide separate oscilloscopes to display the area scan and angle scan information.

The simple system described is applicable to a double deflection system located below the objective lens. However, it can also be used if only one set of deflection coils is located below the lens, using either a single deflection system in the gap of the objective lens (as described below) or a double deflection system above the lens.

Other types of deflection systems, for use when the working distance is very short, will be described elsewhere. By judicious location of the deflection coils, it is possible to avoid the use of double deflection systems, and it is also possible to use real instead of virtual aperture stops.

APPLICATION OF A SYSTEM FOR AREA AND ANGLE SCANS

Some of the principles described have been tested using a commercial electron probe microanalyzer (EMX-SM) with a smaller objective aperture than normally employed ($50\ \mu$ instead of $300\ \mu$). This instrument is provided with deflection coils located in the gap of the lens. A second set of coils was used below the lens on a special sample holder. This sample holder also contained two silicon solar cells used as backscattered electron detectors.⁹⁾ The experimental arrangement is shown schematically in Fig. 3.

Area and angle scans obtained on a silicon bicrystal are shown in Fig. 4. The angle scan shown in Fig. 4(a) was taken on a selected area of the (111) oriented crystal, and the angle scan

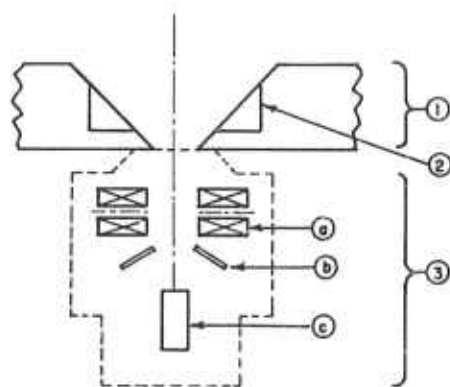


Fig. 3. Schematic diagram of experimental deflection system showing: (1) The objective lens of the microprobe, (2) the scanning coils of the microprobe, and (3) special sample holder containing (a) deflection coils (b) backscatter detectors, and (c) specimen.

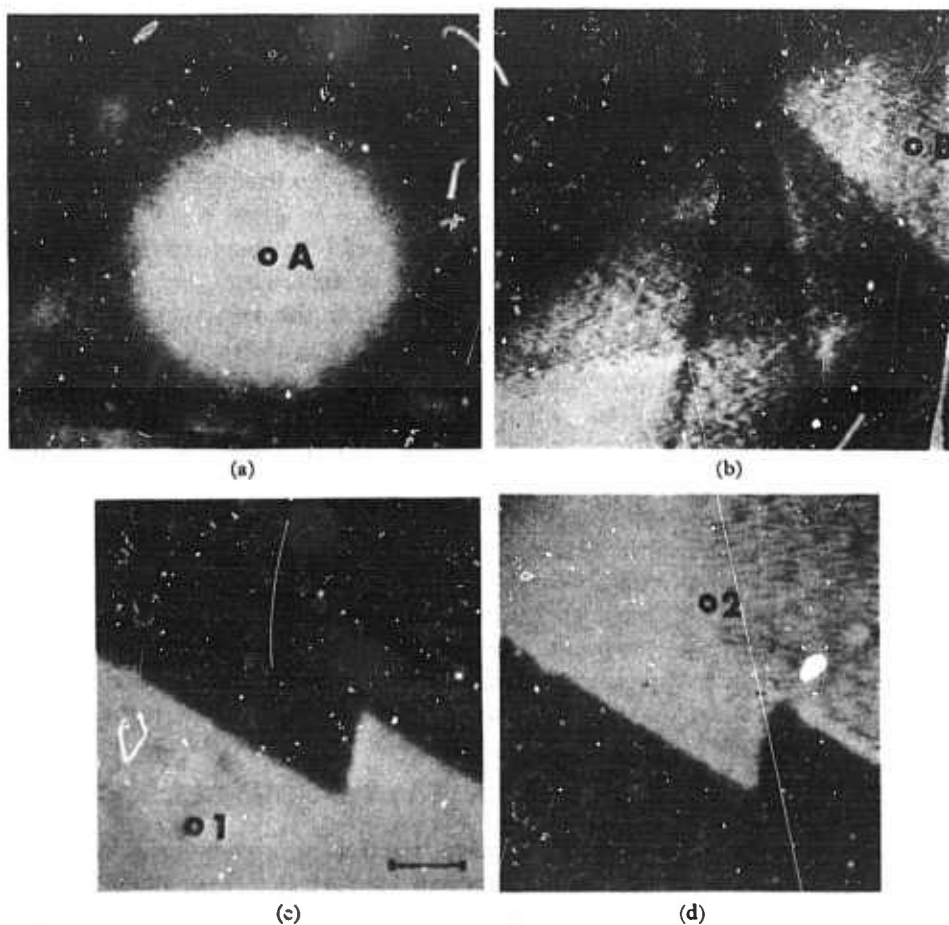


Fig. 4. Area and angle scans obtained on a silicon bicrystal: (a) An angle scan of the (111) oriented crystal (Area 1); (b) an angle scan of the twin (Area 2); (c) an area scan with beam angle A; and (d) an area scan with beam angle B. The scale of the area scans is indicated by the marker in c which is 100 μ long.

Solidification of Off-Eutectic Al-Be Alloy

to the solidification direction. With a little imagination, one can visualize cells, perhaps even aluminum dendrites, in these regions.

The fibrous habit of the beryllium, particularly in the quenched zones, was somewhat surprising. Beryllium is a low entropy of fusion material ($\Delta H_f/T_fR = 1.1$, from Reference 21) and, according to Jackson's theory [22, 23], should grow nonfaceted. Therefore, we would expect to find metallic-type dendrites of beryllium rather than needles, particularly in a quenched beryllium-rich melt. The nonuniform spacing of the beryllium fibers also indicated faceted growth with strongly anisotropic growth kinetics. Another possibility is that the growth rate was so low that the diffusion fields were insufficient to cause completely cooperative growth. Since beryllium did show such a strong preference for a fibrous morphology, we suspect that it may be possible to produce oriented composites without elaborate precautions to assure interface stability. This has been demonstrated with an organic analog of the beryllium-aluminum system [24], and with Cu_6Sn_5 in Sn [10].

The origin of the aluminum cores in many of the beryllium fibers remains a mystery. Perhaps they were caused by the freezing rate fluctuations, as follows. The fibers would thicken with a slight decrease in the rate. When the rate then increased, they might not have been able to contract because of the facets on the sides, thus causing a depression to form in the center of the fibers. If aluminum nucleates easily on beryllium, it would have nucleated in the depressions and formed a solid core growing along with the beryllium fibers. This is, of course, pure speculation.

VI. CONCLUSIONS

It has been shown that aligned composites of aluminum 20 wt% beryllium alloys can be grown by zone melting techniques. The strong preference of the beryllium to grow fibers indicates that oriented composites might be possible even with an irregularly shaped interface. Analytical expressions were derived for compositional transients with a constant freezing rate and for freezing rate changes in zone melting with large amounts of convection.

REFERENCES

1. S. W. Bradstreet, "Principles Affecting High Strength to Density Composites With Fibers or Flakes," Technical Report AFML-TR-64-85, Wright-Patterson Air Force Base, Ohio (1964).
2. M. Hansen, *Constitution of Binary Alloys*, McGraw-Hill (1958).
3. J. D. Baird, G. A. Geach, A. G. Knapton, and K. B. C. West, *Proceedings of the U.N. International Conference on Peaceful Uses of Atomic Energy*, Geneva, Pergamon Press (1958).
4. W. I. Mischeva, "The Solubility of Beryllium in Aluminum," *Izv. Akad. Nauk. SSSR. Ser. Khim.* (1940), p. 775.
5. J. Trottier and R. Graf, "Sur la Structure des Alliages Eutectiques Aluminium-Béryllium Obtenus par Solidification Unidirectionnelle," *Compt. Rend. Acad. Sci. Paris*, Vol. 271 (1970), p. 613.

R. T. Pepper and W. R. Wilcox

6. F. R. Mollard and M. C. Flemings, "Growth of Composites From the Melt—Part II," *Trans. TMS-AIME*, Vol. 239 (1967), p. 1534.
7. H. E. Cline, "Lamellar Stability in Lead-Tin Alloys," *Trans. TMS-AIME*, Vol. 239 (1967), p. 1489.
8. W. R. Wilcox, "Incomplete Liquid Mixing in Crystal Growth From the Melt," *J. Applied Physics*, Vol. 35 (1964), p. 636.
9. M. Zief and W. R. Wilcox, ed., *Fractional Solidification*, Dekker (1967).
10. G. S. Davies, "The Growth of Fiber Structures From the Melt," Ch. 14 in *High Strength Materials*, V. F. Zackay, ed., Wiley (1965), p. 303.
11. K. A. Jackson and J. D. Hunt, "Lamellar and Rod Eutectic Growth," *Trans. TMS-AIME*, Vol. 235 (1966), p. 1129.
12. W. R. Wilcox, "Crystallization Flow," *J. Crystal Growth* (in press).
13. W. R. Wilcox, "Validity of the Stagnant Film Approximation for Mass Transfer in Crystal Growth and Dissolution," *Mat. Res. Bull.*, Vol. 4 (1969), p. 265.
14. W. R. Wilcox, in *Preparation and Properties of Solid State Materials*, R. Lefever, ed., Dekker (1971).
15. W. R. Wilcox, "Fractional Solidification of Eutectic-Forming Mixtures," *Ind. Eng. Chem. Fund.*, Vol. 3 (1964), p. 235.
16. F. R. Mollard and M. C. Flemings, "Growth of Composites From the Melt—Part II," *Trans. TMS-AIME*, Vol. 239 (1967), p. 1526.
17. W. R. Wilcox and L. D. Fullmer, "Turbulent Free Convection in Czochralski Crystal Growth," *J. Applied Physics*, Vol. 36 (1965), p. 2201.
18. J. R. Carruthers, "Thermal Convection in Horizontal Crystal Growth," *J. Crystal Growth*, Vol. 2 (1968), p. 1.
19. D. T. J. Hurle, J. Gillman, and E. J. Harp, "Spectral Analysis of Temperature Fluctuations in Molten Metals," *Phil. Mag.*, Vol. 14 (1966), p. 205.
20. H. P. Utech, W. S. Brower, and J. G. Early, "Thermal Convection and Crystal Growth in Horizontal Boats: Flow Pattern, Velocity Measurement, and Solute Distribution," p. 201 in *Crystal Growth*, H. S. Peiser, ed., Pergamon (1967).
21. C. J. Smithells, *Metals Reference Book*, Interscience/Wiley (1955).
22. J. D. Hunt and K. A. Jackson, "Binary Eutectic Solidification," *Trans. TMS-AIME*, Vol. 236 (1966), p. 343.
23. K. A. Jackson, D. R. Uhlmann, and J. D. Hunt, "On the Nature of Crystal Growth From the Melt," *J. Crystal Growth*, Vol. 1 (1967), p. 1.
24. W. R. Wilcox and J. R. Teviotdale, "Oriented Composites by Solidification of Off-Eutectic Mixtures," *J. Composite Materials*, Vol. 3 (1969), p. 364.
25. J. D. Livingston, H. E. Cline, E. F. Koch, and R. R. Russell, "High-Speed Solidification of Several Eutectic Alloys," *Acta Met.*, Vol. 18 (1970), p. 399.

Crystal orientation by cleavage plane reflected laser beam

J E Green† and J M Whelan

Department of Materials Science, University of Southern California, Los Angeles, California 90007, USA

MS received 28 February 1972



Abstract An apparatus is described for the orientation and transfer of single crystals which have well-defined cleavage planes. It is based upon the reflection of a 6328 Å He-Ne laser beam from the cleavage planes. Orientation and subsequent transfer of a GaAs crystal to a wafering machine can be done with a cumulative error of less than 0.15°.

1 Introduction

An oriented crystal is one whose orientation with respect to a fixed coordinate system is known. Any other orientation may then be found by means of a set of rotations read from a stereographic projection chart. Thus, a crystal orientor must provide a means of distinguishing crystal planes and contain a facility for rotating the crystal into any desired orientation with respect to the fixed reference.

The cleavage planes of many crystals, and III-V compound semiconductors in particular, exhibit extreme flatness and parallelity. GaAs, for example, cleaves to a surface of flat mirror-like steps along (110) planes. Examination of GaAs cleaved surfaces by MacRae and Gobeli (1964) with a 1000× optical microscope failed to resolve any imperfections. Electron microscope examinations showed the cleavage planes to be flat and parallel to within the resolution of the instrument, 30 to 40 Å in height, along steps that were 3000 to 10 000 Å in length. Step heights ranged from 50 to 200 Å.

The cleaved planes can be used as mirrors to reflect a well collimated light beam back upon itself. The light beam serves as one reference coordinate in a convenient space coordinate system and a cleaved plane fixes one of the crystallographic coordinates. By knowing the location of two different (111) faces and the angle between them (60° or 90°), one can locate any other plane by performing the proper rotations.

2 Apparatus

Accurate alignment requires an ultraflat face to obtain a well-defined reflection. Polished surfaces, even those of a very high quality, are generally not adequate; the back reflected beam is too diffuse. A He-Ne laser ($\lambda = 6328 \text{ Å}$) was used to test the flatness of typical GaAs cleavage planes which ranged in area from about 20 mm² to 1 cm². The laser was mounted on a lathe carriage so that the beam could be made to traverse the cleaved surface. The path length between the laser and the sample was 76.2 cm. Upon traversing a typical cleaved surface it was noted that the back reflected beam spot, which was 1.5 mm in diameter, never moved more than one-half of the spot diameter. This indicated that the cleavage planes in that surface were parallel to within 0.06°.

A goniometer manufactured by the Angle Computer Company, Los Angeles, was used as the crystal holder.

† Now at Departments of Mechanical and Industrial Engineering and Metallurgy, University of Illinois at Urbana-Champaign, Urbana, Illinois 61801, USA

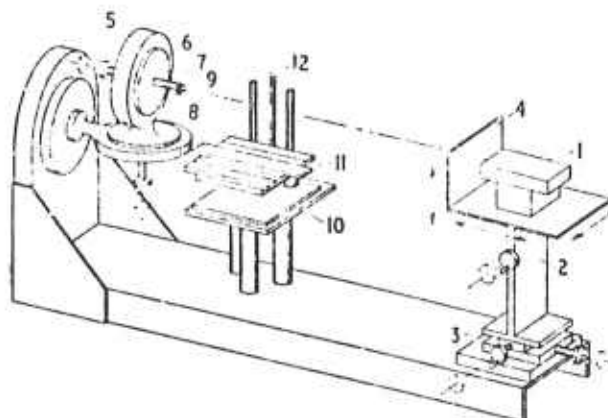


Figure 1 Schematic representation of the instrument: 1, He-Ne laser; 2, microscope elevator; 3, jeweller's lathe carriage; 4, screen for back-reflection; 5, optical goniometer; 6, machined flat reference; 7, stand-off; 8, wax; 9, crystal; 10, die set; 11, transfer plate; 12, threaded rod

The instrument has the ability to perform all three orthogonal rotations to an accuracy of 0.001° as read on a vernier scale. The front face of the goniometer has a machined flat which is used as a reference for the laser beam. A parallel optically flat evaporated gold mirror is placed over the machined flat. The laser beam can then be adjusted perpendicular to the reference plane of the goniometer to within 0.038°.

Figure 1 is a schematic drawing of the apparatus. The crystal is mounted on a short stand-off on the optical goniometer by means of Duxseal wax manufactured by the Johns-Manville Corporation. A rough adjustment can be made by moving the crystal in the wax and by rotating the stand-off which is attached to a ball bearing. After rough alignment of the cleavage face with the laser beam, the bearing plate is tightened to hold the crystal firmly in place. Further rotation is accomplished by means of the optical goniometer itself.

The laser is mounted on a microscope elevator which is in turn mounted on a jeweller's carriage. The elevator has a total vertical displacement of four inches. The laser can be translated in the horizontal plane both parallel and perpendicular to the beam by adjusting the cross feed on the lathe. The maximum horizontal displacement is 10 in. Adjustment of the translational displacements is not critical, but it is important that there be no rotation of the laser during the adjustment procedure. The laser beam itself is aimed through a 2 mm hole in a flat black screen and back-reflected on to an 'x' scribed 2 mm above the pinhole. The error introduced by not being able to observe the light reflected directly back on to itself is inversely proportional to the path length and is 0.15° in 76.2 cm. However, this error can be avoided by using a corrected axis which bisects the incident and reflected beams. All rotations are then performed with respect to this axis.

Transfer of the oriented crystal is accomplished by means of a precision machined plate whose longitudinal axis is parallel with the laser beam as is shown in figure 1. The transfer plate must have the facility to be translated in three orthogonal directions so that it may be located directly under the oriented crystal. This is accomplished by mounting the plate on a Danly commercial die set modified for use as a rigid accurate elevator by inserting a threaded rod between the guide posts. The elevator is located directly in front of

the goniometer. Both the elevator platform and the transfer plate have longitudinally cut steps which allow the plate to slide in a direction parallel to the laser beam and move the steps perpendicular to the beam. The entire assembly (laser, optical goniometer and transfer device) is mounted on a 10 in \times 2.5 in \times .48 in aluminium channel which is fastened to a steel table with provisions for levelling and vibration damping.

After orientation, the crystal is rotated 90° with respect to the laser beam so that its oriented face is now parallel with the longitudinal edge of the transfer plate. Plaster of Paris is used to attach the crystal to the transfer plate and the wax is removed after the plaster sets. The plate with the oriented crystal can then be transferred directly to a magnetic chuck on a lathe machine. A lip has been accurately machined on the transfer plate for alignment with the magnetic chuck.

3 Conclusions

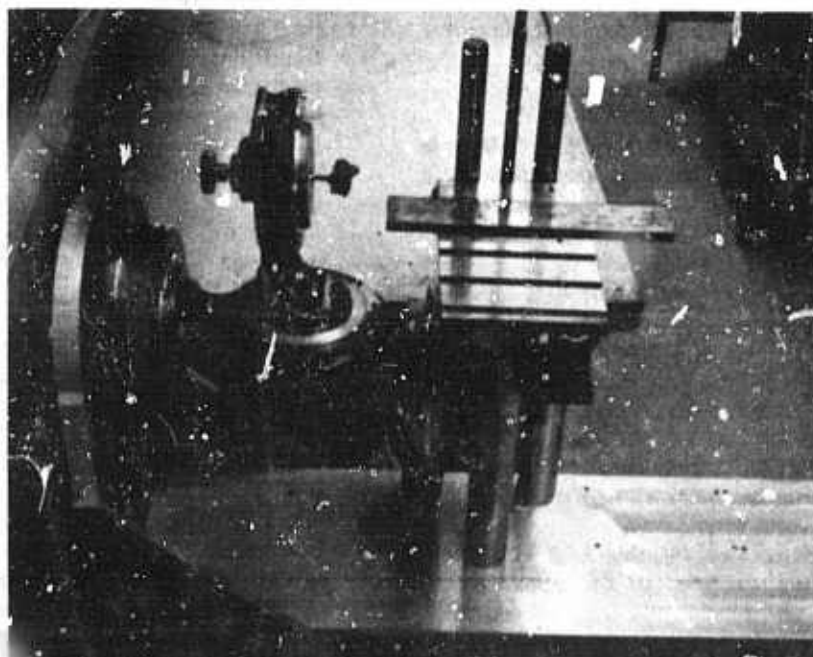
The system is a compact, simple laboratory tool which is quick and easy to use. A crystal may be oriented in less than five minutes and the transfer time is only dependent on the media used for adhesion (20 minutes for quick setting plaster of Paris). The possible errors due to the transfer procedure are misalignment of the transfer plate, misalignment of the saw chuck and walking or wobble of the saw blade. All these errors compounded, however, are less than the 0.1° error due to off axis back reflection of the laser beam. The orientation of sliced wafers has been checked by Bragg diffraction and found to always be within the accuracy of the x ray machine, 0.20°.

Acknowledgments

We wish to thank Mr William Krebs for the fabrication of the apparatus. This work was sponsored in part by the Advanced Project Agency under Grant Number DAAH-15-71-G-6.

References

- MacRae A U and Gobeli G W 1964 *J. Appl. Phys.* 35 1629
Journal of Physics E: Scientific Instruments 1972 Volume 5
Printed in Great Britain © 1972



278<

Optical goniometer and transfer assembly.

Glow-discharge optical spectroscopy for the analysis of thin films

J. E. Greene* and J. M. Whelan

Department of Materials Science, University of Southern California, Los Angeles, California 90007
(Received 2 August 1971; in final form 26 February 1973)

Available techniques for the chemical analysis of epitaxial semiconductor films are limited because of typical sample thicknesses of 0.7–10 μm . The use of glow-discharge optical spectroscopy was investigated as an analytical technique. GaAs was dc sputtered in Ar and the glow discharge monitored for the electroluminescence associated with one or more target elements. The present detection limit for Sn in GaAs is 3×10^{16} atoms cm^{-3} for a volume sputtering rate of 1.5×10^{-5} cm^3/min . The luminescent intensities combined with sputtering rates were used to estimate concentration profiles as a function of depth for $\text{GaAs}_{1-x}\text{Sb}_x$ films grown on GaAs. Sputtering yields have been measured for GaAs over the range 0.5–3 kV and found to vary with orientation in the following order: (111)As, (111)Ga, (211), and (110).

INTRODUCTION

We have investigated glow-discharge optical spectroscopy (GDOS)¹ as a method for trace analysis of thin films. In this technique, the target is sputtered in a low-pressure gas discharge. The discharge is operated in the abnormal glow mode, and its spectra are monitored for the electroluminescence associated with the desired sputtered target elements. Under suitable conditions, the intensity of the spectral line of an element in the target is proportional to the density of that element material in the region of the discharge under observation.

The presently available methods for trace analysis which may be applied to thin films are limited primarily by the small volume of sample available. Typical dimensions of the GaAs thin films used in the following experiments are 0.7–10 μm in thickness by 0.3–0.5 cm^2 in area. For a sample volume of 4×10^{-5} cm^3 and an impurity concentration of 10^{17} atoms/ cm^3 there are only 4×10^{12} total impurity atoms available for analysis. If the dopant is a heavy metal such as Sn, the total mass of impurity atoms is 7×10^{-10} g.

The use of sputtering as a means for atomizing the sample offers several distinct advantages. The etch or depth removal rate can be varied over a wide range (0.01–10 $\mu\text{m}/\text{min}$). No surface preparation of the sample is required. Sample contamination is not a problem since the film does not have to be chemically dissolved in a solvent. Most importantly, sputtering is basically a process which "etches" the sample in an "atom-by-atom" fashion. The discharge associated with sputtering in the abnormal glow regime provides a controllable source of excitation for sputtered atoms. Dc sputtering is convenient for metals and semiconductors, whereas rf sputtering can be used for insulators.

EXPERIMENTAL DESIGN

Figure 1(a) shows the plan view of the sputtering module. The module itself is Pyrex glass with the exception of the window which is Ge type 151 uv-transmitting quartz. The anode and cathode are aluminum and are water cooled. A grounded cylindrical aluminum sputter shield fits over the cathode. The sputter shield and cathode are insulated by means of a quartz sleeve and a Delrin plastic spacer with Delrin screws. All vacuum

seals are made with viton O-rings. Details of the cathode assembly are indicated in Fig. 1(b).

The cathode-anode gap distance can be adjusted by sliding the anode through a modified Veeco C-112 vacuum quick disconnect. Spacing screws allow the distance to be adjusted to within 0.5 mm. The target sample is mounted with silver paste on a demountable aluminum pedestal which screws to the cathode. Pyrex shields are used to mask any exposed aluminum on the cathode assembly from the plasma. This prevents arcing between the pedestal and the grounded shield. It also prevents sputtering of the pedestal. The gas inlet was placed next to the window to minimize the deposition of sputtered material on it.

In operation, the system is purged several times with argon gas and pumped down to a pressure of less than 10^{-3} Torr with a rotary vane pump. The outlet line from the sputtering module is isolated from the mechanical pump by a liquid-nitrogen cold trap. Ar used in these experiments had an initial purity of 99.998%. It was passed through a quartz trap containing titanium sponge at 900°C to remove traces of O_2 , N_2 , hydrocarbons, and water vapor. After the initial pumpdown, the operating Ar pressure of 0.1 Torr was maintained by bleeding the purified gas into the pumped module at an approximate rate of 0.5 $\text{cm}^3/\text{atm}/\text{min}$.

A voltage is established between the cathode and the anode which ionizes the gas and accelerates the Ar ions which bombard the target. Target atoms are ejected primarily in their neutral ground states and are subsequently excited in the plasma. As shown schematically in Fig. 2, the electroluminescence is focused by a set of mirrors, chopped at a frequency synchronized with a phase-sensitive lock-in amplifier, monochromatized by a scanning spectrometer, and detected by an EMI 6256S photomultiplier. The 1200-groove/mm grating in the spectrometer was blazed for a wavelength of 2000 Å. The f number of the spectrometer was $f/8$, but the geometry of the mirrors was such that the effective f number of the optical system was $f/16$. The amplified signal was recorded as either intensity vs wavelength or intensity vs time.

EXPERIMENTS

Experiments were performed to determine in which region of the discharge the maximum target atom electro-

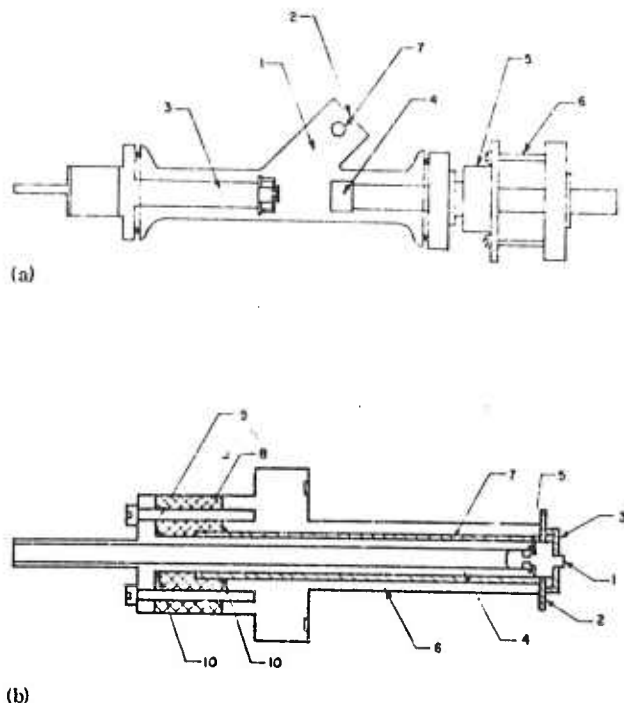


FIG. 1. (a) Plan view of sputtering module: (1) Pyrex module, (2) quartz window, (3) aluminum cathode, (4) aluminum anode, (5) modified Veeeco C-112 vacuum quick disconnect, (6) spacing screws, and (7) gas inlet. (b) Cross-sectional view of cathode assembly: (1) sample holder, (2) Pyrex shield (3) Pyrex shield, (4) cathode, (5) Viton O-ring, (6) aluminum sputter shield, (7) Pyrex sleeve, (8) Delrin insulator, (9) Delrin screws, and (10) Viton O-ring.

luminescence occurs. A module with the snout perpendicular to the cylindrical axis was used. Two alignment slits were placed between the module window and the plane mirror. Using this arrangement, the light incident upon the spectrometer slit originated from a narrow slice of the discharge. The module was mounted on the tracks of an optical bench so that it could be translated in a horizontal plane perpendicular to the spectrometer slit. This permitted the spectra to be examined as a function of distance between the electrodes. Figure 3 shows the neutral As 2860.4-Å line intensity as a function of distance from the GaAs target. The smaller slope on the left-hand side of the maximum is due to the discharge geometry. The maximum intensity occurs in the cathode glow region approximately 2.5 mm from the target surface. Calculations also showed that this is the region in which the ejected target atoms have experienced enough collisions to have given up their initial ejection kinetic energies. In these calculations the mean free path for a "hot" atom in a thermalized gas was used. The ejection energies were estimated from the work of Stuart and co-workers.^{2,3} Elastic collisions and random-walk isotropic scattering were assumed although a correction was made for the "persistence" of velocity.⁴

Knowledge of the intensity distribution in Fig. 3 provided the basis for selecting the analysis module shown in Fig. 2. This module configuration ensured that the measured electroluminescent intensities were independent

of minor uncertainties in alignment. The use of glow-discharge spectroscopy for chemical analysis requires that the luminescent intensity due to a particular target constituent be proportional to the sputtering rate. That this is indeed the case was suggested by the prior work of Stuart and Wehner.^{5,6} To establish this proportionality we measured the relative spectroscopic yield curves for several GaAs orientations and established that these could be normalized with absolute yield data. Yield curves were measured for the following orientations: (111)Ga, (111)As, (110), and (211). All samples used were single crystals with chemically polished planes corresponding to one of the above orientations.

The spectroscopic yield is presently defined as the emission intensity measured in arbitrary units divided by the cathode current. The emission intensity was monitored for transitions from neutral excited states to neutral ground states. The relative yield curves for all orientations mentioned above were measured and checked using both Ga and As lines at 2874.2 and 2860.4 Å, respectively. Data points were taken at intervals of 50 or 100 V, and the results are summarized as the solid curves in Fig. 4.

Each curve in Fig. 4 was normalized with an absolute yield measurement, and the normalization was checked with other absolute yield data. Absolute or mass yield is defined here in as the number of target atoms sputtered per second per unit of cathode current in electronic charges per second. This definition of mass yield is identical to the usual one, the number of target atoms ejected per incident Ar⁺ ion, if current contributions by secondary electrons and multiply charged ions are neglected. These current components are less than 20% of the total. Absolute measurements were made using the "change-in-mass" technique as discussed in detail by Kaminsky.⁷ The absolute yield data are indicated by circles in Fig. 4. The normalized spectroscopic yield curves agreed to within 6% of the absolute yield data. These results established the proportionality between the sputtering rates and the luminescent intensities. The

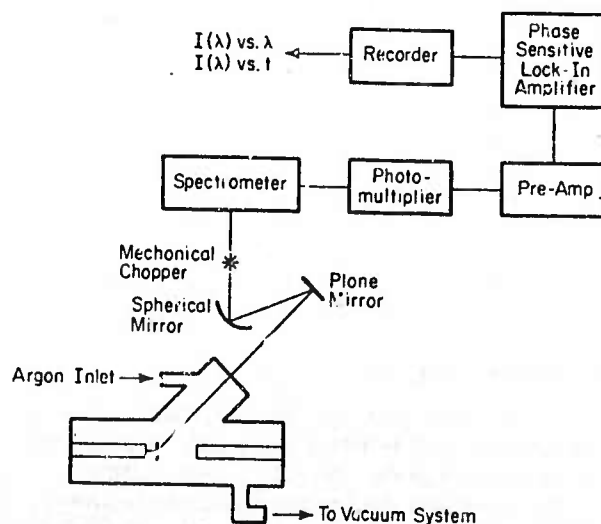


FIG. 2. Schematic diagram of the optical and electronic detection system.

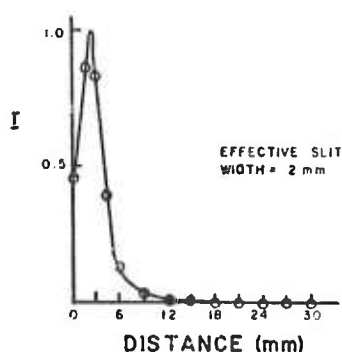


FIG. 3. Target atom emission intensity (arbitrary units) vs distance between target and anode.

yield curves proved to be highly reproducible and served as a sensitive monitor of the sputtering rate. Errors in the absolute yield measurements are estimated to be less than 3%.

From Fig. 4 it can be seen that the sputtering yield varies as the crystal transparency,^{3,9} i.e., the number of atoms per unit area in a plane normal to a particular direction. The more tightly packed planes exhibit higher sputtering yields. Channeling effects¹⁰ may also play some role especially at the higher energies. A polarity effect is evident in the (111) planes. The (111)As plane sputters faster, in agreement with chemical etching work done by Gatos and Lavine.¹¹ These authors showed that the As face is the more reactive with respect to chemical etches. In addition, there is a change in the energy dependence of the yield function between 1300 and 1700 V. The knee in the yield curve occurs at lower energies for planes with higher sputtering rates.

TRACE ANALYSIS

Tin was selected as the main impurity to be studied in GaAs for three reasons: (i) It has a high emission intensity in a copper arc¹²; (ii) it is an important dopant in GaAs; (iii) the tin peak at 2849 Å occurs in a spectral region in which Ar is fairly transparent, which thereby minimizes background intensity problems. Figure 5 shows two superimposed spectra that were taken to establish the detection limit for Sn in GaAs. The solid curve is the spectrum for a GaAs sample containing 9×10^{17} Sn atoms cm^{-3} and the dotted line is for a GaAs sample containing no Sn. Both samples had the same area and they were sputtered under the same conditions. The Sn concentration in the intentionally doped sample was obtained from room-temperature Hall data. Because Sn is weakly amphoteric, this estimate may be low by 10–30%. However, this error is partially compensated by the presence of donors other than Sn, introduced during growth at concentrations of $(0.3-1) \times 10^{17}$ atoms cm^{-3} .

The spectral resolution in these measurements was better than 1 Å. All peaks not labeled, including the shoulder peak at 2841 Å on the Sn line, are due to Ar. Variations in the background intensities of the Ar spectral peaks are less than 10% from one run to another. Within these limits the observed Sn emission line can be corrected for the Ar background. Intensities of the Sn

spectral line were proportional to the sputtering rates as was already demonstrated with the Ga and As spectral lines. The concentration of Sn in a given GaAs sample is estimated by comparing the intensity of the Sn line with that of a GaAs standard containing a known amount of Sn. For each sample the Sn line intensities are measured in units of either a Ga or As peak intensity which is highly reproducible as indicated by the repeatability of the yield curves.

The current detection limit for Sn in GaAs was estimated from the spectra in Fig. 5 and the sputtering conditions, i.e., a sample area of 0.38 cm^2 and a sputtering rate of 0.07 $\mu\text{m}/\text{min}$. The detection limit was conservatively selected as the Sn concentration for which the intensity of the Sn peak is equal to that of the Ar shoulder peak at 2481 Å. Sn can be detected at lower levels, but the reproducibility is less. By using this definition of detection limits, the minimum weight of Sn that can presently be detected is 6×10^{-10} g. The minimum concentration of Sn that we can detect is 3×10^{16} atoms cm^{-3} . This is for a sample with an area of 0.5 cm^2 , a thickness of 2.0 μm , and a sputtering rate of 0.3 $\mu\text{m}/\text{min}$. A Sn concentration of 5×10^{17} atoms cm^{-3} can be detected in a GaAs film only 0.5 μm thick with a surface area of 0.4 cm^2 . The reproducibility of all of these measurements is within 10%.

In addition to Sn the following elements have also been detected: Ga, As, Sb, Al, and Cu. Detection limits have not been established for these elements. Estimated limits are $\sim 5 \times 10^{17}$ atoms cm^{-3} .

The sensitivity of GDOS can be increased by increasing the number of electrons in the plasma available for excitation. Two possible methods for achieving this are the use of a transverse magnetic field or a hot filament. However, both of these methods cause nonuniform sputtering. Another possibility is to use a coherent light source of the proper wavelength for exciting the desired impurity. Lasers are becoming increasingly more available in the uv. However, light scattering may cause problems and would have to be considered.

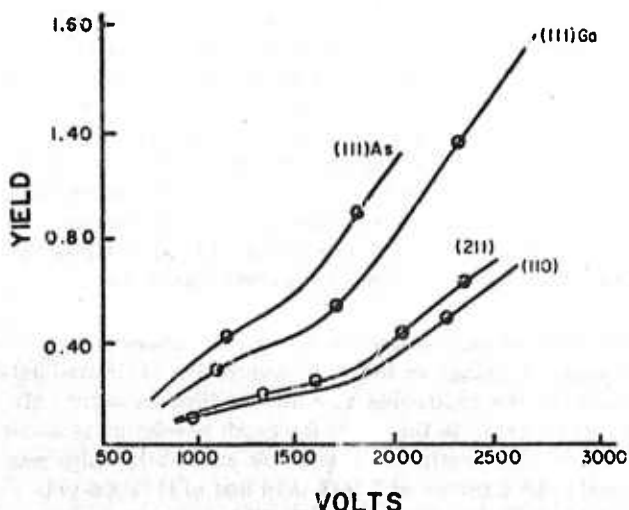


FIG. 4. Sputtering yield (target atoms sputtered per unit of cathode current) vs applied voltage for different orientations of GaAs.

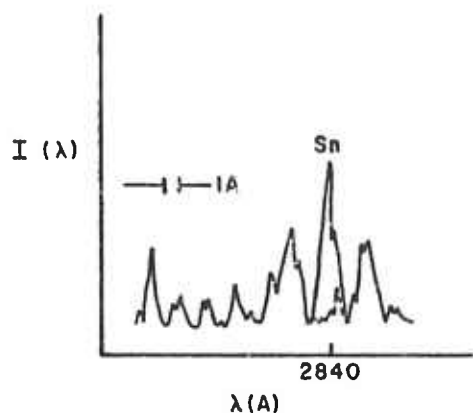


FIG. 5. Emission intensity vs wavelength from the cathode glow portion of the discharge for two superimposed spectra. The solid line corresponds to a GaAs sample containing 9×10^{17} atoms cm^{-3} of Sn, the broken line is the spectrum for a GaAs sample containing no Sn.

The use of different sputtering gases should also be studied for two reasons. First, one should select a gas which is as transparent as possible in the spectral region of interest. Second, one should consider gases with low ionization potentials to increase the number of free electrons available for excitation. The use of Xe (which has a lower ionization potential than Ar), mixtures of rare gases, and specialty gases such as those used in nuclear detector tubes should be considered. However, care must be taken to choose a gas which does not react with the target species in the gas phase to produce species with lower emission intensities. Additives to a rare gas must also not form undesirable masking deposits on the target during sputtering.

CONCENTRATION PROFILING

Another application for GDOS that we have investigated is the concentration profiling of alloy thin films. This technique can be used to estimate the concentration of the constituents as a function of depth through the alloy film. Figure 6 shows a scan that was made while monitoring the Sb concentration in a $\text{GaAs}_{0.952}\text{Sb}_{0.048}$ film. The film was grown on a (111)As-oriented GaAs substrate, and was about $10 \mu\text{m}$ thick. The sputtering rate was $0.3 \mu\text{m}/\text{min}$, and the intensity of the Sb line at 2598 Å was monitored. The upper plateau is flat to within 10%, i.e., $\Delta x \leq 0.1x$, where x is the relative mole fraction of Sb. This indicates that the distribution of Sb is homogeneous to within 10%, which is consistent with x-ray line broadening and photoluminescent measurements reported by Li.¹⁵ The variation is also within the range expected from the alloy growth conditions.

The depth of sample over which one can observe a meaningful change in the Sb concentration is limited primarily by the sputtering rate and the time constants of the amplifiers. In this case the depth resolution is about $0.2 \mu\text{m}$. The sputtering rate of the above alloy film was found to be a factor of 2 less than that of (111)As-oriented bulk GaAs. The reason for this is not obvious to us.

The variations in the upper plateau of Fig. 6 are greater than expected from background noise. They correspond to either small changes in the sputtering rate or inhomogeneities within the film. After the profile was taken, the GaAs substrate was sputtered under the same conditions except that this time the Ga line was monitored. The intensity response was flat to within 1% over the same length of time. In future alloy profiling experiments we intend to monitor the sputtering rate directly for each alloy sample. The Sb profile tails off within $\sim 1 \mu\text{m}$, which is more than the estimated distance for the film-substrate transition region. However, there are several reasons why this tail off region should not be interpreted too closely at present. It probably reflects simultaneous sputtering of the film and substrate caused by a variation in the film thickness over the sample area. Also, some slight rounding of the sample occurs at the edges during sputtering. Finally, the difference in the sputtering yields between the film and the substrate tends to exaggerate the depth of the transition region. In subsequent experiments it is suggested that either a guard ring or a SiO_2 window be employed to minimize sample rounding. Irregularities in sample surface topography after sputtering were far too small to account for the tailing.

CONCLUSIONS

Glow-discharge optical spectroscopy (GDOS) provides an analytical technique for measuring and profiling the concentrations of constituents in thin films. For Sn in GaAs the detection limit is 3×10^{16} atoms cm^{-3} or 0.4 ppm by weight. In addition, we have shown that emission spectroscopy is a quick and sensitive method for measuring sputtering rate. The use of rf sputtering allows GDOS to be applied to nonconducting targets. Background problems can be minimized by a judicious choice of the sputtering gas used. In the future, GDOS may find other applications such as diffusion studies and "non-destructive analysis" where removal of $\sim 1\text{-}\mu\text{m}$ -thick layers is acceptable.

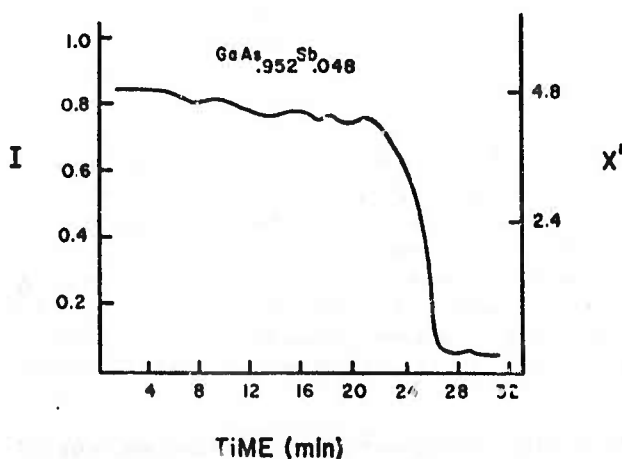


FIG. 6. Emission intensity (arbitrary units) of the 2598-Å Sb line as a function of time. Target was an epitaxial $\text{GaAs}_{0.952}\text{Sb}_{0.048}$ film on a GaAs substrate. x' is the relative mole fraction of Sb.

ACKNOWLEDGMENTS

The authors wish to thank Dr. C. T. Li for providing the gallium arsenide-antimonide film. This work was supported by the Advanced Research Projects Agency, the National Science Foundation, and the Joint Services Electronics Program.

*Departments of Mechanical Engineering, Metallurgy, and the Coordinated Science Laboratory, University of Illinois, Champaign-Urbana, Ill.

¹J. E. Greene and J. M. Whelan, *Bull. Am. Phys. Soc.* **15**, 1614 (1970).

²R. V. Stuart and G. K. Wehner, *J. Appl. Phys.* **35**, 1819 (1964).

³R. V. Stuart, K. Brower, and W. Mayer, *Rev. Sci. Instrum.* **35**, 425 (1963).

⁴J. Jeans, *Kinetic Theory of Gases* (Cambridge U.P., Cambridge, England, 1967).

⁵R. V. Stuart and G. K. Wehner, *Phys. Rev. Lett.* **4**, 409 (1960).

⁶R. V. Stuart and G. K. Wehner, *J. Appl. Phys.* **33**, 2345 (1962).

⁷M. Kaminsky, *Atomic and Ionic Impact Phenomena on Metal Surfaces* (Academic, New York, 1965).

⁸G. D. Magnuson and C. E. Carlston, *J. Appl. Phys.* **34**, 3267 (1963).

⁹A. L. Southern, W. R. Willis, and M. T. Robinson, *J. Appl. Phys.* **34**, 153 (1963).

¹⁰M. T. Robinson and O. S. Oen, *Appl. Phys. Lett.* **2**, 30 (1963).

¹¹H. C. Gatos and M. C. Lavine, *J. Electrochem. Soc.* **107**, A427 (1960).

¹²*Tables of Spectral Line Intensities*, Natl. Bur. Std. (U.S.) Monograph No. 53 (U.S. GPO, Washington, D.C., 1962), part 1.

¹³C. T. Li, Ph.D. dissertation (University of Southern California, 1971) (unpublished).

Cathodoluminescence study of plastically deformed GaAs[†]

A.L. Esquivel, W.N. Lin, and D.B. Wittry

Department of Materials Science, University of Southern California,
Los Angeles, California 90007

(Received 23 January 1977)

Infrared cathodoluminescence (IR-CL) micrographs were taken of surfaces perpendicular (112) and parallel (021) to the bend axis [112] of GaAs single crystals bent at 700 °C in four-point bending to introduce α -Ga and β -As dislocations. At the bend center, light and dark checkered patterns associated with dislocations could be observed only in the IR-CL micrographs but not by optical, infrared, or secondary electron emission microscopy. Dislocation densities to $\rho \approx 5 \times 10^6 \text{ cm}^{-2}$ could be determined nondestructively to within 20% of the theoretical values. No significant changes related to the type of dislocation or dislocation density were observed either in the peak half-width or peak position at $E = 1.411 \text{ eV}$. However, decreases of 40–70% in the relative IR-CL intensity were observed in the bent samples with predominantly α or β dislocations.

Dislocations in GaAs are typically studied by etching low-index planes.¹ In our case, we wished to preserve our plastically deformed samples for further electrical measurements, hence our search for a method not involving any chemical dissolution of the sample surface. The purpose of the present letter is to demonstrate a nondestructive method of characterizing the plastically deformed surfaces of III-V compound semiconductors by using electron-beam-excited cathodoluminescence and to determine the effect of dislocations on the intensity of infrared cathodoluminescence (IR-CL) in plastically deformed GaAs.

Single crystals of GaAs were oriented [Figs. 1(a) and 1(b)] so that an excess of either α -Ga or β -As dislocations were introduced by four-point bending reported previously.² 15- and 17-mm-long samples of 1-mm-sq cross section were cut from an undoped horizontal Bridgman (No. HB-105) and a Te-doped (10^{17} cm^{-3}) Czochralski crystal (No. CZ-16), and bent to progressively increasing dislocation densities as shown in Tables I and II. Dislocation densities were calculated from the measured radii of curvature using Nye's relationship.³ The samples listed in Tables I and II were examined in an electron microprobe (ARL, Model EMX) operated at 40 kV, and with sample currents ranging from 0.46 to 0.70 μA . Most of the micrographs were taken at 200 \times magnification, and the surfaces examined represent square areas [indicated by numbered black rectangles in Figs. 1(a) and 1(b)] from 350 to 400 μ along each edge.

Figures 1(c) and 1(d) are secondary electron emission (SEE) micrographs taken from the bend center (area 1) of the horizontal Bridgman samples containing an excess of α [Fig. 1(c)] and β [Fig. 1(d)] dislocations and different dislocation densities (8.0×10^6 and $5.8 \times 10^6 \text{ cm}^{-2}$, respectively). While the SEE micrographs do not show features related to plastic deformation, the infrared cathodoluminescence (IR-CL) micrographs of the same areas [Figs. 1(e) and 1(f)] reveal a checkered pattern [Fig. 1(e)] and a subsurface flaw indicated by arrows in Fig. 1(f). A line scan (not shown) taken across the surface and normal to the flaw exhibited a decrease in IR-CL intensity in the "shadow" region of the flaw, thus suggesting probably some void or inhomogeneity. None of these features were observed by optical or transmission ir microscopy.

Examination of the checkered pattern in Fig. 1(e) sug-

gests that the regular array of black dots (approximately 3 μ in diameter and indicated by an arrow) is probably related to dislocations lying on (111) slip planes (trace indicated) inclined at 45° relative to the left-hand edge of the photograph and terminating on the (112) surface (plane of the micrograph). An average count of these dots in the IR-CL micrograph yields a dislocation density of $5.0 \times 10^6 \text{ cm}^{-2}$, compared to the calculated value of $8.0 \times 10^6 \text{ cm}^{-2}$. Thus, from IR-CL micrographs a qualitative indication of the dislocation density can be obtained without chemically etching the surface. By determining an optimum level for the bias, it is hoped to improve the resolution of the micrographs and thus also to improve the dislocation density count.

Since the samples were bent at 700 °C in an argon atmosphere, the effect of such short-term heating (15 min) was also investigated. Figures 2(a) and 2(b) show, respectively, IR-CL micrographs of the as-grown (unheated) and heated (unbent) control samples. Dark stripes in Fig. 2(a) represent growth bands on (111) planes inclined at 45° relative to the (021) plane in the as-grown unheated sample. After heating, the small particles in Fig. 2(a) have coarsened and the distance between the bands appears to have increased [Fig. 2(b)], which indicates that impurities responsible for the darker regions in the bands coalesced with the small particles to form larger clusters.

To determine the extent of the deformed regions seen as a checkered pattern in Fig. 1(e), other areas of the bent sample [2, 3, and 4 in Fig. 1(b)] were examined. The IR-CL micrographs in Figs. 2(c) and 2(d) show that the checkered pattern associated with the deformed region [Fig. 2(c)] at the bend center (area 1) disappears near the tip (area 2) of the same Bridgman sample [Fig. 2(d)]. Thus, the principal areas of damage appear confined to the region between the two inner knife edges of the bend apparatus. The deformation, however, at the tensile side of the bend center (area 3) in Fig. 2(e) appears more severe than the damage at the compressive side (area 1) because regions possibly indicating microcracks (arrow) are visible near the sample edge. A checkered pattern similar to that observed in areas 1 and 3 is also found in area 4 [Fig. 2(f)] on the (021) plane, thus indicating that the deformed regions are not confined to the (112) surface.

To obtain semiquantitative data related to the type and density of dislocations, the intensity, peak position, and

TABLE I. Infrared cathodoluminescence intensity, half-width, and peak position for control and bent GaAs samples. Horizontal Bridgman (HB-105) undoped.

No.	Sample No.	Condition excess dislocation type	Calculated dislocation density ρ (cm ⁻²)	Peak position λ_p (Å)		Half-width HW (Å)		Relative peak Intensity, I		% change in intensity relative to tip
				Center	Tip	Center	Tip	Center	Tip	
1										
1	F11-A-AG2	As-grown	$\sim 10^4$ ^a	8780	...	228	...	0.95	0.90	+5
2	F11-B-H2	Heated	...	8800	...	228	...	3.30	3.10	+6
3	F13-C-B1	Bent β	5.8×10^6	b	...	b
4	F11-C-B2	Bent α	5.0×10^6	8790	8810	224	228	1.64	3.20	-49
5	F12-C-B3	Bent α	9.4×10^6	8320	8830	228	228	1.62	4.08	-60
6	F10-C-B4	Bent β	1.7×10^7	8830	8830	225	230	2.10	3.52	-40

^aFrom etch pits on (111) plane.^bNot determined.

half-width of the ir peak at an emission energy of $E = 1.41$ eV were recorded from areas 1, 2, and 3 on the (112) surface of the control and bent samples. In all cases the results are average values obtained by using an electron beam focal spot of ~ 20 - μ diameter. Tables I and II show that the principal changes occurred in the peak intensity and that the peak position and peak half-width remained unaffected by the heat treatment and the type or density of dislocations.

For both the undoped and doped GaAs samples a significant increase in ir intensity is noted after heating (Tables I and II). This increase appears genuine since the peak intensities recorded represent the average of eight to nineteen measurements along the length of each sample. Furthermore, the peak intensity of the heated sample approximated the intensities observed from the tips of the bent doped and undoped samples (Tables I and II). Thus, short-term heating at 700 °C for 15 min produced

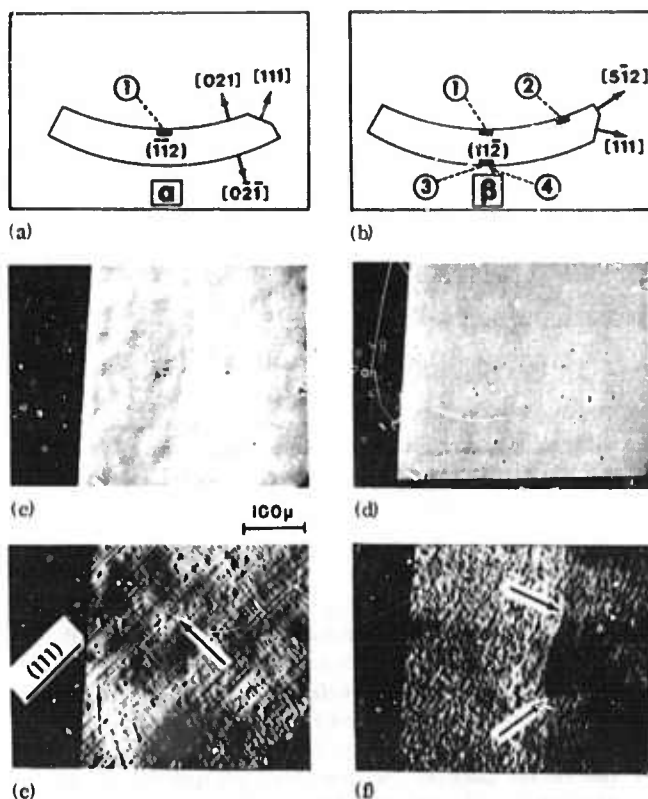


FIG. 1. (a) and (b) are schematic diagrams of orientations used in four-point bending to introduce an excess of α or β dislocations in III-V compound semiconductors. Areas on the (112) surface examined in the electron microprobe are Nos. 1-3. Area 4 lies on the (021) plane. (c) and (d) are secondary electron emission (SEE) micrographs of area 1 in single crystals of GaAs bent according to the scheme in (a) and (b), respectively. (e) and (f) are infrared cathodoluminescence (IR-CL) micrographs of the same area 1 as in (c) and (d), respectively. In (e), arrow points to black dots associated with end point of dislocation of (112) surface. Trace of (111) plane on (112) surface is indicated. In (f), arrows point to subsurface flaw.

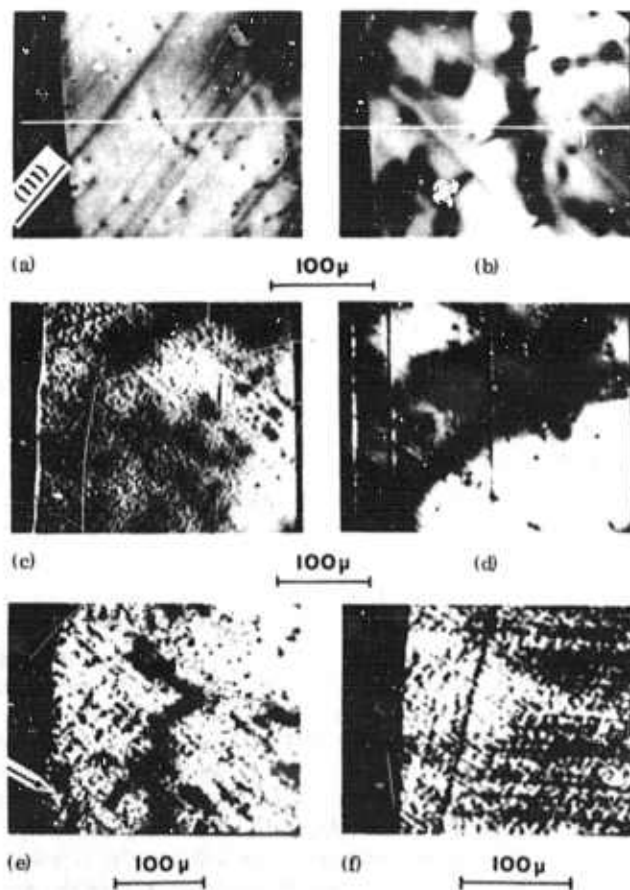


FIG. 2. (a) and (b) are IR-CL micrographs of control samples of Czochozalski-grown GaAs. In (a), as-grown unheated unbent sample; in (b), the heated (700 °C/15 min) unbent sample. (c) and (d) are IR-CL micrographs of bent horizontal Bridgman-grown GaAs. (c) was taken from area 1, and (d) from area 2 of the same sample. (e) and (f) are IR-CL micrographs of same sample as in (c) but are taken from areas 3 and 4, respectively. Arrow in (e) points to possible site for microcracks.

TABLE II. Infrared cathodoluminescence intensity, half-width, and peak position for control and bent GaAs samples. Czochralski (CZ-16) doped Te (10^{17} cm $^{-3}$).

No.	Sample No.	Condition excess dislocation type	Calculated dislocation density ρ (cm $^{-2}$)	Peak position λ_p (Å)		Half-width HW (Å)		Relative peak intensity, I		% change in intensity relative to tip
				Center	Tip	Center	Tip	Center	Tip	
1	9A-AG1	As-grown	$\sim 10^3$ ^a	8780	...	245	...	1.75	1.60	+9
2	9B-W1	Heated	...	8780	...	240	...	3.06	3.44	-11
3	10F-B1	Bent α	4.3×10^6	8790	8790	245	245	1.85	2.72	-32
4	10E-B2	Bent β	4.6×10^6	8790	8790	250	240	1.74	2.47	-30
5	10C-B3	Bent β	8.6×10^6	8760	8790	250	245	0.81	2.82	-71
6	10D-B4	Bent β	1.5×10^7	8790	8790	245	246	2.21	3.54	-38

^aFrom etch pits on (111) plane.

an annealing effect on the dislocations in the as-grown sample as well as a probable redistribution of impurities. Both these processes appear to enhance radiative recombination at the observed wavelength in the heated sample and in the relatively undeformed tips of the bent samples.

Although no systematic decrease in ir intensity was observed with increasing calculated dislocation density in the bent samples, it was observed that the ir intensity from the central portion of the bent sample was consistently lower (from 40 to 70%) than the intensity from the relatively undeformed tip of the same sample. This observation was found true in both the Bridgman and Czochralski samples (Tables I and II). To eliminate the possibility of excessive inhomogeneity within the same sample, the regions between the center (area 1) and tip (area 2) as well as between the tensile (area 3) and compressive (area 1) surfaces of the bent samples were examined for changes in the ir intensity. The results (not shown) indicate a systematic decrease in ir intensity with increasing dislocation density associated with regions extending from the tip to the bend center. That the dislocation density increased upon approaching the bend center has been observed in micrographs similar to those in Figs. 2(c) and 2(d).

Although the process of recombination of excess carriers at dislocations is not fully understood, it is known that dislocations in germanium introduce deep acceptor

levels which act as traps for minority carriers.⁴⁻⁷ Dislocations in GaAs, however, would be expected to behave in the same way. Thus, in portions of the bent sample where the dislocation density is high, there is a corresponding high density of traps so that a decrease in radiative recombination takes place. There is also the possibility that dislocations act as recombination centers which emit ir radiation at a wavelength which falls beyond the range (0.6–1.1 μ) of our $S=1$ ir detector, so that the observed low ir intensity represents merely a portion of the complete ir spectrum. Further study with a detection system capable of recording ir radiation at wavelengths greater than 1.1 μ should resolve this question.

The authors would like to thank Professor William R. Wilcox for his interest and encouragement and S. Sen for assistance with part of the experimental work.

[†]Work supported by the Advanced Research Projects Agency.
¹M.S. Abrahams and C.J. Bulocchi, J. Appl. Phys. 36, 2855 (1965).

²A.L. Esquivel and S. Sen, Bull. Am. Phys. Soc. 17, 61 (1972).

³J.F. Nye, Acta Metall. 1, 153 (1953).

⁴S.R. Morrison, Phys. Rev. 104, 619 (1956).

⁵T. Figielski, Phys. Status Solidi 9, 555 (1965).

⁶T. Figielski, Phys. Status Solidi 10, 75 (1965).

⁷G.K. Wertheim and G.L. Pearson, Phys. Rev. 107, 694 (1953).

286<

Reprinted from
PROCEEDINGS OF THE SIXTH INTERNATIONAL CONFERENCE ON
X-RAY OPTICS AND MICROANALYSIS

Edited by G. SHINODA, K. KOHRA and T. ICHINOKAWA

UNIVERSITY OF TOKYO PRESS, 1972

Crystallographic Information from Scanning Electron Microscope Images

K

D. B. WITTRY

*Departments of Materials Science and Electrical Engineering, University of Southern California,
Los Angeles, California, U.S.A.*

In conventional scanning electron microscopes, the angle of incidence of the electron beam varies as the electron beam scans over an extended area. In this paper, a scanning mode is described that provides controlled crystallographic contrast by maintaining a constant but controllable angle of incidence. This mode, called an area scan mode, is complementary to the angle scan mode employed in selected area channeling patterns. The advantage of a scanning system that provides for rapid switching between area scan and angle scan modes is emphasized and an example of application to a silicon bicrystal is given.

INTRODUCTION

In conventional scanning electron microscopes, the angle of incidence of the beam changes as the beam scans over an extended area. In such a case, contrast due to crystallographic effects is mixed with contrast due to changes in composition or topography. Since the contrast due to crystallographic effects depends only on the angle of incidence of the beam, several authors have proposed methods for obtaining diffraction (or channeling) patterns by changing the angle of incidence of the beam while the point of impact of the beam remains fixed. These methods, which are analogous to the method of selected area diffraction in transmission electron microscopy, have included rocking the specimen mechanically,¹ double deflection of the incident beam,² and single deflection of the incident beam combined with the converging action of the objective lens.³

In the present paper, we consider two independent scanning modes, the angle scan, in which the beam position remains fixed and the angle of incidence is scanned as described above, and the area scan, in which the beam scans an extended area at a predetermined constant angle with respect to the specimen's surface. These two modes of operation are completely analogous to the two modes of operation of the transmission electron microscope, namely the diffraction mode and the imaging mode.

In transmission electron microscopy, it is possible to switch quickly back and forth between the diffraction mode and the imaging mode. Rapid switching between these two modes is essential in order to realize the full potential of both modes. In the diffraction mode, one can observe the angular distribution of transmitted electrons and use this information to select the position of angle-defining stop that is employed for image formation. In the imaging mode, one can observe the size and shape of various regions and use this information to position the area-defining stop that is employed for the diffraction mode.

The scanning electron microscope can provide similar advantages for the study of crystalline materials but only if the scanning modes employed clearly separate angle-dependent information from area-dependent information. The angle scan and area scan modes provide this separation.

This paper is concerned with special scanning systems that can provide both angle and

area scans and gives an example of the application such a scanning system to the examination of a silicon bicrystal.

THE AREA SCAN MODE

Most SEM results reported in the literature involve a mixture of the area and angle scan modes because of the type of scanning systems normally available in scanning microscopes. Because of the interest in crystallographic contrast in scanning microscopy, several methods for obtaining pure angle scans have been reported.¹⁻³⁾

In contrast, there have been few examples of pure area scans. One such example, which was devised for scanning electron mirror microscopy, was described by Garrood and Nixon.⁴⁾ This scanning system provided only for scanning the specimen at a fixed angle (normal to the surface) so that reflected electrons could be collected. It was not used for observation of crystallographic effects. A second example was given by Philibert and Tixier,⁵⁾ who showed interesting contrast effects on polycrystalline specimens using a microanalyzer in which scanning was accomplished by mechanical displacement of the specimen in one direction. In the instrument they used, the mechanical scanning was dictated by requirements of scanning X-ray microanalysis and was not intentionally provided for obtaining diffraction contrast effects.

A useful area scan mode must not only provide for scanning an area of the specimen at a constant angle, but must also provide for changing this angle in a controlled manner. Scanning systems providing this feature in order to obtain stereo pairs have been described by Okano *et al.*⁶⁾ and by Dinnis.⁷⁾ Okano used an offset of the objective aperture between exposures while Dinnis used a postlens double deflection system. However, neither of these systems was used to obtain pure angle scans or to obtain crystallographic contrast.

DEFLECTION SYSTEMS FOR BOTH AREA AND ANGLE SCANS

The importance of being able to switch rapidly between the area and angle scan modes has already been emphasized. Hence, in practical cases, it is necessary to give equal consideration to both modes of operation. For purposes of illustration, we shall consider a double deflection system and neglect the effect of beam deflection on the focusing of the electron probe. Such a system is shown schematically in Fig. 1. The ac drive to the two sets of deflection coils has

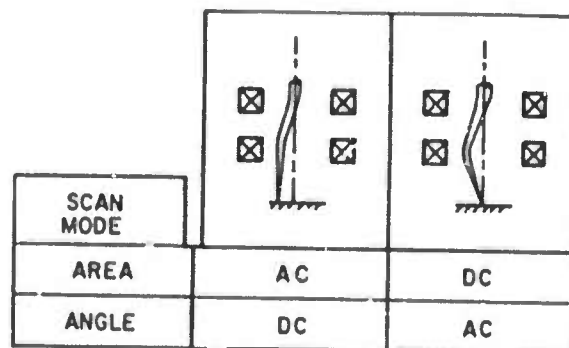


Fig. 1 Simplified diagram of beam deflections for area and angle scans including provision for positioning the probe for angle scans and for setting the angle of incidence of the beam during area scans.

which is valid for

$$\frac{V_2}{V_1} > \frac{w_o - w_e}{1 - w_e} \quad (12)$$

For V_2/V_1 less than this, $w_s = 1$ (pure beryllium). Immediately after a change in freezing rate, $(\partial w/\partial x)$, begins to change and continues to change until a new quasi-steady state is reached, from Equations (2) and (7)

$$w_s = w_e + \frac{1 - \exp\left(-\frac{\delta V_1}{D} \frac{\rho_s}{\rho_l}\right)}{1 - \exp\left(-\frac{\delta V_2}{D} \frac{\rho_s}{\rho_l}\right)} (w_o - w_e). \quad (13)$$

In the present experiments, we estimate that $\delta \sim 100 \mu$ and that $D \sim 4 \times 10^{-5} \text{ cm}^2/\text{sec}$. Thus, $\delta V/D \sim 0.007$ and Equation (13) reduces to Equation (11). Thus, the transient before the quasi-steady state is reached is unimportant. For a true steady state to be reached, the bulk zone concentration w_s must change until $w_s = w_o$ once again. If the initial transient in the stagnant film is ignored, we find from Equations (2), (5), (7), and (13) that the solid concentration after a sudden change in freezing rate varies according to

$$\frac{w_s - w_o}{w_e - w_o} = \frac{\exp\left(-\frac{\delta V_1}{D} \frac{\rho_s}{\rho_l}\right) - \exp\left(-\frac{\delta V_2}{D} \frac{\rho_s}{\rho_l}\right)}{1 - \exp\left(-\frac{\delta V_2}{D} \frac{\rho_s}{\rho_l}\right)} \exp\left[-\frac{z}{l} \frac{\rho_s}{\rho_l} \frac{1}{1 - \exp\left(-\frac{\delta V_2}{D} \frac{\rho_s}{\rho_l}\right)}\right] \quad (14)$$

which can be compared with Equation (4), the analogous relationship for progressive freezing (with $\rho_s = \rho_l$). When $\delta V_2/D$ is very small, the readjustment to steady state is rapid. Since $\delta V_2/D \approx 0.007$ in the present experiments, the solid concentration would have completed $(1 - 1/e) = 63\%$ of its readjustment to steady state in a distance equal to 0.007 of the zone length, or about 180μ . This is somewhat larger than the smallest bands observed (Figure 3), indicating that many of the freezing rate fluctuations were more rapid than the relaxation time of the melt.

The effect of any arbitrary variation in freezing rate may also be calculated with the same quasi-steady-state approach. Numerical integration of Equation (5) may be required.

To the first approximation, the interface stability criterion for slow freezing of off-eutectics may be found from elementary constitutional super-cooling considerations. Thus, the interface is predicted to be stable for

$$\left(\frac{dT}{dx}\right)_i \geq \left(\frac{dT_f}{dx}\right)_i = \left(\frac{dw}{dx}\right)_i \left(\frac{\partial T_f}{\partial w}\right)_i \quad (15)$$

where T is the actual temperature and T_f is the freezing point of the mixture at distance x from the interface. For steady-state operation, $(dw/dx)_i$ may be found from Equation (2) with $w_i = w_o$ and $w_i = w_e$. Letting $m_e = (\partial T_f / \partial w)_i$ and $G = (dT/dx)_i$, we find that the stability criterion is

$$\frac{G}{V} > \frac{m_e \rho_i}{D} (w_o - w_e) \quad (16)$$

which is the same as for progressive freezing, indicating that convection has no influence on stability of the interface. From Hansen [2] we estimate that for the beryllium-rich side of the eutectic, $m_e = 7380^\circ\text{C}/\text{wt fraction Be}$.

Assuming $\rho_i/\rho_l \approx 1$ and using a temperature gradient of $1000^\circ\text{C}/\text{cm}$, we estimate that we need $V < (1000)(4 \times 10^{-3})/(7380)(0.20 - 0.009) = 2.8 \times 10^{-3} \text{ cm/sec} = 1.02 \text{ mm/hr}$.

V. DISCUSSION

Several interesting features of the microstructures warrant discussion. Figures 2 and 3 indicate that significant growth rate fluctuations occurred. The fluctuations in fiber size seen in Figure 2 were probably caused by relatively rapid fluctuations in temperature. Such temperature fluctuations, caused by free convection [17-20], have been observed in virtually all solidification systems in which a significant temperature gradient was present in the melt. The banding shown in Figure 3 was caused by large freezing rate variations of several minutes duration. These variations probably resulted both from sticking of the ingot in the heating entrance and exit and in the cooler, and from variations in power input to the heater and helium flow to the cooler. It is interesting to note that the microstructure corresponds roughly to our theoretical expectations. A few beryllium bands were obtained, corresponding to suddenly reduced growth rates. Aluminum-rich bands of near-eutectic composition were formed, corresponding to suddenly increased growth rates. The fiber spacing was much smaller in the aluminum-rich bands as expected from the faster growth rates. If we assume that an initial steady-state condition existed at a zone travel rate of 1 mm/hr , Equation (11) shows that a sudden decrease in rate to 0.2 mm/hr or lower would be required to produce a band of beryllium. An increase of about an order of magnitude would be required to approach the eutectic composition. The $\sim 40 \mu$ spacing of fibers corresponds to a growth rate of $\sim 0.2 \text{ mm/hr}$, extrapolating to previous results on the Be-Al eutectic [15] and on other eutectics [25]. Thus, we estimate that the true freezing rate varied between about 0.1 and 10 mm/hr , corresponding to about a ten-fold variation in fiber spacing, as roughly observed.

No evidence of interface instability was noted, except in the aluminum-rich bands. In Figure 3, the beryllium fibers in the aluminum-rich band were almost absent in certain areas and were growing as colonies at various angles

shown in Fig. 4(b) was taken on its twin (see Figs. 4(c) and (d) for the location of these areas). Figures 4(c) and (d) show area scan images with different contrast for two different angles of incidence of the beam during the scan (refer to Figs. 4(a) and (b) for the location of these angles with respect to the angle scan patterns). All images were recorded with a beam current of $1 \mu\text{A}$ and 40 kV.

Noise in the images of Fig. 4 is due partly to the low signal level and partly to low contrast. These limitations were due to the need to shunt the detectors with a small resistor (200Ω) to improve their frequency response and to the difficulties in obtaining a damage-free surface on the silicon. Pattern distortion and also minimum size for the selected area ($\sim 20 \mu$) is due to imperfect balancing of the scan controls and imperfect alignment of the deflection coils.

While the results shown are very crude, they illustrate the advantage of images in which there is a clear distinction between angle-dependent information and position-dependent information. These results show that one can obtain controlled crystallographic contrast in SEM by using scanning systems in which it is possible to switch rapidly between angle and area scan modes.

Acknowledgments

This work was supported by the National Science Foundation under Grant No. GK 3904, by the Advanced Research Projects Agency of the Department of Defense under Grant No. DAHC 15-70-G14, and by the Joint Services Electronics Program through the Air Force Office of Scientific Research (AFOSR), United States Air Force, under contract F44620-71-C-0067. John Potosky provided valuable technical assistance including evaluation of the use of commercial silicon solar cells for backscattered electron detectors. Acknowledgment is also due to Applied Research Laboratories, Inc., for the loan of an additional driver unit for the scanning coils.

REFERENCES

- 1) Coates, D. G., *Proceedings of the 2nd Annual SEM Symposium* (Illinois Institute of Technology, Chicago, 1969) pp. 29-40.
- 2) Van Essen, C. G. and Schulson, E. M., *J. Mat'l's Sci.*, **4**, 336-39 (1969).
- 3) Van Essen, C. G., Schulson, E. M. and Donaghay, R. H., *Nature*, **225**, 847-48 (1970).
- 4) Garrood, J. R. and Nixon, W. C., *Electron Microscopy 1968* (Tipografia Poliglotta Vaticana, Rome, 1968) pp. 94-95.
- 5) Philibert, J. and Tixier, R., *Micron*, **1**, 174-86 (1969).
- 6) Okano, H., Hosoki, S. and Tomura, T., *Proceedings of the Fourth National Conference on Electron Microprobe Analysis*, Pasadena, Cal. (1969).
- 7) Dinnis, A. R., *Proceedings of the Fourth Annual SEM Symposium* (Illinois Institute of Technology, Chicago, 1971) pp. 41-48.
- 8) Potosky, J. C., *Proceedings of the Sixth National Conference on Electron Microprobe Analysis*, Pittsburgh, Pa. (1971).



STUDY OF A DUOPLASMATRON WITH A QUADRUPOLE MASS SPECTROMETER*

J.C. Potosky and D.B. Wittry
Departments of Electrical Engineering and Materials Science
University of Southern California
Los Angeles, California 90007

An ideal ion source for an ion microprobe is characterized by high brightness, small virtual source size, and stability. It is also desirable to produce beams of different atomic or molecular species and charge. The duoplasmatron, invented by Von Ardenne¹ can meet the above requirements² and have been used previously as an ion source for ion microprobes.

The duoplasmatron operates by initiating a discharge through a low pressure gas. The gas is ionized and a plasma is produced in the discharge region. An electric field produced by an intermediate electrode, and a longitudinal magnetic field serve to confine the plasma along the central axis and to produce a high ion density in a small region near the anode. The ion beam is extracted from this region with a suitable electrode.

The duoplasmatron shown in Fig. 1 was constructed for use as an ion source for an ion microprobe. In order to produce ions of reactive gases a cold hollow cathode was used in place of the conventional thermionic cathode as in the work of Liebl et al.³ Initially a 1/4" dia. hollow tantalum tube was used as the cathode. However, it was not satisfactory because of higher pressures required by Paschen's law. The cathode of an OB2 electron tube was found to be a useful hollow cathode because of its low work function and ease of replacement. This cathode provided a larger area of high emissivity and resulted in satisfactory operation. Four inexpensive ring-shaped ferrite magnets (Edmund Scientific Co. #40,482) produce the required magnetic field.

An adjustment was provided to offset the cathode-intermediate electrode axis with respect to the anode aperture. The offset optimizes the extraction of negative ions while reducing electron loadings as shown by Lawrence et al.⁴ A standard 100 micron platinum electron microscope aperture was used in the anode to limit the diameter of the extracted beam. The small aperture also serves to isolate the higher pressure discharge region from the high vacuum column which is maintained at $\sim 5 \times 10^{-5}$ torr by a LN₂ trapped oil diffusion pump (Veeco EP2A-1). Typical duoplasmatron pressures⁵ were .05 to .50 torr with corresponding system pressures of 1 to 5×10^{-5} torr.

The I-V characteristics of the discharge are shown in Fig. 2. This curve is pressure dependent. For maximum beam current the intermediate electrode is biased at +50 volts with respect to the cathode.

The mass spectra of the extracted ion beam were obtained with a quadrupole mass spectrometer (Extranuclear Laboratories Inc. model QPS and Special

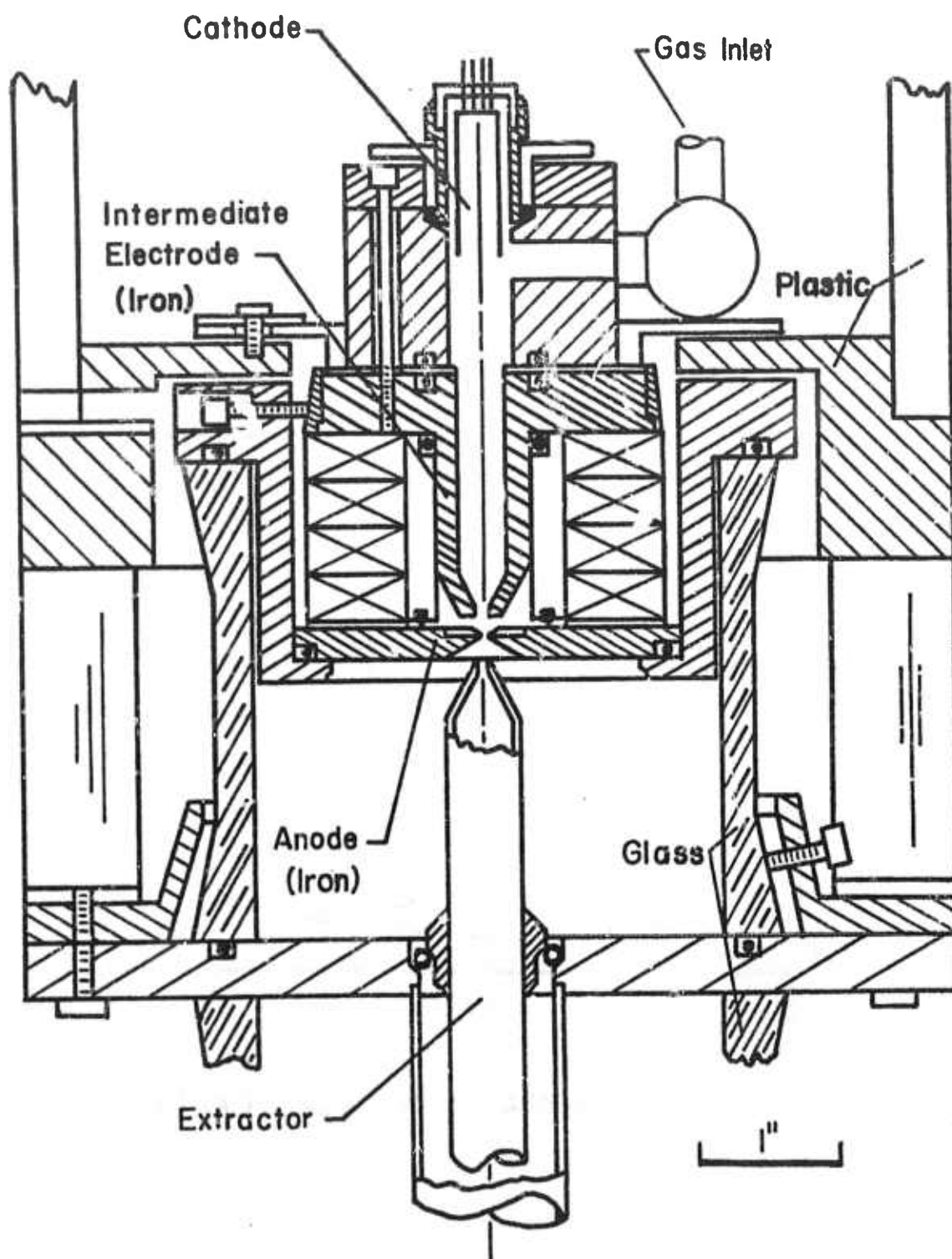


Fig. 1

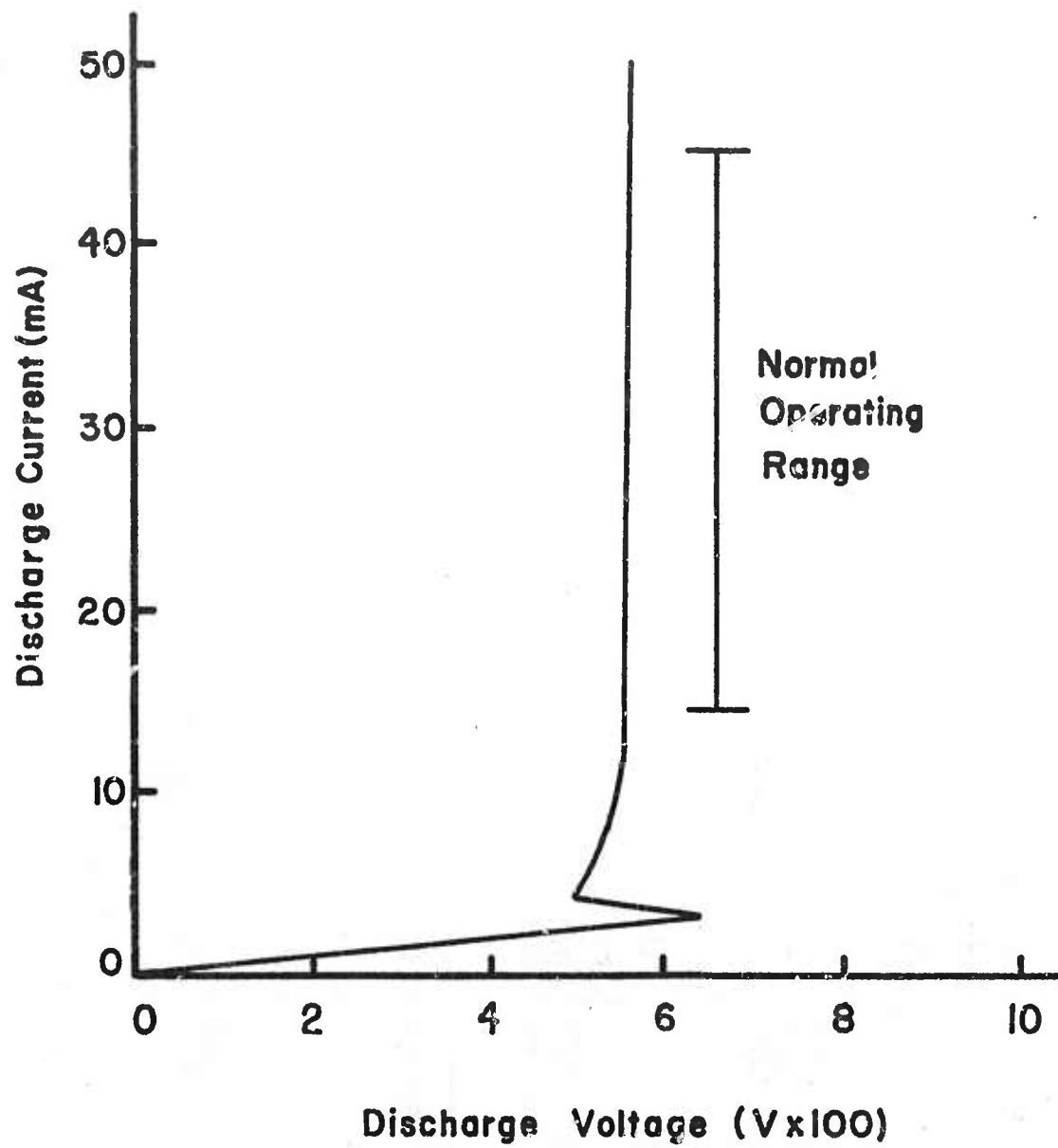


Fig. 2

294<

D-1 High-Q-Head). The body of the spectrometer and mean pole potential was biased near the anode potential for best resolution. It was found desirable to use an electron lens to focus the ion beam into the quadrupole. The experimental arrangement is shown schematically in Fig. 3. The duoplasmatron was run on oxygen and air with negative and positive beams extracted. The spectra obtained are shown in Fig. 4. It should be noted that the intermediate electrode was adjusted to maximize the ion output in each case.

The brightness was not measured. However, if the virtual source size is assumed to be 50 microns, for the ion currents measured (without the quadrupole mass filter but with electron filtering) the brightness could be estimated to be ~ 2 A/cm² ster at 3KV. This may be compared with reported values of 100-200 A/cm² ster. obtained at voltages of 12KV and higher.²

Acknowledgements

N. Gardner assisted in the construction of the apparatus and J. Norris performed some initial tests. H. Roden contributed valuable advice during the construction of the plasmatron.

* This work was sponsored by the Joint Services Electronics Program through the Air Force Office of Scientific Research under grant F44620-71-C-0067 and by the Advanced Research Projects Agency under grant DAHC 15-72-67.

1. M. Von Ardenne, "Tables of Electron Physics, Ion Physics, and Electron Microscopy," Deutscher Verlag der Wissenschaften, Berlin 1, 544-557, 845-862 (1956).
2. H. Liebl, J. Appl. Phys. 38, 5277-83 (1967).
3. C.R. Robinson, H.J. Liebl, and C.A. Anderson, Third Nat. Conf. Electron Microscope Analysis, Chicago, (1968).
4. G.P. Lawrence, R.K. Beuchamp, J.L. McKibben, Nuclear Inst. and Meth. 32, 357-9 (1965).

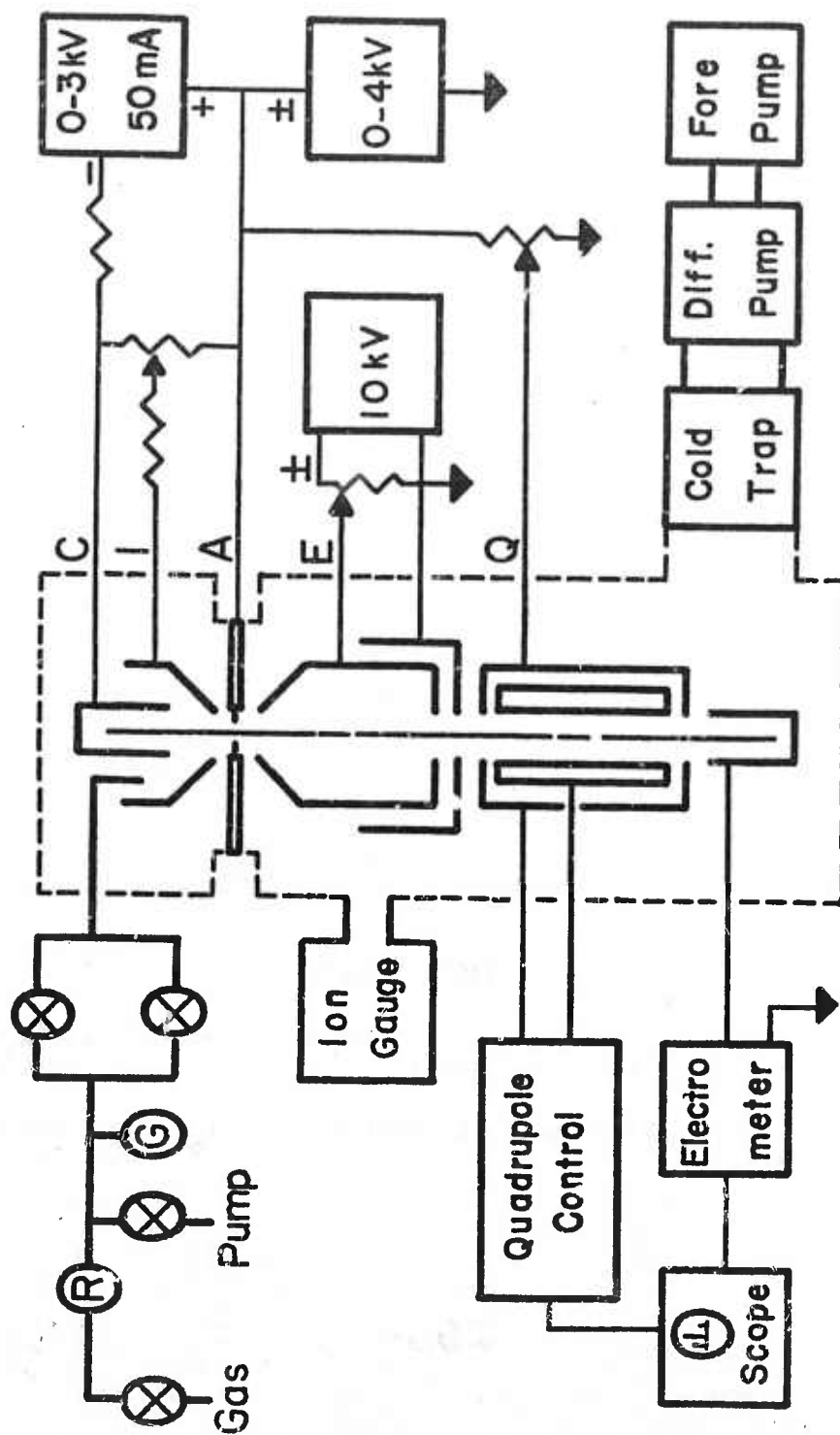


Fig. 3

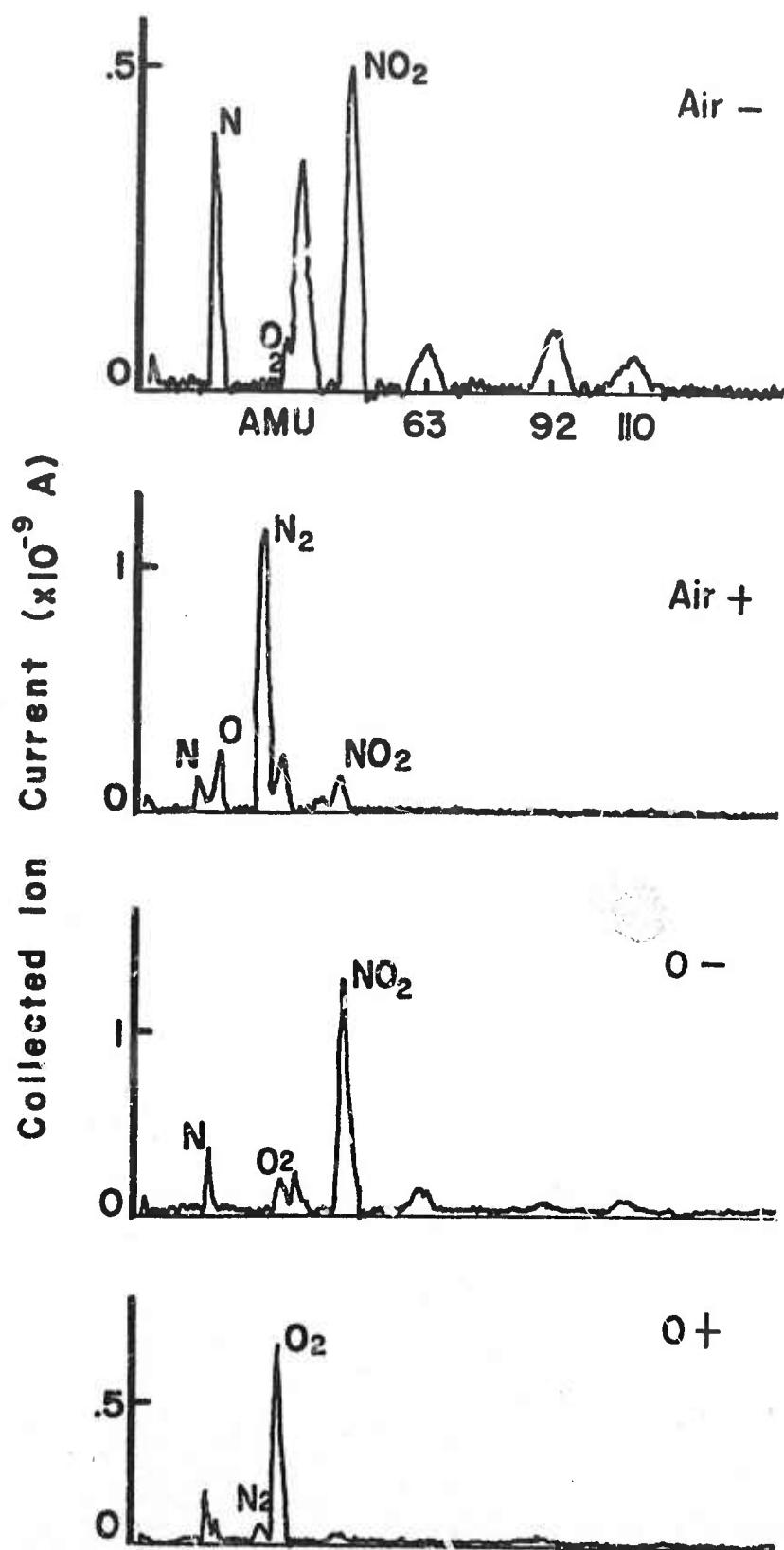


Fig. 4

Reprinted from:

THE REVIEW OF SCIENTIFIC INSTRUMENTS

VOLUME 42, NUMBER 12

DECEMBER 1971

A Clean Vacuum Electron Beam Column for Cathodoluminescence Investigations*

H. C. MARCINIAK AND D. B. WITTRY

Departments of Materials Science and Electrical Engineering, University of Southern California, Los Angeles, California 90007

(Received 28 June 1971)

An instrument is described for investigation of cathodoluminescence at temperatures between 25 and 400 K and beam voltages to 50 kV. Contamination effects are minimized by the use of oil-free pumps, by isolation of the specimen region from sources of organic vapors, and by the use of baffles at liquid nitrogen temperature above and below the specimen region. Preliminary results on the cathodoluminescence of GaAs are reported and compared with the temperature dependence of the bandgap from optical absorption data.

INTRODUCTION

Electron irradiation in conventional electron beam instruments produces contamination deposits on the surface of the sample. The deposits are due to the interaction of the electron beam with organic vapors (from the vacuum pump oil, grease on O-rings, solvents used in cleaning, finger prints, etc.). Effects due to contamination become particularly serious when the specimen is cooled below ambient temperature. One solution to this problem is to construct a fully bakable uhv system. Another solution is to use an oil-free pumping system and to minimize the arrival of organic vapors at the specimen by suitable baffles and cold traps. An instrument based on the latter approach is described in this paper.

Previous experiments have shown that cooling the surfaces near the sample reduces the accumulation of surface contaminants by reducing the partial pressure of vapors in the specimen region.¹ In the present work, the specimen region is isolated from the sources of contamination by a T-shaped tube; a liquid nitrogen cooled baffle is used between this tube and the pumping chamber. The objective lens, which is located outside this tube, is also liquid nitrogen cooled.² With this approach, it is possible to avoid the high cost of a system constructed completely in accord with uhv practices.

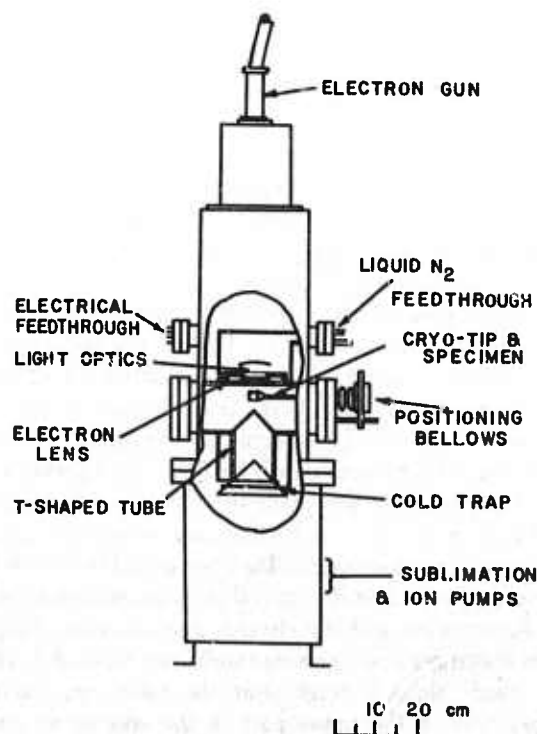
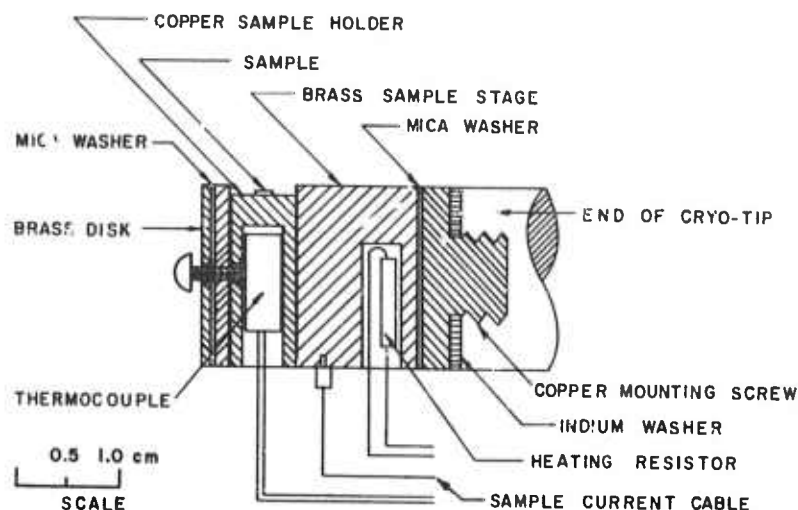


FIG. 1. Schematic diagram of the electron beam column (the scale is only approximate).

FIG. 2. Schematic diagram showing the sample mounting assembly.



VACUUM SYSTEM

The system is shown schematically in Fig. 1. The walls of the chamber are heliarc welded from plates of 304 stainless steel. Vacuum seals use either copper gaskets or Viton-A O-rings. The T-shaped tube located just below the electron lens isolates the specimen region from the rest of the vacuum system. This tube has a 1.27 cm diam hole for the electron beam on top and a large outlet with a cold trap on the bottom communicating directly to the main pumping chamber.

The main pump assembly is a commercially available tabletop uhv system.³ It consists of a liquid nitrogen cooled sorption pump which brings the system's pressure down to 5×10^{-8} Torr, and a combination of titanium sublimation and ion pumps capable of pumping to 10^{-9} Torr and less. In order to minimize the gas load on the sorption pump, an oil-free carbon vane pump⁴ is used to rough the system down to a pressure of 1 Torr.

The choice of materials involved a compromise between cost and minimum outgassing. Certain components that were readily available were not constructed according to uhv practice: these include the electron gun, the electron lens, and the reflecting objective in the optical system.⁵ While these components are all outside the specimen region, every attempt was made to reduce their outgassing. Elastomer seals were used when they were necessary to avoid major reconstruction. These were used mainly in the upper part of the system (optical objective mounting plate and adjustments and the electron gun mounting flange). When elastomer seals were required, only Viton-A O-rings were used; these O-rings limit the maximum bakeout temperature of the upper part of the column to about 100°C. However, because of the low thermal conductivity of stainless steel, the lower half of the chamber could be heated to higher temperature. Bakeout was done by wrapping the chamber with heater tape, the lower half of the chamber being heated more than the upper half.

With this system pressures of 5×10^{-7} Torr are obtained in about 8 h of pumping. With the electron lens and the cold trap cooled with liquid nitrogen the pressure improves to $4-5 \times 10^{-8}$ Torr. No contamination has been observed, even after 3 or 4 h of electron bombardment with the sample at 50 K, and a 5–10 μ spot with a beam current of 0.2 μ A and an accelerating voltage of 50 kV. No visible contamination has been observed during any of the experiments, even when currents of 1.0 μ A were used.

ELECTRON BEAM SYSTEM

The electron beam system consists of a self-biased triode electron gun and a single flat objective lens of the type used in a commercial electron probe microanalyzer.² The gun consists of a V-shaped tungsten filament, a Wehnelt cylinder, and an anode. The accelerating voltage is obtained by a regulated (1 part in 10^4 with line variation of 10%) dc supply which provides voltages up to 50 kV.⁶ Voltages of this magnitude, or even higher, are useful for cathodoluminescence studies to minimize surface recombination effects.⁷ The single electron lens is powered by a constant current power supply⁸ having regulation better than 0.02% + 1 mA for a 10% change in line voltage or load variations from nominal load resistance to zero resistance. Using the lens and high voltage supply described, a spot of about 10 μ and up to 1.5 μ A at 50 kV has been obtained.

SAMPLE HOLDER AND COOLING SYSTEM

The sample holder is mounted at the end of the Joule-Thompson refrigerator.⁹ The refrigerator uses high pressure nitrogen and hydrogen in an open Joule-Thompson cycle. It is capable of achieving temperatures down to 22 K.

Design of the sample holder must include several factors, namely, (1) good thermal contact to the refrigerator, (2) electrical isolation from ground so that sample currents can be measured, (3) a means for temperature sensing, (4) a

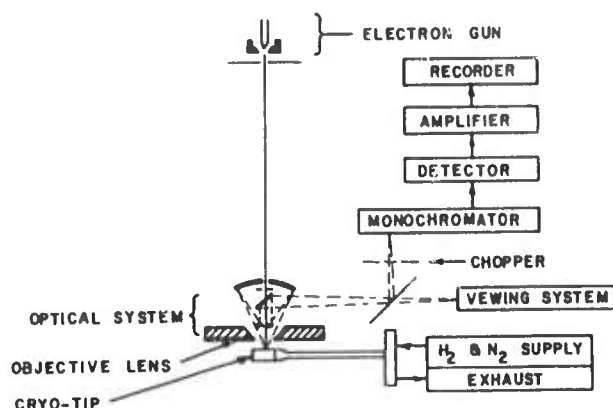


FIG. 3. Schematic diagram showing the electron beam column instrumentation used for cathodoluminescence studies using this instrument.

means for specimen heating, and (5) a minimum mass for rapid cooldown (the refrigeration capacity is only 2 W). Good thermal contact with electrical isolation is difficult to obtain in a clean vacuum system since one cannot use thermally conducting greases as is sometimes done in low temperature work. Two approaches have been tried. The first, shown in Fig. 2, uses two small mica disks which sandwich the brass sample holder. The mica disk nearer the cold end of the refrigerator is 0.05 mm thick. The other method replaces this disk with two anodized aluminum disks sandwiched between two indium washers. The aluminum disks are 0.025 mm thick with a 2.5μ thick Al_2O_3 film on both sides. The soft indium insures good thermal contact between the joined surfaces which are likely to have surface irregularities. Both these methods gave comparable results. About 1 h was required in each case to cool from 290 to 27 K.

The semiconductor specimens are mounted on a small partially hollow copper rod 6.35 mm in diameter. It is held in the brass holder with a setscrew. A thermocouple is soldered in a small stainless steel holder and held in the hollow portion of this copper rod using the same setscrew. Soldering the thermocouple, instead of electrically insulating it from the rest of the sample holder using low vapor pressure epoxy, gives more accurate temperature measurements, at the expense, however, of having to read sample current and temperature sequentially.

Motion of the specimen is obtained by a bellows used to mount the refrigerator to the system. Motion is transmitted by knobs on three threaded rods; these push or pull against a disk mounted on the bellows flange. Springs are used on the screws to balance the force due to atmospheric pressure on the bellows.

To minimize the down time involved in changing specimens, three or four small samples are mounted on the end of the 6.35 mm copper rod. Samples are mounted using indium. The samples are pressed into the indium either

while it is hot or at room temperature. The use of indium eliminates contaminants which could be present if conducting epoxy or silver paint were used.

OPTICAL SYSTEM

The optical system is shown schematically in Fig. 3. The sample is viewed and light produced at the sample is collected by a reflecting objective coaxial with the electron beam. This objective has a numerical aperture of 0.40, a magnification of 28, and a focal length of 10.2 mm. The emerging light is mechanically chopped at 11 Hz and is focused on the entrance slit of a spectrometer¹⁰ whose numerical aperture is 6.6 and whose focal length is 60 cm, with a 1200 groove/mm grating blazed for 7500 Å. Using 0.1 mm entrance and exit slits the resolution is 1 Å. A lens in front of the entrance slit reduces the image size so that a smaller spectrometer slit can be used; this lens is chosen so that the maximum aperture angle of the spectrometer is used, thus providing maximum resolution without loss of signal. Light emerging from the exit slit falls on a photomultiplier whose signal is amplified and recorded by a synchronous amplifier.¹¹

PRELIMINARY RESULTS

Preliminary results obtained with this instrument are shown in Fig. 4. In this figure the peak of the cathodoluminescence spectrum of a heavily doped p-type GaAs sample is plotted as a function of temperature. This sample was used for its high cathodoluminescence efficiency which makes it easy to align the system. The dashed curve is a plot of the absorption edge vs temperature according to Casey and Panish.¹² Experiments performed on lighter doped ($N_A \approx 10^{17} \text{ cm}^{-3}$) p-type GaAs gave two emission peaks separated by 13 meV at temperatures below 90 K as reported by Cusano.¹³ Further studies are in progress, including studies of the temperature dependence of catho-

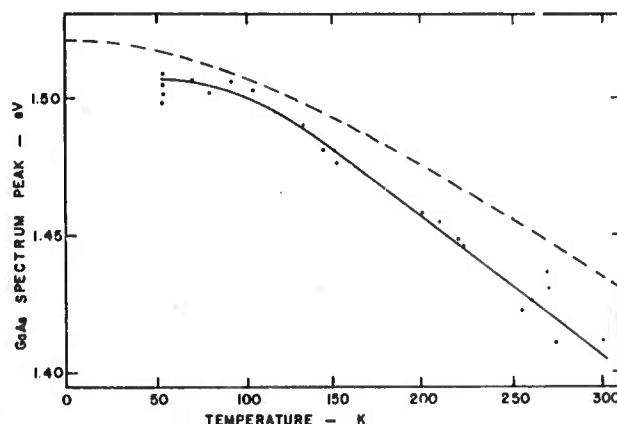


FIG. 4. Peak of the cathodoluminescence spectrum vs temperature of a heavily doped p-type GaAs sample. — Experimental; - - Casey and Panish.

doluminescence in $\text{GaAs}_{1-x}\text{P}_x$ alloys and studies of electron beam excited donor-acceptor pair recombination in GaP.

* Research sponsored by the Air Force Office of Scientific Research, Office of Aerospace Research, United States Air Force, under grant No. AF-AFOSR-68-1414; the National Science Foundation under Grant No. GK3904; and Advanced Research Projects Agency of the Department of Defense under Grant No. DAHC 15-70-G14.

¹A. J. Campbell and R. Gibbons, *The Electron Microprobe* (Wiley, New York, 1966), pp. 75-82.

²Hermann Neuhaus, "Reduction of Contamination Effects in Electron Microprobe Analysis," Nat. Conf. Electron Microprobe Anal. 3rd, No. 19, 1968.

³Ultec TN3 ultrahigh vacuum system, model 7-7389.

⁴Bell and Gossett, model SYL 20-1.

⁵Optical mounting plate from an Applied Research Laboratories electron probe x-ray microanalyzer, model 21 000.

⁶Calmag regulated dc power supply, model 6VT6B.

⁷D. B. Wittry and D. F. Kyser, *J. Appl. Phys.* **38**, 375 (1967).

⁸Power Designs, constant voltage/constant current power source, model 3650R.

⁹Air Products and Chemicals, Inc., heat exchanger, model No. AC-2-109.

¹⁰Spex Industries, Inc., model No. 1700-II.

¹¹Brower Laboratories, Inc., synchronous amplifier-recorder, model 109.

¹²M. B. Panish and H. C. Casey, Jr., *J. Appl. Phys.* **40**, 163 (1969).

¹³D. A. Cusano, *Solid State Commun.* **2**, 353 (1964).



STUDY OF GaAs USING INFRARED MODULATED CATHODOLUMINESCENCE*

W.N. Lin and D.B. Wittry

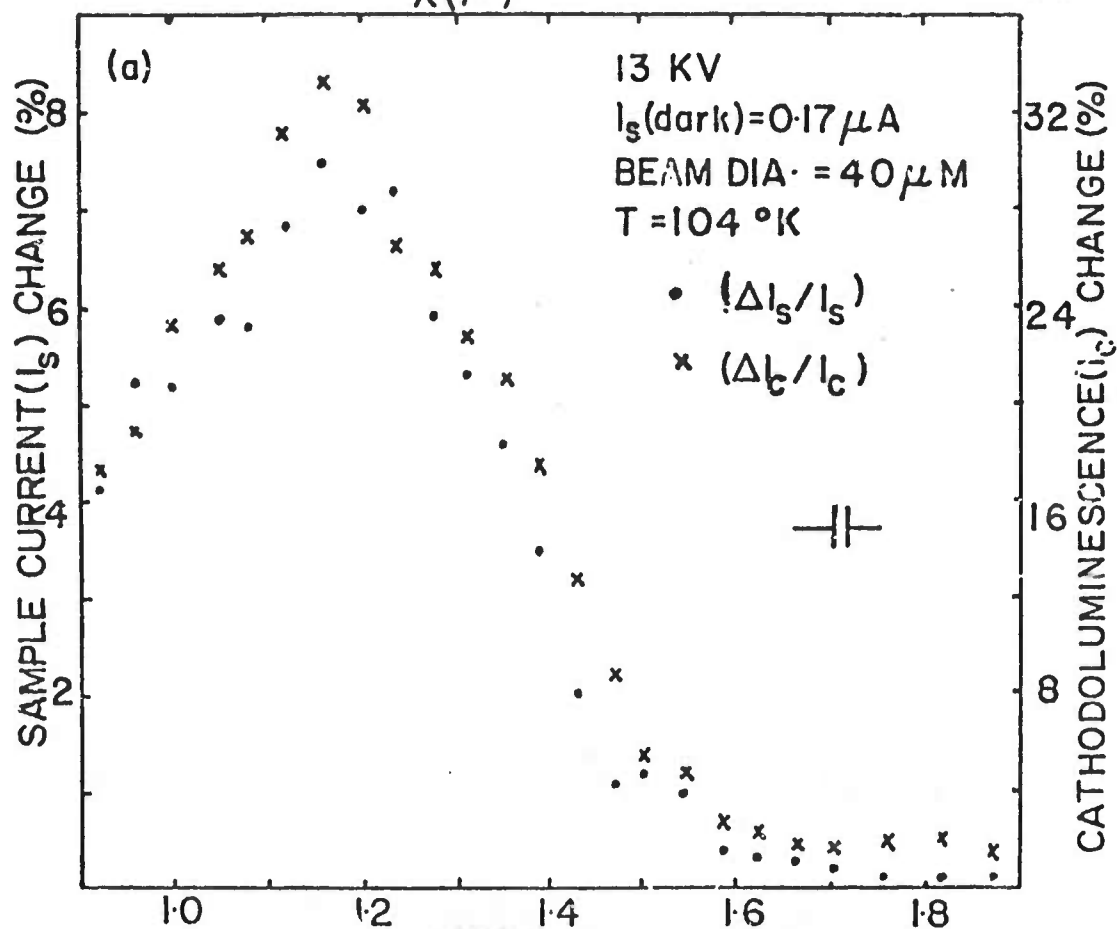
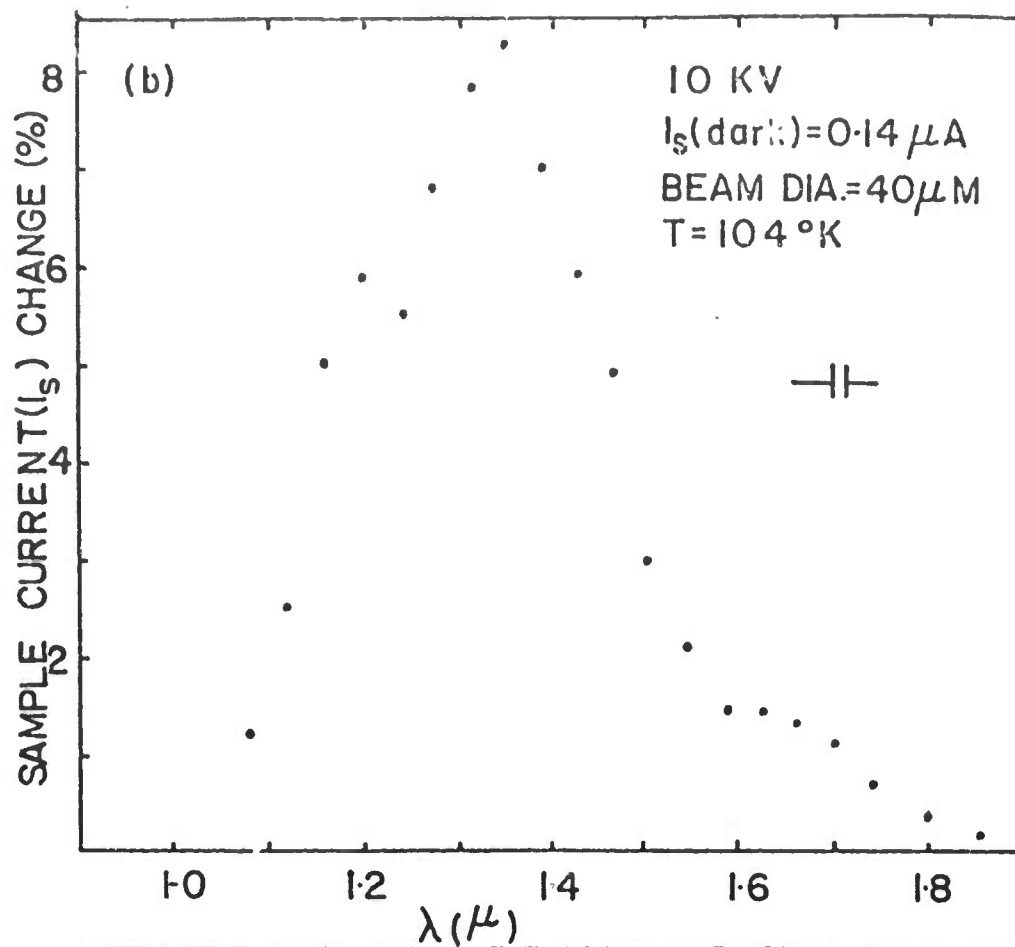
Department of Materials Science

University of Southern California, Los Angeles, California 90007

The study of deep impurity levels in semiconductors is important because of the influence that these levels have on the behavior of semiconductor devices. For example, in GaAs deep lying levels have been found to affect the behavior of diode lamps and transistors. The purpose of the present work is to study a possible new technique for the measurement of the energy of these deep levels.

The effect of light (with energies less than GaAs band gap) on the cathodoluminescence and sample current of semiinsulating GaAs was studied as a function of wavelength. Two Cr-doped and one undoped semiinsulating (resistivity = 10^8 ohm.cm) single crystal GaAs samples were used in experiments performed at 300°K and 104°K. Steady light from a 150 watt quartzline lamp (color temperature 3200°K) passed through a Hilger and Watts D292 plane grating monochromator and was focused on the sample at the same position as the chopped electron beam. The light induced change in cathodoluminescence and sample current as a function of wavelength were recorded simultaneously. The typical curves obtained on the Cr-doped GaAs samples at 104°K are shown in Fig. 1(a). With wavelength λ longer than about 1.6μ (0.77eV), only small increase in cathodoluminescence I_c and sample current I_s were observed. As λ became shorter than 1.6μ , both I_c and I_s increased rapidly with decreasing λ . The energy threshold for the observed increase in I_c and I_s corresponds to the energy level introduced in GaAs by chromium^{1, 2}. The increase in I_c may be attributed to the excitation of electrons from Cr level to the conduction band by light since occupied Cr levels are very efficient hole traps. The increase in I_s is also due to the excitation of electrons from Cr level to conduction band which results in the change of sample conductivity and hence surface potential in such a way as to decrease the secondary electron yield. The energy threshold for the increase in I_c and I_s at 300°K was found to be about the same as that at 104°K (0.77eV). This is in agreement with the suggestion² that the Cr level is associated with conduction band and its distance from the conduction band edge is almost invariant with temperature. For the undoped GaAs sample, two threshold energies were observed at 104°K, namely, a sharp one at 0.77eV (1.6μ) and a much smaller one at 0.6 eV (1.8μ) (Fig. 1(b)). At 300°K, only one threshold energy at 0.70 eV was observed. The observed threshold energies in this sample agree well with those reported^{3, 4} for the undoped high resistivity GaAs.

At constant beam voltage, within our experimental range, the percentage increase in I_c and I_s were found to be proportional to $(I_s)^{-m}$, where m is positive. A plot⁵ of this percentage change vs $(I_s)^{-m}$ will give a straight line. The extrapolation of this straight line gives the value of I_s at which the light effect on I_c and I_s disappears. The concentration⁵ of excess electron hole pair density generated at this excitation should be proportional to the concentration of deep level



303< FIG.1. (a) Cr doped GaAs. (b)undoped GaAs.

impurity responsible for the light effect. In Cr-doped samples, for which the Cr concentration is known, fairly good agreement was obtained between the estimated and true Cr concentration.

It was also found in this experiment, that in Cr-doped GaAs, especially with high Cr doping level ($>10^{17} \text{ cm}^{-3}$), the distribution of Cr atoms tends to be nonuniform which results in the nonuniformity of sample conductivity. In addition to increasing the sample conductivity, the light was also found to make the conductivity more uniform.

From the foregoing, it may be concluded that by choosing a proper beam voltage and current, the light induced change in cathodoluminescence and sample current can be used to measure the energy of deep impurity levels in direct gap semiconductors. Furthermore, it can give information about the concentration of the impurity responsible for the deep level.

* Work supported by the Advanced Research Projects Agency under grant No. DAHC 15-72-G7.

1. G.A. Allen, Brit. J. Appl. Phys., Ser 2, 1, 593 (1968).
2. A.T. Gorelenok, et al, Sov. Phys. - Semicond., 5, 95 (1971).
3. M.D. Sturge, Phys. Rev. 127, 768 (1962).
4. C.M. Gooch, et al, J. Appl. Phys. 32, 2069 (1961).

TEMPERATURE DEPENDENCE OF CATHODOLUMINESCENCE
OF GaAs, GaP, AND GaAs_xP_{1-x}*

H. C. Marciniak and D. B. Wittry

Departments of Materials Science and Electrical Engineering
University of Southern California, Los Angeles, California 90007

A clean vacuum electron beam column^{1,2} in which samples can be irradiated without contamination over the temperature range of 27°-300°K was used in temperature dependence measurements of cathodoluminescence of GaAs, GaP, and GaAs_xP_{1-x}. A beam voltage of 50 kV was used in order to reduce the effects of surface recombination.

Figure 1 shows the peak of the cathodoluminescence spectrum of a lightly doped p-type ($N_A = 7 \times 10^{16} \text{ cm}^{-3}$) GaAs sample as a function of temperature. The dashed curve is a plot of the absorption edge of GaAs versus temperature according to Casey and Panish.³ At low temperatures two emission peaks separated by 11 meV are seen. Cusano⁴ attributes the 1.487 eV peak to conduction band-isolated acceptors recombination. The 1.499 eV peak is probably due to conduction band-valence band recombination. At higher temperatures only one broad emission band is observed.

Figure 2 shows a cathodoluminescence spectrum of GaP taken at 27°K with an accelerating voltage of 50 kV, a beam current of 5nA and a spot size of 15μm. It was expected that donor-acceptor pair recombination between 2.2eV and 2.3eV as reported by Thomas, et al.⁵ at 1.6°K could be observed. However, donor-acceptor pair recombination showing spectra of resolved peaks in GaP has not yet been reported at temperatures above 20°K. Shown in the figure is the "A" line due to the nitrogen bound exciton and the C bound-exciton line due to neutral sulfur donors.⁶ The F line is due to recombination at pairs of isoelectronic nitrogen traps.⁶ The other peaks could be phonon-replicas of the "A" line as discussed by Dean and Thomas.⁷

At the present time cathodoluminescence measurements are made as a function of temperature and beam current of GaAs_xP_{1-x} mixed crystals. It is expected that the nature of the various recombination mechanisms in these crystals can be determined through these studies.

The mixed crystals are first analyzed to determine the "x" value in GaAs_xP_{1-x} using electron probe X-ray microanalysis. The X-ray data is then processed using J. W. Colby's MAGIC⁸ computer program for quantitative electron microprobe analysis. The cathodoluminescence measurements are made on the instrument described in references 1 and 2. Care is taken to analyze the same spot of the samples in both instruments because the samples are polycrystalline and may not be homogeneous.

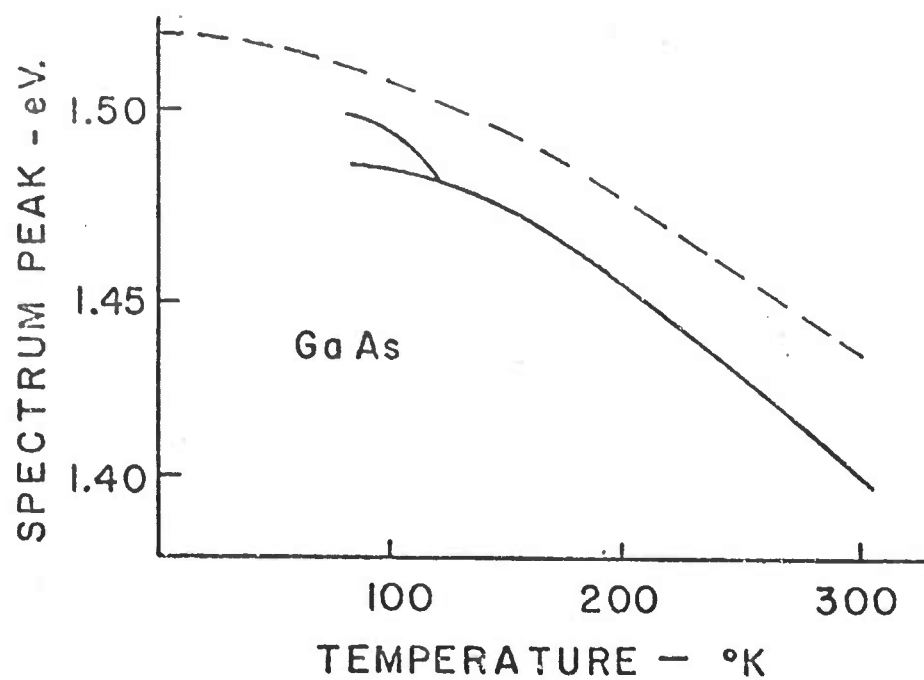


Figure 1

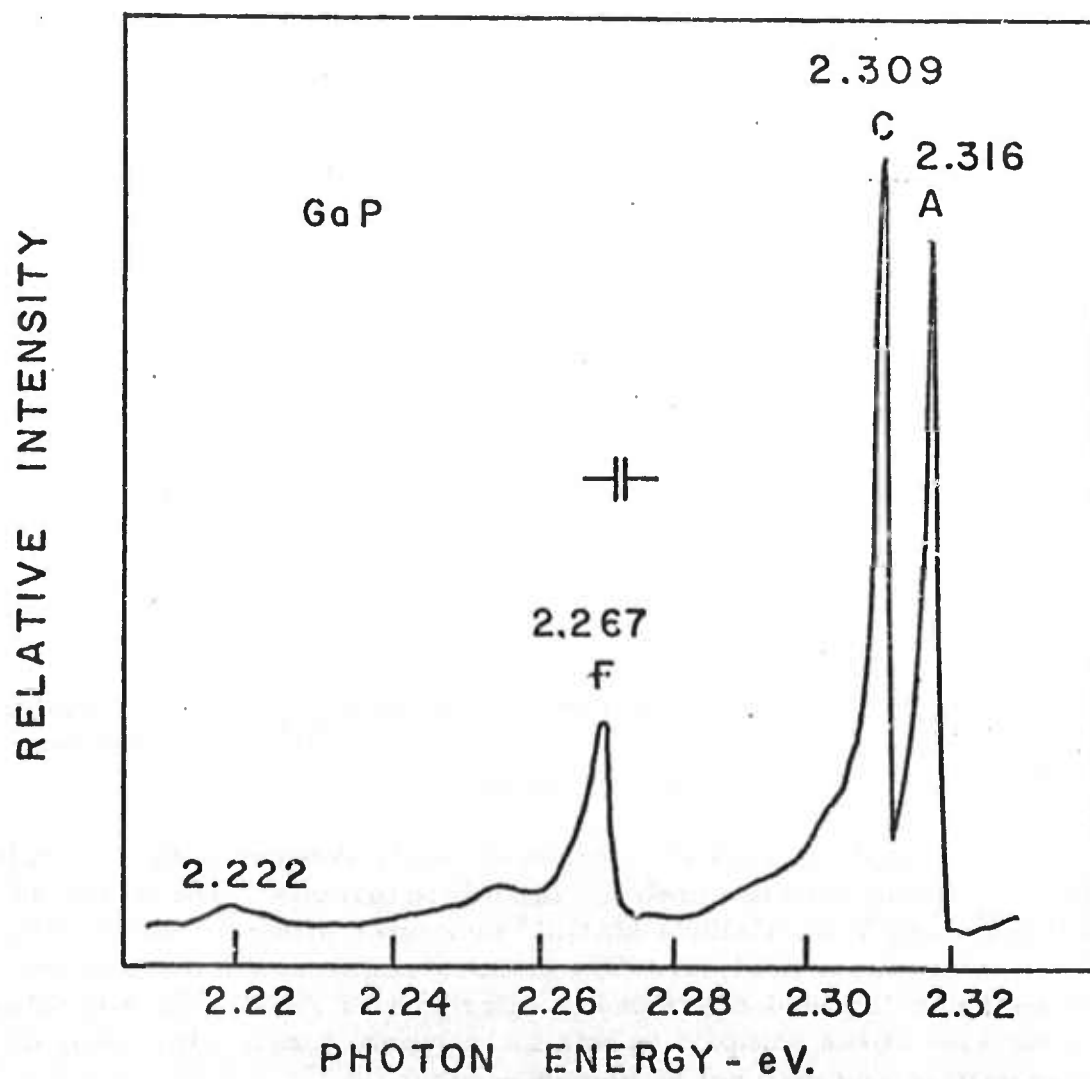


Figure 2

The intensity of the main peaks as a function of current show first a linear dependence which changes to a square root dependence as the current is increased. This sublinear dependence results from the saturation of donor or acceptor levels at a certain beam current when other factors such as accelerating voltage and spot size are kept constant. This sublinear dependence has been observed previously in Zn-O doped GaP⁹ and S-doped GaP.¹⁰

Measurements on these GaAs_xP_{1-x} crystals are being continued with special emphasis on those samples whose values of "x" are near the value at which the band structure changes from direct to indirect.

* Research sponsored by the Air Force Office of Scientific Research, Office of Aerospace Research, United States Air Force, under Grant No. AF-AFOSR-68-1414; the National Science Foundation under Grant No. GK3904; and Advanced Research Projects Agency of the Department of Defense under Grant No. DAHC-15-70-G14.

¹H.C. Marciniak and D.B. Wittry, "A Clean Vacuum Electron Beam Column for Cathodoluminescence Investigations", Fifth National Conference on Electron Probe Analysis; No. 44B, 1970.

²H.C. Marciniak and D.B. Wittry, Rev. of Sci. Instr. 42, 1810 (1971).

³M.B. Panish and H.C. Casey, Jr., Journal of Applied Physics, 40, 163 (1969).

⁴D.A. Cusano, Solid State Communication, 2, 353 (1964).

⁵D.G. Thomas, J.J. Hopfield and K. Colbow (1964) "Light from Distant Pairs." Radiative Recombination in Semiconductors (Paris), 67-77.

⁶M. Gershenzon (1966) "Electroluminescence from p-n Junctions." Luminescence of Inorganic Solids (New York), 625-627.

⁷P.J. Dean and D.G. Thomas, Physical Review, 150, 690-703 (1966).

⁸J.W. Colby, MAGIC - A Computer Program for Quantitative Electron Microprobe Analysis, Bell Telephone Laboratories, Inc., Allentown, Pennsylvania.

⁹H.C. Casey, Jr., and J.S. Jayson, Journal of Applied Physics, 42, 2774 (1971).

¹⁰S. Hosoki and H. Okano, "Scanning Cathodoluminescence Analysis of Compound Semiconductors", Pittsburg Conference on Analytical Chemistry and Applied Spectroscopy; Paper no. 161 (1971).



GAS BUBBLE NUCLEATION DURING CRYSTALLIZATION

WILLIAM R. WILCOX and VINCENT H. S. KUO*

*Chemical Engineering and Materials Science Departments, University of Southern California,
Los Angeles, California 90007, U.S.A.*

Received 23 February 1973; revised manuscript received 16 May 1973

Literature on gas bubble incorporation in growing crystals is reviewed. A theory for nucleation in dilute multicomponent gas solutions was derived. Combined with solute segregation equations, theories result for various forms of crystal growth. The tendency to form gas bubbles increases with increasing growth rate, decreasing stirring, increasing ambient gas pressure, and decreasing height of liquid over crystal. The liquid surface temperature is also an important variable. Homogeneous nucleation of bubbles was found to be possible for melt growth. Bubble formation in solution growth is most likely by heterogeneous nucleation on the crystal surface.

1. Introduction

Gases are usually, if not always, more soluble in a melt than in the corresponding solid. Consequently, crystallization causes the concentration of a dissolved gas to increase in the liquid adjacent to the growing crystal, as is true for any solute with a distribution coefficient $k < 1$. When the concentration becomes sufficiently high, a gas bubble may nucleate¹). The bubble then grows and may either float away, be trapped and incorporated in the solid, or remain at the interface.

The purpose of this paper is to derive the general equations for bubble nucleation and then apply them to specific crystal growth situations, so as to suggest methods for avoiding bubble formation. First, however, we review the prior experimental observations.

Gas bubbles have frequently been found in melt-grown crystals. For example, $\sim 1 \mu\text{m}$ H_2 bubbles were found in MgO and $\text{H}_2 + \text{CO}_2$ bubbles in CaO and SrO grown by electric arc fusion of MgO , CaCO_3 and SrCO_3 ²). The pressure in the bubbles was estimated to be 250 atm at room temperature. Bubbles were not produced when the melts were allowed to sit for several hours before solidification. Bubbles were occasionally observed in vertical gradient-freeze and in Bridgman growth of lanthanum oxysulfide crystals in sealed tungsten crucibles⁴). Isolated bubbles and precipitate bubble pairs were found in yttrium orthoferrite

(YFeO_3) grown by the Bridgman method at rates below 1.5 mm/hr in platinum and 1 atm of oxygen pressure³). Czochralski grown calcium tungstate contained gas bubbles⁵). Barium titanate⁶) and lithium niobate⁷) had large bubbles and sometimes even a hollow core. Formation of oriented rectilinear bubbles in silver bromide was observed⁸). Bubbles were a frequent defect in sapphire grown by the edge-defined film-fed technique^{9,10}). Bubble trapping in Czochralski growth of paratellurite (TeO_2) in oxygen was avoided by decreasing the pull rate to below about 1.5 mm/hr and increasing the seed rotation rate to 40–50 rpm¹¹). When rare earth oxides were added to the melt, Czochralski grown bismuth germanate ($\text{Bi}_4\text{Ge}_3\text{O}_{12}$) crystals tended to contain quantities of bubbles¹²). "Reductions in the pulling and rotation rates were required in order to obtain optical quality commensurate with the undoped crystals." When Nd_2O_3 was added, bands of bubbles were generated when major changes in temperature were made. There appeared to be an orientation dependence for bubble incorporation in pulled crystals of lead germanium oxide¹³). Increasing the rate of seed rotation reduced the number of bubbles and pulling slower than 0.8 mm/hr eliminated all bubbles.

It was found that gas bubbles formed at the interface of naphthalene growing by the vertical gradient freeze technique when the freezing rate was about 3 cm/hr¹⁴). The depth of the melt above the interface was about 6 cm and the temperature gradient in the furnace was 2.5 °C/cm when bubble formation began. One atmosphere of air+naphthalene vapor was over the melt

* Present address: Allied Chemical Corp., Solvay, New York 13209, U.S.A.

surface. When carbon particles were present in vertical Bridgman growth of naphthalene, bubbles formed when the freezing rate exceeded 16 mm/hr¹⁵). A rate of 26 mm/hr was required when the pressure over the melt was reduced to ~ 0.3 Torr. When copper particles were present instead, a freezing rate of 32 mm/hr was insufficient to cause bubble formation at 0.3 Torr ambient pressure. Stirring reduced the tendency to form bubbles. In horizontal zone melting with rotation of the tube, bubbles formed at freezing rates above about 30 mm/hr in the presence of carbon particles only when the rotation rate was low. In vertical zone melting, bubble formation in naphthalene could also be stopped by increasing the heater power, causing the zone size and pressure to increase. (Excessive increases caused the glass tube to burst.)

The generation and trapping of air bubbles by freezing water has long been well known¹⁶). For example, in 1845 distilled water boiled and cooled in air and then frozen contained many bubbles, especially in the last portion to freeze¹⁷). In 1870, bubble-free ice was obtained by directional freezing downward of water boiled in the tube and then sealed to exclude air¹⁸). On the other hand, when water was frozen upward, the upper portion contained bubbles even after three freezings of boiled-out distilled water in vacuum¹⁹). Carte²⁰) observed thin layers of water during directional freezing. Bubbles formed only after a distance on the order of 0.7 mm had frozen. This distance decreased as the freezing rate increased. There was a tendency for the bubbles to form in waves, with clear ice following each wave for a distance slightly smaller than the initial clear portion described above. By application of the segregation equation for convectionless directional freezing, it was estimated that a supersaturation of about 27 was required to nucleate air bubbles. Maeno²¹) showed that air bubbles would form along a scratch on the interface when the supersaturation was insufficient to form bubbles otherwise. Fresh carborundum, lead and glass particles caused bubbles to form behind them, leaving a trail of bubbles in the ice. After treatment of the particles with methanol or dilute hydrochloric acid, their nucleation abilities were lost.

Gas bubbles are also found in solution-grown crystals. These usually, but not always, cohabit with trapped solution, with the gas to solution ratio often vary-

ing widely for inclusions in the same crystal. One can argue that the gas bubbles form after growth because of temperature changes. This undoubtedly occurs very frequently, but in formation of inclusions containing all or mostly gas the bubbles must have been generated prior to trapping. Indeed it has been shown that a bubble can initiate formation of a cavity by reducing access of solution to the crystal surface²²). For completeness, we must also point out that air can be introduced into solvent inclusions by placing the crystal in a temperature gradient, causing the inclusion to move to the surface, exchange ambient gas for a portion of the solvent, and then move back into the crystal^{23,24}). Large increases in temperature can also cause vaporization of small inclusions²⁵) and boiling in large inclusions²⁵).

Gas bubbles were found in crystals of the following reagent grade chemicals²³): $\text{Na}_2\text{S}_2\text{O}_3 \cdot 5 \text{H}_2\text{O}$, $\text{Na}_2\text{B}_4\text{O}_7 \cdot 10 \text{H}_2\text{O}$, $\text{Ba}(\text{NO}_3)_2$, $(\text{NH}_4)_2\text{Ce}(\text{NO}_3)_6$, KIO_3 , KI , KBrO_3 , KClO_3 , "anhydrous" Na_2CO_3 , benzoic acid and hexamethylenetetramine. Solvent inclusions usually contained gas bubbles in sodium chloride²⁶) and in alum²⁷). Growth waves on potassium bromide butterfly twins produced tubular inclusions both of solution and of gas bubbles²⁸). Air bubbles both alone and with MoO_3 have been identified in beryllium oxide crystals grown from molybdate fluxes²⁹). Powers^{30,31}) found some inclusions in sucrose that consisted entirely of gas. He suggested that "the probable origin is that air dissolved in the original crystallizing syrup became supersaturated and formed as bubbles on the growing face." Both liquid plus gas and entirely gaseous inclusions have also been found in terrestrial³¹⁻³⁶) and lunar^{37,38}) minerals.

Gas bubbles and voids have also been found in cast ingots of metals³⁹). "Microporosity, present in nearly all castings and ingots, is always interdendritic in nature and may be large enough to be seen on a polished surface with the naked eye"⁴⁰). Directionally solidified castings of low-alloy steel had 10^{-4} to 10^{-3} volume fraction porosity⁴⁰). The porosity increased significantly from the bottoms to the tops of the ingots, with a vacuum-melted ingot having slightly lower porosity than an air-melted ingot.

2. Homogeneous nucleation rate of gas bubbles

As for any other form of homogeneous nucleation,

the nucleation rate J may be expressed by:

$$J = A \exp(-\Delta F^*/kT), \quad (1)$$

where ΔF^* is the free energy of formation of a critical embryo, k is Boltzmann's constant, and T is absolute temperature. Many arguments have appeared in the literature regarding the exact form and magnitude of the pre-exponential A in various types of nucleation. For the present problem, the following has been suggested⁴¹:

$$A = (\alpha C_l v_v / v_g^*) \left(\frac{2\sigma}{\pi M} \right)^{\frac{1}{2}}, \quad (2)$$

where α is the accommodation coefficient (fraction sticking) for gas molecules striking the gas-liquid interface, C_l is the molecular concentration in the liquid, v_v is the volume of a vacancy in the liquid ($C_l v_v \sim 1$), $v_g^* = kTz/P_g^*$ is the molecular volume in the critical embryo, z is the compressibility factor ($= 1$ for ideal gas), P_g^* is the pressure inside the critical embryo, σ is the gas-liquid surface energy and M is the mass of a molecule in the bubble. This predicts a nucleation rate independent of the dissolved gas concentration. Possibly C_l should be defined as the dissolved gas concentration.

The free change required to form the critical bubble is⁴¹⁻⁴³

$$\Delta F^* = 16\pi\sigma^3/3(P_g^* - P_l)^2, \quad (3)$$

where P_l is the hydrostatic pressure in the liquid at the point where the bubble is forming. Levine⁴⁴ showed that one must also take account of the electrostatic energy density in any chemisorbed layer at the embryo surface. With oxygen dissolved in zirconia, this makes nucleation of a gas bubble much easier than otherwise.

The foregoing is for homogeneous nucleation. However, we do have a solid surface present in our problem - the crystal surface. If the surface is planar, the critical free energy change is^{41,42}

$$\Delta F^* = 16\pi\sigma^3\phi/3(P_g^* - P_l)^2, \quad (4)$$

$$\text{where } \phi = (2 - \cos \theta)(1 + \cos \theta)^2/4. \quad (5)$$

Here θ is the equilibrium contact angle between a liquid drop and the crystal surface in the presence of the gas being considered. For $-1 < \cos \theta < +1$ it is given by

$$\cos \theta = (\sigma_{cg} - \sigma_{cl})/\sigma, \quad (6)$$

where σ_{cg} is the surface energy between gas and crystal, and σ_{cl} is the surface energy between crystal and liquid. When $(\sigma_{cg} - \sigma_{cl}) \geq \sigma$, $\theta = 0$ so that the liquid perfectly wets the crystal and nucleation is unaffected ($\phi = 1$). When $(\sigma_{cg} - \sigma_{cl}) \leq -\sigma$, $\theta = 180^\circ$, the liquid does not wet the crystal at all, and nucleation can take place when the vapor pressure only slightly exceeds the hydrostatic pressure. Chalmers¹) claimed that in melt growth the crystal surface is unlikely to greatly influence bubble nucleation because $\sigma_{cg} \gg \sigma_{cl}$ and generally $\sigma_{cg} > \sigma$ [Knight⁴⁵) found, for example, that $\theta \sim 0$ for air bubbles in water contacting the basal plane of ice.] However, the large gas concentrations required for nucleation may very well change the surface energies so that this is no longer true. These conditions are not necessarily true for solution growth, however, and nucleation may very well be greatly enhanced in some cases. For example, the contact angle of gallium on a (111) gallium arsenide surface is 142° , relatively independent of temperature from 46 to 479°C ⁴⁶). This gives a value of $\phi = 0.028$, which would greatly enhance nucleation. We estimate using the data of refs. 47-49 that if $\sigma_{cg} \approx \sigma + \sigma_{cl} = 116.6$ dyne/cm for pure water, then addition of 1 M NaCl would yield $\theta \approx 33^\circ$ and $\phi \sim 0.98$. Nucleation is even more enhanced on a rough surface when $\theta < 180^\circ$ ⁵⁰). The activation energy for nucleation may go to zero when $\theta < 90^\circ$ if the surface is very rough.

Foreign particles may be effective at enhancing nucleation, as indicated in the examples cited earlier. Surface energies and roughness of particles may make them more efficacious than the crystal surface. Submicroscopic gas bubbles may also be trapped in the interstices of the particles, so that nucleation is not required and the bubbles will grow when the vapor pressure is sufficient to overcome the surface forces.

A minimum nucleation rate J_{\min} on the order of 1 event/cm³sec is necessary for it to be observable. From eqs. (1), (2) and (4), nucleation would be observed when

$$P_g^* \geq P_l + (16\pi\sigma^3\phi)^{\frac{1}{2}} \times \left\{ 3kT \ln \left[\frac{\alpha C_l v_v P_g^*}{z k T J_{\min}} \left(\frac{2\sigma}{\pi M} \right)^{\frac{1}{2}} \right] \right\}^{-\frac{1}{2}}, \quad (7)$$

which is easily solved by successive approximations, for example, by first setting $P_g^* = P_l$ in the logarithm. Thus, for example, for homogeneous nucleation of air

in naphthalene we take $\sigma = 2.2 \text{ dyne/cm}^{51}$, $\phi = 1$, $k = 1.38 \times 10^{-16} \text{ erg/}^\circ\text{K}$, $T = 353^\circ\text{K}$, $\alpha c_1 v_0 = 1$, $z = 1$, $J_{\min} = 1/\text{sec cm}^2$ and $MN_A = 29$, to obtain $(P_g^* - P_l) = 380 \text{ atm}$. Similarly for air in water we take $\sigma = 75.6 \text{ dyne/cm}$, $\phi = 1$, $T = 273^\circ\text{K}$, and $\alpha c_1 v_0 / z J_{\min} = 1$ to obtain $(P_g^* - P_l) = 1720 \text{ atm}$.

3. Dilute gas mixtures

In principle, all of the parameters in the nucleation rate expressions are either known or are capable of measurement, except for the pressure P_g^* in the critical embryo. The critical embryo must satisfy conditions of chemical equilibrium and mechanical equilibrium. The mechanical equilibrium condition is³⁹⁻⁴¹

$$r^* = 2\sigma / (P_g^* - P_l) \quad (8)$$

where r^* is the radius of the critical nucleus. Actually this expression was used in derivation of eq. (3), and is not needed further. Using our estimates for $P_g^* - P_l$, this gives $r^* = 16.8 \text{ \AA}$ for air in naphthalene and 8.6 \AA for air in water.

The condition of chemical equilibrium requires that the chemical potential of each component be the same in both phases. The result of this is that the partial pressure of each component in the critical gas bubble is equal to its ordinary vapor pressure over liquid at P_l ⁵². For a low concentration of dissolved gas j it is often found that the activity coefficients in both phases are constant and that the vapor pressure is given by:

$$(p_j)_g = K_j (x_j)_l^{n_j} \quad (9)$$

where K_j is an equilibrium constant at P_l and T , $(x_j)_l$ is the mole fraction of j in the liquid, and n_j is an integer representing the number of atoms into which each gas molecule dissociates in the liquid. For many gas-liquid combinations $n = 1$ and this is called Henry's law. For diatomic gases in metals, $n = 2$ because they dissociate into atoms^{53,54}. When the foregoing is true, then the solvent is ideal⁵⁵, with a vapor pressure of

$$(p_s)_g = (x_s)_l P_s^0 \quad (10)$$

where P_s is the vapor pressure of pure solvent at total pressure P_l . This is true when gas and liquid both consist of the same solvent species, and is equivalent to $K_s = P_s$ and $n_s = 1$ in eq. (9). It has been shown that P_s and K_j vary with pressure by only about 0.1 % per atmosphere⁵⁵.

From the foregoing, we see that the total gas pressure in a critical bubble is

$$P_g^* = \sum (p_j)_g = \sum K_j (x_j)_l^{n_j} \quad (11)$$

where j now includes the solvent.

We also note that other concentration units may be employed for the dissolved gases, changing the numerical values of K_j .

4. Segregation

Nucleation will be favored at the location where the dissolved gas concentration is greatest. When gas is rejected by the growing crystal, this occurs at the crystal interface. Pertinent equations for various situations follow.

4.1. CRYSTAL GROWTH WITH STIRRING

For melt growth with stirring the interface concentration is⁵⁶⁻⁵⁸

$$(x_j)_{il} = \frac{(x_j)_{lb}}{k_j + (1 - k_j) \exp [-(\delta_j V / D_j) (\rho_c / \rho_l)]} \quad (12)$$

where $(x_j)_{lb}$ is the mole fraction of j in the bulk liquid,

$$k_j = (x_j)_{cl} / (x_j)_{il}$$

is the interfacial distribution coefficient in mole fraction units, $(x_j)_{cl}$ is the mole fraction of j in the crystal at the interface, δ_j is the stagnant film thickness for mass transfer of j , V is the crystal growth rate, D_j is the diffusion coefficient of j in the melt, ρ_c is the density of the crystal and ρ_l is the density of the melt. Note that δ_j depends on crystal growth rate⁵⁹ and on the diffusion coefficient of j ⁶⁰.

For solution growth at a known growth rate V we can similarly obtain for the molar concentration of gas at the interface⁵⁸

$$(c_j)_{il} = \frac{(c_j)_{lb}}{k'_j + (1 - k'_j) \exp [-(\delta_j V / D_j) (\rho_c / \rho_l)]} \quad (13)$$

where $(c_j)_{lb}$ is the molar concentration of j in the bulk solution,

$$k'_j = (c_j)_{cl} \rho_{cl} / (c_j)_{il} \rho_c$$

is the interfacial distribution coefficient in molar units (as usually defined for melt growth of semiconductors), $(c_j)_{cl}$ is the molar concentration of j in the crystal at the interface, and ρ_{cl} is the density that the crystal would

have if its components had the same partial molar volumes as in the solution. When the solute concentration is known at the interface and in the bulk, rather than the growth rate being known, a different expression may be derived⁵⁸).

4.2. CRYSTAL GROWTH WITH NO STIRRING

If the liquid is not stirred, then the solute concentrations at the interface depend on the length y of the crystal grown (there is also a short transient with stirring⁵⁶). For directional solidification of a long ingot with a planar interface, the interfacial gas composition is^{57,61-63})

$$(x_j)_{li} = \frac{(x_j)_{lb}}{2k_j} \left\{ 1 + \operatorname{erf} \left[\frac{1}{2} \left(\frac{yV}{D_j} \right)^{\frac{1}{2}} \left(\frac{\rho_c}{\rho_l} \right) \right] \right. \\ \left. + (2k_j - 1) \exp \left[-k_j(1 - k_j) \left(\frac{yV}{D_j} \right) \left(\frac{\rho_c}{\rho_l} \right)^2 \right] \right\} \quad (14) \\ \operatorname{erfc} \left[\frac{2k_j - 1}{2} \left(\frac{yV}{D_j} \right) \left(\frac{\rho_c}{\rho_l} \right) \right] \}$$

For $k_j \neq 1$, the interfacial gas concentration increases as solidification proceeds either until the steady state value $1/k_j$ is reached or until nucleation occurs. Theoretical solutions for many other solidification situations (e.g., for zone melting and for $k_j \rightarrow 0$, with and without stirring) were reviewed in ref. 57. Several results have been given recently for a variable distribution coefficient for zone melting and progressive freezing both with and without stirring⁶⁴⁻⁶⁷).

The result for solution growth of a large faceted crystal growing at a constant rate without stirring is the same as eq. (14), only with x_j replaced by C_j , k_j replaced by k'_j and ρ_l replaced by ρ_{cl} . Normally, of course, the bulk supersaturation is constant and the growth rate varies with time. The growth rate has been calculated for large faceted crystals⁶⁸) and for very small spherical crystals^{69,70}). A complete and general time dependent solution for gas segregation would be very difficult to obtain from this. However, if we assume $k'_j = 0$ and $D_j = D_s$, then the gas is concentrated to the same extent at the interface as is the solvent.

4.3. CELLULAR AND DENDRITIC GROWTH

When constitutional supercooling occurs, cells and even dendrites may form. (The gas segregation itself contributes to constitutional supercooling.) Additional

segregation occurs in the cell grooves^{1,70}) and in the melt trapped between the dendrites. When the density of the solid is greater than that of the melt, shrinkage occurs and generates a pressure drop^{1,72,73}), which also enhances nucleation.

5. Nucleation in Bridgman crystal growth

We now apply the preceding to vertical Bridgman growth with height h of melt over the interface. The top of the melt is assumed to be in equilibrium* with a gas mixture at pressure

$$P_a = \sum (p_j)_a = \sum (x_j)_a P_a,$$

where x_j is the mole fraction of component j in this mixture. The total liquid pressure is, therefore,

$$P_l = P_a + \rho_l g h,$$

where g is the gravitational constant. If $(K_j)_a$ is the equilibrium constant at the melt surface (at P_a and the melt surface temperature), then from eq. (9) we see that

$$(x_j)_{lb}^{n_j} = (p_j)_a / (K_j)_a.$$

Combining these with eqs. (11) and (12) we obtain

$$\frac{P_a^* - P_l}{P_a} = \sum \frac{[(K_j)_l / (K_j)_a] (x_j)_a}{k_j + (1 - k_j) \exp [-(\delta_j V / D_j) (\rho_c / \rho_l)]} - \left(\frac{\rho_l g h}{P_a} \right) - 1. \quad (15)$$

Note that the equilibrium constants, the distribution coefficients, and to a certain extent the mass transfer parameters δ_j and D_j depend on the presence and segregation of other components, both volatile and non-volatile. Thus, for example, at 25 °C the solubility of air in water is decreased by 84% by addition of 25.6 wt% NaCl⁷⁴). Addition of 20% Cr increases the solubility of O₂ in Fe by 500% at 1600 °C, while 20% Ni decreases the solubility slightly⁷⁴). Although the solubility of gases in liquids usually increases with decreasing temperature, this is not always true. For example, the solubility of nitrogen in iron increases with temperature, while that in niobium and tantalum de-

* Equilibrium is not always readily achieved. With low concentrations, the driving force for mass transfer is small. Surface kinetics may also be limiting. Smithells⁵²) indicates that "the inert gases do not dissolve in true metals from a neutral gas phase since their atoms are not chemisorbed on metallic surfaces. ...equilibrium with the gas phase cannot be established".¹).

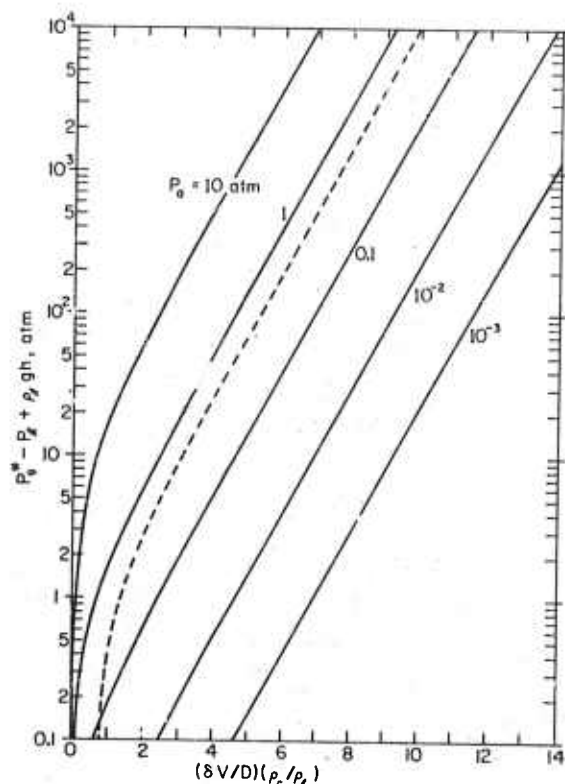


Fig. 1. Gas supersaturation plus liquid head for a single volatile component insoluble in the crystal, as a function of dimensionless freezing rate and ambient gas pressure P_a . From eq. (15). Solid lines: $K_a = K_l$; dashed line: $K_a = 2K_l$, $P_a = 1$ atm

creases⁵³). The solubility of argon in water-ethyl alcohol mixtures increases with increasing temperature when the alcohol content exceeds 18% m, while the reverse is true below 13% m alcohol⁵⁴).

In order to clarify the influence of the variables, eq. (15) is plotted in fig. 1 for the special case of only one volatile component ($x_a = 1$), zero solid solubility ($k = 0$), and the same temperature at the melt and crystal surfaces ($K_l/K_a = 1$). Homogeneous nucleation is observable only if $(P_g^* - P_l + \rho_l g h)$ exceeds the value of $(P_g^* - P_l)$ given by eq. (7) by at least $\rho_l g h$. Bubble growth is possible only if $(P_g^* - P_l + \rho_l g h) > 0$. Noting that a water head of 10.3 meters is required to generate a pressure of 1 atm, it is seen that the liquid head has an appreciable effect only at low supersaturations, i.e., with heterogeneous nucleation.

It is interesting to compare these calculations with our experimental observation that air bubbles formed in vertical gradient freeze growth of naphthalene when the freezing rate exceeded about 3 cm/hr. Using $(P_g^* -$

$P_l) \geq 380$ atm for nucleation to be observable, as previously estimated, we find $(\delta V/D) \sim 6$. With $D \sim 10^{-5}$ cm²/sec this gives $\delta \sim 0.7$ mm, which is very reasonable⁵⁷).

The dashed curve in the figure is for $K_a = 2K_l$ and $P_a = 1$ atm. At high supersaturations, the nucleation driving force is very nearly proportional to K_l/K_a . Thus if gas solubility decreases with increasing temperature, gas nucleation can be reduced by increasing the melt temperature. Likewise at high supersaturation the nucleation driving force is proportional to ambient pressure P_a . Thus the nucleation driving force can be reduced to near zero by adjusting the total pressure to near the vapor pressure of the melt at its surface. For example, one should be able to prepare bubble-free ice simply by holding the surface temperature of the water at 100°C during freezing.

The tendency to form bubbles increases as Bridgman growth proceeds. There are several reasons for this. The segregation transient causes the interfacial gas concentration to increase with distance. The height of the liquid decreases. The surface temperature of the liquid decreases as it approaches the cooler, although it may increase in the beginning as it moves to the temperature maximum in the heater. The bulk gas concentration may also increase if mass transfer with the ambient gas is too slow. If growth takes place in a sealed ampoule, then the gas concentration increases because the gas is unable to escape and the ambient pressure increases. The extent of this increase will depend on gas solubility and on the volume of the gas space over the melt relative to that of the melt itself.

6. Nucleation in Czochralski growth

Stirring is much more vigorous in Czochralski growth, and so $(\delta V/D)$ is generally less than 1. The resulting driving force $(P_g^* - P_l)$ will probably be too small for homogeneous nucleation of gas bubbles, even if one accounts for the decreases in P_l caused by crystal rotation⁷) and by a concave interface.

7. Gas bubbles in solution growth

Solution crystal growth is usually sufficiently slow that $(\delta V/D) \ll 1$, and little increase in gas concentration would be expected at the interface. The change in gas solubility with solution composition might actually be more significant. In any event, the probable

driving force for nucleation is so small that heterogeneous nucleation must have occurred in formation of inclusions containing all or mostly gas.

It is interesting to note that geologists use gas-bubble-containing solvent inclusions as a geological thermometer^{32,36}). The assumption is that gas bubbles form after trapping of solvent, because of volumetric changes due to decreases in temperature. The mineral-formation temperature is taken to be that at which the bubble redissolves. Roedder⁷⁵) has pointed out that nucleation does not always occur in trapped inclusions, even in geological time. We also see here that possible sources of error include formation of a gas bubble prior to sealing over the inclusion, and trapping of solvent supersaturated in dissolved gas.

8. Bubble growth and trapping

Once the embryo has exceeded the critical size, growth can occur. Theories have been developed for growth of gas bubbles in an isotropic supersaturated solution⁷⁶⁻⁷⁸). However, in crystal growth the solution composition and temperature vary with distance from the crystal. This causes the gas-liquid surface tension to vary, leading to instabilities such as vibration or circulation of the bubble surface^{15,24,79}).

It is known that gas bubbles may either be trapped as discrete bubbles, as chains of bubbles, as tubes, or they may float away. Little experimental study and no theoretical work has been performed on this aspect.

9. Conclusions

We have seen that the tendency to form gas bubbles increases as the crystal growth rate increases, as stirring decreases, as the height of the liquid over the interface decreases, and as the ambient pressure increases. Increases in liquid surface temperature either increase or decrease the tendency to nucleate bubbles depending on whether the gas solubility increases or decreases with increasing temperature. Intuitively we feel that the nucleation rate should also increase as the gas solubility increases, but this is not reflected by the current theory.

We have also seen that homogeneous nucleation of gas bubbles is possible in melt growth, but not in solution growth.

Acknowledgement

This research was supported by the Advanced Re-

search Projects Agency of the Department of Defense under Grant No. DAHC 15-72-G7.

References

- 1) B. Chalmers, *Principles of Solidification* (Wiley, New York, 1964) pp. 186-194.
- 2) Y. Chen and M. M. Abraham, *Growth of High-Purity and Doped Alkaline-Earth Oxides*, Second Natl. Conf. Am. Assoc. for Crystal Growth, Princeton, N.J., 1972.
- 3) S. L. Blank, L. K. Shick and J. W. Nielsen, *J. Appl. Phys.* **42** (1971) 1556.
- 4) L. E. Sobon, K. A. Wickersheim, R. A. Buchanan and R. V. Alves, in: *Proc. Eighth Rare Earth Research Conference*, Reno, Nevada, 1970, p. 400.
- 5) K. Nassau and A. M. Broyer, *J. Appl. Phys.* **33** (1962) 3064.
- 6) K. Nassau, *J. Am. Ceram. Soc.* **45** (1962) 474.
- 7) J. R. Carruthers and K. Nassau, *J. Appl. Phys.* **39** (1968) 5205.
- 8) V. I. Saunders and W. West, *Mater. Res. Bull.* **4** (1969) 303.
- 9) J. T. A. Pollock, *J. Mater. Sci.* **7** (1972) 631.
- 10) J. T. A. Pollock, *J. Mater. Sci.* **7** (1972) 787.
- 11) S. Mijazawa and H. Iwasaki, *Japan. J. Appl. Phys.* **9** (1970) 441.
- 12) S. K. Dickenson, R. M. Hilton and H. G. Lipson, *Mater. Res. Bull.* **7** (1972) 181.
- 13) K. Sugii, H. Iwasaki and S. Miyozawa, *J. Crystal Growth* **10** (1971) 127.
- 14) C. E. Chang, private communication, University of Southern California (1972).
- 15) V. H. S. Kuo, *Removal and Separation of Particles by Crystallization*, Ph. D. Dissertation, University of Southern California (1973).
- 16) N. E. Dorsey, *Properties of Ordinary Water-Substance* (Reinhold, New York, 1940) pp. 414, 415.
- 17) C. Brunner, *Ann. Physik (Pogg.)* **64** (1845) 113.
- 18) R. Bunsen, *Ann. Physik (Pogg.)* **141** (1870) 1.
- 19) A. Leduc, *Compt. Rend.* **142** (1906) 149.
- 20) A. E. Corte, *Proc. Phys. Soc. (London)* **77** (1961) 757.
- 21) N. Maeno, in: *Physics of Snow and Ice*, Vol. 1, Part 1, Ed. H. Oura (Inst. of Low Temperature Science, Hokkaido Univ, Sapporo, Japan, 1967) p. 207.
- 22) M. O. Kliia and I. G. Sokolova, *Soviet Phys.-Cryst.* **3** (1958) 217.
- 23) W. R. Wilcox, *Ind. Eng. Chem.* **60** (March 1968) 15.
- 24) W. R. Wilcox, *Ind. Eng. Chem.* **61** (March 1969) 76.
- 25) K. H. Chen and W. R. Wilcox, *Ind. Eng. Chem. Fundamentals* **11** (1972) 563.
- 26) H. Gerlach and S. Heller, *Ber. Deutsch. Ges. Geol. Wiss.-B-Miner. Lagerstättenf.* **11** (1966) 195.
- 27) M. G. Friedel, *Bull. Soc. Franc. Mineral.* **48** (1925) 6.
- 28) W. R. Wilcox and A. Leon, *J. Crystal Growth* **8** (1971) 230.
- 29) M. F. Ehman and J. E. Hanna, *J. Crystal Growth* **30** (1958) 715.
- 30) H. E. C. Powers, *Nature* **180** (1958) 715.
- 31) H. E. C. Powers, *Intern. Sugar J.* **61** (1959) 17.
- 32) E. Roedder, *Sci. Am.* **207** (Oct. 1962) 38.
- 33) K. A. Kvenvolden and E. Roedder, *Geochem. Cosmochim. Acta* **35** (1971) 1209.
- 34) E. Roedder, *Economic Geol.* **66** (1971) 777.
- 35) E. J. Gubelin, *Inclusions as a Means of Gemstone Identification* (Gemological Institute of America, Los Angeles, 1953).
- 36) E. A. Roedder, ed., *Fluid Inclusion Research, Proc. COFFI* (U.S. Geological Survey, Wash., D.C., 1968).

- 37) E. A. Roedder and P. W. Weiblen, in: *Proc. Apollo 11 Lunar Sci. Conf.*
- 38) E. A. Roedder and P. W. Weiblen, *Science* **167** (1970) 641.
- 39) J. Walker, *Foundry Trade J.* (1969) 943.
- 40) A. A. Tzavaras and M. C. Flemings, *Trans. AIME* **233** (1965) 355.
- 41) J. P. Hirth, G. M. Pound and G. R. St. Pierre, *Met. Trans.* **1** (1970) 939.
- 42) J. P. Hirth and G. M. Pound, *Condensation and Evaporation*, in: *Progress in Materials Science*, Vol. 11 (Macmillan, New York, 1963) ch. F.
- 43) L. D. Landau and E. M. Lifshitz, *Statistical Physics*, 2nd ed. (Addison-Wesley, Reading, Mass., 1969) pp. 460-462, 472-474.
- 44) H. S. Levine, *J. Phys. Chem.* **76** (1972) 2609.
- 45) C. A. Knight, *Phil. Mag.* **23** (1971) 153.
- 46) B. E. Liefert and Z. A. Munir, *J. Electrochem. Soc.* **118** (1971) 368.
- 47) D. R. H. Jones and G. A. Chadwick, *Phil. Mag.* **22** (1970) 291.
- 48) D. R. H. Jones and G. A. Chadwick, *J. Crystal Growth* **11** (1971) 260.
- 49) R. C. Weast, ed., *Handbook of Chemistry and Physics*, 51 ed. (Chem. Rubber Co., Cleveland, 1970).
- 50) B. K. Chakraverty and G. M. Pound, *Acta Met.* **12** (1964) 851.
- 51) O. R. Quayle, *Chem. Rev.* **53** (1953) 439.
- 52) C. A. Ward, A. Balakrishnan and F. C. Hopper, *J. Basic Eng.* **92** (1970) 695.
- 53) C. J. Smithells, *Metals Reference Book*, Vol. II, 4th ed. (Plenum, New York, 1967) p. 605.
- 54) R. Battino and H. L. Clever, *Chem. Rev.* **66** (1966) 395.
- 55) I. Prigogine and R. Defay, *Chemical Thermodynamics* (Longmans, Green and Co., London, 1954) p. 332.
- 56) W. R. Wilcox, *J. Appl. Phys.* **35** (1964) 636.
- 57) W. R. Wilcox, in: *Fractional Solidification*, Eds. M. Zief and W. R. Wilcox (Dekker, New York, 1967) ch. 3.
- 58) W. R. Wilcox, *J. Crystal Growth* **12** (1972) 93.
- 59) W. R. Wilcox, *Mater. Res. Bull.* **4** (1969) 265.
- 60) W. R. Wilcox, in: *Preparation and Properties of Solid State Materials*, Ed. R. A. Lefever (Dekker, New York, 1971).
- 61) V. G. Smith, W. A. Tiller and J. W. Rutter, *Can. J. Phys.* **33** (1955) 723.
- 62) K. F. Hulme, *Proc. Phys. Soc. (London)* **B68** (1955) 393.
- 63) D. W. Memlink, *Philips Res. Rept.* **11** (1956) 183.
- 64) C. H. Li, *J. Appl. Phys.* **38** (1967) 3793.
- 65) C. H. Li, *Brit. J. Appl. Phys.* **18** (1967) 359.
- 66) S. C. Mathur and D. C. Singh, *Phys. Status Solidi* **3** (1970) K45.
- 67) D. C. Singh and S. C. Mathur, *Sep. Sci.* **7** (1972) 243.
- 68) A. R. Cooper, Jr., *Trans. Faraday Soc.* **58** (1962) 2468.
- 69) N. A. Clontz and W. L. McCabe, *Chem. Eng. Sci.* **27** (1972) 307.
- 70) R. J. Schaefer and M. E. Glicksman, *J. Crystal Growth* **5** (1969) 44.
- 71) J. J. Kramer, G. F. Bolling and W. A. Tiller, *Trans. AIME* **227** (1963) 374.
- 72) T. S. Piwonka and M. C. Flemings, *Trans. AIME* **236** (1966) 1157.
- 73) J. Campbell, *Trans. AIME* **245** (1969) 2325.
- 74) *Londolt-Börnstein Zahlenwerte und Funktionen*, 6th ed., Vol. II, Part 2b (Springer, Berlin, 1962).
- 75) E. Roedder, in: *Proc. IAGOD-IMA Meeting*, Tokyo-Kyoto, 1970.
- 76) T. Theofanous, L. Biasi and H. S. Isbin, *Chem. Eng. Sci.* **24** (1969) 885.
- 77) J. Szekeley and G. P. Martins, *Chem. Eng. Sci.* **26** (1971) 147.
- 78) D. E. Rosner and M. Epstein, *Chem. Eng. Sci.* **27** (1972) 69.
- 79) W. R. Wilcox, *Separation Sci.* **4** (1969) 95.

LETTERS TO THE EDITORS

LIQUID-SEAL CZOCHRALSKI GROWTH OF GALLIUM ARSENIDE

P. C. LEUNG and W. P. ALLRED

Department of Materials Science, University of Southern California, Los Angeles, California 90007, U.S.A.

Received 12 May 1973

A new technique of using molten B_2O_3 as a push-pull, rotary seal for Czochralski growth of gallium arsenide is described. This system has some advantages over previous techniques. The most attractive feature of this system is that it is very simple, economical to construct, and easy to operate.

Czochralski growth of gallium arsenide has presented some problems primarily because of the volatility of arsenic. The arsenic vapor pressure at the melting point is about 1 atm. A vapor space over the melt can permit transport of arsenic and condensation of solid arsenic on any cool portions of a sealed system. Condensation may be avoided by maintaining the entire enclosure at a temperature such that the vapor pressure of pure arsenic is greater than the arsenic partial pressure over the melt. Since the temperature needed to provide a stoichiometric pressure is 610 °C, a problem arises in providing a seal for the pulling mechanism which will withstand this temperature. A second problem is the high reactivity of the arsenic vapor with many materials at 600 °C. We report here the development of a new technique for Czochralski growth of gallium arsenide possessing some advantages over previous techniques.

Several methods have been employed previously to avoid loss of arsenic from the melt. The earliest technique is the magnetic-type puller developed by Gremmelmaier¹). This method uses magnets to support and rotate the seed rod which is sealed within the quartz chamber. Since there is no mechanical feed through, the temperature of the entire quartz envelope can be heated to a temperature in excess of 610 °C. One of the major disadvantages of the magnetic puller is that the seed crystal, which is driven by rotating magnets, is subject to considerable vibration. This problem is caused by the loose coupling of the magnet and by the friction of the quartz bearing surfaces. In addition, the

system is very complex, costly, and difficult to use.

A second method uses a liquid gallium seal to contain the arsenic vapor²). However, it proved to have little practical use because of its complexity and the fact that the arsenic in the growth chamber reacts with the gallium seal to form solid gallium arsenide. Arsenic is also lost through the gallium seal.

The third method is the liquid encapsulation technique^{3,4}). This system uses a layer of molten B_2O_3 on the surface of the GaAs melt to prevent the escape of arsenic. The B_2O_3 enables the use of conventional Ge or Si growers for the growth of GaAs. The growing crystal is pulled through the B_2O_3 layer. A layer of B_2O_3 adheres to the crystal and generates stresses as it cools due to the differences in thermal expansion. Because the B_2O_3 is in direct contact with the melt, impurities in the B_2O_3 are thereby transferred directly to the melt, leading to erratic electronic properties in the crystals. It is also difficult to react elemental gallium and arsenic under the B_2O_3 layer, making it necessary to use prereacted GaAs for the starting material.

We present here a high temperature push-pull rotary seal that can be used with Czochralski growth of gallium arsenide. This technique overcomes many of the previously mentioned difficulties. This system uses a molten B_2O_3 seal, not in contact with the melt, to prevent arsenic escape. As shown in fig. 1, the pull rod rotates through the liquid seal so that a direct mechanical drive similar to that used in conventional Ge or Si growers can be used. The two resistance furnaces are used to maintain proper temperatures for different

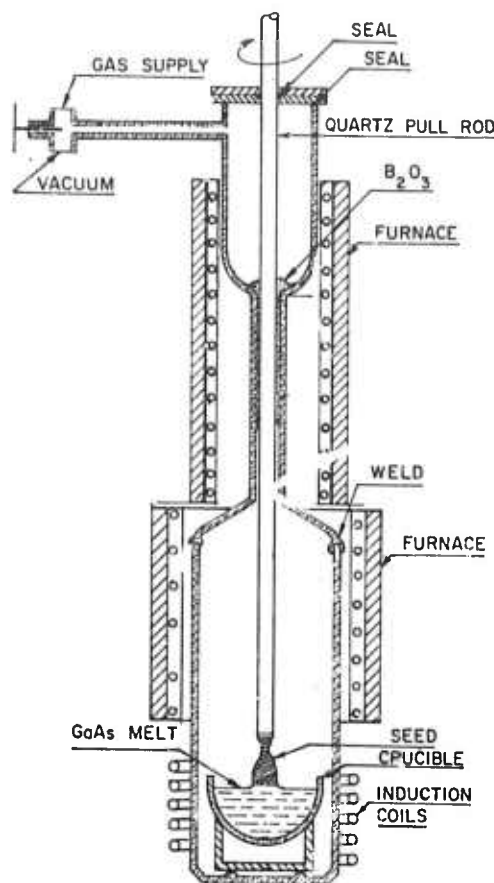


Fig. 1. Illustration of the liquid-seal Czochralski GaAs grower.

regions of the growth system during growth. A stoichiometric amount of gallium and arsenic is placed in the crucible. An additional amount of arsenic is added to provide an arsenic vapor pressure above the melt. A seed is fastened to the quartz pull rod and the bottom growth chamber containing the crucible and melt is then welded to the top section.

The high temperature, vacuum tight, rotating seal required for the growth of GaAs is formed by first placing solid B_2O_3 above the narrow quartz neck. The system is then closed and evacuated. After outgassing the B_2O_3 and the system under vacuum at about $300^\circ C$ the B_2O_3 is melted by heating the top furnace to $900^\circ C$. This temperature is maintained until all the moisture in the B_2O_3 is dissipated. The B_2O_3 is then driven between the pull rod and the surrounding small bore tubing by back filling the section above the B_2O_3 with helium or argon gas. The B_2O_3 is then cooled to between $610^\circ C$ and $650^\circ C$. The seal thus formed is



Fig. 2. Photograph of a GaAs crystal grown by the liquid-seal Czochralski technique.

vacuum tight and can be rotated and moved vertically without the loss of vacuum or arsenic vapor from the lower section. Due to the high viscosity of the B_2O_3 at $650^\circ C$, the differential pressure between the helium filled section and the growth chamber is not critical. A helium pressure of one or two atmospheres is used with consistent success.

After the seal is formed, the lower furnace is then heated to above $600^\circ C$ while the induction heater is used to react the gallium and arsenic and to bring the GaAs melt to the growth temperature. The seed is then lowered into contact with the melt and the crystal can be grown. After the crystal is grown, the furnaces are allowed to cool. The differences in thermal expansion of the B_2O_3 and the quartz causes the pull rod and the surrounding quartz tubing to fracture. This necessitates replacement of the quartz pull rod and the surrounding tubing for each crystal grown.

This system has an advantage over the magnetic-type

grower in that it does not use magnets to effect the vertical displacement and rotation of the seed crystal. Since a direct mechanical drive is used, the smoothness of the rotation and pull is limited only by the mechanical system. This grower also has advantages over the liquid encapsulated Czochralski technique in that pre-reacted material is not necessary because gallium and arsenic can be reacted directly in the system. Since the B_2O_3 is not in direct contact with the GaAs melt, there should be less contamination from the B_2O_3 . In addition, the problem of B_2O_3 adhering to the crystal is eliminated. The most attractive feature of this technique is its simplicity. It is economical to construct, easy to load and keep clean.

A somewhat similar technique⁵) has been developed by using the principle of pressure balancing. In this system, the dissociation pressure of the compound is dynamically balanced by a pressure of inert gas. The new liquid-seal technique presented here differs in that it does not attempt to balance the differential pressure. It utilizes the fact that the B_2O_3 is extremely viscous at 650 °C. The liquid B_2O_3 seal remains in position during the entire crystal growth process and prevents the leakage of arsenic from the growth chamber. The complex pressure balancing apparatus is therefore unnecessary for the growth of GaAs. Thus this liquid-seal technique is much simpler than the pressure balancing technique.

Single GaAs crystals have been grown as a matter of routine by using the liquid-seal Czochralski technique. During the course of growing over fifty crystals, there has been no leakage of arsenic through the B_2O_3 seal. Fig. 2 shows one of the GaAs crystals grown by this technique. Typical crystals weigh 50–100 g, and

are 1–2 cm in diameter and 4–10 cm in length. However, the size of the crystals is limited only by the size of the quartz chamber and crucibles used. The system can be easily adapted for the growth of larger crystals. In this work, carbon crucibles 50 mm in diameter and 20 mm high have been used.

With the liquid-seal and direct mechanical drive, there has been no difficulty in necking down the seed to a diameter of 1–2 mm before enlarging the diameter of the crystal. Using this necking down procedure⁶), single crystals of extremely low dislocation have been grown. Most of the crystals have dislocation densities less than 100 pits/cm² and some of them appear to be dislocation free. Some of the undoped crystals have very high resistivity, probably due to contamination from the carbon crucibles used.

The authors wish to express their appreciation to W. R. Wilcox for his interest in this work and many valuable suggestions, and to G. Mueller for his expert technical assistance. This research was supported by the Advanced Research Projects Agency under Grant No. DAHC 15-72-G7.

References

- 1) R. Gremmelmaier, Z. Naturforsch. 11a (1956) 511.
- 2) J. L. Richards, J. Appl. Phys. 34 (1957) 239.
- 3) J. B. Mullin, B. W. Straughan and W. S. Brickell, J. Phys. Chem. Solids 26 (1965) 782.
- 4) M. E. Weiner, D. T. Lassota and B. Schwartz, J. Electrochem. Soc. 118 (1971) 301.
- 5) J. B. Mullin, W. R. Macewan, C. H. Holliday and A. E. V. Webb, J. Crystal Growth 13/14 (1972) 629.
- 6) A. Steinmann and V. Zimmerli, in: *Crystal Growth*, Ed. H. S. Peiser (Pergamon, Oxford, 1967).

R

COMMUNICATION

Particle Chromatography

VINCENT H. S. KUO* and WILLIAM R. WILCOX

CHEMICAL ENGINEERING AND MATERIALS SCIENCE DEPARTMENTS
UNIVERSITY OF SOUTHERN CALIFORNIA
LOS ANGELES, CALIFORNIA 90007

Abstract

Particle mixtures can be separated into bands by slowly increasing the freezing rate during directional solidification. Continuous size classification of spherical particles can similarly be obtained.

We (1, 2) and others (3-9) have shown that a foreign particle is generally rejected during solidification unless the freezing rate exceeds a critical value V_c . Above V_c the particle is trapped and incorporated in the solid. Values for V_c are sensitive to the particle-melt combination. Although one cannot yet predict V_c for a particular pair, it is expected that factors such as relative thermal conductivity, melt viscosity, and surface properties of particle and solid all influence V_c . The critical freezing rate of spherical particles has been found to vary roughly with the reciprocal of particle diameter. The critical rate for rough particles is higher than for spherical particles and is less size dependent.

These previous results suggest that one might use this particle pushing phenomenon to separate particle mixtures by size and type. The idea is to disperse the particles in a relatively pure liquid which does not act as a solvent for the particles, and then directional-freeze the liquid at a

* Present address: Allied Chemical Corporation, Solvay, New York 13209.

steadily increasing rate—programmed solidification. As V_c is exceeded for each type of particle, it will be trapped in a band. Thus the name "particle chromatography." Because of the specificity of V_c , it might also be possible to identify particles by determining V_c in several liquids.

The purpose of the experiments reported here was to test this concept of particle chromatography.

EXPERIMENTAL METHODS

Two experimental techniques were tried—the vertical Bridgman-Stockbarger technique and horizontal zone melting with rotation—as discussed in detail elsewhere (2). Carbon, copper, red ferric oxide, and silver particles were ultrasonically dispersed in molten naphthalene which was then poured into 10.5 mm i.d. Pyrex tubes. Particles were included only in material at the front end of the tube, in tubes intended for zone melting experiments, so that the initial zone contained all particles present. The remainder of the naphthalene contained no particles. All but the smallest particles of each type settled to rest on the interface during the Bridgman experiments. Particles were completely suspended in the rotating zone-melting experiments.

In a preliminary Bridgman experiment with ferric oxide and carbon particles, bubbles formed at the interface and caused irregular trapping of particles, preventing appreciable separation. Bubble formation was prevented in subsequent experiments by sealing the tube containing solidified naphthalene in a vacuum of 0.05 Torr prior to performing the experiments. Although bubbles were not a problem in horizontal zone melting, most of the gas was removed by a preliminary rapid zone pass of the naphthalene which initially contained no particles.

In order to avoid trapping at the wall, it was also found necessary to use a concave interface.

RESULTS

Carbon and copper were quantitatively separated by horizontal zone melting with rotation at 44 rpm, as shown in Fig. 1. The zone travel rate was increased from 25 to 75 mm/hr over 4 hr. Carbon particles began to be trapped at 34 mm/hr. The carbon was all trapped in the center of the ingot over a length of 2 cm. Copper was trapped uniformly across the ingot from 54 to 75 mm/hr.

Carbon and copper were also separated by the vertical Bridgman method, although the trapping order was reversed. By programming the

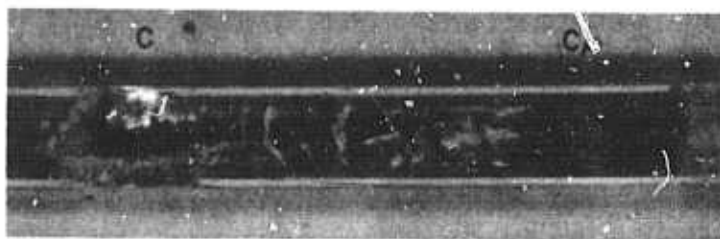


FIG. 1. Carbon and copper particles were separated during programmed solidification of naphthalene in horizontal zone-refining with rotation (HP-16 M).

tube lowering rate from 10 to 40 mm/hr, copper was trapped in the middle of the tube and carbon in the upper portion.

A limited amount of size classification was obtained for silver particles using the Bridgman-Stockbarger method by increasing the freezing rate from 6 to 26 mm/hr. The bottom contained predominantly large particles. The problems probably arose from the irregular shapes of the particles and the polycrystallinity of the solid naphthalene. Spherical particles with a single crystal solid should yield perfect continuous size classification even of submicron particles.

Acknowledgments

This research was supported by Grant No. 4528-AC6 from the Petroleum Research Fund (administered by the American Chemical Society) and by Grant No. DAHCl5-72-G7 from the Advanced Research Projects Agency of the Department of Defense.

REFERENCES

1. V. H. S. Kuo and W. R. Wilcox, *Ind. Eng. Chem., Process Des. Develop.*, in press.
2. V. H. S. Kuo, "Removal and Separation of Particles by Crystallization," Ph.D. Dissertation, University of Southern California, Los Angeles, 1973.
3. C. W. Correns, *Discussions Faraday Soc.*, 5, 267 (1949).
4. A. E. Corte, *J. Geophys. Res.*, 67, 1085 (1962).
5. D. R. Uhlmann, B. Chalmers, and K. A. Jackson, *J. Appl. Phys.*, 35, 2856 (1964).
6. P. Hoekstra and R. D. Miller, *J. Colloid Interface Sci.*, 25, 166 (1967).
7. J. Cisse and G. F. Bolling, *J. Crystal Growth*, 11, 25 (1971).
8. J. Cisse and G. F. Bolling, *Ibid.*, 10, 67 (1971).
9. M. V. Pikunov, *Metalloved. i Obrabotka Tsvetnykh Metal. i Splavov*, Sbornik State, 1957, 35; through *Chem. Abstr.*, 52 16826c (1958).

Received by editor December 12, 1972



A CONVENIENT OPERATIONAL EQUIVALENT TO THE FOWLER PHOTOTHRESHOLD PLOT†

C. R. CROWELL

*Departments of Materials Science and Electrical Engineering, University of
Southern California, Los Angeles, California 90007, U.S.A.*

T. W. KAO

*Department of Electrical Engineering, Loyola University, Los Angeles,
California 90045, U.S.A.*

C. L. ANDERSON* and V. L. RIDEOUT**

*Departments of Materials Science and Electrical Engineering, University of
Southern California, Los Angeles California 90007, U.S.A.*

Received 16 February 1972

A simple universal curve which is operationally equivalent to the Fowler universal photoemission curve is presented which predicts the difference between the true phototreshold and the "apparent" phototreshold, ϕ_a , defined by the intercept of a plot of $R^{\frac{1}{2}}$ versus $h\nu$ on the $h\nu$ axis or

$$q\phi_a \equiv h\nu - 2[d \ln R / d h\nu]^{-1},$$

where R is the photoresponse per absorbed photon of energy $h\nu$. This difference arises because of thermal effects which are customarily ignored when the Fowler theory is applied to metal-semiconductor (Schottky barrier) contacts, and may be significant in many practical situations. The analysis also shows that no information about the true phototreshold is obtained if $h\nu - q\phi_a \approx 2kT$.

Fowler¹⁾ originally derived a universal relationship between the number of electrons, R , emitted from a metal into vacuum per absorbed photon of energy $h\nu$, and $(h\nu - q\phi_b)$, where $q\phi_b$ is the phototreshold energy measured relative to the Fermi energy in the metal. Fowler assumed a parabolic density of states in the metal, an energy-independent matrix element for absorption of a quantum, and a classical probability for electron transmission over the

† This research was supported by the Advanced Research Projects Agency of the Department of Defense under grant No. DAHC 15-71-G-6.

* Howard Hughes Doctoral Fellow, Hughes Research Lab, Malibu, California 90265, U.S.A.

** NASA Trainee; present address: IBM Research Laboratories, Yorktown Heights, New York 10598, U.S.A.

energy barrier. Then

$$R = C \frac{k^2 T^2}{(E_f - kT\mu)^{\frac{1}{2}}} \int_0^{\infty} \ln \{1 + e^{-y+\mu}\} dy, \quad (1)$$

where T is the absolute temperature, k is the Boltzmann's constant, E_f is the Fermi kinetic energy, C is a proportionality constant and

$$\mu \equiv \left(\frac{h\nu - q\phi_b}{kT} \right). \quad (2)$$

Eq. (1) can be expressed in series form: if $\mu \leq 0$

$$R = C \frac{k^2 T^2}{(E_f - kT\mu)^{\frac{1}{2}}} \left[e^{\mu} - \frac{e^{2\mu}}{2^2} + \frac{e^{3\mu}}{3^2} \dots \right], \quad (3)$$

while if $\mu \geq 0$

$$R = C \frac{k^2 T^2}{(E_f - kT\mu)^{\frac{1}{2}}} \left[\frac{\pi^2}{6} + \frac{1}{2}\mu^2 - \left\{ e^{-\mu} - \frac{e^{-2\mu}}{2^2} + \frac{e^{-3\mu}}{3^2} \dots \right\} \right]. \quad (4)$$

Fowler suggested that ϕ_b and C could be determined by a sliding graphical fit of $\ln R$ versus $(h\nu/kT)$ to his universal curve. A more convenient though in principle less accurate approach is in effect a zero temperature approximation. This approximation had been in earlier use and has been used recently to determine Schottky barrier energies^{2,3}. In this approach the intercept $q\phi_b$ of a plot of $R^{\frac{1}{2}}$ versus $h\nu$ on the $h\nu$ axis is assumed to yield the true barrier energy. In many cases, however, it is not possible to measure R over a large enough range of frequency that a linear $R^{\frac{1}{2}}$ versus $h\nu$ relationship is observed. In addition, it is frequently tempting to fit the data to a pseudo-straight line of best fit and to ignore the systematic deviations from linearity.

The following procedure combines the accuracy of a graphical fit to Fowler's universal curve with the convenience of an $R^{\frac{1}{2}}$ plot. First use the slope of an $R^{\frac{1}{2}}$ versus $h\nu$ plot at a convenient datum point to find the intercept on the $h\nu$ axis, $q\phi_b$, made by a tangent to the $R^{\frac{1}{2}}$ plot (cf. fig. 1). The intercept defines a first approximation to the threshold energy. For the tangent

$$dR^{\frac{1}{2}}/d h\nu = R^{\frac{1}{2}}/(h\nu - q\phi_b). \quad (5)$$

In terms of Fowler's universal curve, however, R is a unique function of $(h\nu - q\phi_b)/kT$ (if we ignore the term in E_f , a procedure which is usually

justifiable). Thus implicit in eq. (5) is a relationship between ϕ_b and ϕ_a , i.e.

$$\frac{\ln(1 - e^\mu)}{\int_0^\infty \ln(1 + e^{-y+\mu}) dy} = \frac{2}{\mu_a}, \quad (6)$$

where

$$\mu_a \equiv (h\nu - q\phi_a)/kT. \quad (7)$$

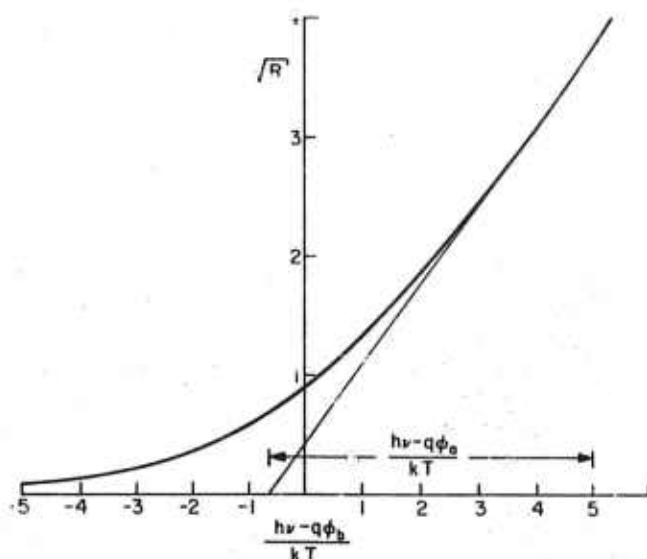


Fig. 1. Photoresponse per absorbed photon (arbitrary units) versus $(h\nu - q\phi_b)/kT$. A sample construction to determine $q\phi_a$ is also shown.

Thus $q(\phi_b - \phi_a)/kT$ is a universal function of $(h\nu - q\phi_a)/kT$. This relationship is plotted in fig. 2. Note that from eq. (6), for $\mu \ll 0$, μ_a has an asymptotic value of 2. Thus the extreme tail of any photoresponse curve contains no information about the photothreshold; in general one should experience considerable difficulty in obtaining an accurate barrier height measurement if $\mu_a < 3$. For $\mu_a \geq 3$, however, the correction can frequently be of use.

Eq. (5) can also be rearranged to yield

$$\phi_a = \frac{h\nu}{q} - \frac{2}{q} [d \ln R / d h\nu]^{-1}, \quad (8)$$

i.e. $(h\nu - q\phi_a)$ can also be defined in terms of the slope of a semilog plot of R versus $h\nu$. Fig. 2 thus allows an objective correction to the first approxi-

mation in photothreshold measurements, even if the photoresponse is plotted as $\ln R$ versus $h\nu$. In many cases, the barrier energy is sufficiently close to the semiconductor band gap that photoresponse data within 0.1 eV of the photothreshold must be used to measure Schottky barrier energies. Then the room temperature correction to $q\phi_a$ is in excess of kT . The correction

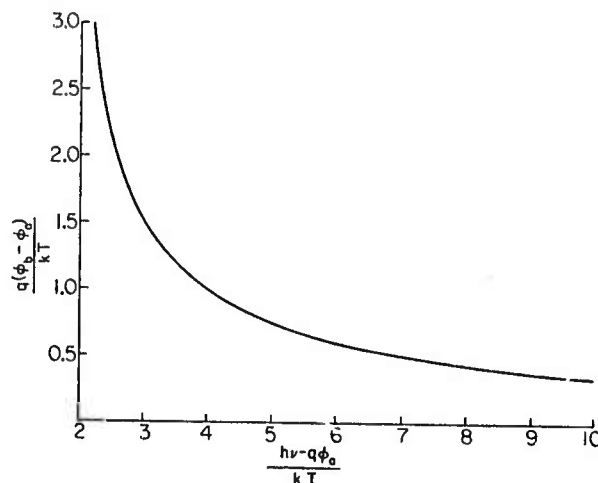


Fig. 2. Universal curve for correction to first approximation to barrier height versus $(h\nu - q\phi_a)$ all in units of kT .

remains comparable to kT over a large range of $(h\nu - q\phi_a)$. Schottky barrier models and preparation techniques are now sufficiently well refined that discrepancies of the order of 0.02 eV in barrier height measured by different techniques (e.g. capacitance-voltage and current-voltage measurements) should be given consideration. Thus the above correction may be significant in many cases. At temperatures well below 300°K this correction should become negligible, but an appreciable correction due to tunneling may be needed⁴⁾.

References

- 1) R. H. Fowler, Phys. Rev. **38** (1931) 45.
- 2) C. R. Crowell, W. G. Spitzer, L. E. Howarth and E. E. LaBate, Phys. Rev. **127** (1962) 2006.
- 3) S. M. Sze, C. R. Crowell and D. Kahng, J. Appl. Phys. **35** (1964) 2534.
- 4) C. L. Anderson, T. W. Kao and C. R. Crowell, to be published.